Dynamics of dust and gas in Star Formation: Dust Evolution, Disk Formation, and Jet Launching

Yisheng Tu (涂以晟)
NanChang, JiangXi, China (中国，江西，南昌)

B.S. Physics & Astronomy; Mathematics, University of Rochester, 2020

A Dissertation Presented to the
Graduate Faculty of the
University of Virginia
in Candidacy for the Degree of
Doctor of Philosophy

Department of Astronomy

University of Virginia
June 2025

Committee Members:
Zhi-Yun Li
Zhaohuan Zhu
Phil Arras
Shane Davis
Kent Yagi

© Copyright by

Yisheng Tu (涂以晟)

All rights reserved

August 8th, 2025

Abstract

Star and planet formation is a hierarchical, multi-stage process governed by complex dynamics. The earliest phase, spanning from the collapse of a molecular cloud core to the emergence of a protostar and protostellar disk, establishes the initial conditions for the subsequent evolution of the star-disk system and eventual planet formation. However, the detailed evolution of this early stage and the interactions among key ingredients—such as gas, dust, and magnetic fields—remain poorly understood. Observational challenges arise due to the small size of the protostar, obscuration by the surrounding envelope, and the rapid timescales of early evolution. As a result, numerical simulations are essential for uncovering the fundamental physical processes shaping this stage. This thesis provides theoretical and numerical insights into the early stages of star formation from three distinct projects, each focusing on a key aspect of the problem.

The first project investigates dust dynamics and grain growth. Observations suggest that grain growth begins early in the star formation process, yet the underlying mechanisms driving this growth remain unclear. Using numerical models that incorporate gas dynamics, grain dynamics, and grain growth, we demonstrate that grain growth is slow in laminar protostellar disks, indicating the need for additional mechanisms to accelerate the process. Furthermore, we derive a simple analytic estimate for the grain growth timescale, providing a useful framework for interpreting obser-

vational constraints.

The second project examines the collapse of a dense molecular cloud core leading to the formation of stars and disks. Using non-ideal magnetohydrodynamic (MHD) models, we show that the evolution of the protostellar envelope is governed by the formation of "gravo-magneto-sheetlets"—thin, dense structures that arise from the interplay between turbulence, gravity, and magnetic fields. These sheetlets play a crucial role in delivering mass, angular momentum, and magnetic flux to the forming protostar and protostellar disk, with the efficiency of this process regulated by non-ideal MHD effects, which redistribute magnetic flux relative to the gas. If a molecular cloud core possesses sufficient mass, initial angular momentum, and strong non-ideal MHD effects, it can undergo "fragmentation", forming multiple stars. After the first protostar emerges, a "Dense Rotation-Dominated (DROD) structure" develops between the gravo-magneto-sheetlets and the newly formed star. The dynamics within this DROD can give rise to companion stars, provided that the structure is sufficiently demagnetized. This "DROD-fragmentation mechanism" offers a novel pathway for the formation of close, 100-au scale multiple systems with misaligned protostellar disks, providing new insights into the origins of compact stellar multiples.

The third project of this thesis explores the launching mechanisms of jets and outflows from Young Stellar Objects (YSOs). Using a combination of 2D axisymmetric and 3D global non-ideal MHD models, we demonstrate that a circumstellar disk alone—if threaded by a vertical open magnetic field—can launch both a jet and a disk wind driven primarily by toroidal magnetic pressure. While this mechanism shares some similarities with the traditional magneto-centrifugal and magnetic-tower models in terms of outflow properties, it operates through a distinct process that questions some observational interpretations. Additionally, disk-driven outflows tend to develop asymmetries between the two hemispheres due to asymmetry in magnetic

field geometry and configuration. In contrast, simulations that include the stellar magnetosphere reveal that magnetosphere-disk interactions generate more powerful and highly collimated bipolar jets. The jet is launched through a "load–fire–reload" cycle, in which differential rotation between the star and disk winds up toroidal magnetic fields ("load"), the resulting pressure gradient accelerates gas vertically into a jet ("fire"), and magnetic reconnection resets the field configuration ("reload"). In this case, the field geometry naturally favors the formation of bipolar outflows by channeling rotational energy from both the star and disk into the polar region.

Acknowledgements

Completing this thesis has been a journey shaped by the guidance, encouragement, and unwavering support of many remarkable individuals. While these pages bear my name, they are the product of countless contributions—both intellectual and personal—from those who have inspired, challenged, and stood by me along the way. It is with deepest gratitude that I acknowledge the people who made this work possible.

First and foremost, I would like to express my deepest gratitude to my family – my parents, in particular – for their unwavering support throughout my academic journey. None of this would have been possible without you. From laying the foundation of my education to enabling my research pursuits, your emotional and practical encouragement has been indispensable. Your selflessness, including supporting my decision not to return home for the past six years, has allowed me to fully dedicate myself to this endeavor.

I am profoundly grateful to my advisor, Prof. Zhi-Yun Li, for his exceptional guidance and inspiring physical intuition—evidenced, for instance, by his remarkable ability to immediately deduce the value of Equation 2.37 at first glance. Our discussions have been nothing short of enlightening. I deeply appreciate your support in pursuing my research interests while steering me away from potential dead ends (a few times). My sincere thanks also go to my second advisor, Prof. Zhaohuan Zhu, whose parting insight sparked an entirely new direction of research. Your ideas have

always been inspiring throughout our collaboration.

Additionally, I owe immense gratitude to my undergraduate mentors – Prof. Adam Frank, Prof. Eric Blackman, Dr. Luke Chamandy, Dr. Tanaji Sen, and Dr. Jean-Francois Ostiguy – for introducing me to the world of research and nurturing my early academic development. I am especially thankful for the opportunity to engage with complex numerical simulations in high-energy astrophysics and the engineering-driven theories in accelerator science.

To Youfang—my greatest fortune. Together, we have marveled at meteor showers, total solar eclipses, and auroras, sharing moments of cosmic wonder. Thank you for your endless support, understanding, and companionship over the years, and for the adventures yet to come.

To my senior groupmate – Ka Ho Lam, thank you for teaching me high-performance programming and how to utilize the full potential of a computer. I learned a lot from you and my Ph.D. would be much harder without your help. To my other groupmates – Daniel, Korash, Renato, and especially, Chun-Yen. Our discussions were always insightful, and I look forward to discussions and collaborations in the future.

To my fellow graduate students at UVA–Alejandro, Andres, Jordan, Erica, Mengyao, Xiaoshan, Xinlun, Deven, Chase, Aayush, Minli, Lianis, Simran, Connor, and Noshin –I deeply value our formal and informal discussions, whether in meetings, hallway chats, or over drinks; on topics about astronomy or more earthly; in the department, in Richmond, on I-64, VA-29, above Charlottesville, or anywhere else. I cherish our conversation and collaborations and look forward to many more.

To my badminton friends at the UVA Badminton Club, especially Alexa, Gosia, Rong, and Boyuan—you have brought joy and vibrancy to my life, both on and off the court. Playing alongside you in tournaments and casual matches has been a highlight of my time here. I hope our paths cross again for more thrilling games in the future.

Finally, to you, the reader, thank you for your time and attention in engaging with this work. To those who navigated language barriers or used translators to read these pages, your dedication moves me deeply. May this thesis inspire dialogue, curiosity, or even friendly debate—because science grows when ideas cross languages and cultures. Thank you for being part of this journey.

To my ~~girlfriend~~ fiancée, for helping me shape my life goals and in planning and carrying out the decisions that have defined ~~my~~ our path

Table of Contents

Abstract **iii**

Acknowledgements **vii**

List of Figures **xli**

List of Tables **xliii**

1 Introduction **1**
1.1 Overview of Star and Planet Formation . . . 3
1.2 Proto-Stars and Disk Formation . . . 10
1.3 Dust Dynamics and grain growth . . . 14
1.4 Outflow Dynamics . . . 18
1.5 Numerical methods . . . 23
1.6 Thesis Outline . . . 25

2 Grain Growth During Protostellar Disk Formation **27**
2.1 Introduction . . . 28
2.2 Problem Setup . . . 32
2.2.1 Governing Equations for Gas Dynamics . . . 32
2.2.2 Hydrodynamic Numerical Method . . . 33
2.2.3 Modeling Grain Dynamics and Growth . . . 35
2.2.4 Lagrangian Treatment of Dust Particles . . . 42
2.3 Hydro results . . . 43
2.4 Dust Results . . . 48
2.4.1 The Baseline Model . . . 48
2.4.2 Model with Enhanced Grain-Grain Collision Speed . . . 50
2.5 Grain Growth Timescale . . . 60
2.5.1 One-Zone Model . . . 63
2.5.2 Semi-analytic Estimate of Grain Growth time . . . 67
2.5.3 Physical Interpretation of η . . . 72
2.6 Discussion . . . 73

2.6.1 Validity of the terminal velocity approximation 73
2.6.2 Slow Grain Growth in a Laminar Protostellar Disk 74
2.6.3 Enhanced Growth Through Higher Grain-Grain Collision Speeds 76
2.7 Conclusion 79
2.8 Acknowledgements 80

3 Protostellar Disks Fed By Dense Collapsing Gravo-Magneto-Sheetlets 81
3.1 Introduction 82
3.2 Problem Setup 85
3.3 Overview of Simulation Results 89
3.4 Magnetically Structured Protostellar Envelopes 94
3.4.1 Dense Collapsing Gravo-Magneto-Sheetlets 95
3.4.2 Role of Sheetlets in Envelope Structure and Dynamics 100
3.5 The Envelope-Disk Connection 104
3.5.1 Level of Envelope and Disk Magnetization 105
3.5.2 Magnetic Collapse-Retarding Force and Rotating-Braking Torque 111
3.5.3 Sheetlet-Fed Envelope Accretion onto Disk 113
3.6 Protostellar Disk Structure and Evolution 116
3.6.1 Are Early Disks Gravitational Stable? 116
3.6.2 Magnetically or Gravitational Driven Angular Momentum Evolution? 119
3.6.3 Kinematically Perturbed Early Disks 122
3.7 Discussion 125
3.7.1 Towards a Picture of Protostellar Envelope Dominated by Gravo-Magneto-Sheetlets 125
3.7.2 Magnetically Driven Evolution of Heterogeneous Protostellar Disks 127
3.8 Conclusion 131
3.9 Acknowledgements 133

4 Fragmentation of Dense Rotation-Dominated Structures Fed by Collapsing Gravo-magneto-Sheetlets and Origin of Misaligned 100 au-Scale Binaries and Multiple Systems 135
4.1 Introduction 136
4.2 Problem Setup 139
4.2.1 Post-process Lagrangian tracer particles 143
4.3 Overview of Results 144
4.4 Origins of Dense Binary/Multiple-Forming Gas Structures 148
4.4.1 Large-Scale Collapsing Gravo-magneto-Sheetlets 148
4.4.2 Dense Rotation-Dominated Structures 153
4.5 Conditions for DROD Fragmentation 157
4.5.1 Toomre-Q unstable structures 157

4.5.2 Collision-Induced Fragmentation . . . 160
4.5.3 The Role of Demagnetization in Fragmentation . . . 163
4.6 Discussion . . . 165
4.6.1 Close Misaligned Companion Formation Through DROD Fragmentation . . . 165
4.6.2 Connection to Observations . . . 173
4.7 Conclusions . . . 176
4.8 Acknowledgements . . . 177

5 YSO Jets Magnetocentrifugally Driven by Reconnecting Atmospheric Avalanche Accretion Streams Above Inner Circumstellar Disks 179
5.1 Introduction . . . 180
5.2 Simulation Setup . . . 183
5.2.1 Magnetic diffusivity . . . 187
5.3 Simulation Results . . . 189
5.3.1 Overview . . . 189
5.3.2 Raised Disk Atmosphere . . . 195
5.3.3 Avalanche Accretion Streams . . . 196
5.3.4 Magnetocentrifugal Jet Driven by Avalanche Accretion Streams 198
5.4 Discussion . . . 203
5.4.1 Towards a new picture of protostellar jet formation . . . 203
5.4.2 Implications and limitations . . . 208
5.5 Conclusion . . . 210
5.6 acknowledgments . . . 211

6 Highly Variable Magnetic Pressure-Driven YSO Jets in the Polar Cavity from Toroidal Fields Generated by Inner Disk Accretion 213
6.1 Introduction . . . 214
6.2 Methods . . . 218
6.2.1 Sink Treatment . . . 221
6.2.2 Magnetic diffusivity . . . 222
6.3 Result overview . . . 224
6.3.1 The polar jet . . . 227
6.3.2 The disk wind . . . 232
6.3.3 The MRI-active turbulent inner disk wind . . . 233
6.4 A lightly-loaded toroidal magnetic field pressure-driven jet . . . 240
6.4.1 A geometric argument for magnetic field structure above and below the disk . . . 240
6.4.2 B_ϕ in the disk . . . 242
6.4.3 Avalanche accretion streams . . . 243
6.4.4 Jet from magnetic energy release in the polar cavity . . . 245
6.5 Comparison to axisymmetric steady-state outflows . . . 251

6.5.1 Connection to the axisymmetric steady-state outflow 251
6.5.2 Differences from the magneto-centrifugal model 254
6.5.3 Differences from axisymmetric steady-state jets 255
6.6 Discussion 262
6.6.1 Mass and angular momentum fluxes carried by the jet and disk wind 262
6.6.2 In-situ toroidal field generation 265
6.7 Conclusions 267
6.8 acknowledgments 271

7 YSO Jets Driven by Magnetic Pressure Generated through Stellar Magnetosphere–Disk Interaction 273
7.1 Introduction 274
7.2 Method 278
7.3 Result 282
7.3.1 Magnetic flux evolution 285
7.3.2 Disk Wind from Opened Magnetospheric Field 286
7.3.3 Opened Stellar Field 289
7.3.4 Magnetospheric jet 291
7.4 Jet launching mechanism: "Load-fire-reload" 293
7.4.1 Load: charging B_ϕ by star-disk differential rotation 293
7.4.2 Fire: releasing magnetic energy by global field geometry . . . 301
7.4.3 Reload: replenishing jet gas by magnetic reconnection 305
7.5 Discussion 307
7.5.1 Magnetospheric accretion and outflow 307
7.5.2 Comparing to the disk-field-only jet model 310
7.5.3 Comparison with previous 2D models 315
7.5.4 Connection to the axisymmetric steady-state outflow 316
7.6 Conclusions 319
7.7 acknowledgments 322

8 Arcturus: A post-process tracer and dust particle simulation framework 323
8.1 Introduction 324
8.2 Numerical method 325
8.3 Benchmark test 328
8.3.1 Triangular Shaped Cloud 328
8.3.2 Tracer 329
8.3.3 Dust particle 331
8.3.4 Dust particle and gravity 334
8.4 summary 336

9 Summary **337**

Appendix A 介绍 **343**
A.1 恒星与行星形成概述 344
A.2 原恒星与盘的形成 347
A.3 尘埃动力学与颗粒生长 349
A.4 外流动力学 351
A.5 数值方法 354
A.6 论文结构 356

Appendix B Additional Information for Chapter 2 **358**
B.1 Brownian motion 358

Appendix C Additional Information for Chapter 4 **361**
C.1 3D Visualization with Unity 361

Appendix D Additional Information for Chapter 5 **363**
D.1 Limits on the toroidal magnetic field strength in the active disk zone 363

Appendix E Additional Information for Chapter 6 **365**
E.1 Insensitivity to the inner boundary condition 365

References **369**

List of Figures

1.1 Figure illustrating the evolutionary sequence from a pre-stellar core through Class 0–III phases, ultimately leading to a planetary system. Adapted from Persson (2014). 5

1.2 ALMA image of representative Class I-II object: HL Tau. Multiple rings and gaps are seen in the protoplanetary disk. The image is adapted from (ALMA Partnership et al., 2015) 7

1.3 Representative Class 0 and Class I protostellar objects. **Left panel:** Image of VLA 1623, adapted from (Sadavoy et al., 2024); **Right panel:** Image of IRS 04302+2247, adapted from (Lin et al., 2023). 9

1.4 Image of magnetic field vectors inferred from dust polarization observation of B335 Class 0 protostellar core. Figure adapted from Le Gouellec et al. (2023) 13

1.5 A sketch of the planet-formation process and rough size scales of the largest bodies. Image adapted from Meech & Raymond (2020) 15

1.6 Jame Web Space Telescope (JWST) image of jet from YSO HH211, showing an extended and colluminated jet. Image adapted from (NASA, 2023) 20

2.1 Stellar properties and disk mass during the gas simulation. The solid and dash-dotted lines are the star mass and disk mass respectively; dotted line and dashed line are the star luminosity (L_*) and total luminosity (L in equation 2.8) respectively. The vertical line at $t = 40,000$ years shows the starting time of the dust simulations. 44

2.2 Hydrodynamical disk densities. Four panels are the disk density when the disk is approximately 100, 150, 200 and 250 au. Corresponding times of the frames are shown in each panel. The black dashed line is the location where gas density is 4×10^{-16}g cm^{-3}, where our definition of the boundary of the disk is located. The solid black line is the boundary in which dust coagulation is calculated, where gas density is $> 4 \times 10^{-17}$g cm^{-3}. 46

2.3 The speeds in $\hat{r}$ direction and $\hat{\theta}$ direction are shown in the upper and lower panels respectively. The figure is taken when the disk radius is about 200 au. At other times in the simulation when there is a disk, the velocity field is similar to the ones showing here. 47

2.4 Sub-Keplerian rotation. Plotted are the rotation speed near the disk midplane, the local Keplerian speed (including the contribution from the self-gravity), and the fractional deviation of the azimuthal speed from the local Keplerian speed when the disk radius is about 200 au (solid line). The fractional deviation is close to the analytic estimate from Nakagawa et al. (1986, labeled "NSH1986"). 49

2.5 Cumulative grain mass as a function of the grain size. The mass includes both the grains in the active computational domain and those already advected through the inner boundary at $r = 10$ au. The total grain mass is conserved throughout the simulation, with a value of 4520 $M_\oplus$ determined at the beginning of the dust model (40,000 years). At later times, the total mass of the grains is calculated by summing all mass that has gone through the central boundary over time and adding all mass in the active computation domain (10 to 10,000 au). The value at each grain size is the mass fraction of the grains at or larger than that size. The black lines shows the cumulative grain mass at four different disk sizes and times in the baseline model ($\chi = 1$ in equation 2.22). The red lines are the cumulative values at the same times as the black lines with the same line style, but for the $\chi = 4$ model. 51

2.6 Spatial distributions of dust mass densities per logarithmic size decade of 6 size bins when the disk is at 250 au in the model with increased grain-grain collision speeds ($\chi = 4$ in equation 2.22). Each panel is the density of one size bin as noted in the upper left corner of each panel. Note the scale is different between the left four panels and the right two panels. We only show the inner disk regions in the two right panels since these are where the mm/cm-sized grains are concentrated. The black dashed contour is the boundary of the hydro disk, where the gas density is 4×10^{-16}g/cc. The dotted contour is at gas density of 4×10^{-14}g/cc to emphasize to scale difference between the left and right panels. Because we only simulated the upper hemisphere, the lower hemisphere is a reflection of the upper hemisphere about the midplane. 52

2.7 The distributions of the dust mass density per size decade in each logarithmic size bin as a function of the grain size at different heights from the midplane (one curve for each height, with the height specified by the colorbar) at a representative cylindrical radius of 50 au. This example frame is taken at 86250 years, when the disk is at 250 au in radius. The highest red line, peaking around 0.5 mm, shows that the largest grains are concentrated near the midplane. 53

2.8 Grain advection and formation time scale for grains in six representative size bins when the disk reaches 250au. The upper six panels are advection time scale and the lower six panels are formation (growth) time scale. The defintion of the time scales is in section § 2.4.2, equation 2.28 and 2.29. Small grains are being advected into the disk constantly, supplying the growth to larger grains in the protostellar disk. The gain due to formation time scale is shorter than the loss due to advection time scale for large grains in general. 55

2.9 Comparison of in-situ formation rate and advection rate. The three black lines are for > 1 mm-sized grains, showing that the in-situ formation rate in the midplane region (solid black line) is much larger than the rate with which such grains are advected into the midplane region (dashed black line) and the formation rate outside the midplane region (dotted black line; not visible due to overlap with the dashed line). Also plotted are the in-situ formation rate for > 1 μm-sized grains in the midplane region (red solid line) and the advection rate of < 1 μm grains into the midplane region (blue solid line), showing that more than half of the small (< 1 μm) grains from the initial MRN distribution advected into the midplane region are turned into larger (> 1 μm) grains. 58

2.10 Dust-to-gas ratio on the disk midplane including grains with different sizes. The solid line is the dust-to-gas ratio including all dust grains. At around ~ 50 au the dust-to-gas ratio reaches 0.03, three times the initial ISM value of 0.01 (dashed horizontal line). The colored lines are the dust-to-gas ratios on the midplane including only grains within a certain size decade. These colored lines show the contribution of dust in each size decade to the local dust-to-gas ratio. For example, $0.1 \sim 1$mm-sized grains contribute most to the dust mass around 45 au. 59

2.11 The distribution of grain mass density $\rho_{\rm d}$ per log size decade as a function of grain size at two times distinguished by line style: the solid line is taken at 25,000 years and the dashed line at 64,000 years. Each color denotes a different initial grain size power-law index q. The similarity of the curves at different times and for different initial size distributions indicates that the grain evolution is nearly self-similar in time and insensitive to the initial size distribution. The time for the grains to grow by one order in this example is about 19500 years (with $\chi = 4$). 65

2.12 **Left panel:** the distribution of the characteristic timescale η in units of 10^4 years assuming a dust-to-gas ratio of 0.01 everywhere and $\chi = 4$ and using the gas density ρ_g, thermal speed $v_{\rm th}$, and the acceleration from aerodynamic drag ζ at a representative time $t = 85000$ years. **Right panel:** Fitting of the peak grain size $s_{\rm peak}$ as a function of time using equation 2.39. Each line corresponds to one location labeled in the left panel. The fitting agrees well the results of the one-zone simulations, proving the validity of equation 2.39. 67

2.13 Schematic of the self-similar evolution of the grain mass density distribution as a function of size, showing the relation between the depletion of small grains (on a time scale $t_{\rm depl}$) due to growth to larger grains and the increase of grain size (on a timescale $t_{\rm size}$) also due to growth. 69

2.14 Values of $-f(s_k; s_s, s_l, q_s)$ (equation 2.37). Each line is a different choice of parameters s_s, s_l or q_s. Each linestyle represents a different q_s, with the dashed, solid and dotted lines have $q_s = 1.5, 2.1$ and 2.7 respectively. Note that the solid lines with $q_s = 2.1$ fits the left half of self-similar and attractive solution in Fig. 2.11 well. Each color denotes a different set of choice of s_s and s_l, with values noted in the legend. The evalution of $f(s_k; s_s, s_l, q_s)$ is only done between s_s and s_l. In all cases, if $s_k \ll s_l$, then $-f(s_k; s_s, s_l, q_s) \approx 1$ (the horizontal dashed gray line). 71

2.15 **Left three panels**: Percentage difference between the terminal velocities used in the Eulerian simulation and those calculated in the Lagrangian simulation for mm-sized grains. The black lines are isodensity contours that are the same in each plot. **Right**: the spatial distribution of the mm-sized grains in the Eulerian simulation with $\chi = 4$, showing that such large grains are concentrated in the high density regions where the terminal velocity approximation is good to the percent-level. 74

3.1 Time evolution of the stellar mass M_* (panel a; dashed lines) and disk mass M_d (panel b) as a function of time for all six models listed in Table 3.1. Also plotted in panel (a) is the combined star and disk mass M_{d*} (solid lines). 89

3.2 Face-on (first and third row) and edge-on (second and fourth row) views of the column density distributions of all six models listed in Table 3.1, showing the formation of a dense disk surrounded by a filamentary inner envelope at a representative time when the combined mass of the star and disk $M_{d*} = 0.2$ $M_\odot$. The model name is shown in each panel. The animated version is available in the online supplementary material. 90

3.3 3D visualization of the reference model (M1.0AD1.0) showing that most of the inner envelope mass is concentrated into warped but coherent sheet-like structures (termed "gravo-magneto-sheetlets" or simply "sheetlets" in the text). The animated version is available in the online supplementary material. 93

3.4 Illustration of a highly inhomogeneous magnetically-structured protostellar envelope. Panel (a) plots the mass density ρ on an x-z plane, showing thin dense filaments (sheetlets in 3D) embedded in a low-density background. The field lines (white) demonstrate that the dense structures are associated with strong field pinching, as in the case of an unperturbed pseudo-disk. Panel (b) shows that the density increase in the dense structures does not have a corresponding increase in the total field strength. Panel (c) displays the plasma-β, showing the dense structures are much less magnetized relative to their masses than the background. Panel (d) shows that the envelope tends to collapse radially at a sub-free-fall speed (with flow streamlines superposed to illustrate the velocity field). Panel (e) displays the cosine of the angle between the velocity and magnetic field vectors, showing the magnetically guided flows in the low-density background and the gravity-driven collapse in the cross-field direction in the dense structures. Panel (f) displays the distribution of the current density $|\mathbf{J}|$, showing that the current (and thus the magnetic force) is concentrated in the dense structures. The animated version is available in the online supplementary material. 97

3.5 Spherically average properties of dense sheetlets and their contributions to the structure and dynamics of the inner protostellar envelope for models with different ambipolar diffusivities. Panel (a) displays the characteristic density ρ_c that separates the dense sheetlets from the diffuse background. Panel (b) shows that the dense sheetlets occupy an increasingly small fraction of the volume towards the center, reaching values as low as $\sim 10\%$. Panel (c) displays the plasma-β for the sheetlets (solid lines) and background (dashed), showing an order-of-magnitude difference between the two. Panel (d) plots the radial infall speed normalized by the local free-fall speed, showing that both the sheetlets and background collapse radially at substantially sub-free-fall speeds. Panel (e) shows the fraction of the radial mass flux carried by the dense sheetlets. Panel (f) displays the fraction of the $z-$component of the angular momentum carried by the dense sheetlets. The solid dot on each line approximately marks the transition radius between the disk and envelope on the disk midplane. 101

3.6 Comparison of the total flow speed v with the local free-fall speed $v_{\rm ff}$. Panel (a) plots the ratio $v/v_{\rm ff}$ on an x-z plane for the reference model M1.0AD1.0 at the same representative time as in Fig. 3.4, showing dense sheetlets tend to move more slowly than the background medium. Panel (b) plots the spherically averaged total speed normalized by the local free-fall speed as a function of radius for models with different diffusivities. The blue lines are for model M1.0AD0.1, green for M1.0AD1.0, cyan for M1.0AD2.0, and red for M1.0AD10. The solid curves are for the dense sheetlets and dashed for the background. The solid dot on each line approximately marks the transition radius between the disk and envelope on the disk midplane. 103

3.7 Magnetization of the inner envelope and disk at a representative time when $M_{d*} = 0.25$ M$_\odot$ for the reference model M1.0AD1.0 (top panels) and for models with different magnetic diffusivities (bottom panels). Panel (a) displays the vertical component of the magnetic field on the midplane $B_{z,mid}$ for the reference model, showing the lack of a large jump in the disk-envelope transition region. Panel (b) is a density map on the same plane (with flow streamlines superposed), showing a dense disk surrounded by a much lower-density envelope. Panel (c) plots the plasma-β_z corresponding to $B_{z,mid}$. Panels (d)-(f) plot, respectively, the azimuthally averaged $B_{z,mid}$, ρ_{mid}, and $\beta_{z,mid}$ for models of different magnetic diffusivities. The solid dot on each line approximately marks the transition radius between the disk and envelope. The animated version is available in the online supplementary material. 106

3.8 Evolution of the disk magnetic field as a function of the combined star and disk mass M_{d*}. Plotted are (a) the vertical magnetic flux threading the disk midplane vertically $\Psi_{z,mid}$; (b) the disk magnetic flux fraction f_Ψ defined in equation (3.8) of the text; (c) the vertical field strength averaged over the disk midplane, and (d) two versions of plasma-β, β_z (solid lines) and β (dashed), averaged over the disk midplane. 108

3.9 Plotted as a function of radius are (a) the ratio of the spherically averaged radial components of the magnetic and gravitational forces and (b) the $z-$component of the magnetic torque per unit radius for the four turbulent models with different magnetic diffusivities at the representative time. 111

3.10 Highly anisotropic envelope mass accretion onto the disk. Plotted are the mass accretion rate per unit area through the six surfaces of a rectangular box enclosing the disk for the reference model at the representative time. Accretion into the box/disk is colored blue and out of the box/disk brown. 114

3.11 Gravitational stability of disks in formation. Plotted are the column density maps (top row) and the distributions of the Toomre Q parameter for disk gravitational stability (bottom row) for models M1.0AD1.0, M1.0AD2.0, and M1.0AD10 at the representative time. 117

3.12 Cumulative magnetic (solid lines) and gravitational (dashed) torques inside the disk up to a given cylindrical radius R at the representative time. 119

3.13 The ratio between the specific angular momentum carried by the infalling envelope material above (panel a) and below (panel b) the disk and that required for staying in a Keplerian orbit at the projected cylindrical radii on the disk midplane. The black contours in both panels are the projected disk midplane outline. The green curves are contours of mass feeding rate per unit area, highlighting where most envelope material lands on the disk surfaces. 122

3.14 Perturbed disk kinematics for models M1.0AD1.0 (upper panels) and M1.0AD10 (lower) at a relatively early time when $M_{d*} = 0.2\ M_\odot$. **Panels (a) and (c)**: gas radial velocity on the disk midplane. The black line in each panel is a representative flow streamline. **Panels (b) and (d)**: Statistics of the gas radial velocity in the disk. A black dot represents each cell in the disk. The red lines are the averaged gas radial velocity at each radius. 123

4.1 **Left Panel (a):** The time evolution of the total mass of all stars formed in each of the first four models listed in Table 4.1, starting from the time of the primary formation. The "star" on each curve marks the formation of the secondary, if any. **Right Panels (b)-(e):** The time evolution of the masses of individual stars for the four models. The quantity M_0 above the panels refers to the mass of the primary, M_1 that of the first stellar companion (or the secondary), and M_2 that of the second stellar companion, etc. 145

4.2 Column density distributions within a 800 au^3 central region along the $\hat{z}-$ (left column), $\hat{y}-$ (middle column), and $\hat{x}-$direction (right column), respectively at a representative time, with the model name shown in each panel. The "stars" in each panel mark the projected locations of the sink particles. An animation of this figure can be found at `https://virginia.box.com/s/nju7yjqycbecpfbgsoem7x7yj7ygp3ip` 147

4.3 Dense demagnetized sheetlets embedded in a strongly magnetized diffuse background. Plotted are the distributions of the mass density (panel [a], with field lines superposed), the quantity $\cos(\theta_{\rm ali})$ (panel [b], where $\theta_{\rm ali}$ is the angle between the magnetic and velocity field), and the plasma-β (panel [c]) on an xz-slice through the reference model at a representative time on a relatively large ($\sim$1000 au) scale. The thin, wiggly, bluish filaments in the middle panel (where dense demagnetized gas collapses across field lines) mark the 2D (xz-)cross-section of the 3D gravo-magneto-sheetlets. The low-density, strongly magnetically dominated cavities above and below the sheetlets are magnetically driven outflow lobes. 149

4.4 Sheetlets in 3D. Plotted are the 3D structures of the gravo-magneto-sheetlets at the representative time for the reference model shown in Fig. 4.3. The color in panel (a) shows the local density. It shows the rotation speed around the center of the mass normalized by the local Keplerian speed in panel (b). Note the large-scale, relatively open spirals in the flattened sheetlets, which turn into more tightly wound spirals on the smaller scale. An animation of the figure at different times can be found at `https://virginia.box.com/s/l8zm7qg1h17h47b0aze7gy3xy6b7s199` (for the left panel) and `https://virginia.box.com/s/m5g0tr2ydxkyw8nttfsezicu7y69g6ba` (for the right panel). An animation of the left panel viewed from different angles can be found at `https://virginia.box.com/s/3wh123bq9jaj84j6hm80osx0smw86ugh` 150

4.5 A 3D view of the dense rotation-dominated DROD structure (DROD for short) that is fed by the larger-scale sheetlets; it is the formation site for (often misaligned) stellar companions (see Figs. 4.12 and § 4.6.1 below). An animated version of this figure viewed from different angles can be found at `https://virginia.box.com/s/wkasilbfccszie1pz2o6udqwifplf12a` 154

4.6 Total mass of the stars and their disks (defined in sec. 4.4.2, red solid line) and total mass of the DROD (green dashed line). The stars on both curves mark the formation time of each star. 155

4.7 Potential for fragmentation as measured by the Toomre parameter Q (middle panels) and the effects of the magnetic field as measured by the magnetic Toomre parameter Q_m (right panels), for the least diffusive model M1.0AD1.0 (top row) and reference model M1.0AD2.0 (bottom row). The column density is shown in the left panels for comparison. 158

4.8 Collisions of dense spiraling filaments leading to stellar companion formation. Each column shows three representative snapshots during the formation of each of the five stellar companions of the reference model, highlighting the dense spiraling filaments that collided to form the companion (see the thin black lines). The time before the companion formation is marked in each panel (e.g., -200 yrs). The companions are numbered in the bottom panels. An animation of this figure can be found at `https://virginia.box.com/s/2uul0la2ekysemd9rhoa47cu73f0rwnz` 161

4.9 3D view of the collisions of dense spiraling filaments leading to the formation of the fifth stellar companion in the reference model. Plotted are Lagrangian tracers, which highlight the colliding filaments leading to the fifth companion's formation. The black circle in each panel highlights the filament collision site. An animation of the figure can be found at `https://virginia.box.com/s/2s8h7l7w9y9zz21g8m28l854tq4n54nw`. 163

4.10 Role of plasma-β in fragmentation. Plotted are the distributions of the density and plasma-β on the "midplane" for Model M1.0AD2.0 (panels [a] and [b], respectively) and M1.0AD1.0 (panels [d] and [e], respectively). The green dashed circle in each panel marks a DROD collision site with significant cross-B field motions, as shown by the distribution of $\cos\theta_{\rm ali}$ plotted in panel (c), which is significantly below unity. Panels (b) and (e) show that the collision site in Model M1.0AD2.0 (where fragmentation occurs) is more demagnetized (with a higher plasma-β) than that in Model M1.0AD1.0, which is further quantified in panel (f), where the distribution of the plasma-β is plotted. 164

4.11 Cumulative angular momentum transport rates by gravitational (dashed lines) and magnetic torques (solid) for different models. The magnetic torque dominates angular momentum transport in the M1.0AD2.0, M1.0AD1.0, and M1.0AD2.0 models. In the M1.0AD10 model, gravity and magnetic fields transport angular momentum at comparable rates within the innermost 100 au. 167

4.12 Circumstellar disk misalignment in Models M1.0AD2.0 (upper panels) and PRM2.0AD2.0 (lower panels). The left panels ([a] and [c]) plot the evolution of the angles between the circumstellar disk axes of stellar companions and that of the primary, showing disk misalignment, particularly at late times. The right panels ([b] and [d]) show a visualization of the circumstellar disk misalignment at the time marked by the vertical dashed line in the corresponding left panel. An animated version of the figure can be found at `https://virginia.box.com/s/c5c0y27s4pfd3rz5a389unzyis6dpb99`. 169

4.13 Key components of the DROD fragmentation mechanism for binary/multiple formation. The circumstellar disk around each star is shown in red. The irregular, orange-colored structure is the DROD, which is fed by larger-scale sheetlets (shown in blue). An animated version of this figure can be found at `https://virginia.box.com/s/0t02kcktstho6xmc1rxpye8jz2y5kvag`172

4.14 A simulated triple system analogous to L1448 IRS3B, but formed through collisions of dense rotationally dominated structures (DRODs). The figure is the column density in the M1.0AD2.0 model. 174

5.1 3D rendition of the disk-jet system at a representative time $t = 3.0$ yr, showing a fast (> 100 km/s) collimated bipolar jet (colored red) driven from a highly dynamic dense equatorial disk (colored purple and blue). The jet maintains its fast speed reaching the upper and lower edges of this rendition, which are at the boundaries of the simulation domain (10 au in the $\hat{z}$ direction). The horizontal black structure is a representation of the disk up to 5 au in radius; all features in the disk representation are rendering effects. An animated version of this figure is available in the online journal. The movie is 9 seconds long, showcasing a continuous jet launched in our model. 190

5.2 Overview of the simulation result on a meridional plane at a representative time $t = 3.0$ yr. The upper panels show (a) the density, (b) radial velocity v_r, and (c) the mass flux, respectively. The lower panels show (d) the magnetic field strength, (e) plasma-β, and (f) the ratio between the toroidal field and the poloidal field, respectively. An animated version of this figure is available in the online journal. The movie is 27 seconds long, showing an overview of the disk and outflow evolution in our model. 191

5.3 Key components of the avalanche accretion stream driven jet-launching model. The green zone is the low-density magnetic poloidal zone (with the dominant poloidal field highlighted by gray dashed lines with arrows), surrounded by the jet. The gray zone is the raised disk atmosphere (discussed in sec. 5.3.2), and the orange stream is the avalanche accretion stream (discussed in sec. 5.3.3). The disk is divided into the active (red) and the dead zone (black). The cyan and magenta line segments highlight the magnetic field geometry, with a sharp pinch on the avalanche accretion stream (discussed in sec. 5.3.4). The black arrows highlight the gas motion in the avalanche accretion stream and the jet. 193

5.4 The properties of the raised disk atmosphere (RDA), roughly located to the right of the dashed black line, at a representative time of $t = 3.2$ yr. Plotted are (a) the density distribution, (b) the vertical gas velocity normalized by the local free-fall speed, and (c) the fraction of mass coming from the material originally near the disk surface (see text). Overplotted in panel (b) are the poloidal velocity streamlines, and in panel (c) are the poloidal magnetic field lines. 194

5.5 The disk and outflow properties at a representative time of $t = 3.01$ yr when a prominent avalanche accretion stream is present. Panels (a) and (b) show the squared poloidal and toroidal magnetic field strength, respectively. Panel (c) shows the ratio of the toroidal velocity and local Keplerian velocity, with the poloidal velocity streamlines overplotted. The lower panels show (d) the radial gas velocity v_r, (e) the specific angular momentum, and (f) the vertical magnetic acceleration, respectively. The poloidal magnetic field lines on the lower panels are plotted as contours of equal radial magnetic flux. A representative poloidal field line threading the avalanche accretion stream is highlighted in panels (c)-(f), with its pinch tip dividing the highlighted field line into two branches. The upper branch is colored magenta, and the lower branch is colored cyan. Flow acceleration along this representative field line is discussed in Section 5.3.4 below. 197

5.6 Quantities along the highlighted magnetic field line in Fig. 5.5. $s = 0$ on the horizontal axis corresponds to the tip of the pinched field line; the $s > 0$ section follows the upper branch of the field line (along the magenta field line), and the $s < 0$ section follows the lower branch (along the cyan field line). The distances shown are projected along the field line on the meridian plane. The upper panels are the four conserved quantities defined in equ. 5.18, 5.19, 5.20, 5.21 respectively. Panel (e) shows the ratio between the magnitude of the poloidal velocity and the poloidal Alfvén wave speed. The gas speed becomes super-Alfvénic at ~ 1.2 au along the magenta field line. Panel (f), (g), and (h) show the gas and magnetic components of equ. 5.15, 5.16, and 5.17 respectively. The gas components are the first terms in equ. 5.15, 5.16, and 5.17; the magnetic components are the second terms in equ. 5.15, 5.16, and the third term in equ. 5.17. 199

5.7 A representative magnetic reconnection event in our model. The four panels are a time sequence of reconnecting magnetic field lines. The magnetic field lines are specified by their values of the poloidal magnetic flux so that individual field lines can be traced over time. The magenta field line highlights a specific reconnecting magnetic field line. An animated version of this figure is available in the online journal. The movie is 27 seconds long, which highlights the magnetic reconnection along the avalanche accretion stream. The highlighted magenta field line reconnected multiple times during the movie. 204

6.1 3D rendition of the jet, disk wind, and the disk at a representative time $t = 4.5$ yr. The colors are the $\hat{z}$-direction velocity, showing a fast (> 100 km/s) collimated bipolar jet (colored red and blue, close to the polar axis), surrounded by a slower disk wind (colored yellow and green, further away from the polar axis). The disk is represented by the gray structure on the equatorial plane. The jet is highly variable in space and time, as seen from the animated version available at `https://figshare.com/s/899801ea6282e9c06261?file=53753738`. The animated version is 50 seconds long, featuring a 3D rendition of the outflow in our model. We encourage readers to view it for a clearer impression of the outflow structure and dynamics. 225

6.2 Overview of the simulation result, showing a slice through the plane at $y = 0$. The upper and lower panels show two representative times at 4.5 and 9.0 yr, respectively. Panels (a) and (c) show the density, and panels (b) and (d) show the projected z direction velocity (equ. 6.18). The three main components of the outflow - jet, disk wind, and MRI-active disk wind (MRI DW) - are labeled in panel (b). An animated version is available at `https://figshare.com/s/8b13ca47b44adf6e3db9`. The animated version is 50 seconds long, showing an overview of our simulation result and the evolution of the outflow in our model. 228

6.3 The gas properties near the base of the jet. Plotted are the azimuthally averaged projected z direction velocity (equ. 6.18), plasma-β, kinetic-β (equ. 6.19), and the comparison between the local specific angular momentum and the Keplerian value, respectively, at a representative time $t = 4.5$ yr. The green contour highlights the lower part of the jet (where $v_z^p \geq 3 \times 10^6$ cm/s), where the plasma-β is much less than unity, and the kinetic-β is close to or less than unity. An animated version is available at `https://figshare.com/s/219f51de0c77cbcf17f1`. The animated version is 25 seconds long, showing an overview of the jet properties in our model. 229

6.4 The gas acceleration near the base of the jet. The values are the $\hat{z}$-projected values, where a positive value means the force is pointing away from the disk midplane and a negative value points towards the midplane. The five panels show the total magnetic acceleration, gas acceleration due to magnetic tension, gas acceleration due to magnetic pressure, the gas acceleration due to the "effective magnetic tension" (defined in equ. 6.24), and the gas acceleration due to the "effective magnetic pressure" (defined in equ. 6.23). The outflow is launched by the toroidal magnetic pressure gradient, which provides the acceleration away from the disk in both the upper and lower hemispheres. Magnetic tension is unable to launch an outflow as it points towards the disk. An animated version is available at `https://figshare.com/s/d0d617e992b70dd720fb`. The animated version is 50 seconds long, confirming that the magnetic forces remain consistent throughout the simulation and validating the representative frame shown here. It illustrates the dominant role of toroidal magnetic pressure in driving the outflow. 230

6.5 The gas properties of the disk wind. The four panels show the same quantities as in fig. 6.3, at the same representative time but on a larger scale. The cyan line shows the approximate boundary between the disk wind and the jet, and the magenta line shows the approximate boundary between the disk wind and the expanded disk atmosphere. Compared to the jet, the disk is less magnetically dominated as the kinetic-β is above order unity. An animated version is available at `https://figshare.com/s/668556d9b7090225b367`. The animated version is 25 seconds long, showing an overview of the disk wind launched in our model. 234

6.6 A comparison between different forces in the disk wind. **Panel (a)** shows the ratio between the centrifugal acceleration and the gravitational acceleration in the cylindrical-$\hat{R}$ direction; **panel (b)** shows the ratio between the centrifugal acceleration and magnetic acceleration. Negative values in panels (a) and (b) indicate that the centrifugal acceleration points in the opposite direction to both gravity and the magnetic field. **Panel (c) and (d)** show the $\hat{z}$ direction magnetic acceleration and $\hat{z}$ direction "effective" magnetic pressure acceleration (defined in equ. 6.23) normalized by gravitational acceleration in the $\hat{z}$ direction respectively. Toroidal magnetic pressure drives the disk wind upwards in the $\hat{z}$ direction. An animated version is available at `https://figshare.com/s/86c130e6b25e55d81200`. The animated version is 50 seconds long, showing the force ratios in the disk wind are similar to those in the representative frame we show here throughout the simulation. 235

6.7 A x-y slice through the simulation domain at $z = -1.0$ au showing the projected z-direction velocity (equ. 6.18). The jet stands out at the center of the slice as the dark red (with $v_z^p \geq 10^7$ cm/s) circle with radius ~ 0.3 au; the disk wind is the annulus in lighter red at ~ 1.5 au; in between the jet and the disk wind is the MRI-active turbulent disk wind, where the gas alternates between infall toward the disk and outflow. An animated version is available at `https://figshare.com/s/5d5a3c8cb83a94170519`. The animated version is 50 seconds long, showing the outflow structure described above is persistent in our model before the MRI-active turbulent disk wind chokes the jet at later times. 237

6.8 Properties of the MRI-active turbulent disk wind region, enclosed by the green line. **Panel (a)** shows the projected z-direction velocity (equ. 6.18), overplotted with velocity streamlines; **panel (b)** shows the ratio between local rotation velocity v_ϕ and the local Keplerian velocity v_K, overplotted with magnetic field lines. **Panel (c)** shows the normalized most unstable MRI wavelength (equ. 6.26), where $10^{-1} < q < 10^{1}$ is the most optimal range to activate MRI. An animated version is available at `https://figshare.com/s/2a211268b205eb9a2dd1`. The animated version is 25 seconds long, showing the evolution of the MRI active turbulent disk wind region in our model. The highlighted features in each panel are persistent in the animation. 238

6.9 Geometric argument for the magnetic field geometry (sec. 6.4.1), assuming the disk is threaded by open, $+\hat{z}$-direction magnetic field lines. The signs of the magnetic field and two magnetic field gradients above and below the disk in cylindrical coordinates are shown for the upper and lower hemispheres, respectively, showing magnetic tension force (equ. 6.24) is unable to drive an outflow, whereas magnetic pressure force (equ. 6.23) can. 241

6.10 Properties of the disk surface avalanche accretion stream and the jet-launching cavity at two representative times: 4.5 yr (upper panels) and 9.0 yr (lower panels). The arrows in the two leftmost panels point to the locations of the avalanche accretion stream. **Panels (a) and (e)** show B_ϕ, which switches direction inside the disk between 4.5 yr and 9.0 yr. **Panels (b) and (f)** display the gas density distribution. The disk surface avalanche accretion stream is located where B_ϕ switches sign spatially, roughly coinciding with the pinching of poloidal magnetic field lines. Low-density outflow cavities exist in both hemispheres at 4.5 yr (larger in the lower hemisphere), but much more prominently in the upper hemisphere at 9.0 yr, where B_ϕ spatially changes sign. **Panels (c) and (g)** illustrate the magnetic energy density, symmetric about the disk midplane at both times. **Panels (d) and (h)** show the magnetic energy per unit mass, which is large only in the low-density outflow cavities. An animated version can be found at `https://figshare.com/s/763d65cae5aa7d452442`. The animated version is 50 seconds long, showing the evolution of the magnetic field structure and magnetic energy density evolution in our model. The animation highlights the role of the avalanche accretion stream, located where B_ϕ switches sign, in limiting the disk expansion and facilitating jet launching. 244

6.11 Ratios between energy advection through two components of the Poynting flux and gas kinetic energy *for the jet*, outlined by the cyan contour. The left three panels focus on the base of the jet, and the cyan contour is at 10^6 cm s^{-1}. The right two panels zoom out to larger scales, with the cyan contour at 10^7 cm s^{-1}. **Panel (a)** shows the ratio between the magnetic pressure component of the Poynting flux (equ. 6.30) and kinetic energy flux in the $\hat{z}$ direction; **panel (b)** shows the ratio between the magnetic tension component of the Poynting flux (equ. 6.31) and kinetic energy flux, and panel (c) shows the ratio between magnetic energy and tension components of the Poynting flux, illustrating the dominance of energy transportation by the advection of the toroidal field. **Panels (d) and (e)** show the same ratios as panels (a) and (b), but on a larger scale. Kinetic energy flux gradually becomes more important as the jet propagates to a larger distance. 246

6.12 Quantities along magnetic field lines passing through the avalanche accretion stream. **Panel (a)** shows three consecutive fieldlines in 3D. The avalanche accretion stream is located at the pinching point of these fieldlines, marked by a solid dot. All other panels traces various quantities along these fieldlines, with $s = 0$ located at the solid dot and positive direction tracing the fieldline upward: the vertical dashed line at $s \approx 0.075$ au corresponds to the "star" along each magnetic fieldline. **Panels (b), (c), (d), and (e)** shows the density, radial direction velocity v_r, azimuthal velocity v_ϕ, and toroidal magnetic field B_ϕ respectively, with line colors matching the respective field lines in panel (a). The similarities between these three magnetic field lines show a consistent evolution along the magnetic field lines advected by the avalanche accretion stream. **Panels (f), (g), and (h)** focuses on the black fieldline in panel (a), showing Poynting flux (and its terms, defined in equ. 6.29, 6.31, 6.30 respectively), Poynting flux per unit mass, and magnetic acceleration on the gas (defined in equ. 6.23 and equ. 6.24) respectively. An animated version showing the 3D structure of the fieldlines is available at `https://figshare.com/s/ff9d053534f58e00f774`. The animation is 4 seconds long, showing a 3D view of panel (a) 249

6.13 Quantities along a magnetic field line at the representative time $t = 4.5$ yr. All values are azimuthally averaged to minimize numerical effects. **Panel (a)** shows the projected v_z velocity (equ. 6.18). The representative field line analyzed is highlighted in cyan, where the positive direction traces the field line away from the disk midplane. **Panels (b), (c), (e), and (f)** shows the four dimensionless conserved quantity defined in equ. 6.36, 6.37, 6.38, 6.39 respectively. **Panel (d)** shows the Alfvénic Mach number and the poloidal Alfvénic Mach number along the magnetic field line. 251

6.14 Deviation from the expectations of the magneto-centrifugal model. **Panel (a)** shows the pitch angle of the poloidal magnetic field line is more than 60 degrees from the disk midplane; **panel (b) and (c)** shows although centrifugal force is strong in the jet, magnetic force in the cylindrical-$\hat{R}$ direction is stronger. 256

6.15 Comparison between the jet and disk wind in our model and the steady-state solutions from Ferreira et al. (2006). The outflow is divided into the jet and disk wind based on geometry (see sec. 6.5.3). Each cell is represented by a dot, colored according to its vertical distance from the disk midplane ($|z|$). **Panels (a) and (b)** show the jet and disk wind in the upper hemisphere, respectively; **panels (c) and (d)** show the same cells as a and b, but with values extrapolated assuming all angular momentum and kinetic energy carried by the magnetic field are released into the gas. The lower panels present the same quantities as the upper panels but use cells in the lower hemisphere. 261

6.16 **Left panel:** Disk accretion rate and outflow mass flux. A negative sign is added to the accretion rate, so the values are positive. **Right panel:** The "Keplerian angular momentum radius" R_a (defined in equ. 6.59) for the jet and the disk wind. The horizontal lines in both panels are the averaged values between 4.0 yr and 10.0 yr for each line. 265

6.17 Ratios of energy advection rates and forces for the *disk wind*. The magnetic tension component of the Poynting flux (equ. 6.31) dominates over the magnetic pressure component (equ. 6.30) in transporting energy in the $\hat{z}$ direction near the outflow base at small radii (left panel). However, the dominance in energy transport does not translate to a dominance in force: magnetic pressure force dominates over magnetic tension force everywhere in the disk wind (right panel). 266

6.18 Azimuthally averaged magnetic field strength, generation, and advection. **Left panel:** azimuthal magnetic field B_ϕ at the representative time. **Middle panel**: generation of azimuthal magnetic field through differential rotation, as defined in equ. 6.60; **Right panel:** advection of azimuthal magnetic field through gas motion, as defined in equ. 6.61. The green line in each panel shows where $\beta_K = 1$ (defined in equ. 6.19), with the polar regions being magnetically dominated ($\beta_K < 1$). Note that a negative generation or advection rate in a negative B_ϕ region is an *increase* in magnetic field strength. 268

7.1 3D rendition of the bipolar jet launched in our model. The outer red and blue shells are isosurface contours at 100 km s^{-1}, whereas the inner ones are at 200 km s^{-1}. The gray structure on the equatorial plane represents the disk. For reference, the green and yellow lines each have a length of 5 au, illustrating the physical scale of the system. An animated version of this figure can be found at: `https://virginia.box.com/s/uctiv36qbwj4tgr5bbjfs8kq4jzu3zwb`. The movie is 27 seconds long, highlighting the strong bipolar outflow from the simulation's beginning (0 yr) to the end (5.5 yr). 283

7.2 Magnetic field geometry after the initial adjustment in the simulation. The background color map shows the projected $\hat{z}$-direction velocity v_z^p (equ. 7.9). The magnetic field structure can be roughly divided into four distinct zones, delineated by the magenta, cyan, and green lines. The magenta line encloses the permanently closed stellar magnetosphere; the cyan line marks the boundary of opened stellar field lines that still thread the star; the green line outlines the extent of the large-scale magnetic field lines threading the disk. The region between the cyan and green lines corresponds to a reconnecting, outflow-driving zone where the interaction between stellar and disk fields powers the outflow. 284

7.3 Magnetic flux evolution in the simulation. **The left panel** shows the total magnetospheric flux (black line), defined as the maximum magnitude of the total downward $\hat{z}$-directed magnetic flux integrated azimuthally at each cylindrical radius. The red and blue lines indicate the amount of opened stellar magnetosphere flux, measured as the maximum magnitude of azimuthally-integrated downward B_z at $z = \pm 5$ au above and below the disk midplane, respectively. **The right panel** shows the time evolution of the enclosed magnetic flux at each cylindrical radius at the midplane. The stellar magnetosphere primarily contributes to the negative flux at small radii, while the disk field dominates the positive flux at larger radii. 286

7.4 Overview of the outflow, particularly the disk wind at a large cylindrical radius surrounding the jet. **Panel (a) and (b)** show the density and projected $\hat{z}$-direction velocity (v_z^p, equ. 7.9) respectively; **panel (c)** shows the normalized MRI-turbulence wavelength (equ. 7.10; **panel (d) and (e)** show the plasma-β and (equ. 7.12) kinetic-β (equ. 7.13) respectively. The lower panels compare different force components in the disk wind. **Panel (f)** shows the ratio between the cylindrical-$\hat{R}$ direction magnetic force and centrifugal force. **Panel (g), (h), (i), and (j)** show the magnitude of the gas acceleration due to magnetic forces. The quantities are total gas acceleration in cylindrical-$\hat{R}$ direction, total magnetic acceleration in $\hat{z}$- irection, the effective magnetic pressure component (equ. 7.15), and the effective magnetic tension component (equ. 7.16) respectively. These disk wind properties and forces show that the disk wind in this model is very similar to the disk wind in Tu et al. (2025a). 290

7.5 A zoom-in view focusing on the permanently closed stellar magnetosphere (around the midplane) and the opened stellar magnetic field threading the star (in the polar region above and below the star). **Panel (a)** shows the real density traced by the "passive scalars", highlighting the magnetospheric accretion streams. The sphere in the middle is the inner boundary $r_{\rm fix}$, where a star resides (see sec. 7.2 for a more detailed description of the setup). **Panels (b) and (c)** show the B_z field strength and v_z^p (equ. 7.9) respectively, illustrating the magnetic and dynamical properties of the region close to the star. **Panels (d) and (e)** show the plasma-β (equ. 7.12) and kinetic-β (equ. 7.13) respectively, indicating the magnetosphere and the polar cavity are both magnetically dominated. 291

7.6 Overview of the jet. Upper panels focus on the magneto-hydrodynamic properties of the jet; lower panels focus on the magnetic forces. **Panels (a) and (b)** show the density and projected $\hat{z}$-direction (v_z^p, equ. 7.9) respectively, showing the jet lies in the low-density polar cavity. **Panels (c) and (d)** show the plasma-β (equ. 7.12) and kinetic-β (equ. 7.13) respectively, showing the jet is a magnetically-dominated structure. **Panels (e), (f), (g), and (h)** show the total magnetic force, the effective magnetic tension force (equ. 7.16), the effective magnetic pressure force (equ. 7.15), and the toroidal magnetic pressure force (equ. 7.17) respectively. 294

7.7 Toroidal magnetic field generation in the jet-launching region. The quantities plotted are azimuthally averaged. **Panel (a) and (b)** show the density and projected $\hat{z}$-direction velocity (v_z^p, equ. 7.9) respectively, showing the density structure and the location of the jet. **Panel (c)** shows the kinetic-β (equ. 7.13), highlighting the transition from the magnetically-dominated polar cavity to the mass-dominated disk. **Panel (d)** shows the angular velocity, normalized by the local Keplerian value. The lower panels show toroidal magnetic field dynamics. **Panel (e)** shows the toroidal magnetic field; **Panels (f), (g), and (h)** show the total change in toroidal field strength (equ. 7.20), toroidal field generation by differential rotation (equ. 7.18), and toroidal field advection by flux-freezing (equ. 7.19) respectively. The black dashed contour highlights the $\beta_K = 1$ surface. The magenta and green field lines are 2D projections of representative 3D field lines shown in Figure 7.8. An animated version is available at `https://virginia.box.com/s/ijkmmcxee9f6mchph57zp8zdptgbt07p`. 296

7.8 3D rendition of the two fieldlines highlighted in Figure 7.7, colored by the local kinetic-β (equ. 7.13). The yellow sphere at the center represents the star. The magenta fieldline in Figure 7.7 is located on the right, with one low kinetic-β end on the star and one high kinetic-β end in the disk. The green field line from Figure7.7 is shown on the left: most of this field line resides in regions where $\beta_K < 1$, indicating magnetic dominance, except for a localized segment with $\beta_K > 1$, where kinetic energy becomes dominant. 297

7.9 Magnetic energy evolution in the jet-launching region. The top panels illustrate the cylindrical $\hat{R}$-direction current and its components. Given the toroidal magnetic field structure (Figure 7.7[e]), a positive current is required to exert a force directly away from the disk. **Panels (a) and (b)** show meridional slices of the two components of the $\hat{R}$-directed current (equ. 7.22 and 7.23), respectively. The component due to azimuthal asymmetry (equ. 7.22) points toward the midplane, while the component arising from global field geometry (equ. 7.23) points away from the disk. **Panel (c)** shows the azimuthally averaged current at a representative time, revealing a positive current along the surfaces of both the magnetosphere and disk—sufficient to drive outflows. To reduce transient effects and emphasize large-scale features, panels (d), (e), and (f) present time-averaged (over ±0.1 yr centered on 4.0 yr) and azimuthally averaged quantities. **Panel (d)** shows toroidal field generation concentrated along narrow streams at the magnetosphere and disk surfaces, highlighting the origin of the current. **Panels (e) and (f)** display the projected Poynting flux in the $\hat{z}$- and $\hat{R}$-directions, respectively, demonstrating how magnetic energy generated near the star is transported outward to power the jet. The dashed contours in panels (c)–(f) outline the approximate extent of the jet. 298

7.10 3D rendition of the protostar, accreting magnetosphere, and magnetic field lines. The disk is shown as semi-transparent density isosurfaces at around 10^{-12} g cm^{-3}. The protostar is represented by the central red solid sphere. White lines depict magnetic field lines, including permanently closed magnetospheric loops and twisted field lines resulting from magnetosphere–disk interactions (e.g., the prominent twisted fieldline near the top-center of the image). An animated version of this figure is available at: `https://virginia.box.com/s/w3f0wjnpakciejrlxnurnvlaxwi24sdx`. 304

7.11 Illustration of the "reload" stage where magnetic reconnection resets the field geometry. While individual reconnection event occurs rapidly and is unrealistic to show explicitly in 3D simulations, we illustrate the cumulative effect using azimuthally integrated magnetic flux surfaces. The panels present a time sequence of the flux surface evolution. The background color shows the radial velocity in spherical coordinates (v_r), highlighting the jet's location. Black lines represent azimuthally averaged magnetic flux surfaces, which can also be interpreted as approximate magnetic field line locations. The thick black line shows magnetic reconnection by tracing a representative field line along the $B_r = 0$ surface, which is marked by the magenta dash-dot line. 306

7.12 Accretion and outflow properties. **Panel (a)** shows a 3D rendition of the accretion streams by only choosing cells with real $\rho > 10^{-13}$ g cm^{-3} and kinetic-$\beta < 1$. **Panel (b)** quantifies the landing locations of the mass accretion rate streams on the star at each polar angle, showing off-midplane accretion along magnetosphere fieldlines. **Panel (c)** shows the total mass accretion rate (black line on top), jet outflow rate (red line at the bottom), and the disk wind outflow rate (blue line in the middle). The red dashed line is the jet outflow rate using the real gas only, showing the density floor's minimal effect on the outflow. **Panel (d)** shows the "Keplerian angular momentum radius" (R_a, equ. 7.26) of the jet (lower red line) and the disk wind (upper blue line). The horizontal dashed lines mark the averaged R_a over the time shown. . 310

7.13 Illustration of the resulting large-scale toroidal magnetic field configuration, shaped by the poloidal field geometry established through the presence and partial opening of the stellar magnetosphere. In contrast to the disk-only case (Tu et al., 2025a), where the magnetic field direction reverses in only one hemisphere, both the poloidal and toroidal components exhibit reversal in both the upper and lower hemispheres in the case with a stellar magnetosphere. 313

7.14 Mass-weighted average conserved quantities (upper four panels) and outflow properties (lower two panels) at different heights. **Panels (a), (b), (c), and (d)** show the mass loading parameter (equ. 7.27), angular velocity (equ. 7.28), angular momentum (equ. 7.29), and energy (equ. 7.30) respectively. **Panel (e)** shows the plasma-β (equ. 7.12), kinetic-β (equ. 7.13), and the poloidal kinetic-β (equ. 7.31). **Panel (f)** shows the ratios of toroidal to poloidal components for both velocity and magnetic field, illustrating the changing dominance of flow and field geometry with height. 320

8.1 Numerical accuracy of the TSC interpolation algorithm with different functions $[f(x)]$, resolution between $[0, 1]$ (n), and distance from the origin (x). 329

8.2 Fractional error in the tracer particle test as a function of radius in a model tracing circular orbits. The simulation setup is described in Section 8.3.2. 331

8.3 Fractional error in the dust particle test as a function of initial dust velocity in a model with stationary gas background. The simulation setup is described in Section 8.3.3. 333

8.4 Fractional error in the gravity module of dust particle test as a function radius from the center in a model with minimal gas drag and the dust in Keplerian orbit around the center. The simulation setup is described in Section 8.3.4. 335

B.1 Cumulative grain mass as a function of grain size similar to Fig. 2.5 but with the Brownian motion included. The mass includes both the grains in the active computational domain and those advected through the inner boundary. The black and red lines are the baseline models for $\chi = 1$ and 4 respectively without Brownian motion; the blue and green lines are the corresponding models with Brownian motion included. . 360

C.1 One representative frame of the artististic rendering of the M1.0AD2.0 model with Unity (Unity Technologies, 2024). The movie can be found on YouTube at `https://www.youtube.com/watch?v=s-eHv7cAObw` . 362

E.1 Comparison between the NOROT and STROT at the same time (9.0 yr). The upper row shows a slice through the NOROT model and the lower row shows the STROT model. The four columns show density, projected z-direction velocity (v_z^p, equ. 6.18), azimuthal magnetic field, and magnetic energy per unit mass, respectively. Although these two models are not expected to be identical due to their turbulent nature, they are qualitatively similar. An animated showing the evolution can be found at `https://figshare.com/s/04e8a31b7f92218f24bb`. The animated version is 50 seconds long, showing the evolution of the NOROT and STROT models from the initial condition to 10 yrs. The animation shows the qualitative similarities between these two models. 367

List of Tables

3.1 $\mathcal{M}$ is the initial turbulent Mach number and η_R the reference ambipolar diffusion coefficient. 88

4.1 Summary of each simulation model's initial conditions and outcome. $\mathcal{M}$ is the Mach number of the initial turbulence; $\tilde{\eta}_0$ is the scaling of the ambipolar diffusivity coefficient defined in equ. 4.8; $N_{\rm star}$ is the number of stars at the end of the simulation (excluding merged stars; stellar companion 2 merged with stellar companion 1 in Model M1.0AD2.0, and stellar companion 5 merged with stellar companion 4 in Model M1.0AD10); $N_{\rm tot}$ is the total number of stars formed in the simulation (including merged stars); $t_{\rm primary}$ is the formation time of the primary in years. 143

5.1 Atomic species included in the thermal ionization calculation using the Saha equation. m_s in the second column is the atomic mass of each element in the unit of proton mass m_p. The abundances in the third column are taken from Asplund et al. (2009), assuming 1% of the metal is in the gas phase. The last column is the ionization potential e_I. . . 189

6.1 Parameters for calculating the thermal ionization fraction with the Saha equation. m_s, the atomic mass of each element, is in the unit of proton mass m_p. The relative abundances with respect to H_2 are taken from Asplund et al. (2009), assuming the gas phase metal in the protoplanetary disk is 1% of the solar photosphere abundance. 224

Chapter 1

Introduction

天高地迥，觉宇宙之无穷；兴尽悲来，识盈虚之有数。

- (唐) 王勃,《滕王阁序》

本章节的中文版在附录A. A Chinese version of this chapter is in Appendix A

The formation and evolution of planetary systems—from our solar system to distant exoplanets—represents one of astrophysics' most fundamental quests. These universal processes create the physical conditions that shape planetary environments, ultimately determining their potential for habitability and life. For centuries, our understanding was limited to a single example: our own solar system. This changed forever in 1995 with the discovery of 51 Pegasi b (Mayor & Queloz, 1995), the first confirmed exoplanet orbiting a Sun-like star. This groundbreaking revelation shattered our assumptions about planetary system architecture and launched a revolutionary era of astrophysical discovery. By studying how planets, moons, and smaller bodies form and evolve, we not only trace our cosmic origins but also confront profound questions about life's prevalence and humanity's place in the universe.

Philosophically, the remarkable diversity of exoplanetary systems challenges our assumptions about Earth's uniqueness, compelling us to reconsider our cosmic perspective. Biologically, this line of research seeks to reveal the precise physical and chemical conditions necessary for life, providing crucial insights into its potential distribution throughout the cosmos. From a planetary science viewpoint, reconstructing stellar system formation explains the observed variety among stars, planets, and debris disks. Practically, this knowledge proves indispensable—it directly informs the exploration and utilization of space resources, from nearby asteroids to the outer solar system's untapped potential.

Progress in these areas requires a multidisciplinary approach that combines theoretical models, advanced simulations, and cutting-edge observations from both ground- and space-based facilities. Beyond its academic significance, this understanding plays a vital role in humanity's future as it drives advancements in space technology and establishes the foundation for our sustainable expansion beyond Earth.

1.1 Overview of Star and Planet Formation

The formation of planetary systems is a cosmic odyssey that begins within the vast, enigmatic nurseries of giant molecular clouds (GMCs)—colossal structures that serve as the coldest and densest reservoirs of the interstellar medium. These GMCs, spanning hundreds of parsecs in size (with 1 parsec approximating 3.26 light-years) and harboring masses exceeding 10^5 solar masses ($M_\odot$) (Großschedl et al., 2018), are dynamic laboratories of star formation. Within their turbulent interiors (Elmegreen & Scalo, 2004), supersonic motions—driven by a combination of gravitational instabilities, magnetic fields, and feedback from stars—generate chaotic, shock-dominated environments. This turbulence produces intricate, filamentary substructures across the clouds, channeling gas and dust into dense, elongated networks (Men'shchikov et al., 2010). Over time, gravitational instabilities amplify within these filaments, leading to localized material accumulations (Könyves et al., 2015). These overdensities, termed molecular cloud cores, represent the critical precursors to stellar birth (André et al., 2010). As a core accumulates sufficient mass, its self-gravity overwhelms the opposing forces of thermal pressure, magnetic support, and turbulent motions, triggering a cascade of collapse. The process culminates in the formation of a protostellar system, which may eventually coalesce into single stars, binary systems, or small stellar clusters, while remnant material in the protostellar disk assembles into planets, asteroids, and comets (Könyves et al., 2015). Studying low-mass star formation is crucial for understanding the origins of systems like our own solar system. These stars, with masses up to a few times that of the Sun, serve as ideal models for investigating the processes that lead to star and planet formation. Additionally, many low-mass star-forming regions are located relatively close to Earth, offering unique opportunities to observe and analyze these processes in detail. By examining

these regions, we can gain insights into the early stages of stellar evolution and the conditions that foster planet formation.

The transformation of molecular cloud cores into stars and planetary systems follows a sequence of four evolutionary stages (Class 0, I, II, III, Fig. 1.1)—a classification scheme originally defined by observational traits but now recognized as a chronological progression tied to physical evolution (Barsony, 1994; Kristensen & Dunham, 2018). The Class 0 phase, first identified through its dominant submillimeter emission, represents the initial collapse of a dense core (Andre et al., 1993). At this stage (lasts $\sim 10^4$-10^5 years), the protostar remains deeply embedded in a massive envelope, with a large fraction of its final mass still in the surrounding material. The transition to Class I ($\sim 10^5$ years) is marked by a shift to a spectral energy distribution (SED) more dominated by emission at longer infrared wavelengths as the envelope continues to dissipate and funnel material onto the protostar and its growing disk. Collimated jets and outflows—powered by magnetic processes driven by disk accretion—are prominent during this phase, sculpting the surrounding environment and ejecting material at supersonic speeds (Ray & Ferreira, 2021; Caratti o Garatti et al., 2024a).

By the Class II phase ($\sim 10^6$ years), the envelope is almost fully accreted by the star and disk and/or removed by protostellar outflows, leaving a pre-main-sequence star with a luminous[1] protoplanetary disk emitting strongly in the near-infrared. This stage showcases advanced dust evolution, with small (micron-sized) grains aggregating into pebbles and planetesimals within a disk now structured by gaps and rings, likely signifying embedded protoplanets (Dong et al., 2017; Dipierro et al., 2018; Lorek & Johansen, 2022). Finally, the Class III phase begins as the disk disperses through photoevaporation and dynamical interactions (e.g., through interaction with the stel-

[1]brighter than the star at relatively long (near- and mid-infrared) wavelengths.

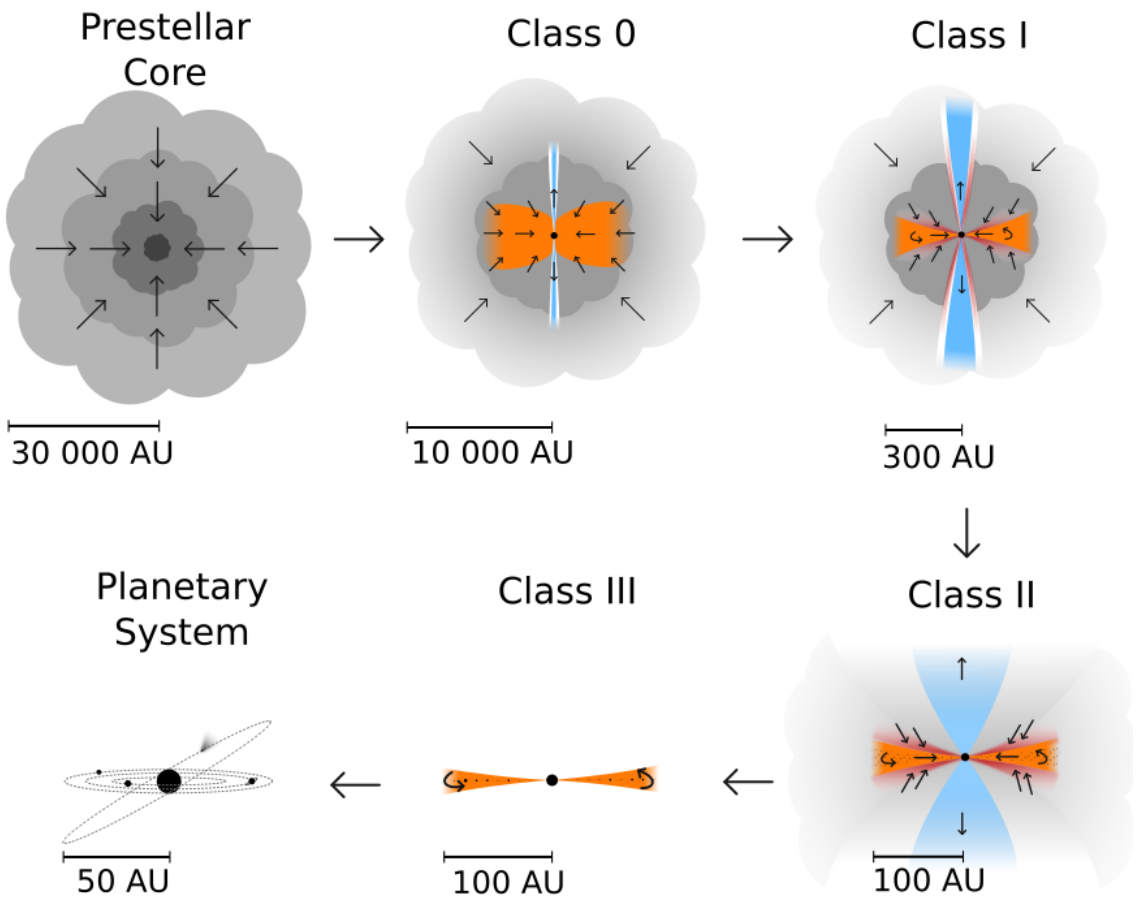


Figure 1.1: Figure illustrating the evolutionary sequence from a pre-stellar core through Class 0–III phases, ultimately leading to a planetary system. Adapted from Persson (2014).

lar wind), leaving a debris disk or a young planetary system. Residual gas is expelled, while planets migrate to stable orbits—a process mirrored in our Solar System's early history (Lovell et al., 2021).

The evolutionary stages of star formation have been rigorously investigated through multi-wavelength observations, particularly in nearby giant molecular clouds (GMCs) such as the Taurus, Orion, Ophiuchus, and Perseus Molecular Clouds, which serve as astrophysical laboratories for studying young stellar objects. Among these phases, the Class II stage is observed more frequently due to their extended lifetimes compared to earlier phases. A paradigmatic example is HL Tau (e.g. ALMA Partnership et al., 2015, Fig. 1.2), a Class I-II system[2] in the Taurus Molecular Cloud. Its proximity ($\sim$ 140 parsecs; [1 parsec = 206265 au $\approx$ 3.26 light year]) and advancements in facilities such as the Atacama Large Millimeter/submillimeter Array (ALMA) have enabled spatially resolved imaging of its protoplanetary disk, revealing concentric rings and gaps. These features are widely attributed to dynamic interactions with forming planets or pressure bumps (e.g. ALMA Partnership et al., 2015). Recent high-resolution studies of HL Tau and similar Class I-II systems have mapped their chemical inventories (e.g., the detection of water, Facchini et al., 2024) and polarized dust structures (Stephens et al., 2014, 2023), providing more detailed insights into their physical properties and furthering our understanding of later-stage disk evolution and planet formation processes.

Observational studies of Class 0 and early Class I objects—the earliest phases of star formation—remain comparatively limited due to two intrinsic challenges: their short lifetimes and their extreme obscuration by dense, dusty envelopes. At these stages, the nascent protostar and its immediate surroundings are shrouded in opti-

[2]There are uncertainties in the classification due to, e.g., observation angle of the system, so the classification is not rigorous.

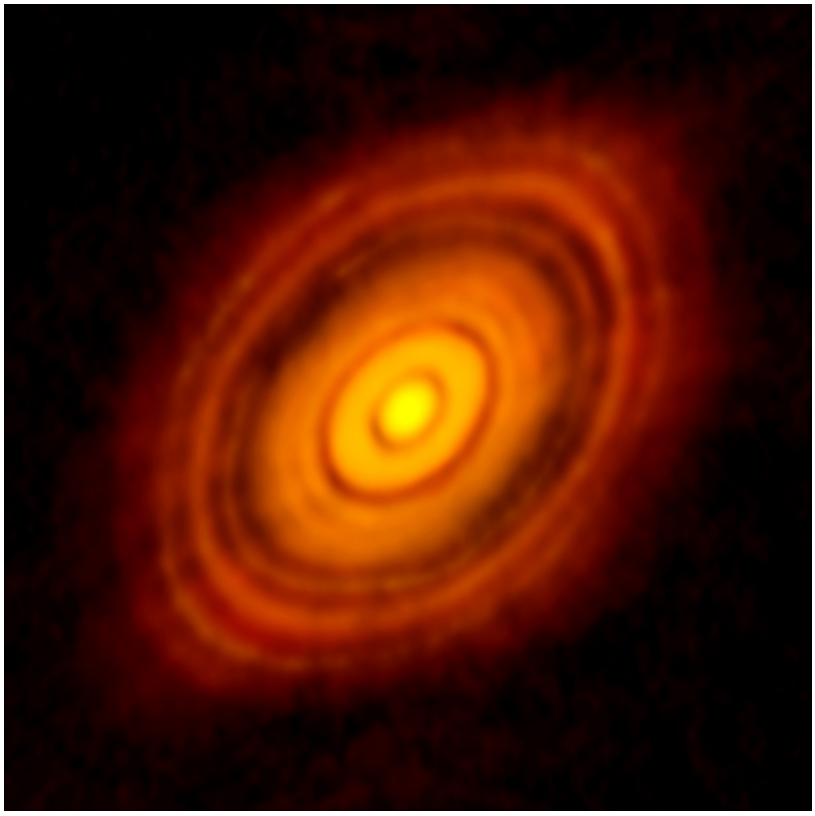


Figure 1.2: ALMA image of representative Class I-II object: HL Tau. Multiple rings and gaps are seen in the protoplanetary disk. The image is adapted from (ALMA Partnership et al., 2015)

cally thick material, rendering the inner regions invisible at optical and near-infrared wavelengths. Observations instead rely on submillimeter/millimeter (e.g., ALMA) and near-to-mid-infrared (e.g., JWST, Spitzer) facilities to penetrate the envelope and probe accretion dynamics.

A representative Class 0 protostar is VLA 1623 (left panel of Fig. 1.3), located in the Ophiuchus molecular cloud (Andre et al., 1993). This system, one of the youngest known, consists of a trio of protostars actively accreting from a shared envelope (Harris et al., 2018). Observations reveal vigorous, collimated bipolar outflows—jets of material ejected perpendicular to the accretion disk—powered by the release of gravitational energy as gas spirals onto the protostars. These outflows, a hallmark of early accretion activity, are traced via shocked molecular gas (e.g., SiO) and serve as signposts of ongoing mass ejection and angular momentum redistribution (Codella et al., 2024). In the early Class I phase, exemplified by the edge-on system IRAS 04302+2247 (Taurus Molecular Cloud, right panel of Fig. 1.3), the envelope continues to dissipate, offering glimpses of the developing protostellar disk at shorter wavelengths (Lucas & Roche, 1998). High-resolution ALMA observations of IRAS 04302+2247 show that dust grains remain unsettled toward the midplane (Lin et al., 2023). This suggests persistent turbulence or magnetic activity counteracting gravitational settling in contrast to the ordered, settled dust layers seen in older Class II disks.

Despite significant observational advancements, the physical mechanisms governing Class 0 and Class I stages remain poorly constrained. Understanding these early phases is crucial, as they play a foundational role in setting the stage for later stellar and planetary evolution, influencing the mass, composition, and dynamics of both the forming star and its surrounding protoplanetary disk. The Class 0 and class I phases are governed by a tangle of interdependent processes: gravitational collapse competes

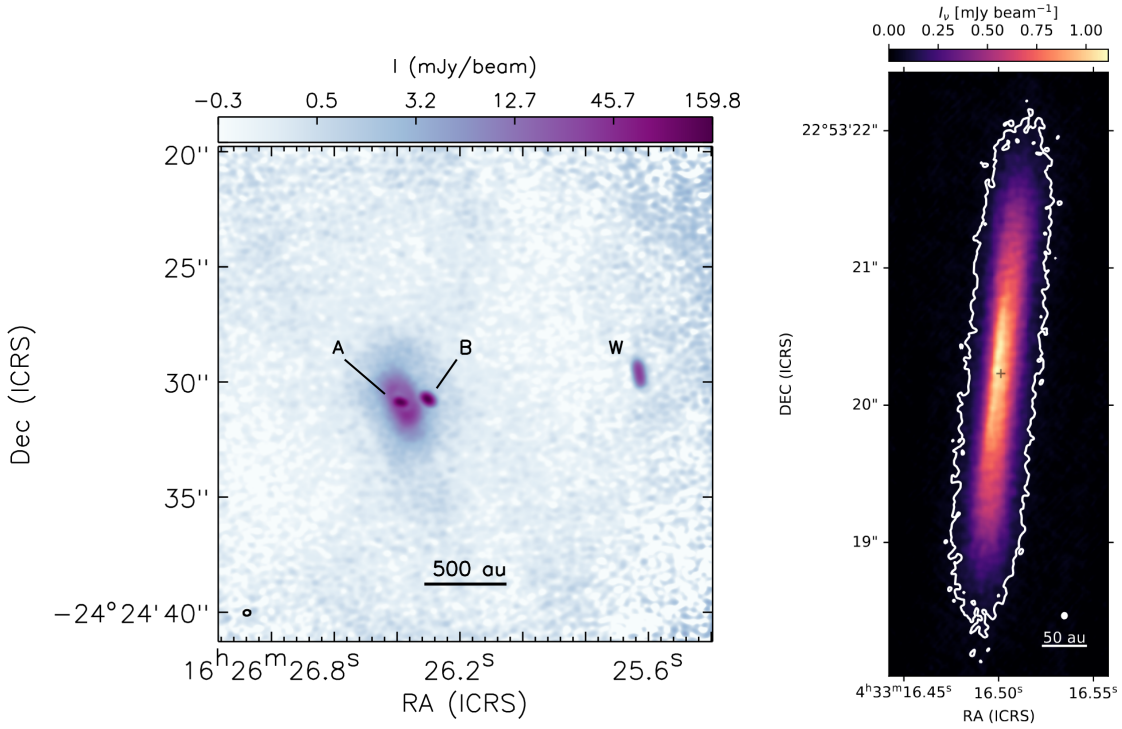


Figure 1.3: Representative Class 0 and Class I protostellar objects. **Left panel:** Image of VLA 1623, adapted from (Sadavoy et al., 2024); **Right panel:** Image of IRS 04302+2247, adapted from (Lin et al., 2023).

with turbulent and magnetic support; gas-magnetic field interactions complicate and alter angular momentum transport; accretion-driven outflows interact with infalling envelopes; and nascent disks form within chaotic, asymmetric environments. Observational snapshots, while invaluable, struggle to disentangle these dynamics, as they capture only a single epoch in systems evolving over timescales much longer than human lifetimes. Similarly, idealized analytic models, though foundational, often oversimplify the non-linear interactions inherent to these stages (e.g., the feedback between gas evolution and magnetic field advection).

To unravel this complexity, numerical simulations have become indispensable. By coupling magnetohydrodynamics (MHD), radiative transfer, and chemistry, simulations allow researchers to conduct controlled experiments—varying initial conditions (e.g., turbulence, magnetic field strength) and tracking outcomes over millennia in a computational framework. In the sections that follow, we introduce some pivotal questions in early star formation and describe the essence of numerical modeling.

1.2 Proto-Stars and Disk Formation

Protostars and protostellar disks (Class 0 and Class I objects) represent the earliest phases of star formation. Although this stage is relatively brief compared to the later protoplanetary phase, its dynamics play a crucial role in shaping the architecture of the emerging system—determining whether it evolves into a single star with a disk or a multiple-star system. During this period, a pre-stellar core collapses to form the stars and the disks. The majority of the stellar mass is accreted in this stage, either through direct accretion from the protostellar envelope or via, more likely, the protostellar disk (Fiorellino et al., 2023). This phase also sets the foundation for later disk evolution, with its properties influencing the subsequent evolution of the protoplanetary disk and, ultimately, the potential for planet formation.

Magnetic fields are a fundamental component of protostellar systems, with their presence at every stage of star formation (Liu et al., 2022; Seifried et al., 2014). These fields act as "elastic wires" in astrophysical systems, dynamically linking different components of the evolving protostellar environment. For example, angular momentum can be transferred along magnetic field from faster-rotating gas to slower ones (usually named "magnetic braking"). The magnetic field can be carried along by gas flows, influencing the system's evolution. In the ideal magnetohydrodynamic (MHD) regime, magnetic fields are assumed to be frozen in the gas, meaning the field and gas move together without separation. However, in reality, non-ideal MHD effects can decouple the magnetic field from the gas, allowing them to move independently. There are three non-ideal MHD effects: ambipolar diffusion, the Hall effect, and Ohmic dissipation. Their relative importance depends on local conditions such as gas density, ionization fraction, and magnetic field strength, which influence the degree of coupling between gas and magnetic fields. The evolution of magnetic fields during the protostellar phase is particularly important (e.g., Tsukamoto, 2016), and non-ideal MHD processes can redistribute or remove magnetic fields, influencing the magnetic flux carried from the protostellar phase to the protoplanetary phase and determining the field strength available for subsequent protoplanetary disk evolution.

Observing magnetic fields in star formation is challenging, particularly in protostellar environments where the magnetic field strength is relatively weak compared to the strong magnetic fields found on stellar surfaces. Direct observations typically rely on the Zeeman effect, where spectral lines split into different components due to the presence of a magnetic field (e.g., as reviewed by Crutcher & Kemball, 2019). Although this is a powerful technique for detecting magnetic fields, the signal from Zeeman splitting is weak and requires high sensitivity and long observation times, often pushing the limits of current instruments. Alternatively, magnetic fields can be

inferred indirectly by measuring dust polarization (e.g. Ohashi et al., 2025). Small, elongated dust grains align their spin axes with the magnetic field, emitting light in a way that produces observable polarized light (e.g., Le Gouellec et al., 2023, Fig. 1.4). However, this method assumes that dust grains align with the magnetic field, but other processes, such as gas drag, can also result in their alignment, making this assumption uncertain (Lin et al., 2024). Additionally, this method primarily reveals information about the magnetic field's geometry, offering only limited constraints on its strength. As a result, constraining and understanding magnetic fields in star formation is highly challenging, compounded by the time-dependent evolution of magnetic fields due to non-ideal MHD effects, which come with additional observational uncertainties. To bridge the gap between observed gas dynamics and magnetic field behavior, non-ideal MHD simulations are crucial for understanding magnetic field evolution in these environments.

An additional complexity in our understanding of star formation arises from the presence of turbulence. The turbulence in star-forming pre-stellar cores originates from larger-scale giant molecular clouds, where strong, supersonic turbulence is ubiquitous (e.g., Mac Low & Klessen, 2004; Orkisz et al., 2017). Although turbulence weakens—typically becoming subsonic—in dense pre-stellar cores (Chen et al., 2019), its impact on gas dynamics and magnetic field evolution remains important and uncertain. For the gas, turbulence can disrupt the laminar collapse of dense pre-stellar cores, altering the flow patterns and influencing the architecture of the forming system. Turbulence also affects magnetic fields by reshaping their geometry, leading to enhanced magnetic reconnection, where oppositely directed field lines reconnect and modify the overall field structure. This process can significantly influence the redistribution of magnetic flux within the system. Due to the interplay between turbulence, gas dynamics, and magnetic fields, numerical simulations are essential for capturing

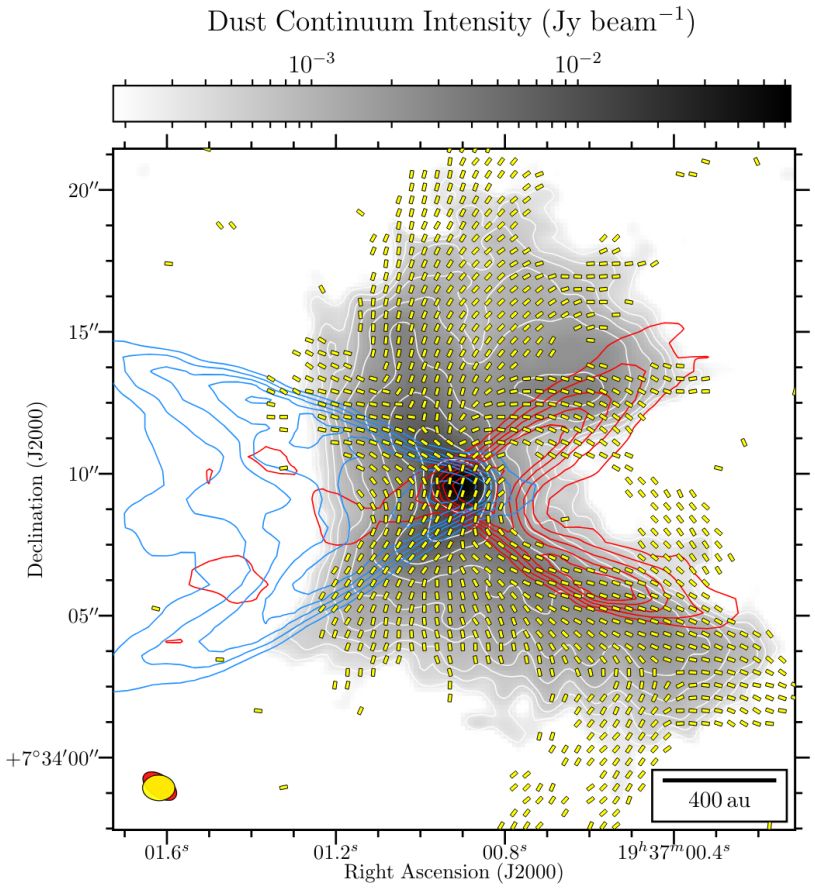


Figure 1.4: Image of magnetic field vectors inferred from dust polarization observation of B335 Class 0 protostellar core. Figure adapted from Le Gouellec et al. (2023)

these local processes and their broader impact on star formation. The numerical methods and simulation results will be discussed in later chapters.

1.3 Dust Dynamics and grain growth

The terrestrial planets (Mercury, Venus, Earth, and Mars) and the asteroids in the solar system are primarily composed of solid materials, consisting of rocks and metals. In dense molecular cloud cores, these solids (in the form of dust) are relatively rare compared to gas, with a typical mass ratio of dust : gas = 1 : 100 (Bohlin et al., 1978). Moreover, the size of this dust is very small in dense cores, typically around 1 microns (10^{-4} cm) in size or smaller (Mathis et al., 1977a; Weingartner & Draine, 2001). How these tiny dust grains found each other and eventually formed the planets we live on (6.4×10^8 cm) remains an open question.

The leading model of planet formation follows a bottom-up approach, where solids gradually grow from small to large sizes. This process occurs in several stages (fig. 1.5). The first stage is "grain coagulation," in which small (micron-sized) dust grains collide and stick together, forming larger aggregates. Once the grains reach approximately millimeter to centimeter sizes, their interaction with the gas can trigger the "streaming instability," leading to dust concentration and collapse into objects ranging from kilometers to a few tens of kilometers in size (Youdin & Goodman, 2005a). These 100-km-sized objects continue to grow either by accreting smaller dust grains through "pebble accretion" (Bitsch et al., 2015; Visser & Ormel, 2016) or by colliding with other 100-km-sized objects (Gabriel & Cambioni, 2023). Through these processes, they eventually form terrestrial planets or the cores of giant planets such as Jupiter and Saturn in the solar system.

The exact process of the initial grain coagulation stage remains unclear, introducing uncertainties in subsequent evolutionary steps. One major unanswered question

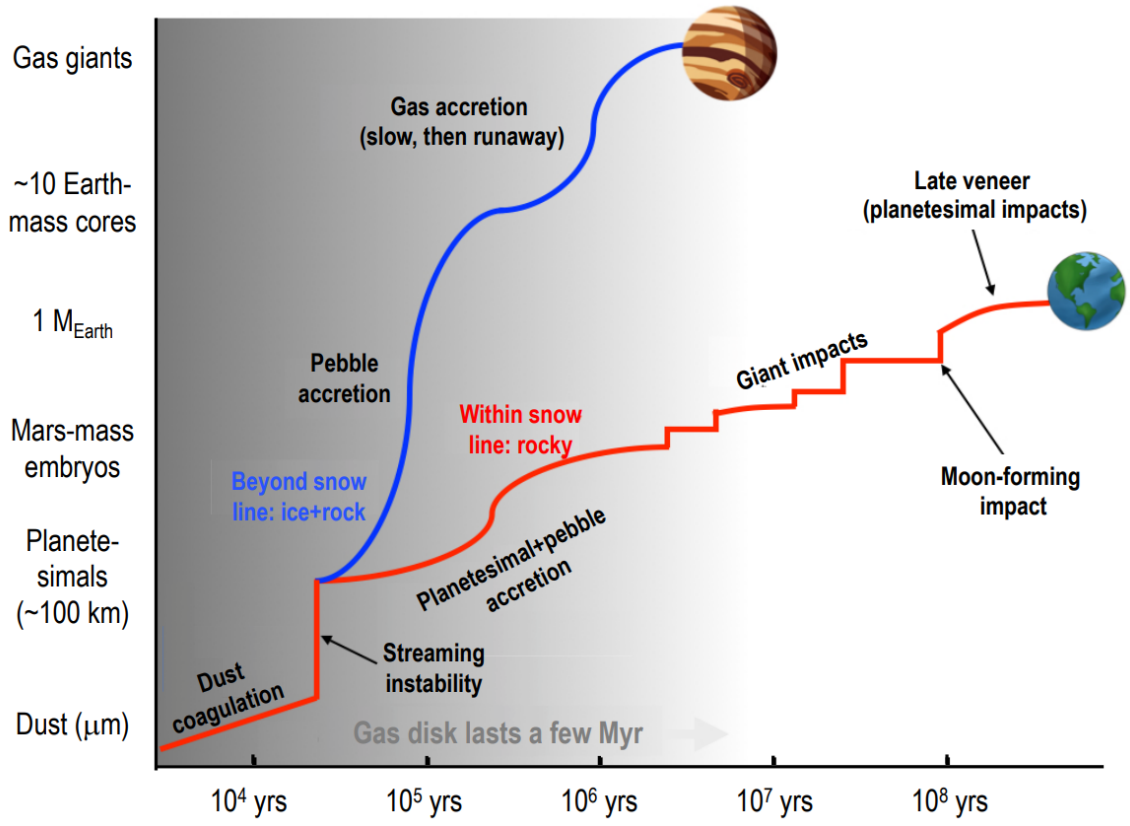


Figure 1.5: A sketch of the planet-formation process and rough size scales of the largest bodies. Image adapted from Meech & Raymond (2020)

is "During which evolutionary stage (in which Class of object) does grain growth happen primarily?" Although it is becoming a consensus that grain growth starts early in the Class 0 phase or the Class I phase, conflicting evidences from observations are presented to whether large (mm-sized or cm-sized) grains present in the Class 0 and Class I disks (Jørgensen et al., 2007; Kwon et al., 2009; Chiang et al., 2012; Han et al., 2023; Zamponi et al., 2024) or not (Zamponi et al., 2021; Ohashi et al., 2022). It is thus crucial to understand the physics and mechanism of grain growth so interpretation of observations can be guided by theory.

A key challenge for grain growth in a gas-dominated environment is that small dust grains tend to co-move with the gas due to efficient gas drag, leading to infrequent collisions with other grains and hindering growth. When grains are smaller than the mean free path of the surrounding gas particles, the gas drag acceleration on dust, given a dust-gas relative velocity Δv, follows the Epstein regime (Epstein, 1924):

$$a_{\rm drag} = \frac{\Delta v}{t_s}, \tag{1.1}$$

where t_s is the "stopping time", describing the degree of coupling between the gas and dust. When the grain size is small, t_s is also small, generally indicating strong gas-dust coupling.

Determining whether t_s is small is not always intuitive, making it useful to compare it with the characteristic dynamical time of the gas. This motivates the definition of the "Stokes number", given by

$$\mathrm{St} = \frac{t_s}{t_L} \tag{1.2}$$

where t_L represents a typical gas turn-over time—generally the time required for the gas to complete one full rotation or cycle, though its exact definition depends on the

context. In circumstellar disks, t_L is typically taken as the local Keplerian period at the dust's location. In the case of turbulence, which governs smaller-scale dynamics within disks, t_L is usually defined as the eddy turn-over time, and the value of St depends on the turbulence intensity. If grain growth in a laminar environment is insufficient to explain observed grain sizes, turbulence is often invoked to enhance grain growth rates.

However, incorporating turbulence into grain growth models presents significant challenges. One major difficulty is the highly nonlinear relationship between the Stokes number and grain-grain collision speed, a key parameter in grain growth (see, e.g., Voelk et al., 1980; Markiewicz et al., 1991a; Pan & Padoan, 2013, 2015). Although numerous studies have explored this relationship using analytical models and numerical simulations in local environments, a complete theoretical framework for grain collisions in turbulent conditions remains elusive.

Further complicating the picture, local models of grain dynamics in turbulence provide only limited insight because grain growth is inherently a non-local process. As grains grow larger (i.e., as St increases), they decouple from the gas and begin to drift relative to the gas, leading to grain concentration and depletion—effects that can only be captured in global models (e.g. Birnstiel et al., 2010, 2012). Since these global models are computationally expensive, they often require parameterization and simplifications, introducing uncertainties into the results.

Additional complexities arise when considering factors such as grain internal structure, grain surface chemistry, and variability in grain-grain collision outcomes. While grains are often modeled as perfect spheres, their actual shapes and structures can be far more intricate, with features like porosity affecting their physical behavior (Dominik & Tielens, 1997; Blum, 2004). Additionally, grain surfaces may be coated with ice, particularly in early, low-temperature environments, altering dust-gas interactions

and influencing collision outcomes (Potapov et al., 2020).

The results of grain-grain collisions typically fall into three categories: coagulation, where grains stick and grow in mass; bouncing, where they collide but retain their original sizes; and fragmentation, where smaller grains break off from the collision. These outcomes have been studied through theoretical models, such as the JKRS theory (Johnson et al., 1971; Sperling, 1964) for grain surface mechanics, and through laboratory experiments such as simulated zero-gravity environment in drop towers (e.g. Blum & Münch, 1993; Weidling et al., 2012). However, the complexities of grain structure and collision parameters introduce significant uncertainties in these predictions.

Despite these challenges, understanding grain growth remains essential for deciphering the early stages of planet formation and laying the groundwork for subsequent evolutionary steps. For instance, the Streaming Instability typically requires a local dust-to-gas mass ratio exceeding 1 (Zhu & Yang, 2020)—one hundred times higher than in dense molecular cloud cores. Achieving such an enhancement requires substantial dust-gas decoupling, likely driven by grain growth. As a result, ongoing studies continue to investigate grain growth from multiple angles, seeking to bridge the gap between theoretical models, simulations, experiments, and observations.

1.4 Outflow Dynamics

Star and planet formation is typically perceived as a process driven by infall (as shown in Fig. 1.1), but the reverse process—outflow—is equally, if not more, important in shaping star formation.

Outflows play a crucial role in redistributing angular momentum in star and planet formation environments, influencing the evolution of stars, disks, and planets. During the earliest accretion phases (early to mid-Class 0), if gas infall is well-ordered (Basu

et al., 2024), outflow can be driven by magnetic fields outside the rotationally supported disk (through magnetic braking of the infalling and rotating inner envelope) even during the earliest Class 0 infall phase, facilitating the transportation of angular momentum (as discussed in sec. 1.2). In the Class 0 and Class I stages, outflows can be launched from either the star or the disk, carrying away angular momentum from their respective sources. If stellar-driven, outflows contribute to the stellar spin regulation; without outflow, stars would rotate much faster than observed. For instance, the Sun, which rotates with a 28-day period, would have retained a much shorter spin period without angular momentum loss. Similarly, circumstellar disks require angular momentum transport to evolve (Hartmann, 1998; Goodson & Winglee, 1999; Mellon & Li, 2008); without efficient redistribution, disk accretion and subsequent planet formation would stall.

Observationally, jets and outflows can be detected due to their size and brightness at some wavelengths (e.g., Fe II emission lines, see Assani et al., 2024), making them accessible probes of star formation (Ray & Ferreira, 2021; Lee et al., 2018, see e.g., fig. 1.6). High-resolution observations continue to refine our understanding of their structure while raising new questions about their origins (Pascucci et al., 2023). Magnetic fields, which connect and regulate gas dynamics across scales, are thought to be the primary driver of jets and outflows. Since jet-scale dynamics are more easily observable than their launching regions near the star or inner disk, studying outflows provides crucial indirect constraints on the conditions and mechanisms governing their formation. Understanding jet launching is, therefore, essential for interpreting observations and linking them to underlying physical processes.

The impact of outflows extends far beyond star and planet formation. A primary component of outflows is the jet, the most energetic form of YSO outflow. In high-mass star formation ($\gtrsim 10 M_\odot$), jets can extend several parsecs in length (e.g.,



Figure 1.6: Jame Web Space Telescope (JWST) image of jet from YSO HH211, showing an extended and colluminated jet. Image adapted from (NASA, 2023)

Fedriani et al., 2018), while in low-mass star formation ($\simeq 1M_{\odot}$), jets can reach distances exceeding 10^4 au (e.g., Caratti o Garatti et al., 2024b). The gas in these jets moves at hypersonic speeds (> 100 km s^{-1}), injecting significant energy back into the surrounding interstellar medium (ISM). On a large scale, these long-reaching jets modify the conditions of surrounding molecular cloud cores, potentially halting star formation within those cores (Federrath, 2016). This has a significant impact on the initial mass function (IMF, the statistical mass distribution of newly formed stars on a giant molecular cloud scale), which is a crucial parameter in galaxy formation and evolution (Guszejnov et al., 2021).

Understanding how jets are powered is crucial for assessing their impact across different scales. Jets are generally believed to originate near the star, yet the star alone cannot drive them—evidenced by the absence of jets around isolated stars, including

our Sun. This suggests that the inner disk plays a central role in jet launching. One possible mechanism is photoevaporative winds, where stellar radiation heats the disk surface and thermally drives an outflow. However, photoevaporative processes are generally too weak to produce the highly collimated and powerful jets observed, particularly jets with speeds greater than 100 km/s (Macías et al., 2016; Rodenkirch et al., 2020).

Instead, magnetic fields in the disk—either inherited from the molecular cloud core or influenced by the stellar magnetic field—are thought to be crucial in launching jets. Since magnetic fields dynamically couple different components of the system, they can, in principle, mediate the transfer of disk rotational energy to power the jet. However, the exact mechanisms behind this process remain uncertain.

Observations of jet rotation have reinforced the idea that rotational energy extracted by magnetic field drives outflows (Chrysostomou et al., 2008). One leading class of models invokes the centrifugal effect (both the magneto-centrifugal disk wind and X-wind model, as discussed in e.g., Blandford & Payne, 1982; Pudritz & Norman, 1983; Shu et al., 1994, 2000), where angular momentum is transferred from the disk to the gas via nearly rigid magnetic field lines. This process accelerates the gas to super-Keplerian rotational speeds, allowing centrifugal forces to launch the outflow. Another class of models focuses on the energetics of rotation (Poynting flux jet and magnetic tower jet, as described in, e.g., Shibata & Uchida, 1986; Lovelace et al., 2001; Lynden-Bell, 2003, 1996), where rotational energy is initially transferred to the magnetic field, generating a strong toroidal component that drives a significant Poynting flux above the disk. This flux then channels energy back into the gas, propelling the outflow. While both classes of models have been extensively studied, a fully self-consistent framework that reproduces key observational features—including the energetics, morphology, and collimation of jets—remains elusive.

Another key component of the outflow is the disk wind, a slower outflow (a few km s^{-1}) compared to the jet, with a wider opening angle of a few tens of degrees (Pascucci et al., 2023). While it provides less feedback on the scale of giant molecular clouds, it dominates mass transport in outflows, making it a crucial factor in regulating disk evolution (Tabone et al., 2020), particularly in governing angular momentum transport. Like jets, disk winds are also believed to be magnetohydrodynamically (MHD)-driven, yet their exact relationship with jets remains unclear. In particular, whether substructures exist within both the disk wind and the jet (de Valon et al., 2022), and if so, how these substructures form, remains an open question.

The dynamics within the jet-launching region is important not only on its own but also for understanding the formation and evolution of the Solar System. Evidence of early solar system evolution, including the possible existence of early solar jets, is recorded in asteroids and meteorites, whose properties and compositions provide a unique probe into the history of the early solar nebula. The outflow may affect, in particular, chondritic meteorites, a type of stony meteorite, that is composed of chondrules—small, spherical grain inclusions—embedded in a silicate matrix. These chondrules are typically millimeter-sized and often display a spherical morphology.

A distinct type of chondrule is the Calcium-Aluminum-rich Inclusion (CAI). Unlike typical chondrules, which are predominantly composed of magnesium-iron silicates, CAIs are enriched in refractory elements that have relatively high sublimation temperatures (Lodders, 2003). Around the young Sun, high temperatures vaporize all elements into the gas phase, and as the gas cools, elements condense sequentially based on their condensation temperatures. Due to their high condensation temperature, CAIs are the first solids to reappear, forming Ca-Al-rich grains near the young star (Woitke et al., 2024).

Meteorite evidence also confirms that CAIs were the earliest solids to form in the

protoplanetary disk, possibly dating back to the Class I or early Class II phase of our solar nebula (see e.g., Bekaert et al., 2021, and references within). However, a longstanding question remains: how did CAIs form so close to the young Sun yet get transported outward to the outer solar system, where they were eventually incorporated into meteorites that later fell to Earth? One proposed mechanism for outward transport is turbulent diffusion, where disk turbulence stochastically spreads particles over large distances (Brownlee et al., 2006; Cuzzi et al., 2003). Another promising candidate is transport by jets and outflows, which, given their direct connection to the inner disk and protostar, could potentially carry CAIs outward while shaping the structure of our protoplanetary disk (Ciesla, 2009).

1.5 Numerical methods

The intricate nature of astrophysical systems often requires numerical simulations to decode their governing mechanisms. While an exhaustive review of simulation techniques lies beyond the scope of this thesis, we summarize the conceptual foundations of these computational tools and outline the principles guiding their application in astrophysical research.

Astrophysical systems–from molecular clouds to galaxies–are predominantly composed of gas[3], which serves as the primary component in most models. Depending on the physical regime being studied, supplementary processes such as magnetohydrodynamics (MHD), gravitational interactions, relativistic effects, and radiation may be incorporated. To enhance realism, additional components such as dust, chemical species, and charged particles may also be included, though these additions increase the complexity and computational cost of simulations. In the context of star and

[3]on very large, cosmological scales, other components, such as dark matter, can become important.

planet formation, the interaction between hydrodynamics (gas and dust dynamics) and magnetic fields plays a crucial role. Therefore, we will focus on the computational techniques used to model these processes.

A cornerstone of astrophysical simulations is strict adherence to conservation laws: mass, momentum, and energy must remain invariant over time. Given the vast spatial scales and extended timescales inherent to these systems, even minor numerical errors in conservation can compound catastrophically. For this reason, preserving these quantities robustly is non-negotiable. While methods such as smoothed particle hydrodynamics (SPH) are also employed (e.g., Price et al., 2018), the finite volume method (FVM) has emerged as the preferred numerical scheme in astrophysics due to its inherent conservation of the five core variables: mass, three components of momentum, and energy (e.g., Fryxell et al., 2000; Teyssier, 2002; Stone et al., 2020).

The finite volume method works by decomposing the simulation domain into discrete cells (control volumes), each small enough to assume uniform gas properties within. At each timestep, the method resolves how conserved quantities propagate between adjacent cells by solving the Riemann problem–a mathematical description of the interaction between two fluid states separated by a discontinuity. For example, when gas in one cell has higher pressure than its neighbor, their interaction generates waves (e.g., shocks or rarefactions) that redistribute mass and energy. A Godunov-type solver approximates these wave dynamics at every cell interface, calculating the net flux of conserved variables across boundaries. This approach ensures strict conservation while naturally capturing discontinuities like shock fronts in supernovae or turbulence in star-forming clouds (Toro, 2009).

Magnetic fields play a pivotal role in many astrophysical systems and are now routinely included in modern simulations. The fidelity of magnetic field evolution hinges on maintaining the divergence-free condition ($\nabla \cdot \mathbf{B} = 0$), a fundamental

constraint from Maxwell's equations. The state-of-the-art constrained transport (CT) algorithm enforces this condition by design, ensuring the magnetic flux through each cell remains zero at all times (Evans & Hawley, 1988). CT achieves this by evolving the magnetic field components on a staggered grid—where the magnetic fields are stored at cell faces—and updating them using the electric field's curl computed at cell edges. This geometric approach inherently preserves $\nabla \cdot \mathbf{B} = 0$ discretely, avoiding ad-hoc corrections required by divergence-cleaning methods. By coupling fluid dynamics with magnetic field evolution, MHD simulations capture critical phenomena such as jet launching, accretion disk stability, and interstellar medium turbulence.

In contrast to continuum-based methods, simulations of discrete systems–such as planetary orbits or dust particle trajectories in gas–focus on solving the equations of motion for individual point masses (e.g., Rein & Liu, 2012). For example, the trajectory of a dust particle is governed by Newton's second law:

$$\frac{d^2\boldsymbol{x}}{dt^2} = \mathbf{a}(\boldsymbol{x}, t), \tag{1.3}$$

where $\mathbf{a}(\boldsymbol{x}, t)$ represents the net acceleration (e.g., gravitational or drag forces). When combined with gas dynamics, this particle-tracking approach enables studies of dust-gas coupling in protoplanetary disks or planetary migration in evolving systems.

1.6 Thesis Outline

This thesis aims to shed light on several key scientific questions outlined in Sections 1.2, 1.3, and 1.4. These questions are investigated in detail in the subsequent chapters through a series of numerical simulations and theoretical analyses. Chapter 2 models grain dynamics and grain growth in protostellar environments, demonstrating that grain growth is slow in laminar protostellar disks. Chapters 3 and 4 model

the collapse of a protostellar core leading to the formation of stars and disks, with a focus on the structure of the protostellar envelope, the effects of non-ideal MHD on disk formation, and the emergence of close ($\sim$100 au) multiple systems with misaligned disks. Chapters 5, 6, and 7 examine jets and outflows, investigating their launching mechanisms. Chapters 5 and 6 utilize 2D axisymmetric and 3D models to study jet launching driven solely by the disk magnetic field. Chapter 7 incorporates a stellar magnetosphere and explores how magnetosphere-disk interactions alter jet-launching behavior compared to the disk-only models. In addition, Chapter 8 presents a post-processing tracer and dust simulation framework, `Arcturus`, which is applied in Chapters 2 and 4 to highlight key processes in each context. The main conclusions of this thesis are summarized in Chapter 9.

Chapter 2

Grain Growth During Protostellar Disk Formation

The work presented in this chapter has been published in the Monthly Notices of the Royal Astronomical Society (MNRAS) with Zhi-Yun Li and Ka Ho Lam as coauthors (Tu et al., 2022).

Abstract: Recent observations indicate that mm/cm-sized grains may exist in the embedded protostellar disks. How such large grains grow from the micron size (or less) in the earliest phase of star formation remains relatively unexplored. In this study we take a first step to model the grain growth in the protostellar environment, using two-dimensional (2D axisymmetric) radiation hydrodynamic and grain growth simulations. We show that the grain growth calculations can be greatly simplified by the "terminal velocity approximation", where the dust drift velocity relative to the gas is proportional to its stopping time, which is proportional to the grain size. We find that the grain-grain collision from size-dependent terminal velocity alone is too slow to convert a significant fraction of the initially micron-sized grains into mm/cm sizes during the deeply embedded Class 0 phase. Substantial grain growth is achieved when the grain-grain collision speed is enhanced by a factor of 4. The dust growth above and below the disk midplane enables the grains to settle faster towards the midplane, which increases the local dust-to-gas ratio, which, in turn, speeds up further growth there. How this needed enhancement can be achieved is unclear, although turbulence is a strong possibility that deserves further exploration.

2.1 INTRODUCTION

The formation of a stellar system can be categorized generally into four classes based on their observational properties such as their spectral energy distribution (Lada, 1987; Andre et al., 1993). These observational differences are believed to be associated with their stages of evolution in the process of star (and planet) formation. In Class 0 sources, the protostar is deeply embedded in the surrounding envelope (Chandler et al., 1998), and during the evolution from Class 0 to Class I, the mass in the envelope is transferred to the protostar and protostellar disk. The system depletes its envelope in the Class II phase, forming a protoplanetary disk. The disk

is eventually depleted in the Class III phase, leaving behind planets orbiting a stellar system.

Planets are formed in circumstellar disks, but exactly when and how their formation starts in the disk remains uncertain. Recent high-resolution surveys of Class II (protoplanetary) disks show substructures that potentially indicate the presence of planets (Zhang et al., 2016; Isella et al., 2016; Fedele, D. et al., 2018; Andrews et al., 2018; Andrews, 2020). Such substructures have now been observed in the younger Class I (Sheehan & Eisner, 2018; Segura-Cox et al., 2020) and even Class 0 disks (Sheehan et al., 2020). Some of the putative planets have inferred masses of the Jupiter or even larger, and may have reached the end of their growth judging from their low accretion rates (Haffert et al., 2019; Cridland et al., 2022).

These observational evidences suggest that at least some planets must have formed early in the process of star formation. In order to form planets, dust grains in the protostellar disk must have grown from their sizes in the interstellar medium (ISM), typically of order ~ 0.1 μm (Mathis et al., 1977b), to sizes that are large enough to partially decouple from the gas and potentially trigger streaming instability to start the formation of planetesimals and ultimately planets. This process demands the formation of a substantial amount of mm/cm-sized grains during the protostellar phase.

There are evidences for large mm/cm sized grains in protostellar sources based on the spectral energy distribution (Testi et al., 2014). Specifically, a value of the opacity index β in the millimeter regime ($= \alpha - 2$ in the optically thin limit, where α is the spectral index) of order 1 or less is usually interpreted as evidence for mm/cm-sized grains (Draine, 2006; Beckwith, 1999). For example, Galametz et al. (2019) found 7 out of 10 observed Class 0 sources exhibit $\beta_{1-3\mathrm{mm}} < 1$ within 1σ after accounting for free-free emission coming from the central protostar. Other observational studies

such as Jørgensen et al. (2007), Tobin et al. (2013) and Kwon et al. (2015) have shown additional examples of protostellar sources exhibiting $\beta < 1$, indicating that mm/cm-sized grains are prevalent in the earliest phases of star formation[1].

How the grains grow from (sub)μm sizes to mm/cm sizes in the protostellar phase is unclear. An early attempt to address this question was made by Morfill et al. (1978), who performed a dust evolution calculation on a coarse 2D (axisymmetric) grid with an underlying analytic 1D (spherical) gas dynamic model. They found early grain growth to sizes up to $\sim 100\mu$m in the collapsing envelope around the protostar on a time scale of 1.67 Myr, and proposed the idea that fast grain growth during the protostellar collapse may form seeds to later planet formation. Birnstiel et al. (2010) improved upon Morfill et al. (1978) by including both the collapsing protostellar envelope and a growing protostellar disk, as well as new physical ingredients for grain growth, notably, turbulence-enhanced grain-grain collision speeds (see e.g. Voelk et al., 1980; Markiewicz et al., 1991b; Ormel & Cuzzi, 2007). However, their analytical treatment of the gas dynamics is essentially one dimensional (in the cylindrically radial direction), which leaves open the question of how the dust and gas enter the growing disk from the collapsing envelope from all directions and how the grains move and grow inside the disk as they gradually settle towards the midplane gravitationally. Suttner & Yorke (2001) performed a series of 2D (axisymmetry) models, but their calculations focused primarily on the effects of relatively moderate grain growth (to several tens of microns) on the optical/IR appearance of disks through its impact on dust opacities. Hirashita & Li (2013) examined the grain growth in dense molecular cloud cores and concluded that the core lifetime must be several times the free-fall time to grow grains from the classical ISM sizes to micron-sizes (see also Ormel et al.,

[1]There are, however, counter examples where the spatially resolved opacity index β is close to the ISM value that is indicative of small grains (e.g., Ohashi et al. (2022) for the L1527 protostellar disk).

2009). Wong et al. (2016) extended Hirashita & Li (2013) to show that the dense molecular cores have too low densities for grains to grow to mm-sizes effectively. More recently, Ohashi et al. (2021) showed the existence of dust ring structures around Class 0/I objects using analytical arguments assuming the dust growth time scale is comparable to the disk age, which are consistent with the ALMA observations. The existence of a dust ring also agrees with the need for the formation of pebble drifting in inner disks to allow pebble accretion, which can grow planets more effectively than the accretion of large planetsimals (Kobayashi & Tanaka, 2021). Tsukamoto et al. (2021) proposed the idea of increased grain growth rate by circulating large grains in disks via "ash-fall", in which large grains in the inner disk are carried out of the disk by magnetized outflows and re-enter the disk at large radii.

In this work, we aim to investigate the dust dynamics and growth during the protostellar phase of the star and disk formation in two dimensions (2D) using a radiation hydrodynamical code, under the assumption of axisymmetry. We focus on grain growth to mm/cm sizes that are important for (sub)millimeter and centimeter dust continuum observations and planet formation. In section § 2.2 we describe the hydro and dust simulation methods. In section § 2.3 and section § 2.4 we present the results of the hydro and dust models respectively. We find that it is difficult to produce a significant amount of large mm/cm-sized grains during the protostellar phase in the baseline case where grains collide with one another only through the size-dependent dust-gas drift velocities (§ 2.4.1) and that significant growth can be achieved if the grain-grain collision speed is enhanced by a factor of 4 (§ 2.4.2). We obtain a simple expression for the grain size e-folding time in section § 2.5, which is used to understand the numerical results on grain growth in section § 2.6. We conclude in section § 2.7.

2.2 PROBLEM SETUP

2.2.1 Governing Equations for Gas Dynamics

Protostellar disk formation in dense cores of molecular clouds is a complex process involving turbulence and magnetic fields (and associated non-ideal MHD effects; see Li et al., 2014a, for a review). As a first step in exploring how the grains grow as the infalling envelope is transformed into a rotationally supported disk, we have decided to limit our investigation to the simplest case of the collapse of a rotating core without any magnetic field or turbulence. The dynamics of core collapse and disk formation are governed by the following radiation hydrodynamical equations:

$$\frac{\partial \rho}{\partial t} + \nabla \cdot (\rho \boldsymbol{u}) = 0, \tag{2.1}$$

$$\rho \frac{\partial \boldsymbol{u}}{\partial t} + \rho \left(\boldsymbol{u} \cdot \nabla\right) \boldsymbol{u} = -\nabla P - \rho \boldsymbol{g} + \nabla \cdot \boldsymbol{\Pi} - \boldsymbol{G}_r, \tag{2.2}$$

$$\frac{\partial E}{\partial t} + \nabla \cdot [(E + P)\boldsymbol{u} + \boldsymbol{\Pi} \cdot \boldsymbol{v}] = \rho \boldsymbol{u} \cdot \boldsymbol{g} - G_r^0, \tag{2.3}$$

$$\frac{\partial \boldsymbol{I}}{\partial t} + c\boldsymbol{n} \cdot \nabla \boldsymbol{I} = \boldsymbol{S}(\boldsymbol{I}, \boldsymbol{n}), \tag{2.4}$$

where $\rho, \boldsymbol{u}, P, E$ and I are gas density, velocity, gas pressure, total energy density and frequency-integrated specific intensity respectively. $\boldsymbol{g}$ is the gravitational acceleration, including both gas-self gravity and the gravity due to the central protostar. $\boldsymbol{G}_r$ and G_r^0 are radiative force and the radiative heating/cooling rates respectively. The last equation, equation (2.4), is the standard time-dependent radiative transfer equation for the specific intensity I along direction $\boldsymbol{n}$, with S denoting the source term (representing additional cosmic-ray heating).

The quantity $\mathbf{\Pi}$ is the viscous stress tensor given by

$$\Pi_{ij} = \rho\nu\Big(\frac{\partial u_i}{\partial x_j} + \frac{\partial u_j}{\partial x_i} - \frac{2}{3}\delta_{ij}\nabla\cdot\boldsymbol{u}\Big) \tag{2.5}$$

where ν is the the kinematic viscosity. $\mathbf{\Pi}$ is used to model angular momentum transport in the absence of a magnetic field. We adopt a standard β-parametrization for the kinematic viscosity ν (see e.g. Kuiper et al., 2010)

$$\nu = \beta_\nu \Omega_K(r) R^2, \tag{2.6}$$

where R is the cylindrical radius and $\Omega_K(r) = \sqrt{GM(r)/r^3}$, with $M(r)$ denoting the mass enclosed within a sphere of radius r. For a rotationally supported disk, the quantity Ω_K would be the orbital angular velocity and the dimensionless parameter β_ν would be related to the standard $\alpha-$viscosity parameter by $\beta_\nu = \alpha(H/R)^2$ where H is the disk scale height.

2.2.2 Hydrodynamic Numerical Method

The governing equations are solved with the Athena++ code (Stone et al., 2020) under the assumption of (2D) axisymmetry around the rotation axis in a spherical polar coordinate system (r, θ, ϕ). We adopt a computation grid with logarithmic spacing in the radial direction and constant spacing in the θ-direction. Logarithmic spacing has the advantage of providing higher resolution at smaller radii relevant to disk formation, at the expense of producing larger cells at larger radii, which are not as critical for our analysis. The grid extends logarithmically in the radial direction from 10 to 10^4 au with 320 cells, and linearly in the θ-direction from 0 to π with 208 cells.

There are 4 boundary conditions treated in the simulation. The inner and outer

radial boundaries are treated in the same way, with a semi-outflow boundary condition where material is allowed to exit the computational domain but not enter back in. The standard reflective boundary conditions are imposed at the poles.

The simulation is initialized with an uniform temperature of 8K and a power-law density profile following Shu (1977)

$$\rho_{\rm g}(r, t = 0) = \frac{A_s c_s^2}{4\pi G r^2} \tag{2.7}$$

where $c_s = \sqrt{\frac{k_b T}{\mu m_H}}$ is the isothermal sound speed and A_s is chosen to be 3.11. This yields $\sim 1.66 M_\odot$ inside the simulation domain. The central protostar has a small initial mass of $0.0017 M_\odot$, which is increased as mass is accreted across the inner radial boundary. Effects of stellar radiation are included using the stellar evolution model of Hosokawa & Omukai (2009) that assumes an accretion rate $10^{-6} M_\odot$ yr^{-1}. It yields a stellar luminosity L_* and a stellar radius R_* for a given stellar mass M_*. The total luminosity is given by

$$L = L_* + L_{\rm acc} = L_* + \frac{G\ M_*\ \dot{M}_*}{R_*} \tag{2.8}$$

where the accretion rate $\dot{M}_*$ is found by measuring the amount of mass going through inner boundary in our simulation. The total luminosity is then distributed uniformly onto the inner boundary of our simulation at $r = 10$ au for the radiative transfer calculation by the code.

For the radiative transfer in the simulation domain, we adopted an opacity κ_ν model from Laor & Draine (1993) and Kuiper et al. (2010), with a constant dust-to-gas ratio of 0.01. To speed up the simulation, we reduced the speed of light by a factor of 10^4 (see e.g. Chang et al., 2020).

We assume ϕ displacement symmetry but allow for a ϕ direction velocity. The initial ϕ direction velocity is determined by the solid-body rotation rate $\Omega_{\rm init}$, taken to be 3.75 rad/Myr. Viscosity is also included using the model described by equation 2.6, with a constant $\beta_\nu = 0.001$. This combination of parameters yields a hundred au-sized disk towards the end of the simulation.

2.2.3 Modeling Grain Dynamics and Growth

We post-process the hydrodynamical outputs from Athena++ for grain dynamics and coagulation calculations. The hydrodynamical results are output at 50 years intervals so that the hydrodynamical evolution can be reconstructed with linear interpolation between consecutive frames. In this study, we consider spherical dust particles, with radius determined by the mass m of the particle

$$s = \Big(\frac{3\ m}{4\pi\tilde{\rho}_{\rm dm}}\Big)^{1/3} \tag{2.9}$$

where $\tilde{\rho}_{\rm dm}$ is the material density of the grain.

The grains are evolved on a grid with the same resolution as the hydrodynamical grid, but only include the upper hemisphere by taking advantage of the disk being symmetric about the midplane. Reflective boundary conditions are applied on the midplane. The grain sizes are discretized into 105 bins logarithmic spaced from 0.1 μm to 1 cm. The number of size bins is chosen to be as large as possible to minimize numerical diffusion into large grains (see e.g. Lombart & Laibe, 2021), while keeping a reasonable simulation run-time. In all models, the grain everywhere is initialized from 0.1 μm to 1 μm following an MRN-distribution[2] $n(s) \propto s^{-3.5}$ (Mathis et al., 1977b),

[2]Our choice of an initial maximum grain size of 1 μm is motivated by the detection of mid-infrared emission in dense cores of molecular clouds produced via scattering by micron-sized grains (Steinacker et al., 2010)

assuming an initial dust-to-gas mass ratio 0.01. We evolve the number density in each grain size bin (N_i) in our numerical model, which is related to the usual number density per unit size $n(s)$ through

$$N_i = \int_{s_i}^{s_{i+1}} n(s) ds \tag{2.10}$$

where s_i and s_{i+1} are the grain sizes in two adjacent size bins.

The grain distribution on the mesh grid is initialized approximately 2500 years before the appearance of a disk. Because the high density region of the envelope falls quickly through our inner boundary prior to disk formation and the remaining envelope is orders of magnitude less dense than the majority of the disk, grains are not expected to grow significantly before the formation of the disk because of the low density and short core collapse time (see section § 2.5).

Grain dynamics

The acceleration of grains of different sizes can be modeled with the pressure-less non-viscous Navier-Stokes equations in spherical polar coordinate, given by (Acheson & Acheson, 1990)

$$\begin{aligned}
\frac{\partial u_r}{\partial t} &= F_r - u_r \frac{\partial u_r}{\partial r} - \frac{u_\phi}{r \sin\theta} \frac{\partial u_r}{\partial \phi} - \frac{u_\theta}{r} \frac{\partial u_r}{\partial \theta} + \frac{u_\theta^2 + u_\phi^2}{r} \\
\frac{\partial u_\theta}{\partial t} &= F_\theta - u_r \frac{\partial u_\theta}{\partial r} - \frac{u_\phi}{r \sin\theta} \frac{\partial u_\theta}{\partial \phi} - \frac{u_\theta}{r} \frac{\partial u_\theta}{\partial \theta} - \frac{u_r u_\theta - u_\phi^2 \cot\theta}{r} \\
\frac{\partial u_\phi}{\partial t} &= F_\phi - u_r \frac{\partial u_\phi}{\partial r} - \frac{u_\phi}{r \sin\theta} \frac{\partial u_\phi}{\partial \phi} - \frac{u_\theta}{r} \frac{\partial u_\phi}{\partial \theta} - \frac{u_r u_\phi + u_\phi u_\theta \cot\theta}{r}
\end{aligned} \tag{2.11}$$

where F_r, F_θ, and F_ϕ denote the body force per unit mass acting on the dust grains, including both gravity and hydrodynamical drag. u_r, u_θ and u_ϕ are the dust velocities in r, θ and ϕ directions respectively. In the remainder of this subsection, we will use

these notations to represent dust grain speeds. Because we are interested in relatively small grains ($0.1\,\mu\text{m} \rightarrow 1\,\text{cm}$), the drag force is in the Epstein regime, where the stopping time t_s is given by (Epstein, 1924; Armitage, 2015)

$$t_s = \frac{\tilde{\rho}_{\text{dm}} s}{\rho_{\text{g}} v_{\text{th}}} \tag{2.12}$$

where $v_{\text{th}} = \sqrt{\frac{8k_bT}{\pi\mu m_H}}$ is the gas thermal velocity, k_b and T are the Boltzmann constant and temperature respectively, $\mu = 2.33$ and m_H are the mean particle weight and hydrogen mass, and ρ_{g} is the gas density at the location of the dust grains. The force per unit volume $\boldsymbol{F}$ is given by

$$\boldsymbol{F} = \rho\boldsymbol{g} + \rho\frac{\boldsymbol{u}_{\text{gas}} - \boldsymbol{u}_{\text{dust}}}{t_s} \tag{2.13}$$

where $\boldsymbol{g}$ is the local gravitaional acceleration and $\boldsymbol{u}_{\text{gas}}$ and $\boldsymbol{u}_{\text{dust}}$ are gas and dust velocities respectively.

As we show in section § 2.6.1, in the parameter regime of interest to us, the dust velocity is close to the "terminal velocity" (the velocity that enables the gas drag to balance all other forces acting on a grain), especially in the disk where most of the grain growth occurs. We are thus motivated to adopt the terminal velocity approximation, where the dust velocity components are given by

$$\boldsymbol{u}_{\text{dust}} = \boldsymbol{u}_{\text{gas}} + \zeta t_s \tag{2.14}$$

where the vector ζ is the sum of all forces except the gas drag acting on a unit dust mass (i.e., the net dust acceleration to be balanced by gas drag force per unit mass),

with its three components given by

$$\begin{aligned}\zeta_r &= g_r + \frac{u_{\phi,\mathrm{gas}}^2 + u_{\theta,\mathrm{gas}}^2}{r} \\ \zeta_\theta &= g_\theta - \frac{u_{\mathrm{r,gas}} u_{\theta,\mathrm{gas}} - u_{\phi,\mathrm{gas}}^2 \cot\theta}{r} \\ \zeta_\phi &= g_\phi - \frac{u_{\mathrm{r,gas}} u_{\phi,\mathrm{gas}} + u_{\phi,\mathrm{gas}} u_{\theta,\mathrm{gas}} \cot\theta}{r}\end{aligned} \tag{2.15}$$

This approximation is equivalent to the steady-state assumption adopted by Nakagawa et al. (1986) for the dust dynamics. It greatly simplifies the treatment of the grain dynamics, enabling us to focus on grain growth, which is more computationally expensive.

Grain spatial transportation

The grain spatial transportation is modeled with the advection equation

$$\frac{\partial N}{\partial t} = -\nabla \cdot (N \boldsymbol{u}) \tag{2.16}$$

where N and $\boldsymbol{u}$ are local dust number density and dust velocity respectively. We ignore diffusion because the thermal speed of all grains are less than a few cm/s, which is negligible comparing to their bulk speed ($> 10^3$ cm/s). For the i^{th} grain size bin in a cell located at (I, J) ($\hat{r}$ direction indexed by $\{I\}$ and $\hat{\theta}$ indexed by $\{J\}$), we evolve the number density by solving the discretized advection equation at cell edges:

$$\Delta N_i^{(I,J)} = \Big(\sum_{\text{edges}} \text{Flux} \Big) \Delta t \tag{2.17}$$

In our models, there are two edges in the $\hat{r}$ direction and two edges in the $\hat{\theta}$ direction. The flux through the radial boundary between cells indexing $(I-1, J)$ and (I, J) is

$$\text{Flux}_{I-\frac{1}{2}} = \begin{cases} u_{r,i}^{(I-\frac{1}{2},J)} A^{(I-\frac{1}{2},J)} N_i^{(I-1,J)}, & \text{if } u_{r,i}^{(I-\frac{1}{2},J)} > 0 \\ u_{r,i}^{(I-\frac{1}{2},J)} A^{(I-\frac{1}{2},J)} N_i^{(I,J)}, & \text{if } u_{r,i}^{(I-\frac{1}{2},J)} < 0. \end{cases} \tag{2.18}$$

where $u_{r,i}^{(I-\frac{1}{2},J)}$ is the interpolated radial speed at cell edge and $A^{(I-\frac{1}{2},J)}$ is the area of the cell edge.

Similarly the flux through the radial boundary between cells indexing (I, J) and $(I+1, J)$ is

$$\text{Flux}_{I+\frac{1}{2}} = \begin{cases} -u_{r,i}^{(I+\frac{1}{2},J)} A^{(I+\frac{1}{2},J)} N_i^{(I,J)}, & \text{if } u_{r,i}^{(I+\frac{1}{2},J)} > 0 \\ -u_{r,i}^{(I+\frac{1}{2},J)} A^{(I+\frac{1}{2},J)} N_i^{(I+1,J)}, & \text{if } u_{r,i}^{(I+\frac{1}{2},J)} < 0. \end{cases} \tag{2.19}$$

where $u_{r,i}^{(I+\frac{1}{2},J)}$ is the interpolated radial speed at cell edge and $A^{(I+\frac{1}{2},J)}$ is the area of the cell edge. Note the leading negative sign in equation 2.19 reflects the causation that a positive flux from cell (I, J) to cell $(I+1, J)$ results in a net lost in cell (I, J). Flux in the $\hat{\theta}$ direction can be calculated with the same method. The algorithm is similar to the one used in Birnstiel et al. (2010) (equation A4, A5 within).

At the boundaries in the radial direction, the speed at each boundary is taken to be the value at the nearest cell if the flow is outbound from the simulation domain and zero if the flow is inbound. At the boundaries in the θ direction, the speed at each boundary is taken to be 0 because of symmetry.

Grain growth

Grain growth is calculated within each cell at each time step with the Smoluchowski equation (Smoluchowski, 1916) following Birnstiel et al. (2010). We adopted

the Smoluchowski equation for re-distributing grain species i, j, k within a cell:

$$\frac{\partial n_k}{\partial t} = \iint_0^\infty M_{ijk} n_i n_j ds_i ds_j \tag{2.20}$$

where the kernal M_{ijk} is defined as

$$\begin{aligned} M_{ijk} =& \frac{1}{2} K_{ij} \delta(m_i + m_j - m_k) - K_{ij} \delta(m_j - m_k) \\ &+ \frac{1}{2} L_{ij} S_{ijk} - L_{ij} \delta(m_j - m_k) \end{aligned} \tag{2.21}$$

where m_i, m_j and m_k are the masses of individual grains and K_{ij} and L_{ij} are the coagulation kernel and fragmentation kernel respectively. S_{ijk} describes the distribution of fragments in a collision. In reality, the best description of grain coagulation and fragmentation is to use a function describing the distribution of grain mass in the aftermath of a collision (see e.g. Hasegawa et al., 2021; Kobayashi & Tanaka, 2010). As a first step to understand the grain growth in an actively forming protostellar disk, we have included coagulation but not fragmentation, which should yield an upper limit to the growth. We emphasize this idealized assumption by separating perfect sticking from all other processes in equ. 2.21. As we will see in § 2.4.1 below, even with this optimistic assumption, it is difficult to grow a substantial amount of large mm/cm grains in the simplest, baseline case. Including fragmentation would exacerbate the difficulty.

Under the assumption above, we have

$$K_{ij} = \chi \cdot \Delta u_{ij} \sigma_{\mathrm{geo},ij} = \chi \cdot \Delta u_{ij} \cdot \pi (s_i + s_j)^2 \tag{2.22}$$

$$L_{ij} = 0 \tag{2.23}$$

where Δu_{ij} is the relative speed between grains in bin i and j; $\sigma_{\mathrm{geo},ij}$ is the geometric cross-sectional area between grains of size s_i and s_j. $\Delta u_{ij} = |\boldsymbol{u}_i - \boldsymbol{u}_j|$ describes the relative speed between grains in two size bins with speeds $\boldsymbol{u}_i$ and $\boldsymbol{u}_j$, whose values are taken to be grain speeds at the cell centers.

Note that we used only the grain drift velocity relative to the gas due to the body force in computing the relative speed for grain coagulation. This relative speed can potentially be greatly increased by effects not included in our calculations, such as turbulence (Voelk et al., 1980; Markiewicz et al., 1991b; Ormel & Cuzzi, 2007). To account for such possibilities, we have included an enhancement factor χ in the equation (2.22) for the coagulation rate, with $\chi = 1$ corresponding to the lower limit for the grain growth. We show in the Appendix that the Brownian motion does not affect the growth to large grains significantly.

In the numerical model, the Smoluchowski equation must be discretized as

$$\frac{\Delta N_k}{\Delta t} = \sum_{ij} M_{ijk} N_i N_j \tag{2.24}$$

where N_i, N_j and N_k are the number density of grain species i, j and k respectively (equation 2.10). Because of the discretization of grain masses, $m_i + m_j$ can fall between two consecutive bins with m_k and m_{k+1}. In this case we modify the delta function in the kernel (equation 2.21) to distribute the mass into both size bins in the following way:

$$\delta(m_i + m_j - m_k) \rightarrow \begin{cases} \frac{m_i+m_j-m_k}{m_{k+1}-m_k}, & \text{if } m_k \leq m_i + m_j \leq m_{k+1} \\ \frac{m_i+m_j-m_{k-1}}{m_k-m_{k-1}}, & \text{if } m_{k-1} \leq m_i + m_j \leq m_k \\ 0, & \text{otherwise.} \end{cases} \tag{2.25}$$

This modified δ function ensures mass conservation and suppresses the numerical

"leak" of grains to larger size (see e.g. Lombart & Laibe, 2021). Because grain growth rate is significant only in and around the disk, where the density is highest, we perform grain coagulation calculations only in cells where hydro density is higher than $4 \cdot 10^{-17}$ g/cm^3. This region includes the entire disk at all times.

2.2.4 Lagrangian Treatment of Dust Particles

To verify the velocities obtained by the terminal velocity approximation (equation 2.14) is a reasonable estimate of the grain speeds at the cell locations, we perform a series of simulations with the Lagrangian dust particles, and compare the speeds obtained with the terminal velocity approximation. Similar to the Eulerian dust simulation outlined in the last subsection, the Lagrangian particle simulations are done by post-processing the hydrodynamic simulation.

Each particle in the Lagrangian simulation is independently evolved in a 3D Cartesian coordinate. The particles move within the gas under the influence of both gravity and hydrodynamics drag force. The location of each particle is updated at every time step, with

$$\Delta \boldsymbol{x} = \boldsymbol{u}_{\rm par} \Delta t + \frac{1}{2} \boldsymbol{a} \Delta t^2 \tag{2.26}$$

where Δt is the integration time step, $\boldsymbol{u}_{\rm par}$ is the dust velocity at the last time step and $\boldsymbol{a}$ is the instantaneous acceleration, given by

$$\boldsymbol{a} = \boldsymbol{g} + \boldsymbol{a}_{\rm drag} = \boldsymbol{g} + \frac{\boldsymbol{u}_{\rm gas} - \boldsymbol{u}_{\rm par}}{t_s} \tag{2.27}$$

where $\boldsymbol{g}$ is the local gravitational acceleration, $\boldsymbol{u}_{\rm gas}$ is the local gas velocity, $\boldsymbol{u}_{\rm par}$ is the velocity of the particle, and t_s is the stopping time. The stopping time can be very small for the smallest grains in the highest density regions of the disk, which severely limits the time step Δt that is used to evolve all Lagrangian particles at

the same time. To speed up the computation, we force those particles with stopping times smaller than a small floor value of $t_{s,\min} = 0.01$ yrs to move together with the gas, which is physically reasonable since such particles are essentially tracer particles of the gas. This approximation does not affect the main purpose of the Lagrangian simulation, which is to test the validity of the terminal velocity approximation for relatively large particles (e.g., mm/cm sized grains; see § 2.6.1 below), which tend to have stopping times much larger than 0.01 years.

The local hydrodynamical quantities (ρ, T, $\boldsymbol{g}$, $\boldsymbol{u}_{\rm gas}$) at the locations of the dust particles are obtained using the Triangular-Shaped-Cloud (TSC) algorithm (Hockney & Eastwood, 1981) and projected onto the Cartesian coordinate.

The Lagrangian particle simulations are initialized at the same time as the Euler simulations. At initialization, we put 400,000 particles with the same size in the simulation domain between 10 and 8000 au with pseudo-random locations, with proportionally more particles at locations where the gas density is higher. The particles are then evolved spatially with integration method described by equation (2.26).

2.3 Hydro results

We start with a discussion of the gas dynamics of the core collapse and disk formation and evolution, which forms the basis for our grain growth calculations.

Fig. 2.1 shows the mass and luminosity of the central protostar in our model. The vertical line shows the stellar properties at the time ($t = 40,000$ yrs) when the dust simulation was initialized. During the simulation of dust grains, the star grows from ~ 0.3 to 0.6 $M_\odot$. The total (stellar and accretion) luminosity stays between 25 and 30 $L_\odot$ after the disk forms; the sudden drop in luminosity at ~ 42000 years is caused by the reduction of mass accretion rate onto the central star due to disk formation.

Fig. 2.1 also shows the mass of the "disk", defined to be anywhere with the gas

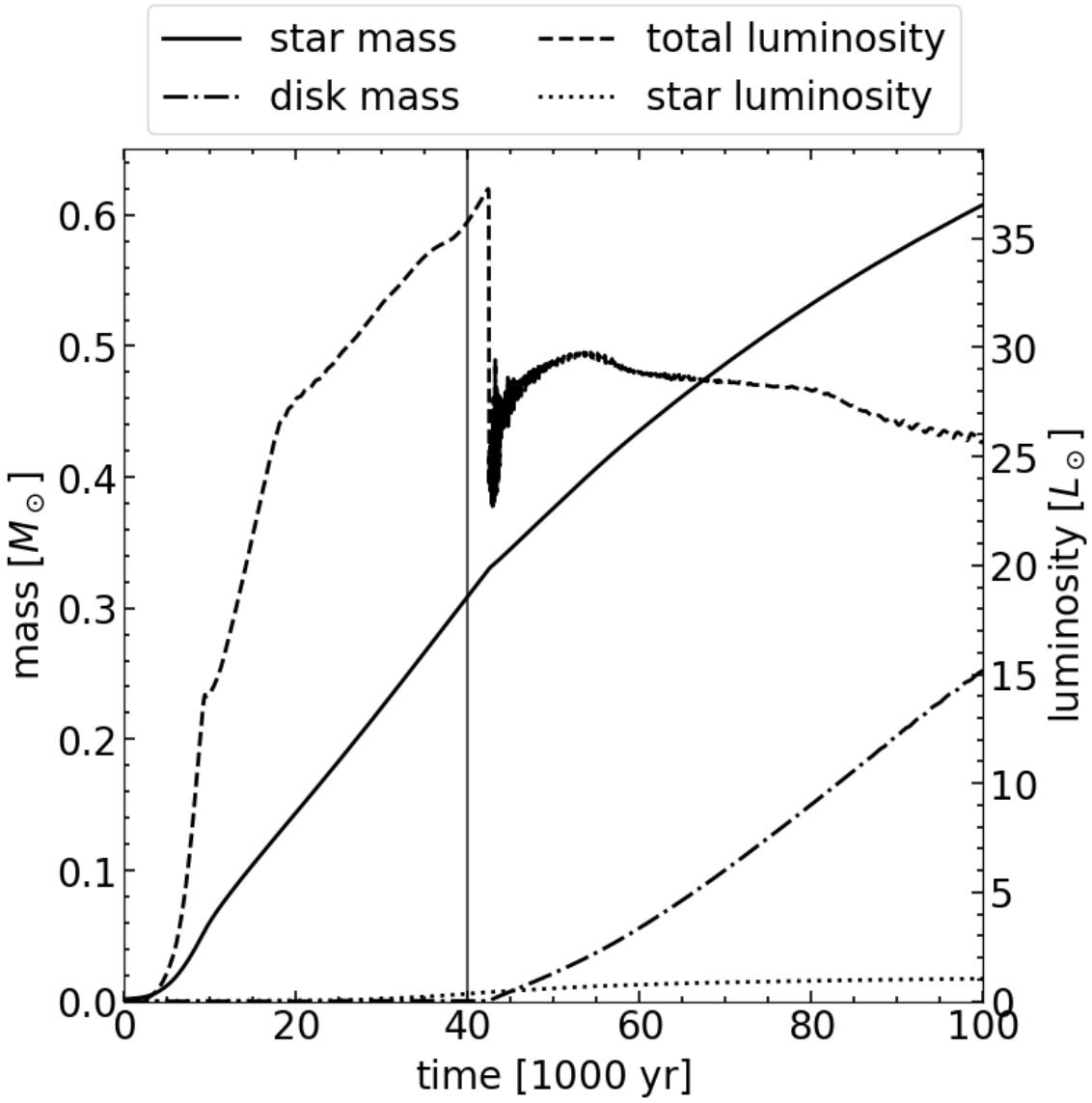


Figure 2.1: Stellar properties and disk mass during the gas simulation. The solid and dash-dotted lines are the star mass and disk mass respectively; dotted line and dashed line are the star luminosity (L_*) and total luminosity (L in equation 2.8) respectively. The vertical line at $t = 40,000$ years shows the starting time of the dust simulations.

density $> 4 \cdot 10^{-16}$ g cm^{-3}. In fig. 2.2 we show the meridian density distributions at four representative times, when the disk size is, respectively, 100, 150, 200 and 250 au, with the "disk" boundary marked by the black dashed contour in each panel. Our analysis of the dust below will focus on the latter three times. We choose the $4 \cdot 10^{-16}$ g cm^{-3} cut-off density because its location is close to a sudden density increase from the rapidly infalling "envelope" to the "disk" at most times during the simulation. The solid black contour is the boundary in which dust coagulation is calculated, located at a gas density $4 \cdot 10^{-17}$ g cm^{-3}. The region is chosen to fully enclose where dust coagulation happens rapidly. Dust coagulation outside occurs at a negligible rate that can be ignored.

The meridional gas velocities in the $\hat{r}$ and $\hat{\theta}$ directions are shown in fig. 2.3. Gas velocities at other times are similar to the selected frame. We observe that u_r is positive in some parts of the disk due to (viscous) angular momentum transport. In the majority of the disk, u_θ is pointing towards the midplane, with the exception at the innermost part of the disk and the edge of the disk. At the innermost part of the disk, an outgoing flow at the edge of the disk "shears" the in-going disk midplane, causing a circular motion at $\sim$ 20 au. This feature can be numerical due to the existence of an inner boundary at 10 au. At the outer (radial) edge of the disk, quickly infalling envelope encounters the expanding disk, forcing some of the gas to go around the disk and to move away from the midplane.

As expected, the gas in the disk rotates at a speed below the local Keplerian speed because of the outward pressure gradient force. In Fig. 2.4, we plot the rotation speed and the local Keplerian speed as well as the fractional deviation from the local Keplerian speed on the midplane, $|u_\phi - v_K|/v_K$, at the time when the disk radius is about 200 au. For comparison, we have plotted the analytic prediction from Nakagawa et al. (1986). The slight difference between the numerical and analytical values are

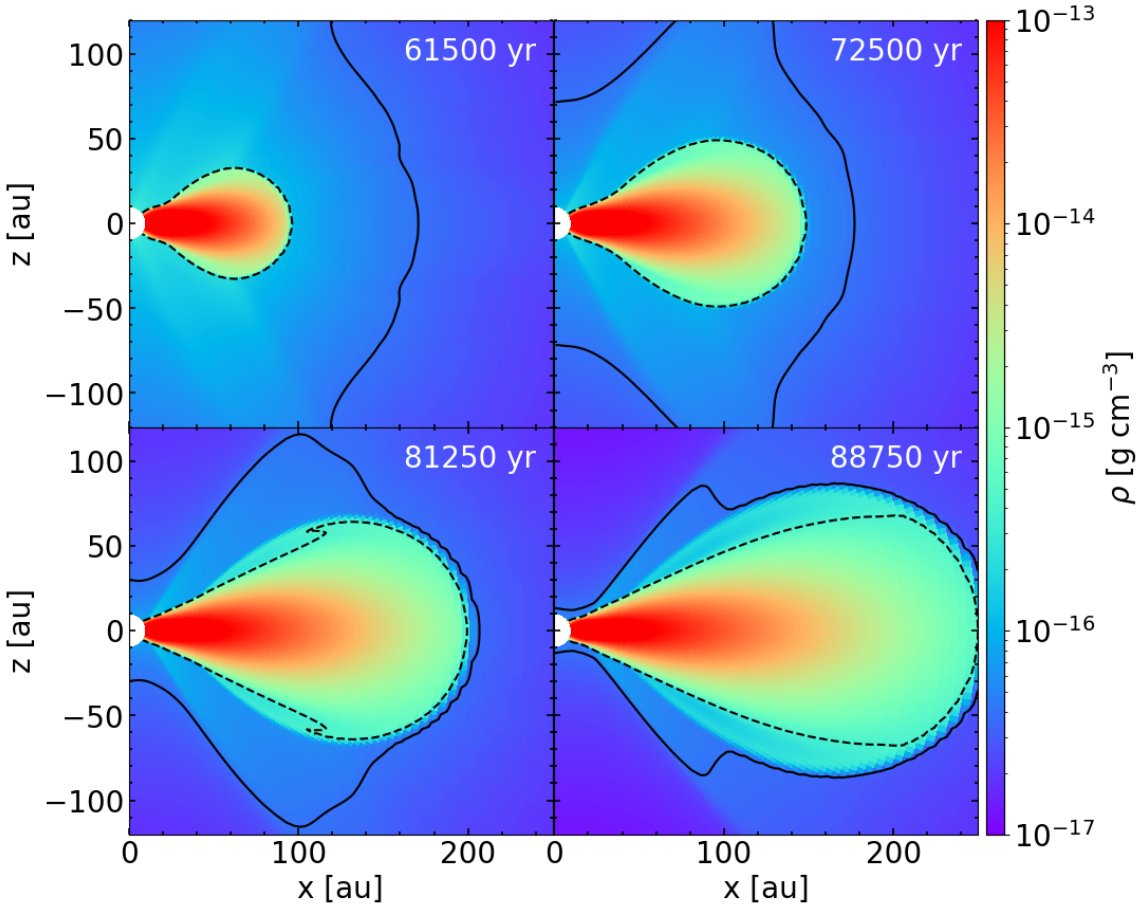


Figure 2.2: Hydrodynamical disk densities. Four panels are the disk density when the disk is approximately 100, 150, 200 and 250 au. Corresponding times of the frames are shown in each panel. The black dashed line is the location where gas density is 4×10^{-16}g cm^{-3}, where our definition of the boundary of the disk is located. The solid black line is the boundary in which dust coagulation is calculated, where gas density is $> 4 \times 10^{-17}$g cm^{-3}.

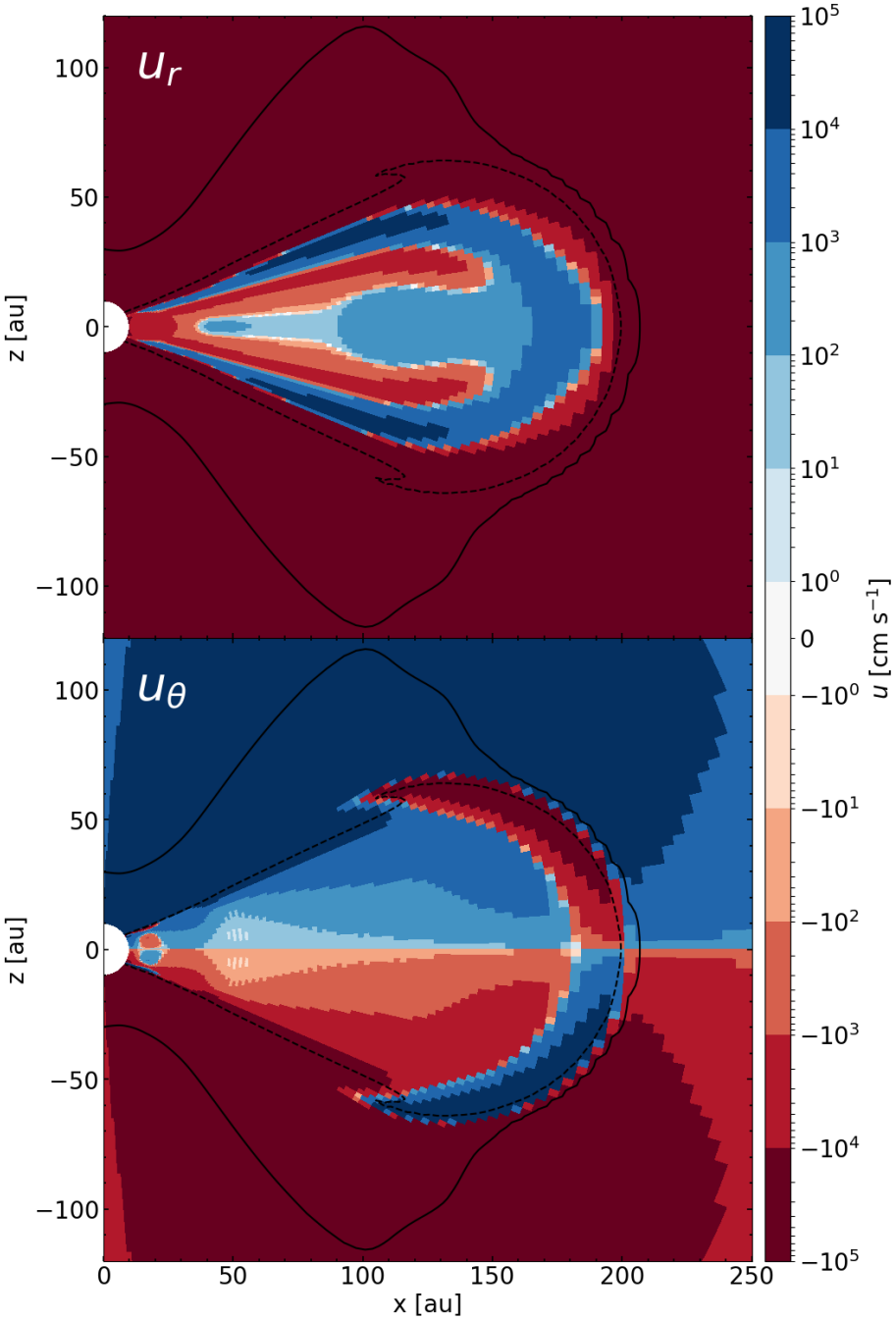


Figure 2.3: The speeds in $\hat{r}$ direction and $\hat{\theta}$ direction are shown in the upper and lower panels respectively. The figure is taken when the disk radius is about 200 au. At other times in the simulation when there is a disk, the velocity field is similar to the ones showing here.

due to the inclusion of self-gravity in our simulation. As is well known, this sub-Keplerian gas rotation is the cause of the inward radial dust migration, which plays a key role in the grain growth and loss near the disk midplane.

2.4 Dust Results

Because dust coagulation is only modeled in the Eulerian models, we focus on the Eulerian results in this section. The Lagrangian results will be discussed in section § 2.6.1 in connection with the terminal velocity approximation.

2.4.1 The Baseline Model

In the baseline model, we only consider the bulk drift motion of the dust grains in the laminar disk without any sub-grid model to enhance the grain-grain collision speed (i.e., setting the enhancement factor χ in equation (2.22) to $\chi = 1$). In fig. 2.5 we show the cumulative mass and mass fraction of the grains from large to small, including all the mass in the simulation domain since the initialization of the dust simulation (that includes those going into the center during the simulation). Mass is well-conserved in the simulation with a total mass of 4520 $M_\oplus$. Fig. 2.5 shows that about 8% (by mass) of the dust has grown to sizes beyond the original maximum size of 1 μm by the time that the disk is 250 au in radius. However, at this time, less than 0.01% of the dust has grown beyond 10 μm. This result demonstrates that it is difficult to produce a substantial population of large grains by relying solely on the differential drift velocities of grains between different sizes to generate the relative grain-grain collision speed. The reason will be explored in detail in § 2.5 and § 2.6. Here, we briefly state that the low grain growth rate is due to the initially micron-sized (or smaller) grains being well coupled to the relatively dense gas in the disk, which makes the grain-gas drift velocity (and thus the grain-grain collision speed)

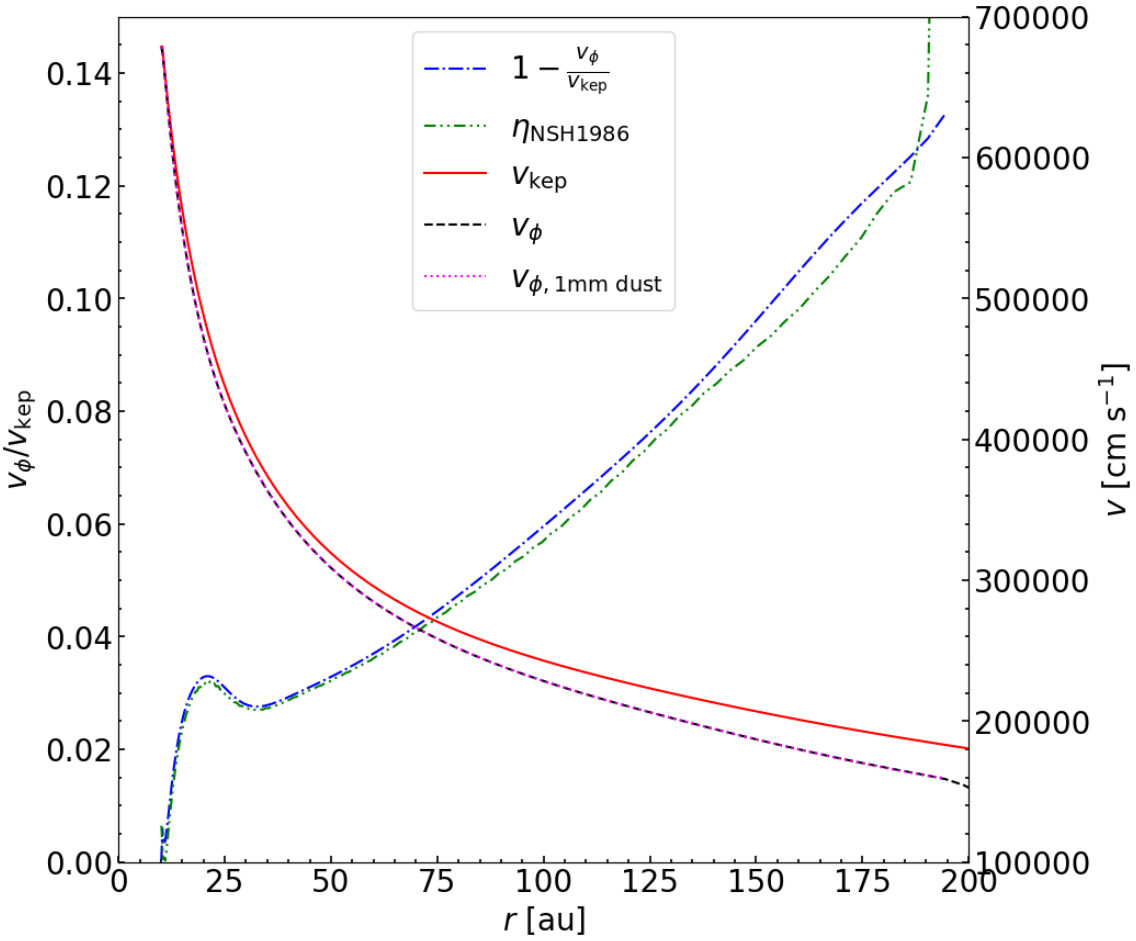


Figure 2.4: Sub-Keplerian rotation. Plotted are the rotation speed near the disk midplane, the local Keplerian speed (including the contribution from the self-gravity), and the fractional deviation of the azimuthal speed from the local Keplerian speed when the disk radius is about 200 au (solid line). The fractional deviation is close to the analytic estimate from Nakagawa et al. (1986, labeled "NSH1986").

small and the grain growth slow.

2.4.2 Model with Enhanced Grain-Grain Collision Speed

Since observational studies suggest that there might be a significant amount of large grains in protostellar disks in order to explain the dust emission at relatively long wavelengths (§ 2.1), we are motivated to increase the grain growth rate over the baseline value $\chi = 1$ in equation (2.22). We experimented with different enhancement factors and found that $\chi = 4$ yields reasonable grain growth to large sizes. Fig. 2.5 shows the cumulative mass and mass percentage in the model with the increased growth rate. At the latest time shown (when the disk grows to 250 au), about 140 $M_\oplus$ of the initially small grains are converted to grains larger than 0.1 mm, and ~ 15 $M_\oplus$ has grown beyond 1 mm.

Fig. 2.6 shows the spatial distributions of the mass densities per logarithmic size decade ($\rho_{\mathrm{d,i}}$) of dust grains of 6 representative sizes when the disk is at 250 au ($t =$ 88750 years). While the 0.1μm and 1μm sized grains are almost everywhere in the protostellar disk, grains larger than 10μm are only concentrated at or around the disk midplane. The larger the grain size is, the smaller the vertical extent of its concentration becomes. Nearly all mm-sized grains are concentrated on the disk midplane, extending ~ 50 au in radius. The largest, cm-sized grains are concentrated within 20 au from the protostar on the disk midplane.

To illustrate the substantial grain growth in this model more vividly, we plot in Fig. 2.7 the density per logarithmic size decade at different heights above the midplane at a representative cylindrical radius of 50 au. Well above the midplane near the disk boundary, the size distribution is close to the initial MRN distribution. These are the "raw material" for later growth to larger grain sizes. As the grains move closer to the midplane, their distributions become more dominated by larger

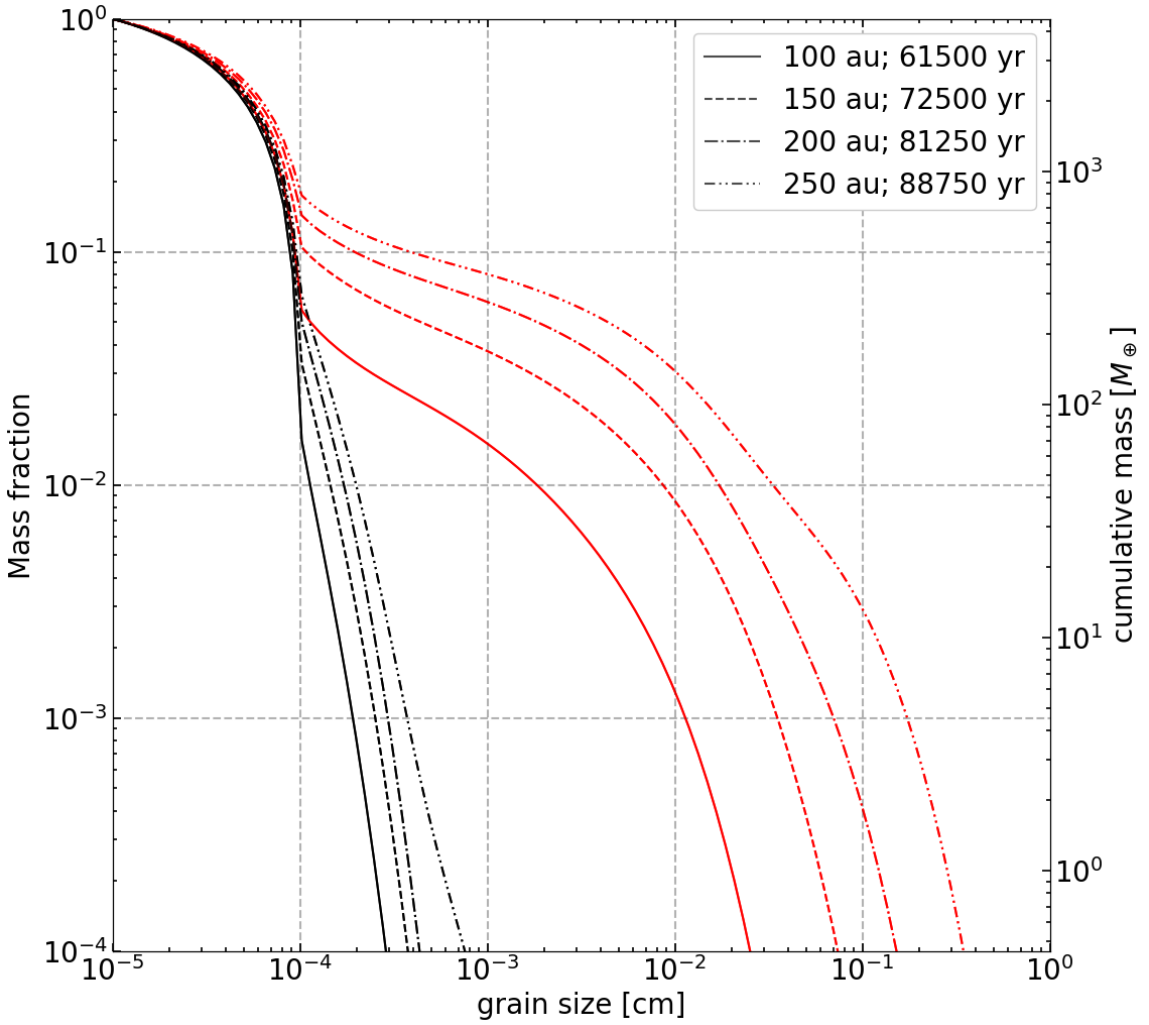


Figure 2.5: Cumulative grain mass as a function of the grain size. The mass includes both the grains in the active computational domain and those already advected through the inner boundary at $r = 10$ au. The total grain mass is conserved throughout the simulation, with a value of 4520 $M_\oplus$ determined at the beginning of the dust model (40,000 years). At later times, the total mass of the grains is calculated by summing all mass that has gone through the central boundary over time and adding all mass in the active computation domain (10 to 10,000 au). The value at each grain size is the mass fraction of the grains at or larger than that size. The black lines shows the cumulative grain mass at four different disk sizes and times in the baseline model ($\chi = 1$ in equation 2.22). The red lines are the cumulative values at the same times as the black lines with the same line style, but for the $\chi = 4$ model.

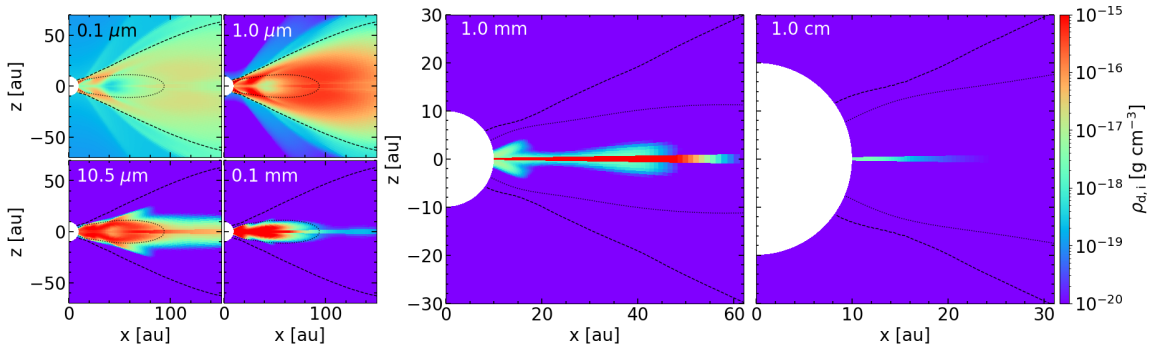


Figure 2.6: Spatial distributions of dust mass densities per logarithmic size decade of 6 size bins when the disk is at 250 au in the model with increased grain-grain collision speeds ($\chi = 4$ in equation 2.22). Each panel is the density of one size bin as noted in the upper left corner of each panel. Note the scale is different between the left four panels and the right two panels. We only show the inner disk regions in the two right panels since these are where the mm/cm-sized grains are concentrated. The black dashed contour is the boundary of the hydro disk, where the gas density is 4×10^{-16}g/cc. The dotted contour is at gas density of 4×10^{-14}g/cc to emphasize to scale difference between the left and right panels. Because we only simulated the upper hemisphere, the lower hemisphere is a reflection of the upper hemisphere about the midplane.

grains. Around a height $\sim$ 15 au above the midplane, the size that dominates the grain mass (i.e., the peak of the distribution, $s_{\rm peak}$) suddenly increases from ~ 1 μm (10^{-4} cm) to ~ 10 μm. Then $s_{\rm peak}$ grows more slowly with decreasing height. Closer to the midplane at a height between $\sim$ 1 and 5 au, most of the grain mass resides in rather large grains of ~ 100 μm. Near the midplane, the distribution is dominated by the even larger, ~ 0.5 mm-sized grains (see the rightmost curve in Fig. 2.7). A similar increase in grain size towards the midplane is observed at other cylindrical radii, indicating wide-spread grain growth throughout the protostellar disk. In what follows, we seek to understand how the grain growth occurs in the simulation.

Interplay between drift and growth

Because both the gravity and the polar component of the gas velocity u_θ point towards the midplane, naturally the velocity vectors of most grains point towards

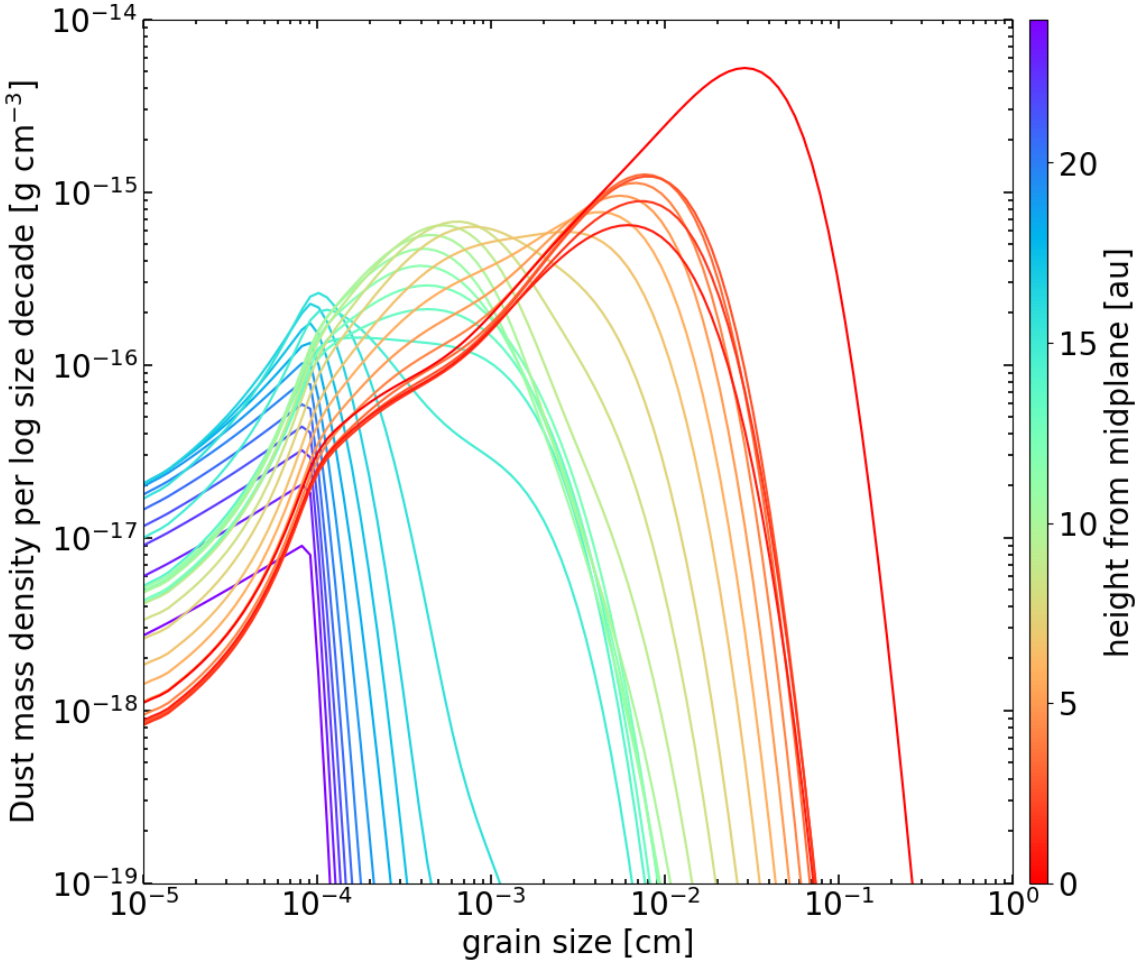


Figure 2.7: The distributions of the dust mass density per size decade in each logarithmic size bin as a function of the grain size at different heights from the midplane (one curve for each height, with the height specified by the colorbar) at a representative cylindrical radius of 50 au. This example frame is taken at 86250 years, when the disk is at 250 au in radius. The highest red line, peaking around 0.5 mm, shows that the largest grains are concentrated near the midplane.

the midplane in the majority of the disk. With the dust grains exerting no pressure force on each other, the midplane is a natural place for grains to concentrate. This concentration is the key to understanding the growth pattern that we see.

As shown in Fig. 2.6, most of the largest grains are concentrated near the midplane. To understand whether such grains are formed in situ or advected from higher up in the disk, we first examine the advection and growth rates in the protostellar disk. In Fig. 2.8 we show the advection time scale of the grains in six representative size bins at different times. The advection time scale for grains in a given size bin i is defined as

$$t_{\mathrm{adv},i} = \frac{m_i}{f_i} \tag{2.28}$$

where m_i is the total mass of the grains in the ith size bin within a cell and f_i is the net flux of these grains through all boundaries of the cell. If $f_i > 0$, $t_{\mathrm{adv,i}}$ is the characteristic time scale for advection to fill the cell; if $f_i < 0$, $t_{\mathrm{adv,i}}$ is the characteristic time scale for advection to remove all grains within the cell.

The formation (growth) time scale is defined in the same way,

$$t_{\mathrm{grow},i} = \frac{m_i}{(dm_i/dt)} \tag{2.29}$$

where dm_i/dt is the net growth rate calculated from the Smoluchowski equation (equ. 2.20). The time scales for other frames are similar to that of the frame shown.

For sub-micron sized grains (< 1 μm), the advection time scale on the disk is generally positive, which means that these small grains are effectively replenished by the infall from the envelope. These grains are the seeds for growing to larger grains. As the grain size increases, the vertical extent of the region with a positive advection time scale shrinks closer to the midplane (see top panels of Fig. 2.8, from left to right).

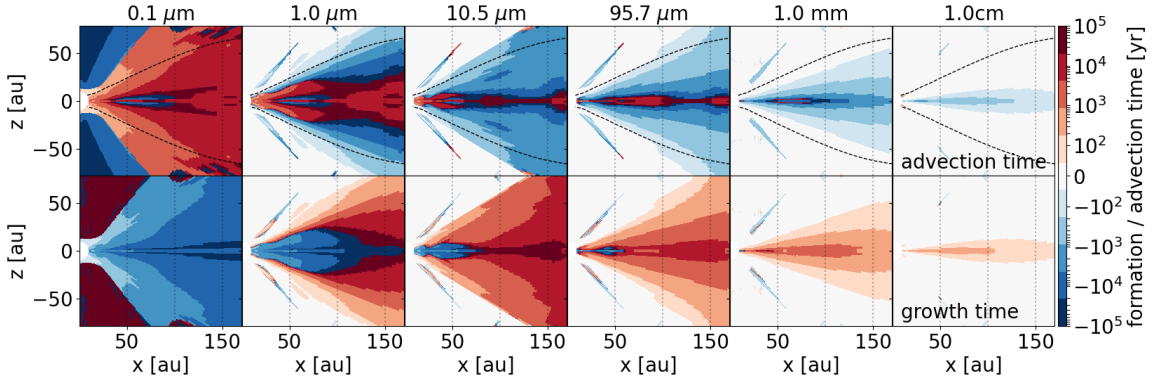


Figure 2.8: Grain advection and formation time scale for grains in six representative size bins when the disk reaches 250au. The upper six panels are advection time scale and the lower six panels are formation (growth) time scale. The defintion of the time scales is in section § 2.4.2, equation 2.28 and 2.29. Small grains are being advected into the disk constantly, supplying the growth to larger grains in the protostellar disk. The gain due to formation time scale is shorter than the loss due to advection time scale for large grains in general.

This is a reflection of the general tendency for the grains that have grown beyond the initial sizes to move towards the midplane, which leads to a net depletion of the grown grains at high altitudes (and hence a negative advection time scale) and a net gain of the grown grains at low altitudes (and hence a positive advection time scale).

The transition from a net advective loss to a net advective gain moves closer to the midplane for larger grains, until the grains are large enough that their radial drift towards the central protostar prohibits this transition from happening.

This effect is seen for the two largest grain sizes shown in Fig. 2.8 (1 mm and 1 cm): advection leads to a net loss nearly everywhere in the disk, even at the disk midplane.

Quantitatively, for 10 μm sized grains and 100 μm sized grains, in the majority of the disk the advection time scale is between -10^3 and -10^4 years. This time scale is short compared to the simulation time scale of $4 \cdot 10^4$ years, which means that the grains are effectively removed from the atmosphere of the disk and are being advected

to the disk midplane or to the central protostar. The advection time scale for mm and cm-sized are shorter than those of the smaller size bins, meaning they are removed from the upper parts of the disk even more effectively.

To compare the formation time scale with the drift time scale, we point out that if $t_{\rm grow}$ and $t_{\rm adv}$ have the same sign (both negative or both positive), then the grains either are quickly lost from that location (both negative) or quickly accumulated (both positive). The more subtle cases are when their signs are different. If $t_{\rm grow} > 0 > t_{\rm adv}$ and $|t_{\rm adv}| > t_{\rm grow}$, then the presence of grains at that location is due to fast grain growth since the in-situ growth rate is faster than the advective removal rate. This is the case near the midplane for mm and cm-sized grains, and is generally true for 100 μm and 10 μm sized grains at relatively high altitudes as well. Qualitatively, this shows that the large grains, especially the largest ones, are formed in-situ more rapidly than they are removed. The "raw materials" (micron or sub-micron sized grains) that supply the growth process are progressively being advected from the envelope to the disk.

To quantitatively examine whether the concentration of the largest grains near the midplane we observe in the density plots of Fig. 2.6 is due to the grains formed locally, we compare the total mass of >1 mm size grain advected to the midplane and the total mass of those that grew there locally. Fig. 2.9 shows the midplane formation rate of the grains larger than 1 mm (dashed line) and their formation rate anywhere else (dotted line), as well as the rate at which such grains are advected to the midplane (solid black line). Because the midplane surface in our simulation is a cell boundary instead of a cell center, we define the disk midplane to be one cell above or below the midplane surface and has a gas density greater than 4×10^{-16}g cm^{-3}. The flux into this region is defined to be the total flux into the region but excluding the loss through the inner boundary at $r = 10$ au. We find that the amount of >mm

size dust advected to the midplane and formed everywhere else are both negligible compared to the ones formed on the midplane locally. These results show that the largest grains that we see in the simulation are formed locally on the midplane instead of being advected from higher up in the disk.

In Fig. 2.9 we also plot the advection rate of all grains smaller than 1 μm and the formation rate of all grains larger than 1 μm on the midplane. Since mass is conserved during advection and formation, the advected small grains to the midplane are turned into the larger ones. The rate of growth into larger grains ($>$1 μm) is about 60% of the advection rate of the small grains almost at all times. In other words, more than half of the small grains are constantly being turned into larger ones. It supports a scenario where the small grains are carried to the midplane, converted to larger grains, which stay near the midplane or are advected radially to the central protostar.

Dust-to-gas ratio

For the eventual formation of planets, one important quality to characterize is the dust-to-gas ratio since a high ratio is required to form planetesimals through streaming instability. We seek to understand the dust-to-gas ratio in our simulation.

In Fig. 2.10 we plot the midplane dust-to-gas ratio as a function of radius at 85,000 years. The solid black line includes grains of all sizes. Each of the colored lines is the contribution of the grains in one size decade to the local dust-to-gas ratio. The total dust-to-gas ratio reaches ~ 0.03 at a radius of ~ 50 au, and the value decreases to slightly above the ISM value of 0.01 at and beyond $\sim$ 125 au. This increased concentration of dust grains will be important for our understanding of why grains grow on the disk midplane in § 2.5 and § 2.6.

In terms of the contribution by grains within each size decade, there is a "layering"

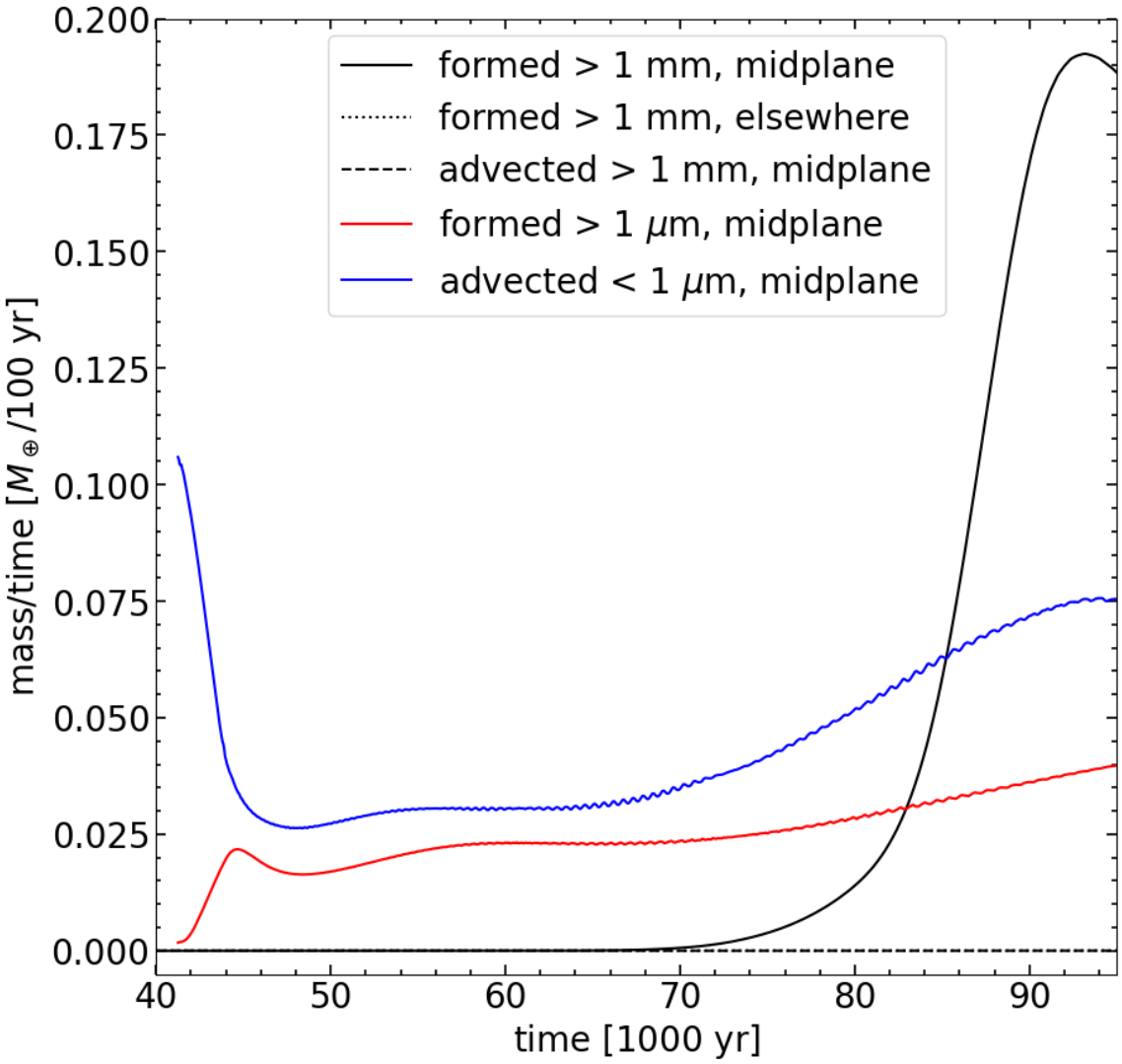


Figure 2.9: Comparison of in-situ formation rate and advection rate. The three black lines are for $>$ 1 mm-sized grains, showing that the in-situ formation rate in the midplane region (solid black line) is much larger than the rate with which such grains are advected into the midplane region (dashed black line) and the formation rate outside the midplane region (dotted black line; not visible due to overlap with the dashed line). Also plotted are the in-situ formation rate for $>$ 1 μm-sized grains in the midplane region (red solid line) and the advection rate of $<$ 1 μm grains into the midplane region (blue solid line), showing that more than half of the small ($<$ 1 μm) grains from the initial MRN distribution advected into the midplane region are turned into larger ($>$ 1 μm) grains.

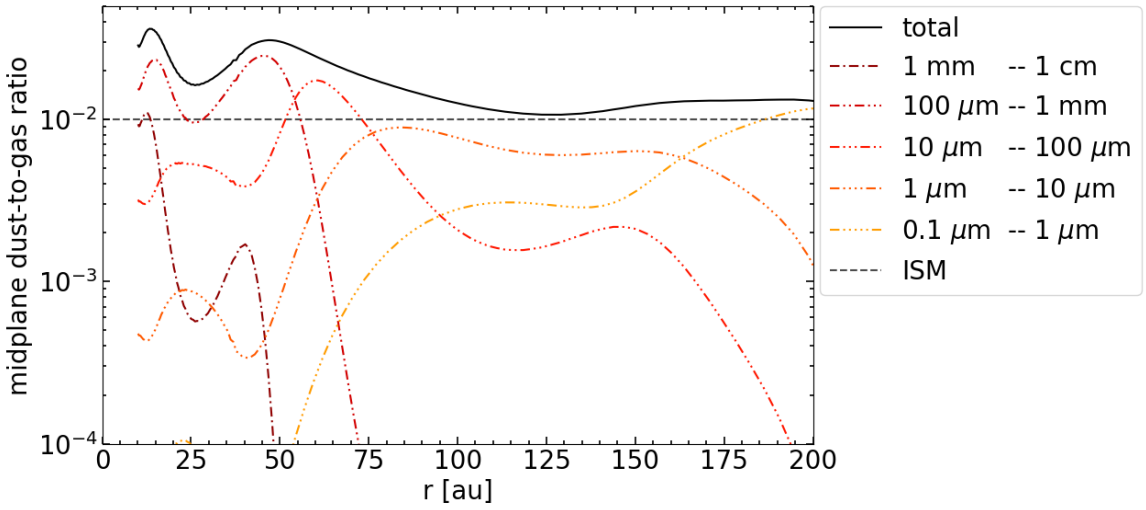


Figure 2.10: Dust-to-gas ratio on the disk midplane including grains with different sizes. The solid line is the dust-to-gas ratio including all dust grains. At around $\sim$ 50 au the dust-to-gas ratio reaches 0.03, three times the initial ISM value of 0.01 (dashed horizontal line). The colored lines are the dust-to-gas ratios on the midplane including only grains within a certain size decade. These colored lines show the contribution of dust in each size decade to the local dust-to-gas ratio. For example, 0.1 $\sim$ 1mm-sized grains contribute most to the dust mass around 45 au.

of the highest contribution as a function of grain size and radius. Ignoring the peaks within 20 au which may be affected by the inner boundary, we find that the greatest contributor to dust-to-gas ratio near 45 au are the grains between 100 μm and 1 mm; the greatest contributor changes to grains between 10 μm and 100 μm at about 60 au. At 90 au the greatest contributor shifts to grains between 1 μm and 10 μm. Outside 160 au, the initial MRN grains dominate the contribution to the dust-to-gas ratio. With increased grain sizes, the region where the grains concentrate moves inward. The reason for this layering is the differential drift, with larger grains drifting inwards faster than smaller ones in the low density regions. Once the large grains reach a high density region, there is a "traffic jam" that concentrates them at those locations. This differential drift also explains why the largest (mm to cm-sized) grains do not contribute much to the dust-to-gas ratio at all radius: their radial drift is so

fast that they hardly have time to accumulate in the disk. This quick radial drift can also be seen in Fig. 2.8, where the cm-sized grains are advected away on a time scale of ~ 1000 years. If there are substructures, such as dense rings, in the gas disk, the large grains may be trapped on the disk. The dust trapping may make it possible to increase the local dust-to-gas ratio further, potentially to values that are conducive to the onset of the streaming instability (~ 0.1, Youdin & Goodman, 2005b).

2.5 GRAIN GROWTH TIMESCALE

To understand the dust simulation results, we seek to obtain an estimate of the grain growth timescale using the Smoluchowski equation (equation 2.20). In our case, the kernel M_{ijk} is determined by the differential drift speed between grains of different sizes only. Using the terminal velocity approximation (equation 2.14), we can write

$$\Delta u_{ij} = \chi\zeta|t_{si} - t_{sj}| = \chi\zeta\frac{\tilde{\rho}_{\rm dm}}{\rho_{\rm g} v_{\rm th}}|s_i - s_j| \tag{2.30}$$

where Δu_{ij} is the relative speed defined in equation (2.22), $\zeta = |\zeta|$ is the magnitude of the net grain acceleration from all forces other than the gas drag that is balanced by the acceleration from the gas drag (equ. 2.15); it depends only on the gas properties. The quantity t_{si} is the stopping time for the i-th dust size bin as defined in equation (2.12). We include χ here for later discussions. Considering coagulation only, the net change of the number density of grains of a certain size s_k is

$$\begin{aligned}\frac{dn_k}{dt} = &\frac{1}{2}\iint_0^\infty \chi\zeta\frac{\tilde{\rho}_{\rm dm}}{\rho_{\rm g} v_{\rm th}}|s_i - s_j|(s_i + s_j)^2\delta_{ijk}n_i n_j ds_i ds_j \\ &- \iint_0^\infty \chi\zeta\frac{\tilde{\rho}_{\rm dm}}{\rho_{\rm g} v_{\rm th}}|s_i - s_j|(s_i + s_j)^2 n_i n_j \delta_{jk} ds_i ds_j\end{aligned} \tag{2.31}$$

where the first term on the right hand side (RHS) describes the gain via coagulation and the second term describes the lost due to coagulation. $\delta_{ijk} = 1$ if $s_i^3 + s_j^3 = s_k^3$ and 0 otherwise; $\delta_{jk} = 1$ if $s_j = s_k$ and 0 otherwise. Assume the grain number density follows a power law $n_i(s_i) = A s_i^{-q}$ from s_s to s_l (note that $q = 3.5$ is the MRN distribution). If the total grain mass density is given by $\rho_{\rm d,tot}$, the coefficient A can be written as

$$A = \frac{3(4-q)\rho_{\rm d,tot}}{4\pi\tilde{\rho}_{\rm dm}(s_l^{4-q} - s_s^{4-q})} \tag{2.32}$$

A growth time-scale can be obtained by evaluating $n_k/(dn_k/dt)$. Each of the two δ functions in equation 2.31 can be absorbed with one of the two integrals respectively, and we have

$$\begin{aligned}\frac{dn_k}{dt} = &\frac{1}{2}\int_{s_s}^{s_k} \chi\zeta\frac{\tilde{\rho}_{\rm dm}}{\rho_{\rm g} v_{\rm th}}|s_j^{\rm gain} - s_i|(s_j^{\rm gain} + s_i)^2 n_i n_j^{\rm gain} ds_i \\ &- \int_{s_s}^{s_l} \chi\zeta\frac{\tilde{\rho}_{\rm dm}}{\rho_{\rm g} v_{\rm th}}|s_j^{\rm lost} - s_i|(s_j^{\rm lost} + s_i)^2 n_i n_j^{\rm lost} ds_i\end{aligned} \tag{2.33}$$

where

$$\begin{aligned}s_j^{\rm gain} &= [s_k^3 - s_i^3]^{1/3} \\ s_j^{\rm lost} &= s_k \\ n_j^{\rm gain/lost} &= A\left(s_j^{\rm gain/lost}\right)^{-q}\end{aligned} \tag{2.34}$$

Equation 2.33 can be evaluated by plugging in n_i, A and simplify. Before writing out the result, we define one important parameter that governs the grain growth rate:

$$\eta = \frac{4\rho_{\rm g} v_{\rm th}}{3\chi\rho_{\rm d,tot}\zeta} \tag{2.35}$$

and two expressions to simplify notations:

$$w_{\rm gain/lost}(s_i,q) \equiv |s_j^{\rm gain/lost} - s_i|(s_j^{\rm gain/lost} + s_i)^2 s_i^{-q}\left(s_j^{\rm gain/lost}\right)^{-q} \tag{2.36}$$

and

$$f(s_k;s_s,s_l,q) \equiv \frac{s_k^{-q}(s_l^{4-q} - s_s^{4-q})/(4-q)}{\frac{1}{2}\int_{\rm gain} w_{\rm gain}(s_i,q)ds_i - \int_{\rm lost} w_{\rm lost}(s_i,q)ds_i} \tag{2.37}$$

where $\int_{\rm gain}$ and $\int_{\rm lost}$ are the integration bounds of the first and second term in equation 2.33 respectively.

Using these definitions, equation 2.33 can be written as a time scale

$$t_{\rm depl} \equiv -\frac{dt}{d\ln n_k} = -\frac{n_k}{\frac{dn_k}{dt}} = -\eta\ f(s_k;s_s,s_l,q), \tag{2.38}$$

Physically, $t_{\rm depl}$ is the time scale to deplete small grains of a given size (k) due to growth to larger sizes. It is positive for $\frac{dn_k}{dt} < 0$. As we show below, it is related to the time scale $t_{\rm size}$ to increase the grain size where the dust mass distribution peaks (see equation 2.43 below).

Since $f(s_k;s_s,s_l,q)$ is a dimensionless quantity, the quantity η has the unit of time, which can easily be confirmed from its definition in equation (2.35). It will be referred to as "the characteristic timescale" hereafter.

Note that all physical properties of the disk, such as its gas density $\rho_{\rm g}$, thermal speed ($v_{\rm th}$ (and thus temperature), grain acceleration from gas drag ζ, as well as the dust-gas drift speed enhancement factor χ, affect the grain growth only through the timescale η. If η is increased (or decreased), the timescale for the grains to evolve would increase (or decrease) proportionally.

In the next subsection (§ 2.5.1) we will use a one-zone model to show numerically that there is a simple relationship between the timescale for the grain size to increase

by a factor of e (the size e-folding time $t_{\rm size}$) and the characteristic timescale η. We will then validate this relationship semi-analytically using equation (2.38) in the following sub-section (§ 2.5.2).

2.5.1 One-Zone Model

To quantify the role of the characteristic timescale η in grain growth, we develop a so-called "one-zone model," where we keep the hydro properties in a representative cell in the hydro simulation fixed and evolve the grain size distribution in time through coagulation from an initial distribution, keeping the dust-to-gas ratio to 0.01 (i.e., no outflow from or inflow into the cell). The algorithm for grain growth is identical to the one described in section § 2.2.3, but with two slight modifications: the number of grain bins is increased to 1050, 10 times the resolution used in the full model. This is to minimize possible numerical effects in our model due to the discretization of grain sizes (see e.g. Lombart & Laibe, 2021). The integration time step is chosen to be the smaller value between 1 year and the depletion time of a grain species. This adaptive time step is implemented to speed up the calculation with little loss of precision. For the rest of the discussion, the hydro background is chosen to be the disk at 85,000 years, when the disk size is between 200 and 250 au.

We first study the effects of the initial grain size power-law index q in the Smoluchowski equation (equation 2.20, 2.21 and 2.22). We first take the hydro background to be the one cell on the midplane at 26 au (referred to as the "fiducial cell" hereafter). We integrate the Smoluchowski equation with different values of initial q and plot the resultant dust mass density per size decade in Fig. 2.11. To speed up the calculations, we uses $\chi = 4$ to conduct the one-zone models. The value chosen is identical to the χ used in the increased grain growth model (§ 2.4.2).

The solid lines in Fig. 2.11 are the solutions at 25,000 years after the initiation

of grain growth and the dashed lines are at 64,000 years. Comparing models with different values of initial q, we find that the solutions are self-similar in time and share almost exactly the same shape (except in the 0.1 μm to 1 μm part, where all grains are initialized) regardless of the initial distribution. Although in the $q = 6$ case the distribution is lagging behind the other lines in moving to the larger size end by about 4000 years, the rate at which it is moving is the same as the other lines. These findings show that the solution to the Smoluchowski equation in a closed environment is a self-similar, attractive solution moving from small grain sizes to large grain sizes as a function of time. Therefore, we define the "grain growth rate" to be the rate that this self-similar and attractive solution moves to the larger grain side.

In equation 2.38, the part of the expression that is independent of the grain size s and the size power-law index q is the characteristic timescale η, as defined in equation 2.35. The existence of a self-similar and attractive solution means that the grain growth rate is solely governed by the parameter η. For the purpose of later discussions, we approximate the dust mass density per logarithmic size decade $\rho_{d,i}$ as a function of s_i as a power-law with index p_s: $\rho_{\mathrm{d,i}} \propto s_i^{p_s}$. From the one-zone models, we obtain $p_s \sim 1.9$.

Next, we seek to find a relationship between the characteristic timescale η, defined in equation 2.35 and the rate at which the self-similar distribution moves to the large grain side (the grain size increase rate). To find this relationship we pick 20 cells, distributed inside the disk at radii $26, 41, 63, 97$ and 150 au and angles $0, 0.01\pi, 0.04\pi$ and 0.1π from the midplane. The cells are labeled in the left panel of Fig. 2.12, where the spatial distribution of the characteristic timescale η (with the dust-to-gas ratio fixed at 0.01 and $\chi = 4$) is plotted. The grain size distributions in the other 19 chosen cells are similar to that of the fiducial cell (located on the midplane at 26 au) shown in Fig. 2.11, but the grain growth rates are different.

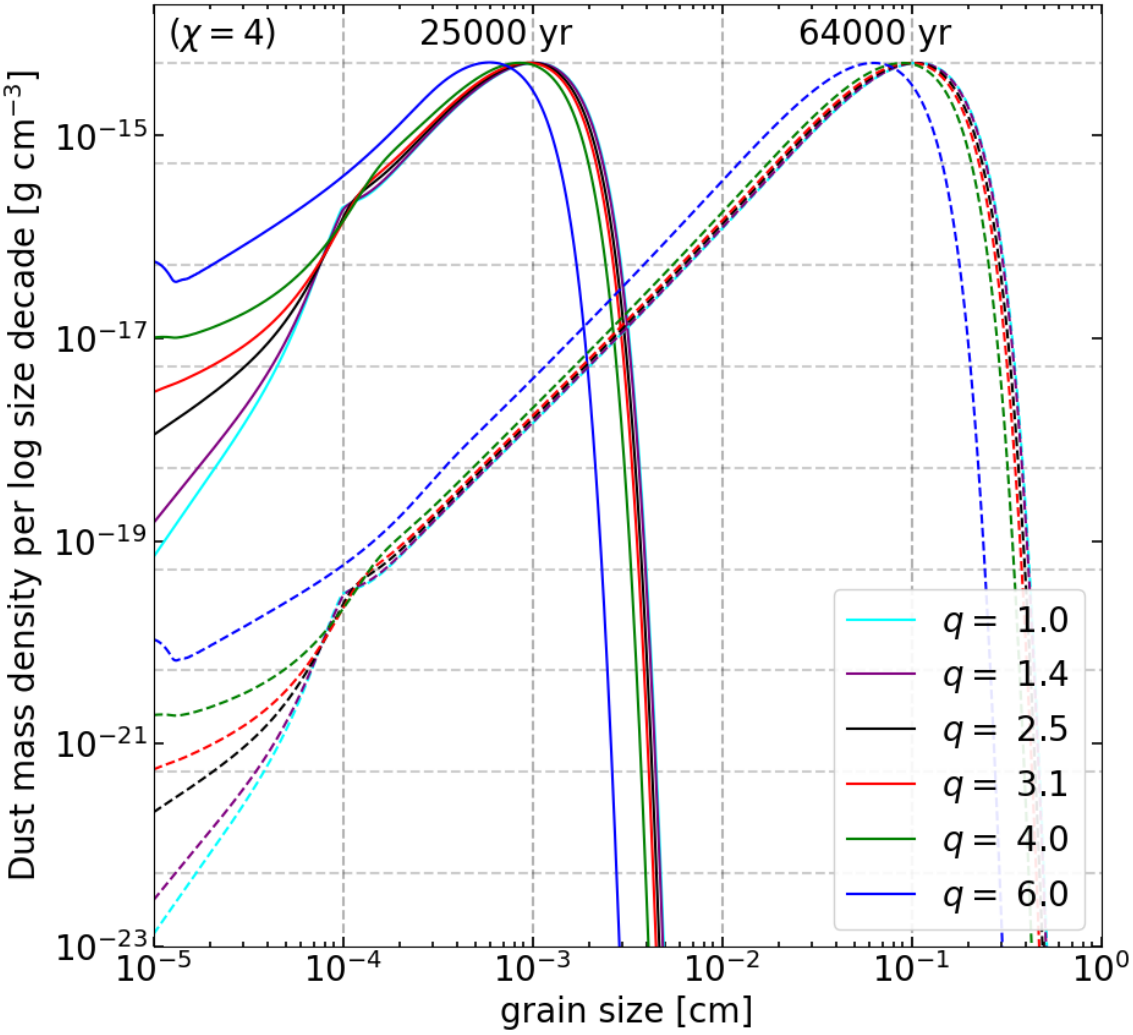


Figure 2.11: The distribution of grain mass density $\rho_{\rm d}$ per log size decade as a function of grain size at two times distinguished by line style: the solid line is taken at 25,000 years and the dashed line at 64,000 years. Each color denotes a different initial grain size power-law index q. The similarity of the curves at different times and for different initial size distributions indicates that the grain evolution is nearly self-similar in time and insensitive to the initial size distribution. The time for the grains to grow by one order in this example is about 19500 years (with $\chi = 4$).

At each time, there is a grain size bin that has more mass than any other bins. We term the grain size in this bin "the peak size" and denote it by $s_{\rm peak}$. For example, $s_{\rm peak} \sim 10$ μm in the fiducial cell at 25,000 years (see Fig. 2.11). In principle there are other ways to define a representative grain size, such as the mass weighted average size (Kobayashi et al., 2016). However, because the grain mass distribution is self-similar over time, our conclusion regarding the grain growth time scale is expected to be insensitive to how the representative grain size is chosen, as we verified explicitly for the case of mass weighted average size. We can fit the peak size as a function of time. Because at the beginning of the simulation the peak size is determined by the initial condition rather than grain growth, we only perform the fitting using integration results when the peak size is between 10 μm and 1 mm. We fit the peak size as a function of time to

$$s_{\rm peak} = \exp\left\{\frac{t}{t_{\rm size}} + c\right\} \tag{2.39}$$

where $t_{\rm size}$ is the peak size growth timescale, which is to be fitted together with the constant c, and t is the time. The fitting yields a pair of $t_{\rm size}$ and c in each cell. Because the Smoluchowski equation is governed by the characteristic timescale η, we can fit $t_{\rm size}$ and c as functions of η. We use a simple linear regression for the fitting of both. The best fit results are

$$t_{\rm size} = 1.84 \cdot \eta \tag{2.40}$$

and

$$c = -9.91. \tag{2.41}$$

Fig. 2.12 shows that the peak size obtained from the fitted expression (equation 2.39) agrees well with the numerical results from the one-zone simulations. In what follows,

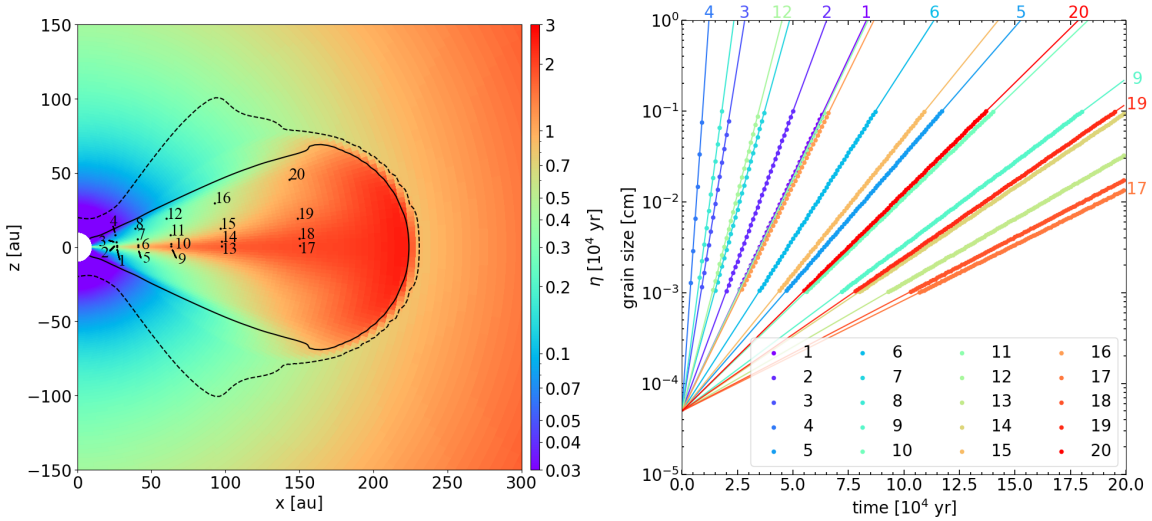


Figure 2.12: **Left panel:** the distribution of the characteristic timescale η in units of 10^4 years assuming a dust-to-gas ratio of 0.01 everywhere and $\chi = 4$ and using the gas density ρ_g, thermal speed $v_{\rm th}$, and the acceleration from aerodynamic drag ζ at a representative time $t = 85000$ years. **Right panel:** Fitting of the peak grain size $s_{\rm peak}$ as a function of time using equation 2.39. Each line corresponds to one location labeled in the left panel. The fitting agrees well the results of the one-zone simulations, proving the validity of equation 2.39.

we will validate the relationship between $t_{\rm size}$ and η (equation 2.40) semi-analytically.

2.5.2 Semi-analytic Estimate of Grain Growth time

In the last subsection, we found that when the one-zone models run long enough, the effects of initial conditions wear off, with all solutions converging to $\rho_{\rm d,i} \propto s_i^{p_s}$, where $\rho_{\rm d,i}$ is the mass density per log size decade of the dust of size s_i and $p_s \sim 1.9$ is the power-law index of the converged self-similar solution. This self-similar and attractive solution can also be described by a power law for the dust number density per (linear) size bin $n_i \propto s_i^{-q_s}$ and note that $p_s + q_s = 4$ by definition.[3] For a semi-analytic treatment in this subsection, we will idealize the late-time dust mass density distribution shown in Fig. 2.11 as a power-law with a sharp cut-off beyond the peak

[3] $\rho_{\rm d,i} = \frac{4}{3}\pi\tilde{\rho}_{\rm dm}s_i^3\Delta s_i n_i = \frac{4}{3}\pi\tilde{\rho}_{\rm dm}s_i^3\tilde{A}s_i A s_i^{-q} \propto s_i^{4-q_s} \propto s_i^{p_s}$, where $\Delta s_i = \tilde{A}s_i$, since our grain size bins are linear in log space. Thus $4 - q_s = p_s$.

size $s_{\rm peak}$, as shown in Fig. 2.13.

To determine the (e-folding) time $t_{\rm size}$ for the peak grain size $s_{\rm peak}$ to increase by a factor of e for the self-similar dust evolution sketched in Fig. 2.13, we note that it is related to the (e-folding) time $t_{\rm depl}$ for the small grains at a fixed size to deplete by a factor of e through

$$t_{\rm size} \equiv \frac{dt}{d\ln s_{\rm peak}} = p_s \; t_{\rm depl}. \tag{2.42}$$

The depletion time $t_{\rm depl}$ for grains of a given size s_k is given by

$$t_{\rm depl} \equiv \frac{dt}{d\ln \rho_{\rm d,k}} = \frac{dt}{d\ln n_k} = -\eta \; f(s_k, s_s, s_l, q_s), \tag{2.43}$$

where equation 2.38 is used in the last equality, with the parameters s_s and s_l denoting, respectively, the lower and upper limit of the size integral in the expression for the function f (see equation 2.37).

We numerically integrate the function $-f(s_k; s_s, s_l, q_s)$ for four pairs of s_s and s_l, and three values of q_s (including the approximate value for the self-similar evolution, 2.1). The results are shown in Fig. 2.14). For the purposes of comparison with the time scale for the peak grain size increase obtained numerically in the one-zone models (equation 2.40), the relevant values of the function f are those for relatively small grains (much smaller than the maximum grain size, i.e., $s_k \ll s_l$) because the deviation of the size distribution near the maximum in the one-zone models is not captured by the strict power-law with a sharp cut-off adopted here. In the relevant limit $s_k \ll s_l$, the value of $-f(s_k; s_s, s_l, q_s)$ converges to 1 independent of the choice of s_s, s_l and q_s. Therefore, we have $t_{\rm depl} \approx \eta$ from equation (2.43) which, when plugged

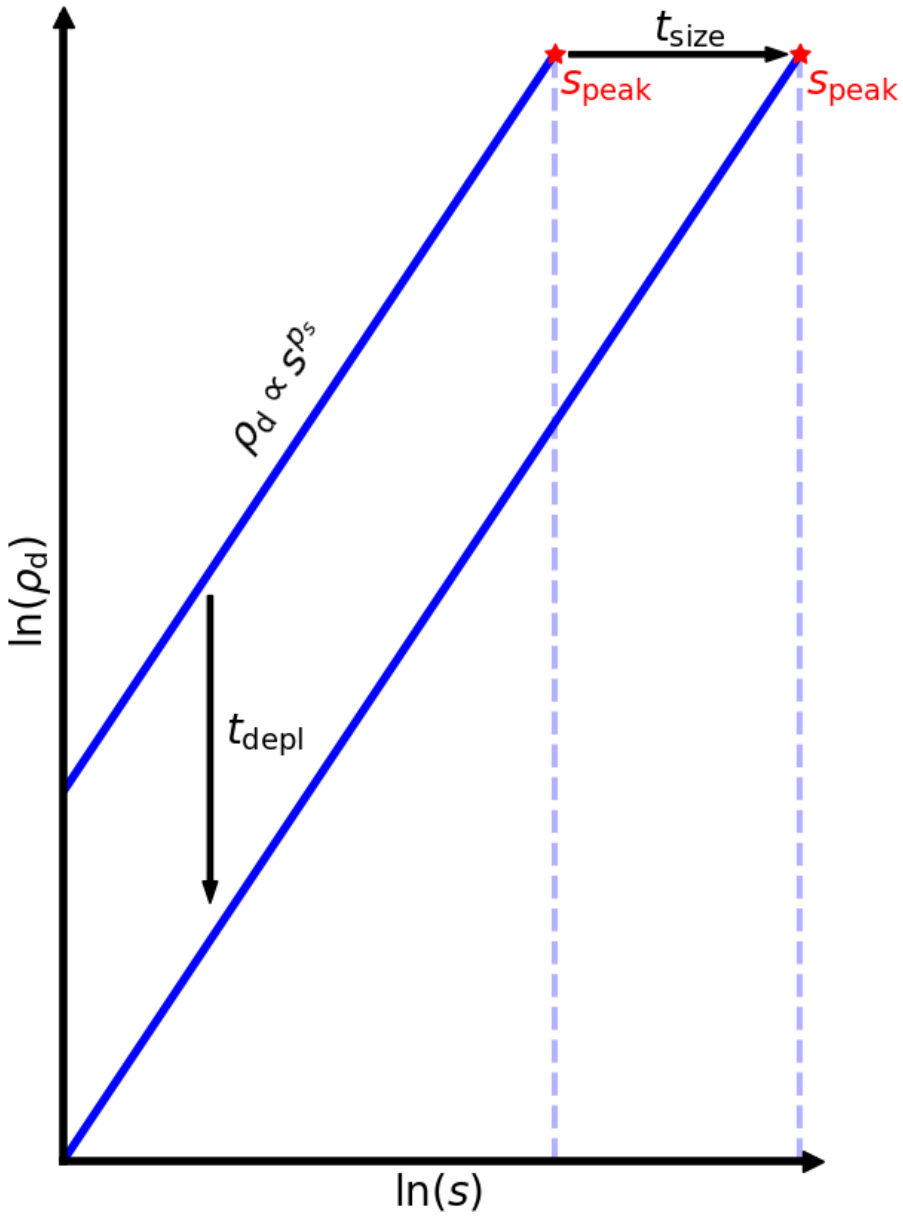


Figure 2.13: Schematic of the self-similar evolution of the grain mass density distribution as a function of size, showing the relation between the depletion of small grains (on a time scale $t_{\rm depl}$) due to growth to larger grains and the increase of grain size (on a timescale $t_{\rm size}$) also due to growth.

into equation (2.42), yields

$$t_{\rm size} \approx p_s\ \eta = 1.9\ \eta = 2.5\ \frac{\rho_g\ v_{\rm th}}{\chi\ \rho_{\rm d,tot}\ \zeta}, \tag{2.44}$$

which is remarkably close to the value of 1.84 η numerically obtained from the one-zone models (see equation 2.40). We have used the definition of η (equation 2.35) in the last equality.

It is important to note that the time scale for the grain size increase $t_{\rm size}$ depends only on the local gas quantities through the quantity η. To give a feel for the physical value of η (and thus $t_{\rm size}$), we scale the disk quantities to their values in the fiducial cell (cell #1 in Fig. 2.12)

$$t_{\rm size} \approx 8680\ {\rm year}\ \Big(\frac{0.01}{R_{\rm d-g}}\Big)\Big(\frac{v_{\rm th}}{10^5\ {\rm cm\ s^{-1}}}\Big) \Big(\frac{2.5\cdot 10^{-5}\ {\rm cm\ s^{-2}}}{\zeta}\Big)\Big(\frac{4}{\chi}\Big), \tag{2.45}$$

where $R_{\rm d-g} = \frac{\rho_{\rm d,tot}}{\rho_{\rm g}}$ is the local dust-to-gas ratio; $v_{\rm th}$ is the gas thermal speed, ζ is the dust acceleration from gas drag defined in equation 2.30. The time scale for the grain size to increase by one order of magnitude, $t_{\rm size-10}$, would be ln(10) times longer, so that

$$t_{\rm size-10} \approx 20000\ {\rm year}\ \Big(\frac{0.01}{R_{\rm d-g}}\Big)\Big(\frac{v_{\rm th}}{10^5\ {\rm cm\ s^{-1}}}\Big) \Big(\frac{2.5\cdot 10^{-5}\ {\rm cm\ s^{-2}}}{\zeta}\Big)\Big(\frac{4}{\chi}\Big). \tag{2.46}$$

This estimate holds as long as the grain-grain collision speed is given by $\Delta u_{ij} = \chi\zeta|t_{s_i} - t_{s_j}|$. The typical values of $t_{\rm size}$ are estimated in the discussion section (§ 2.6) below.

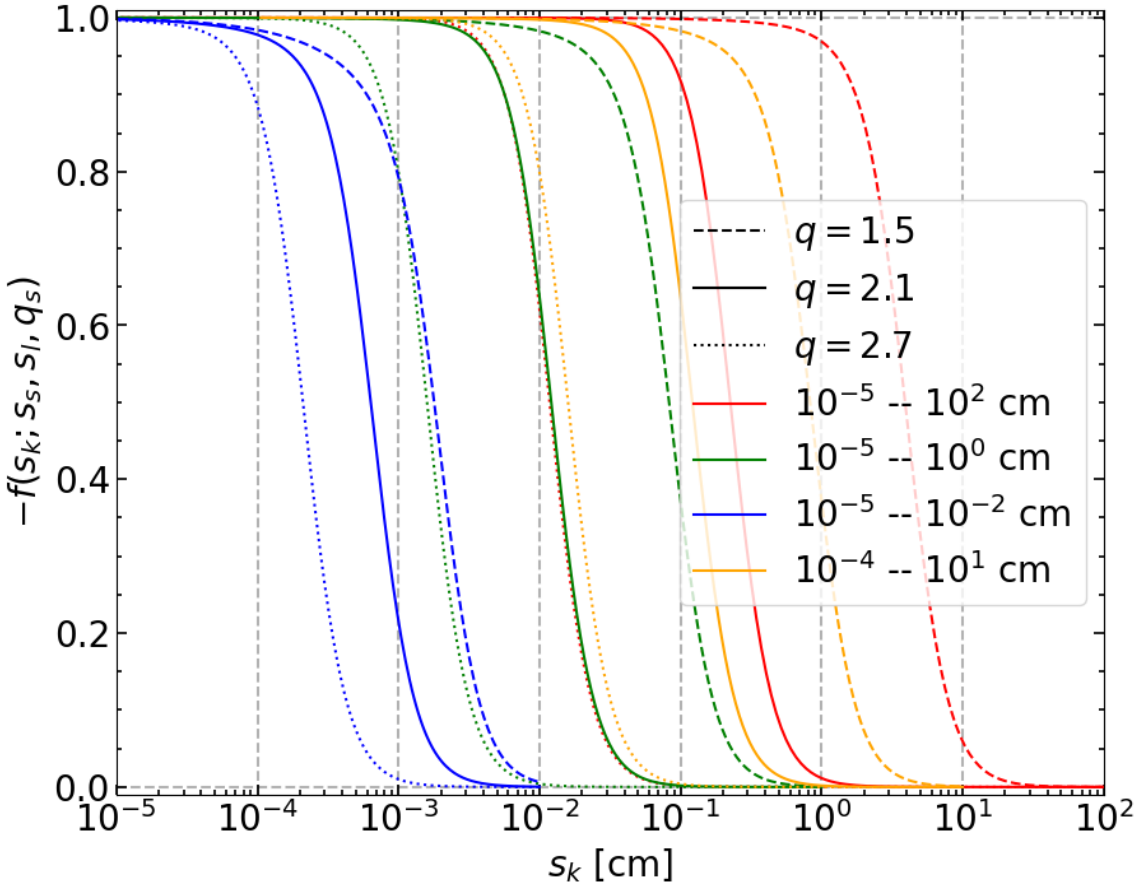


Figure 2.14: Values of $-f(s_k; s_s, s_l, q_s)$ (equation 2.37). Each line is a different choice of parameters s_s, s_l or q_s. Each linestyle represents a different q_s, with the dashed, solid and dotted lines have $q_s = 1.5, 2.1$ and 2.7 respectively. Note that the solid lines with $q_s = 2.1$ fits the left half of self-similar and attractive solution in Fig. 2.11 well. Each color denotes a different set of choice of s_s and s_l, with values noted in the legend. The evalution of $f(s_k; s_s, s_l, q_s)$ is only done between s_s and s_l. In all cases, if $s_k \ll s_l$, then $-f(s_k; s_s, s_l, q_s) \approx 1$ (the horizontal dashed gray line).

2.5.3 Physical Interpretation of η

As discussed above, the quantity η defined in equation 2.35 is a crucial parameter for grain growth: it is about half of the time-scale $t_{\rm size}$ for the maximum grain size to increase by a factor of e (see equation 2.44). The physical meaning of this parameter can be obtained from the following consideration.

Since the grain mass distribution typically peaks around some size $s_{\rm peak}$ (see Figs. 2.11 and 2.13), we can obtain a rough estimate of the number density $n_{\rm peak}$ of the grains with the peak size by assuming all of the dust mass is contained in such grains:

$$n_{\rm peak} \approx \frac{3\rho_{\rm d,tot}}{4\pi s_{\rm peak}^3 \tilde{\rho}_{\rm dm}}, \tag{2.47}$$

where $\rho_{\rm d,tot}$ is the total grain mass density and $\tilde{\rho}_{\rm dm}$ is the dust material density. This, combined with the cross-section $\pi s_{\rm peak}^2$, yields the mean-free-path for a collision with grains of size $s_{\rm peak}$:

$$l_{\rm peak} = \frac{1}{\pi s_{\rm peak}^2 n_{\rm peak}} \approx \frac{4\tilde{\rho}_{\rm dm} s_{\rm peak}}{3\rho_{\rm d,tot}}. \tag{2.48}$$

Since the grains of the peak size drift relative to gas at a terminal speed of

$$u_{\rm d,peak} = \chi\zeta \frac{\tilde{\rho}_{\rm dm}\ s_{\rm peak}}{\rho_{\rm g}\ u_{\rm th}}, \tag{2.49}$$

we have from the definition of η (equation 2.35) that

$$\eta \approx \frac{l_{\rm peak}}{u_{\rm d,peak}}. \tag{2.50}$$

In other words, the parameter η is basically the time it takes a grain near the peak size (where most of the dust mass resides) to collide with another grain of comparable size, which sets the timescale for grain growth. It is basically the same as the characteristic

time of grain-grain collision estimated by Nakagawa et al. (1981, see their equation (9)).

2.6 Discussion

2.6.1 Validity of the terminal velocity approximation

The grain velocities used in the Eulerian models are the "terminal velocities" (equation 2.14) of the grains at their respective locations. To test their validity, we compare them to those obtained from the Lagrangian simulation, where the particle velocities are calculated self-consistently, as described in § 2.2.4. Because the Lagrangian particles are usually not located at cell centers where the gas quantities in the (Eulerian) hydro simulation are defined, we use the TSC interpolation algorithm (see section § 2.2.4) to obtain the gas quantities at the grain locations. Fig. 2.15 shows the percentage difference between the velocities in the Eulerian and Lagrangian models for mm-sized grains (the left three panels), as well as the spatial distribution of such grains in the $\chi = 4$ Eulerian model (the rightmost panel). We see that most mm-sized grains in the Eulerian model are concentrated within the dashed-dotted line (where the gas density is greater than $4 \cdot 10^{-14}$g cm^{-2}), where the difference is $< 1\%$. A larger difference exists in the lower density regions (particularly beyond the dotted line marking $4 \cdot 10^{-15}$g cm^{-2}) where mm-sized grains coming from the envelope in one hemisphere can pass through the disk midplane to the other hemisphere before settling back to the midplane (see, e.g. Bate & Lorén-Aguilar, 2016). Such a behavior cannot be captured by the Eulerian model but there are very few mm-sized grains in the envelope and the low-density part of the disk, so the difference is inconsequential as far as grain growth is concerned. The situation is similar for the cm-sized grains, which are concentrated in even higher density regions. The terminal velocity

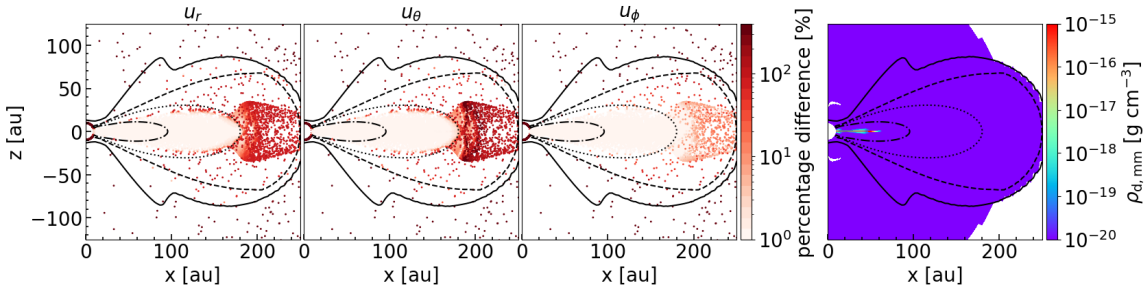


Figure 2.15: **Left three panels**: Percentage difference between the terminal velocities used in the Eulerian simulation and those calculated in the Lagrangian simulation for mm-sized grains. The black lines are iso-density contours that are the same in each plot. **Right**: the spatial distribution of the mm-sized grains in the Eulerian simulation with $\chi = 4$, showing that such large grains are concentrated in the high density regions where the terminal velocity approximation is good to the percent-level.

approximation is even better for the smaller grains, which are better coupled to the gas.

2.6.2 Slow Grain Growth in a Laminar Protostellar Disk

In a laminar disk without any turbulence, the main driver for grain growth is the force that causes grains of different sizes to move at different (terminal) speeds. In the vertical direction, this force is the vertical component of the gravity acting on the grain that is balanced by the aerodynamic drag. At a given cylindrical radius R, this force points towards the disk midplane, and increases roughly linearly with the distance from the midplane. Its characteristic value can be estimated at one disk scale height $h = R\ c_s/V_K$:

$$g_{\rm z,h} \approx \frac{GM_*}{R^2}\frac{h}{R} \approx \Omega_K c_s \tag{2.51}$$

where $c_s = \sqrt{\frac{k_b T}{\mu m_H}}$ is the isothermal sound speed, V_K the local Keplerian speed, and $\Omega_K = V_K/R$ is the orbital frequency.

Using $g_{\rm z,h}$ to approximate the dust acceleration to be balanced by the aerodynamic

drag, ζ, we obtain an estimate for the grain size e-folding time at one scale height:

$$\begin{aligned} t_{\rm size,h} \approx 1.9\ \eta\ &= 2.53 \frac{1}{\chi R_{\rm d-g}} \frac{v_{\rm th}}{g_{\rm z,h}} \approx \frac{64}{\chi} \left(\frac{0.01}{R_{\rm d-g}} \right)\ P_K \\ &= 90,000\ ({\rm years})\ \left(\frac{1}{\chi} \right) \left(\frac{0.01}{R_{\rm d-g}} \right)\ \left(\frac{0.5 M_\odot}{M_*} \right)^{1/2} \left(\frac{R}{100\ {\rm au}} \right)^{3/2}, \end{aligned} \tag{2.52}$$

where $P_K = 2\pi/\Omega_K$ is the local orbital period. Note that this e-folding time is similar to (but ~ 2.5 times longer than) the estimate of grain growth time given in Tanaka et al. (2005, their equation (23)), which was taken from Nakagawa et al. (1981) but with a factor of 4/3 removed (i.e., the value adopted in Tanaka et al. (2005) is only 75% of that of Nakagawa et al. (1981)).

We have checked the above estimate against the baseline model without any enhancement (i.e., $\chi = 1$) and found that the above estimate is about 50% longer than that obtained numerically in the model. The reason for the discrepancy is that the protostellar disk formed in our simulation is relatively massive, with a significant self-gravity in the vertical direction that is about half of that from the central star at one scale height; the disk self-gravity increases the dust settling (and thus grain-grain collision) speed somewhat, with a corresponding reduction in the grain growth time. Nevertheless, the above equation provides a reasonable estimate for the grain size e-folding timescale.

Equation (2.52) highlights the fundamental difficulty with grain growth from micron-sizes to mm-sizes in large (100 au-sized), laminar protostellar disks revealed by our baseline model (see Fig. 2.5). Increasing the grain size by a factor of 10^3 (from 1 μm to 1 mm) requires 6.9 e-folding times, which corresponds to $\sim 6.2 \times 10^5$ years for the fiducial stellar mass and radius adopted in equation (2.52). It is significantly longer than the time scale for the Class 0 stage of star formation of $\sim 1.6 \times 10^5$ years estimated by (Evans et al., 2009). If we choose a smaller characteristic height than

the pressure scale height h to evaluate the net dust acceleration to be balanced by the drag acceleration (ζ), as may be appropriate for large grains, the grain size $e-$folding time would be even longer because of a smaller local vertical gravity that would drive a slower grain-grain collision. The longer size $e-$folding time would strengthen our conclusion, namely, in order to produce a substantial amount of mm-sized grains in the relatively short deeply embedded Class 0 phase of star formation, the grain-grain collision speeds must be enhanced over those of the baseline laminar case.

2.6.3 Enhanced Growth Through Higher Grain-Grain Collision Speeds

To illustrate how a higher grain-grain collision speed enhances the grain growth, we carried out a simulation with a factor of $\chi = 4$ higher speed in § 2.4.2. We found that, by the time $t = 88,750$ years (or 48,750 years after the formation of the disk and the grain growth in it, when the disk radius reaches 250 au), about 140 $M_\oplus$ of grains have grown beyond 0.1 mm and about 15 $M_\oplus$ beyond 1 mm (see Fig. 2.5).

Part of the reason for the substantial grain growth in this case can be understood from the size e-folding time $t_{\rm size,h}$ at one scale height (equation 2.52). For an enhancement factor of $\chi = 4$, $t_{\rm size,h}$ is reduced to about 22,500 years at 100 au, which is well within the timescale for the disk to form and grow. This is reflected, for example, in Fig. 2.7, which shows the progression of the grain size increase from the disk upper surface towards the midplane at a representative cylindrical radius 50 au, where $t_{\rm size,h}$ is shorter still (about 8,000 years). The grain size peaks around 40 μm at a height of ~ 10 au. Most of the grains grown at relatively large vertical heights are quickly advected towards the midplane (see Fig. 2.6 for an example of advection timescale), where they grow further. Further growth near the midplane may appear surprising at the first sight, because the vertical component of the gravity g_z, which drives the

grain growth through dust-gas drift at relatively large vertical heights, disappears on the midplane.

However, near the midplane, the grains can drift radially inward relative to the gas because of the gas pressure gradient. We can estimate the acceleration due to this gradient as

$$a_p = \left| \frac{1}{\rho} \frac{d\ P}{d\ R} \right| \approx \alpha_p \frac{c_s^2}{R} \approx \alpha_p \frac{c_s}{V_K} g_{\rm z,h} \approx \alpha_p \frac{h}{R} g_{\rm z,h}, \tag{2.53}$$

where α_p is the exponent in the pressure distribution $P \propto R^{-\alpha_p}$, R the cylindrical radius, $c_s = \sqrt{P/\rho}$ the isothermal sound, V_K the Keplerian speed, and $g_{\rm z,h} \approx \Omega_K\ c_s$ the vertical component of the stellar gravity at one scale height (see equation 2.51). Using a_p to approximate the dust acceleration from aerodynamic drag, ζ, we obtain an estimate for the grain size e-folding time on the disk midplane:

$$\begin{aligned} t_{\rm size,mid} \approx 1.9\ \eta\ &= 2.53 \frac{1}{\chi R_{\rm d-g}} \frac{v_{\rm th}}{a_p} \approx \frac{64}{\chi} \left(\frac{0.01}{R_{\rm d-g}} \right)\ \frac{1}{\alpha_p}\ \frac{1}{h/R}\ P_K \\ &= 3 \times 10^5 ({\rm yrs}) \left(\frac{1}{\chi} \right) \left(\frac{0.01}{R_{\rm d-g}} \right) \left(\frac{3}{\alpha_p} \right) \left(\frac{0.1}{h/R} \right) \left(\frac{0.5 M_\odot}{M_*} \right)^{1/2} \left(\frac{R}{10^2 {\rm au}} \right)^{3/2}. \end{aligned} \tag{2.54}$$

Note that the force due to the radial pressure gradient on the midplane is smaller than the vertical gravity at one scale height by a factor of $\sim \alpha_p\ h/R$ (or ~ 0.3 for the adopted fiducial values of $\alpha_p = 3$ and $h/R = 0.1$), which translates to a longer size e-folding time on the midplane (by a factor of $\sim 10/3$) compared to that at one scale height, with everything else being equal. However, the advection of dust grains towards the midplane makes the midplane dust-to-gas ratio $R_{\rm d-g}$ substantially higher than the initial value of 0.01 in the envelope, reaching $R_{\rm d-g} \approx 0.03$ near the inner edge of the disk and at a radius $R \approx 50$ au (see Fig. 2.10). The higher dust-to-gas ratio leads to a shorter grain growth time scale.

For example, with $R_{\rm d-g} \approx 0.03$ and $\chi = 4$, the size e-folding time at a radius around 50 au on the midplane becomes $t_{\rm size,mid} \approx 8,840$ years if other parameters are held at their fiducial values. This is significantly shorter than the disk formation and evolution time during the Class 0 phase. The relatively short size e-folding timescale is consistent with the fact that, at this midplane location, the majority of the grains have already grown to a size of order 300 μm by the time shown in Fig. 2.7 (46,250 years after the disk formation and the start of grain growth; see the right-most curve).

A salient feature of the $\chi = 4$ model with an enhanced grain-grain collision speed is that grain growth in the atmosphere of the disk at relatively large heights can lead to a faster settling of the grown dust to the midplane, which increases the local dust-to-gas ratio, which, in turn, speeds up further growth there. Whether such an enhancement of collision speed can be achieved in protostellar disks is unclear. We believe that it is plausible during the Class 0 stage of star formation, when the protostar is expected to accrete most of its final mass. Yen et al. (2017) estimated a mass accretion rate of order 10^{-6} – 10^{-5} $M_\odot$ yr^{-1}, which is 2 to 3 orders of magnitude higher than the typical value for classical T Tauri stars. What drives the fast accretion in Class 0 disks is still unclear. If it is due to turbulent motions (from, e.g., magneto-rotational instability; Balbus & Hawley, 1991), the required turbulent speed would be comparable to the sound speed (i.e., with an effective α-parameter of order unity as opposed to the typical value of 10^{-2} for classical T Tauri disks). It is well known that turbulence can in principle promote grain growth by increasing the grain-grain collision speed (Voelk et al., 1980; Markiewicz et al., 1991b; Ormel & Cuzzi, 2007). However, turbulence can also puff up the vertical dust distribution, which can make the grain growth more difficult by reducing the dust number density, particularly for relatively large grains (Ohashi et al., 2021). The degree of enhancement depends on the details of the turbulence in the Class 0 disks, which are currently unknown. Our

results highlight the pressing need to tackle the problem of enhanced grain growth through disk turbulence or other means during the earliest deeply embedded phase of star formation.

2.7 Conclusion

We have studied the growth of dust grains during the formation of protostellar disks. We follow the disk formation out of the gravitational collapse of a rotating molecular cloud core using 2D (axisymmetric) radiation hydrodynamic simulations, which form the basis for the grain growth calculations that are performed as a post-processing step. Our main conclusions are as follows:

1. We find that the so-called "terminal velocity approximation" (equation 2.14) holds in most of the laminar protostellar disks, particularly the relatively dense regions that are of the most interest to grain growth (see Fig. 2.15). The approximation greatly simplifies the calculations of the dust drift speed relative to the gas and thus the collision speeds between grains of different sizes, which control the rate of grain growth in our simulations.

2. We find numerically that the grain-grain collision from differential (size-dependent) terminal velocities alone is too slow to convert a significant fraction of the grains into mm/cm sizes during the deeply embedded Class 0 phase (§ 2.4.1). This difficulty is caused by a rather long grain size e-folding time, which is estimated to be nearly two orders of magnitude longer than the local orbital period (or $\sim 10^5$ years on the 100 au scale; see equation (2.52) and the need for several e-folding times to grow from μm to mm sizes). Enhanced grain-grain collision speeds are required to produce enough mm/cm sized grains for, e.g., giant planet formation through core accretion in the Class 0 phase.

3. We find substantial grain growth when the grain-grain collision speed is en-

hanced by a factor of 4 (§ 2.4.2), with $\sim$ 15 $M_\oplus$ of grains larger than 1 mm and $\sim$ 140 $M_\oplus$ larger than 0.1 mm when the disk size reaches 250 au (see Fig. 2.5). As the grains grow bigger in the atmosphere of the disk, they settle faster towards the midplane, which increases the local dust-to-gas ratio, which, in turn, speeds up further growth there. Most of the largest, mm/cm-sized grains are formed near the midplane in the inner part of the disk (see Fig. 2.6).

4. If a substantial amount of mm/cm sized grains exist in Class 0 disks, as indicated by thermal dust emission at cm wavelengths and required if planets are to form in this earliest phase of star formation, the grain-grain collision speeds must be increased well beyond that given by the differential (size-dependent) terminal velocities. How this enhancement is achieved is unclear, although turbulence is a strong possibility. Our study highlights the urgent need for quantifying the level of turbulence in Class 0 disks and its effect on grain growth.

2.8 ACKNOWLEDGEMENTS

We thank Hiroyuki Hirashita, Zhaohuan Zhu and Jon Ramsey for useful discussions and the referee, H. Kobayashi, for constructive comments that improved the presentation of the paper. YT acknowledges support from an interdisciplinary fellowship and a computing allocation from the University of Virginia, NSF AST-1815784, and a NASA High-End Computing allocation. ZYL is supported in part by NASA 80NSSC20K0533 and NSF AST-1716259. KHL acknowledges support from SOFIA grant 07-0235.

Chapter 3

Protostellar Disks Fed By Dense Collapsing Gravo-Magneto-Sheetlets

The work presented in this chapter has been published in the Monthly Notices of the Royal Astronomical Society (MNRAS) with Zhi-Yun Li, Ka Ho Lam, Kengo Tomida, and Chun-Yen Hsu as coauthors (Tu et al., 2024a).

Abstract: Stars form from the gravitational collapse of turbulent, magnetized molecular cloud cores. Our non-ideal MHD simulations reveal that the intrinsically anisotropic magnetic resistance to gravity during the core collapse naturally generates dense gravo-magneto-sheetlets within inner protostellar envelopes – disrupted versions of classical sheet-like pseudodisks. They are embedded in a magnetically dominant background, where less dense materials flow along the local magnetic field lines and accumulate in the dense sheetlets. The sheetlets, which feed the disk predominantly through its upper and lower surfaces, are the primary channels for mass and angular momentum transfer from the envelope to the disk. The protostellar disk inherits a small fraction (up to 10%) of the magnetic flux from the envelope, resulting in a disk-averaged net vertical field strength of 1-10 mG and a somewhat stronger toroidal field, potentially detectable through ALMA Zeeman observations. The inherited magnetic field from the envelope plays a dominant role in disk angular momentum evolution, enabling the formation of gravitationally stable disks in cases where the disk field is relatively well-coupled to the gas. Its influence remains significant even in marginally gravitationally unstable disks formed in the more magnetically diffusive cases, removing angular momentum at a rate comparable to or greater than that caused by spiral arms. The magnetically driven disk evolution is consistent with the apparent scarcity of prominent spirals capable of driving rapid accretion in deeply embedded protostellar disks. The dense gravo-magneto-sheetlets observed in our simulations may correspond to the "accretion streamers" increasingly detected around protostars.

3.1 INTRODUCTION

Circumstellar disks play a central role in the formation of both stars and planets. How they form and evolve has been a topic of active research for decades. Much of the recent effort has been focused on the role of magnetic fields in disk formation, as

reviewed in, e.g. Li et al. (2014b); Wurster & Li (2018); Zhao et al. (2020); Tsukamoto et al. (2023b). There appears to be a general agreement that the magnetic field can strongly modify but does not prevent the formation of a rotationally supported disk in the presence of a realistic level of magnetic diffusion. With the question of whether disks can form in magnetized molecular cloud cores largely settled, it is natural to shift the focus to characterizing the properties of the formed protostellar disks and their connection with the collapsing envelope feeding them.

The protostellar disk's magnetic field strength is particularly important to quantify. It determines not only the structure and evolution of the disk during the protostellar phase but also sets the initial conditions for the subsequent disk evolution in the protoplanetary phase. For example, if little or no magnetic flux is inherited from the envelope, the disk would have to rely on gravitational torque to transport angular momentum, with its structure and evolution dominated by spiral arms rather than magneto-rotation instability or magnetically driven winds, as recently reviewed by Lesur et al. (2023). These authors emphasized: "A major uncertainty here is the field strength, which is not predicted by any complete theory, and for which we have few empirical constraints." We fully agree with this assessment. Some empirical constraints on the field strength on the disk scale have recently been obtained with ALMA CN Zeeman observations, which provided upper limits of several to tens of milli-Gausses (Vlemmings et al., 2019; Harrison et al., 2021). Our investigation aims to take initial steps toward a complete theory capable of predicting the disk field strength and confronting the prediction with observations.

Another goal is to quantify the role of the magnetic field in structuring the inner protostellar envelope. It is timely because ALMA has been observing the inner envelope in detail in molecular lines and, increasingly, dust continuum polarization (e.g. Pattle et al., 2023a); the latter trace magnetic fields on the envelope scale. It is

natural to ask how the observationally accessible magnetic field affects the envelope's structure and dynamics and how the magnetic structuring of the envelope affects the disk formation.

There is little doubt that a dynamically significant magnetic field can strongly affect the mass distribution of the collapsing protostellar envelope. It is well known that magnetic fields tend to deflect the gravity-induced collapsing motions toward a direction along the field lines through a tension force, forming a dense gravo-magneto-sheet near the magnetic equator – the classical "pseudodisk" (Galli & Shu, 1993a). Its formation is an unavoidable consequence of the anisotropic nature of the magnetic resistance to gravity. A realistic level of turbulence is expected to warp the dense sheet out of the equatorial plane and potentially break it up into smaller pieces, forming a highly perturbed three-dimensional structure that we will term "gravo-magneto-sheetlets" (or "sheetlets" for short). They show up as filaments in the column density maps of many disk formation simulations that include both magnetic fields and turbulence (e.g. Santos-Lima et al., 2012; Seifried et al., 2013; Li et al., 2014a; Seifried et al., 2015; Kuffmeier et al., 2017; Matsumoto et al., 2017; Gray et al., 2018; Lam et al., 2019; Wurster & Lewis, 2020a,b; see Tsukamoto et al., 2023b for a review), although the deep connection between the apparent filaments in the column density map and the classical pseudodisk of Galli & Shu (1993a) was rarely recognized. We aim to build a conceptual framework of protostellar envelopes dominated by gravo-magneto-sheetlets by examining such dense thin structures more closely than before, focusing on their contributions to the envelope's mass and angular momentum budgets, their effects on disk formation, and their connection to observations, particularly accretion streamers that are increasingly detected around Class 0 (e.g. Hsieh et al., 2020; Pineda et al., 2020; Murillo et al., 2022; Thieme et al., 2022) and Class I protostars (e.g. Yen et al., 2014, 2019; Valdivia-Mena et al., 2022).

The paper is organized as follows. Section 3.2 describes the numerical setup of the problem, while section 3.3 overviews our simulation results and defines terms used in our analysis. We focus on the formation of gravo-magneto-sheetlets and their leading roles in the structure and dynamics of the inner protostellar envelope in § 3.4. It is followed by a discussion of the transition between the envelope and disk in § 3.5, emphasizing the magnetic flux fraction the disk inherits from the envelope. Section 3.6 discusses the properties of the formed disks, focusing on the role of the magnetic field in transporting angular momentum. We discuss our main results in § 3.7 and conclude in § 3.8.

3.2 Problem Setup

The formation of protostellar disks from the collapse of dense magnetized molecular cloud cores is a complex process involving non-ideal MHD effects (particularly ambipolar diffusion) and turbulence. The following set of equations governs this turbulent, non-ideal MHD process:

$$\frac{\partial \rho}{\partial t} + \nabla \cdot (\rho \boldsymbol{v}) = 0, \tag{3.1}$$

$$\rho \frac{\partial \boldsymbol{u}}{\partial t} + \rho(\boldsymbol{u} \cdot \nabla)\boldsymbol{u} = -\nabla P + \frac{1}{c}\boldsymbol{J} \times \boldsymbol{B} - \rho \nabla \Phi_g, \tag{3.2}$$

$$\frac{\partial \boldsymbol{B}}{\partial t} = \nabla \times (\boldsymbol{v} \times \boldsymbol{B}) - \frac{4\pi}{c} \nabla \times (\eta_A \boldsymbol{J}_\perp), \tag{3.3}$$

$$\nabla^2 \Phi_g = 4\pi G \rho \tag{3.4}$$

where $\boldsymbol{J} = (c/4\pi)\nabla \times \boldsymbol{B}$ is the current density, $\boldsymbol{J}_\perp = [(\boldsymbol{J} \times \boldsymbol{B}) \times \boldsymbol{B}]/B^2$ the component of current density perpendicular to the magnetic field, and η_A the ambipolar diffusivity. Other symbols have their usual meanings.

To simplify calculations, we adopted an equation of state consisting of four power-

laws in four different density regimes based on the radiation magnetohydrodynamic calculations of Tomida et al. (2013). The transition densities between the power-laws are chosen as $\rho_1 = 10^{-13}$g cm^{-3}, $\rho_2 = 3.16\times10^{-12}$g cm^{-3} and $\rho_3 = 5.66\times10^{-9}$g cm^{-3}, with corresponding adiabatic constant $\gamma_1 = 5/3$, $\gamma_2 = 1.4$, and $\gamma_3 = 1.1$, respectively. At low densities $\rho < \rho_1$, we assume the gas is isothermal with $\gamma_0 = 1$.

Our simulation setup closely follows that of Lam et al. (2019), except for our use of Adaptive Mesh Refinement (AMR), which is required to better resolve the formed disks, a key goal of our investigation. The AMR capability is afforded by the ATHENA++ code (Stone et al., 2008, 2020), which includes a newly developed self-gravity solver specifically designed for AMR (Tomida & Stone, 2023). We used the full multigrid (FMG) mode of the multigrid self-gravity solver and obtained the boundary conditions for the gravitation potential using multipole expansion (Tomida & Stone, 2023). The governing equations are solved in a Cartesian coordinate system, with standard outflow boundary conditions implemented at all simulation domain boundaries.

We used four strategies to speed up the simulations so that they could be completed in a reasonable amount of time. Firstly, we use the AMR capability to concentrate computational resources around the central star region. A refinement level is added when the local cell size exceeds 1/16 of the local Jeans length. Secondly, we adopt the sink particle technique of Lam et al. (2019) to treat protostellar accretion. A sink particle is created when the grid reaches the highest refinement level, and the local cell size exceeds 1/16 of the local Jeans length. After creation on the finest grid, the sink particle accretes mass and the radial component of the linear momentum from a sink region of $3 \times 3 \times 3$ cells, leaving the magnetic field untouched in the sink region. Thirdly, we cap the ambipolar diffusion using equation (7) of Lam et al. (2019) to avoid prohibitively small time steps. This treatment primarily affects very

low-density regions, and we monitor the simulation to make sure that its effect is minimal. Finally, we cap the Alfvén speed by adding small amounts of mass in highly evacuated cells and monitor the total added mass to ensure that it stays negligible compared to the mass in the computation domain. With these strategies, the models presented in this work each cost between 50,000 to 100,000 CPU core hours.

The simulation is initialized by putting a pseudo-Bonner-Ebert sphere of mass 0.5 $M_\odot$ and radius 2000 au at the center of the simulation domain with a box size of 10,000 au on each side. The density profile of the pesudo-Bonner-Ebert sphere is given by

$$\rho(r) = \frac{\rho_0}{1 + (r/r_c)^2} \tag{3.5}$$

where $\rho_0 = 4.6 \times 10^{-17}$ g cm^{-3} is the central density, and $r_c \approx 670$ au is a radius characterizing the size of the central region of relatively uniform density distribution. We fill the space outside the sphere with diffuse material of a low density 4.56×10^{-20} g cm^{-3}. The total mass in the simulation domain is $0.56 M_\odot$, enough to form a star of a few tenths of the solar mass that is typical of low-mass stars (e.g. Offner et al., 2014). We assume the core has an initial solid body rotation rate of 6.16×10^{-13} s^{-1} along the $\hat{z}$ axis and an initially uniform magnetic field of 2.2×10^{-4} G (corresponding to a dimensionless mass-to-flux ratio of 2.6 in units of the critical value $1/[2\pi G^{1/2}]$), also along the $\hat{z}$ axis.

As in Lam et al. (2019), we initialize the simulation with a turbulent velocity field of an k^{-2} power spectrum (Kolmogorov, 1941; Gong & Ostriker, 2011). The net angular momentum from the turbulence is removed from the initial state. The velocity field's amplitude is normalized to obtain a root-mean-square Mach number $\mathcal{M} = 1$ for most of our runs. We also consider two cases with, respectively, weaker turbulence of $\mathcal{M} = 0.5$ and no turbulence ($\mathcal{M} = 0$). The parameters of all models

Model name	$\mathcal{M}$	η_0/η_R	Comments
M1.0AD1.0	1.0	1.0	Reference model
M0.5AD1.0	0.5	1.0	Weaker turbulence model
M0.0AD1.0	0.0	1.0	Non-turbulent model
M1.0AD2.0	1.0	2.0	More diffusive model
M1.0AD10.	1.0	10.	Most diffusive model
M1.0AD0.1	1.0	0.1	Least diffusive model

Table 3.1: $\mathcal{M}$ is the initial turbulent Mach number and η_R the reference ambipolar diffusion coefficient.

considered in this paper are summarized in Table 3.1.

The ambipolar diffusivity η_A in the governing equations is uncertain. It is strongly affected by the size distribution of dust grains and the abundance of metals (such as Mg) in the gas phase, which are uncertain (e.g. Lesur, 2021). Following Lam et al. (2019), we choose to parameterize it in the following way for efficient parameter exploration:

$$\eta_A = \frac{B^2}{4\pi\gamma\rho\rho_i}, \tag{3.6}$$

where $\gamma = \langle\sigma v\rangle/(m + m_i)$ is the ion-neutral drag coefficient and $\rho_i = C\rho^{1/2}$ is the ion density, with the coefficient C proportional to the square root of the cosmic ray ionization rate (Shu, 1991; Draine et al., 1983); we postpone a more detailed treatment of the ambipolar diffusivity using chemical networks to a future investigation. With these approximations, the ambipolar diffusivity can be written as

$$\eta_A = \eta_0 \frac{B^2}{4\pi\rho^{3/2}}, \tag{3.7}$$

with $\eta_0 = 1/(\gamma C)$. For the standard cosmic ionization rate of 10^{-17} s^{-1}, we have $\gamma = 3.5 \times 10^{13}$cm^{3}g^{-1}s^{-1} and $C = 3 \times 10^{-16}$ cm$^{-3/2}$ g$^{1/2}$ (Shu, 1991), yielding a "reference" value for η_0 of $\eta_R = 95.2$ g$^{1/2}$ cm$^{-3/2}$ s. Besides η_R, we also explore a wide range of values for η_0, from 0.1 to 10 $\times$ η_R (see Table 3.1).

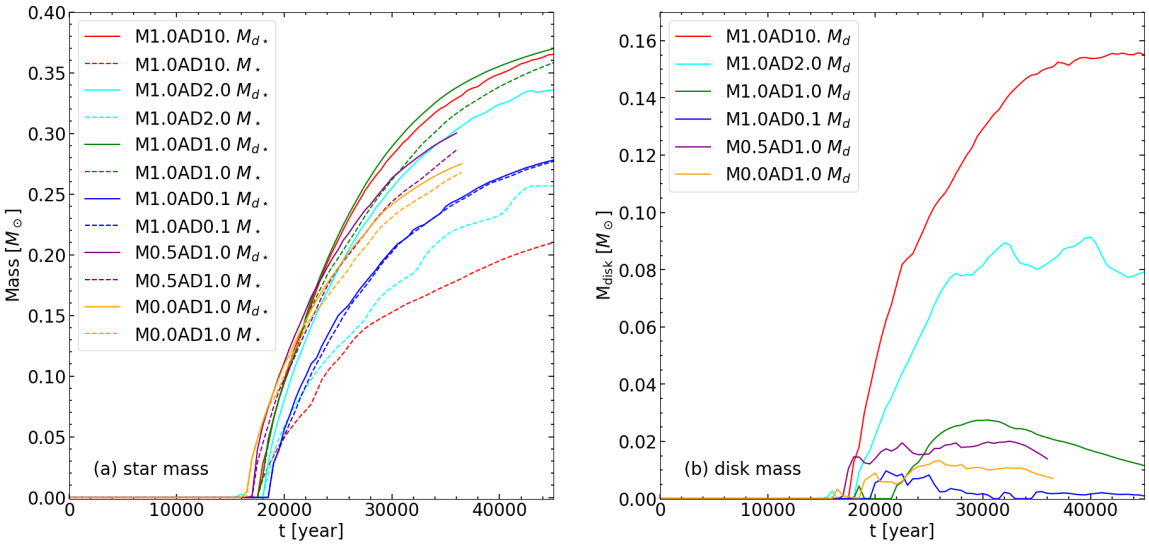


Figure 3.1: Time evolution of the stellar mass M_* (panel a; dashed lines) and disk mass M_d (panel b) as a function of time for all six models listed in Table 3.1. Also plotted in panel (a) is the combined star and disk mass M_{d*} (solid lines).

We choose 6 levels of mesh refinement, with the finest cell size of 1.22 au at the highest level of refinement. We ensure that the sink particle always stays on the finest grid so that the resolution for the protostellar disk, if formed, is maximized.

3.3 Overview of Simulation Results

To give a first impression of the simulation results, we show in Figs. 1 and 2 some broad features of all six models listed in Table 3.1. Fig. 1 plots the masses of the protostar (sink particle, panel a) and the protostellar disk (panel b) as a function of time, and Fig. 2 displays the face-on (along the $z-$axis) and edge-on views of the column density distribution, showing a dense, flatted disk-like structure surrounded by a filamentary inner envelope in all cases. The disk is persistent and well defined in some cases (e.g., Models M1.0AD2.0 and M1.0AD10) but highly transient and irregular in others (e.g., Model M1.0AD0.1; see the animated version of Fig. 3.2 in the supplementary material).

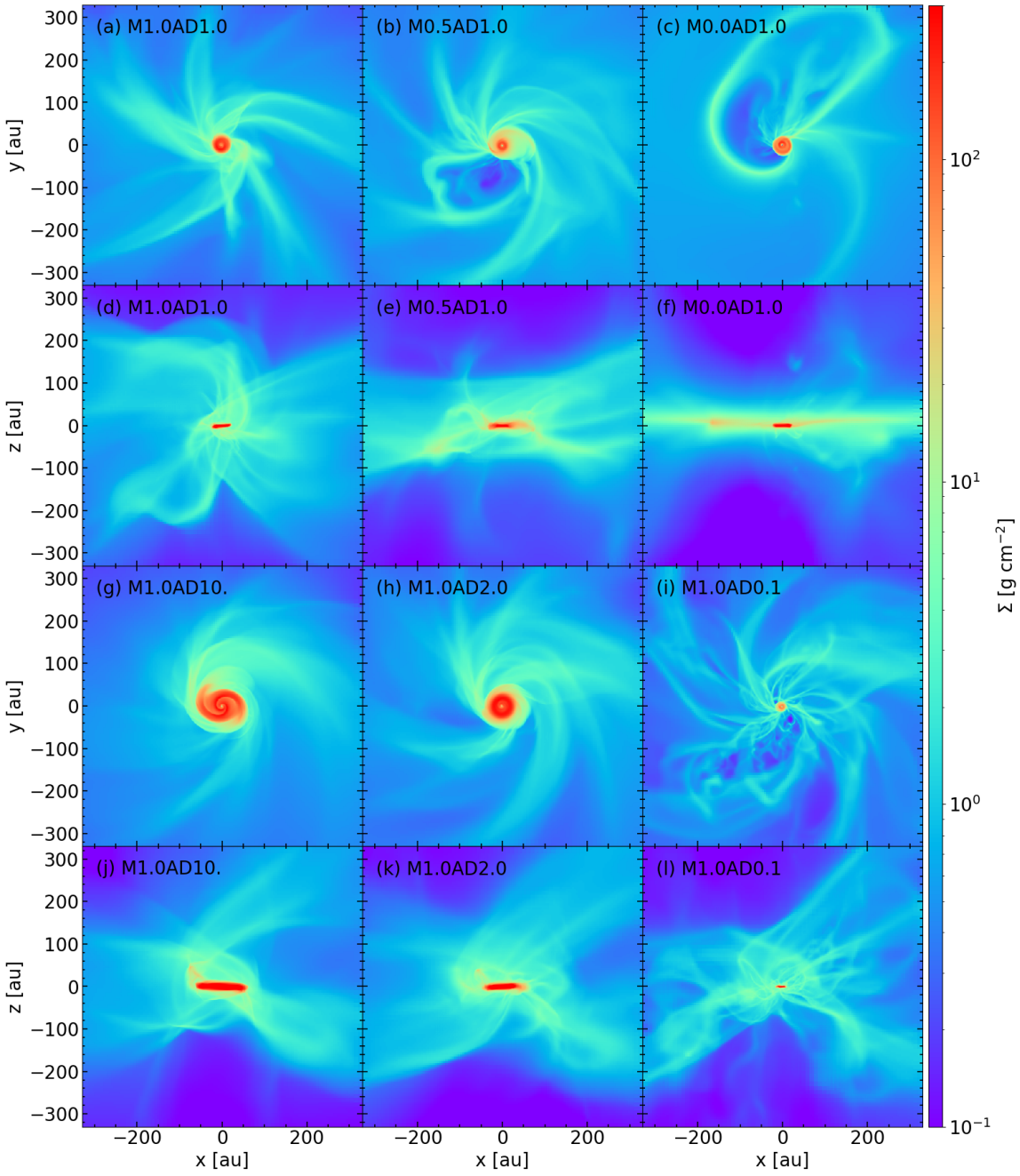


Figure 3.2: Face-on (first and third row) and edge-on (second and fourth row) views of the column density distributions of all six models listed in Table 3.1, showing the formation of a dense disk surrounded by a filamentary inner envelope at a representative time when the combined mass of the star and disk $M_{d*} = 0.2$ M$_\odot$. The model name is shown in each panel. The animated version is available in the online supplementary material.

To facilitate a quantitative analysis, we define the disk in two steps. Firstly, we identify a disk "midplane," which satisfies the following two criteria: (a) it passes through the protostar (the sink particle), and (b) its average distance to the densest 10,000 cells in the simulation is minimized. A region on this plane is considered to be part of the disk if it is rotationally supported with $v_\phi > 0.8\ v_{\rm K}$ where $v_{\rm K}$ is the local Keplerian speed) and denser than $\rho_{\rm disk}$. We have empirically varied the threshold density $\rho_{\rm disk}$ and found that a value of 5×10^{-15} g/cm^3 describes well the boundaries of the relatively small disks formed in all cases other than the two most magnetically diffusive models (M1.0AD2.0 and M1.0AD10), where the disks are substantially larger and less dense (see Fig. 3.2 below). For these two cases, we apply a lower density threshold of 1×10^{-15} g/cm^3, which captures the full extents of the larger and lower-density disks better (see, e.g., Fig. 3.11). Secondly, we identify the rest of the disk by examining regions on planes parallel to, and at increasing distances from, the midplane. A region on a plane is considered part of the disk if (a) its density is greater than $\rho_{\rm disk}$, (b) its location lies within the disk boundary when projected onto the midplane, (c) its rotational motion dominates over the vertical motion, with $v_\phi > 2\ |v_z|$ (following Masson et al. 2016). In addition, we require that the disk cells form nearly closed circles around the midplane axis, to exclude irregular, rotationally dominated accretion streams that can extend tens of AUs above and below the disk midplane; these streams can be seen in, e.g., panel (d) of Fig. 3.2 and will be discussed in § 3.5 below.

We can quantify the disk's mass with the above definition, as shown in Fig. 3.1b. The disk mass is determined primarily by the magnetic diffusivity, with more massive disks formed in the more diffusive models (M1.0AD10 and M1.0AD2.0). The more massive disks are also larger, as shown in panels (g) and (h) of Fig. 3.2. Conversely, the less diffusive (i.e., best magnetically coupled) model, M1.0AD0.1, barely has a

rotationally supported disk (see Fig. 3.2i), especially at late times, when the disk mass goes to almost zero (see the blue curve in Fig. 3.1b). The reference run, M1.0AD1.0, lies between these two extremes, with a well-defined disk over most of the simulation duration, although both its mass and radius decrease at later times. As we will show in § 3.6 below, the disk formed in this case evolves quickly, with the material accreted from the envelope passing through the disk in only several orbital periods.

Compared to the disk mass M_d, the stellar mass M_* varies less across the different models, as shown by the dashed lines in Fig. 3.1a. The difference between the largest M_* (for the reference model M1.0AD1.0) and the least massive one (for the most diffusive model M1.0AD10) is less than a factor of two (compare the green and red dashed curves in the panel). The difference is even less for the combined stellar and disk mass M_{d*} because smaller stellar masses in more diffusive models are compensated somewhat by larger disk masses (see the solid lines in the panel). Nevertheless, there is some difference in M_{d*} across the models, with the largest value in the reference model and the lowest value in the best magnetically coupled model M1.0AD0.1, indicating a difference in the structure and dynamics of the protostellar envelope, which controls the envelope accretion onto the disk-plus-star system, and/or in the outflow rate.

We discuss the structure and dynamics of the protostellar envelope in detail in the next section (§ 3.4). It is followed by a discussion of the connection between the envelope and the disk in § 3.5 and the structure and evolution of the formed disk in § 3.6.

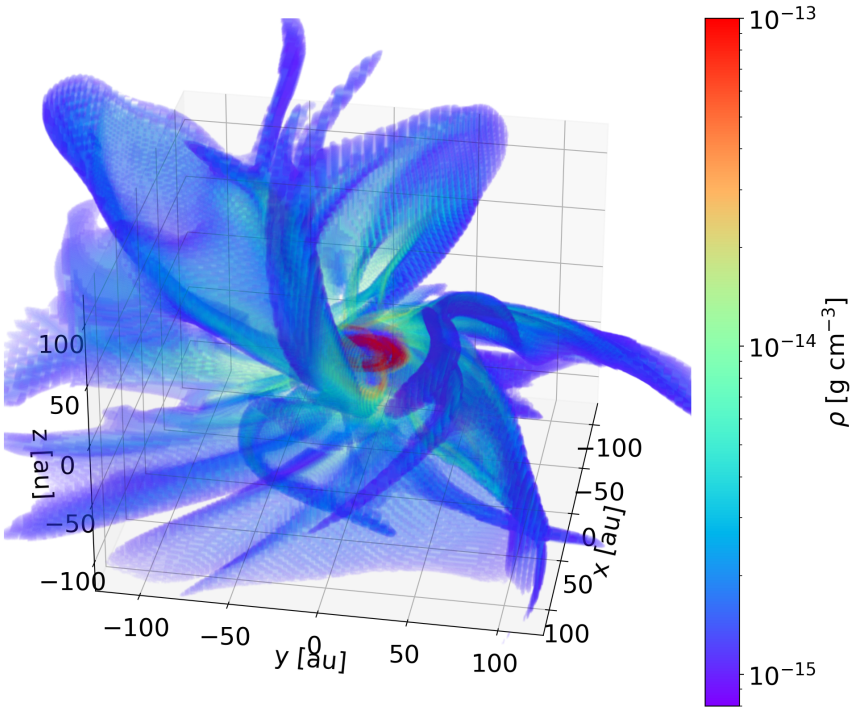


Figure 3.3: 3D visualization of the reference model (M1.0AD1.0) showing that most of the inner envelope mass is concentrated into warped but coherent sheet-like structures (termed "gravo-magneto-sheetlets" or simply "sheetlets" in the text). The animated version is available in the online supplementary material.

3.4 MAGNETICALLY STRUCTURED PROTOSTELLAR ENVELOPES

As mentioned in the introduction, one of our focuses is on how the interplay between the magnetic field, turbulence, and gravity shapes the structure and dynamics of the protostellar envelope. The inner protostellar envelopes are highly structured, as illustrated by the representative column density maps shown in Fig. 3.2. To highlight the envelope, we pick a representative time that is relatively early when the combined stellar and disk mass reaches $M_{d*} = 0.2\ M_\odot$ in this section (§ 3.4). The envelope becomes more inhomogeneous and filamentary with an increasing initial turbulence strength (compare Models M1.0AD1.0, M0.5AD1.0, and M0.0AD1.0). In the non-turbulent model M0.0AD1.0 (panels c and f), the gas in the envelope concentrates near the midplane, forming an infalling disk-like structure that is not rotationally supported – the pseudodisk[1]. In the more turbulent model M0.5AD1.0, the pseudodisk puffs up into a visually filamentary structure with a vertical height of about 150 au at the time shown (panel e). In the most turbulent reference model M1.0AD1.0, the envelope material falls onto the disk from all directions in dense filaments (panel d).

Although the dense filaments in the column density maps of the reference model appear to be independent of one another, they are spatially connected in 3D. The spatial connectivity is illustrated in Fig. 3.3, where we highlight the high-density regions in 3D with colored dots at the same time as in Fig. 3.2. The figure shows only the densest regions above a density threshold $\rho_c(r)$ that contains 70% of the mass at each radius r (see more discussion in § 3.4.2 below). Regions with densities below 4×10^{-16} g cm^{-3} are removed from the visualization for clarity. Most of the inner envelope

[1]The low-density cavity in Fig. 3.2c is filled with the magnetic flux released by the mass already accreted to the central protostar, as first discussed in Zhao et al. (2011).

material is concentrated into warped sheet-like structures. These 3D structures can be seen even more clearly in the animation included in the online supplementary materials. They show up as the long, curved filaments in the (projected) column density maps (see Fig. 3.2a,d)[2].

The dense warped sheet-like structures also exist in models with different ambipolar diffusivities, as shown in the column density maps of Models M1.0AD10, M1.0AD2.0, and M1.0AD0.1 in Fig. 3.2. There is a clear trend that the inner envelope is more inhomogeneous and filamentary when the magnetic field is better coupled to the gas (i.e., for a lower ambipolar diffusivity). Since the ambipolar diffusivity controls the efficiency of magnetic braking and the disk size (as discussed in detail in Section 3.5 below), there is a correlation between the disk size and how filamentary the envelope is, everything else being equal; such a correlation should be searched for in observational data. The sheet-like structures appear to be a generic feature of the turbulent magnetized inner protostellar envelopes. Their ubiquitous presence makes it conceptually appealing to view the inner envelope as a bi-phase medium, with dense sheet-like structures embedded in a low-density background.

3.4.1 Dense Collapsing Gravo-Magneto-Sheetlets

To help illustrate the physical nature of the dense sheet-like structures and their differences from the lower-density background, we plot in Fig. 3.4a the distribution

[2]We should note that some filamentary structures are produced even without an initial turbulence. For example, there is an elongated dense loop in the non-turbulent model M0.0AD1.0 that lines the outer edge of the low-density cavity carved out by the escaping magnetic flux in the equatorial pseudodisk (see Fig. 3.2c and also the lower-left panel of Fig. 2 of Mignon-Risse et al., 2021). It appears different from the filamentary structures produced by the initial turbulence, which warps (rather than carving out) the pseudodisk. The turbulence-induced sheet-like structures tend to be farther away from the equatorial plane (see Fig. 3.2d and more pictorially Fig. 3.3) and generally do not line the edges of any obvious cavities driven by the released magnetic flux. It is conceivable that the released flux could still have an effect on the inner envelope in the presence of an initial turbulence, but it is unlikely to dominate the creation of the dense sheet-like structures shown in Fig. 3.3, which look very different from the equatorial dense structure created by the released flux in the non-turbulent case.

of the mass density ρ on an x-z plane passing through the stellar position for the reference model M1.0AD1.0 at the representative time. It can be seen that dense filaments clearly stand out from the lower-density background. They are the cross-sections of the 3D dense sheet-like structures shown in Fig. 3.3 on the chosen plane. Several magnetic field line segments are superposed on the density map to demonstrate that the dense structures are associated with a strong field line pinching, which is a well-known characteristic of an unperturbed magnetically induced pseudodisk (Galli & Shu, 1993a; see, e.g., Fig. 6 of Li et al., 2014c). The similarity in the local field geometry supports the notion that the dense sheet-like structures are distorted pseudodisks, which are produced by the gravitational accumulation of material along the field lines near the sharp kinks where the gravitational collapse is retarded by the strong magnetic tension force associated with the field pinching. Just as in the case of unperturbed equatorial pseudodisk, the formation of these dense structures is an unavoidable consequence of the intrinsically anisotropic magnetic resistance (mostly through tension forces) to the gravitational collapse. To highlight their common physical origin with the unperturbed pseudodisks that are sheets produced by the interplay between gravitational collapse and anisotropic magnetic resistance, we will term these dense structures "gravo-magneto-sheetlets" or simply "sheetlets" for short hereafter. They are simply pseudodisks distorted and/or disrupted by turbulence or other processes (such as a clumpy mass distribution).

Because the dense sheetlets/filaments are formed by mass accumulation primarily along the field lines, the large density increase is not accompanied by a correspondingly large increase in the field strength, as illustrated in panel (b) of Fig. 3.4. If anything, the field strength in the dense filaments tends to be lower than their surroundings (see, e.g., the two filaments below the disk). It is a direct consequence of the sharp field line pinch across the dense filament, which greatly increases the com-

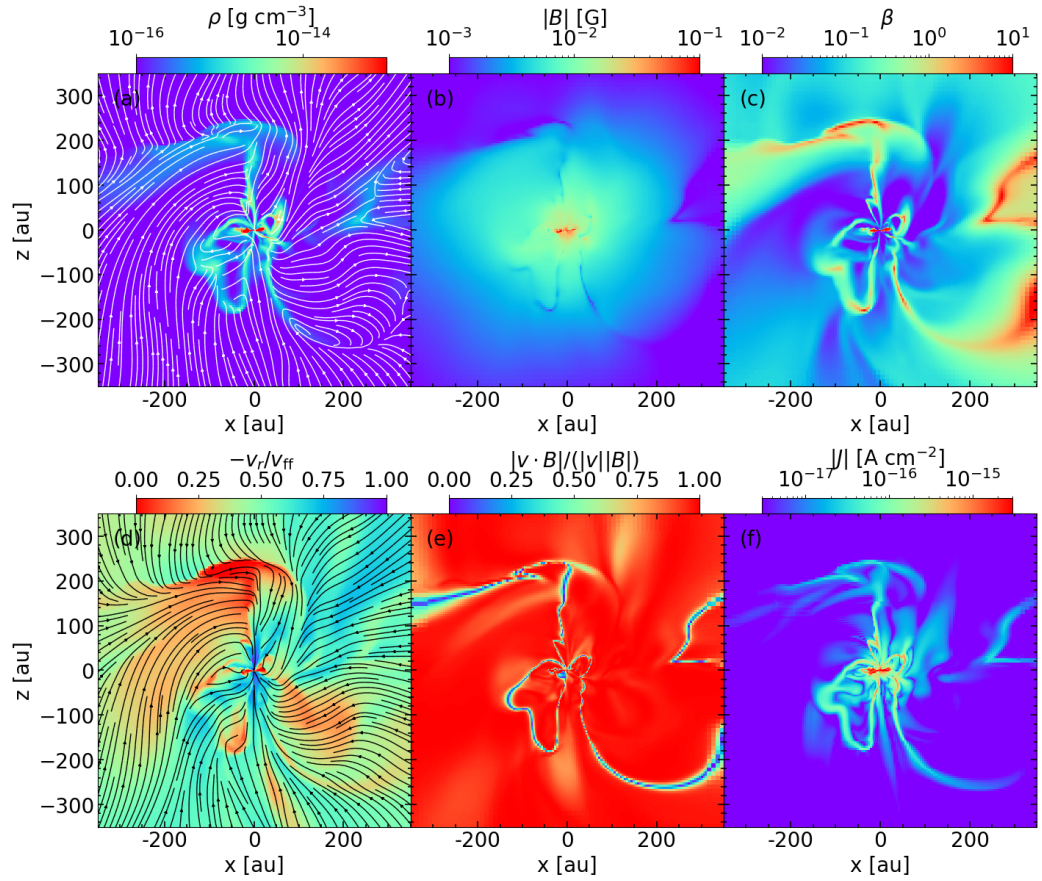


Figure 3.4: Illustration of a highly inhomogeneous magnetically-structured protostellar envelope. Panel (a) plots the mass density ρ on an x-z plane, showing thin dense filaments (sheetlets in 3D) embedded in a low-density background. The field lines (white) demonstrate that the dense structures are associated with strong field pinching, as in the case of an unperturbed pseudo-disk. Panel (b) shows that the density increase in the dense structures does not have a corresponding increase in the total field strength. Panel (c) displays the plasma-β, showing the dense structures are much less magnetized relative to their masses than the background. Panel (d) shows that the envelope tends to collapse radially at a sub-free-fall speed (with flow streamlines superposed to illustrate the velocity field). Panel (e) displays the cosine of the angle between the velocity and magnetic field vectors, showing the magnetically guided flows in the low-density background and the gravity-driven collapse in the cross-field direction in the dense structures. Panel (f) displays the distribution of the current density $|\mathbf{J}|$, showing that the current (and thus the magnetic force) is concentrated in the dense structures. The animated version is available in the online supplementary material.

ponent of the magnetic field parallel to the filament immediately outside it compared to that inside. The combination of higher densities and comparable or weaker magnetic fields makes the dense structures easily distinguishable from their background in the plasma-β, as shown in panel (c). It is clear that, whereas the background is strongly magnetically dominated, with a plasma-β well below unity, the dense structures are much less so, with a plasma-β closer to, or, in some regions, even larger than unity. This difference re-enforces the notion of a bi-phase inner envelope where a magnetically dominated background surrounds a less magnetized (relative to the local density) network of denser filaments (or sheetlets in 3D).

The strong magnetic field in the inner envelope, especially in the low-density background, is expected to affect gas kinematics. Naively, one would expect the inner envelope to collapse more or less radially towards the central stellar object at a speed close to the local free-fall value, with some deflection towards the midplane near the disk because of rotation. However, this is not the case, as illustrated in panel (d), where the streamlines with velocity vectors (black arrows) are displayed. There is a large deviation from the expected radial infall over most of the displayed area, with non-radial motions dominating the radial infall over large patches. It is particularly true in the low plasma-β regions to the upper-left and lower-right of the disk, where the flows are more azimuthal than radial. They broadly follow the magnetic field lines (shown in panel a), indicating that the envelope material in these regions is forced to slide along the rather strong (and thus rigid) field lines, which are not directed radially.

Another major deviation from the naive expectation is that the radial collapse speed is typically significantly below the local free-fall speed (defined as $\sqrt{2|\Phi|}$ where Φ is the local gravitation potential) in the inner envelope (see the color map in panel d), by a factor of 3 or more over large patches. Since these slowly infalling regions

do not have a significant amount of rotational support, their gravitational collapse must be retarded primarily by magnetic forces. The magnetic retardation will be discussed further in Section 3.5.2, and its observation implications will be discussed in Section 3.7.

The most striking difference between the dense sheetlets and the background is the degree of alignment between the flow and magnetic field directions (see panel e). Whereas the low-density gas in the magnetically-dominated (low-plasma-β) background primarily flows along the field lines (with $\cos[\theta] \equiv |\mathbf{v} \cdot \mathbf{B}|/[|\mathbf{v}|\ |\mathbf{B}|]$ close to unity, where θ is the angle between the velocity and magnetic vectors), the dense sheetlets move primarily perpendicular to the field lines. The bimodal behavior leads to a conceptual picture where the envelope material in the low-density background is collected along the (strong) field lines into the dense sheetlets, where the gravity becomes strong enough to overwhelm the magnetic (tension) resistance and pull the gas towards the central protostar in a cross-field direction, pinching the field in the process. In this picture, the gravity-dominated dense sheetlets are the main conduits for the envelope to feed the central disk-plus-star system, while the magnetically-dominated background is the feeder of material to the conduits, analogous to the runoff of rainwater from the land surface feeding rivers. In other words, the magnetized protostellar envelope accretion is fundamentally a two-step process involving two distinct types of regions shaped by the competition between gravity and magnetism – dense gravity-dominated sheetlets and diffuse magnetically-dominated background – with the latter feeding the former, which in turn feeds the central star-disk system. We call this two-step feeding process "bimodal protostellar envelope accretion."

The dense sheetlets/filaments and the background also differ in the current density $\mathbf{J}$, which is displayed in panel (f) of Fig. 3.4. The current density map looks strikingly similar to the mass density map (panel a), with large current densities concentrating in

the dense filaments. The strong correlation is not surprising since the dense filaments are where the field lines are sharply pinched (see panel a). An implication is that the magnetic force ($\propto \mathbf{J} \times \mathbf{B}$) is also concentrated in the dense filaments, including the azimuthal component, which is responsible for regulating the angular momentum content of the envelope through magnetic braking. We will return to discussing magnetic braking and disk formation in § 3.5.

It should be noted that the dense gravo-magneto-sheetlets can be modified by the magnetic flux released near the center, which tends to expand against (and sweep up) the surrounding material, including the sheetlets. In the non-turbulent case (M0.0AD1.0), the magnetic flux release creates a "bubble" on the pseudodisk (fig. 3.2c), which aligns with the disk midplane. In the turbulent models, the magnetic flux release would interact with the dense sheetlets in a similar way, although the flux release is more episodic and harder to quantify.

3.4.2 Role of Sheetlets in Envelope Structure and Dynamics

To quantify the roles of the dense (3D) sheetlets in the structure and dynamics of the protostellar envelope, we define a characteristic density $\rho_c(r)$ at each radius r from the central protostar, with the material denser than ρ_c containing 70% of the mass at that radius. As shown in Fig. 3.3, the material above this density threshold forms multiple sheet-like structures in the reference model – the dense sheetlets. The characteristic density is shown as a function of radius in the inner envelope up to 750 au in Fig. 3.5a for models with the same initially sonic turbulence but different ambipolar diffusivities at the representative time when $M_{d*} = 0.2$ M$_\odot$. The sharp increase in ρ_c towards the center on each curve marks the transition from the envelope to the disk. The dense sheetlets defined this way contain the majority of the envelope mass. However, they are squeezed into an increasingly small fraction of the volume

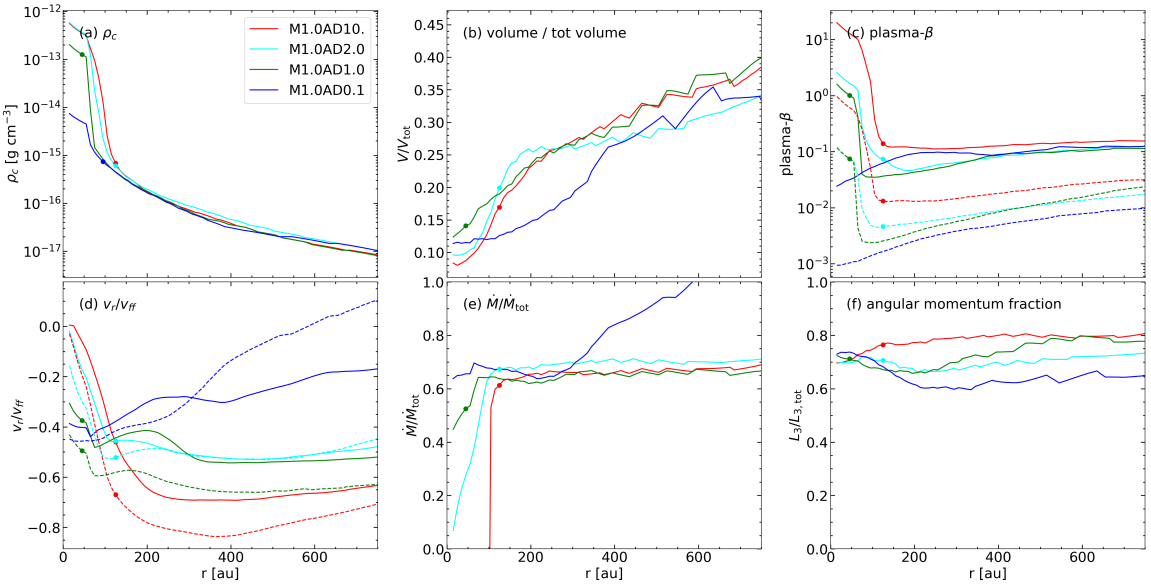


Figure 3.5: Spherically average properties of dense sheetlets and their contributions to the structure and dynamics of the inner protostellar envelope for models with different ambipolar diffusivities. Panel (a) displays the characteristic density ρ_c that separates the dense sheetlets from the diffuse background. Panel (b) shows that the dense sheetlets occupy an increasingly small fraction of the volume towards the center, reaching values as low as $\sim 10\%$. Panel (c) displays the plasma-β for the sheetlets (solid lines) and background (dashed), showing an order-of-magnitude difference between the two. Panel (d) plots the radial infall speed normalized by the local free-fall speed, showing that both the sheetlets and background collapse radially at substantially sub-free-fall speeds. Panel (e) shows the fraction of the radial mass flux carried by the dense sheetlets. Panel (f) displays the fraction of the $z-$component of the angular momentum carried by the dense sheetlets. The solid dot on each line approximately marks the transition radius between the disk and envelope on the disk midplane.

towards the center, reaching values as low as $\sim 10\%$, as shown in panel (b). Panel (c) displays the average plasma-β for the dense sheetlets and diffuse background, showing an order-of-magnitude difference between the two, especially for the least magnetically diffusive model M1.0AD0.1, where the contrast is the highest. Panel (d) plots the radial infall speed normalized by the local free-fall speed. For the reference model M1.0AD1.0, the panel shows that the dense sheetlets collapse at roughly 50% of the local free-fall speed, somewhat slower than the diffuse background, which infalls at about 60% of the free-fall speed. The sub-free-fall radial motions are consistent with the normalized infall speed shown pictorially in the color map of Fig. 3.4d. The infall speed tends to decrease with a smaller magnetic diffusivity. It remains substantially sub-free-fall for all four models shown, indicating that the result is robust. It is primarily a consequence of the magnetic field channeling the flow in the low-plasma β background and resisting gravitational collapse in dense sheetlets, which will be discussed in more detail in § 3.5.

Because the average infall speeds are comparable in the dense sheetlets and diffuse background, the former (which contains 70% of the mass by definition) typically contributes the majority ($\sim 60-70\%$) of the (radial) mass accretion rate in the M1.0AD1.0, M1.0AD2.0, and M1.0AD10 models. The mass accretion contribution by the sheetlets in the lowest diffusivity model M1.0AD0.1 is larger beyond a radius of ~ 300 au, reaching values greater than 100% because the background has a positive average radial speed at such large radii (see panel d) and thus contributes negatively to the mass accretion. Similarly, the dense sheetlets carry the majority ($\sim 60\%$ or more) of the $z-$component of the angular momentum in the envelope in all four cases, as shown in panel (f) of Fig. 3.5, and are thus expected to play a crucial role in disk formation, as discussed further below in § 3.5.

We conclude that, despite the small volume they occupy, the dense sheetlets play

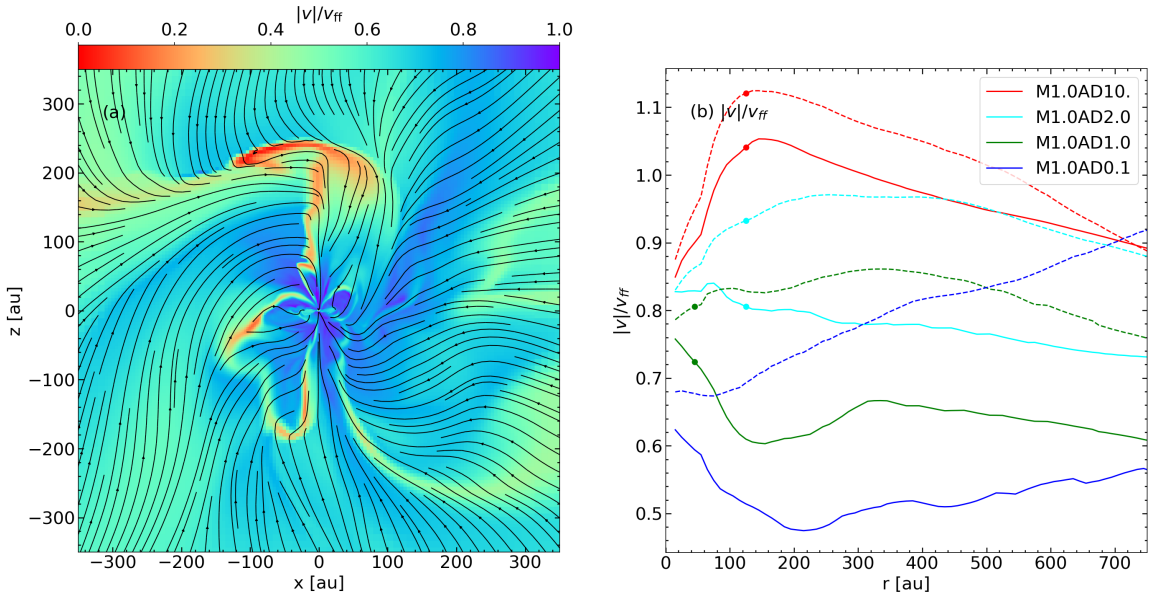


Figure 3.6: Comparison of the total flow speed v with the local free-fall speed $v_{\rm ff}$. Panel (a) plots the ratio $v/v_{\rm ff}$ on an x-z plane for the reference model M1.0AD1.0 at the same representative time as in Fig. 3.4, showing dense sheetlets tend to move more slowly than the background medium. Panel (b) plots the spherically averaged total speed normalized by the local free-fall speed as a function of radius for models with different diffusivities. The blue lines are for model M1.0AD0.1, green for M1.0AD1.0, cyan for M1.0AD2.0, and red for M1.0AD10. The solid curves are for the dense sheetlets and dashed for the background. The solid dot on each line approximately marks the transition radius between the disk and envelope on the disk midplane.

a key role in the structure and dynamics of the protostellar envelope, dominating its mass and angular momentum budgets and mass accretion rate.

Before leaving this subsection, we comment on a few interesting features regarding the total flow speed v compared to the local free-fall speed $v_{\rm ff}$. The ratio $v/v_{\rm ff}$ is plotted on an x-z plane for the reference model M1.0AD1.0 at the same representative time as in Fig. 3.6, so it can be compared directly with Fig. 3.4d, where the radial component of the velocity normalized by the local free-fall speed is plotted. The contrast between the dense sheetlets and the more diffuse background is more clear in the total speed plot than in the radial velocity plot. Specifically, the sheetlets tend

to move significantly slower than the background (with a redder color in Fig. 3.6a) and at a substantially sub-free-fall speed. The difference is quantified in panel (b) of Fig. 3.6, where the spherically averaged total speed normalized by the local free-fall speed is plotted as a function of radius for models with different diffusivities. There is a clear trend for the dense sheetlets to move more slowly for a lower magnetic diffusivity (compare the four solid lines in the panel). In the least magnetically diffusive (best coupled) case of M1.0AD0.1, the sheetlets move at about half of the local free-fall speed on average. They move close to the free-fall speed in the most diffusive case (Model M1.0AD10). Another interesting trend is that the difference in the total speed between the dense sheetlets and their lower-density background is larger for a lower magnetic diffusivity (contrast, e.g., the blue curves with the red ones), which, together with a smaller volume filling factor (see Fig. 3.5b) and higher contrast in plasma-β (see Fig. 3.5c), indicate that the sheetlets become more distinct from their lower-density background as the magnetic field becomes better coupled to the gas.

3.5 The Envelope-Disk Connection

In the last section, we demonstrated the importance of the magnetic field in segregating the envelope material into dense gravo-magneto-sheetlets and a magnetically dominated low-density background. In this section, we first examine the field strength and distribution in some detail, focusing on the vertical field component B_z (§ 3.5.1), which controls the *net* magnetic flux threading the formed disk Ψ_z (a crucial quantity for the subsequent disk dynamics and evolution), and the connection between the inner envelope and the disk. It is followed by a discussion of magnetic retardation of the envelope infall and magnetic braking of rotation in § 3.5.2, and anisotropic (sheetlet-fed) envelope accretion onto the disk in § 3.5.3. In this (§ 3.5) and most of the next

sections (§ 3.6.1 and § 3.6.2), we choose to illustrate the results at a representative time when the stellar and disk mass reaches $M_{d*} = 0.25\ M_\odot$ (somewhat later than that used in the previous envelope-focused section corresponding to $M_{d*} = 0.2\ M_\odot$) to have a larger, more stable disk that facilitates the disk discussion.

3.5.1 Level of Envelope and Disk Magnetization

To illustrate the magnetic field distribution, we plot in Fig. 3.7a the vertical field strength $B_{z,mid}$ on the x-y plane passing through the sink particle (approximately the disk midplane) for the reference run M1.0AD1.0 at the representative time[3]. Clearly, $B_{z,mid}$ varies strongly from one location to another in the inner envelope, which is to be expected given its highly structured mass distribution as discussed in § 3.4. In particular, magnetic field lines are strongly distorted by the collapsing dense sheetlets, which can reverse the direction of the vertical B field in some locations (see, e.g., the field lines to the right of the right filament below the disk in Fig. 3.4a). Such negative B_z is also present on the midplane as shown in Fig. 3.7a. It would reduce the net vertical magnetic flux on the disk if advected to the disk along the midplane.

Despite the strong spatial variation, there is a general trend for $B_{z,mid}$ to increase with decreasing radius towards the center (to be quantified below). Nevertheless, the increase is relatively gentle. In particular, there is no large jump from the infalling envelope to the rotationally supported disk, unlike the mass density on the same plane (ρ_{mid}, which is plotted in Fig. 3.7b for comparison. The dense curving filaments in the envelope in the density map are simply the midplane cross-sections of the 3D gravo-magneto-sheetlets (see Fig. 3.3) that collapse towards the disk (see the flow streamlines). The difference between the distributions of $B_{z,mid}$ and ρ_{mid} highlights

[3]The approximate alignment of the disk axis along the $z-$direction is likely due to the net angular momentum along the $z-$axis. The choice of the x-y plane simplifies the computation of magnetic flux through a surface and best captures the flux of the original z-direction magnetic field.

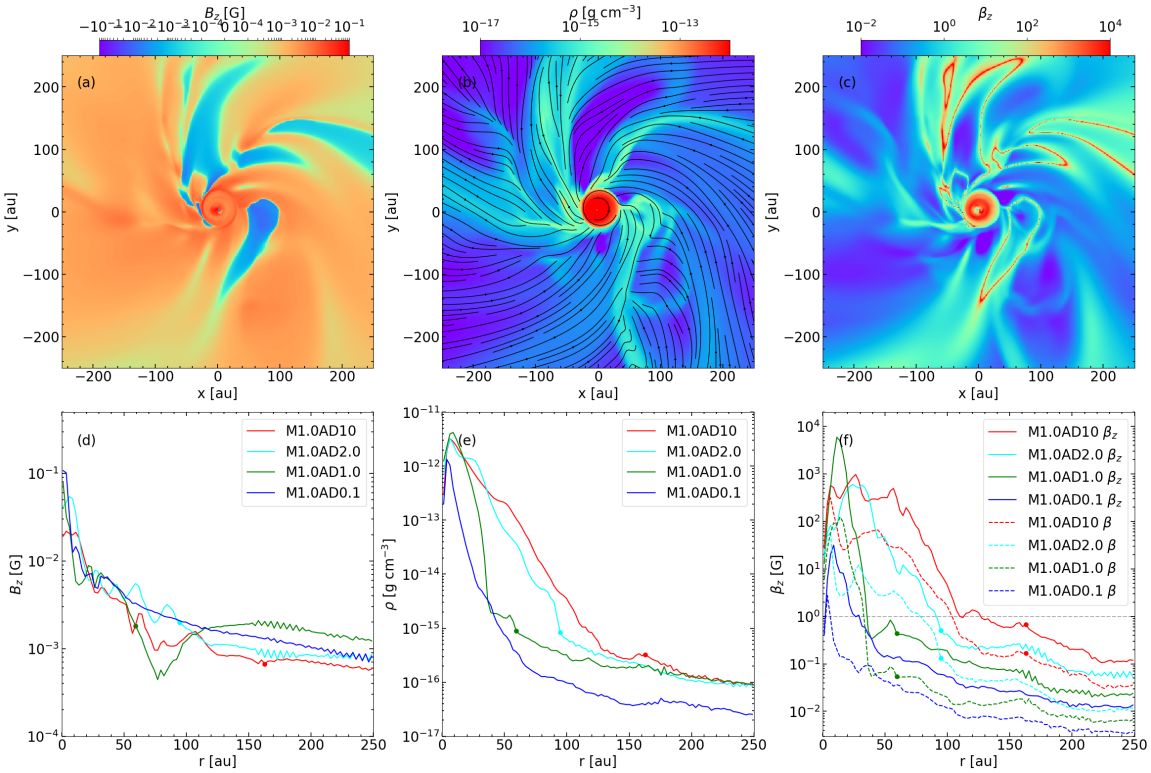


Figure 3.7: Magnetization of the inner envelope and disk at a representative time when $M_{d*} = 0.25$ M$_\odot$ for the reference model M1.0AD1.0 (top panels) and for models with different magnetic diffusivities (bottom panels). Panel (a) displays the vertical component of the magnetic field on the midplane $B_{z,mid}$ for the reference model, showing the lack of a large jump in the disk-envelope transition region. Panel (b) is a density map on the same plane (with flow streamlines superposed), showing a dense disk surrounded by a much lower-density envelope. Panel (c) plots the plasma-β_z corresponding to $B_{z,mid}$. Panels (d)-(f) plot, respectively, the azimuthally averaged $B_{z,mid}$, ρ_{mid}, and $\beta_{z,mid}$ for models of different magnetic diffusivities. The solid dot on each line approximately marks the transition radius between the disk and envelope. The animated version is available in the online supplementary material.

that the large concentration of mass in the disk does not lead to the same degree of magnetic flux concentration there. It is further quantified in panel (c) of Fig. 3.7, where we plot the plasma-$\beta_{z,mid}$ based on the vertical component of the magnetic field $B_{z,mid}$ only. Although there is a strong spatial variation, especially in the inner envelope, $\beta_{z,mid}$ is, on average, much higher in the disk than in the envelope, reaching values as high as 10^4. The large increase comes primarily from the jump in density rather than the field strength, indicating that the disk material is strongly demagnetized relative to its mass compared to the envelope feeding it. This demagnetization is the key for the disk to form in the first place and survive to later times, as discussed in, e.g., Hennebelle et al. (2016a) and recently reviewed by Tsukamoto et al. (2023a).

To quantify the magnetic field and mass distribution further, we azimuthally average $B_{z,mid}$ and ρ_{mid} and show the results in the lower panels of Fig. 3.7. As expected, there is a clear change of the averaged midplane density around the disk-envelope transition region (marked by a solid dot), inside which the density starts to increase steeply with decreasing radius (except for the least magnetic diffusive model M1.0AD0.1 where a well-defined disk does not exist at the time shown and, thus, no solid dot marking disk-envelope transition is plotted). The behavior of the average midplane $B_{z,mid}$ is more complex, partly because negative values of B_z exist in some regions (see panel a), which cause strong variations. The magnetic fields with alternating polarities lead, in particular, to the dip near 70 au for the reference model M1.0AD1.0 (the green curve in panel d). Nevertheless, the azimuthally averaged plasma-β remains well behaved, with the thermally dominated disk region well separated from the magnetically dominated envelope region (panel f of Fig. 3.7). For the most magnetically diffusive model (M1.0AD10) with the best-resolved disk, there is a gradual increase of the averaged plasma-$\beta_{z,mid}$ towards the center, reaching a plateau of ~ 400. The second most diffusive model (M1.0AD2.0) reaches a similar peak value,

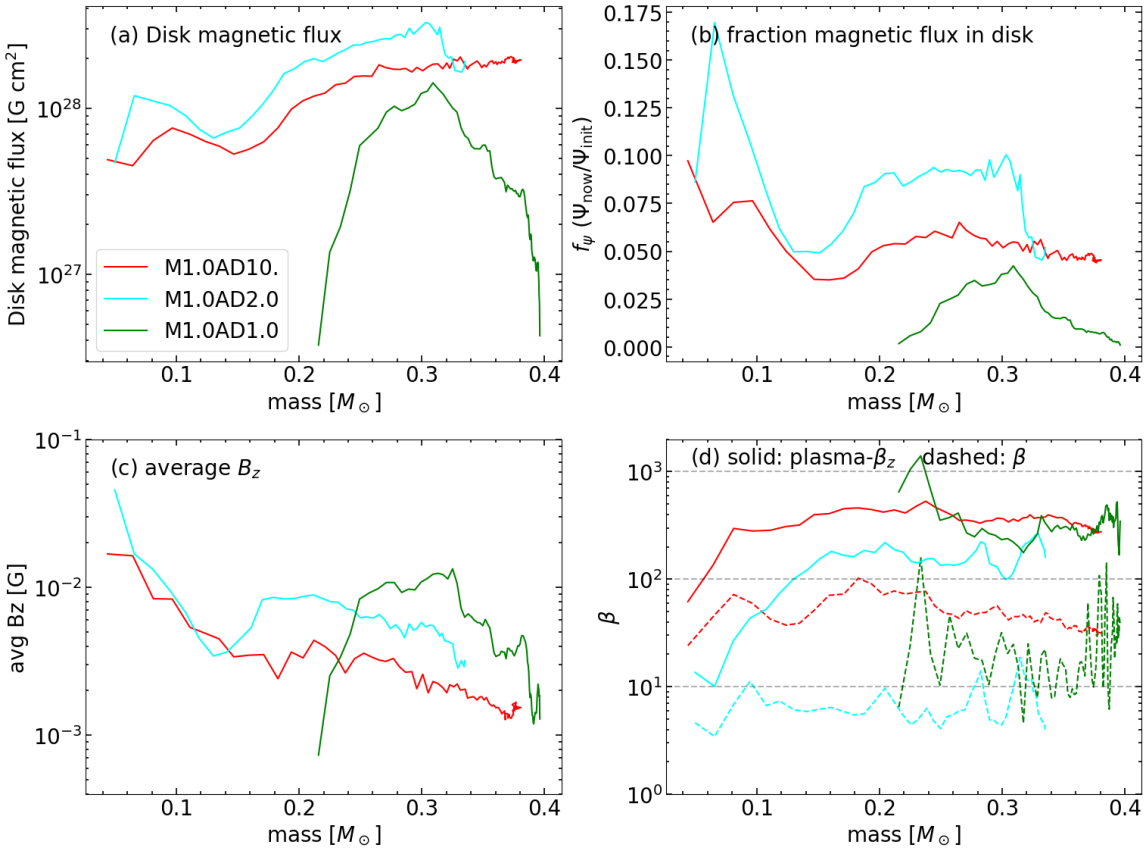


Figure 3.8: Evolution of the disk magnetic field as a function of the combined star and disk mass M_{d*}. Plotted are (a) the vertical magnetic flux threading the disk midplane vertically $\Psi_{z,mid}$; (b) the disk magnetic flux fraction f_Ψ defined in equation (3.8) of the text; (c) the vertical field strength averaged over the disk midplane, and (d) two versions of plasma-β, β_z (solid lines) and β (dashed), averaged over the disk midplane.

although the peak is higher in the reference case. The disk plasma-β based on the total magnetic pressure is lower, typically by about an order of magnitude, indicating that the toroidal magnetic field is stronger than the vertical field by a factor of several on average near the disk midplane.

An important quantity characterizing the degree of global disk magnetization is the total magnetic flux threading vertically through the disk midplane $\Psi_{d,mid}$. Its evolution as a function of the combined star and disk mass M_{d*} is shown in panel (a) of Fig. 3.8. After some initial adjustment, there is a general trend of increasing

disk magnetic flux with increasing mass for the star-disk system; the decline in the reference model M1.0AD1.0 after $M_{d*} \approx 0.3$ $M_\odot$ is primarily caused by a shrinking disk at later times. This general trend is not surprising because more magnetic flux is expected to be dragged into the disk as mass is added to the star-disk system. As an approximate measure of the fraction of the magnetic flux initially associated with the mass of the star and disk that remains trapped on the disk, we define a dimensionless quantity:

$$f_\Psi \equiv \frac{\Psi_{d,mid}}{\Psi_{i,M}}, \tag{3.8}$$

where $\Psi_{i,M}$ is the magnetic flux threading a sphere enclosing the same amount of mass as M_{d*} but at the beginning of the simulation ($t = 0$). From panel (b), we see that the flux fraction f_Ψ ranges from a few percent for the reference model M1.0AD1.0 to about 10% for the intermediate magnetic diffusivity model M1.0AD2.0. Interestingly, the most diffusivity model M1.0AD10 has a flux fraction f_Ψ between the two less diffusive models, with a value of approximately 5%.

The non-monotonic variation of the fraction of the magnetic flux the disk inherits from the envelope, f_Ψ, with respect to the magnetic diffusivity is shaped by two competing effects. On the one hand, the disk size (and thus surface area) increases with increasing magnetic diffusivity, which tends to increase the trapped magnetic flux $\Psi_{z,mid}$. On the other hand, the magnetic field tends to be weaker for a larger diffusivity, lowering the flux. The latter trend is shown explicitly in panel (c), where the vertical field strength averaged over the disk mid-plane $\langle B_{z,mid} \rangle$ is plotted. The averaged net vertical field tends to be weaker for a more magnetically diffusive model, which makes intuitive sense. There is a tendency for $\langle B_{z,mid} \rangle$ to decrease with time, with typical values of order 1-10 mG, which may be detectable through ALMA Zeeman observations (Vlemmings et al., 2019; Mazzei et al., 2020; Harrison et al., 2021),

especially since the disk-averaged toroidal field is significantly stronger than the vertical component.

Interestingly, the late-time decrease in $\langle B_{z,mid} \rangle$ does not translate to a corresponding increase in the mid-plane plasma-β_z based on the vertical field component, as shown in panel (d) of Fig. 3.8. Clearly, β_z plateaus around ~ 300 for both the most and least diffusive models (M1.0AD10 and M1.0AD1.0 of the three shown), with that for the intermediate magnetic diffusivity model (M1.0AD2.0) somewhat lower, but still within a factor of 2. The plasma-β based on the total field is significantly lower, reaching values of order 10 for the two less diffusive models (M1.0AD1.0 and M1.0AD2.0), although there is significant time variation, particularly for the more magnetically coupled case of the two (M1.0AD1.0), indicating a toroidal domination of the disk magnetic field. The total plasma-β for the most diffusive model stays around ~ 40 at late times, which is higher than the less diffusive cases but still about an order of magnitude below its corresponding β_z, indicating that the disk magnetic field is toroidally dominated even in this most diffusive case.

To summarize, the vast majority (of order 90% or more) of the magnetic flux originally threading the mass that has gone into the star and disk is stripped away from the mass, presumably through the physical mechanism of ambipolar diffusion included in the simulation. However, some contribution from the difficult-to-quantify numerical reconnection cannot be ruled out[4]. This demagnetization of the disk and stellar material is likely facilitated by the majority of the envelope material being forced into thin gravo-magneto-sheetlets with highly pinched field lines, which increases the magnetic forces and, thus, the ion-neutral drift that separates the magnetic field relative to the

[4]Gas flowing along magnetic field directly connected to the disk can also lead to a mass increase in the disk without a corresponding increase in field strength, thus contributing to the disk demagnetization. The contribution is expected to be limited because the fraction of the envelope material magnetically connected to the disk is relatively small at any given time.

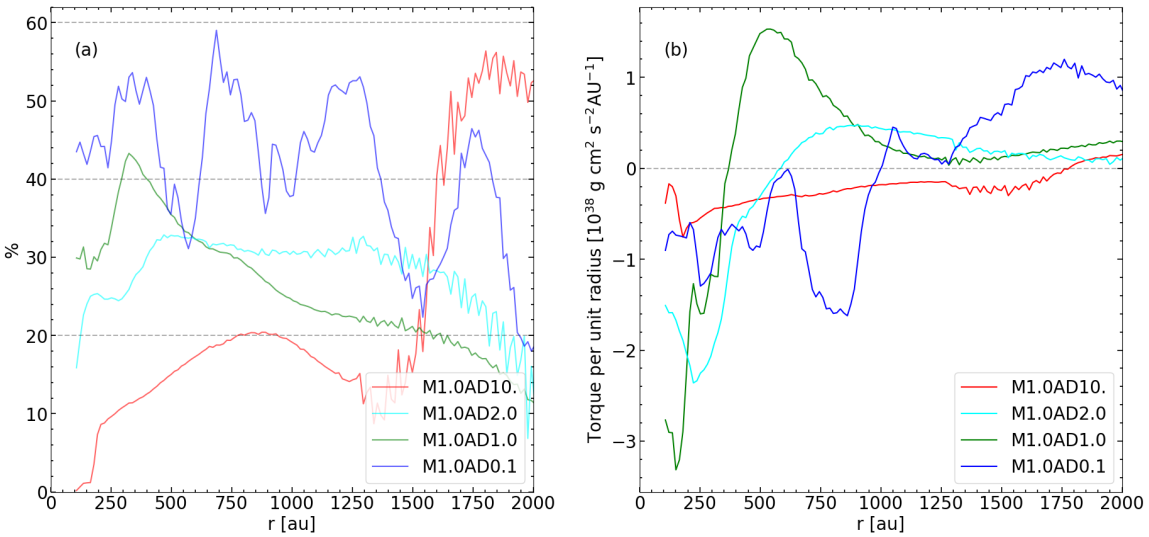


Figure 3.9: Plotted as a function of radius are (a) the ratio of the spherically averaged radial components of the magnetic and gravitational forces and (b) the $z-$component of the magnetic torque per unit radius for the four turbulent models with different magnetic diffusivities at the representative time.

matter. Nevertheless, a small but highly significant fraction of the original magnetic field (up to $\sim 10\%$) is brought into the disk, enabling the disk to remain significantly magnetized (with β_z of a few hundred). The inherited magnetic field plays a key role in the subsequent disk dynamics and evolution, as shown in § 3.6 below.

3.5.2 Magnetic Collapse-Retarding Force and Rotating-Braking Torque

We have already established in § 3.4 that most of the volume of the inner envelope is magnetically dominated, with a plasma-β well below unity, especially in the low-density background (see Fig. 3.4c and Fig. 3.5c), and that the field is strong enough to significantly retard the envelope collapse (see Fig. 3.4d and Fig. 3.5d) and regulate the disk formation through magnetic braking (see Fig. 3.2). In this subsection, we quantify the radial magnetic force that retards the gravitational collapse and the magnetic torque from the toroidal magnetic force that redistributes the angular

momentum. The radial magnetic force density is calculated with

$$F_{B,r} = \boldsymbol{F}_B \cdot \hat{r}_{\rm sph} = \Big[\frac{1}{4\pi}(\nabla \times \boldsymbol{B}) \times \boldsymbol{B}\Big] \cdot \hat{r}_{\rm sph} \tag{3.9}$$

and the z-component of the magnetic torque density is defined as

$$\tau_B = \boldsymbol{F}_B \cdot (\boldsymbol{r}_{\rm cyl} \times \hat{z}) \tag{3.10}$$

where $\hat{r}_{\rm sph}$ is a unit vector in the spherical radial direction with the star at the origin, and $\boldsymbol{r}_{\rm cyl}$ is the radial vector in a cylindrical coordinate centered on the star, with the polar axis along the Cartesian $\hat{z}$ axis.

Panel (a) of Fig. 3.9 plots as a function of radius the ratio of spherically averaged radial components of the magnetic and gravitational forces at the representative time. The least magnetically diffusive model M1.0AD0.1 has the strongest radially outward magnetic force, reaching values of order half of the local gravity, although there is a strong spatial variation. The more severe magnetic retardation is the reason for the slower growth in the mass of its star plus disk compared to other models (see the solid blue curve in the left panel of Fig. 3.1). The radial magnetic force is less extreme for the more diffusive models but remains significant, reaching values typically between $\sim 20 - 40\%$ of the local gravity in the inner envelopes. It explains why the collapse of the inner envelope is significantly sub-free-fall (see Fig. 3.5d).

Panel (b) of Fig. 3.9 plots as a function of radius the $z-$component of the magnetic torque per unit radius

$$\frac{dT_B}{dr} = \int_0^{2\pi} \int_0^{\pi} \tau_B \; r^2 \; \sin(\theta) \; d\theta \; d\phi \tag{3.11}$$

where r, θ, and ϕ are the spherical radius, polar angle, and azimuthal angle in a

spherical polar coordinate system centered on the protostar, and τ_B the $z-$component of the magnetic torque density given in equation (3.10). The magnetic torque is negative in the inner part of the envelope (and disk), indicating that it typically removes angular momentum from the gas at small radii. At larger distances, the magnetic torque generally becomes positive, indicating that the magnetic force acts in the positive azimuthal direction to spin up the gas. The sign change of the torque is a natural consequence of the outward magnetic transport of angular momentum in a collapsing envelope that is magnetized and rotates differentially, with the inner part rotating faster than the outer part on average. The transport is least efficient in the most diffusive model M1.0AD10, enabling a large, massive, persistent disk to form. As the magnetic diffusivity decreases from model M1.0AD10 to M1.0AD2.0 to M1.0AD1.0, the magnetic torque increases, leading to stronger inner envelope braking and forming a smaller, less massive, and more transient disk. For the least diffusive model M1.0AD0.1, there is so little angular momentum left in the inner envelope that a relatively small magnetic torque is enough to transport it outward, leading to a tiny, transient disk.

3.5.3 Sheetlet-Fed Envelope Accretion onto Disk

We have established in § 3.4 that there are two types of regions in the inner envelope – the gravity-dominated dense gravo-magneto-sheetlets and the magnetically dominated low-density background. The background occupies most of the volume, but the sheetlets dominate the mass and mass accretion rate. This bimodal behavior is expected to have an impact on how mass is fed from the inner envelope onto the disk, as we demonstrate in Fig. 3.10.

The figure shows the mass and angular momentum accretion rates across the six surfaces of a flattened rectangular box enclosing the disk for the reference model at

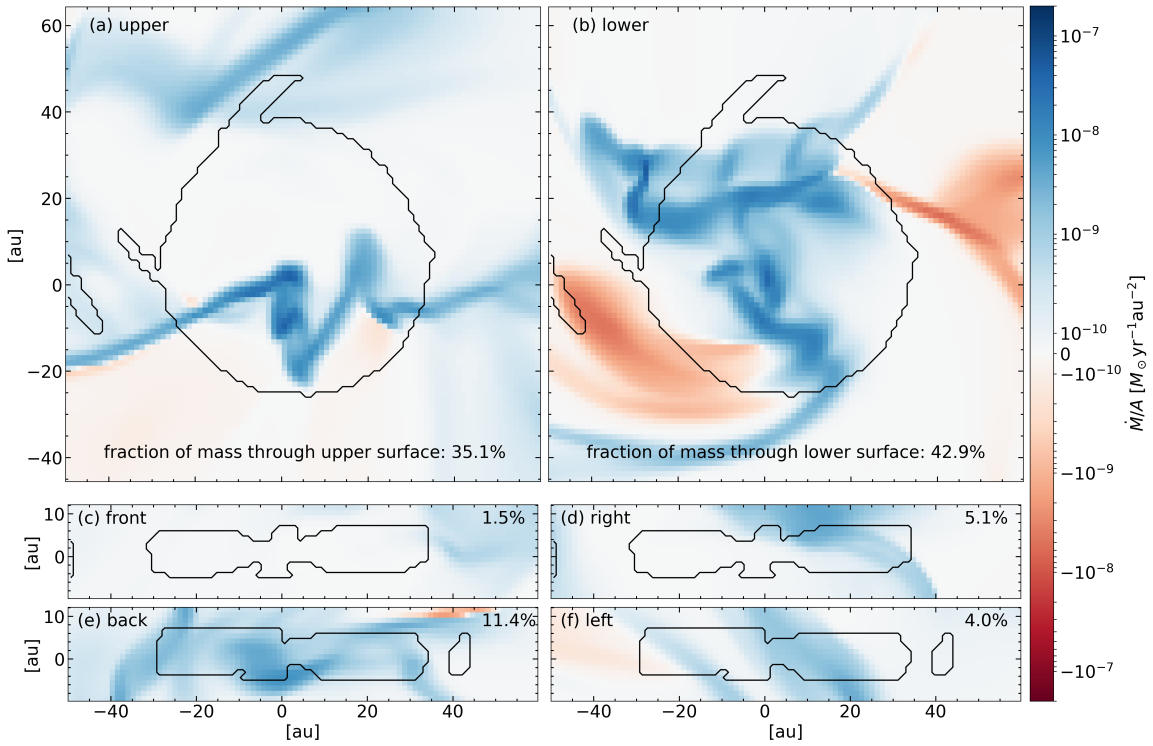


Figure 3.10: Highly anisotropic envelope mass accretion onto the disk. Plotted are the mass accretion rate per unit area through the six surfaces of a rectangular box enclosing the disk for the reference model at the representative time. Accretion into the box/disk is colored blue and out of the box/disk brown.

a representative time. Two features are worth noting. Firstly, a large majority of the mass ($\sim 78\%$) lands on the disk through the upper and lower surfaces rather than the sides. Secondly, the mass accretion onto the upper and lower disk surfaces is highly inhomogeneous, with most of the mass flux concentrated into narrow filaments that span a range of disk radii. Both features are direct consequences of the dense gravo-magneto-sheetlets being warped out of the equatorial plane of the system by turbulence (see Fig. 3.3 and Fig. 3.4); these out-of-the-plane collapsing sheetlets tend to feed the disk through its upper and lower surfaces rather than equatorially through its outer edge.

The mass accretion primarily through the upper and lower disk surfaces has implications on the net magnetic flux Ψ_z threading the disk. As shown in Fig. 3.8b, the disk is drastically demagnetized relatively to the simplest expectation, retaining only a small fraction ($\sim 10\%$ or less) of the original magnetic flux $\Psi_{i,M}$ initially threading the mass M that has gone into the star and disk. Part of this demagnetization occurs in the sheetlets (which are primarily responsible for feeding the disk) before they approach the disk as a result of the ambipolar diffusion, which allows the sheetlet material to collapse without dragging the (highly pinched) field lines along with it at the same speed; the same outward-directing magnetic (tension) force that significantly retards the gravitational collapse of the sheetlets also pushes the field lines to diffuse outward relative to the collapsing material through ambipolar diffusion. The demagnetization is likely helped by the disk mass accretion through the upper and lower surfaces, since vertical accretion through a horizontal plane can add mass to the disk, but not the *net* vertical magnetic flux Ψ_z; the latter is increased primarily through horizontal mass accretion near the equatorial plane, which is greatly reduced by the strong warping of the sheetlets. The dense sheetlets are the primary conduits for supplying the disk with not only mass but also angular momentum and thus are

expected to affect the disk dynamics and evolution. In particular, the specific angular momentum of the sheetlet material landing on the disk may not match that of the Keplerian disk at the landing site. We will discuss this and other aspects of this new mode of disk-feeding in § 3.6 below.

3.6 PROTOSTELLAR DISK STRUCTURE AND EVOLUTION

In this section, we examine more closely the structure and evolution of the disks formed in our simulations, focusing on the roles played by gravity, magnetic fields, and feeding by the highly structured inner envelope in the three models with persistent disks (M1.0AD10., M1.0AD2.0, and M1.0AD1.0; see the top row of Fig. 3.11).

3.6.1 Are Early Disks Gravitational Stable?

We start by addressing whether all early disks are gravitationally unstable. It would be the case if the magnetic field needs to decouple from the matter to such a degree in order to form the disk in the first place that, once a disk has formed, the field becomes too weak and/or too decoupled to the gas to drive the subsequent disk evolution. In such a case, the disk would accumulate mass until it becomes gravitationally unstable, forming spiral arms to redistribute angular momentum and drive disk accretion. Prominent, persistent spiral arms are indeed present in the most diffusive model M1.0AD10 (see Fig. 3.11c), indicating that the disk formed in this case was gravitationally unstable. This conclusion is strengthened by Fig. 3.11, which plots the Toomre parameter:

$$Q = \frac{c_s \Omega}{\pi G \Sigma} \tag{3.12}$$

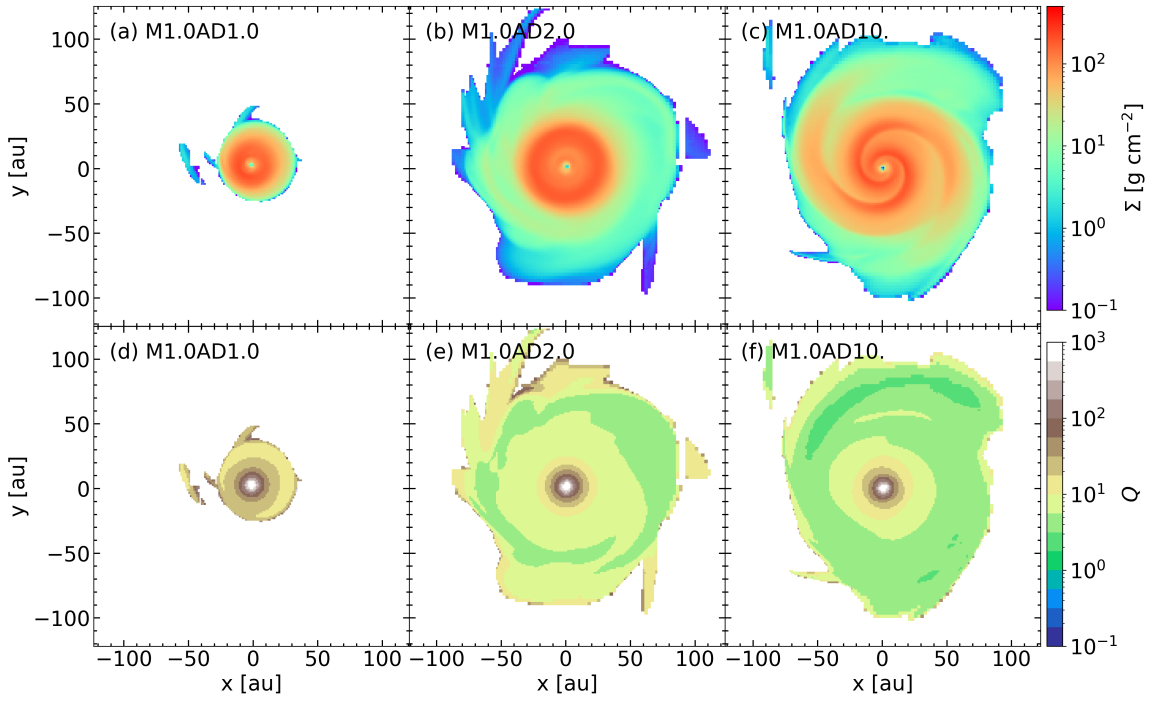


Figure 3.11: Gravitational stability of disks in formation. Plotted are the column density maps (top row) and the distributions of the Toomre Q parameter for disk gravitational stability (bottom row) for models M1.0AD1.0, M1.0AD2.0, and M1.0AD10 at the representative time.

where c_s is the isothermal sound speed, Ω the local Keplerian angular speed, and G and Σ the gravitational constant and disk column density respectively. It is clear from panel (f) that Q is larger than, but close to, unity in the outer half of the disk, where the spirals are the most prominent. Evidently, the non-linear development of the spirals has driven the disk towards a marginally stable state. In the less magnetically diffusive model M1.0AD2.0, the Q parameter remains above ~ 4 everywhere (see panel [e]), indicating the disk is largely gravitational stable at the time shown. However, its outer edge occasionally approaches closer to the gravitational instability, with transient spiral arms developing and disappearing. In contrast, the least magnetic diffusive model of the three, M1.0AD1.0, has a Q parameter of order 10 or more nearly everywhere on the disk (panel d), indicating that the disk formed in this case is gravitationally stable. This is consistent with the surface density distribution, which shows only transient, weak spirals that likely arise from the rotational smearing of patchy materials landed on the disk. We conclude that not all early disks are gravitationally unstable, and whether they become so depends on the magnetic diffusivity. Instability is more likely to develop in more magnetic diffusive cases. It makes physical sense because the disks are bigger and more massive in the more magnetically diffusive cases, as shown in Fig. 3.1.

The fact that some disks become gravitationally unstable while others do not naturally raises the question: which mechanism is more important in driving disk angular momentum evolution: gravitational torque or magnetic braking? We will address this question next.

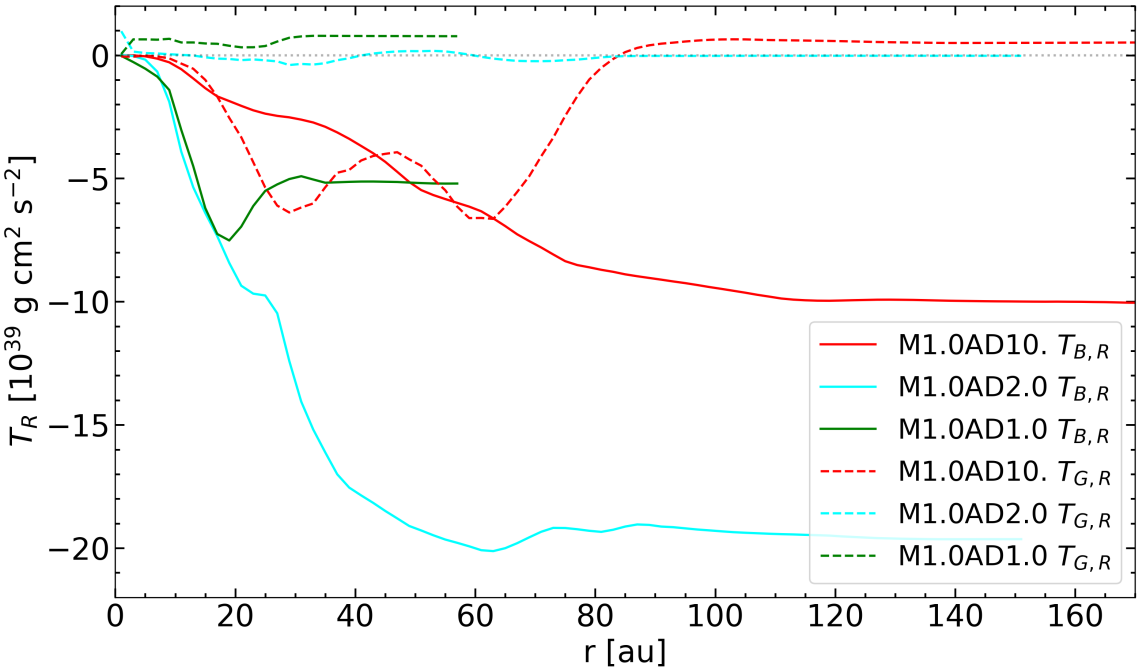


Figure 3.12: Cumulative magnetic (solid lines) and gravitational (dashed) torques inside the disk up to a given cylindrical radius R at the representative time.

3.6.2 Magnetically or Gravitational Driven Angular Momentum Evolution?

To quantify the roles of gravity and magnetic fields in disk angular momentum evolution, we compute the azimuthal components of the gravitational and magnetic force densities, $F_{G,\phi}$ and $F_{B,\phi}$, everywhere inside the disk, multiply them by the cylindrical radius $r_{\rm cyl}$ to obtain the local gravitational and magnetic torque densities, τ_G and τ_B, and then sum all torques up to a given cylindrical radius R to obtain cumulative gravitational and magnetic torques, $T_{G,R}$ and $T_{B,R}$, as a function of the cylindrical radius R:

$$T_{G,R} = \int_{z\in\text{disk}} \int_{\phi\in\text{disk}} \int_{r_{\rm cyl}=0}^{r_{\rm cyl}=R} F_{G,\phi}\ r_{\rm cyl} dV \tag{3.13}$$

$$T_{B,R} = \int_{z\in\text{disk}} \int_{\phi\in\text{disk}} \int_{r_{\text{cyl}}=0}^{r_{\text{cyl}}=R} F_{B,\phi}\ r_{\text{cyl}} dV \tag{3.14}$$

where $F_{G,\phi}$ and $F_{B,\phi}$ are the azimuthal component of the gravitational and magnetic force, respectively, r_{cyl} the cylindrical radius from the $z-$axis, dV the infinitesimal volume element in cylindrical coordinates. The cumulative torques are shown in Fig. 3.12.

We will start the torque discussion with the most diffusive model M1.0AD10, where prominent spirals are present, so the gravitational torque is expected to be significant. In this case, the cumulative gravitational torque $T_{G,R}$ is plotted as the dashed red line in Fig. 3.12. In the inner part of the disk, $T_{G,R}$ decreases with radius R monotonically, reaching a (negative) minimum around a radius $R \sim 30$ au, indicating that the net azimuthal gravitational force in this region is negative, acting to brake the disk rotation and remove its angular momentum. Part of the removed angular momentum is transported outward to the adjacent region between ~ 30 and ~ 45 au, where $T_{G,R}$ increases to a local maximum. This region's net azimuthal gravitational force is positive, speeding up the disk rotation and increasing its angular momentum. As the radius increases, the pattern repeats itself, with gravity first removing angular momentum from the disk before giving it back to the disk. By the outer edge of the disk at $R \sim 100$ au, nearly all of the angular momentum extracted from the disk material by the gravitational torque is returned to the disk, which makes sense because the gravitational torque is mostly internal to the disk and, thus, can redistribute angular momentum between different parts of the disk but not efficiently remove angular momentum from the disk as a whole. This behavior contrasts with the magnetic torque, shown as the solid red line in Fig. 3.12. Although small fluctuations exist, there is a general trend for the cumulative magnetic torque $T_{B,R}$ to decrease (becoming more negative) with radius, indicating that the net azimuthal magnetic

force is predominantly negative and acts to brake the disk rotation. Most importantly, at large radii, $T_{B,R}$ plateaus to a value more negative than the minimum (negative) $T_{G,R}$, indicating that the magnetic torque is important even in this most magnetically diffusive case: it removes angular momentum from the disk at a rate comparable to or larger than the rate with which the gravitational torque redistributes angular momentum from one part of the disk to another.

In the less magnetically diffusive model M1.0AD2.0 where a relatively large, persistent disk is also formed, the gravitational torque acts to redistribute angular momentum within the disk as well, but at a rate far below that of the magnetic torque (compare the dashed and solid cyan curves in Fig. 3.12). Indeed, the magnetic torque removes angular momentum from the disk as a whole at a rate significantly higher than that in the more diffusive model M1.0AD10, likely because its disk is more strongly magnetized (see Fig. 3.8c,d). Therefore, in this case, the magnetic field completely dominates gravity in controlling the disk's angular momentum evolution. The same is true for the least magnetically diffusive, reference model M1.0AD1.0, where the cumulative magnetic torque $T_{B,R}$ is much larger than the cumulative gravitational torque $T_{G,R}$ in magnitude (compare the dashed and solid green curves in Fig. 3.12). Interestingly, $T_{B,R}$ increases with the radius (becoming less negative) near the outer edge of the disk (between ~ 20 and ~ 30 au), indicating that a (relatively small) fraction of the angular momentum extracted magnetically from the inner part of the disk is returned to the outer part. However, there is the possibility that the disk's outer edge is spun up externally by a faster-rotating inner envelope magnetically connected to it. We conclude that enough magnetic flux is carried into the forming disk for the field to play a dominant role in regulating its angular momentum evolution.

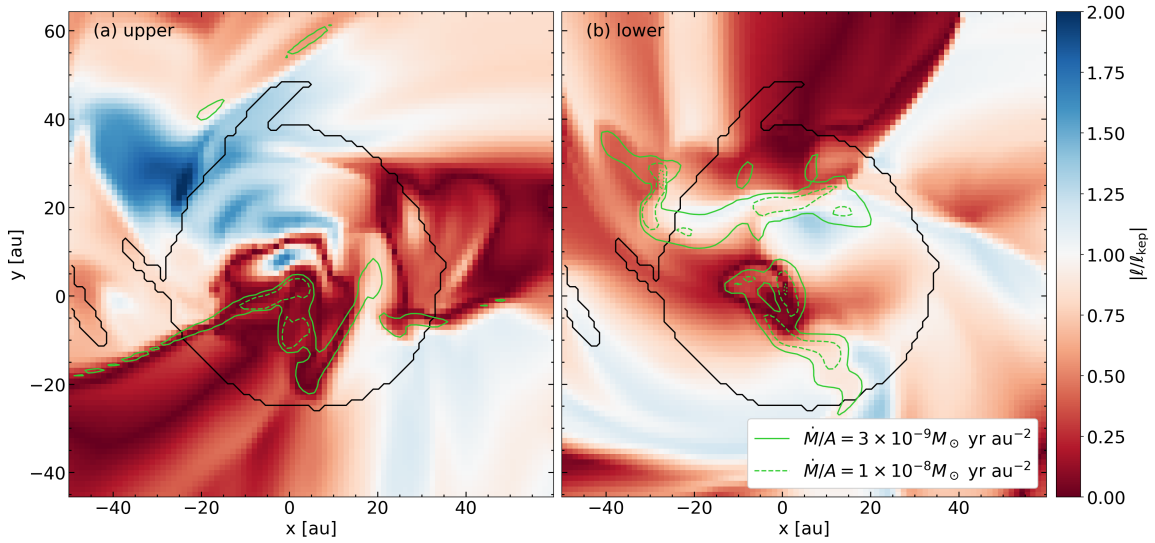


Figure 3.13: The ratio between the specific angular momentum carried by the infalling envelope material above (panel a) and below (panel b) the disk and that required for staying in a Keplerian orbit at the projected cylindrical radii on the disk midplane. The black contours in both panels are the projected disk midplane outline. The green curves are contours of mass feeding rate per unit area, highlighting where most envelope material lands on the disk surfaces.

3.6.3 Kinematically Perturbed Early Disks

Besides the gravitational and magnetic torques discussed in the last section, accretion from the envelope can also significantly affect the disk structure and evolution. It is especially true when the accretion is highly anisotropic, as expected for an inner envelope dominated by dense sheetlets (see, e.g., Fig. 3.3). Since the sheetlets can be strongly magnetically braked, there is no reason for their specific angular momenta to match those of their landing sites on the disk. The mismatch is illustrated in Fig. 3.13, which plots the specific angular momentum above and below the disk normalized by that needed for the rotational support against gravity on the disk midplane for the reference model at the representative time. In this case, most of the mass falls onto the disk with a specific angular momentum well below the local Keplerian value (particularly for the upper disk surface), indicating that substantial mixing with the material

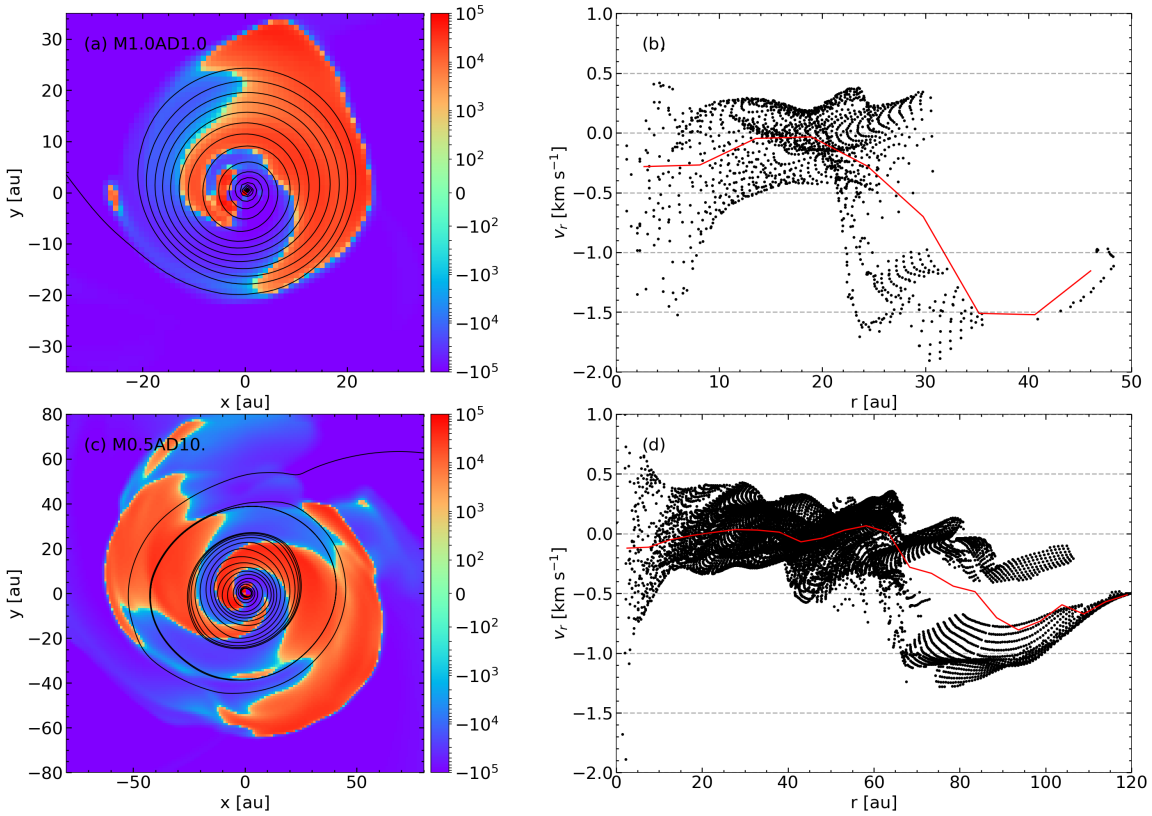


Figure 3.14: Perturbed disk kinematics for models M1.0AD1.0 (upper panels) and M1.0AD10 (lower) at a relatively early time when $M_{d*} = 0.2\ M_\odot$. **Panels (a) and (c)**: gas radial velocity on the disk midplane. The black line in each panel is a representative flow streamline. **Panels (b) and (d)**: Statistics of the gas radial velocity in the disk. A black dot represents each cell in the disk. The red lines are the averaged gas radial velocity at each radius.

already in the disk is required to fully incorporate the newly accreted low-angular-momentum material (which is already magnetically braked before entering the disk) into the Keplerian disk. As a result, the mixed material would have a lower angular momentum than the local Keplerian value and move inward. Therefore, magnetic braking of the inner envelope material at relatively large distances, particularly the dense sheetlets, provides another mechanism to drive the disk accretion by supplying the formed disk with lower angular momentum material.

Given the angular momentum mismatch discussed above and the generally patchy

and episodic nature of the sheetlet-dominated disk-feeding, deviations from a perfectly circular Keplerian disk are to be expected. The deviation from a circular orbit is illustrated in Fig. 3.14a, which plots a representative streamline on the disk midplane for the reference model at a relatively early time when the combined stellar and disk mass is $M_{d*} = 0.2\ M_\odot$. The streamline loops are clearly displaced to the upper side of the protostar and are bunched up closer together in the lower left part of the disk compared to other parts. Interestingly, the trajectory spirals inwards quickly, shrinking in radius by a factor of two in only half a dozen turns. The rapid shrinkage is indicative of a significant radial velocity component, which is indeed the case, as shown by the color map in panel (a) and scatter diagram in panel (b) of Fig. 3.14. Although some regions move inward (the reddish regions in panel [a]) and others outward (purple regions), the inward motions tend to be faster than the outward ones, reaching values as high as ~ 0.5 km/s or more, comparable to the local sound speed. The expanding and contracting regions form a "yin-yang" pattern. It is related to the non-circular orbits highlighted by the streamline. We note that the speeds and distributions of expanding and contracting motions are variable in time, which is not surprising in this (reference) case given that the disk remains significantly magnetized (see Fig. 3.7) and strongly braked (see Fig. 3.12) by both non-uniform magnetic fields and patchy low-angular momentum material accreted from the envelope (see Fig. 3.13).

The disks formed in the more diffusive models contract more slowly on average. It is illustrated in Fig. 3.14d, which plots the radial component of the velocity in each cell of the disk midplane in the most diffusive model M1.0AD10. Although substantial infall exists near the outer edge, the number of cells with expanding and contracting motions are comparable inside a radius of ~ 60 au, leading to little net orbital shrinkage, in agreement with the outermost streamline shown in panel (c). A

prominent "yin-yang" pattern also exists in the radial velocity map, but, unlike the reference case discussed above, it is primarily caused by the spiral arms in the disk surface density, which produces non-circular orbits with misaligned semi-major-axes, as illustrated by the streamlines in the central region. The spiral arms are strong enough to cause significant derivations from the local Keplerian rotation speed (of order 0.2 to 0.8 times the sound speed), which may be detectable with high spatial and spectral resolution ALMA observations. In this case, the gravitationally induced kinematic perturbations dominate those from magnetic braking and patchy envelope accretion.

3.7 Discussion

3.7.1 Towards a Picture of Protostellar Envelope Dominated by Gravo-Magneto-Sheetlets

As stressed in § 3.1, the gravitational collapse of a smooth molecular cloud core threaded by a large-scale, dynamically significant magnetic field naturally leads to a dense, collapsing, equatorial sheet – the classical pseudodisk (Galli & Shu, 1993a) because the magnetic resistance to gravity is intrinsically anisotropic. Turbulence or other perturbations, such as clumpiness, in the star-forming core tend to distort the pseudodisk into dense, collapsing, gravo-magneto-sheetlets, which appear as dense filaments in mass density or column density maps (see, e.g., Fig. 3.1). Such filaments have been reported in many core-collapse simulations with both magnetic fields and turbulence (e.g., Santos-Lima et al., 2012; Seifried et al., 2013; Li et al., 2014a; Seifried et al., 2015; Kuffmeier et al., 2017; Matsumoto et al., 2017; Gray et al., 2018; Lam et al., 2019; Wurster & Lewis, 2020a, Mignon-Risse et al., 2021; see Tsukamoto et al., 2023b for a review). The prevalence of gravo-magneto-sheetlets in numerical simula-

tions, coupled with their simple physical origin, adds weight to the notion that they are an integral part of protostellar envelopes. This emerging picture has implications both observationally and theoretically.

On the observation side, it is tempting to identify the collapsing gravo-magneto-sheetlets with the so-called "accretion streamers" observed around an increasing number of protostars, including, e.g., the Class 0 sources VLA 1623 (Hsieh et al., 2020), IRAS 03292 +3039 (Pineda et al., 2020), IRAS 16293-2422 (Murillo et al., 2022), and Lupus 3-MMS (Thieme et al., 2022), and Class I sources L1498 (Yen et al., 2014), HL Tau (Yen et al., 2019), and Per emb-50 (Valdivia-Mena et al., 2022). To strengthen the identification, additional information is needed. In particular, it would be interesting to determine using, e.g., ALMA, whether the accretion streamers are associated with highly pinched magnetic field lines (e.g. Sanhueza et al., 2021), which is a strong prediction of the picture (see Fig. 3.4a).

Another prediction of the picture is that the inner envelope collapses at a speed substantially below the free-fall speed (see Figs. 3.4d and 3.5d) because of strong magnetic retardation to the gravitational collapse, particularly in the dense gravo-magneto-sheetlets. The sub-free-fall collapse has been inferred around a few protostars, including, e.g., L1527 IRS (Ohashi et al., 2014) and TMC-1A (Aso et al., 2015), which could be due to magnetic support. It remains to be determined whether this is generally true. A difficulty is that an accurate determination of the stellar mass is needed to ascertain the free-fall speed, which is not easy for deeply embedded protostars. Ultimately, the most direct observational test of the picture is a direct measurement of the magnetic field strength in the envelope through the Zeeman effect. Its feasibility with ALMA will be explored in a separate investigation (Mazzei, R. et al. 2023, under review).

On the theory side, the domination by dense gravo-magneto-sheetlets has impli-

cations on several aspects of the protostellar envelope, including chemistry and grain growth. Since the sheetlets are much denser than their surrounding background, chemical reactions and freeze-out of molecules onto dust grains should occur faster there than naively expected for a non-clumpy envelope. Similarly, grain growth in the envelope should be enhanced because the higher density shortens the grain-grain collision time, and the magnetic retardation of collapse allows more time for the grains to grow. It could be further sped up by the sharp pinching of the field lines in the dense sheetlets, which increases the magnetic force and, thus, the relative drift (and thus collision) speed between charged and neutral grains (e.g. Guillet et al., 2020). In addition, the segregation of the inner envelope into a highly structured medium with dense, thin sheetlets embedded in a magnetically dominated background should affect the detailed properties of the local turbulence, which may control the grain growth rate (e.g. Ormel et al., 2009; Tu et al., 2022). It would be interesting to quantify these effects in the future.

3.7.2 Magnetically Driven Evolution of Heterogeneous Protostellar Disks

A direct consequence of the picture of protostellar envelope dominated by gravo-magneto-sheetlets is that the protostellar disk is fed primarily from above and below the equatorial plane (see, e.g., Fig. 3.10)[5]. Such patchy off-the-equatorial plane accretion has been found in other simulations (e.g. Lee et al., 2021) and is more prevalent in more turbulent and better magnetically coupled envelopes. It is expected to produce heterogeneities on the disk that could evolve into substructures such as transient

[5]It is possible for a stellar or inner disk wind (not included in the present model) to clear out the collapsing streams above and below the disk, forcing most of the envelope accretion to the equatorial plane, especially at relatively late times when the outflow cavity has a large opening angle near the base.

spirals as well as rings and gaps (e.g. Kuznetsova et al., 2022). However, the relatively low spatial resolution on the disk scale does not allow us to study the substructure formation properly in our global core collapse and disk formation simulations. Another indication of the protostellar disks being more dynamically active than the more evolved protoplanetary disks is the large deviation from pure Keplerian rotation found in our simulations (see Fig. 3.14).

As mentioned in § 3.1 and stressed by Lesur et al. (2023), a central question for the protostellar disk evolution is: how strong is the disk magnetic field? It is related to the classical magnetic flux problem for the central star, where the stellar field strength would be orders of magnitude above the observed values if all of the magnetic flux on the core scale is dragged into the star (Mestel & Spitzer, 1956). If dragged into the disk instead, it would rapidly brake the rotation, creating a corresponding "magnetic flux problem for the disk." Therefore, a crucial task for magnetized disk formation calculations is to evaluate the fraction of magnetic flux dragged from the envelope into the disk f_Ψ.

We find that the fraction f_Ψ depends on the magnetic diffusivity in a complex manner. One may expect a smaller flux fraction f_Ψ for a more magnetically diffusive case. However, our most magnetically diffusive model M1.0AD10 has a larger f_Ψ than the reference model M1.0AD1.0 (see Fig. 3.8b), which is less diffusive by a factor of ten. One reason for this counter-intuitive result is that the disk is larger in the former case. Another (less obvious) reason is that the gravo-magneto-sheetlets become thinner with more sharply pinched field lines in the less diffusive case, facilitating the de-magnetization of the dense material in the sheetlets through ambipolar diffusion.

Our simulations show that f_Ψ ranges from a few to $\sim 10\%$ for the three models with persistent disks (see Fig. 3.8b). They yield a disk-averaged vertical field strength between ~ 1 to ~ 10 mG (see Fig. 3.8c), which is about one order of magnitude lower

than the values found by Masson et al. (2016, see their Fig. 1) and Xu & Kunz (2021a, see their Fig. 2), as reviewed by Tsukamoto et al. (2023a)[6]. Nevertheless, the vertical field is strong enough to yield a disk-averaged plasma-β_z based on this component alone of order a few hundred, which, as already stressed by others (e.g. Lam et al., 2019; Hennebelle et al., 2020; Lee et al., 2021), is much lower than the values of order 10^4-10^5 typically adopted for MHD simulations of evolved (Class II) protoplanetary disks. The disk-averaged plasma-β based on the total field strength is significantly lower still, reaching values as low as ~ 10.

The relatively low values of plasma-β make it possible for the magnetic field to dominate the disk angular momentum evolution in our relatively less magnetically diffusive models M1.0AD1.0 and M1.0AD2.0. These models illustrate an important conceptual point that is not obvious a priori: it is possible to de-magnetize the collapsing envelope enough for a persistent disk to form but not so much as to render the magnetic field insignificant in driving the subsequent disk evolution. These disks are gravitational stable, with a Toomre Q-parameter well above unity. This conclusion is strengthened by the high-resolution non-ideal MHD simulations of Lee et al. (2021), where a similarly gravitationally stable disk was formed with a strong enough disk field to drive fast accretion. Even in our most magnetically diffusive model M1.0AD10, the magnetic field remains significant in removing angular momentum from the marginally gravitational unstable disk with prominent spiral arms.

In contrast, Xu & Kunz (2021b,a) found that the protostellar disks in their 3D simulations are marginally gravitationally unstable, and the magnetic field plays little

[6]The lower average vertical field strengths in our disks compared to those of Masson et al. (2016) and Xu & Kunz (2021a) may come from different ambipolar diffusivities used in our simulations compared to theirs (e.g., Marchand et al., 2016). For example, a higher diffusivity in the envelope would lower the magnetic flux delivered by the protostellar collapse to the disk region (and hence reducing the field strength there). It is also possible that the turbulence included in our simulations (but not theirs) enabled a more efficient outward magnetic flux transport relative to mass in the envelope for a given microscopic ambipolar diffusivity.

role in the disk angular momentum transport despite a much higher field strength than in our simulations. We believe the inefficient magnetic braking is caused by a large magnetic diffusivity on the disk that essentially decouples the field lines from the disk material, as evidenced by the nearly vertical and uniform disk field with a much smaller toroidal component.

We conclude that the disk can inherit enough magnetic flux from the envelope for the field to play a significant, even dominant, role in the disk angular momentum transport if it remains sufficiently well coupled to the bulk disk material. The degree of coupling depends on several uncertain factors, including the abundance of small grains, the depletion factor for metals such as Mg, and the cosmic ray ionization rate ζ (e.g. Lesur, 2021). For example, ζ can be reduced by a magnetized outflow from the disk and/or central star that can severely attenuate low-energy cosmic rays (e.g. Cleeves et al., 2013). On the other hand, the cosmic ray flux can potentially be enhanced by local particle acceleration at shocks near the stellar surface or in protostellar jets (Padovani et al., 2018; Offner et al., 2019). Ultimately, the degree of magnetic coupling must be constrained by comparing model predictions (e.g. Kuffmeier et al., 2020) with detailed observations of dust and gas, particularly molecular ions (e.g. Aikawa et al., 2021).

If the magnetic field is inefficient in transporting angular momentum, disk evolution must rely on gravitational torque from spiral arms. Although spiral arms have been detected in some protostellar disks (e.g. Lee et al., 2020), they are uncommon. A large optical depth at the observing wavelength or a low resolution could hinder the detection. High-resolution ($0.04''$, or ~ 7 au) observations are now available for 12 Class 0 and 7 Class I disks in nearby star formation regions from the ALMA Large Program eDisk (Ohashi et al., 2023). None of the disks shows obvious spirals. While it is important to quantify the extent to which the optical depth and other

effects (such as the disk inclination) hinder their detection through detailed modeling and additional observations, the simplest conclusion based on the currently available data is that there is little compelling observational evidence for the majority of these early disks to have strong spirals capable of driving their fast accretion. We conclude that magnetic transport of angular momentum remains a viable option for driving protostellar disk evolution. It does not preclude gravitational torque from playing a significant, even dominant, role in some cases.

3.8 Conclusion

We extended the non-ideal MHD simulations by Lam et al. (2019) to study magnetized cloud core collapse and disk formation including ambipolar diffusion and turbulence. Our improved simulations incorporated adaptive mesh refinement, enabling better resolution of the disk scale. Our key findings are as follows:

1. Turbulent magnetized protostellar envelopes are dominated by dense collapsing 3D gravo-magneto-sheetlets in their inner regions. These sheetlets, which are disrupted versions of classical sheet-like pseudodisks, are embedded in a magnetically dominant (low plasma-β) background where less dense materials flow along local magnetic field lines and accumulate in the sheetlets. The gravitational collapse of the dense sheetlets, occurring across locally pinched field lines, serves as the primary mechanism for the envelope to feed mass and angular momentum to the central disk-plus-star. Due to strong magnetic retardation, the collapse of the inner envelope is typically slower than the local free-fall rate.

2. The collapsing sheetlets primarily feed the disk through its upper and lower surfaces, contributing materials with specific angular momenta that typically deviate from Keplerian values at their landing sites on the disk. Sheetlets that experience significant magnetic braking in the envelope can supply low-angular momentum ma-

terials to the disk, thereby driving disk accretion along with gravitational torque and magnetic stresses.

3. The protostellar disk inherits a small fraction (up to 10%) of the magnetic flux from the envelope, resulting in a disk-averaged net vertical field strength of around 1-10 mG and a stronger toroidal field. Such field strengths can potentially be measured through ALMA Zeeman observations. The plasma-β_z based solely on the vertical field component is typically a few hundred, significantly lower than the values commonly assumed for Class II protoplanetary disks. The plasma-β based on the total field strength is even lower, reaching values as low as approximately 10.

4. The inherited magnetic field from the envelope plays a dominant role in the evolution of disk angular momentum, facilitating the formation of gravitationally stable disks in our well-coupled models. This magnetic field's influence remains significant even in our least coupled model, as it removes angular momentum from the marginally gravitationally unstable disk at a rate comparable to or greater than that caused by spiral arms. It is thus possible to demagnetize the collapsing envelope enough to allow for the formation of a persistent disk without rendering the disk field too weak to drive subsequent evolution. This magnetically driven disk evolution is consistent with the apparent scarcity of prominent spirals capable of driving rapid accretion in deeply embedded protostellar disks. However, detecting these spirals may be hindered by optical depth and resolution effects.

5. Early disks in the active formation stage experience significant perturbations in both morphology and kinematics. These perturbations arise from the rapid inward spiraling of disk material on eccentric orbits when the magnetic field remains relatively well coupled to the disk material and from spiral arms in more magnetically diffusive cases.

6. The dense collapsing gravo-magneto-sheetlets observed in our simulations may

correspond to the "accretion streamers" observed around protostars. Additional observations are necessary to confirm whether these streamers are associated with the predicted highly pinched magnetic field and exhibit sub-free-fall speeds indicative of significant magnetic retardation.

3.9 Acknowledgements

We thank the referee for a constructive report. Resources supporting this work were provided by the NASA High-End Computing (HEC) Program through the NASA Advanced Supercomputing (NAS) Division at Ames Research Center and the RIVANNA supercomputer at the University of Virginia. YT acknowledges support from an interdisciplinary fellowship from the University of Virginia. ZYL is supported in part by NSF AST-2308199, AST-1910106, and NASA 80NSSC20K0533. KT is supported by the Japan Society for the Promotion of Science (JSPS) KAKENHI Grant Numbers JP21H04487, JP21H04495, and JP22KK0043.

Chapter 4

Fragmentation of Dense Rotation-Dominated Structures Fed by Collapsing Gravo-magneto-Sheetlets and Origin of Misaligned 100 au-Scale Binaries and Multiple Systems

The work presented in this chapter has been published in the Monthly Notices of the Royal Astronomical Society (MNRAS) with Zhi-Yun Li, Zhaohuan Zhu, and Chun-Yen Hsu as coauthors (Tu et al., 2024b).

Abstract: The majority of stars are in binary/multiple systems. How such systems form in turbulent, magnetized cores of molecular clouds in the presence of non-ideal MHD effects remains relatively under-explored. Through ATHENA++-based non-ideal MHD AMR simulations with ambipolar diffusion, we show that the collapsing protostellar envelope is dominated by dense gravo-magneto-sheetlets, a turbulence-warped version of the classic pseudodisk produced by anisotropic magnetic resistance to the gravitational collapse, in agreement with previous simulations of turbulent, magnetized single-star formation. The sheetlets feed mass, magnetic fields, and angular momentum to a Dense ROtation-Dominated (DROD) structure, which fragments into binary/multiple systems. This DROD fragmentation scenario is a more dynamic variant of the traditional disk fragmentation scenario for binary/multiple formation, with dense spiral filaments created by inhomogeneous feeding from the highly structured larger-scale sheetlets rather than the need for angular momentum transport, which is dominated by magnetic braking. Provided that the local material is sufficiently demagnetized, with a plasma-β of 10 or more, collisions between the dense spiraling filaments play a key role in facilitating gravitational collapse and stellar companion formation by pushing the local magnetic Toomre parameter $Q_{\rm m}$ below unity. This mechanism can naturally produce *in situ* misaligned systems on the 100-au scale, often detected with high-resolution Atacama Large Millimeter Array (ALMA) observations. Our simulations also highlight the importance of non-ideal MHD effects, which affect whether fragmentation occurs and, if so, the masses and orbital parameters of the stellar companions formed.

4.1 Introduction

The majority of stars are in binary or multiple systems. How binaries/multiples form is a fundamental problem in star formation with a long and distinguished history,

as reviewed by, e.g., Tohline (2002) and Offner et al. (2023). At the heart of the problem lies how the star-forming gas is condensed and how the condensed gas evolves into independent centers of gravitational collapse, a process commonly referred to as fragmentation.

Early work focused on the role of the rotation rate and the degree of elongation of dense collapsing cloud cores (e.g., Tohline, 2002). More recent work included turbulence on relatively large scales, which creates independent collapse centers, typically yielding binary/multiple systems of relatively wide separations (e.g. Offner et al., 2016; Kuffmeier et al., 2019). It is widely believed that binary/multiple systems on the 100-au scale or closer are formed primarily through disk fragmentation (Offner et al., 2023). However, there is an increasing number of 100-au scale binaries/multiples whose disks are significantly misaligned, e.g., HK Tau (Jensen & Akeson, 2014), L1448 IRAS2A (Tobin et al., 2015), and VLA1623 (Ohashi et al., 2022). It is difficult to form such misaligned systems via the traditional scenario of fragmentation of a well-ordered, co-planar disk. This paper aims to develop a more dynamic picture of the fragmentation of the so-called "Dense ROtation-Dominated structures" (DROD structures or DRODs for short) that are much more inhomogeneous and dynamically active than the traditional disks and that can naturally produce misaligned binary/multiple systems. In this picture, a strong interplay between magnetic fields, turbulence, and gravity drives the inhomogeneities and dynamic activities of the dense fragmenting gas.

Magnetic fields are expected to play a crucial role in binary/multiple star formation because they can efficiently remove the angular momentum needed for binary/multiple formation through magnetic braking, potentially suppressing fragmentation altogether, leading to the so-called "fragmentation crisis" in the ideal MHD limit (Hennebelle & Fromang, 2008). Similarly, efficient angular momentum removal

during core collapse can potentially suppress disk formation, leading to the so-called "magnetic braking catastrophe" (Li et al., 2014b). Both crises highlight the importance of non-ideal MHD effects, which weaken the coupling between the magnetic field and the bulk neutral gas (and thus the magnetic braking) in both disk and binary/multiple formation. Thus, non-ideal MHD effects are included in our investigation.

Previous studies have stressed different aspects of the role of magnetic fields in binary/multiple formation. For example, Machida et al. (2008) and Price & Bate (2008) explored the effects of the initial magnetic field strength on the number of stellar objects formed, and their subsequent evolution, whereas Harada et al. (2021) stressed the importance of the relative orientation between the magnetic field and the rotation axis. Non-ideal MHD effects were explored extensively in the related problem of disk formation (as reviewed in, e.g., Li et al., 2014b and Tsukamoto et al., 2023a), but less so in the context of binary/multiple formation (see, however, Wurster & Bate, 2019 and Mignon-Risse et al., 2023). Exploring the role of non-ideal MHD, particularly ambipolar diffusion, is a focus of this investigation.

Specifically, we will concentrate on how the interplay between the magnetic field, turbulence, and gravity affects binary/multiple star formation in the presence of ambipolar diffusion. We have previously demonstrated that the interplay produces the so-called "gravo-magneto-sheetlets" that dominate the mass and angular momentum contents of the inner protostellar envelope that feeds the central protostellar disk (Lam et al., 2019; Tu et al., 2024a, see their Fig.3 for a 3D visualization of the structure); they are the strongly perturbed version of the classic pseudo-disk of Galli & Shu (1993b) that has long been recognized to play a central role in disk formation (e.g., Xu & Kunz, 2021b). Given how closely related the problems of disk and binary/multiple star formation are, it is natural to expect the "gravo-magneto-sheetlets" ("sheetlets"

for short hereafter) to play an important role in the binary/multiple formation as well. In this paper, we will demonstrate that this is indeed the case.

In particular, we will show that the highly dynamic collapsing sheetlets feed a highly dynamic dense rotation-dominated structure (DROD) around the primary star on a smaller, 100-au scale, which produces stellar companions through collisions of dense spiraling filaments. The rest of the paper is organized as follows. In § 4.2, we describe the problem setup. It is followed by an overview of the simulation results in § 4.3. In § 4.4, we describe the transformation of the collapsing sheetlets that dominate the structure and dynamics of the inner protostellar envelope into the dense rotation-dominated structures that set the stage for fragmentation. It is followed by a discussion of the conditions for fragmentation and stellar companion formation in § 4.5. Our main results and their observational implications are discussed in § 4.6 and summarized in § 4.7.

4.2 Problem Setup

The formation of stars and their associated structures through the collapse of a molecular cloud core is a complex process involving non-ideal magneto-hydrodynamics (particularly ambipolar diffusion) and turbulence. The following set of equations governs the process:

$$\frac{\partial \rho}{\partial t} + \nabla \cdot (\rho \boldsymbol{v}) = 0, \tag{4.1}$$

$$\rho \frac{\partial \boldsymbol{v}}{\partial t} + \rho(\boldsymbol{v} \cdot \nabla)\boldsymbol{v} = -\nabla P + \frac{1}{c}\boldsymbol{J} \times \boldsymbol{B} - \rho \nabla \Phi_g, \tag{4.2}$$

$$\frac{\partial \boldsymbol{B}}{\partial t} = \nabla \times (\boldsymbol{v} \times \boldsymbol{B}) - \frac{4\pi}{c} \nabla \times (\eta_A \boldsymbol{J}_\perp), \tag{4.3}$$

$$\nabla^2 \Phi_g = 4\pi G \rho, \tag{4.4}$$

where $\boldsymbol{J} = (c/4\pi)\nabla \times \boldsymbol{B}$ is the current density, $\boldsymbol{J}_\perp = [(\boldsymbol{J} \times \boldsymbol{B}) \times \boldsymbol{B}]/B^2$ the component of current density perpendicular to the magnetic field, and η_A the ambipolar diffusivity. Other symbols have their usual meanings.

Our setup closely follows that of Tu et al. (2024a) and Lam et al. (2019). In particular, we use the ATHENA++ code with adaptive mesh refinement (AMR) and the full multigrid (FMG) mode of the multigrid self-gravity solver. The boundary conditions of the self-gravity solver are obtained using multipole expansion for the gravitation potential (Stone et al., 2020; Tomida & Stone, 2023). The simulations are conducted in Cartesian coordinates, with outflow boundary conditions employed at all simulation boundaries.

We use five techniques to speed up the calculations. First, we use the same simplified, four power-laws equation of state (EOS) in Tu et al. (2024a). The adiabatic constant as a function of density is divided into four segments, with $\gamma_1 = 1$, $\gamma_2 = 1.1$, $\gamma_3 = 1.4$ and $\gamma_4 = 5/3$ separated by densities $\rho_{1-2} = 10^{-13}$g cm^{-3}, $\rho_{2-3} = 3.16 \times 10^{-12}$g cm^{-3} and $\rho_{3-4} = 5.66 \times 10^{-9}$g cm^{-3} respectively. Second, we use the AMR capacity to concentrate computational resources in the densest, dynamically active region. A refinement level is added when the local cell size exceeds 1/16 of the local Jeans length. In the most refined region, the cell size is about 1.22 au. Third, we use the same sink particle treatment as in Tu et al. (2024a) to avoid prohibitively small simulation time-step and represent protostars' formation. A sink particle is created when the simulation reaches the highest refinement level and the local cell size exceeds 1/8 of the local Jeans length. The formed sink particle then accretes both mass and momentum from its nearby $3 \times 3 \times 3$ cells. If more than one sink particle is created, two sink particles would merge only if the two sink particles are separated by less than 2 cells (about 2.4 au). Fourth, we cap the ambipolar diffusion coefficient using equation (7) of Lam et al. (2019) to avoid prohibitively small time

steps. Finally, we cap the Alfvén speed by adding small amounts of mass in highly evacuated cells. The last two treatments primarily affect very low-density regions, and we monitor the simulation to ensure the mass added stays negligible compared to the mass in the computation domain.

The simulation is initialized by putting a 1.0 $M_\odot$ perturbed pseudo-Bonner-Ebert sphere of radius $r_{\rm max} = 2000$ au at the center of the 10,000 au size cubic simulation box. The initial density is prescribed by

$$\rho(r) = \frac{\rho_0}{1 + (r/r_c)}(1 + \delta_p) \tag{4.5}$$

where

$$\delta_p = A_\theta \frac{r^2}{r_{\rm max}^2} \cos(2\theta) \tag{4.6}$$

where r is the spherical radius, θ the polar angle from the $z-$axis, and $A_\theta = 0.2$ determines the magnitude of the initial density perturbation. We chose a characteristic radius of $r_c = 1,000$ au, which yields a central density of $\rho_0 = 5.29 \times 10^{-17}$ g cm^{-3}. The rest of the space is filled with low-density gas of 4.56×10^{-20} g cm^{-3}. We assume the core has an initial solid body rotation around the z-axis, with a rate of 1.27×10^{-12} s^{-1}. The setup yields a ratio between the total gas thermal energy and the absolute value of the total gravitational energy of $\alpha = 0.32$ and a ratio between the rotational energy and the absolute value of the total gravitational energy of $\beta_0 = 0.08$. The initial uniform z-direction magnetic field has a strength of 3.28×10^{-4} G, corresponding to a dimensionless mass-to-flux ratio about 3.5 in units of the critical value $1/(2\pi G^{1/2})$.

To simulate a turbulent pre-stellar core (Bergin & Tafalla, 2007), we include an initial turbulence in our models, as in Lam et al. (2019) and Tu et al. (2024a). The

turbulence could be inherited from the larger-scale cloud in which the core is embedded. A root-mean-square Mach number $\mathcal{M} = 1$ is obtained by normalizing the velocity field's amplitude for all of the turbulent models. One difference between the models in this paper and those in Tu et al. (2024a) is the angular momentum of the turbulence isn't removed from the initial rotation. The angular momentum in the turbulence results in a tilted structure in this paper.

Ambipolar diffusivity is treated similarly as in Tu et al. (2024a) to parameterize the uncertainty in the ambipolar diffusivity coefficient associated with the uncertainties in the ionization level (caused by, e.g., uncertain grain size distribution and cosmic ray ionization rate). Following Lam et al. (2019), we choose to parameterize it in the following way for efficient parameter exploration:

$$\eta_A = \frac{B^2}{4\pi\gamma\rho\rho_i}, \tag{4.7}$$

where $\gamma = \langle\sigma v\rangle/(m + m_i)$ is the ion-neutral drag coefficient, and $\rho_i = C\rho^{1/2}$ is the ion density, with the coefficient C proportional to the square root of the cosmic ray ionization rate (Shu, 1991; Draine et al., 1983). With these approximations, the ambipolar diffusivity can be written as

$$\eta_A = \eta_0 \frac{B^2}{4\pi\rho^{3/2}}, \tag{4.8}$$

where $\eta_0 = \tilde{\eta}_0/(\gamma C)$, with $\gamma = 3.5 \times 10^{13}\mathrm{cm^3 g^{-1} s^{-1}}$ and $C = 3 \times 10^{-16}$ $\mathrm{cm^{-3/2}}$ $\mathrm{g^{1/2}}$ (Shu, 1991). The $\tilde{\eta}_0$ is a free scaling parameter for the ambipolar diffusivity coefficient, with $\tilde{\eta}_0 = 1$ corresponding to the standard cosmic ionization rate of 10^{-17} $\mathrm{s^{-1}}$. We consider three values of $\tilde{\eta}_0$: 1, 2, and 10 (see Table 4.1). In addition, we consider a variant of the $\tilde{\eta}_0 = 2$ model that does not have any initial turbulence (Model M0.0AD2.0)

Model	$\mathcal{M}$	$\tilde{\eta}_0$	$N_{\rm star}$	$N_{\rm tot}$	$t_{\rm primary}$	comment
M1.0AD2.0	1	2	5	6	13560	reference
M0.0AD2.0	0	2	3	3	12050	no turbulence
M1.0AD1.0	1	1	1	1	13670	low diffusivity
M1.0AD10	1	10	5	6	13110	high diffusivity
PRM2.0AD2.0	2	2	2	2	16290	$\boldsymbol{\Omega}_0 \perp \boldsymbol{B}_0$

Table 4.1: Summary of each simulation model's initial conditions and outcome. $\mathcal{M}$ is the Mach number of the initial turbulence; $\tilde{\eta}_0$ is the scaling of the ambipolar diffusivity coefficient defined in equ. 4.8; $N_{\rm star}$ is the number of stars at the end of the simulation (excluding merged stars; stellar companion 2 merged with stellar companion 1 in Model M1.0AD2.0, and stellar companion 5 merged with stellar companion 4 in Model M1.0AD10); $N_{\rm tot}$ is the total number of stars formed in the simulation (including merged stars); $t_{\rm primary}$ is the formation time of the primary in years.

and another variant where the turbulence Mach number is twice as large and the initial magnetic field and rotation axis are perpendicular (Model PRM2.0AD2.0).

4.2.1 Post-process Lagrangian tracer particles

To better understand the gas evolution during the simulation, particularly in the period leading up to stellar companion formation (see fig. 4.9 below), we developed a post-process Lagrangian tracer particle code to trace the gas trajectory. We solve the equation of motion of tracer particles and update their velocities and positions at every time step. The equation of motion is given by

$$\frac{d\boldsymbol{x}}{dt} = \boldsymbol{v}_{\rm gas} \tag{4.9}$$

where $\boldsymbol{v}_{\rm gas}$ is the instantaneous gas velocity at the location of the tracer particle. We obtain the gas property information at every location ($\boldsymbol{x}$) at every time step (t) in two steps. Firstly, we interpolate the gas properties spatially using the Triangular-Shaped-Cloud (TSC) interpolation method (Hockney & Eastwood, 1981) at the hydro frames immediately before (denoted with a subscript "1", e.g., v_1 and t_1) and after

(denoted with a subscript "2", e.g., v_2 and t_2) the time of interest. Secondly, we get the hydro quantities at the time of interest using a linear interpolation of their values at t_1 and t_2, e.g.,

$$v_t = v_1 + \frac{(v_2 - v_1)(t - t_1)}{t_2 - t_1} \tag{4.10}$$

Finally, we solve the equation of motion using the second-order Runge-Kutta method.

To maximize the efficiency of the post-process simulation, we allow each particle to evolve using its own time steps by taking advantage of the fact that the hydro information is known. We only require the time steps for all particles to synchronize at the time of output. The time step for each particle is determined by its instantaneous speed $\boldsymbol{v}_t$ and the local cell size $dx_{\rm grid}$, and is given by

$$dt = 0.3 \times \min\left(dt_{\rm max}, \frac{dx_{\rm grid}}{|\boldsymbol{v}_t|}\right) \tag{4.11}$$

This guarantees that a particle travels no more than 0.3 times the local cell size each time step (similar to the CFL condition described in Courant et al., 1928). The maximum time step $dt_{\rm max} = 1$ yr caps the time step so that it does not become too large when the tracer is almost stationary.

4.3 Overview of Results

In this section, we give a general impression of the simulation results by highlighting some broad features in Fig. 4.1 and 4.2. Fig. 4.1 shows the time evolution of the total mass of all protostellar objects (sinks) after the formation of the first object (referred to as the "primary" hereafter) in each of the first four models listed in Table 4.1 (left panel) and the mass evolution of each individual object (right panels); the last model in the table (PRM2.0AD2.0) will be discussed separately in § 4.6 below. The "star" on each curve in panel (a) corresponds to the formation time of the first stellar

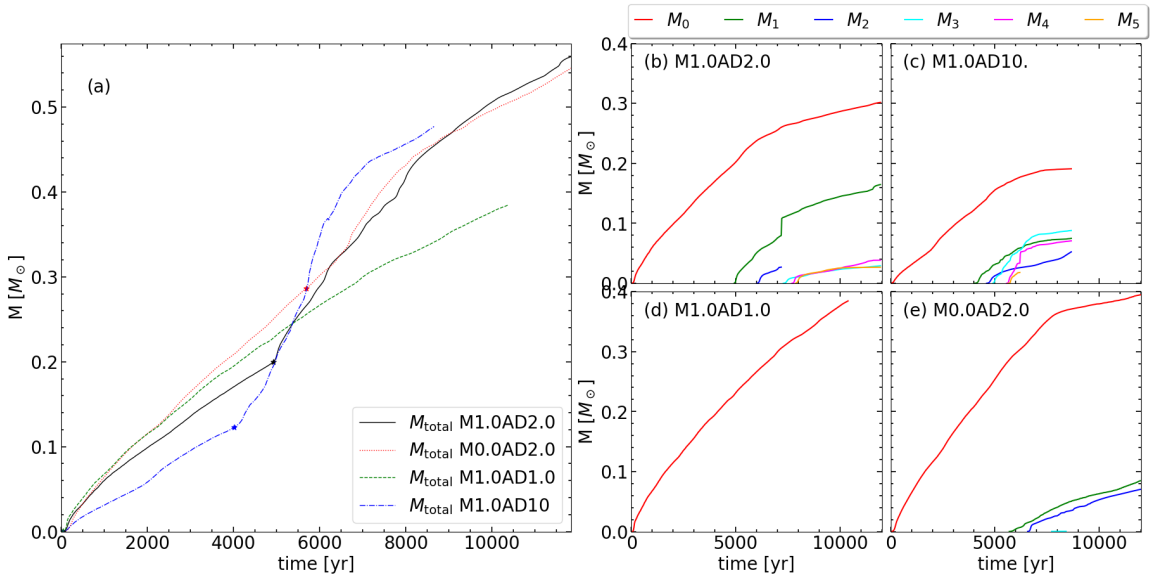


Figure 4.1: **Left Panel (a):** The time evolution of the total mass of all stars formed in each of the first four models listed in Table 4.1, starting from the time of the primary formation. The "star" on each curve marks the formation of the secondary, if any. **Right Panels (b)-(e):** The time evolution of the masses of individual stars for the four models. The quantity M_0 above the panels refers to the mass of the primary, M_1 that of the first stellar companion (or the secondary), and M_2 that of the second stellar companion, etc.

companion (referred to as the "secondary" hereafter). In the least magnetically diffusive model (M1.0AD1.0 model), there is no "star" on the curve, which means there is only a single object in this model at all times. Only in the more diffusive cases does a secondary form. After the primary formation, the secondary forms the earliest in the M1.0AD10 model and the latest in Model M0.0AD2.0, with Model M1.0AD2.0 in between the two limits. After the secondary formation, the slope of the total stellar mass as a function of time changes suddenly because mass is now accreted onto the second star in addition to the primary (Fig. 4.1a). Because Model M1.0AD2.0 has multiple stellar objects formed at well-defined times (see Fig. 4.1b), it will be the focus of our detailed analysis and be referred to as the "reference" model hereafter.

To give a general impression of the spatial distribution of the protostars and the gas structures around them, we show in Fig. 4.2 the column density distribution and the projected sink particle positions at a representative time when all stars have formed and grown beyond $0.02M_{\odot}$. Each plot is centered on the center-of-mass of the simulation. Fig. 4.2 shows that most of the dense gas and formed stars reside in a relatively flat structure, which is particularly evident when viewed along the $\hat{x}-$direction (see the right panels). In the simplest case of the non-turbulent model M0.0AD2.0, the dense flattened structure lies on the equatorial plane perpendicular to the initial magnetic field and rotation axis (see Fig. 4.2e,f). It is tilted and modified by the turbulence included in the reference model M1.0AD2.0, which apparently facilitated an earlier formation of the secondary (see Fig. 4.1a) and the formation of more companions at later times (Fig. 4.1b). The comparison of these two models clearly illustrates the beneficial effects of turbulence on the fragmentation of dense gas that leads to the formation of binary/multiple systems.

The dense gas fragmentation also depends on the magnetic diffusivity. The dependence is illustrated most vividly by the least magnetic diffusive model M1.0AD1.0,

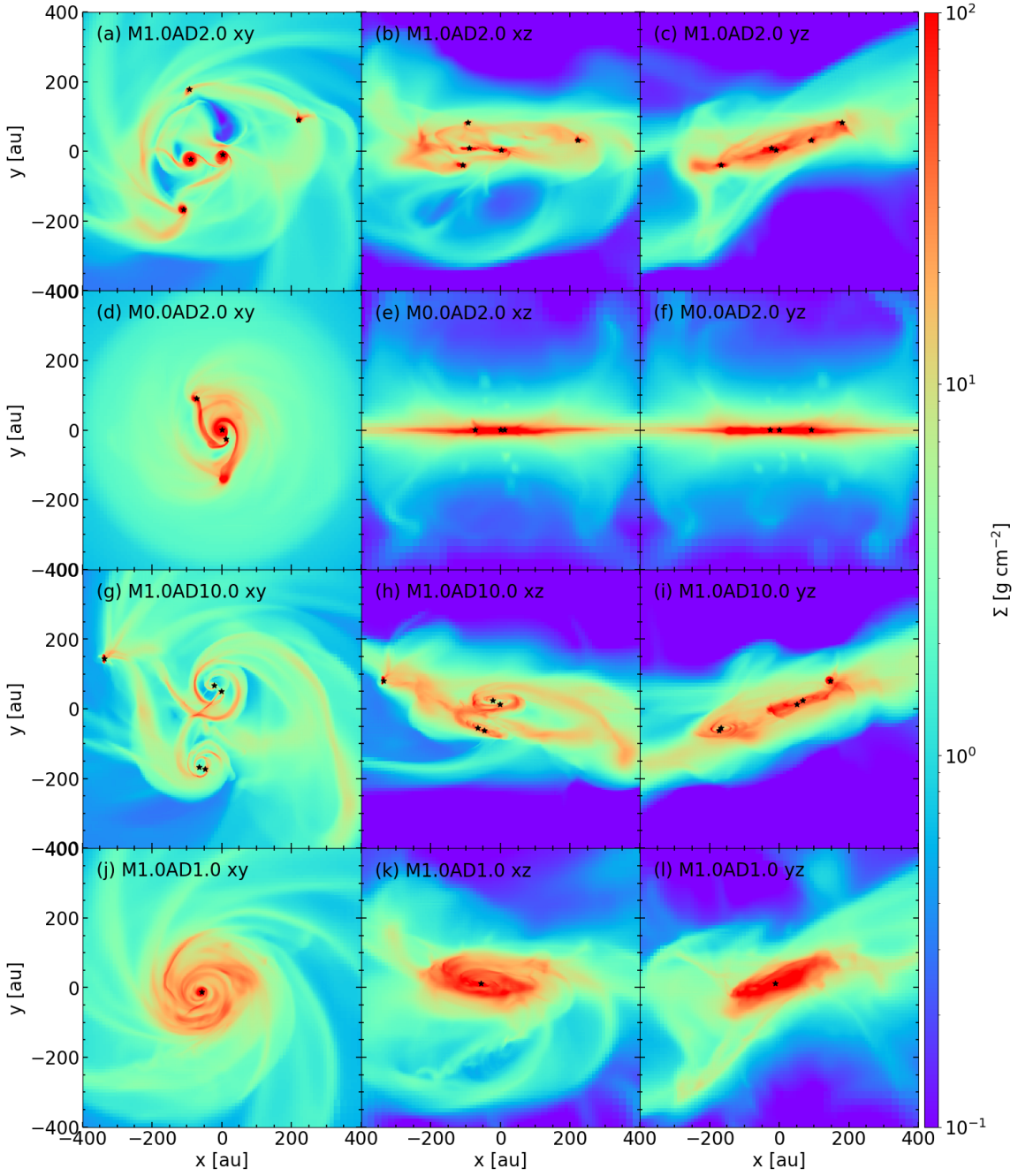


Figure 4.2: Column density distributions within a 800 au^3 central region along the $\hat{z}-$ (left column), $\hat{y}-$ (middle column), and $\hat{x}-$direction (right column), respectively at a representative time, with the model name shown in each panel. The "stars" in each panel mark the projected locations of the sink particles. An animation of this figure can be found at `https://virginia.box.com/s/nju7yjqycbecpfbgsoem7x7yj7ygp3ip`

where fragmentation does not occur at all, despite the presence of initial turbulence as in the reference model. In contrast, several stars are formed in the more magnetically diffusive models, Models M1.0AD2.0 and M1.0AD10. This result is consistent with the finding of earlier work that a dynamically important magnetic field tends to suppress fragmentation in the ideal MHD limit, leading to a potential binary/multiple star formation crisis (e.g. Hennebelle & Fromang, 2008; Boss & Keiser, 2013; Zhao & Li, 2013). Our models demonstrate that non-ideal MHD effects (specifically ambipolar diffusion) can avert the fragmentation crisis, provided the magnetic diffusivity is large enough. The value of the diffusivity can also strongly affect the properties of the formed stellar systems (such as the number of stars and their mass distribution and orbital parameters) when fragmentation does occur, as can be seen from a comparison of Model M1.0AD2.0 (top row of Fig. 4.2 and Fig. 4.1b) and Model M1.0AD10 (third row of Fig. 4.2 and Fig. 4.1c), whose diffusivities differ by a factor of 5.

Since the formation and evolution of dense structures lie at the heart of gas fragmentation and binary/multiple formation, they will be discussed first (§ 4.4). It is followed by a discussion of the conditions for binary/multiple formation (§ 4.5).

4.4 Origins of Dense Binary/Multiple-Forming Gas Structures

4.4.1 Large-Scale Collapsing Gravo-magneto-Sheetlets

The concentration of gas in a collapsing molecular cloud core and the subsequent evolution of the dense gas set the stage for fragmentation and binary/multiple formation. Both processes are shaped by a complex interplay between several processes, including gravitational collapse, rotation, turbulence, and the magnetic field. In particular, in the presence of an ordered, dynamically important magnetic field, the

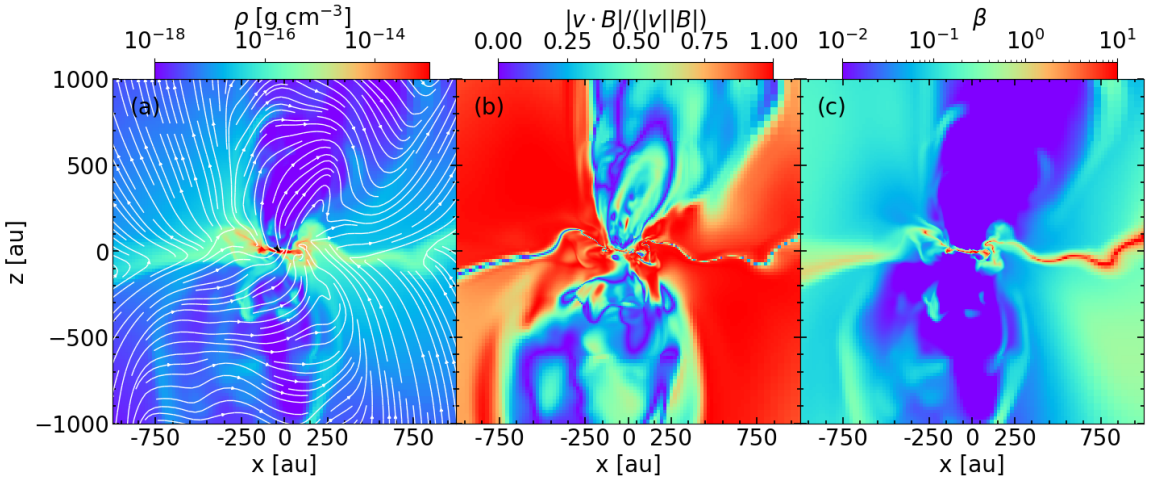


Figure 4.3: Dense demagnetized sheetlets embedded in a strongly magnetized diffuse background. Plotted are the distributions of the mass density (panel [a], with field lines superposed), the quantity $\cos(\theta_{\rm ali})$ (panel [b], where $\theta_{\rm ali}$ is the angle between the magnetic and velocity field), and the plasma-β (panel [c]) on an xz-slice through the reference model at a representative time on a relatively large ($\sim$1000 au) scale. The thin, wiggly, bluish filaments in the middle panel (where dense demagnetized gas collapses across field lines) mark the 2D (xz-)cross-section of the 3D gravo-magneto-sheetlets. The low-density, strongly magnetically dominated cavities above and below the sheetlets are magnetically driven outflow lobes.

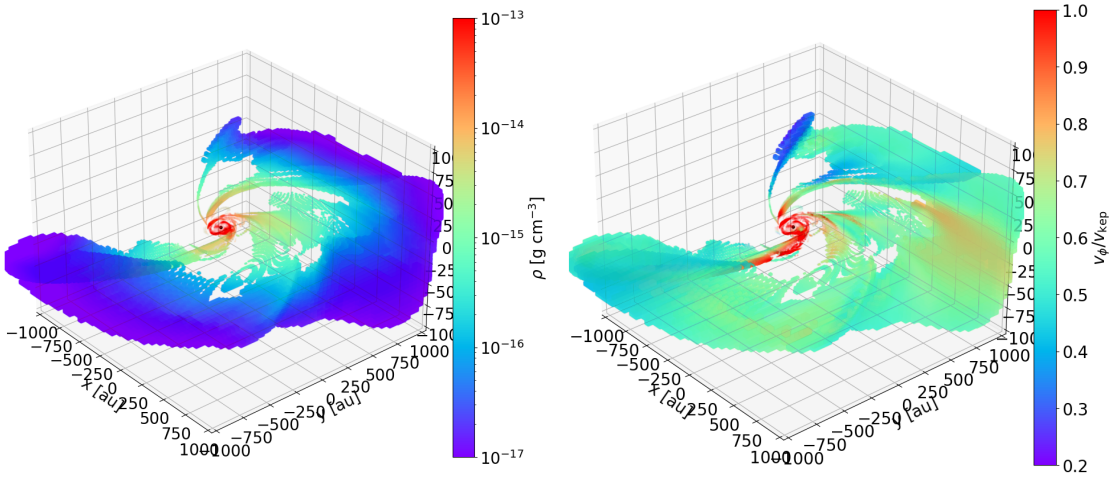


Figure 4.4: Sheetlets in 3D. Plotted are the 3D structures of the gravo-magneto-sheetlets at the representative time for the reference model shown in Fig. 4.3. The color in panel (a) shows the local density. It shows the rotation speed around the center of the mass normalized by the local Keplerian speed in panel (b). Note the large-scale, relatively open spirals in the flattened sheetlets, which turn into more tightly wound spirals on the smaller scale. An animation of the figure at different times can be found at `https://virginia.box.com/s/l8zm7qg1h17h47b0aze7gy3xy6b7s199` (for the left panel) and `https://virginia.box.com/s/m5g0tr2ydxkyw8nttfsezicu7y69g6ba` (for the right panel). An animation of the left panel viewed from different angles can be found at `https://virginia.box.com/s/3wh123bq9jaj84j6hm80osx0smw86ugh`.

gravitational collapse tends to funnel the collapsing material along the field lines towards a dense flattened structure that is spatially coherent - the classic "pseudodisk" in the simplest case of the collapse of a non-turbulent initially uniformly magnetized singular isothermal sphere (Galli & Shu, 1993b). This product of the interplay between the gravitational collapse and anisotropic magnetic resistance to it shows up clearly in our non-turbulent model M0.0AD2.0 as a dense equatorial sheet that is the main conduit for delivering the dense gas close to the center, where fragmentation leading to binary/multiple systems occurs (see Fig. 4.2, second row). In the presence of turbulence, the flat gravo-magneto-sheet is warped and fragmented into more irregular gravo-magneto-sheetlets, which show up in the column density maps as filaments connecting to the densest region near the center (see, e.g., Fig. 4.2c,i). Tu et al. (2024a) showed that these filamentary column-density structures are spatially connected in 3D, which they termed "gravo-magneto-sheetlets" (or "sheetlets" for short; see their Fig. 3 for a 3D visualization of the structure).

Tu et al. (2024a) found two defining characteristics of the sheetlets: (1) they are less magnetized compared to the background (with a significantly higher plasma-β) and (2) they tend to move across the field lines, with a relatively small value of the quantity $\cos\theta_{\rm ali} = |\boldsymbol{v}\cdot\boldsymbol{B}|/(|\boldsymbol{v}||\boldsymbol{B}|)$, where $\theta_{\rm ali}$ is the angle between the magnetic field and velocity field. The latter contrasts with the lower-density background, where the strongly magnetized (low plasma-β) gas tends to flow along the field lines, with $\cos\theta_{\rm ali}$ close to unity. These two characteristics are illustrated in Fig. 4.3, which shows the distributions of the mass density, $\cos\theta_{\rm ali}$, and the plasma-β of the reference model M1.0AD2.0 on a xz-slide through the primary at a representative time $t = 19,000$ years after the start of the simulation, when the primary mass reached $M_0 = 0.2M_\odot$. The most striking feature is present in the distribution of $\cos\theta_{\rm ali}$ in the middle panels where thin wiggly blue filaments of small $\cos\theta_{\rm ali}$ are embedded in a red

background of $\cos\theta_{\rm ali} \approx 1$. These filaments have higher plasma-β (see right panels) and higher density (left panels) than the surrounding background. They also have sharp pinching of the local field lines (see the white lines in the left panels), which is produced by the field dragging by the cross-field gravitational collapse, as expected in the dense sheetlets (Tu et al., 2024a)[1].

To show the true shape of the turbulence-perturbed gravo-magneto-sheetlets in 3D, we make use of their two defining characteristics and search for all cells where the plasma-$\beta > 2.51$ and $\cos\theta_{\rm ali} < 0.6$. Fig. 4.4 displays a 3D visualization of the ridges of the sheetlets identified with the above two criteria in the reference model at the same time ($t = 19,000$ years, corresponding to 5500 years after the primary formation) as shown in Fig. 4.3 on a relatively large scale of 1000 au. Note that with these two selection criteria, we are picking out only the densest part (the "spline") of the sheetlet identified in Tu et al. (2024a), where the sheetlet is identified by a density threshold using mass contained. The reader is encouraged to view the animation of the figure from different viewing angles to get a more vivid impression of this crucial 3D structure, which is the main conduit to funnel the dense material collected from the more diffuse regions of the protostellar envelope along magnetic field lines to the central region where fragmentation and binary/multiple star formation occurs (e.g., Tu et al., 2024a, their Fig.5e). It contains several large-scale spirals with relatively open arms, which are caused by a relatively fast gravitational collapse compared to the rotation. The gravitational collapse is integral to the density increase in the sheetlets. However, it limits the mass the sheetlets can collect to form binary/multiple systems locally through gravitational instability because of mass continuity: for a given mass

[1]We note dense filaments similar to those shown in Fig. 4.2 are also observed in disk formation simulations starting from larger cloud scales that include magnetic fields and turbulence (e.g., Kuffmeier et al., 2017; Lebreuilly et al., 2021). At least some of them are likely gravo-magneto-sheetlets, but we do not have detailed information on their magnetic and velocity fields to be sure.

accretion rate, the faster the infall is, the lower the local density becomes. To collect enough mass to form binary/multiple systems, another mechanism must come into play to slow down the collapse and force the matter to pile up further. It is, of course, through rotational support against gravity, as we demonstrate next.

4.4.2 Dense Rotation-Dominated Structures

The transformation of the large-scale dense collapsing gravo-magneto-sheetlets into even denser, smaller-scale rotation-dominated structures is illustrated in the right panel of Fig. 4.4, which shows (in color) the non-radial speed around the primary star normalized by the local Keplerian speed. Because the primary's mass is relatively small compared to that of the inner envelope at early times, we approximate the local Keplerian speed by $v_{\rm kep}(r) = \sqrt{GM_{\rm in}(r)/r}$ where r is the distance from the primary and $M_{\rm in}(r)$ is the mass enclosed within a sphere of radius r (including the stellar mass)[2]. A comparison of the left and right panels of Fig. 4.4 clearly shows that the transition from an infall-dominated velocity field to one dominated by rotation corresponds to a jump in density. This rotation-induced mass pileup sets the stage for fragmentation and binary/multiple formation.

In Fig. 4.5, we show the dense rotation-dominated structure with a density greater than 3×10^{-15}g cm^{-3} and rotating at $> 90\%$ the local Keplerian speed. We term this structure the "DROD (Dense ROtation-Dominated) structure" (or "DROD" for short) to distinguish it from the traditional circumstellar disk because it is much more irregular and dynamically active (see the online animated version of Fig. 4.5). To distinguish between the circumstellar disk and the DROD structure, we define the circumstellar disk to be the gas in the vicinity of a star, rotating at $> 90\%$

[2]We caution the reader that this approximation of the local Keplerian velocity assumes a gravitational potential dominated by the first (monopole) term in the multipole expansion, which is more accurate at later times when more mass is concentrated at small radii (including the star/sink).

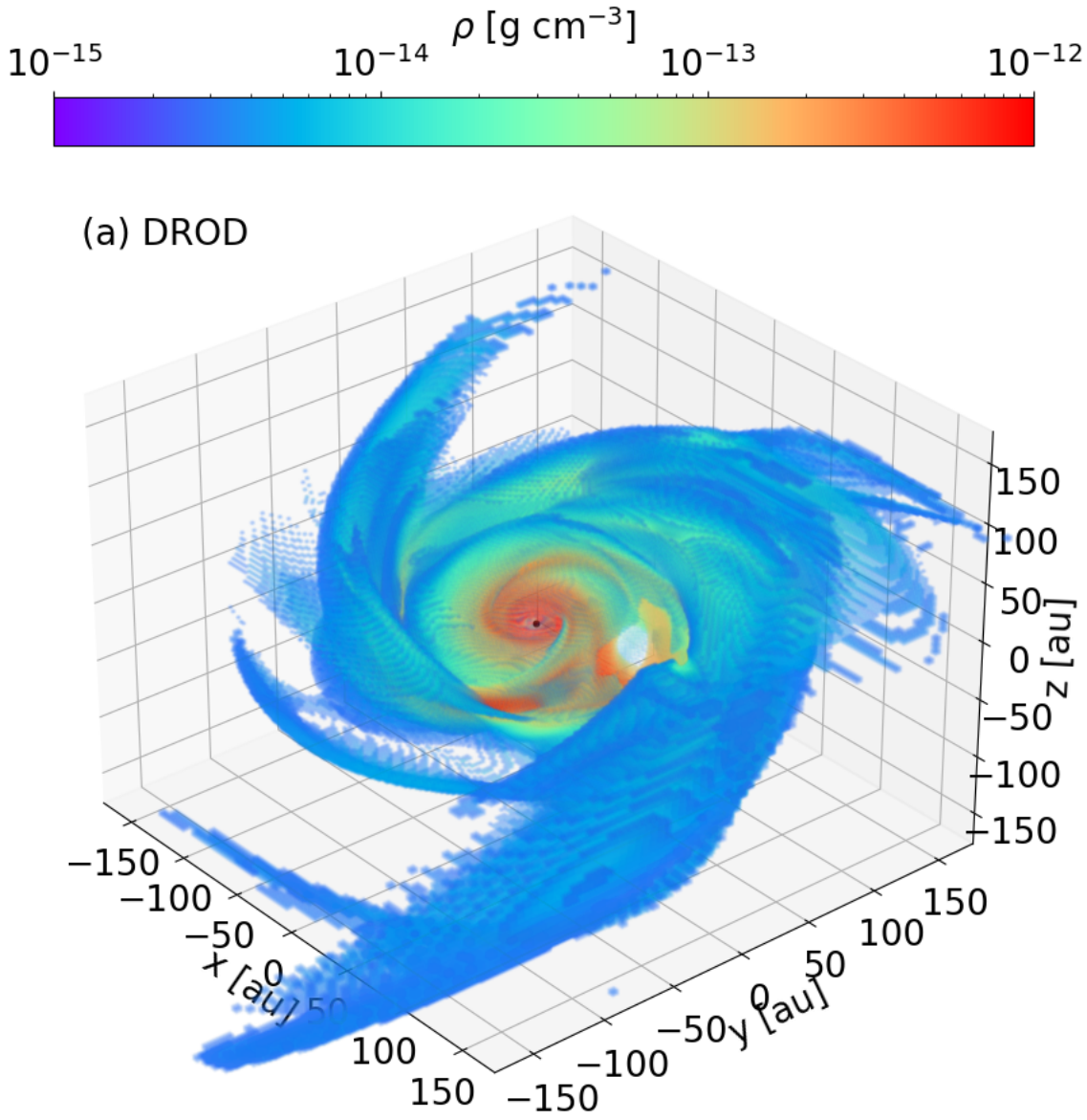


Figure 4.5: A 3D view of the dense rotation-dominated DROD structure (DROD for short) that is fed by the larger-scale sheetlets; it is the formation site for (often misaligned) stellar companions (see Figs. 4.12 and § 4.6.1 below). An animated version of this figure viewed from different angles can be found at `https://virginia.box.com/s/wkasilbfccszie1pz2o6udqwifplf12a`

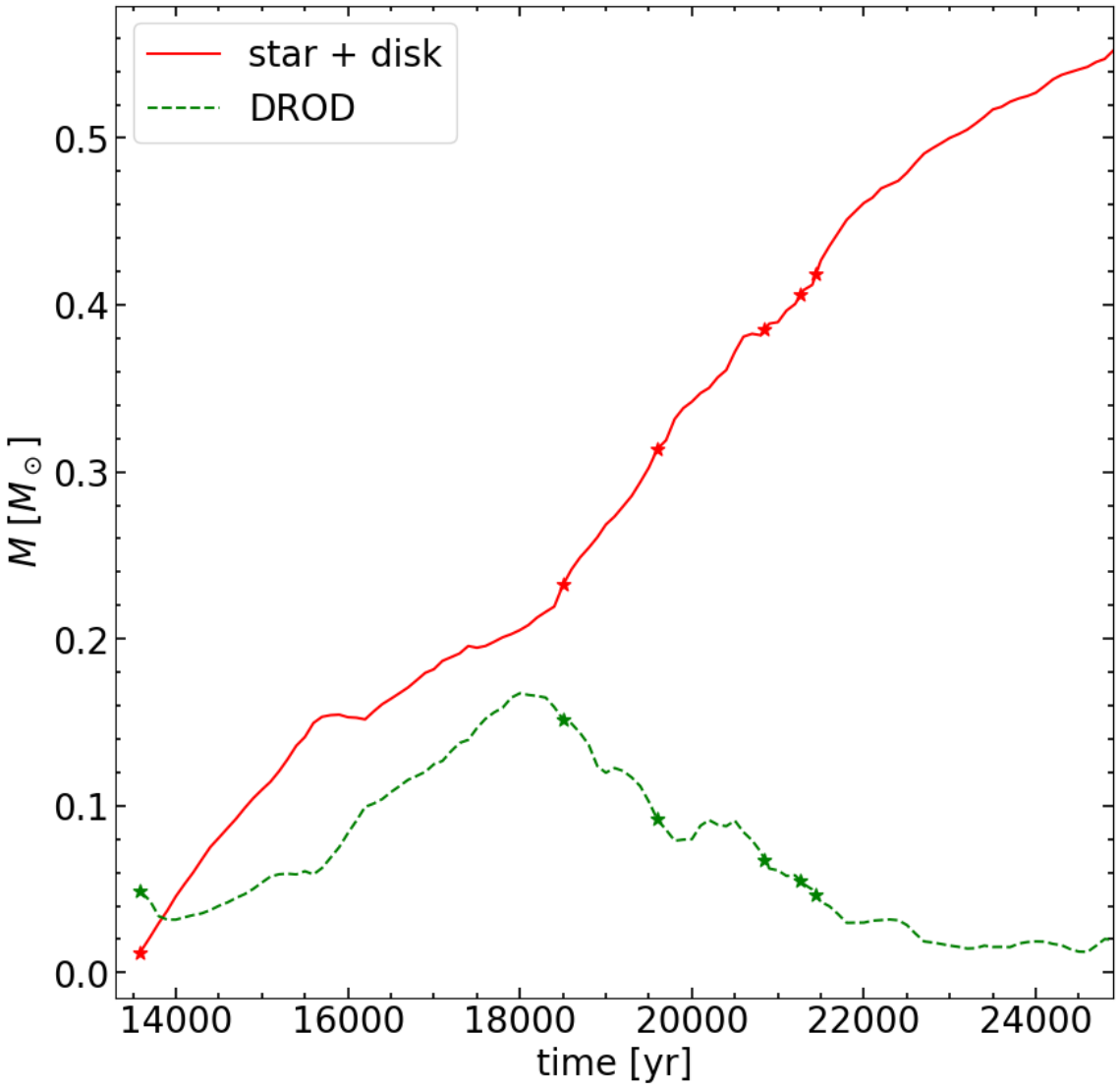


Figure 4.6: Total mass of the stars and their disks (defined in sec. 4.4.2, red solid line) and total mass of the DROD (green dashed line). The stars on both curves mark the formation time of each star.

the local Keplerian speed relative to the host star, and with a density greater than 10^{-12} g cm^{-3}. In Fig. 4.6, we show the mass of the DROD and the star-disk system. The formation times of the stars are marked by the "star" on each line. After the primary formation, the mass of the DROD increases as mass piles up due to rotation. At $\sim$ 18500 yr, the DROD starts to fragment into companion stars and 5 additional stellar objects form within the next 3000 yrs. During this rapid star formation era, the mass of the DROD decreases. After the mass becomes depleted in the DROD at $\sim$ 21500 yr, no more stars form. This picture could be modified if there is additional material accreting onto the DROD from, e.g., the larger cloud scale (e.g., Kuffmeier et al., 2017; Lebreuilly et al., 2021).

Whether the piled-up dense gas in the DROD fragments into a binary/multiple system or not depends on its detailed properties, such as mass and size, which, in the set of models considered in this paper, depend on the magnetic diffusivity. Specifically, the DROD formed in the least magnetically diffusive model, M1.0AD1.0, contains several spirals that connect smoothly to the larger-scale collapsing sheetlets (see Fig. 4.2j and associated animation). It does not accumulate enough mass to become locally self-gravitating for a long enough period to collapse into companion stellar objects. In contrast, the DROD in each of the three more magnetically diffusive models (M1.0AD2.0, M0.0AD2.0, and M1.0AD10) contains denser, more prominent spiraling filaments that are often spatially connected to the larger-scale collapsing gravo-magneto-sheetlets (see, e.g., Fig. 4.2a and Fig. 4.4a and their associated animations) independent of the level of turbulence. Portions of the filaments accumulate enough mass at large enough distances from the primary to collapse locally to form companion stellar objects.

The above difference can be traced to the effects of magnetic diffusivity on the field strength and configuration and their associated magnetic braking efficiency. These

effects have been discussed in depth in Tu et al. (2024a) in the context of disk formation around a single star (see also, e.g. Lam et al., 2019; Hennebelle et al., 2016b; Hennebelle et al., 2020; Lee et al., 2021). Specifically, they showed that, as the magnetic diffusivity increases, the magnetic braking becomes less efficient (see their Fig. 12), resulting in a larger (their Fig. 11, top panels) and more massive (their Fig. 1, right panel) disk, which is closer to being gravitationally unstable as measured by the value of the standard Toomre Q parameter (their Fig. 11, bottom panels). This trend makes physical sense since the braking would go to zero in the limit of infinite magnetic diffusivity (i.e., the field is not coupled to the matter at all). The next section shows that it also holds for the DRODs formed in our simulations.

4.5 Conditions for DROD Fragmentation

4.5.1 Toomre-Q unstable structures

A traditional measure for disk fragmentation is the Toomre Q parameter, defined as

$$Q = \frac{c_s \Omega}{\pi G \Sigma} \tag{4.12}$$

where c_s and Σ are the isothermal sound speed and gas column density, respectively, and Ω is the disk rotation frequency around the central star. Even though the stability condition on the Toomre-Q parameter was initially derived mathematically for axisymmetic perturbations (Toomre, 1964), it has often been used to diagnose and predict gravitational fragmentation. Although the DRODs formed in our simulations are not necessarily smooth, well-defined disks (see Fig. 4.5 and discussion in § 4.6.1 below), we will stick with this quantity because it continues to provide a measure of how self-gravitating a region is locally against thermal pressure support and shearing by tidal forces.

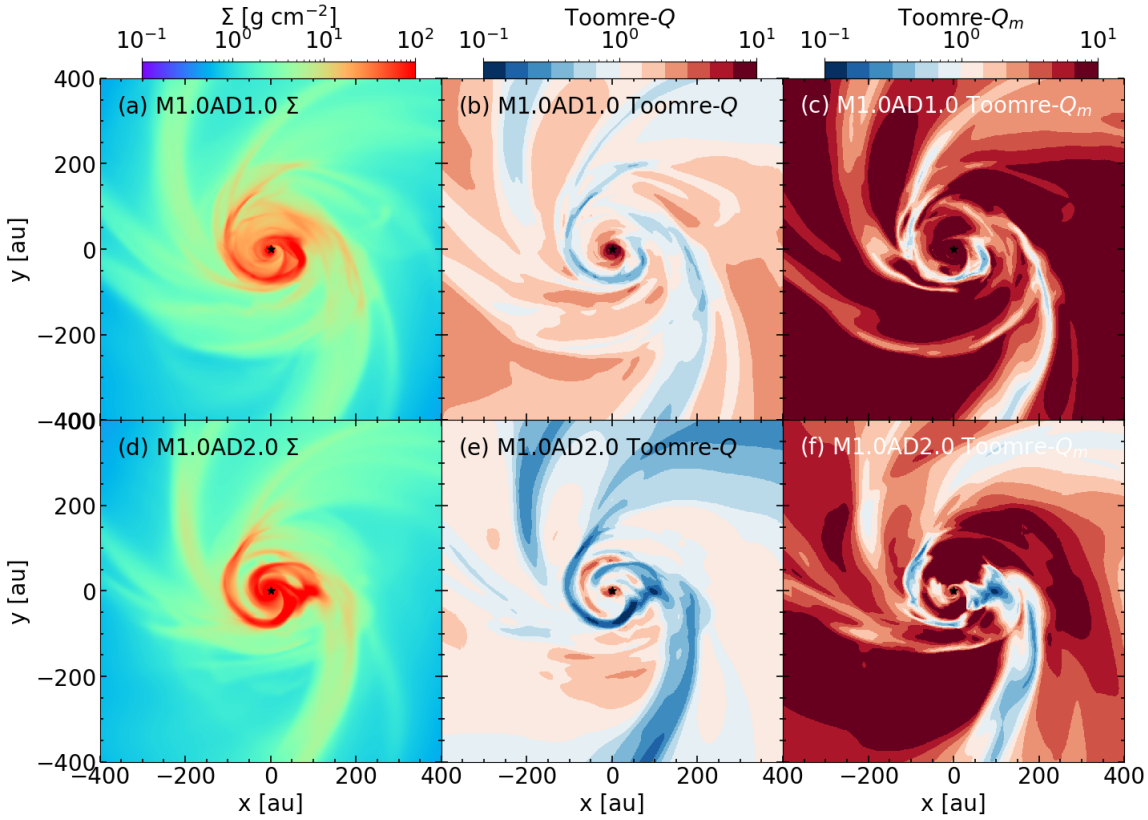


Figure 4.7: Potential for fragmentation as measured by the Toomre parameter Q (middle panels) and the effects of the magnetic field as measured by the magnetic Toomre parameter Q_m (right panels), for the least diffusive model M1.0AD1.0 (top row) and reference model M1.0AD2.0 (bottom row). The column density is shown in the left panels for comparison.

To compute the Toomre Q parameter, we must first determine a "midplane" of the simulation, which is the plane that best captures the rotation-dominated structure in each model and is not aligned with any of the coordinate directions. In the least diffusive M1.0AD1.0 model, where only a single star forms, the midplane is defined as the plane through the star that minimizes its distance to the densest 1000 cells, following the definition used in Tu et al. (2024a). To best capture the DRODs in models with multiple stars, we define the midplane as the plane that minimizes its distance to all stars' orbit over all times and goes through the primary star at the time of interest. The sound speed c_s and Keplerian rotation speed Ω are computed on the midplane. The column density Σ is computed by integrating 400 au in both directions perpendicular to the midplane. For the least magnetically diffusive model M1.0AD1.0, we find values of Q well below unity in the prominent spirals in the DROD. The apparently gravitationally unstable spirals often connect smoothly to the larger-scale sheetlets with low values of Q, as illustrated in the top middle panel of Fig. 4.7. At the face value, one may expect the spirals to fragment. However, the DROD remains significantly magnetized, which hinders fragmentation.

To account for the magnetic effects, we define a magnetic Toomre parameter (following Kim & Ostriker, 2001):

$$Q_m = \frac{\sqrt{c_s^2 + v_A^2}\Omega}{\pi G \Sigma} \tag{4.13}$$

where v_A is the Alfvén speed computed on the midplane. It is included to account for approximately the magnetic resistance to local gravitational collapse.

The magnetic Toomre parameter Q_m in Model M1.0AD1.0 is significantly higher than Q, as seen by comparing the top right panel of Fig. 4.7 to the top middle panel. The magnetic effects bring most of the apparently Toomre unstable regions with Q

well below unity to marginal stability with $Q_m \sim 1$. In the more diffusive reference model M1.0AD2.0, the apparently Q-unstable regions are more widespread than in Model M1.0AD1.0 (compare the middle panels of Fig. 4.7). Some of these regions remain unstable even after the magnetic effects are considered. A subset of such apparently unstable regions collapses gravitationally to become stellar companions while others are quickly sheared apart. In the latter case, the relatively strong magnetic field remaining in the DROD plays a key role in suppressing the fragmentation, as discussed further in sec. 4.5.3 below.

The presence of regions with $Q_m < 1$ that do not collapse into stars suggests that the magnetic Toomre criterion is a necessary but not sufficient condition for fragmentation. This conclusion is consistent with the finding of Mignon-Risse et al. (2021) that the Toomre parameter alone cannot determine whether a rotationally supported structure would fragment or not. The following subsection will investigate whether collisions between dense filaments inside the DROD can help induce Toomre-unstable regions to collapse and form stellar companions.

4.5.2 Collision-Induced Fragmentation

The rotation-dominated DRODs formed in our simulations are highly dynamic structures, with dense spiraling filaments often colliding with one another. The collisions are key to forming stellar companions. These collisions are seen most clearly in an animated version of the column density distribution of the DROD along the $z-$axis. A link to the animation can be found in the caption of Fig. 4.8, where we highlight the filaments involved in the collisions that form each of the five stellar companions in the reference model, with one column of three panels in the figure for each companion. The formation of the first companion involves the collisions between three dense spiral filaments marked with black line segments in panels (a) through

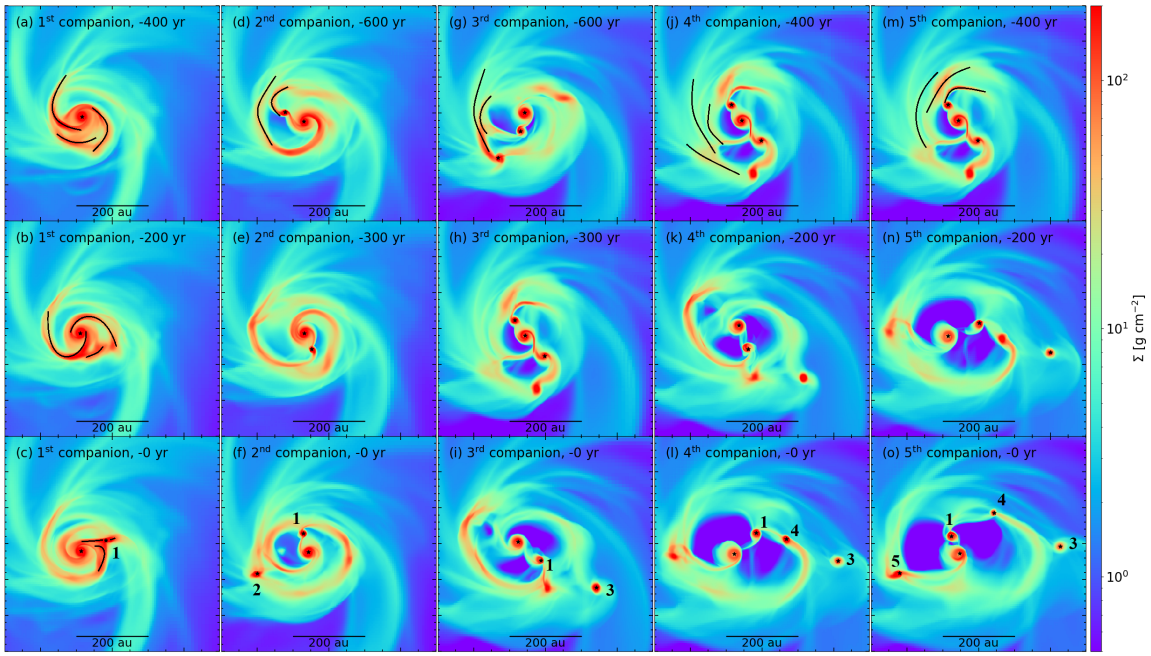


Figure 4.8: Collisions of dense spiraling filaments leading to stellar companion formation. Each column shows three representative snapshots during the formation of each of the five stellar companions of the reference model, highlighting the dense spiraling filaments that collided to form the companion (see the thin black lines). The time before the companion formation is marked in each panel (e.g., -200 yrs). The companions are numbered in the bottom panels. An animation of this figure can be found at `https://virginia.box.com/s/2uul0la2ekysemd9rhoa47cu73f0rwnz`

(c). The filament in the middle is compressed by the collision and becomes the first companion. The formation of the second and third companions involves the collision of two dense spiraling filaments and the continued accretion of material along the merged filament after the collision (see the second and third columns, respectively); the second companion later merged with the first companion. Similar to the formation of the first companion, the formation of the fourth and fifth companions each involves three dense spiraling filaments (see the fourth and fifth columns). In the case of the fourth companion, the outer two filaments collide first, with the merged filament subsequently colliding with the innermost filament to form the companion. In the case of the fifth companion, the inner two filaments collide first, with the merged filament colliding with the outermost filament to form the companion. Some low-density cavities appear in the DROD, particularly at later times (see, e.g., the right 3 columns of Fig. 4.8). They are likely primarily caused by stellar interactions, as in Artymowicz & Lubow (1994), although magnetic fields may have also contributed because the cavities are magnetically dominated (with a plasma-β typically well below unity) and contain a significant fraction of the magnetic flux threading the DROD.

To illustrate the collisions leading to stellar companion formation more vividly, we produced a 3D animation highlighting the dense structures in the DROD using the post-processing Lagrangian tracers described in § 4.2.1. A link to the animation can be found in the caption of Fig. 4.9, which shows the evolution of tracers including the three timeframes in the right column of Fig. 4.8 for the formation of the fifth companion. Figs. 4.8 and 4.9 and their associated animations leave little doubt that collisions of dense spiraling filaments play a key role in stellar companion formation. Our finding agrees with Mignon-Risse et al. (2021), who also stresses the importance of filament collisions.

Similar to the magnetic Toomre parameter $Q_m < 1$ requirement, collision is also a

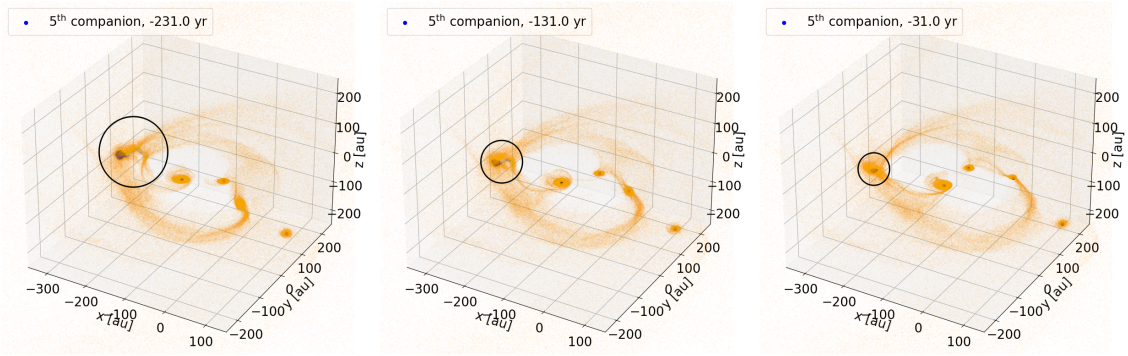


Figure 4.9: 3D view of the collisions of dense spiraling filaments leading to the formation of the fifth stellar companion in the reference model. Plotted are Lagrangian tracers, which highlight the colliding filaments leading to the fifth companion's formation. The black circle in each panel highlights the filament collision site. An animation of the figure can be found at `https://virginia.box.com/s/2s8h7l7w9y9zz21g8m28l854tq4n54nw`.

necessary but not sufficient condition for fragmentation. For example, in the less magnetically diffusive model M1.0AD1.0, collisions between dense filaments also happen, yet none of them triggers fragmentation. Because the colliding filaments typically have low values of Toomre-Q_m at the collision sites, these two requirements are often satisfied simultaneously. The lack of fragmentation in Model M1.0AD1.0 indicates it must be missing some ingredient(s) that enabled fragmentation in the more magnetically diffusive reference model.

4.5.3 The Role of Demagnetization in Fragmentation

By analyzing the collision sites of the DROD that formed stellar companions in Model M1.0AD2.0 and those that didn't in Model M1.0AD1.0, we find that fragmentation tends to happen when the colliding filaments in the DROD are sufficiently demagnetized, with a plasma-β greater than 10 in general. This is illustrated in Fig. 4.10, which plots the distributions of the density and plasma-β on the "midplane" (defined in sec. 4.5) for Models M1.0AD2.0 and M1.0AD1.0 (left and middle

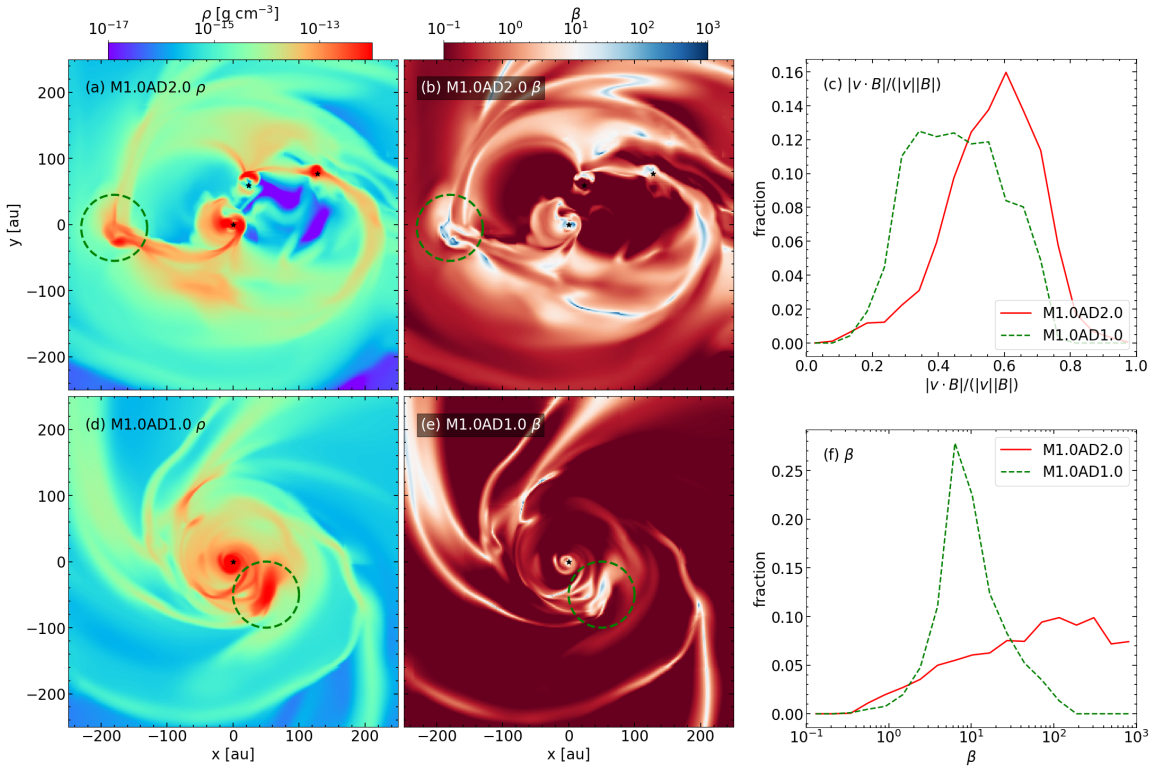


Figure 4.10: Role of plasma-β in fragmentation. Plotted are the distributions of the density and plasma-β on the "midplane" for Model M1.0AD2.0 (panels [a] and [b], respectively) and M1.0AD1.0 (panels [d] and [e], respectively). The green dashed circle in each panel marks a DROD collision site with significant cross-B field motions, as shown by the distribution of $\cos\theta_{\rm ali}$ plotted in panel (c), which is significantly below unity. Panels (b) and (e) show that the collision site in Model M1.0AD2.0 (where fragmentation occurs) is more demagnetized (with a higher plasma-β) than that in Model M1.0AD1.0, which is further quantified in panel (f), where the distribution of the plasma-β is plotted.

panels). The green dashed circle in each panel marks a filament collision site with significant cross-B field motions, as shown by the distribution of $\cos\theta_{\rm ali}$ in panel (c). A comparison of panels (b) and (e) shows that the collision site in Model M1.0AD2.0 (where fragmentation occurs) is more demagnetized (with a higher plasma-β) than that in Model M1.0AD1.0 (where fragmentation does not occur). This difference is quantified in panel (f), where the distribution of the plasma-β of the collision site is plotted. Clearly, the collision site of the non-fragmenting M1.0AD1.0 model remains magnetically dominated, with the plasma-β mostly below 10. In contrast, the collision site of the fragmenting M1.0AD2.0 model is thermally dominated, with the plasma-β mostly above 10.

In summary, we find the stellar companions tend to form in highly dynamic dense rotation-dominated structures (DRODs) that have a relatively low magnetic Toomre parameter ($Q_m < 1$), substantial cross-B field motions generated by collisions (corresponding to a relatively low value of the cosine of the alignment angle $\theta_{\rm ali}$), and are locally thermally dominated (with a plasma-$\beta \gtrsim 10$). These tendencies stress the importance of the non-ideal MHD effects in the formation of multiple stellar systems in molecular cloud cores with dynamically significant magnetic fields.

4.6 Discussion

4.6.1 Close Misaligned Companion Formation Through DROD Fragmentation

As mentioned in § 4.1, disk fragmentation is a widely discussed channel for forming close binary/multiple systems (e.g. Offner et al., 2023). It is thought to happen, in particular, during the deeply embedded phase of star formation, when the mass accretion from the protostellar envelope onto the disk exceeds the mass accretion

rate through the disk onto the central protostar (e.g. Kratter et al., 2010), with the resultant mass accumulation driving the disk fragmentation and stellar companion formation. Two generic expectations for this scenario are: (1) spiral arms develop in the gravitationally unstable disk and dominate the disk angular momentum transport, and (2) the circumstellar disk of the companion, if any, should be aligned with that of the primary. In this subsection, we demonstrate that these expectations are not met in our simulations, pointing to a close binary/multiple formation mechanism related to, but distinct from, the traditional disk fragmentation.

Magnetically Dominated Angular Momentum Transport in DRODs

In our simulations, prominent spiraling filaments are present in both the large-scale gravo-magneto-sheetlets and the small-scale DRODs (see, e.g., Fig. 4.4 and the lower-left panel of Fig. 4.7). The larger-scale spirals in the collapsing sheetlets are produced by the inhomogeneities induced by the initial turbulence unrelated to gravitational instability. The smaller-scale dense spiraling filaments in the DRODs are often spatially connected to the larger-scale spirals in the sheetlets and are thus likely resulting from non-uniform feeding by the sheetlets rather than the need to transport angular momentum from large to small distances. Indeed, the gravitational torque due to the spiraling filaments is substantially smaller than the magnetic torque on the scale of the DROD in the reference model, as illustrated by the red lines in Fig. 4.11, where the accumulative torques up to a given radius from the primary are plotted as a function of radius. The accumulative torque is computed by summing the total gravitational or magnetic torque on the gas within 50 au above or below the midplane (defined in sec. 4.5.1), i.e.

$$T_R(R) = \int_0^{2\pi} \int_{-z}^{z} \int_0^{R} f_\phi \; R dV, \tag{4.14}$$

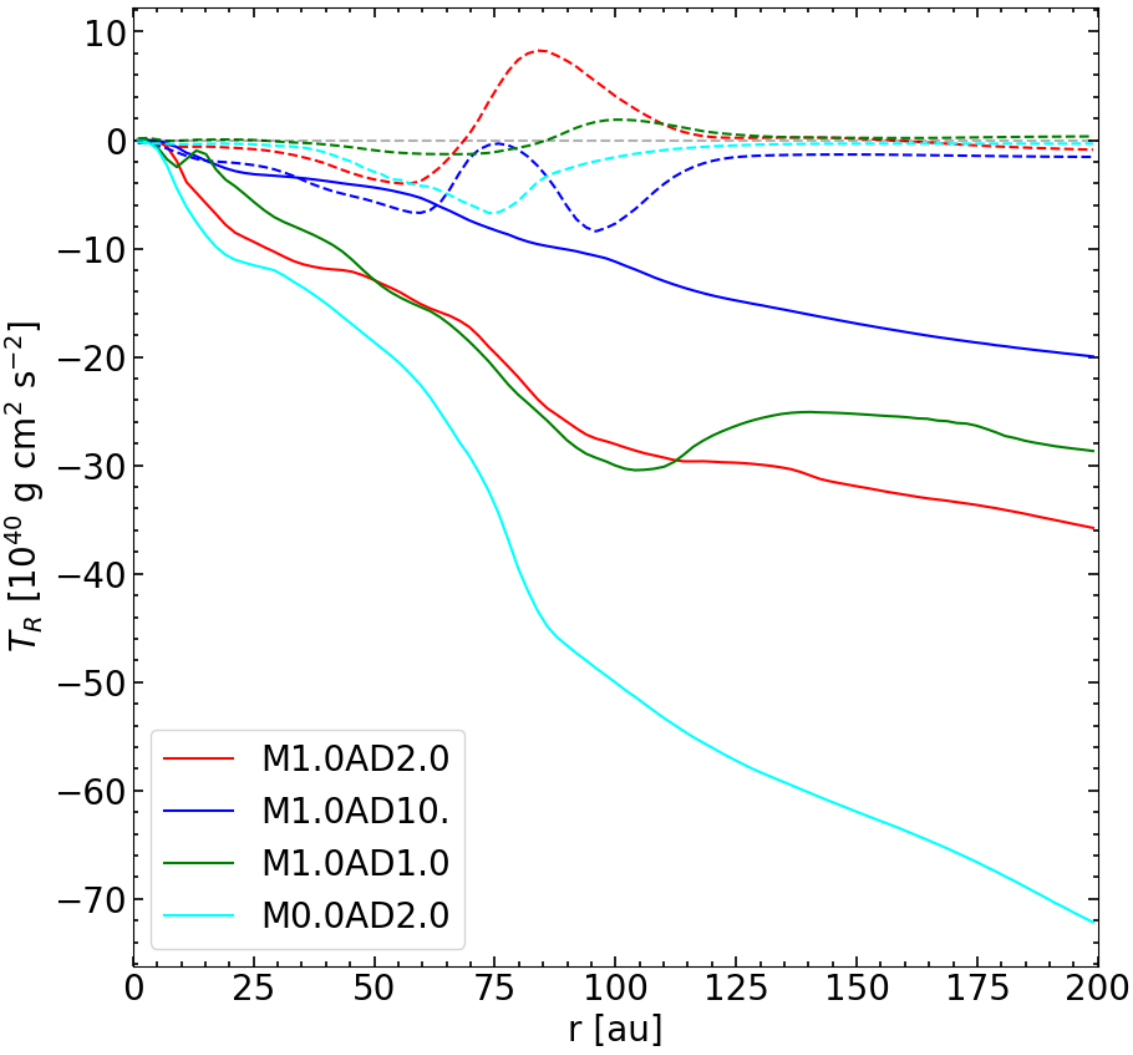


Figure 4.11: Cumulative angular momentum transport rates by gravitational (dashed lines) and magnetic torques (solid) for different models. The magnetic torque dominates angular momentum transport in the M1.0AD2.0, M1.0AD1.0, and M1.0AD2.0 models. In the M1.0AD10 model, gravity and magnetic fields transport angular momentum at comparable rates within the innermost 100 au.

where f_ϕ is the force in the ϕ direction in the cylindrical coordinate with z-axis perpendicular to the midplane and center on the primary; R is the cylindrical radius from the primary. For the models with more than one star formed, the time plotted is chosen to be within 100 years before the secondary formation. Given the overwhelming domination of the gravitational torque by the magnetic torque in the reference model (M1.0AD2.0), it is reasonable to surmise that the spiraling filaments develop in the DROD of this model *not* to transport angular momentum as in the traditional disk fragmentation picture, but as an inheritance from the larger-scale sheetlets that already contain prominent spirals. This difference may have contributed, at least in part, to the frequent collisions of the dense spiraling filaments in the reference model, which are key to stellar companion formation.

In the non-turbulent model M0.0AD2.0 and less magnetically diffusive model M1.0AD1.0, the magnetic torque also dominates over the gravitational torque, similar to the reference model. However, in the more magnetically diffusive model M1.0AD10, the gravitational torque can be comparable to the magnetic torque within the innermost 100 au. Because of the high diffusivity in the M1.0AD10 model, the magnetic field is expected to be weaker than in the other models, so gravity is expected to be more important. It is, therefore, unsurprising that the secondary formation in the M1.0AD10 model is closer to the traditional view of disk fragmentation in the absence of magnetic fields. Without less magnetic pressure hindering the collapse of self-gravitating gas (see sec. 4.5), the secondary formed earlier in this case than in other models (fig. 4.1).

Circumstellar Disk Misalignment

Even more intriguing is the misalignment between the stellar systems, which is not expected in the simplest version of the traditional disk fragmentation scenario. We

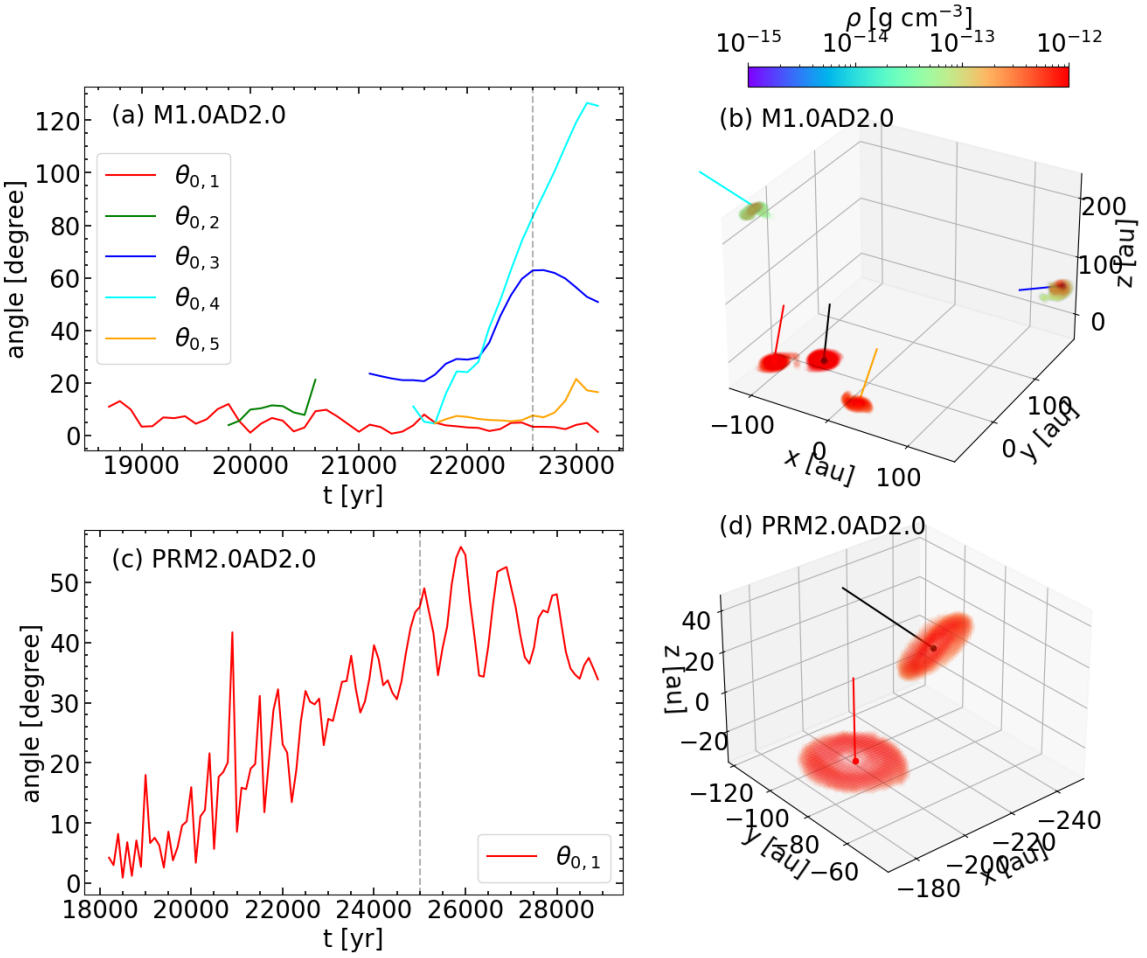


Figure 4.12: Circumstellar disk misalignment in Models M1.0AD2.0 (upper panels) and PRM2.0AD2.0 (lower panels). The left panels ([a] and [c]) plot the evolution of the angles between the circumstellar disk axes of stellar companions and that of the primary, showing disk misalignment, particularly at late times. The right panels ([b] and [d]) show a visualization of the circumstellar disk misalignment at the time marked by the vertical dashed line in the corresponding left panel. An animated version of the figure can be found at `https://virginia.box.com/s/c5c0y27s4pfd3rz5a389unzyis6dpb99`.

will demonstrate the misalignment using two simulations: the reference run, where several stellar objects are formed with moderately misaligned disks, and a new simulation (Model PRM2.0AD2.0 in Table 1), where a binary system is formed with a more pronounced disk misalignment.

We will use the angular momentum axis of the circumstellar material within 25 AU of each stellar object as a proxy for the circumstellar disk axis because the disks are relatively small and may not be adequately resolved. The results are shown in Fig. 4.12, which plots the evolution of the angles between the circumstellar disk axes of the stellar companions and that of the primary for the reference model (M1.0AD2.0, panel [a]) and Model PRM2.0AD2.0 (panel [c]). Both cases show considerable disk misalignment, particularly at relatively late times, as illustrated in the right panels ([b] and [d]), which show a visualization of the circumstellar disk misalignment at the time marked by the vertical dashed line in the corresponding left panel.

Note that the misalignment angle takes a value between 0 and 180 degrees because disks can rotate in opposite directions. In the reference model, the disk axis of the first companion (particle 1) remains aligned rather closely with that of the primary. It is not true for other companions, especially the third and fourth companions. The disk axis of the third companion starts with a 25-degree misalignment from that of the primary disk and increases to as large as 60 degrees. The disk misalignment angle of the fourth companion starts around 15 degrees but quickly increases above 90 degrees, reaching $\sim$ 120 degrees towards the end of the simulation. The counter-rotation is an extreme example of the deviation from the traditional disk fragmentation scenario for companion formation. The reason for the disk misalignment is that the stellar companions in our core-collapse simulations with magnetic fields and turbulence are formed in highly structured DRODs that are much more dynamically active than the circum-primary disk envisioned in the traditional disk fragmentation scenario. The

DRODs are fed from different directions by the larger-scale warped gravo-magneto-sheetlets with directions of angular momentum different from that of the primary disk. It is more so at a later time when the feeding sheetlet material originates from a larger initial distance, where it is expected to be more strongly perturbed by turbulence.

To illustrate the above picture more clearly, we consider a more perturbed version of the reference run with a stronger initial turbulence of rms Mach number of 2 and an initial magnetic field (along x-direction) perpendicular to the rotation axis (along z-direction; Model PRM2.0AD2.0 in Table 4.1). Only a single companion is formed in this simulation, with a disk axis that starts close to that of the primary but becomes increasingly more misaligned later, reaching $\sim 40^\circ$ at the end of the simulation (see the lower panels of Fig. 4.12). The periodic variation in the inclination angle reflects the orbiting of the secondary around the primary. This example reinforced the notion that the collapse of turbulent magnetized cloud cores can naturally lead to close misaligned stellar systems. Our findings agree with the SupAS model of Mignon-Risse et al. (2021), which also produced misaligned close multiple systems (not shown in the paper, private communication).

A Variant of the Disk Fragmentation Mechanism

The circumstellar disk misalignment and magnetic domination of the angular momentum transport motivate us to propose a variant to the traditional disk fragmentation – DROD fragmentation. The key components of this new variant are illustrated in Fig. 4.13, which shows that the DROD (orange-colored, defined in sec. 4.4.2) is fed magnetized material by larger-scale warped gravo-magneto-sheetlets (blue-colored, defined in sec. 4.4.1) from different directions. The resulting DROD contains dense spiraling filaments that do not generate enough gravitational torque to dominate the angular momentum transport. The filaments collide with one another to create

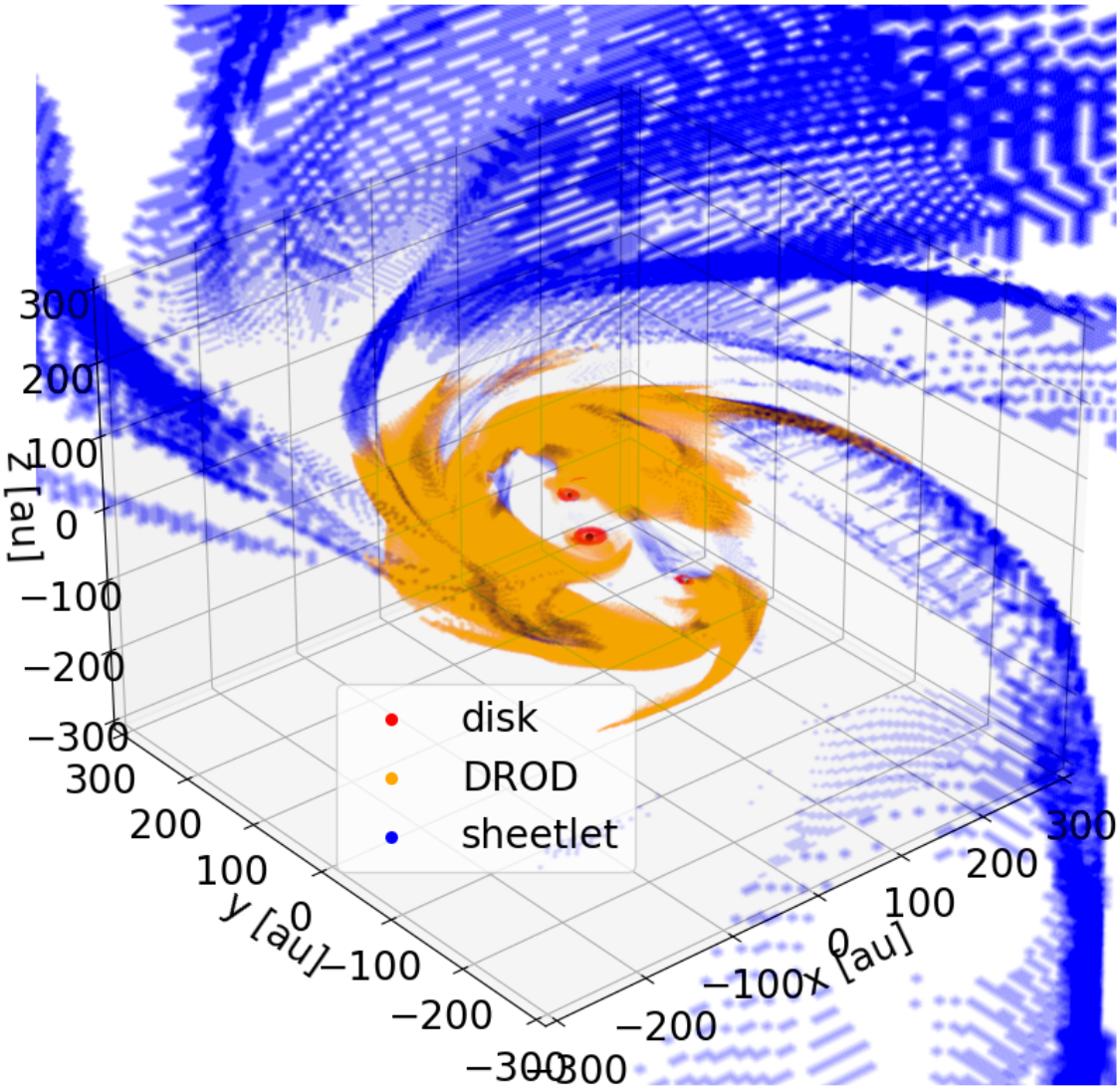


Figure 4.13: Key components of the DROD fragmentation mechanism for binary/multiple formation. The circumstellar disk around each star is shown in red. The irregular, orange-colored structure is the DROD, which is fed by larger-scale sheetlets (shown in blue). An animated version of this figure can be found at `https://virginia.box.com/s/0t02kcktstho6xmc1rxpye8jz2y5kvag`

conditions conducive to fragmentation and stellar companion formation. This more dynamic variant allows for the *in-situ* formation of misaligned systems on the 100-au scale.

4.6.2 Connection to Observations

The DRODs and associated features discussed in the preceding sections can be used to interpret observations of binary/multiple protostellar systems. For illustration purposes, we will focus on three representative systems: L1448 IRS3B, NGC 1333 IRAS2A, and VLA1623.

L1448 IRS3B is a Class 0 triple system considered to be the prototype of multiple systems formed through disk fragmentation (Tobin et al., 2016a). Two stellar objects have already formed, and a third object appears to be caught in formation in the circumbinary disk of the binary. A key piece of evidence for disk fragmentation was that the Toomre Q parameter was estimated to be close to unity near the tertiary (Reynolds et al., 2021). However, a low Toomre-Q value is not definitive proof that the stellar companion formed through the traditional disk fragmentation, where spiral arms necessitated by the need to redistribute disk angular momentum become self-gravitating and collapse gravitationally. Our reference simulation (Model M1.0AD2.0) passes through a phase that resembles the observed system, with two stars already formed and a third on its way, as shown in Fig. 4.14. In our case, the third stellar object (the second stellar companion) was formed through collisions between different streams of dense material with Toomre Q below unity (see, e.g., Fig. 4.7e) that are fed by, and spatially connected to, the larger scale collapsing gravo-magneto-sheetlets.

NGC 1333 IRAS2A is a sub-arcsecond Class 0 protobinary system (separated by ~ 143 au) studied in detail by Tobin et al. (2015, 2016b) as part of the VLA/ALMA Nascent Disk and Multiplicity (VANDAM) survey. A salient feature of this sys-

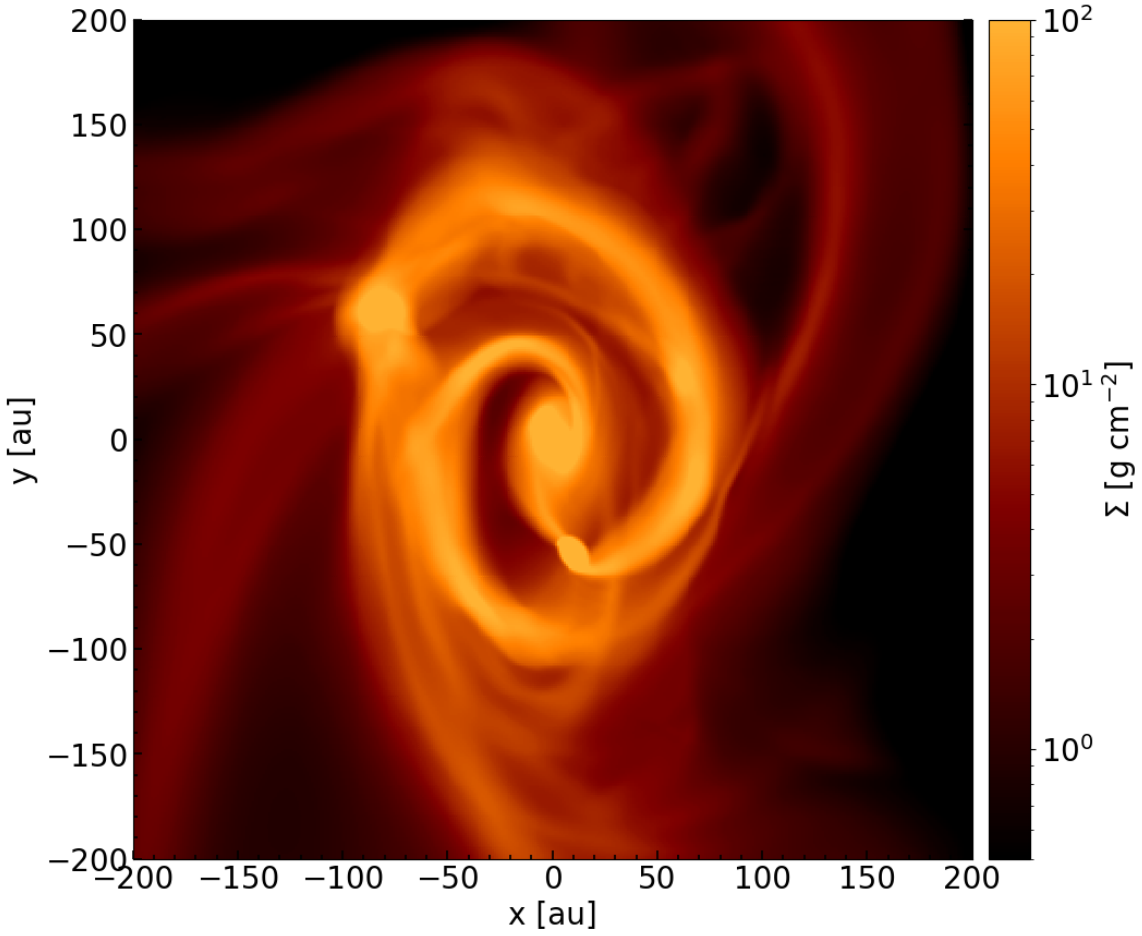


Figure 4.14: A simulated triple system analogous to L1448 IRS3B, but formed through collisions of dense rotationally dominated structures (DRODs). The figure is the column density in the M1.0AD2.0 model.

tem is that the two protostars drive two nearly orthogonal CO outflows (see their Fig. 6). The large misalignment led to the suggestion that the two stellar components were formed independently at a much larger initial distance through turbulent fragmentation and subsequently moved closer together, as found in some turbulent fragmentation simulations (e.g., Offner et al., 2010). However, we have demonstrated that highly misaligned systems on the 100-au scale can be formed *in situ* (i.e., without the need for orbital tightening by a large factor) from dense rotationally dominated structures that are much more disorganized and dynamically active than the traditional disks (see, e.g., Fig. 4.12d). The larger-scale warped sheetlets deliver materials with different angular momentum directions to the stellar companions, which is key to producing and maintaining the misalignment.

An even more extreme case of misalignment is VLA1623, the first Class 0 object observed and a prototype of the class (Andre et al., 1993). It is a deeply embedded quadruple system consisting of a close binary pair (VLA1623A1 and VLA1623A2), a relatively close companion with $\sim$ 100 au separation (VLA1623B) and another companion much farther away (VLA1623W). The disk of component "B" is highly inclined with respect to the circumbinary disk around components "A1" and "A2," and rotates in a direction opposite to that of the circumbinary disk (see Ohashi et al., 2022, their Fig. 21). It is unlikely to have formed through traditional disk fragmentation. A clue for its origin may come from the spatially and kinematically distinct accretion streams identified by Hsieh et al. (2020, see their Fig. 19; see also Codella et al., 2024), which may have formed and maintained the highly misaligned system. It is plausible that the accretion streams correspond to the collapsing sheetlets in our picture, although magnetic field information and more detailed analysis are needed to firm up the identification[3] In any case, this protostellar multiple system presents

[3]We note that dense filaments are produced in many star and disk formation simulations including

a challenge to the traditional disk fragmentation scenario but could be produced through the more dynamic scenario of DROD fragmentation proposed here, which can produce counter-rotating circumstellar structures (see the cyan line in Fig. 4.12a, which shows that the misalignment angle for the fourth stellar companion goes beyond 90° at late times).

4.7 Conclusions

We have carried out a set of non-ideal MHD simulations of binary/multiple formation from the gravitational collapse of magnetized, turbulent, low-mass molecular cloud cores. Our main conclusions are as follows.

1. As in the case of single star formation in turbulent, magnetized cores, the inner protostellar envelope is dominated by dense gravo-magneto-sheetlets, which are a turbulence-warped version of the classic pseudodisk resulting from the anisotropic magnetic resistance to the gravitational collapse. These sheetlets feed mass, magnetic fields, and angular momentum to a dense rotation-dominated structure – a DROD – where fragmentation leads to binary/multiple star formation. We define a DROD to be the structure where density is larger than 3×10^{-15} g cm^{-3} and rotating at $> 0.9 \times$ local keplerian speed (computed using the enclosed mass).

2. The DROD is a more dynamic version of the traditional disk with dense spiraling filaments created by inhomogeneous feeding from the highly structured larger-scale sheetlets rather than the need for angular momentum transport, which is dominated by magnetic braking. Collisions between the dense rotation-

magnetic fields and turbulence (see, e.g., Kuffmeier et al., 2019). As discussed by Tu et al. (2024a, see their introduction and sec. 7.1, and references therein), many, if not all, of them are likely produced by the interplay between magnetic fields, turbulence, and gravity, as is the case for our sheetlets, although detailed analysis of their magnetic fields and dynamics is needed to be sure.

dominated filaments play a key role in pushing the local magnetic Toomre parameter $Q_{\rm m}$ below unity at the collision sites, leading to gravitational collapse and stellar companion formation provided that the local material is sufficiently demagnetized, with a plasma-β of 10 or more. This DROD fragmentation scenario for binary/multiple star formation is a more dynamic variant of the traditional disk fragmentation in a turbulent, magnetized cloud core. It can naturally produce *in situ* misaligned systems on the 100-au scale, often detected with high-resolution ALMA observations.

3. Our simulations highlight the importance of non-ideal MHD effects in binary/multiple star formation. For our modeled cloud cores, the fragmentation is completely suppressed when the magnetic diffusivity is relatively low (e.g., Model M1.0AD1.0). Fragmentation occurs when the magnetic diffusivity is large enough, with the stellar masses and orbital parameters strongly affected by the diffusivity level (compare, e.g., Model M1.0AD2.0 and M1.0AD10). The magnetic diffusivity depends on the cosmic ray ionization rate and grain size distribution, which are uncertain. The uncertainties make it challenging to develop a complete theory for binary/multiple star formation in magnetized clouds.

4.8 Acknowledgements

We thank the referee, Dr. Raphaël Mignon-Risse, for a detailed and constructive report. This work is supported by NASA 80NSSC18K1095, NASA 80NSSC20K0533, NSF AST-1910106, and NSF AST-2307199. Computing resources were provided by the NASA High-End Computing (HEC) Program through the NASA Advanced Supercomputing (NAS) Division at Ames Research Center and the RIVANNA supercomputer at the University of Virginia. YT acknowledges support from an interdis-

ciplinary fellowship from the University of Virginia.

Chapter 5

YSO Jets Magnetocentrifugally Driven by Reconnecting Atmospheric Avalanche Accretion Streams Above Inner Circumstellar Disks

The work presented in this chapter has been published in the Astrophysical Journal (ApJ) with Zhi-Yun Li, Zhaohuan Zhu, Xiao Hu, and Chun-Yen Hsu as coauthors (Tu et al., 2025b).

Abstract: Fast, collimated jets are ubiquitous features of young stellar objects (YSOs). They are generally thought to be powered by disk accretion, but the details are debated. Through 2D (axisymmetric) MHD simulations, we find that a fast (> 100 km/s) collimated bipolar jet is continuously driven along the north and south poles of the circumstellar disk that is initially magnetized by a large-scale open poloidal field and contains a thermally ionized inner magnetically active zone surrounded by a dead zone. The fast jet is primarily driven magneto-centrifugally by the release of the gravitational binding energy of the so-called "avalanche accretion streams" near the boundary of an evacuated poloidal field-dominated polar region and a thick disk atmosphere raised by a toroidal magnetic field. Specifically, the fast outflow is driven along the upper (open) branch of the highly pinched poloidal field lines threading the (strongly magnetically braked) accretion streams where the density is relatively low so that the lightly loaded material can be accelerated magneto-centrifugally along the open field line to a high speed. The highly pinched poloidal magnetic fields threading the avalanche accretion streams tend to reconnect, enabling mass to accrete to the center without dragging along the poloidal magnetic flux with it. The reconnection provides a potential heating source for producing chondrules and calcium- and aluminum-rich inclusions (CAIs).

5.1 INTRODUCTION

Jets are observed in many astrophysical systems, from young stellar objects (YSOs) to Active Galactic Nuclei (AGNs). The mechanisms that drive these observed jets and whether all jets share the same mechanism are areas of active debate. AGNs can rely on the spinning black hole itself to power the jet electromagnetically (Blandford & Znajek, 1977). YSOs do not have such a luxury and must instead rely on the release of the gravitational binding energy of the circumstellar disk accretion for jet

launching, typically through magnetic fields threading the disk.

Depending on where the jet-launching magnetic fields are rooted on the disk, there are two broad classes of models: the X-wind (Shu et al., 2000; Shang et al., 2007) and disk-wind (Konigl & Pudritz, 2000; Pudritz et al., 2007) models. The former envisions the wind-launching open field lines concentrating near the corotation radius where the stellar magnetosphere truncates the circumstellar disk (see, e.g. Ostriker & Shu, 1995; Zanni & Ferreira, 2009, 2013), potentially carrying away the angular momentum associated with the mass accretion along (deformed) magnetospheric field lines (the so-called "funnel flow") onto the central star, preventing excessive stellar spin-up. The latter class of models posits that the wind-launching field lines are anchored over a range of disk radii. It has the potential to remove angular momentum and drive disk accretion over a wide range of radii.

Our work focuses on the magnetically driven disk-wind model in the YSO context, which has a long and rich history, as reviewed by, e.g., Pudritz et al. (2007, and reference therein) and more recently Ray & Ferreira (2021). A key issue of the magnetic disk-wind theory is the origin and distribution of the wind-launching large-scale poloidal magnetic field on the disk. Since the YSO disks are formed out of dense cores of molecular clouds that are now known to be magnetized by ordered fields (Pattle et al., 2023b), it is reasonable to expect some of the core magnetic flux to be dragged into the disk during its formation stage by the protostellar envelope collapse (e.g. Tu et al., 2024a; Mauxion et al., 2024); there is, therefore, no shortage of poloidal magnetic flux that can in principle thread the disk and drive the disk wind.

What fraction of the core's magnetic flux is inherited by the disk and the subsequent flux evolution on the disk are important (e.g. Yang & Bai, 2021) but open questions. In particular, the wind-driven radial mass accretion has the tendency to drag the wind-launching poloidal magnetic flux inward and concentrate it near the

inner edge of the disk, potentially disrupting the disk, which may, in turn, shut off the wind launching. This magnetic flux problem for jet/disk-wind launching in a disk threaded by a net poloidal flux is analogous to the classic “magnetic flux problem" in star formation (Mestel & Spitzer, 1956).

How the magnetic flux problem in jet/disk-wind launching is resolved remains uncertain. In the lightly ionized outer disk, ambipolar diffusion can allow disk material to accrete across the wind-launching poloidal field lines without dragging them along, as demonstrated semi-analytically (e.g. Wardle & Koenigl, 1993; Li, 1996) and through numerical simulations (e.g. Suriano et al., 2018; Martel & Lesur, 2022). The situation is less clear in the inner disk, where the temperature is high enough that the gas is well coupled to the magnetic field through the thermal ionization of alkali metals and where the fast jet is expected to be launched.

Previous semi-analytic work and numerical simulations of magnetic disk winds from the magnetically well-coupled inner disks have typically assumed a prescribed resistivity, presumably of turbulent origin (e.g. Ferreira & Pelletier, 1993; Li, 1995; Ferreira, 1997; Casse & Keppens, 2002; Tzeferacos et al., 2009; Murphy et al., 2010; Stepanovs & Fendt, 2016), which facilitates radial disk accretion across poloidal field lines, thus alleviating the magnetic flux problem. In particular, Stepanovs & Fendt (2016) demonstrated that resistive disks can drive fast steady magneto-centrifugal outflows over a wide range of disk magnetization. Whether such disks can drive fast jets persistently without a prescribed resistivity remains less explored. It is the main goal of our paper.

There have been several recent simulations of magnetically well-coupled inner disks without an explicitly prescribed resistivity, with a stellar magnetosphere (e.g., Lubow et al., 1994; Pantolmos et al., 2020; Ireland et al., 2021; Takasao et al., 2022; Zhu et al., 2024; Meskini et al., 2024) or without (e.g. Tzeferacos et al., 2009; Fendt

& Sheikhnezami, 2013; Zhu & Stone, 2018; Takasao et al., 2018; Mattia & Fendt, 2020a,b; Jacquemin-Ide et al., 2021). These simulations show that the fast accretion of the thick magnetically dominated surface can counterbalance the field's outward diffusion. As a first step, we will ignore the stellar magnetosphere and focus on the question of whether a fast jet can be driven by the inner disk alone and, if so, what mechanism is responsible for the jet launching and the question of whether the magnetic flux problem can be resolved in the absence of any explicit resistivity. We find that a persistent fast jet is driven magneto-centrifugally along the lightly mass-loaded upper (open) branch of the highly pinched poloidal field lines threading the so-called "avalanche accretion streams" in the elevated disk atmosphere and that the magnetic flux problem is alleviated by the reconnection of the highly pinched field of jet-launching field lines threading the accretion streams.

The paper is organized as follows. The simulation setup and results are described in § 5.2 and § 5.3, respectively. We discuss the results in § 5.4 and conclude in § 5.5.

5.2 Simulation Setup

The launch of a jet from the inner circumstellar disk is a complex process involving non-ideal magneto-hydrodynamics. In particular, Ohmic dissipation is important in the relatively cool dead zone of the disk surrounding the hotter inner active zone, where the gas is close to the ideal MHD limit due to thermal ionization. The system is governed by the following set of equations:

$$\frac{\partial \rho}{\partial t} + \nabla \cdot (\rho \boldsymbol{v}) = 0, \tag{5.1}$$

$$\rho \frac{\partial \boldsymbol{v}}{\partial t} + \rho(\boldsymbol{v} \cdot \nabla)\boldsymbol{v} = -\nabla P + \frac{1}{c}\boldsymbol{J} \times \boldsymbol{B} + \rho \boldsymbol{g}, \tag{5.2}$$

$$\frac{\partial \boldsymbol{B}}{\partial t} = \nabla \times (\boldsymbol{v} \times \boldsymbol{B}) - \frac{4\pi}{c} \nabla \times [\eta_O (\boldsymbol{J} \times \hat{\boldsymbol{B}})], \tag{5.3}$$

where $\boldsymbol{J} = (c/4\pi)\nabla \times \boldsymbol{B}$ is the current density, η_O the Ohmic diffusivity, and $\boldsymbol{g}$ is the gravitational acceleration from the central star, which we assume to have one solar mass. Other symbols have their usual meanings.

The governing equations are solved using the ATHENA++ code (Stone et al., 2020) with static mesh refinement (SMR) in spherical polar coordinates. The simulation domain extends from 0.03 au to 10 au in the radial direction and 0.02 rad to $\pi - 0.02$ rad in the polar direction. The domain is chosen to cover both the magnetically active and dead zones on the disk and the atmosphere and outflow outside the disk. The base resolution has 160 logarithmically spaced cells in the radial direction and 192 uniformly spaced cells in the polar angle direction. To increase the resolution of the jet-launching inner region, one level of static mesh refinement (SMR) is added from the inner boundary to 5 au in the radial direction and from the north polar axis to the south polar axis in the polar direction within the 5 au radius.

For illustration purposes, we adopt a power-law distribution for the initial midplane density:

$$\rho_{\rm mid}(r) = \rho_0 \Big(\frac{r}{r_0} \Big)^p, \tag{5.4}$$

The vertical density distribution within a dimensionless height of $|z/r| = 0.1$ (where z is the vertical height from the disk midplane) has a profile set by hydrostatic equilibrium. We continue the same profile to larger heights (where $|z/r| > 0.1$). To help with numerical stability, particularly at small radii and in the polar regions where

the magnetic field tends to be strong, we adopt a radially varying density floor:

$$\rho_{\rm floor}(r) = \begin{cases} \rho_f; & r \leq r_f, \\ \rho_f (r/r_f)^{-2}; & r > r_f, , \end{cases} \tag{5.5}$$

where $\rho_f = 5.94 \times 10^{-18}$ g cm^{-3} and $r_f = 0.1$ au. We choose $\rho_0 = 10^{-9}$ g cm^{-3}, $r_0 = 6.3 \times 10^{-2}$ au, and $p = -1.35$, which yields a total mass in the 10 au simulation domain of 10^{-3} $M_\odot$.

Following Flock et al. (2016), we set the temperature in the disk (where $|z/r| < 0.1$) as

$$T_{\rm d}(r) = \frac{T_\odot}{\epsilon_T^{0.25}} \left(\frac{R_\odot}{2r} \right)^{1/2} \tag{5.6}$$

where $T_\odot = 5666$K and $R_\odot = 6.943 \times 10^{10}$cm are the surface temperature and radius of the Sun, respectively, and $\epsilon_T = 1/3$. Above the disk surface, we assume a temperature transition region up to an angular height $|z/r| = 0.3$. The temperature above the transition region (where $|z/r| > 0.3$) is assumed to be uniform $T_{\rm env} = 3,000$ K. The temperature in the transition region is given by

$$T_{\rm trans}(r) = (T_{\rm env} - T_{\rm d}) \frac{|z/r| - 0.1}{0.2} + T_{\rm d}; \quad 0.1 \leq \left| \frac{z}{r} \right| \leq 0.3 \tag{5.7}$$

to allow a smooth transition between disk temperature and envelope temperature. To better simulate the active zone and account for accretion heating, we artificially increase the temperature within a radius of 0.1 au and between 0.1 and 0.2 au by, respectively,

$$T_{\rm raised}(r)_{r<0.1{\rm au}} = 2\ T(r) \tag{5.8}$$

and

$$T_{\rm raised}(r)_{0.1{\rm au}\le r<0.2{\rm au}} = \Big(3 - \frac{r}{0.1{\rm au}}\Big)T(r) \tag{5.9}$$

This temperature profile gives an active zone spanning from the inner boundary at $r = 0.03$ au to about 0.13 au. We assume the spatial temperature profile remains unchanged throughout the simulation to simplify the calculation and increase numerical stability.

The initial magnetic field is calculated by taking the curl of a vector potential to ensure a divergence-free magnetic field. Following Wang et al. (2019), the vector potential is given by $\boldsymbol{A} = \langle 0, 0, A_\phi \rangle$, where

$$A_\phi = \frac{4}{3}\frac{B_{z,0}(r/r_0)^{-0.25}}{[1 + 1/(\mu \tan\theta)^2]^{0.625}}; \tag{5.10}$$

$\mu = 0.5$ determines how curved the initial field is. We set the scale for the magnetic field strength $B_{z,0} = 9\times10^{-3}$ G so the plasma-β at 1 au is about 10^5. We note that this vector potential yields a purely poloidal field that initially threads the disk and opens to infinity. It is used to parameterize the intrinsic disk field (inherited, e.g., from the magnetized star-forming molecular cloud cores, Tu et al., 2024a), rather than that from the stellar magnetosphere since our goal is to study the limiting case of purely disk-driven outflow in the absence of a stellar magnetosphere. The initial disk field is about 1 G at the inner edge of the disk at a radius of 0.03 au, which is weaker than the typical stellar magnetospheric field expected at a similar radius. Nevertheless, it is quickly amplified by differential rotation, leading to a much stronger toroidal field at later times (Sec. 5.3.1). A stronger initial poloidal field may launch a faster outflow, everything else being equal.

In the radial direction, the hydro boundary conditions for both the inner and the

outer boundary is the "no inflow" boundary: if the gas flows out of the simulation domain, the gas velocity at the boundary is copied into the ghost zone; if the gas flows into the simulation domain, the gas velocity is set to 0 in the ghost zones. The magnetic boundary conditions at both radial boundaries are the "standard" zero-gradient boundary conditions, where the value at the first active cell is copied into the ghost zones. This is a conservative boundary condition to ensure that only the outflow driven by the processes inside the computation domain is captured in the simulation; the outflow could be stronger than what we simulate here if the poloidal field lines passing through the inner radial boundary are attached to rapidly rotating material inside the boundary and constantly twisted by it. Reflective boundary conditions are used in the polar direction.

5.2.1 Magnetic diffusivity

Ohmic dissipation is included in our model since it is important in the relatively cool midplane region of the disk (roughly beyond 0.13 au in our model) where the gas is insufficiently ionized thermally or by (attenuated) cosmic rays (e.g. Gammie, 1996). The Ohmic diffusivity is calculated by combining the contributions of two ionization sources: thermal ionization and cosmic ray ionization. It is given by

$$\eta_O = \frac{c^2}{4\pi\sigma_O}, \tag{5.11}$$

where c is the speed of light and the conductivity σ_O is dominated by electrons

$$\sigma_O \approx \frac{n_e e^2}{m_e \gamma_s \rho} \tag{5.12}$$

where n_e and m_e are the electron number density and mass, and γ_s is the momentum transfer rate between electrons and neutrals.

In the innermost part of the disk, where the temperature exceeds $\sim 10^3$ K, thermal ionization dominates. We compute the electron number density n_e from the Saha equation, including four elements with relatively low ionization potential e_I (see Table 5.1). In the cooler region at larger radii, the ionization fraction drops rapidly, leading to a dead zone with a very large Ohmic diffusivity. To prevent the time scale for the magnetic diffusion from becoming prohibitively small, we include cosmic ray ionization using the simple prescription of Shu (1991):

$$n_e = n_i = \frac{C\sqrt{\rho}}{m_i}, \tag{5.13}$$

where n_i is the number density of the dominant molecular ion and $m_i \approx 29\ m_H$. ρ is the local gas density. We choose $C = 9.5 \times 10^{-18}$ cm$^{-3/2}$ g$^{1/2}$, corresponding to a cosmic ray ionization rate 10^3 times lower than the canonical value of 10^{-17} s^{-1} to account for the cosmic ray attenuation expected in the dead zone; it is also comparable to the ionization rate expected from radioactive nuclides (Umebayashi & Nakano, 2009). The better magnetic coupling in the surface layer and envelope of the disk (which is more ionized by the less attenuated cosmic rays and energetic photons such as UV and X-rays) is represented by an increased temperature and its associated thermal ionization.

Following Wang et al. (2019), we include an inner buffer zone from a radius $r = 0.045$ au to the inner boundary at $r = 0.03$ au to increase numerical stability, where the magnetic diffusivity is gradually decreased from its original value (at 0.045 au) to 0 (at 0.03 au). Since the magnetic field is already well coupled to the gas due to a relatively high temperature (and associated efficient ionization of alkali metals), we do not expect the further reduction in the magnetic diffusivity to affect the results significantly. We do not include any anomalous magnetic diffusivity (due to, e.g.,

Species	m_s [m_p]	$n/n_{\rm H2}$	e_I [erg]
K	39	2.14×10^{-9}	6.95×10^{-12}
Ca	40	4.38×10^{-8}	9.76×10^{-12}
Na	23	3.47×10^{-8}	8.2×10^{-12}
Mg	24	7.96×10^{-8}	1.2×10^{-11}

Table 5.1: Atomic species included in the thermal ionization calculation using the Saha equation. m_s in the second column is the atomic mass of each element in the unit of proton mass m_p. The abundances in the third column are taken from Asplund et al. (2009), assuming 1% of the metal is in the gas phase. The last column is the ionization potential e_I.

sub-grid turbulence) in the simulation, which may affect the magnetic field evolution and gas dynamics in magnetically well-coupled regions that are MRI active, although some effective turbulent magnetic diffusion due to reconnection is captured in our simulation (see Section 5.4.1).

5.3 Simulation Results

5.3.1 Overview

To give a first impression of the disk-jet system, we show in Fig. 5.1 a representative frame of an animation of the simulation. It shows clearly that a fast (> 100 km/s) collimated bipolar jet (colored red)[1] is continuously driven along the north and south poles of the dense circumstellar disk (colored black and gray). Fig. 5.2 gives a more detailed view of the distributions of various flow quantities in the inner part of the simulation, focusing on the upper hemisphere.

The top row of Fig. 5.2 shows the density (panel a), radial direction velocity v_r (panel b), and the mass flux ρv_r (panel c) at a representative time $t = 3.0$ yr, corresponding to about 577 times the orbital period at the inner disk edge. The

[1]The minimum (threshold) speed of 100 km/s for highlighting the jet in the animation is chosen somewhat arbitrarily; it is on the low side of the observed range of YSO jet speed, especially for the atomic jets from relatively evolved Class II sources. It does not mean that all jet materials move at 100 km/s; they have a range of speed up to at least 500 km/s.

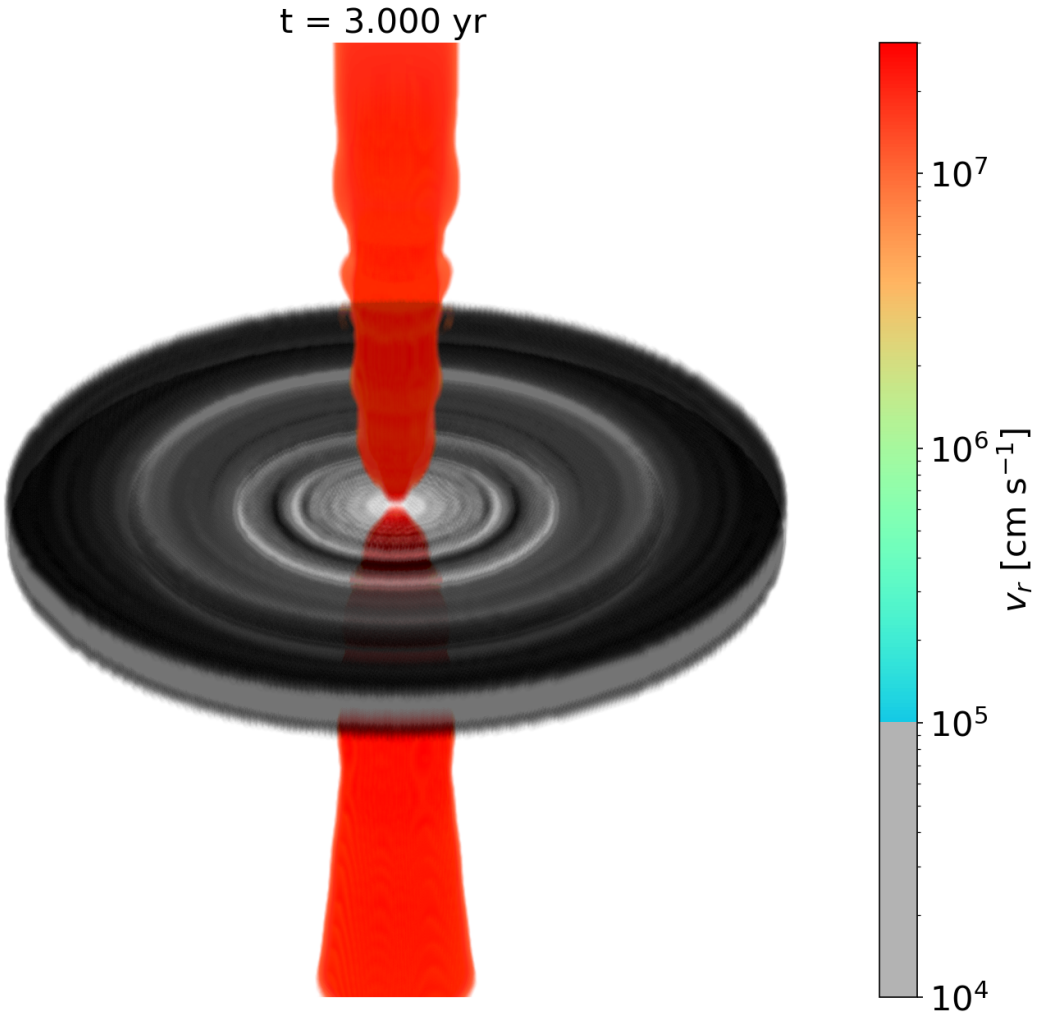


Figure 5.1: 3D rendition of the disk-jet system at a representative time $t = 3.0$ yr, showing a fast (> 100 km/s) collimated bipolar jet (colored red) driven from a highly dynamic dense equatorial disk (colored purple and blue). The jet maintains its fast speed reaching the upper and lower edges of this rendition, which are at the boundaries of the simulation domain (10 au in the $\hat{z}$ direction). The horizontal black structure is a representation of the disk up to 5 au in radius; all features in the disk representation are rendering effects. An animated version of this figure is available in the online journal. The movie is 9 seconds long, showcasing a continuous jet launched in our model.

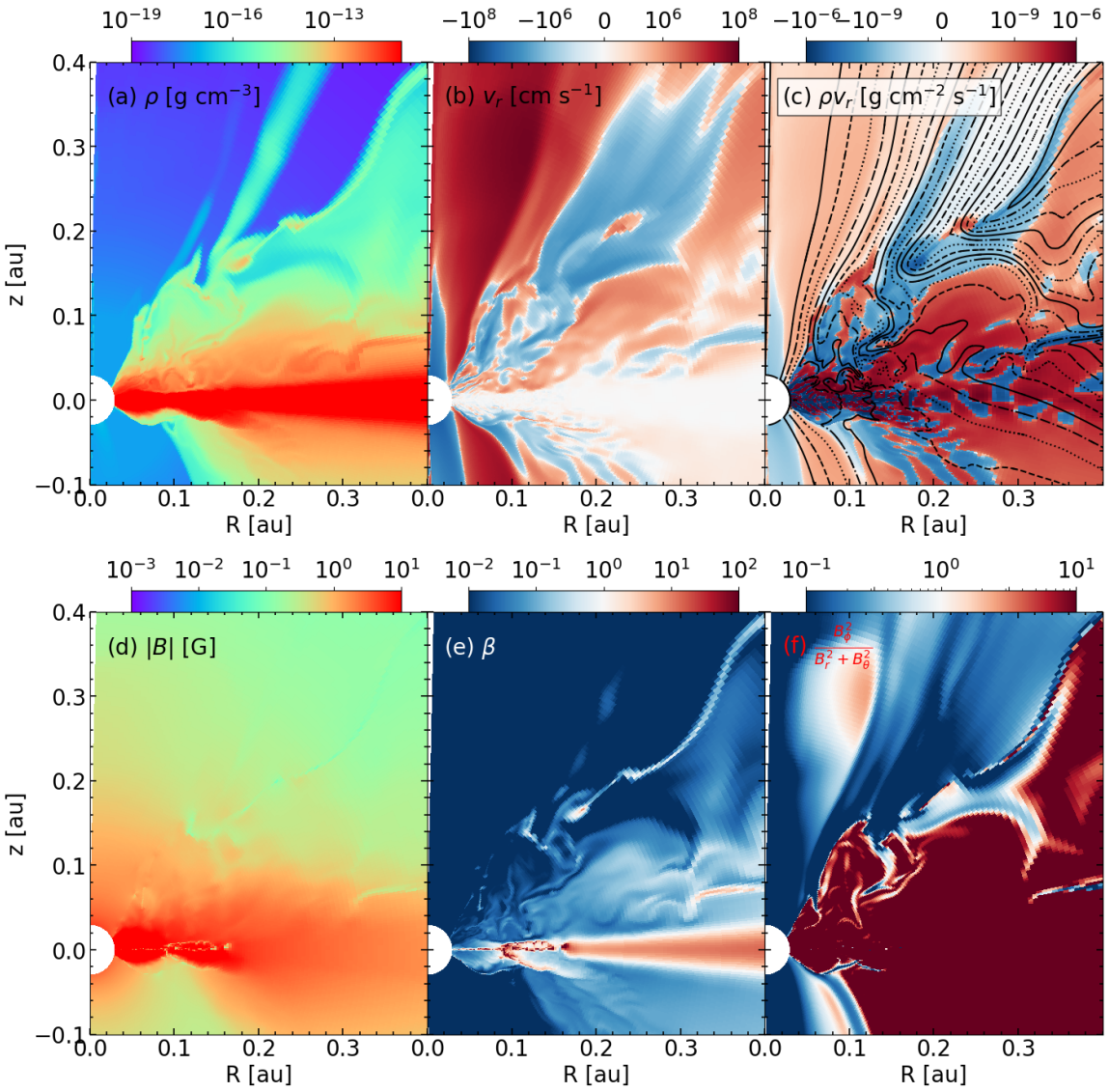


Figure 5.2: Overview of the simulation result on a meridional plane at a representative time $t = 3.0$ yr. The upper panels show (a) the density, (b) radial velocity v_r, and (c) the mass flux, respectively. The lower panels show (d) the magnetic field strength, (e) plasma-β, and (f) the ratio between the toroidal field and the poloidal field, respectively. An animated version of this figure is available in the online journal. The movie is 27 seconds long, showing an overview of the disk and outflow evolution in our model.

poloidal magnetic field lines, with an equally spaced poloidal magnetic flux between adjacent field lines, are overplotted on the mass flux panel. The disk resides near the equatorial plane where $z = 0$, highlighted by the high density and low v_r. It is surrounded by a more diffuse and faster-moving atmosphere. Close to the polar axis is an outflow (jet), where the density is lower, and flow is faster, reaching values as high as $\sim 10^8$ cm/s. The poloidal magnetic field lines are concentrated in the jet region, suggesting a close relationship between the outflow and the magnetic field.

The magnetic field of the simulation is quantified in the lower panels of Fig. 5.2, which display the magnetic field strength (panel d), plasma-β (panel e), and the ratio between toroidal magnetic pressure and poloidal magnetic pressure ($B_\phi^2/(B_\theta^2 + B_r^2)$ (panel f). The strongest magnetic field region in panel (d) is the active zone on the disk (extending to about 0.13 au in radius), where the temperature is high enough to ionize metals with low ionization potentials. The gas is close to the ideal MHD limit in this region. As a result, the magnetic field builds up through differential rotation in the active zone, reaching a strength $>$ 10G. Consequently, the plasma-β in the active zone stays mostly of order or below unity. Outside the active zone in the disk is the dead zone, where the temperature near the midplane is insufficient to ionize the metals. Ohmic dissipation is strong enough to prevent rapid amplification of the magnetic field, resulting in a plasma-β greater than 1. The gas is well ionized in the disk atmosphere so that it is close to the ideal MHD limit. Fig. 5.2f shows that the poloidal field dominates the polar region (the solid blue region close to the poles), whereas the toroidal field dominates the disk and part of the disk atmosphere (the solid red regions). Between these two extremes is a region where the toroidal and poloidal field components are more comparable. The fast jet resides in this region (Fig. 5.2b).

To facilitate the discussion of the jet launching mechanism, we conceptually divide

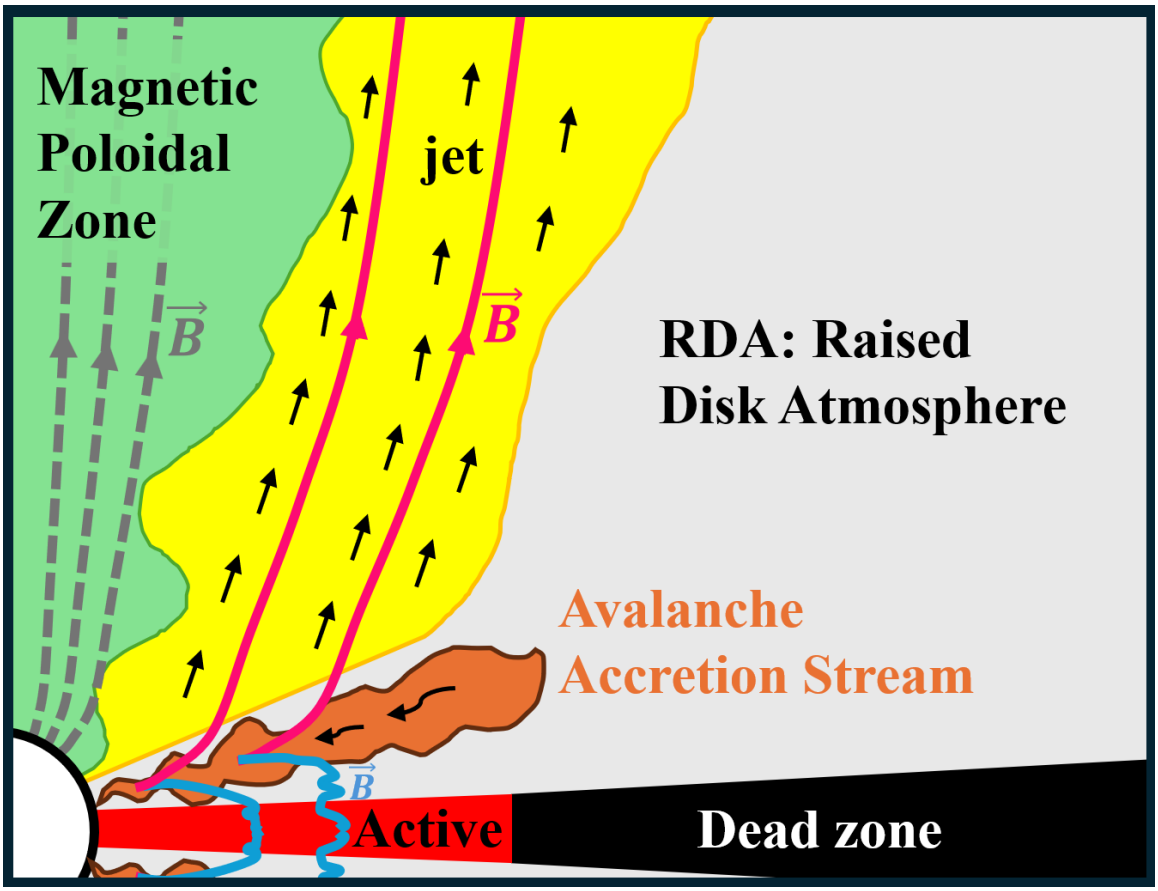


Figure 5.3: Key components of the avalanche accretion stream driven jet-launching model. The green zone is the low-density magnetic poloidal zone (with the dominant poloidal field highlighted by gray dashed lines with arrows), surrounded by the jet. The gray zone is the raised disk atmosphere (discussed in sec. 5.3.2), and the orange stream is the avalanche accretion stream (discussed in sec. 5.3.3). The disk is divided into the active (red) and the dead zone (black). The cyan and magenta line segments highlight the magnetic field geometry, with a sharp pinch on the avalanche accretion stream (discussed in sec. 5.3.4). The black arrows highlight the gas motion in the avalanche accretion stream and the jet.

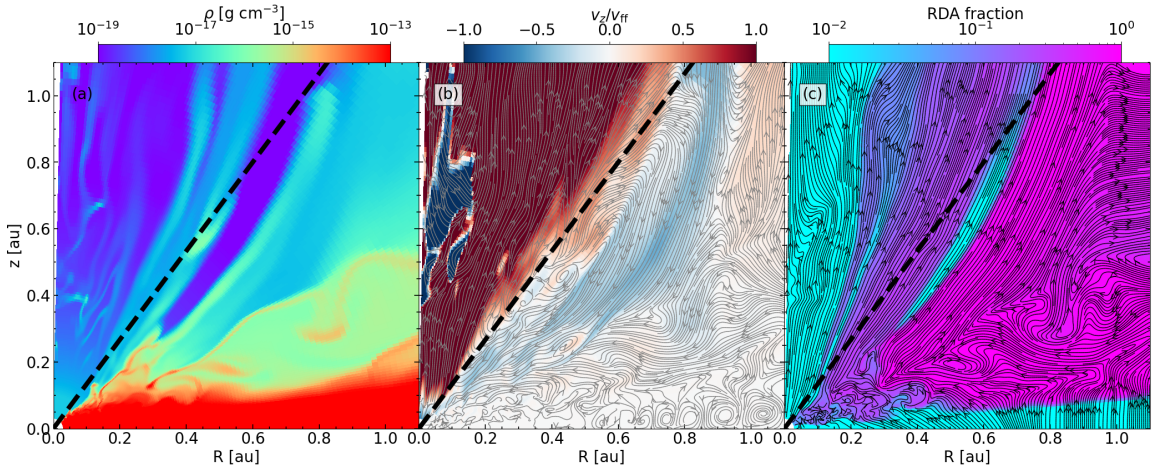


Figure 5.4: The properties of the raised disk atmosphere (RDA), roughly located to the right of the dashed black line, at a representative time of $t = 3.2$ yr. Plotted are (a) the density distribution, (b) the vertical gas velocity normalized by the local free-fall speed, and (c) the fraction of mass coming from the material originally near the disk surface (see text). Overplotted in panel (b) are the poloidal velocity streamlines, and in panel (c) are the poloidal magnetic field lines.

the simulation domain into several zones based on their physical characteristics. The zoning is sketched in Fig. 5.3. The disk is divided into an inner active and outer dead zone based on their temperatures. Above the disk is the avalanche accretion stream, which drags the poloidal magnetic fields (the magenta and cyan lines) into a sharply pinched configuration. A jet is launched above the avalanche accretion stream along the upper (magenta-colored) branch of the pinched field line (the yellow region, with arrows showing the gas flow direction). The avalanche accretion streams are embedded in a thick atmosphere (colored gray in the sketch), which surrounds the jet region in the cylindrically radial direction and helps confine it laterally. Since the jet-launching avalanche streams reside in the raised atmosphere, it will be discussed next.

5.3.2 Raised Disk Atmosphere

Fig. 5.4a and b show the density and vertical velocity component normalized by the local free-fall speed $v_z/v_{\rm ff}$ of the raised disk atmosphere (RDA), respectively. The RDA is the clumpy region above the disk with a relatively high density (compared to the more evacuated polar region) but a relatively low vertical velocity v_z compared to the local free-fall (or escape) speed, indicating that it remains bound to the disk through stellar gravity. Although some parts of the RDA move away from the disk, the motion is too slow to escape from the star's gravity. Thus, distinct from the much faster-moving jet in the polar region, this RDA is essentially a quasi-static structure enveloping the disk, i.e., a raised disk atmosphere. Above the active disk zone and the inner dead zone, we find that the magnetic pressure dominates the thermal pressure, with the magnetic pressure gradient from the toroidal field primarily responsible for raising the atmosphere. At larger radii, the thermal pressure gradient becomes relatively more significant, although it takes longer for the toroidal field to grow through the differential twisting of the initial poloidal field at larger distances.

To illustrate more pictorially that the vertically raised atmosphere was part of the material originally closer to the disk, we mark the material initially in the disk surface region between $0.1 < |z/r| < 0.15$ and $r > 0.2$ au with a scalar of 1. Fig. 5.4c plots the spatial distribution of the scalar value at the representative time, showing that the material originally close to the disk surface is now raised to occupy most of the atmosphere (the pink region in the panel). The poloidal magnetic field lines are overplotted in the panel, showing pinched morphologies in several regions of the atmosphere, particularly in the lower-left quadrant of the panel. These pinched magnetic field lines characterize the avalanche accretion streams, which we will focus on in the following subsection.

5.3.3 Avalanche Accretion Streams

We now switch our focus to smaller cylindrical radii, where the magnetic poloidal zone, jet zone, active disk zone, and prominent avalanche accretion streams reside. Since the avalanche accretion streams are crucial to jet-launching (sec. 5.3.4), we describe their properties and formation in this subsection.

The avalanche accretion stream is sandwiched between the active disk zone and the magnetic poloidal zone, where the poloidal magnetic flux accumulates through mass accretion. At the time shown in Fig. 5.5, the poloidal magnetic flux threading the inner (spherical) boundary in the region from $\theta = 0$ to $\theta = \pi/4$ increases by about a factor of ~ 6 compared to the initial flux. The magnetic field strength in the active disk zone is amplified when the poloidal field is winded into the toroidal field. Because the active zone is close to the ideal MHD limit, non-ideal MHD effects cannot remove the generated toroidal flux. As a result, a strong toroidal field develops in the active zone. To show the magnetic properties of these two zones more vividly, we show in Fig. 5.5a and b the square of the poloidal and toroidal field strength, respectively. The magnetic poloidal zone is dominated by a strong poloidal field (see Fig. 5.5a), while the active disk zone and the atmosphere immediately above it are dominated by a strong toroidal field (see Fig. 5.5b).

These two zones occupy most of the volume and angular space around the inner (radial) boundary. To accrete the raised atmosphere through the inner boundary, both zones must be avoided along the trajectory of an accreting gas parcel. As a result, the gas can only travel through a narrow corridor between these two zones, in the form of narrow streams. In order for the streams to accrete rapidly, they must be braked strongly.

Fig. 5.5c shows the avalanche accretion stream in the narrow corridor is braked

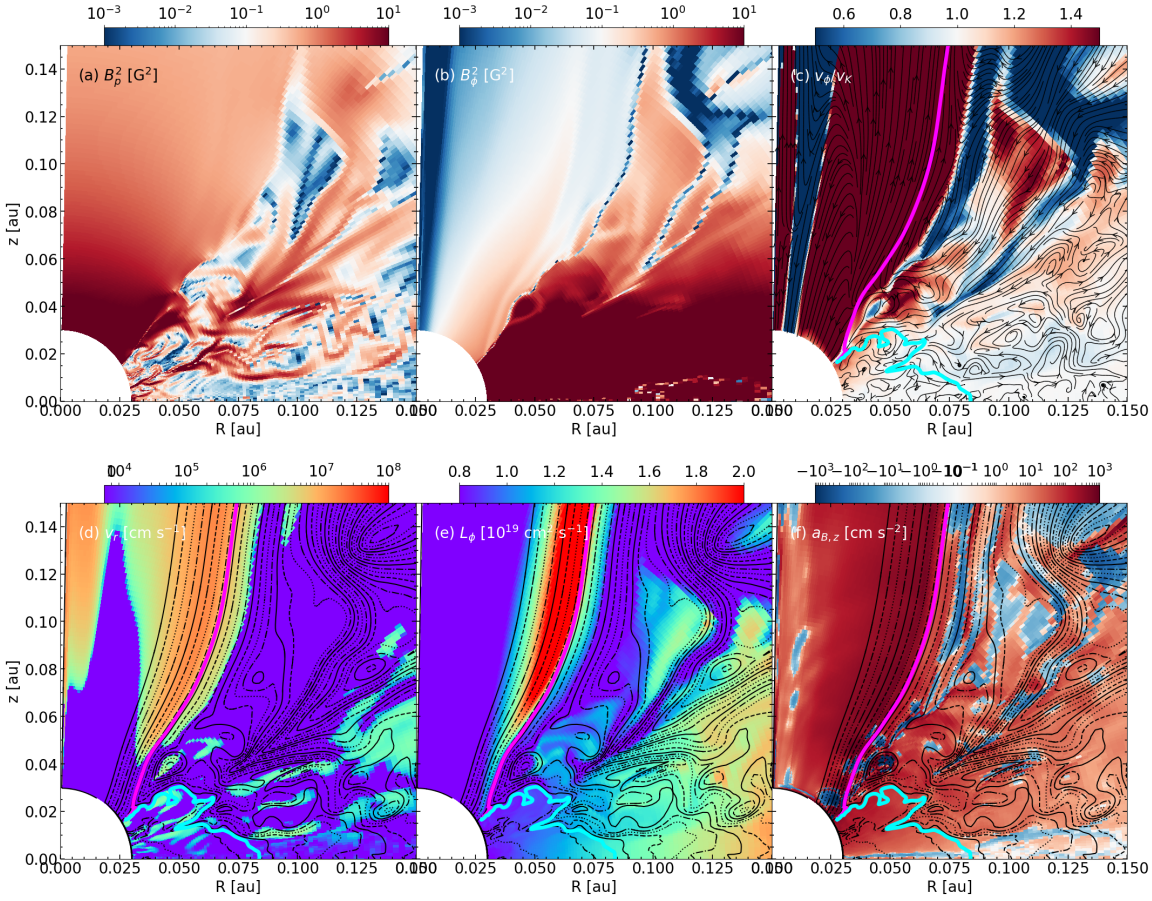


Figure 5.5: The disk and outflow properties at a representative time of $t = 3.01$ yr when a prominent avalanche accretion stream is present. Panels (a) and (b) show the squared poloidal and toroidal magnetic field strength, respectively. Panel (c) shows the ratio of the toroidal velocity and local Keplerian velocity, with the poloidal velocity streamlines overplotted. The lower panels show (d) the radial gas velocity v_r, (e) the specific angular momentum, and (f) the vertical magnetic acceleration, respectively. The poloidal magnetic field lines on the lower panels are plotted as contours of equal radial magnetic flux. A representative poloidal field line threading the avalanche accretion stream is highlighted in panels (c)-(f), with its pinch tip dividing the highlighted field line into two branches. The upper branch is colored magenta, and the lower branch is colored cyan. Flow acceleration along this representative field line is discussed in Section 5.3.4 below.

so strongly that it rotates at a significantly sub-Keplerian speed. The sub-Keplerian nature of the accretion flow results from a positive feedback loop between magnetic braking and accretion, where angular momentum removal by magnetic braking enables the gas near the tip of the pinched poloidal field to sink closer to the central star, where it rotates faster and is magnetically braked more strongly, leading to an avalanche-like gas falling, which is a form of the magneto-rotational instability (e.g. Kudoh et al., 1998; Suriano et al., 2017; Zhu & Stone, 2018; Mishra et al., 2020). Specifically, a gas parcel moving radially inwards along the narrow corridor pinches the poloidal magnetic field line on a meridional $(R-z)$ plane (see Fig. 5.5c) and the toroidal magnetic field line on the cylindrical $\phi - z$ plane. The pinch on the cylindrical $\phi - z$ plane brakes the gas rotation magnetically. We can divide the poloidal magnetic field line from the tip of the pinch into two branches, as illustrated by the highlighted fieldline in Fig. 5.5c. The upper branch is colored magenta, and the lower is colored cyan. Because the upper branch is restricted radially by the magnetic poloidal zone and the lower one is embedded in the heavily mass-loaded active disk zone, neither branch of the magnetic field line can move inwards together with the tip of the pinch. As a result, when the gas accretes further, the poloidal field line becomes more pinched, which, in turn, brakes the gas harder, facilitating further infall. This feedback loop creates the avalanche accretion stream, which is responsible for fast outflow launching, as we demonstrate next.

5.3.4 Magnetocentrifugal Jet Driven by Avalanche Accretion Streams

From Fig. 5.2 and its associated animation, we observe that fast outflow tends to be driven along the upper branch of the highly pinched poloidal magnetic field of an avalanche accretion stream that extends to a large radius in a relatively evacuated

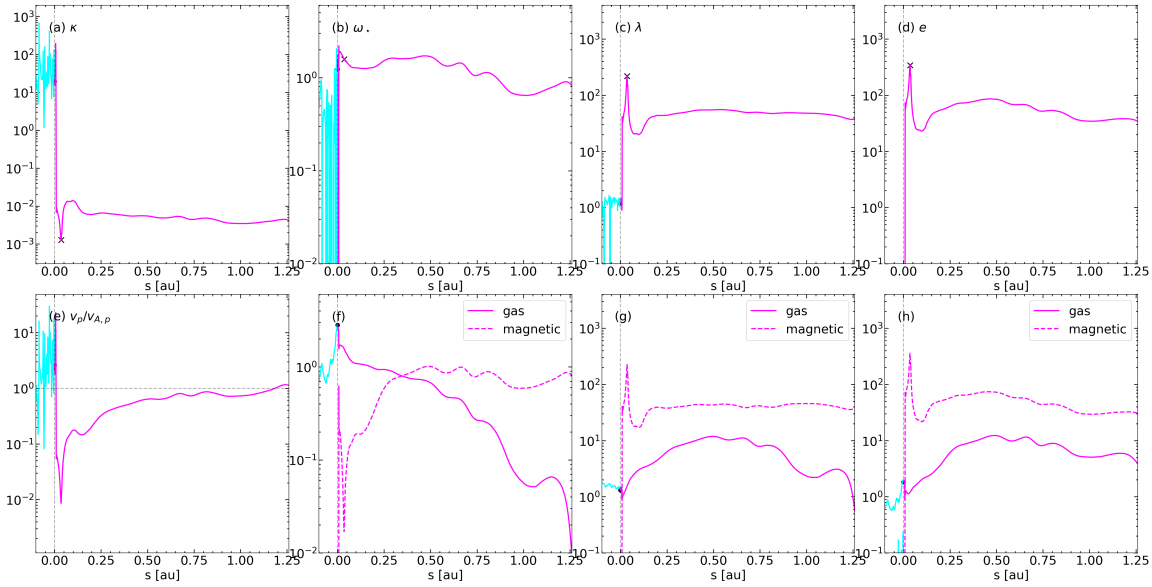


Figure 5.6: Quantities along the highlighted magnetic field line in Fig. 5.5. $s = 0$ on the horizontal axis corresponds to the tip of the pinched field line; the $s > 0$ section follows the upper branch of the field line (along the magenta field line), and the $s < 0$ section follows the lower branch (along the cyan field line). The distances shown are projected along the field line on the meridian plane. The upper panels are the four conserved quantities defined in equ. 5.18, 5.19, 5.20, 5.21 respectively. Panel (e) shows the ratio between the magnitude of the poloidal velocity and the poloidal Alfvén wave speed. The gas speed becomes super-Alfvénic at ~ 1.2 au along the magenta field line. Panel (f), (g), and (h) show the gas and magnetic components of equ. 5.15, 5.16, and 5.17 respectively. The gas components are the first terms in equ. 5.15, 5.16, and 5.17; the magnetic components are the second terms in equ. 5.15, 5.16, and the third term in equ. 5.17.

region, such as the magenta line in Fig. 5.5. The outflow is generated by the conversion of magnetic energy into gas kinetic energy, as in a standard MHD wind (see, e.g., Spruit, 2006, for a review). Although the outflow is highly time variable, it is still instructive to analyze the four quantities that are conserved along a magnetic field line for a steady axisymmetric wind (Weber & Davis, 1967; Blandford & Payne, 1982): the mass loading parameter

$$k = \frac{4\pi\rho v_p}{B_p}; \tag{5.14}$$

the angular speed

$$\omega_s = \frac{v_\phi}{R} - \frac{kB_\phi}{4\pi\rho R}; \tag{5.15}$$

the specific angular momentum

$$l = Rv_\phi - \frac{RB_\phi}{k}; \tag{5.16}$$

and the specific energy

$$E = \frac{1}{2}v^2 + \Phi - \frac{\omega_s R B_\phi}{k} + h, \tag{5.17}$$

where R is the cylindrical radius, $v_p^2 = v_r^2 + v_\theta^2$, $B_p^2 = B_r^2 + B_\theta^2$, and h is the enthalpy per unit mass. These dimensional quantities can be non-dimensionalized using the gas properties at the base of the outflow, which is taken to be the slow magnetosonic point (denoted with a subscript "SM," Jacquemin-Ide et al., 2021; Blandford & Payne, 1982)

$$\kappa = k\frac{v_{\rm K,SM}}{B_{\rm z,SM}} \tag{5.18}$$

$$\omega_\star = \frac{\omega_s}{\Omega_{\rm K,SM}}; \tag{5.19}$$

$$\lambda = \frac{l}{R_{\rm SM} v_{\rm K,SM}}; \tag{5.20}$$

$$e = \frac{E}{v_{\rm K,SM}^2}, \tag{5.21}$$

where the subscript "K" denotes the Keplerian value, with $v_{\rm K,SM} = R_{\rm SM}\Omega_{\rm K,SM}$. Note that the normalization for the specific energy, $v_{\rm K,SM}^2$, is consistent with that in Blandford & Payne (1982), which is a factor of 2 larger than that used in Jacquemin-Ide et al. (2021).

Fig. 5.6 shows these four dimensionless conserved quantities on the magnetic field line highlighted in the lower panels of Fig. 5.5 and the contributions by the fluid and magnetic field to three of the conserved quantities on the last three lower panels. The dimensionless mass loading parameter κ (Fig. 5.6a) is around 30 along the lower branch (colored cyan) of the magnetic field line. The value decreases abruptly to $\sim 10^{-3}$ crossing the tip of the pinched field line from the lower branch to the upper branch (colored magenta) before settling to a value $\sim 4 \times 10^{-3}$. The sudden decrease of the mass-loading parameter highlights the transition from the dense magnetically supported quasi-static inner disk atmosphere to the much more tenuous magnetically driven outflow zone. At around 1.2 au along the lightly loaded magnetic field line (see panel e), the gas poloidal velocity exceeds the poloidal Alfvén velocity (Fig. 5.6e), defined as $v_{A,p} = \sqrt{\frac{B_p^2}{4\pi\rho}}$ based on the poloidal field strength[2].

The panel (b) of Fig. 5.6 shows that the dimensionless quantity ω_* stays roughly constant outside the slow magnetosonic point (marked by a cross). It is initially dominated by the fluid rotation but becomes increasingly more dominated by the magnetic contribution as the gas angular speed decreases at larger distances. The

[2]Note that the flow in the cyan part of the field line in Fig. 5.6e is super-Alfvénic with respect to the poloidal magnetic field. The reason is that this part of the field line is located in the much denser part of the disk and disk atmosphere where relatively fast, chaotic poloidal motions are driven by magnetically mediated angular momentum transfer (see Fig. 5.5c) and the poloidal Alfvén speed $v_{A,p}$ is low because of a weak poloidal field. The relatively fast chaotic poloidal motions do not lead to an excessively large mass accretion rate, however, because of the cancellation of inward and outward mass fluxes. Indeed, the average (net) accretion speed (based on the net mass accretion rate) is well below the Alfvén speed.

dimensionless specific angular momentum also approaches an approximately constant value of ~ 40 (panel c). The magnetic contribution is more significant than the fluid contribution, but there is a conversion of the former into the latter along the field line (panel g), which gives rise to the super-Keplerian rotation in the jet zone shown in Fig. 5.5c, which, in turn, facilitates centrifugal outflow acceleration.

The dimensionless specific energy is also roughly constant in the outflow region (see panel d). It is entirely dominated by the magnetic contribution, even at the largest distance from the base of the outflow shown in the plot (1.2 au), where the magnetic energy remains nearly one order of magnitude higher than the flow kinetic energy (see panel h). Nevertheless, the gas velocity reaches a few $\times\ 10^7$ cm/s along the magnetic field line, well above the local escape velocity.

We note that jet-launching pinched poloidal field lines like the one highlighted in the lower panels of Fig. 5.5 are cut at the inner (radial) boundary when their tips are dragged across the boundary by the accretion streams. A fast outflow persists along the upper branch of the field line immediately after the cut, as the already magneto-centrifugally accelerated material continues to move outward (see, e.g., the dot-dashed and dotted field lines to the immediate right of the magenta line). However, the cut field lines are no longer attached to the dense accreting streams that powered their acceleration before the cut, likely rendering the acceleration captured in the simulation domain a lower limit.

To summarize, a standard magneto-centrifugal outflow appears to be driven from the upper branch of the highly pinched poloidal magnetic field of the avalanche accretion stream in the raised atmosphere of the inner accretion disk. It is collimated into a jet along the rotation axis by the vertically extended, raised disk atmosphere surrounding the outflow, as shown in Fig. 5.4c.

5.4 Discussion

5.4.1 Towards a new picture of protostellar jet formation

It is unsurprising that the atmospheric avalanche accretion stream drives the jet. This is because the energy for the jet launching ultimately comes from the release of the gravitational binding energy of mass accretion, which is concentrated in the atmospheric avalanche streams.

The scenario of the avalanche accretion stream-driven jet is a variant of one of the traditional scenarios of jet launching, where the jet is driven magneto-centrifugally directly from the inner disk (e.g. Konigl & Pudritz, 2000; Krasnopolsky et al., 2003, the other is the X-wind picture; Shu et al., 2000). A longstanding concern with the traditional disk-wind picture is that the magneto-centrifugal jet would remove angular momentum from the launching region on the disk so efficiently that it would accrete supersonically, leading to an excessively large accretion rate and rapid depletion of the inner disk as well as accumulation of an excessive poloidal magnetic flux that may cause disk disruption, which may, in turn, choke the jet launching. This “magnetic flux problem" of jet launching was often alleviated using a prescribed “turbulent" resistivity that enables the poloidal field to diffuse outward relative to the accreting material (e.g. Stepanovs & Fendt, 2016).

Rapid inflow is also present in the atmospheric avalanche accretion stream in our picture, but it does not lead to a mass accretion rate as large nor a poloidal magnetic flux accumulation as fast as in the traditional picture. The former is because the rapid inflow involves only a small fraction of the raised disk atmosphere, which is much less dense than the disk midplane. The latter is because the highly pinched poloidal field lines in the accretion streams are prone to reconnection, allowing the

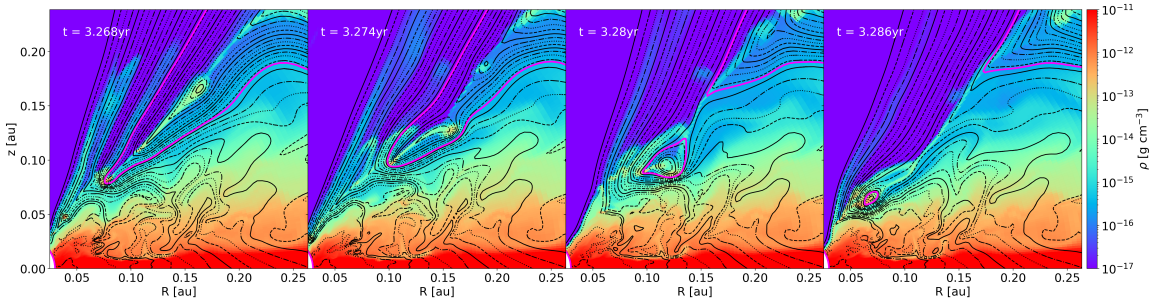


Figure 5.7: A representative magnetic reconnection event in our model. The four panels are a time sequence of reconnecting magnetic field lines. The magnetic field lines are specified by their values of the poloidal magnetic flux so that individual field lines can be traced over time. The magenta field line highlights a specific reconnecting magnetic field line. An animated version of this figure is available in the online journal. The movie is 27 seconds long, which highlights the magnetic reconnection along the avalanche accretion stream. The highlighted magenta field line reconnected multiple times during the movie.

mass to accrete without dragging along the field lines.

In Fig. 5.7, we show an example of the poloidal field line evolution involving reconnection. The lines shown are the contour lines of the poloidal magnetic flux, with each field line specified by a distinct flux value; for example, the magenta line in different panels marks the same field line at different times. From the time sequence, it is clear that the highlighted field line reconnected. For example, the highly pinched field line in the first and second panels has reconnected in the third and fourth panels, with the detached magnetic loop falling inward and the remaining reconnected open field line moving outward. This is a clear demonstration that accreting matter with a closed magnetic loop does not lead to the accretion of magnetic flux (open field line), which is left behind. The same process repeats itself, as shown in the animated version of Fig. 5.7 (see the figure caption for a link to the animation).

The reconnecting atmospheric avalanche accretion streams that play an essential role in mass accretion and outflow launching correspond to the so-called “turbulent atmosphere" defined by Jacquemin-Ide et al. (2021) in their 3D simulations (marked

as "TA" in their Fig. 3, top panel). The ridges of these streams have weaker magnetic fields than their surroundings because of the sharp pinching of field lines in both poloidal and toroidal directions. This leads to vanishing field components along the accretion stream and in the toroidal direction at the locations where the field lines reverse direction. We believe this is why the time-averaged field strength in their "turbulent" layer has a dip (see the red line in the shaded regions near the polar angle $\theta = \pi/4$ and $3\pi/4$ in their Fig. 7), which makes it easier for the time-averaged component of the field strength to drop below the time-varying (fluctuating) component (see the blue dashed line of the figure), the defining characteristic of their turbulent atmosphere. The correspondence can be seen even more explicitly from the top panel of their Fig. 8, which shows that their turbulent atmosphere is near the region where their time-averaged poloidal field lines are sharply pinched, as in our (axisymmetric) avalanche accretion streams.

One advantage of our 2D (axisymmetric) simulations is that each poloidal field line can be labeled by the poloidal magnetic flux it encloses, which enables us to show explicitly the reconnection of the field lines in the avalanche accretion streams (see Fig. 5.7 and especially its animated version). The reconnection is crucial for the outward transport of the poloidal magnetic flux related to the accreted gas, which was attributed to a turbulent "effective" resistivity by Jacquemin-Ide et al. (2021). We conclude that the fast outflows in our and their simulations are both driven by atmospheric avalanche accretion streams, but the results are interpreted from different perspectives.

Atmospheric avalanche accretion streams have been observed in other simulations in the context of both AGN (Active Galactic Nucleus) and YSO (Young Stellar Object) disk accretion, particularly when the disk is initially threaded with a relatively weak large-scale open poloidal field. For example, Matsumoto et al. (1996) carried

out 2D (axisymmetric) ideal MHD simulations of the accretion of an initially thick toroid threaded by a uniform poloidal field onto a central black hole. They found a fast outflow driven by magnetically braked surface accretion streams, which they first termed “avalanche accretion." They interpreted the outflow launching as a consequence of the outward propagation of non-linear Alfvén waves due to twisted field lines. Despite the differences in our simulation setup and somewhat different interpretations of the outflow production (magneto-centrifugal launching vs Alfvén waves), the jet production mechanism explored in this paper can be viewed as the YSO counterpart to their mechanism. Similarly, Beckwith et al. (2009) simulated the accretion of a magnetized toroid onto a central black hole in 3D, finding high-latitude accretion streams with highly pinched poloidal field lines (which they called "hairpins") and evidence for reconnection (as in our case). However, their focus was on magnetic flux transport rather than outflow generation.

In the context of YSO disk accretion, Takasao et al. (2018) appears to contradict our results because it has prominent accretion streams but no obvious fast outflow. Their accretion streams are located near the outer boundary enclosing a low-density polar region filled with a strong, ordered, poloidal magnetic field referred to as a “funnel." They are termed “funnel-wall accretion," which plays a crucial role in their picture of mass accretion onto a non-magnetized central star. These funnel-wall accretion streams are produced by strong magnetic braking, just like our avalanche flows, but they do not appear to drive an easily discernable fast outflow. It is not exactly clear why a fast outflow is driven magnetically by the accretion streams in our case but not theirs. One possibility is that the magnetically driven fast outflow may be masked by the powerful thermally driven stellar wind included in their case; the absence of a stellar wind may have allowed the accretion stream-driven fast outflow to show up more clearly in our case. Another difference is that their simulations

are 3D, while ours are 2D (axisymmetric), which could exaggerate the avalanche accretion stream features and their associated outflows. We note, however, that the 3D simulations of Zhu & Stone (2018) clearly show a lightly loaded fast wind that is driven magneto-centrifugally from high-latitude accretion streams. Indeed, our simulations can be viewed as a specialization of their simulations to the young star case that includes a nearly ideal MHD inner disk surrounded by a midplane dead zone at larger radii, with a focus on the innermost part of the simulation domain, which is where most of the gravitational binding energy of the avalanche accretion is released and where the fastest outflow is driven. The presence of a disk midplane dead zone at relatively large radii does not fundamentally change the basic features of the magnetically active regions at smaller radii.

The prevalence of atmospheric avalanche accretion streams and their associated outflows in simulations similar to ours indicate that they are robust features of magnetized accretion, particularly near the rotation axis where the low density and strong (accumulated) poloidal field combine to enable the upper branch of the stream's pinched field line to magneto-centrifugally accelerate the lightly loaded material to a high speed, forming a protostellar jet.

Although the poloidal magnetic field in the inner active disk zone remains relatively weak in the current generation of simulations, including ours, the question remains whether the poloidal field can become strong enough to disrupt the inner disk through magnetic flux accumulation and drive a fast outflow through accretion across the strong field (similar to magnetically arrested disks (MAD) in black hole accretion, e.g., Igumenshchev, 2008). It is a possibility worth exploring but will be challenging to simulate because of strong magnetization and mass depletion.

5.4.2 Implications and limitations

The disk, atmosphere, and outflow structure produced in our simulations should affect the transport and thermal processing of dust particles in the inner disk, with implications for the formation of chondrules and calcium- and aluminum-rich inclusions (CAIs). The rather turbulent meridional flows in the active disk zone may lift the dust grains to the magnetically raised atmosphere, where they can be funneled by gas flow into the atmospheric avalanche accretion streams. The raised streams allow the dust grains to be directly exposed to stellar irradiation, facilitating their heating/melting. Perhaps more intriguingly, the frequent magnetic reconnection events in the avalanche streams provide another powerful dust heating/melting mechanism often invoked in chondrule/CAI formation (e.g., Shu et al., 2001). Just as importantly, some of the molten or partially molten dust droplets can potentially be quickly advected outward by the fast outflow connected to (and launched from) the avalanche streams, where they can cool rapidly, decouple from the outflow, and fall back to the disk at large distances from the central protostar.

The above picture is broadly similar to the X-wind picture of the chondrule/CAI formation of Shu et al. (2001) but has several notable differences. Firstly, the fast avalanche streams may quickly deliver dust grains from the relatively cool outer regions of the active disk zone outside the dust sublimation radius to the inner disk edge (the “X-region" in Shu et al., 2001), which may otherwise be dust-free (Desch et al., 2010). Secondly, the molten dust particles are transported outward by an outflow driven by magnetized disk atmospheric avalanche accretion streams rather than the X-wind driven by the stellar magnetospheric magnetic field near the inner disk edge opened by disk interaction. Furthermore, magnetic reconnections potentially capable of dust-melting occur in the disk atmospheric avalanche streams beyond the

inner disk edge rather than in the reconnection ring near the disk midplane interior to the disk inner edge. Whether this variant of Shu et al. (2001)'s picture works quantitatively remains to be determined.

A limitation of the current simulations is the assumption of axisymmetry. This assumption was adopted as a first step to explore efficiently, with reasonable computational costs, the dynamics of the inner disk and jet launching, which requires high spatial resolution and non-ideal MHD effects (i.e., Ohmic dissipation). In particular, high resolution in the θ-direction is required to capture the sharp pinching of the poloidal field lines, which is a key feature of the jet-launching avalanche accretion streams. The assumption of axisymmetry also enabled us to clearly identify reconnecting magnetic field lines using contours of enclosed poloidal magnetic flux. However, some features we observe in the 2D may be modified by 3D effects.

One feature of the 2D model is the azimuthal magnetic field strength in the active disk zone can be significantly stronger than that in 3D simulations (e.g. Takasao et al., 2019; Jacquemin-Ide et al., 2021; Zhu et al., 2024; Mishra et al., 2020; Parfrey & Tchekhovskoy, 2023; Porth et al., 2021). The difference can be attributed to the additional freedom in the azimuthal direction in 3D, allowing easier magnetic field removal through processes unavailable in 2D. For example, magnetic reconnection in the azimuthal direction is only possible in 3D, which can lower the strength of B_ϕ. Furthermore, magnetic bubbles can form in 3D simulations at some azimuthal locations (e.g. Porth et al., 2021), carrying away poloidal magnetic flux. Because the twist of poloidal magnetic fields generates B_ϕ, removing poloidal magnetic flux helps reduce the strength of the toroidal magnetic field. Nevertheless, the toroidal magnetic field cannot grow indefinitely in the disk. It is limited by the advection of the toroidal field out of its generation region, which tends to limit the energy density of the toroidal field well below the kinetic energy of the disk rotation, as we

demonstrate in the Appendix.

5.5 CONCLUSION

We carried out a 2D (axisymmetric) non-ideal MHD simulation of the disk around an accreting young stellar object, including a thermally ionized inner active zone surrounded by a magnetically dead zone initially threaded by a relatively weak, large-scale, open poloidal magnetic field. Our main conclusions are as follows.

- We find that a fast (> 100 km/s) collimated bipolar jet is continuously driven along the north and south poles of the circumstellar disk initially magnetized by a large-scale open poloidal field.

- The disk-jet system has several distinct components, which, besides the fast-moving jet, include a low-density polar region filled with a strong poloidal magnetic field from magnetic flux accumulation near the axis, a dense equatorial disk that is magnetically active in the inner part surrounded by a magnetically dead zone near the equator at larger radii, a quasi-static atmosphere that is raised above the disk primarily by the toroidal magnetic field and bound to the disk by the stellar gravity, and narrow avalanche accretion streams in the raised atmosphere produced by efficient local magnetic braking.

- The fast jet is primarily driven magneto-centrifugally by the release of the gravitational binding energy of the avalanche accretion streams near the boundary of the evacuated poloidal field-dominated polar region and the denser raised disk atmosphere. In particular, the fast outflow is driven along the upper (open) branch of the highly pinched poloidal field lines threading the accretion streams where the density is relatively low so that the lightly loaded material can be accelerated magneto-centrifugally along the open field line to a high speed.

- We find explicit evidence for repeated reconnection of the highly pinched poloidal magnetic fields threading the avalanche accretion streams, which enables mass to accrete to the center without dragging along the poloidal magnetic flux with it, thus alleviating the problem of excessive magnetic flux accumulation that may disrupt the inner disk and choke the jet launching. It also provides a potential heating source for producing chondrules and CAIs which, after formation, may then be transported to larger distances by the fast outflow connected to (and driven by) the reconnecting avalanche accretion streams.

5.6 ACKNOWLEDGMENTS

We thank Brandt Gaches, Jonathan Tan, and Etienne Martel for helpful discussions at the early stage of this project and the referee for prompt and constructive comments. This work is supported by NASA 80NSSC20K0533 and NSF AST-2307199. Computing resources were provided by the NASA High-End Computing (HEC) Program through the NASA Advanced Supercomputing (NAS) Division at Ames Research Center and the RIVANNA supercomputer at the University of Virginia. YT acknowledges support from an interdisciplinary fellowship from the University of Virginia.

Chapter 6

Highly Variable Magnetic Pressure-Driven YSO Jets in the Polar Cavity from Toroidal Fields Generated by Inner Disk Accretion

The work presented in this chapter has been accepted for publication in the Astrophysical Journal (ApJ) with Zhi-Yun Li, Zhaohuan Zhu, Chun-Yen Hsu, and Xiao Hu as coauthors (Tu et al., 2025a).

Abstract: Jets and outflows are commonly observed in young stellar objects (YSOs), yet their origins remain debated. Using 3D non-ideal magnetohydrodynamic (MHD) simulations of a circumstellar disk threaded by a large-scale open poloidal magnetic field, we identify three components in the disk-driven outflow: (1) a fast, collimated jet, (2) a less collimated, slower laminar disk wind, and (3) a magneto-rotational instability (MRI)-active turbulent disk wind that separates the former two. At high altitudes, the MRI-active wind merges with the laminar disk wind, leaving only the jet and disk wind as distinct components. The jet is powered by a novel mechanism in the star formation context: a lightly mass-loaded outflow driven by toroidal magnetic pressure in the low-density polar funnel near the system's rotation axis. A geometric analysis of the magnetic field structure confirms that magnetic tension does not contribute to the outflow acceleration, with magnetic pressure acting as the dominant driver. While the outflow in our model shares similarities with the magneto-centrifugal model-such as angular momentum extraction from the accreting disk-centrifugal forces play a negligible role in jet acceleration. In particular, the flow near the jet base does not satisfy the conditions for magneto-centrifugal wind launching. Additionally, the jet in our simulation exhibits strong spatial and temporal variability. These differences challenge the applicability of rotation-outflow velocity relations derived from steady-state, axisymmetric magneto-centrifugal jet models for estimating the jet's launching radius. For the slower disk wind, vertical motion is driven by toroidal magnetic pressure, while centrifugal forces widen the wind's opening angle.

6.1 Introduction

Outflows from young stellar objects (YSOs) play a crucial role in the process of star formation. Observationally, they bridge the dynamics at small scales near the

star and disk to larger-scale phenomena, providing indirect evidence of the physical processes occurring close to the star and along the disk surface. Outflows from YSOs are generally categorized into two components: the jet and the disk wind. Jets are highly collimated, fast outflows that can extend hundreds of au or even parsecs from the YSO (McGroarty & Ray, 2004; Ray & Ferreira, 2021; Whelan et al., 2024; Chauhan et al., 2024), while disk winds are slower and less collimated, observable primarily closer to the star (Klaassen et al., 2013; Bjerkeli et al., 2016; Launhardt et al., 2023). Both components play essential roles in star formation by removing angular momentum from the disk (and potentially the star), thereby driving accretion onto the star and facilitating disk evolution (Bouvier et al., 2007; Frank et al., 2014; Pascucci et al., 2023). Despite their importance, the mechanisms driving jets and disk winds, as well as whether they share a common origin, remain areas of active research (Pudritz et al., 2007; Shang et al., 2007; McKinney & Narayan, 2007; Bai et al., 2016; Jacquemin-Ide et al., 2019; Banzatti et al., 2022; López-Vázquez et al., 2024a; Zimniak et al., 2024).

Numerous studies have explored the driving mechanisms of outflows from YSOs over the past decades, with a growing consensus that they are most likely magnetically driven (Pudritz et al., 2007; Shang et al., 2007; Ray & Ferreira, 2021). While the presence of magnetic fields in the disk is expected (Wurster & Li, 2018; Vlemmings et al., 2019; Galametz et al., 2020; Tu et al., 2024a; Ohashi et al., 2025), the exact process of utilizing these fields to launch outflows remains a topic of active debate. The leading model for jets in YSOs is the class of magneto-centrifugal models, including the disk-wind model (Blandford & Payne, 1982; Pudritz & Norman, 1983) and the X-wind model (Shu et al., 1994, 2000; Ferreira et al., 2000). In this class of models, rigid magnetic field lines efficiently transport angular momentum from the disk to the gas above. If the field lines are sufficiently inclined, the centrifugal

force can overcome gravity along the lines, leading to strong gas acceleration, like "beads on a wire." This accelerated gas is subsequently collimated into a jet, either by magnetic tension forces or through external confinement. To maintain the rigid magnetic field lines necessary for efficient centrifugal gas acceleration, only a small amount of gas can be loaded onto these lines, resulting in a "lightly loaded" wind (Bai & Stone, 2013; Hawley et al., 2015). This model effectively explains angular momentum transport and jet launching, and is particularly well developed under the assumptions of steady-state and axisymmetry (e.g. Ferreira et al., 2006), which are often used to interpret observational data (e.g. López-Vázquez et al., 2024a).

Another class of models suggests that jets are primarily powered by Poynting flux (Shibata & Uchida, 1986; Lovelace et al., 2001; Lovelace & Romanova, 2009), with toroidal magnetic energy dominating over kinetic energy in the jet acceleration region. A related model is the so-called "magnetic tower model," where field lines form loop-like structures stacked atop one another (Contopoulos, 1995; Lynden-Bell, 1996, 2003). The gas acceleration in this scenario is more gradual compared to the classic lightly-loaded magneto-centrifugal model since the field is more heavily loaded and the acceleration results from the expansion driven by magnetic pressure within the tower.

Both classes of models have undergone extensive investigations using numerical simulations. The magneto-centrifugal models are investigated with 2D axisymmetric (e.g. Casse & Keppens, 2002; Kato et al., 2002; Fendt et al., 2011; Fendt & Sheikhnezami, 2013; Tzeferacos et al., 2009; Stepanovs & Fendt, 2016; Ramsey & Clarke, 2019; Mattia & Fendt, 2020a,b; Jannaud et al., 2023; Tu et al., 2025c; Zanni & Ferreira, 2013, 2009) and 3D (e.g. Anderson et al., 2006; Zhu & Stone, 2018; Mishra et al., 2020; Jacquemin-Ide et al., 2021; Takasao et al., 2022) simulations, typically with ideal MHD or a prescribed (turbulence) diffusivity that focuses on the

outer wind-launching region. The Poynting-flux/magnetic tower model was investigated with a prescribed disk property (Ustyugova et al., 2000; Huarte-Espinosa et al., 2012). A 3D model with a more realistic treatment of non-ideal MHD effect based on thermal ionization focusing on the innermost disk that distinguishes between the disk active zone and dead zone (Flock et al., 2016) is still lacking. Furthermore, a detailed force analysis in the jet-launching region is needed to determine the jet-launching mechanism. These will be the focus of this paper.

A primary objective is to identify the dominant jet-launching mechanism in YSOs and determine whether it aligns more closely with the classic magneto-centrifugal model or the magnetic tower model. This study extends the 2D axisymmetric model of Tu et al. (2025c) to 3D to investigate the jet-launching mechanism in greater detail. In the 2D model, the "avalanche accretion stream" along the disk surface was identified as a key driver of the jet, transferring angular momentum from the accretion stream to the low-density gas above via open magnetic field lines. Here, we aim to determine whether this feature persists in 3D and retains its role in jet launching. To overcome the limitations of the previous approach, we transition from spherical-polar to Cartesian coordinates, resolving challenges posed by the polar and radial boundaries and allowing the jet to evolve naturally around the polar axis. The stellar magnetosphere is excluded in this study to isolate the role of the disk's magnetic field and its associated disk accretion in jet launching; the magnetosphere will be included in a subsequent investigation.

This paper is organized as follows: we describe our model setup in sec. 6.2. Sec. 6.3 shows an overview of the simulation result and a description of the outflow component in our model. The forces driving each outflow component are also discussed in sec. 6.3. The jet-launching mechanism is discussed in detail in sec. 6.4, and a comparison to the expectations of steady-state jet solution and the magneto-centrifugal model is

discussed in sec. 6.5. Sec. 6.6 focuses on the implications of our jet-launching model on observation and interpretations of the jet-launching mechanism. We conclude in sec. 6.7.

6.2 Methods

In a jet-launching inner disk around a young stellar object (YSO), the following set of equations governs the disk accretion and jet-launching processes:

$$\frac{\partial \rho}{\partial t} + \nabla \cdot (\rho \boldsymbol{v}) = 0, \tag{6.1}$$

$$\rho \frac{\partial \boldsymbol{v}}{\partial t} + \rho(\boldsymbol{v} \cdot \nabla)\boldsymbol{v} = -\nabla P + \frac{1}{c}\boldsymbol{J} \times \boldsymbol{B} - \rho \boldsymbol{g}, \tag{6.2}$$

$$\frac{\partial \boldsymbol{B}}{\partial t} = \nabla \times (\boldsymbol{v} \times \boldsymbol{B}) - \frac{4\pi}{c}\nabla \times (\eta_O \boldsymbol{J}), \tag{6.3}$$

where $\boldsymbol{J} = (c/4\pi)\nabla \times \boldsymbol{B}$ is the current density, and η_O the Ohmic dissipation coefficient. Other symbols have their usual meanings.

We use the ATHENA++ code (Stone et al., 2020) with static mesh refinement (SMR) to solve the governing equations in Cartesian coordinates. The simulation domain is cubic, extending from -10 au to 10 au in all three directions. The base resolution is 64^3, and we use 7 levels of mesh refinement to focus on the jet-launching inner disk region, yielding a smallest cell size of 0.0024 au. The finest level (level 7) extends from -0.15 au to 0.15 au in the $\hat{x}$ and $\hat{y}$ directions and from -0.08 au to 0.08 au in the $\hat{z}$ direction, covering the magnetically active inner zone of the disk in the simulation. To better resolve the launched jet without significantly increasing computational cost, an additional refinement of level 6 is added, from -0.15 au to 0.15 au in $\hat{x}$ and $\hat{y}$ directions, and from -0.32 au to 0.32 au in $\hat{z}$ directions. The rest of the refinement is automatically generated, enforcing the criteria that adjacent

mesh blocks must have refinement levels that differ by exactly one. This refinement strategy is chosen to optimize the resolution of the inner disk and the jet-launching region while maintaining a reasonable computational cost.

Since a major goal of this work is to extend the 2D (axisymmetric) simulations of Tu et al. (2025c) to 3D, our initial setup of the problem will closely follow theirs. Specifically, the following power-law is adopted for the midplane gas density:

$$\rho_{\rm mid}(r) = \rho_0 \Big(\frac{r}{r_0}\Big)^p, \tag{6.4}$$

where $\rho_0 = 10^{-9}$ g cm^{-3}; $r_0 = 6.3 \times 10^{-2}$ au and $p = -1.35$. The midplane density within 0.06 au of the origin is gradually reduced to a floored density profile (see equation 6.5 below) to mimic the expected transition between the inner disk and circumstellar cavity caused presumably by the stellar magnetosphere, which is not included in this study to isolate the role of the disk magnetic field and its associated accretion in jet launching; the combined effects of the disk and stellar magnetic fields will be explored elsewhere. The disk density away from the midplane is calculated assuming vertical isothermal hydrostatic equilibrium with a dimensionless disk scale height of $h = H/R = 0.1$ (where H is the scale height and R is the cylindrical radius). We extrapolate the disk's vertical density profile into the atmosphere above and below the disk.

To help with numerical stability, particularly in the polar regions where the magnetic field is expected to be strong and gas is depleted due to rapid infall, we imple-

ment a similar radially varying density floor as in Tu et al. (2025c)[1]:

$$\rho_{\rm floor}(r) = \begin{cases} \rho_f; & r < r_f, \\ \rho_f (r/r_f)^{-2}; & \text{otherwise}, \end{cases} \tag{6.5}$$

where $\rho_f = 5.94 \times 10^{-17}$ g cm^{-3} and $r_f = 0.025$ au. Both the disk and envelope are initially in Keplerian rotation. To speed up the development of potential instabilities such as current-driven instabilities in toroidal magnetic field-dominated parts of jets, such as the nonaxisymmetric helical kink m = 1 mode (see, e.g. McKinney & Blandford, 2009), a random perturbation with a magnitude of up to 1% of the local velocity is added to the system. This is in addition to the grid-level numerical noise that can also break the axisymmetry of the initial conditions and seed potential instabilities.

The temperature in the disk (where $|z/r| < 0.1$) follows that of Flock et al. (2016):

$$T_{\rm disk}(r) = T_i \frac{T_\odot}{\epsilon_T^{0.25}} \left(\frac{R_\odot}{2r} \right)^{1/2} \tag{6.6}$$

where $T_\odot = 5666$ K and $R_\odot = 6.943 \times 10^{10}$ cm are the solar surface temperature and radius respectively; $\epsilon_T = 1/3$. Following Tu et al. (2025c), we set the parameter T_i as

$$T_i = \begin{cases} 2 & r < 0.1 \text{ au}, \\ 3 - \frac{r}{0.1 \text{ au}} & 0.1 \text{ au} \leq r < 0.2 \text{ au}, \\ 1 & \text{otherwise}. \end{cases} \tag{6.7}$$

to increase the midplane temperature inside 0.2 au to mimic accretion heating and produce a well-defined magnetically active inner disk region inside ~ 0.13 au. A

[1]The inclusion of a stellar wind, as done by Meskini et al. (2024), may alleviate the need for the density floor in future simulations.

temperature transition zone lies between the disk and the envelope, where the temperature is given by

$$T_{\rm trans}(r) = (T_{\rm env} - T_{\rm disk})\frac{|z/r| - 0.1}{0.2} + T_{\rm disk}; \quad 0.1 \leq \left|\frac{z}{r}\right| \leq 0.3, \tag{6.8}$$

where $T_{\rm env} = 3,000$ K is the temperature of the envelope above the transition zone (where $|z/r| > 0.3$); it is adopted primarily to ensure that the envelope remains well coupled to the magnetic field as generally expected, although a more self-consistent temperature treatment is desirable in future investigations. For simplicity and to ensure numerical stability, we assume that the spatial distribution of the temperature remains the same throughout the simulation.

The initial magnetic field is calculated from a vector potential $\boldsymbol{A} = \langle 0, 0, A_\phi \rangle$ following Wang et al. (2019)

$$A_\phi = \frac{4}{3}\frac{A_{z,0}(r/r_0)^{-0.25}}{[1 + 1/(\mu \tan\theta)^2]^{0.625}}, \tag{6.9}$$

where $\mu = 0.5$ determines how curved the initial field is. The scale for the magnetic field strength is chosen to be $A_{z,0} = 0.009$ G au so the plasma-β at 1 au is about 10^5.

6.2.1 Sink Treatment

Since our focus is on outflow driven by disk accretion, we will adopt a simplified treatment of the central star and ignore, for now, the stellar magnetosphere. We define a spherical "sink" region of radius $r_{\rm fix} = 0.025$ au (the same as the radius of the plateau density floor r_f in equ. 6.5), where all hydrodynamic quantities are reset to their initial values at each step, but the magnetic field is allowed to evolve over time. To gauge the potential effects of stellar rotation on jet launching, we adopt two simple prescriptions for the velocity field in the sink region within $r_{\rm fix}$. In the "NOROT"

model, the velocity is set to 0 in all three directions. In the "strot" model, the gas within $r_{\rm fix}$ is assumed to rotate as a solid body with an angular velocity equal to half the Keplerian rate at $r_{\rm fix}$. This translates to a stellar spin period of approximately 2.9 days, typical of those observed in YSOs (Herbst et al., 2007).

Our sink treatment also includes a softening of the stellar gravity:

$$a_g(r) = \begin{cases} -\frac{GM_\star \hat{\boldsymbol{r}}}{r^2} \ \frac{(r-r_s)^2}{(r-r_s)^2+r_s^2}; & r > r_s, \\ 0; & \text{otherwise}, \end{cases} \tag{6.10}$$

where $M_\star = 1 M_\odot$ is the stellar mass and $r_s = 0.005$ au is the softening radius, which resides well within the sink region of radius $r_{\rm fix}$. The gravitational acceleration is close to the unsoftened value (within $\sim 5\%$) outside the sink region ($r = r_{\rm fix}$).

6.2.2 Magnetic diffusivity

Our simulation captures both the inner magnetically active disk and magnetically inactive dead zone at larger distances by including Ohmic dissipation. The coefficient η_O is calculated by combining the contributions of two ionization sources: cosmic ray ionization and thermal ionization, following Tu et al. (2025c). It is given by (Bai, 2011)

$$\eta_O = \frac{c^2}{4\pi\sigma_O}, \tag{6.11}$$

where c is the speed of light. The conductivity σ_O is given by

$$\sigma_O = \frac{ec}{B}\sum_j n_j Z_j \beta_j, \tag{6.12}$$

with

$$\beta_j = \frac{Z_j e B}{m_j c}\frac{1}{\gamma_j \rho}, \tag{6.13}$$

where n_j, m_j, Z_j, and γ_j are the number density, mass, electric charge, and momentum transfer rate between the jth charged species and the neutrals, respectively. The parameter β_j characterizes the relative importance between the Lorentz force and the neutral drag.

The conductivity due to cosmic ray ionization is computed using two charged species: the ions and the electrons. The ion abundance is given by

$$n_i = \frac{C\sqrt{\rho}}{m_i} \tag{6.14}$$

where the coefficient $C = 9.5 \times 10^{-18}$ cm$^{-3/2}$ g$^{1/2}$ is determined by a cosmic ray ionization rate of 10^{-20} s^{-1}. The value is chosen to account for the screening effect due to the disk column density and the ionization due to decaying radioactive atoms (Umebayashi & Nakano, 2009). The momentum transfer coefficient between the ions and the neutral is $\gamma_{\rm i,cr} = 3.5 \times 10^{13}$ cm^3 s^{-1} (Shu, 1991). The electron abundance is assumed to be the same as the ion abundance. The electron momentum transfer coefficient is given by (Bai, 2011)

$$\gamma_e = 8.3 \times 10^{-10}\sqrt{T}\ \text{cm}^3\ \text{s}^{-1}, \tag{6.15}$$

where T is the temperature of the gas.

The conductivity due to thermal ionization is computed using five charged species: potassium, calcium, magnesium, sodium, and electron. The total number density of each metal is obtained from its relative abundance to H_2 shown in Table 6.1. The number density of each metal ion is calculated with the Saha equation, and the electron density is taken as the sum of the number densities of all metal ions. The

Species	m_s [m_p]	$n/n_{\rm H2}$	e_I [erg]
K	39	2.14×10^{-9}	6.95×10^{-12}
Ca	40	4.38×10^{-8}	9.76×10^{-12}
Na	23	3.48×10^{-8}	8.2×10^{-12}
Mg	24	7.96×10^{-7}	1.2×10^{-11}

Table 6.1: Parameters for calculating the thermal ionization fraction with the Saha equation. m_s, the atomic mass of each element, is in the unit of proton mass m_p. The relative abundances with respect to H_2 are taken from Asplund et al. (2009), assuming the gas phase metal in the protoplanetary disk is 1% of the solar photosphere abundance.

momentum transfer rate between the metals and the neutral is given by (Bai, 2011)

$$\gamma_j = \frac{2 \times 10^{-9}}{m_n + m_j} \Big(\frac{m_H}{\mu} \Big)^{1/2} \ {\rm cm}^3 \ {\rm s}^{-1}, \tag{6.16}$$

where

$$\mu = \frac{m_j m_n}{m_j + m_n} \tag{6.17}$$

is the reduced mass in the collision between the jth metal ion and the neutral (with mass m_n).

The total conductivity is computed by summing the contributions of each component, and the diffusivity is calculated according to equ. 6.11.

6.3 Result overview

In this section, we present an overview of some broad features of the reference model NOROT with a non-rotating sink region; the STROT model (with a rotating sink region) will be discussed in Appendix E.1. Fig. 6.1 displays a 3D view of the simulation at a representative time of $t = 4.5$ yr, showing a bipolar outflow with a vertical velocity away from the disk larger than 10^6 cm s^{-1}. The disk is represented by the gray torus near the equatorial plane with density $> 10^{-12}$ g cm^{-3}. At this

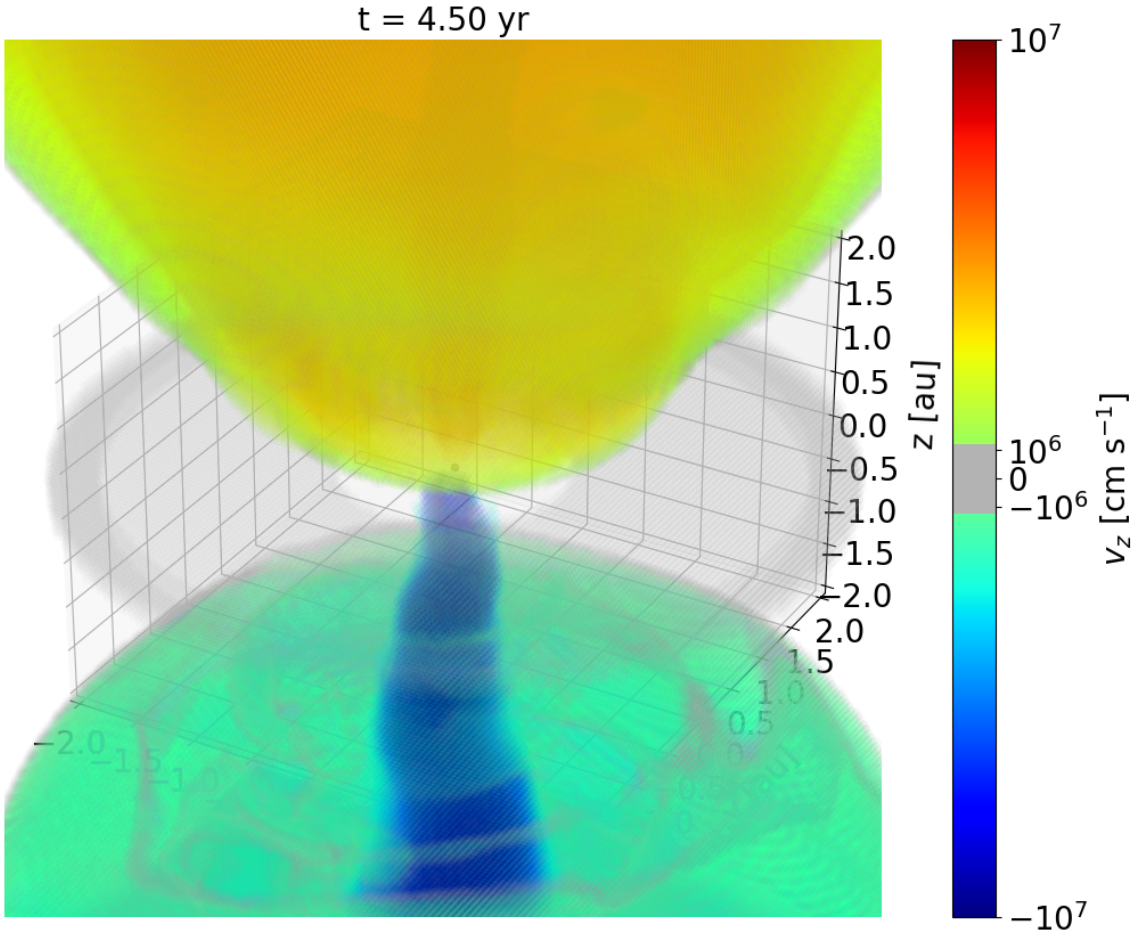


Figure 6.1: 3D rendition of the jet, disk wind, and the disk at a representative time $t = 4.5$ yr. The colors are the $\hat{z}$-direction velocity, showing a fast (> 100 km/s) collimated bipolar jet (colored red and blue, close to the polar axis), surrounded by a slower disk wind (colored yellow and green, further away from the polar axis). The disk is represented by the gray structure on the equatorial plane. The jet is highly variable in space and time, as seen from the animated version available at `https://figshare.com/s/899801ea6282e9c06261?file=53753738`. The animated version is 50 seconds long, featuring a 3D rendition of the outflow in our model. We encourage readers to view it for a clearer impression of the outflow structure and dynamics.

time, the narrow jet in the lower hemisphere is faster and more prominent than its counterpart in the upper hemisphere, although both jet components are highly variable in time, as can be seen from the animated version of the figure (see the figure caption for a link). Both jet components are surrounded by a wider, slower outflow – the disk wind component. All models presented here cover a simulation time span of 10 years. While the system is highly variable and does not reach a true steady state, this duration is sufficient for the overall accretion and outflow properties to settle into a quasi-steady configuration and the key structural and dynamical features of the outflow remain qualitatively stable after ∼4 yr.

To show the outflow more quantitatively, Fig. 6.2 presents two x-z slices at the two representative times: $t = 4.5$ and 9.0 yr. For each row, the horizontal panels show, respectively, the density ρ and the projected z-direction velocity (v_z^p), defined as

$$v_z^p = v_z \; z/|z|. \tag{6.18}$$

A positive value of v_z^p means that the flow is away from the disk midplane (i.e., an outflow). The density is broadly symmetric about the midplane at both 4.5 and 9.0 yr, although there is significantly more mass in the polar region in the lower hemisphere at 9.0 yr. The fast jet, defined as the region where $v_z^p \geq 10^7$ cm s^{-1}, is stronger in the lower hemisphere at 4.5 yr as mentioned earlier, but becomes stronger in the upper hemisphere at 9.0 yr. The reason behind this change in jet strength and its relationship to the density structure will be discussed in sec. 6.4. Readers are encouraged to view the animated version of this figure to better visualize the evolution of our model, especially its strong time variability.

Surrounding the jet, but also moving away from the disk midplane, is a slower-moving disk wind. The disk wind is prominent at 4.5 yr as the wide-angle structure

outflows on both hemispheres. The disk wind persists at 9.0 yr, particularly in the lower hemisphere, where a jet is absent. Between the jet and the disk wind lies an MRI-active disk wind region. We will focus on these three components one by one in the following subsections.

6.3.1 The polar jet

As shown in panel (a) of Fig. 6.2, the magnetic field lines threading the jet are connected to the inner active zone of the disk and the central boundary. Thus, we focus on these two regions to examine the jet-launching mechanism.

Fig 6.3(a) shows the azimuthally-averaged v_z^p near the base of the jet-launching region. The green contour traces the jet in both the upper and lower hemispheres. The specific angular momentum in the jet launching region is well above the local Keplerian value as a result of angular momentum transport from the disk into the jet region. The importance of the magnetic field is evident: the plasma-β is well below order unity (fig. 6.3[b]) in both the jet region and the magnetically active inner disk zone. Magnetic energy also dominates over kinetic energy in the jet region, as illustrated in Fig 6.3(c), which shows that the kinetic-β

$$\beta_K = \frac{\rho v^2/2}{B^2/8\pi}, \tag{6.19}$$

is below unity in the jet region, particularly in the lower hemisphere, where the outflow is stronger at 4.5 yr. In contrast, the kinetic-β in the disk is above order unity, suggesting that the outflow-launching region contains two components: a kinetic energy-dominated disk and a magnetically dominated jet-launching region.

To understand the jet production mechanism in the magnetically-dominated jet-launching region, we show in Fig. 6.4 the $\hat{z}$-direction projected total magnetic ac-

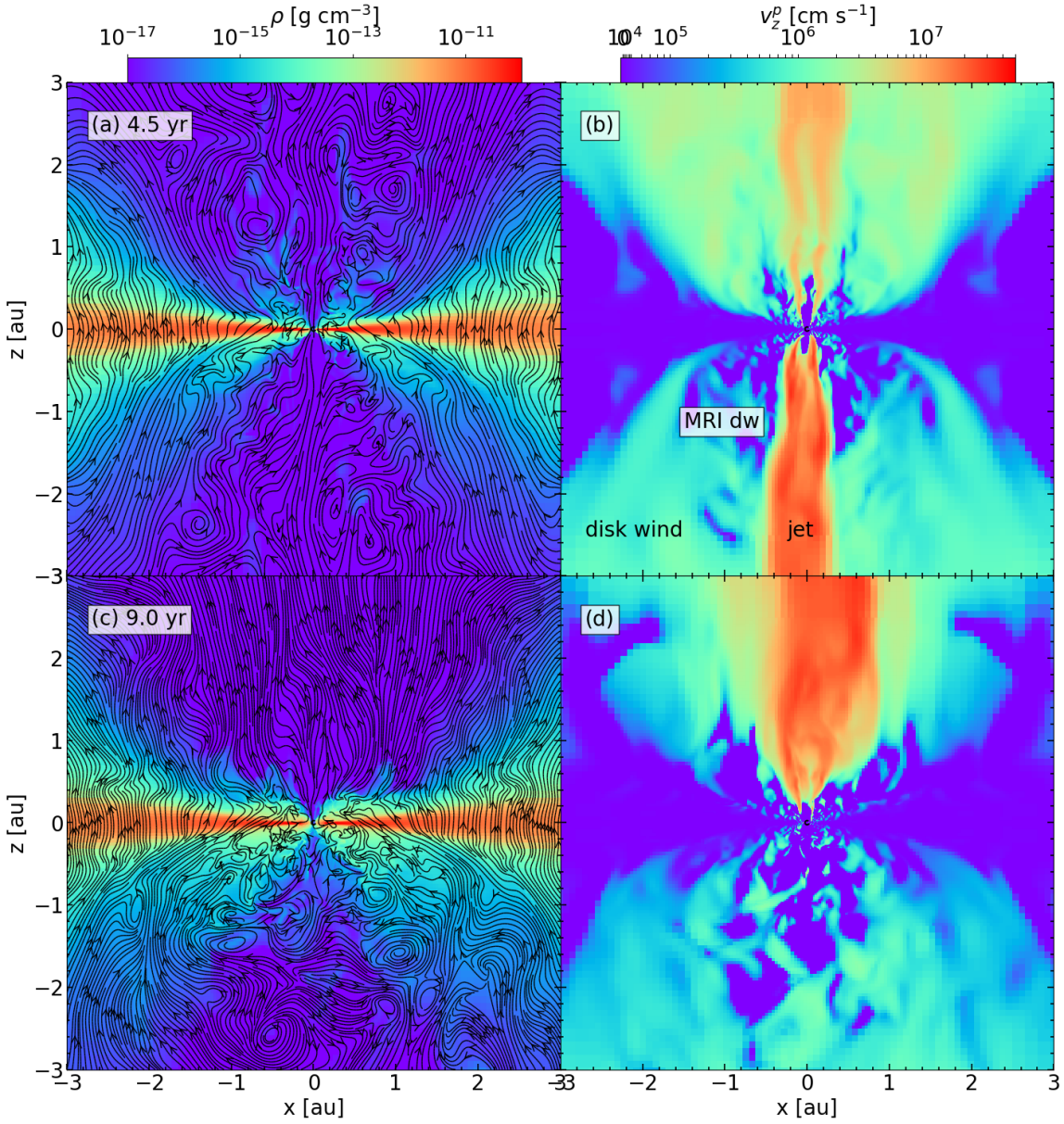


Figure 6.2: Overview of the simulation result, showing a slice through the plane at $y = 0$. The upper and lower panels show two representative times at 4.5 and 9.0 yr, respectively. Panels (a) and (c) show the density, and panels (b) and (d) show the projected z direction velocity (equ. 6.18). The three main components of the outflow - jet, disk wind, and MRI-active disk wind (MRI DW) - are labeled in panel (b). An animated version is available at `https://figshare.com/s/8b13ca47b44adf6e3db9`. The animated version is 50 seconds long, showing an overview of our simulation result and the evolution of the outflow in our model.

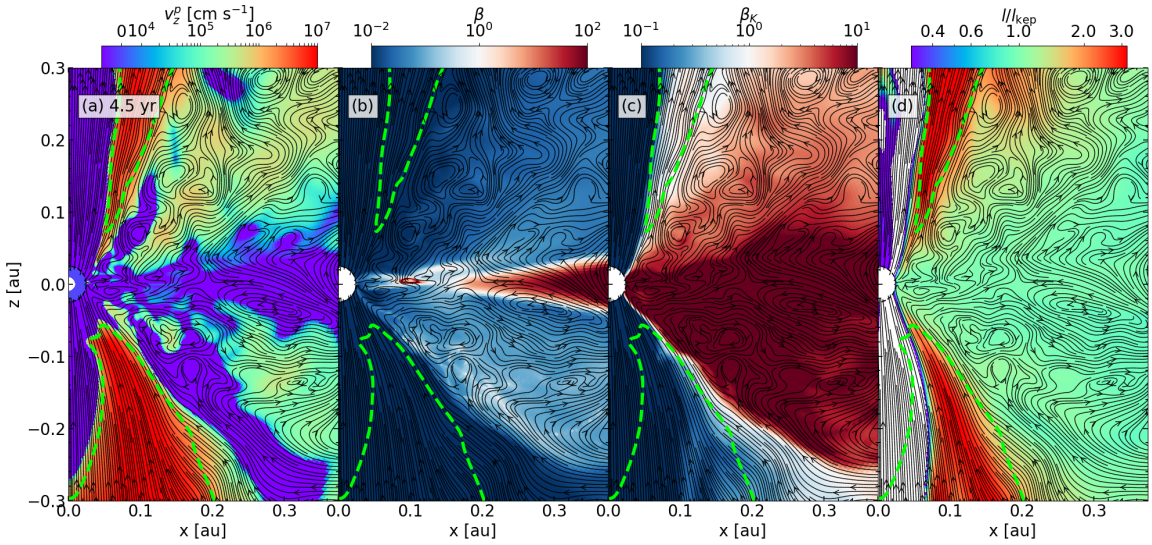


Figure 6.3: The gas properties near the base of the jet. Plotted are the azimuthally averaged projected z direction velocity (equ. 6.18), plasma-β, kinetic-β (equ. 6.19), and the comparison between the local specific angular momentum and the Keplerian value, respectively, at a representative time $t = 4.5$ yr. The green contour highlights the lower part of the jet (where $v_z^p \geq 3 \times 10^6$ cm/s), where the plasma-β is much less than unity, and the kinetic-β is close to or less than unity. An animated version is available at `https://figshare.com/s/219f51de0c77cbcf17f1`. The animated version is 25 seconds long, showing an overview of the jet properties in our model.

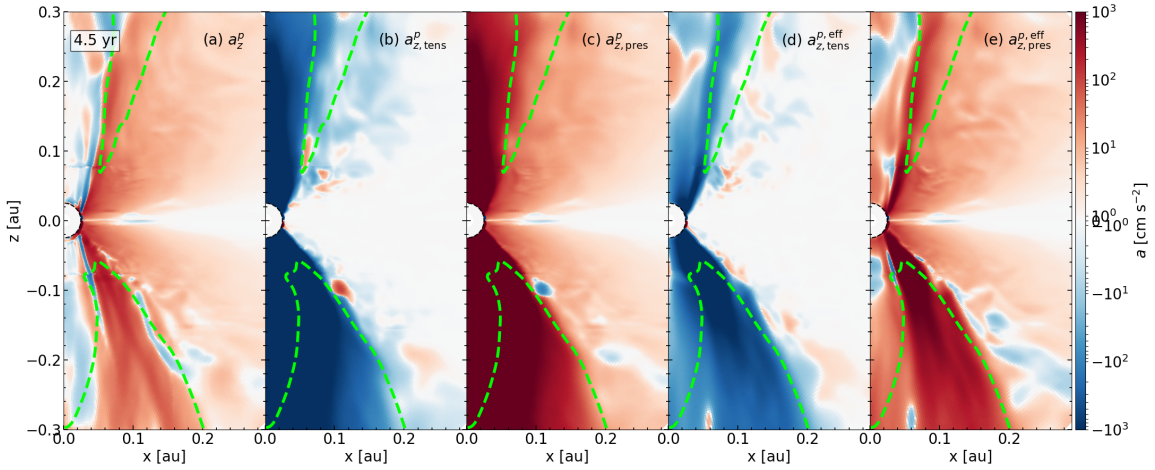


Figure 6.4: The gas acceleration near the base of the jet. The values are the $\hat{z}$-projected values, where a positive value means the force is pointing away from the disk midplane and a negative value points towards the midplane. The five panels show the total magnetic acceleration, gas acceleration due to magnetic tension, gas acceleration due to magnetic pressure, the gas acceleration due to the "effective magnetic tension" (defined in equ. 6.24), and the gas acceleration due to the "effective magnetic pressure" (defined in equ. 6.23). The outflow is launched by the toroidal magnetic pressure gradient, which provides the acceleration away from the disk in both the upper and lower hemispheres. Magnetic tension is unable to launch an outflow as it points towards the disk. An animated version is available at `https://figshare.com/s/d0d617e992b70dd720fb`. The animated version is 50 seconds long, confirming that the magnetic forces remain consistent throughout the simulation and validating the representative frame shown here. It illustrates the dominant role of toroidal magnetic pressure in driving the outflow.

celeration (a_z^p, panel [a]), magnetic tension acceleration ($a_{z,\rm tens}^p$, panel [b]), magnetic pressure acceleration ($a_{z,\rm pres}^p$, panel [c]), and the projected $\hat{z}$-direction magnetic acceleration due to poloidal magnetic tension (panel [d]) and toroidal magnetic field gradient (panel [e]). The projected z-direction magnetic acceleration in cylindrical coordinates is defined as

$$a_z^p = \frac{z}{|z|}\Big[\frac{1}{4\pi\rho}(\nabla\times\boldsymbol{B})\times\boldsymbol{B}\Big]_z; \tag{6.20}$$

$$\begin{aligned} a_{z,\rm tens}^p &= \frac{z}{|z|}\Big[\frac{1}{4\pi\rho}(\nabla\cdot\boldsymbol{B})\boldsymbol{B}\Big]_z \\ &= \frac{z}{|z|}\frac{1}{4\pi\rho}\Big[B_R\frac{\partial B_z}{\partial R}+B_\phi\frac{\partial B_z}{\partial\phi}+B_z\frac{\partial B_z}{\partial z}\Big]; \end{aligned} \tag{6.21}$$

$$\begin{aligned} a_{z,\rm pres}^p &= -\frac{z}{|z|}\Big[\frac{1}{8\pi\rho}(\nabla\cdot\boldsymbol{B}^2)\Big]_z \\ &= -\frac{z}{|z|}\frac{1}{4\pi\rho}\Big[B_R\frac{\partial B_R}{\partial z}+B_\phi\frac{\partial B_\phi}{\partial z}+B_z\frac{\partial B_z}{\partial z}\Big], \end{aligned} \tag{6.22}$$

where the $\frac{z}{|z|}$ is the projection in the direction away from the disk midplane. Note that the z-direction magnetic acceleration term $B_z\frac{\partial B_z}{\partial z}$ is in both the magnetic tension acceleration (equ. 6.21) and the magnetic pressure acceleration (equ. 6.22) equations, and has opposite signs in these two equations, which means the *net* effect of the $B_z\frac{\partial B_z}{\partial z}$ term is zero in launching of the outflow. Thus we can rewrite equ. 6.22 excluding this term to define an "effective magnetic pressure acceleration"

$$\begin{aligned} a_{z,\rm pres}^{p,\rm eff} &= -\frac{z}{|z|}\frac{1}{4\pi\rho}\Big[B_R\frac{\partial B_R}{\partial z}+B_\phi\frac{\partial B_\phi}{\partial z}\Big] \\ &\approx -\frac{z}{|z|}\frac{1}{4\pi\rho}\frac{\partial B_\phi}{\partial z}B_\phi, \end{aligned} \tag{6.23}$$

The last approximation uses the fact that the toroidal field dominates the outflow region. A similar argument can be applied to equ. 6.21 to define an "effective magnetic

tension acceleration"

$$a_{\rm z,tens}^{p,\rm eff} = \frac{z}{|z|}\frac{1}{4\pi\rho}B_R\frac{\partial B_z}{\partial R}, \tag{6.24}$$

assuming azimuthal symmetry.

Fig. 6.4(d) and (e) illustrate these two effective accelerations. While $a_{z,\rm tens}^{p,\rm eff}$ always acts toward the disk and therefore cannot drive the jet, $a_{z,\rm pres}^{p,\rm eff}$ is directed away from the disk, playing a crucial role in jet acceleration. It overcomes $a_{z,\rm tens}^{p,\rm eff}$ and contributes positively to the net magnetic acceleration (a_z), as shown in Fig. 6.4(a). A geometric argument for why only magnetic pressure, not magnetic tension, can accelerate a jet will be presented in sec. 6.4. We stress here that the jet is primarily accelerated by the toroidal magnetic pressure gradient.

6.3.2 The disk wind

Surrounding the jet but further away from the polar axis is a slower disk wind (e.g. fig. 6.2[b]). The z-direction gas velocity in the disk wind is around 10^6cm s^{-1}, which is slower than the jet. In this section, we focus on the launching mechanism of the disk wind.

Fig. 6.5(a) shows the v_z^p in the disk wind region. The disk wind is the region between the cyan dashed line (the approximate boundary between the jet and the disk wind) and the magenta line (the boundary between the disk wind and the expanded disk atmosphere). Fig. 6.5(b) and (c) show the plasma-β and kinetic-β in the disk wind region respectively. While plasma-β is still well below order unity in the disk wind region, the kinetic-β is above unity. Unlike the jet, which is completely magnetically dominated, the kinetic energy (primarily from rotation) is important in the disk wind region. Similar to the jet, the specific angular momentum in the disk wind region exceeds the local Keplerian value (by a factor of at least 3, see Fig. 6.5[d]).

Because both magnetic and kinetic energy are important for the disk wind, we

will examine both the acceleration by the magnetic field and by momentum (centrifugal force) to understand the acceleration of the disk wind. Fig. 6.6 shows the centrifugal force in the cylindrical-$\hat{R}$ direction ($a_{R,\rm centrifugal}$), magnetic force in the cylindrical-$\hat{R}$ direction ($a_{R,\rm magnetic}$) and $\hat{z}$ directions, and effective magnetic pressure force (equ. 6.23) respectively. In the disk wind region, $a_{R,\rm centrifugal}$ opposes both the gravitational acceleration (g_R) and $a_{R,\rm magnetic}$, which direct inward. The magnitude of $a_{R,\rm centrifugal}$ exceeds the g_R by more than a factor of 2 and generally dominates over $a_{R,\rm magnetic}$. This outward dominance of centrifugal force over both the magnetic field and gravity (as shown in fig. 6.5[d], where the gas is super-Keperian in the disk wind region) drives the gas horizontally outward. In the $\hat{z}$ direction, magnetic force provides a $\hat{z}$-direction acceleration away from the disk midplane against gravity (fig. 6.6[c]). The net $\hat{z}$ direction acceleration is comparable to the net cylindrical-$\hat{R}$ direction acceleration, so the net acceleration moves diagonally on a meridional plane, which produces the wide-angle disk wind.

Similar to the jet, toroidal magnetic pressure is the main driver of the disk wind. Fig. 6.6(d) shows the effective $\hat{z}$-direction magnetic acceleration (equ. 6.23), which is very similar to the total $\hat{z}$-direction magnetic acceleration (Fig. 6.6[c]). A similar geometric argument can be used to illustrate why only magnetic pressure can drive a z-direction acceleration, and we leave the detailed illustration to sec. 6.4.1.

6.3.3 The MRI-active turbulent inner disk wind

The inner portion of the disk wind at low altitudes (e.g., near $(x, z) = (1, 1)$ au in fig. 6.6) is a region where the magnetic force alternates between dominating gravity in the vertical direction and being less than it. To show the difference between this region and the jet and the disk wind more vividly, Fig. 6.7 shows a horizontal slice of the v_z^p at $z = -1.0$ au. The jet stands out at the center as the circular structure

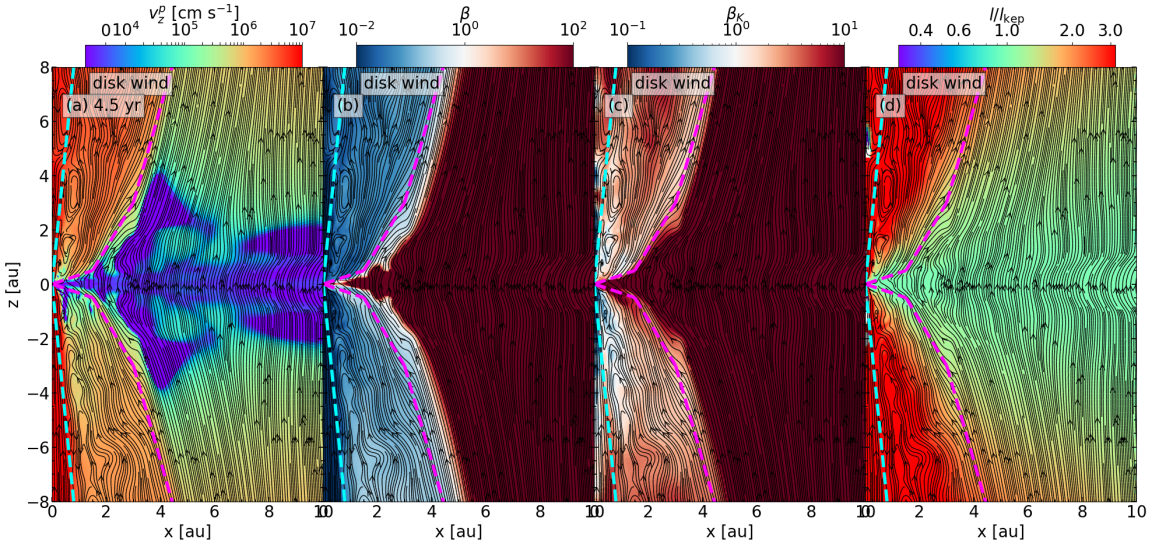


Figure 6.5: The gas properties of the disk wind. The four panels show the same quantities as in fig. 6.3, at the same representative time but on a larger scale. The cyan line shows the approximate boundary between the disk wind and the jet, and the magenta line shows the approximate boundary between the disk wind and the expanded disk atmosphere. Compared to the jet, the disk is less magnetically dominated as the kinetic-β is above order unity. An animated version is available at `https://figshare.com/s/668556d9b7090225b367`. The animated version is 25 seconds long, showing an overview of the disk wind launched in our model.

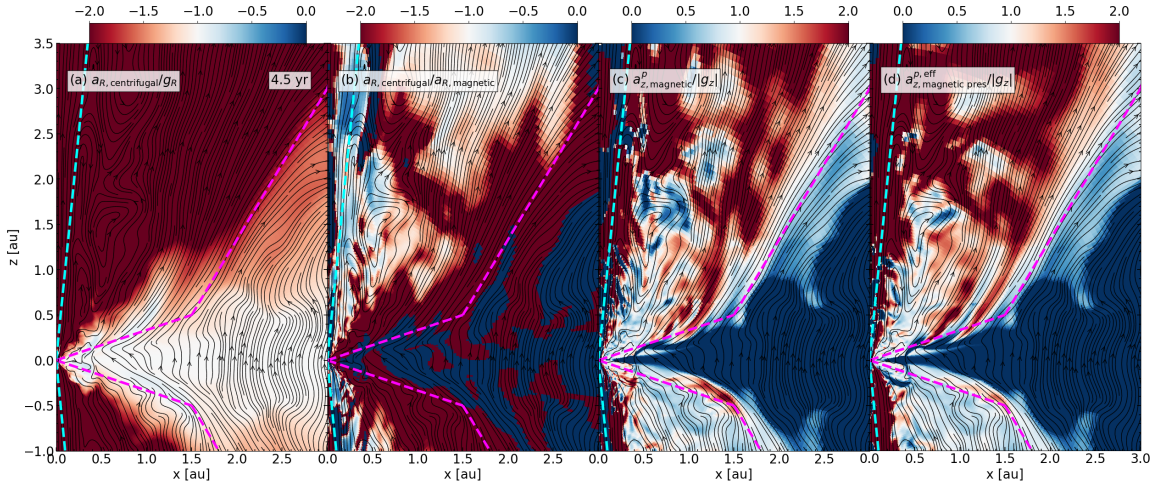


Figure 6.6: A comparison between different forces in the disk wind. **Panel (a)** shows the ratio between the centrifugal acceleration and the gravitational acceleration in the cylindrical-$\hat{R}$ direction; **panel (b)** shows the ratio between the centrifugal acceleration and magnetic acceleration. Negative values in panels (a) and (b) indicate that the centrifugal acceleration points in the opposite direction to both gravity and the magnetic field. **Panel (c) and (d)** show the $\hat{z}$ direction magnetic acceleration and $\hat{z}$ direction "effective" magnetic pressure acceleration (defined in equ. 6.23) normalized by gravitational acceleration in the $\hat{z}$ direction respectively. Toroidal magnetic pressure drives the disk wind upwards in the $\hat{z}$ direction. An animated version is available at `https://figshare.com/s/86c130e6b25e55d81200`. The animated version is 50 seconds long, showing the force ratios in the disk wind are similar to those in the representative frame we show here throughout the simulation.

moving at a speed $> 10^7$ cm s^{-1}. The disk wind is the slower outward-moving ring located at $R \approx 1.5 \sim 2$ au. Between the jet and the disk wind is a region with slow outflow *and* slow infall. This middle region, an MRI-active turbulent disk wind region, separates the jet from the outer laminar disk wind.

To illustrate the physical origin of the MRI-active turbulent disk wind region, we show the azimuthally-averaged v_z^p in Fig. 6.8(a). The green lines denote rough boundaries between the jet, the middle MRI-active turbulent disk wind region, and the more laminar disk wind at a larger cylindrical radius. The velocity streamlines are overplotted in Fig. 6.8, showing that the middle region identified in Fig. 6.7 originates around the boundary between the dead zone and active zone of the disk. Fig. 6.8(b) shows the ratio between the $\hat{\phi}$-direction velocity and the local Keplerian velocity, where the base of the middle region stands out as the sub-Keplerian region sandwiched between the super-Keplerian jet and super-Keplerian disk wind. Because the velocity streamlines are more chaotic in the middle region than in both the jet and the disk wind, the magnetic field lines (shown in Fig. 6.8[b]) are also more tangled in the MRI-active turbulent disk wind region. This disordered magnetic fieldline means that the usual expectation that angular momentum can be transferred along an (ordered) magnetic field line to gas at a larger cylindrical radius cannot be met in the MRI-active turbulent disk wind region. Thus, the disk surface in the MRI-active turbulent disk wind region expands outward as a result of magnetic pressure without gaining angular momentum, resulting in the sub-Keplerian region.

The reason for the chaotic gas flow pattern and the disordered fieldline in the middle region is that this region is unstable to turbulence induced by magneto-rotational instability (MRI). The most unstable turbulent MRI wavelength is given by (Noble

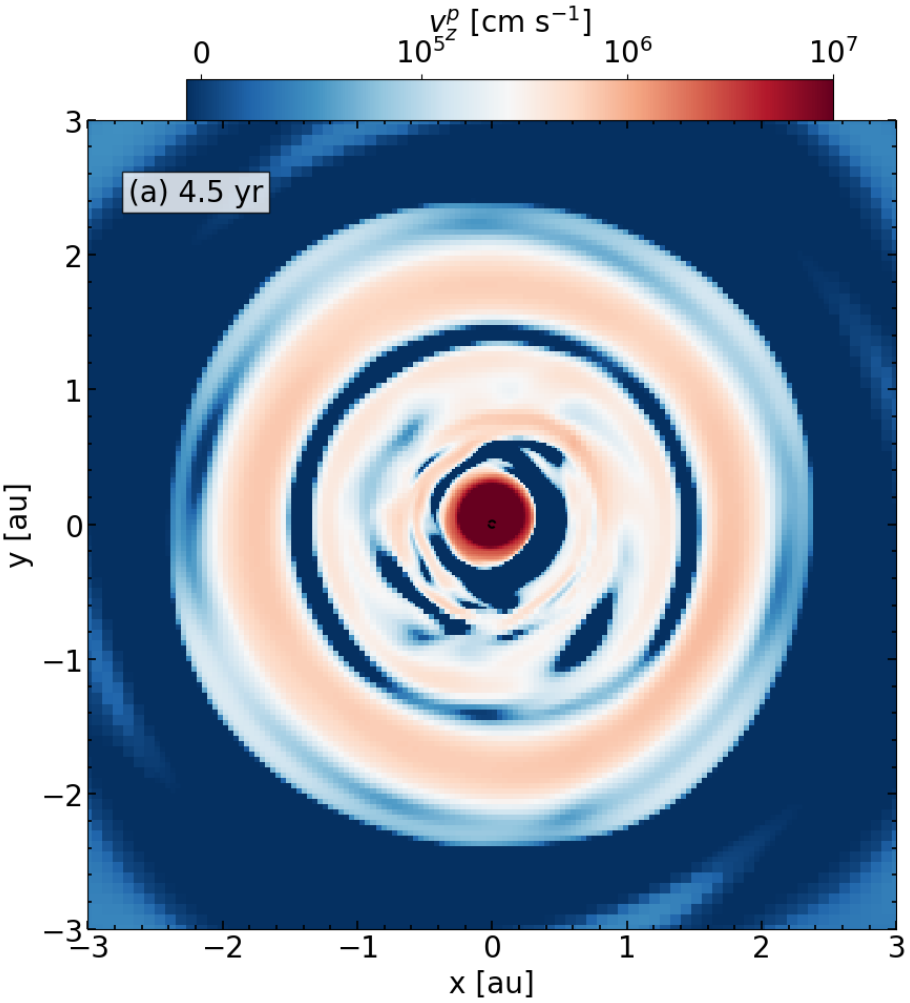


Figure 6.7: A x-y slice through the simulation domain at $z = -1.0$ au showing the projected z-direction velocity (equ. 6.18). The jet stands out at the center of the slice as the dark red (with $v_z^p \geq 10^7$ cm/s) circle with radius ~ 0.3 au; the disk wind is the annulus in lighter red at ~ 1.5 au; in between the jet and the disk wind is the MRI-active turbulent disk wind, where the gas alternates between infall toward the disk and outflow. An animated version is available at `https://figshare.com/s/5d5a3c8cb83a94170519`. The animated version is 50 seconds long, showing the outflow structure described above is persistent in our model before the MRI-active turbulent disk wind chokes the jet at later times.

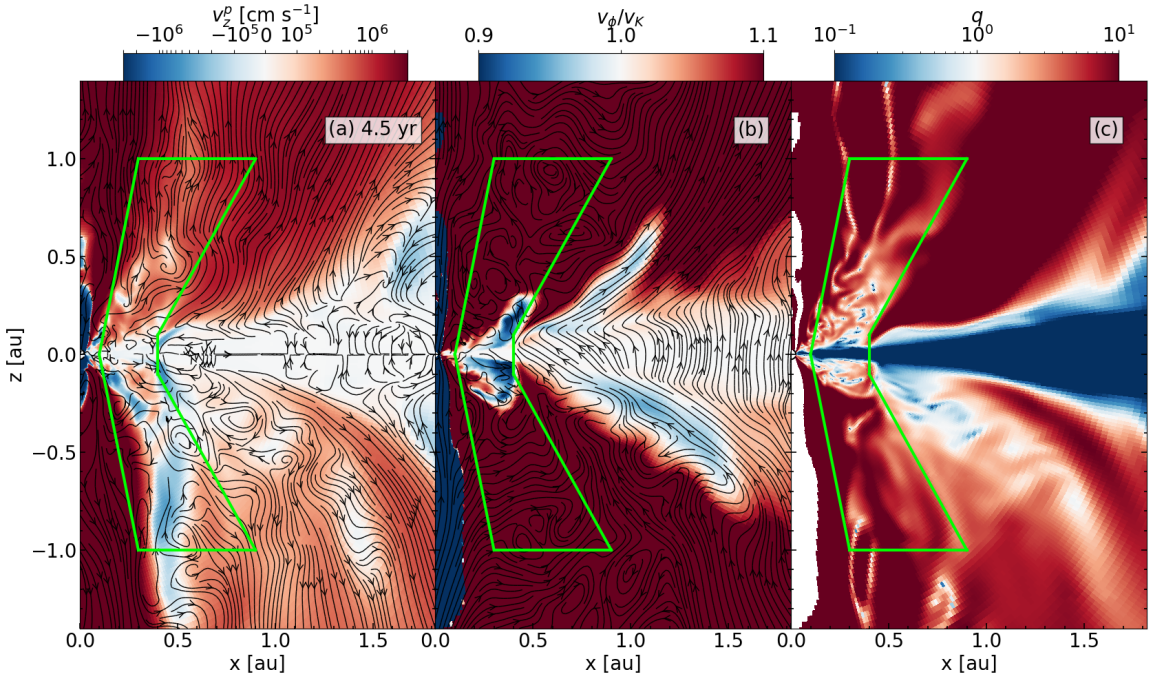


Figure 6.8: Properties of the MRI-active turbulent disk wind region, enclosed by the green line. **Panel (a)** shows the projected z-direction velocity (equ. 6.18), overplotted with velocity streamlines; **panel (b)** shows the ratio between local rotation velocity v_ϕ and the local Keplerian velocity v_K, overplotted with magnetic field lines. **Panel (c)** shows the normalized most unstable MRI wavelength (equ. 6.26), where $10^{-1} < q < 10^1$ is the most optimal range to activate MRI. An animated version is available at `https://figshare.com/s/2a211268b205eb9a2dd1`. The animated version is 25 seconds long, showing the evolution of the MRI active turbulent disk wind region in our model. The highlighted features in each panel are persistent in the animation.

et al., 2010)

$$\lambda = 2\pi\sqrt{\frac{16}{15}}\frac{v_A}{\Omega}. \tag{6.25}$$

For MRI to be active, the wavelength must not be too long such that the MRI wavelength cannot fit into the disk (Porth et al., 2021), and the wavelength must also not be too short such that the MRI effect is too weak (Balbus & Hawley, 1991; Hawley & Balbus, 1991). To identify the region where MRI is active, we first define a dimensionless wavelength

$$q = \frac{\lambda}{H} \approx \frac{\lambda}{R/10}, \tag{6.26}$$

where H is the scale height of the disk, which can be approximated by one-tenth of the cylindrical radius R. The MRI operates most efficiently when q is of order unity, which motivates us to adopt, for illustrative purposes, the range $0.1 < q < 10$ where the most unstable wavelength is neither too long nor too short.

Fig. 6.8(c) shows q: while the jet, the disk wind, and the disk are all MRI stable ($q > 10$ in the disk wind and the jet; $q < 0.1$ in the disk), the MRI-active turbulent disk wind region lies within the optimal range of MRI. Because this inner disk wind region is MRI-active, both velocity and magnetic field are far from laminar. Thus, although the gas is still moving away from the disk due to the magnetic pressure gradient (Fig. 6.4[c]), an ordered outflow cannot be launched in this region.

The lack of an ordered outflow at a low altitude does not translate to the complete absence of an outflow. When MRI cannot be sustained at a higher altitude, the MRI-active turbulent disk wind becomes a laminar, ordered disk wind. This transition is illustrated in Fig. 6.8(a), where the gas above the region enclosed by the green line is more laminar than the gas within due to MRI not being able to be sustained at a higher altitude (Fig. 6.8[c]). The gas, after the transition from turbulent to laminar, becomes part of the slower disk wind surrounding the jet.

In summary, both the jet and the disk wind are driven by toroidal magnetic pressure. The region responsible for launching the jet is primarily governed by the magnetic field, while the disk wind-launching region is dominated by kinetic energy, with centrifugal forces acting to widen the opening angle of the disk wind. The jet and disk wind are distinct outflows, separated by an MRI-active turbulent disk wind zone, which becomes part of the disk wind at a large altitude when the MRI-induced turbulence can no longer be sustained.

6.4 A lightly-loaded toroidal magnetic field pressure-driven jet

6.4.1 A geometric argument for magnetic field structure above and below the disk

In this section, we present a geometric argument that an outflow can only be launched by a toroidal field pressure gradient, and tension cannot launch an outflow in a global model.

The geometry of the magnetic field is illustrated in Fig. 6.9 in the outflow-launching region. Assuming global $B_z > 0$, $B_\phi < 0$ in the upper hemisphere because the disk has a faster speed compared to the atmosphere; $\frac{dB_\phi}{dz} > 0$, the strength of (the negative) toroidal magnetic field decreases with height due to the decrease of differential rotation at a higher altitude. Thus, the effective magnetic pressure force (equ. 6.22), $a^{p,\mathrm{eff}}_{\mathrm{z,pres}} > 0$, capable of launching an outflow.

The effective magnetic tension force (equ. 6.24), however, always points towards the disk midplane. $B_R > 0$ in the upper hemisphere both because of geometry in the jet-launching region (Fig. 6.3) and the excess of specific angular momentum in the

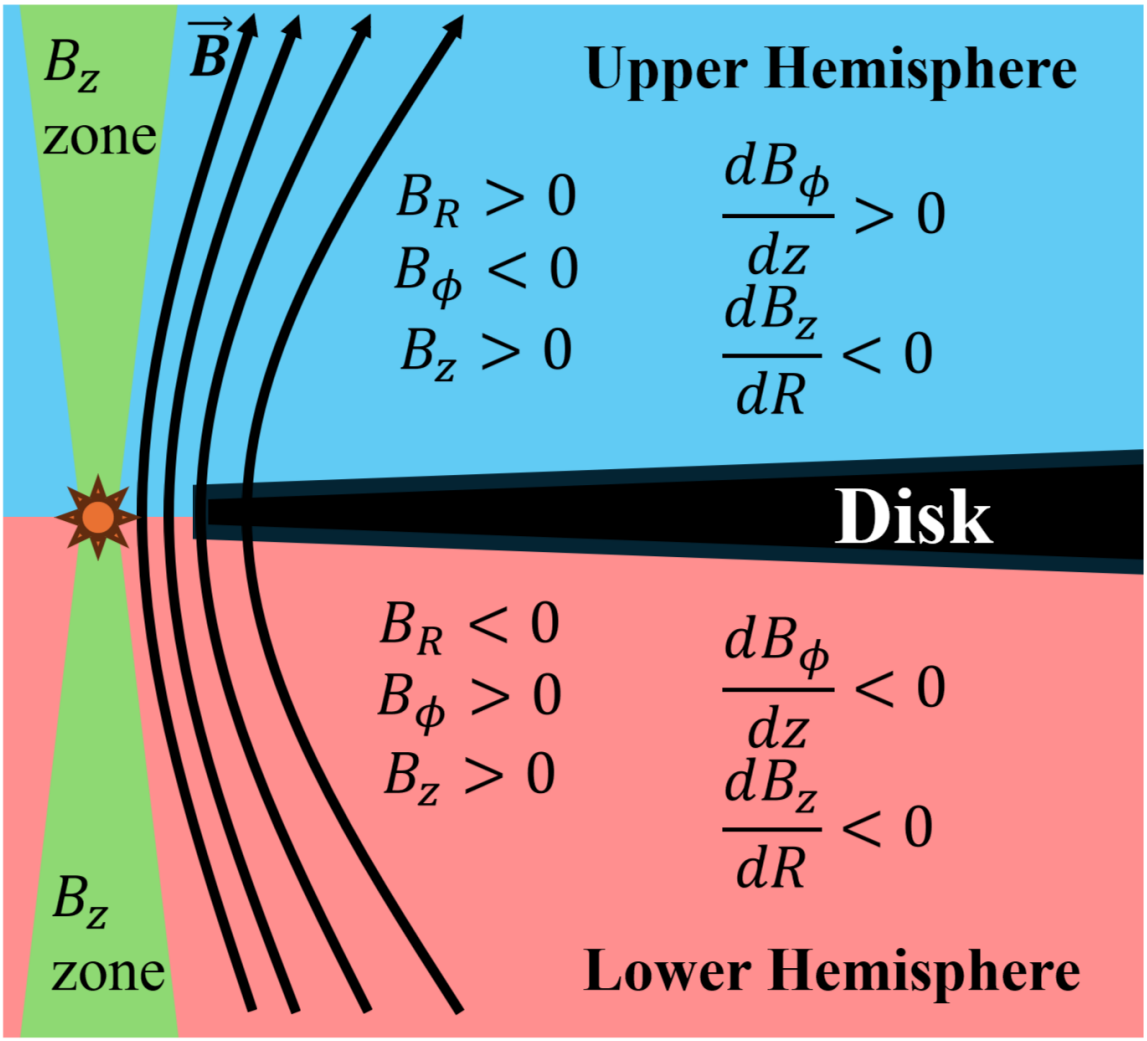


Figure 6.9: Geometric argument for the magnetic field geometry (sec. 6.4.1), assuming the disk is threaded by open, $+\hat{z}$-direction magnetic field lines. The signs of the magnetic field and two magnetic field gradients above and below the disk in cylindrical coordinates are shown for the upper and lower hemispheres, respectively, showing magnetic tension force (equ. 6.24) is unable to drive an outflow, whereas magnetic pressure force (equ. 6.23) can.

disk wind region (Fig. 6.5[d]); $\frac{dB_z}{dR} < 0$, the strength of B_z decreases as cylindrical radius increases. As a result, $a^{p,\mathrm{eff}}_{\mathrm{z,tens}} < 0$, which points to the midplane and is unable to launch an outflow.

This geometric argument and the force analysis (Fig. 6.4) both show that toroidal magnetic pressure launches an outflow (the jet and the disk wind). The only role of rotation is to generate the B_ϕ in the mass-dominated disk required to launch the outflow. Using the same geometric argument, we can show that $B_\phi < 0$ in the upper hemisphere and $B_\phi > 0$ in the lower hemisphere. The B_ϕ in the disk varies in the simulation, determining the location of the "avalanche accretion stream"–a crucial component in jet launching.

6.4.2 B_ϕ in the disk

We have established in sec. 6.3.3 that the inner disk region is turbulent due to MRI. One consequence of being turbulent is that B_ϕ appears to take only one sign in most of the inner disk, probably because rapid magnetic reconnection due to MRI turbulence tends to remove B_ϕ of the opposite direction quickly, particularly in the inner disk region where plasma-$\beta < 1$ (fig. 6.3). This is illustrated in Fig. 6.10 panels (a) and (e), which show B_ϕ at 4.5 and 9.0 yr, respectively. At 4.5 years, B_ϕ is almost universally negative in the disk (albeit a negligible positive B_ϕ region exists), and at 9.0 years, B_ϕ switches to fully positive in the disk.

The sign change in the disk from 4.5 to 9.0 yr is due to one exception to this one-sign rule: the disk B_ϕ can switch sign when B_ϕ changes sign at the region where B_ϕ is most rapidly generated, located at the innermost disk around the inner boundary. In this case, the B_ϕ in the disk would gradually switch to the opposite sign as the B_ϕ of the opposite sign slowly takes over the entire disk. Readers are encouraged to view the animated version of Fig. 6.10 for the transition from negative B_ϕ in the disk at

4.5 yr to positive B_ϕ at 9.0 yr.

6.4.3 Avalanche accretion streams

The avalanche accretion stream is most prominent where the azimuthal magnetic field, B_ϕ, changes sign. Figure 6.10 illustrates such streams at 4.5 and 9.0 yr in the upper and lower rows, respectively. The dense avalanche accretion stream resides where B_ϕ spatially changes sign and the meridian magnetic field line sharply pinches (highlighted by the arrows in the two leftmost panels). Because the avalanche accretion stream is a consequence of magnetic braking that removes angular momentum (Zhu & Stone, 2018; Tu et al., 2025c), the locations where the azimuthal magnetic field pinches (where B_ϕ changes sign) are the most ideal for forming an avalanche accretion stream. Magnetic energy is generated in the disk by differential rotation, producing the toroidal magnetic field, with a magnetic energy density similar in both hemispheres of the disk atmosphere at 4.5 and 9.0 yr (Fig. 6.10[c], [g]). However, while the overall magnetic energy density remains comparable, the magnetic energy per unit mass is more abundant in the upper hemisphere at 9.0 yr, resulting in the differences in the outflows launched from each hemisphere.

The MRI-active inner disk can expand vertically because of the toroidal magnetic pressure. As illustrated in Fig. 6.8, this expansion can reach a high altitude. In some extreme cases, this expansion can fill the entire disk atmosphere, including the jet-launching zone around the polar region, which can choke the jet by loading too much mass onto the magnetic fields. This is the case in the lower hemisphere at 9.0 yr, where the polar region is filled with high-density gas (Fig. 6.10[f]), and no fast jet is launched (Fig. 6.2). In the upper hemisphere at 9.0 years, however, the avalanche accretion stream stops the disk expansion. Because B_ϕ must change sign somewhere in the upper hemisphere, the magnetic field line is pinched azimuthally

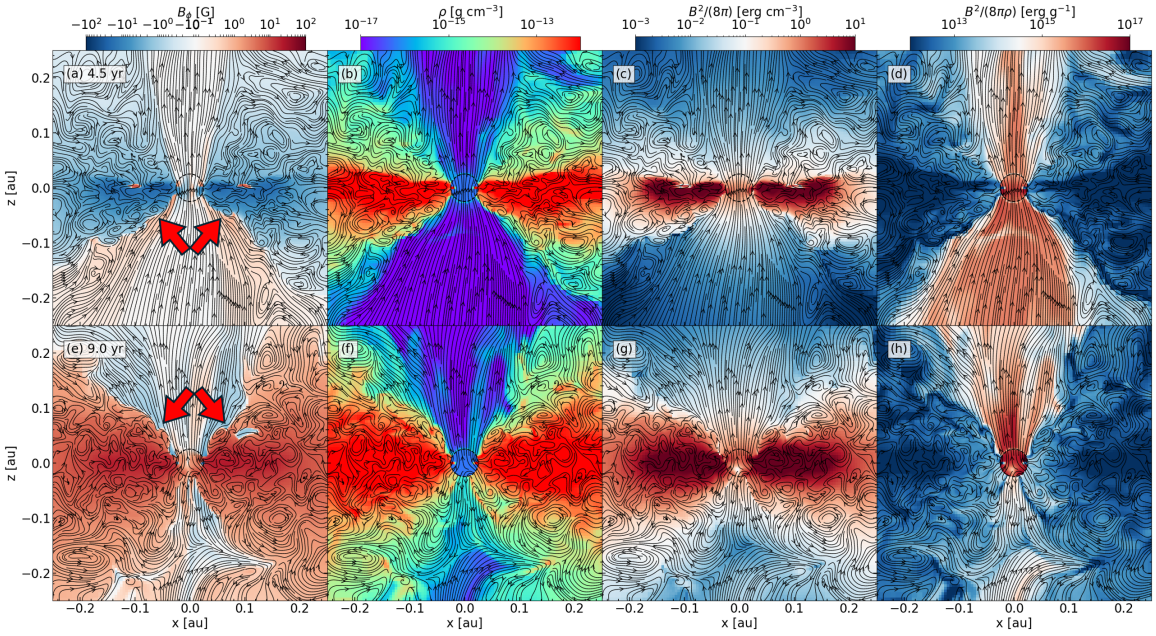


Figure 6.10: Properties of the disk surface avalanche accretion stream and the jet-launching cavity at two representative times: 4.5 yr (upper panels) and 9.0 yr (lower panels). The arrows in the two leftmost panels point to the locations of the avalanche accretion stream. **Panels (a) and (e)** show B_ϕ, which switches direction inside the disk between 4.5 yr and 9.0 yr. **Panels (b) and (f)** display the gas density distribution. The disk surface avalanche accretion stream is located where B_ϕ switches sign spatially, roughly coinciding with the pinching of poloidal magnetic field lines. Low-density outflow cavities exist in both hemispheres at 4.5 yr (larger in the lower hemisphere), but much more prominently in the upper hemisphere at 9.0 yr, where B_ϕ spatially changes sign. **Panels (c) and (g)** illustrate the magnetic energy density, symmetric about the disk midplane at both times. **Panels (d) and (h)** show the magnetic energy per unit mass, which is large only in the low-density outflow cavities. An animated version can be found at `https://figshare.com/s/763d65cae5aa7d452442`. The animated version is 50 seconds long, showing the evolution of the magnetic field structure and magnetic energy density evolution in our model. The animation highlights the role of the avalanche accretion stream, located where B_ϕ switches sign, in limiting the disk expansion and facilitating jet launching.

where $B_\phi = 0$, resulting in strong magnetic braking and facilitating a fast infall. This infall stream naturally separates the heavily mass-loaded raised inner disk atmosphere (where kinetic-$\beta > 1$) and the lightly loaded jet-launching zone in the polar region (where kinetic-$\beta < 1$) near the rotation axis through the formation of an avalanche accretion stream that typically starts somewhere above the inner active zone and ends close to the central radial boundary. The separation reduces the mass-loading in the jet-launching region, allowing a strong magnetic field to accelerate a small amount of gas mass there (Fig. 6.10[h]), forming a jet.

The absence of B_ϕ switching sign in the disk atmosphere, which is necessary for forming an avalanche-accretion stream, is less favorable for jet launching. However, a jet can still form through a similar magnetic-pressure driven mechanism if the polar region remains lightly loaded—that is, if it is not filled with mass lifted by the inner disk MRI-induced turbulence. This is the case for the upper hemisphere at 4.5 yr (Fig. 6.10 upper row): although B_ϕ is ubiquitously negative there, the polar region is not filled with dense gas, so a jet can still be launched. It is, however, less developed (i.e. slower) than the jet in the lower hemisphere at the same time (see, e.g., Fig. 6.2[b]), where a prominent avalanche stream with B_ϕ reversal separates the dense disk atmosphere and much less dense jet zone.

6.4.4 Jet from magnetic energy release in the polar cavity

The low-density polar cavity above the avalanche accretion stream is an ideal environment for jet launching. The magnetic field generated in the disk and along the avalanche accretion stream stores a large amount of energy (Fig. 6.3[c]), and it can drive a jet if the energy is transferred to a small amount of mass. To examine the jet-launching mechanism from an energetic perspective, we demonstrate energy advection and conversion in the jet-launching cavity in this section.

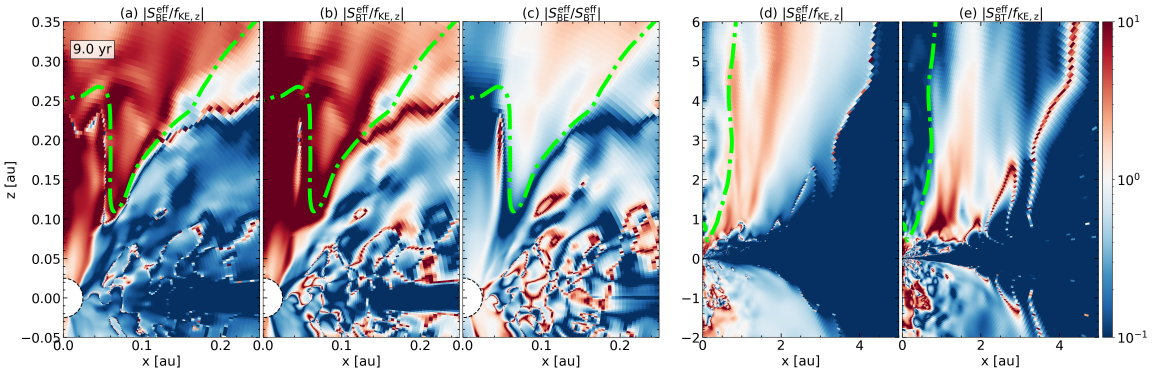


Figure 6.11: Ratios between energy advection through two components of the Poynting flux and gas kinetic energy *for the jet*, outlined by the cyan contour. The left three panels focus on the base of the jet, and the cyan contour is at 10^6 cm s^{-1}. The right two panels zoom out to larger scales, with the cyan contour at 10^7 cm s^{-1}. **Panel (a)** shows the ratio between the magnetic pressure component of the Poynting flux (equ. 6.30) and kinetic energy flux in the $\hat{z}$ direction; **panel (b)** shows the ratio between the magnetic tension component of the Poynting flux (equ. 6.31) and kinetic energy flux, and panel (c) shows the ratio between magnetic energy and tension components of the Poynting flux, illustrating the dominance of energy transportation by the advection of the toroidal field. **Panels (d) and (e)** show the same ratios as panels (a) and (b), but on a larger scale. Kinetic energy flux gradually becomes more important as the jet propagates to a larger distance.

The energy advection is described by the MHD energy equation

$$\frac{dE}{dt} + \nabla \cdot \Big[\Big(\frac{1}{2}\rho \boldsymbol{v}^2 + P + h + \frac{B^2}{4\pi}\Big)\boldsymbol{v} - \frac{1}{4\pi}\boldsymbol{B}(\boldsymbol{B}\cdot\boldsymbol{v}) + \boldsymbol{Q}\Big] = 0, \tag{6.27}$$

where P is the gas thermal pressure; h is the gas internal energy and $\boldsymbol{Q}$ is the heat flux. Since magnetic and fluid kinetic energy fluxes dominate in a jet-launching system, we can keep only two terms while ignoring the others: the kinetic energy flux

$$f_{\rm KE} = \frac{1}{2}\rho v^2 \boldsymbol{v} \tag{6.28}$$

and magnetic energy flux, which is equivalent to the Poynting flux

$$\boldsymbol{S} = \frac{1}{4\pi}(-\boldsymbol{v}\times\boldsymbol{B})\times\boldsymbol{B} = \frac{1}{4\pi}\Big[B^2\boldsymbol{v} - \boldsymbol{B}(\boldsymbol{B}\cdot\boldsymbol{v})\Big]. \tag{6.29}$$

The Poynting flux consists of a magnetic energy advection term and a magnetic tension energy term. In the jet-launching cavity, we focus on the energy advection in the $\hat{z}$ direction. Using a similar argument as in decomposing the magnetic force into effective pressure and effective tension by removing the two terms canceling each other (as done in the derivation of equ. 6.23, 6.24), we can define the "effective magnetic energy advection" as

$$S^{\rm eff}_{\rm BE} = \frac{1}{4\pi}(B_R^2 + B_\phi^2)v_z, \tag{6.30}$$

and the "effective energy advection due to magnetic tension" as

$$S^{\rm eff}_{\rm BT} = -\frac{1}{4\pi}(B_z B_R v_R + B_z B_\phi v_\phi). \tag{6.31}$$

To quantify how energy is advected in the jet-launching cavity, we show the azimuthally-

averaged ratios between $S_{\rm BE}^{\rm eff}$, $S_{\rm BT}^{\rm eff}$, and $f_{\rm KE,z}$ in Fig. 6.11. Panels (a), (b), and (c) focus on the small scale near the base of the jet; panels (d) and (e) show the former two ratios on larger scales. The cyan line outlines the rough location of the outflow. Below the base of the outflow (below the dashed cyan line in fig. 6.11), $S_{\rm BT}^{\rm eff}$ dominates energy transportation over both $S_{\rm BE}^{\rm eff}$ and $f_{\rm KE,z}$. Within the outflow, $S_{\rm BE}^{\rm eff}$ dominates over both $S_{\rm BT}^{\rm eff}$ and $f_{\rm KE,z}$: energy is transported mostly by the advection of toroidal magnetic field. At a larger scale, $f_{\rm KE,z}$ dominates both magnetic terms in the jet as the magnetic energy carried by the toroidal magnetic field is converted into kinetic energy.

To illustrate the connection between the avalanche accretion stream (Section 6.4.3) and energy release, Figure 6.12 traces the 3D spatial evolution of a representative jet-launching magnetic fieldline. Fig. 6.12(a) depicts three consecutive fieldlines along the avalanche accretion stream, each passing through the magnetic pinching point (marked by dots) in the accretion stream, which serves as the reference origin ($s = 0$, the vertical dashed line in panels [b]-[g]) for analyzing physical quantities along the fieldlines. A second point on each fieldline marks the outflow base (where $v_r = 0$), corresponding to the other vertical dashed line (at $s \approx 0.075$ au) in panels (b)-(g) to establish spatial context.

Fig. 6.12(b) and 6.12(c) reveal a stark density contrast (about five orders of magnitude) and radial velocity reversal between the dense accretion stream ($\sim 10^{-12}$ g cm^{-3}) and the low-density outflow ($\sim 10^{-17}$ g cm^{-3}). In Fig. 6.12(d), the azimuthal velocity v_ϕ drops abruptly below the pinching point, signaling intense magnetic braking. The differential rotation around this braking point switches the sign of B_ϕ from positive in the disk to negative in the outflow, as shown in Fig. 6.12(e).

The similarities between the gas properties along the three consecutive fieldlines in Fig. 6.12 show a coherent evolution along the avalanche accretion stream where rapid

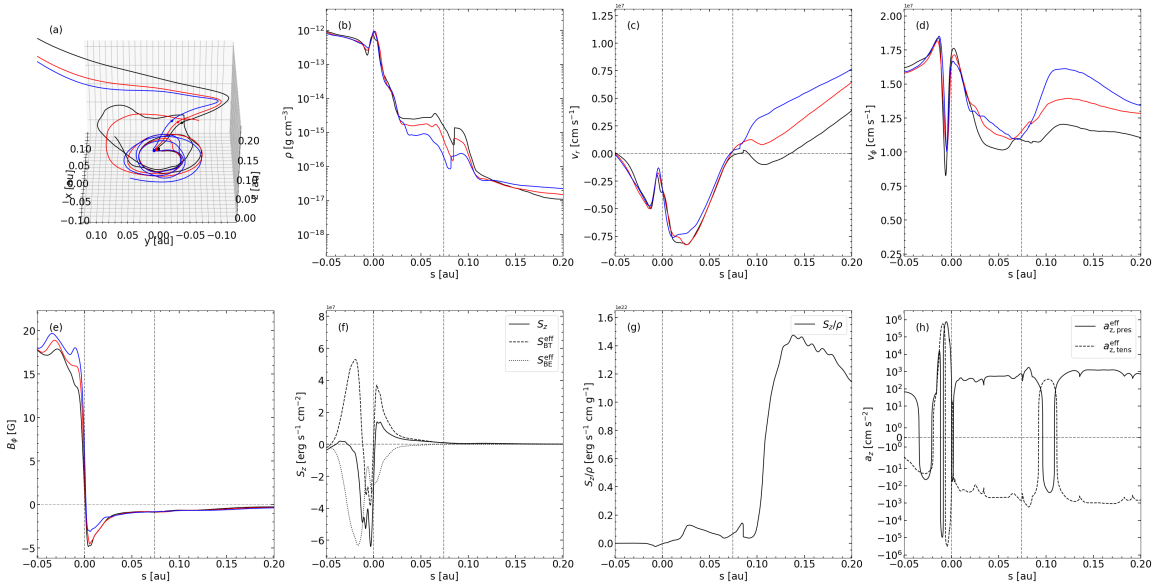


Figure 6.12: Quantities along magnetic field lines passing through the avalanche accretion stream. **Panel (a)** shows three consecutive fieldlines in 3D. The avalanche accretion stream is located at the pinching point of these fieldlines, marked by a solid dot. All other panels traces various quantities along these fieldlines, with $s = 0$ located at the solid dot and positive direction tracing the fieldline upward: the vertical dashed line at $s \approx 0.075$ au corresponds to the "star" along each magnetic fieldline. **Panels (b), (c), (d), and (e)** shows the density, radial direction velocity v_r, azimuthal velocity v_ϕ, and toroidal magnetic field B_ϕ respectively, with line colors matching the respective field lines in panel (a). The similarities between these three magnetic field lines show a consistent evolution along the magnetic field lines advected by the avalanche accretion stream. **Panels (f), (g), and (h)** focuses on the black fieldline in panel (a), showing Poynting flux (and its terms, defined in equ. 6.29, 6.31, 6.30 respectively), Poynting flux per unit mass, and magnetic acceleration on the gas (defined in equ. 6.23 and equ. 6.24) respectively. An animated version showing the 3D structure of the fieldlines is available at `https://figshare.com/s/ff9d053534f58e00f774`. The animation is 4 seconds long, showing a 3D view of panel (a)

infall, efficient magnetic braking, and magnetic field generation constantly supply twisted magnetic field to the outflow-launching cavity. In the following analysis, we will focus on one of the three highlighted fieldlines to illustrate the energy evolution. Immediately above the pinching point, the magnitude of (the negative) B_ϕ reaches a local maximum, and the energy is transported to the outflow-launching region primarily through magnetic tension ($S_{\rm BT}^{\rm eff}$): as the gas is infalling in this region, only magnetic tension can advect energy upstream into the outflow cavity. The magnetic energy flux per unit mass (S/ρ) is much higher in the polar cavity than in the disk (see panel [g]), making it possible to drive the jet to a high speed.

The dominance of magnetic tension in energy transport does not, however, imply its importance as the dominant force in accelerating the outflow. As shown in Fig. 6.12(h), only the magnetic pressure force acts outward (away from the disk); the tension force remains directed toward the mid-plane–a result consistent with the geometric arguments in Section 6.4.1.

To summarize, the jet-launching mechanism in our model operates as follows: energy is transferred from the dense, rapidly rotating gas in the disk to the magnetic field through the winding of the field within the magnetically active inner disk zone. When a polar density cavity forms—particularly on the side of the disk where the toroidal magnetic field changes sign and creates the avalanche accretion stream—the energy stored in the toroidal field can be released into the gas within the low-density cavity, leading to the formation of a fast jet. The model with a rotating inner boundary, "STROT", yields a qualitatively similar result, and we leave a comparison of the model "NOROT" without boundary rotation discussed here and the "STROT" model to Appendix. E.1.

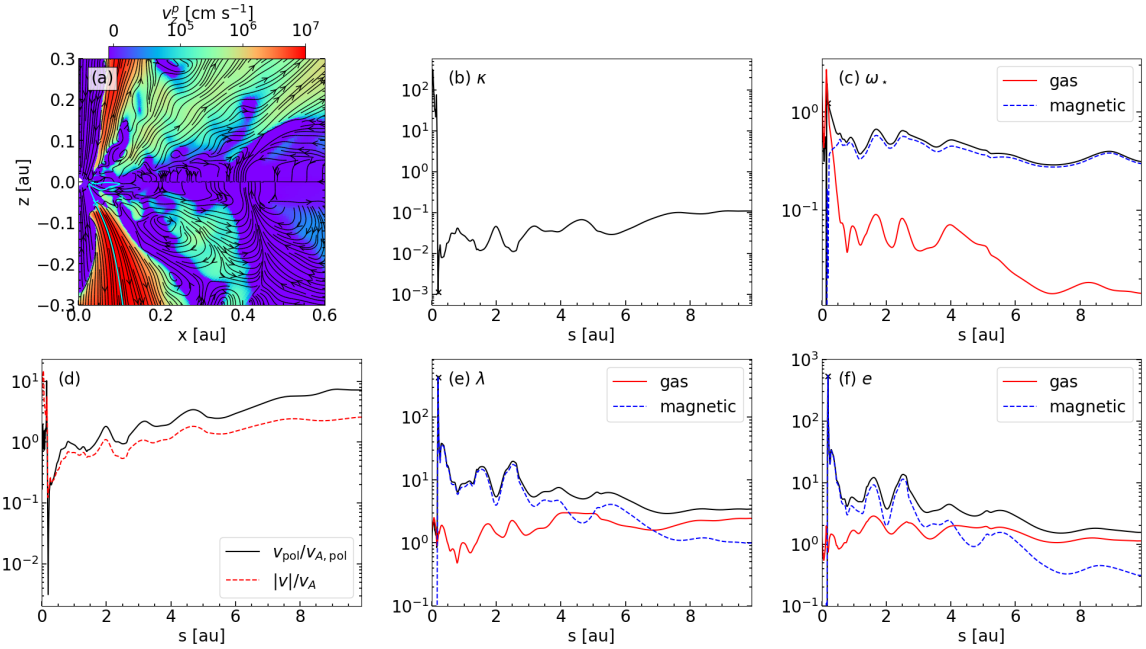


Figure 6.13: Quantities along a magnetic field line at the representative time $t = 4.5$ yr. All values are azimuthally averaged to minimize numerical effects. **Panel (a)** shows the projected v_z velocity (equ. 6.18). The representative field line analyzed is highlighted in cyan, where the positive direction traces the field line away from the disk midplane. **Panels (b), (c), (e), and (f)** shows the four dimensionless conserved quantity defined in equ. 6.36, 6.37, 6.38, 6.39 respectively. **Panel (d)** shows the Alfvénic Mach number and the poloidal Alfvénic Mach number along the magnetic field line.

6.5 Comparison to axisymmetric steady-state outflows

6.5.1 Connection to the axisymmetric steady-state outflow

The jet launched in our model is highly variable in time and non-axisymmetric (as seen, e.g., in the animated version of Fig. 6.1 and Fig. 6.7), but it shares some similarities with the axisymmetric steady-state MHD wind solutions. In this section, we will illustrate the similarities.

In a steady state, an effective method for understanding the outflow is to analyze quantities along a magnetic field line. If the poloidal velocity aligns with the poloidal magnetic field, this approach is qualitatively analogous to examining gas flow along a velocity streamline. Fig. 6.13(b), (c), (e), (f), and (h) are quantities along the magnetic field line highlighted by the cyan line in Fig. 6.13(a). The starting point of the field line is in the disk on the disk midplane, and the positive direction traces backward (relative to the magnetic field direction) along the field line away from the midplane in the lower hemisphere. We chose the lower half of this fieldline because the jet is more prominent in the lower hemisphere at the plotted time of the simulation (4.5 yr).

Kinematically, the gas changes from sub-Alfvénic to super-Alfvénic along a magnetic field line as a result of the conversion from magnetic energy to kinetic energy. Fig. 6.13(d) shows the poloidal Alfvén Mach number, calculated using only the poloidal component of the gas velocity and magnetic field, and the Alfvén Mach number, calculated using all components of velocity and magnetic field. Because the outflow region is initially dominated by the magnetic field, the gas first becomes super-poloidal Alfvénic at ~ 2 au. At ~ 4 au, the gas is fully super Alfvénic, and the importance of the magnetic field decreases along the magnetic field line.

In a steady-state axisymmetric MHD wind solution, there are four conserved quantities along a magnetic field line. Although the outflow in our model is highly time-dependent, it is still instructive to analyze these conserved quantities to make a connection between the toroidal-field launched jet model advocated in this paper and the classic magneto-centrifugal model (Salmeron et al., 2011; Zhu & Stone, 2018).

The first of the four quantities is

$$k = \frac{4\pi\rho v_{\rm pol}}{B_{\rm pol}}, \tag{6.32}$$

which corresponds to the mass loading of the outflow. The second is

$$\omega_s = \frac{v_\phi}{R} - \frac{kB_\phi}{4\pi\rho R}. \tag{6.33}$$

The third quantity

$$l = Rv_\phi - \frac{RB_\phi}{k} \tag{6.34}$$

corresponds to the angular momentum transported from the disk to the wind (Wang et al., 2019). The last is

$$E = \frac{1}{2}v^2 + \Phi - \frac{\omega_s RB_\phi}{k} + h, \tag{6.35}$$

the Bernoulli invariant corresponding to energy flux conservation along a field line (Shu et al., 2000; Konigl & Pudritz, 2000). h is the thermal energy, which is negligible compared to the magnetic energy and kinetic energy (Fig. 6.3,6.5). Following Tu et al. (2025c) and Jacquemin-Ide et al. (2021), we can non-dimensionalize these quantities using the gas quantities at the slow magneto-sonic point (denoted by SM, the location of the slow magneto-sonic point is marked by the "X" in Fig. 6.13)

$$\kappa = k\frac{v_{\rm K,SM}}{B_{\rm z,SM}} \tag{6.36}$$

$$\omega_\star = \frac{\omega_s}{\Omega_{\rm K,SM}}; \tag{6.37}$$

$$\lambda = \frac{l}{R_{\rm SM} v_{\rm K,SM}}; \tag{6.38}$$

$$e = \frac{E}{v_{\rm K,SM}^2}, \tag{6.39}$$

where the subscript K denotes the Keplerian value.

Fig. 6.13 shows these four dimensionless conserved quantities along the magnetic field line highlighted in Fig. 6.13(a). The mass loading parameter decreases from 10^2 to 10^{-2} as the field line goes from inside the disk into the jet-launching region and stays below 10^{-1} along the outflow, indicating that the magnetic field in the jet is lightly loaded with mass, as in the reference magneto-centrifugal wind solution of Blandford & Payne (1982). However, the normalized angular velocity, $\omega_\star$, while staying roughly constant along the field line, is substantially below unity (with an average value of order ~ 0.5), unlike the standard lightly loaded magneto-centrifugal wind. The angular momentum λ and the energy density e both hold almost a constant along the fieldline, despite a slight decrease at large distances. They are dominated by the magnetic field at small radii and transition to being gas-dominated along the fieldline at high altitudes (~ 5 au). These findings are broadly consistent with the results of Tu et al. (2025c).

6.5.2 Differences from the magneto-centrifugal model

The magneto-centrifugal model (as reviewed by, e.g., Spruit, 2010, and references within) proposes that jets are launched by centrifugal forces, as angular momentum is transferred outward along rigid magnetic field lines anchored in a rotating system. In this subsection, we illustrate that, despite some similarities between our model and the magneto-centrifugal model, the requirements and expectations of the magneto-centrifugal mechanism are not met in our model.

Geometrically, the poloidal magnetic field line must be inclined < 60 degrees from

the disk midplane for the centrifugal force to be effective in initiating a cold outflow from a thin disk (e.g. Krasnopolsky et al., 1999), i.e.

$$\theta_B = \arctan\left|\frac{z}{R}\right|, \tag{6.40}$$

where R is the cylindrical radius. Fig. 6.14(a) shows that the poloidal magnetic field in our jet inclines by $\theta_B > 60$ degrees from the disk midplane, deviating from the expectations in the standard magneto-centrifugal model. However, the jet has a higher specific angular momentum compared to that at their launching location due to the transport of angular momentum by magnetic field lines (Fig. 6.3). As a result, the centrifugal force is stronger than the gravity in the cylindrically radial direction, although it is still weaker than the magnetic force that collimates the jet towards the axis (see Fig. 6.14[b] and [c]).

6.5.3 Differences from axisymmetric steady-state jets

As mentioned in sec. 6.5.1, in an axisymmetric steady-state jet model, there are four conserved quantities (equ. 6.32, 6.33, 6.34, 6.35) along magnetic field lines. In such a model, we can establish a relationship between the specific angular momentum Rv_ϕ, the outflow poloidal velocity $v_{\rm pol}$ at large distances from its base, and the radius of the outflow launching point, assuming the outflow originates from the disk plane where specific angular momentum is dominated by gas angular momentum, i.e.

$$l = l_0 = R_0 v_{\phi,0}, \tag{6.41}$$

$$\omega_s = \frac{v_{\phi,0}}{R_0} = \Omega_0. \tag{6.42}$$

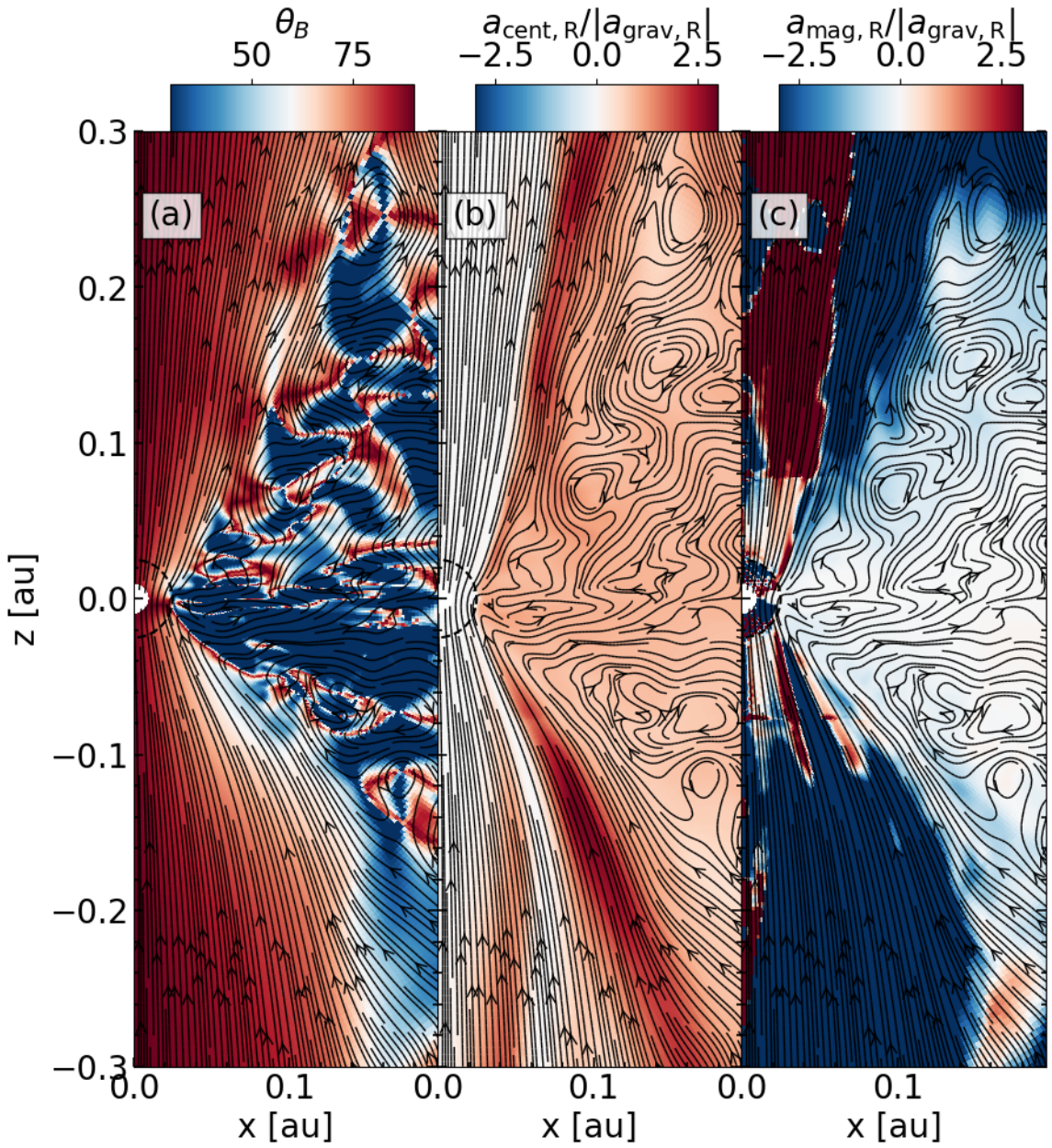


Figure 6.14: Deviation from the expectations of the magneto-centrifugal model. **Panel (a)** shows the pitch angle of the poloidal magnetic field line is more than 60 degrees from the disk midplane; **panel (b) and (c)** shows although centrifugal force is strong in the jet, magnetic force in the cylindrical-$\hat{R}$ direction is stronger.

where the subscript "0" denotes the footpoint of the outflow on the disk plane. The angular velocity ω_s can be substituted into conserved energy:

$$E = \frac{1}{2}v_\phi^2 - \Phi - \frac{\Omega_0 R B_\phi}{k} + h. \tag{6.43}$$

Following Ferreira et al. (2006), we can use equ. 6.43 to parameterize Rv_ϕ and $v_{\rm pol}$ into

$$Rv_\phi = \sqrt{GMR_0}\delta_0\lambda_\phi \tag{6.44}$$

$$v_{\rm pol} = \sqrt{\frac{GM}{R_0}}\sqrt{\delta_0^2(2\lambda_p - 1) - 2 + \beta} \tag{6.45}$$

where

$$\delta_0^2 = \frac{\Omega_0^2 R_0^3}{GM}; \tag{6.46}$$

$$\lambda_\phi = (1-g)\frac{R^2}{R_0^2}; \tag{6.47}$$

$$\lambda_p = \lambda_\phi \frac{1+g}{2}; \tag{6.48}$$

$$g = 1 - \frac{\Omega}{\Omega_0}; \tag{6.49}$$

$$\beta = 2\frac{h_0 - h}{GM/R_0}, \tag{6.50}$$

assuming no heat input along the outflow. Ω is the local gas angular velocity. Ferreira et al. (2006) divides the solutions to Rv_ϕ and $v_{\rm pol}$ into two regimes: the "disk wind" regime, where thermal energy is assumed to be unimportant ($\beta = 0$) and $\lambda_p \approx \lambda_\phi$, and the "stellar wind" regime, where thermal pressure β dominates poloidal velocity.

Fig. 6.15 shows the "disk wind" and "stellar wind" regimes adapted from Ferreira et al. (2006). To compare our model to the steady-state solutions, we select only the cells greater than 6 au from the disk midplane ($|z| > 6$ au) and

$v_z^p > \max(10^6 \text{ cm s}^{-1}, v_{\text{escape}})$, where v_{escape} is the local escape velocity. Since the outflow is asymmetric about the midplane, we show the selected upper hemisphere in the upper row of Fig. 6.15 and the lower hemisphere in the lower row of Fig. 6.15. Because the outflow in our model can be divided into the jet and the disk wind (sec. 6.3), we divide our simulation into two regimes by geometry: the jet, which includes gas within $0.1|z|$ from the polar axis, and the disk wind, which includes the outflow up to 4 au in the cylindrical-$\hat{R}$ direction. Each selected cell is represented by a dot in Fig. 6.15, color-coded by the distance between the cell and the disk midplane (i.e., $|z|$). In both hemispheres, the jet resides beyond the lower left corner of the disk-wind parameter space and exhibits a wide vertical distribution. The disk wind is also clustered off the disk wind parameter space, moving slower but carrying more angular momentum than the jet.

The primary difference between the simulation and the steady-state solutions arises from the assumption regarding the angular momentum at the base of the outflow (equ. 6.42). In our model, due to the highly dynamic and time-dependent nature of the disk's magnetically active zone at the outflow's base, conserved quantities are only applicable after the outflow is launched. For instance, as shown in Fig. 6.13, these quantities are conserved only after some distance beyond the slow magnetosonic point along a magnetic field line. If we position the "footpoint" of the outflow somewhere near the slow magnetosonic point—outside the disk but within the outflow region, the conserved quantities are dominated by the terms with the toroidal field, making it necessary to account for the magnetic component of the conserved angular velocity at the footpoint (denoted again by the subscript "0"), i.e.

$$\omega_{s,0} = \frac{v_{\phi,0}}{R_0} + \frac{kB_{\phi,0}}{4\pi\rho_0 R_0} \tag{6.51}$$

and equ. 6.43 can be updated accordingly

$$E = \frac{1}{2}v_\phi^2 - \Phi - \frac{\Omega_0 R B_\phi}{k} + h + \frac{B_\phi B_{\phi,0} R}{4\pi\rho_0 R_0}, \tag{6.52}$$

which includes an extra term (the last term on the right hand side). At the footpoint of the outflow (where $R = R_0$), this term is twice the toroidal magnetic energy density $E_{B,\phi,0} = \frac{B_{\phi,0}^2}{4\pi\rho_0}$; it represents the Poynting flux, which is dominated by the $B_{\phi,0}^2/(4\pi\rho_0)$ term (sec. 6.4.4). Far away from the footpoint, specific angular momentum is dominated by the gas component (l in Fig. 6.13), so $RB_\phi \ll R_0 B_{\phi,0}$. Defining

$$\chi = 2\frac{\frac{B_{\phi,0}}{4\pi\rho_0}(R_0 B_{\phi,0} - RB_\phi)}{GM/R_0} \approx 2\frac{E_{B,\phi,0}}{GM/R_0}, \tag{6.53}$$

we can rewrite the poloidal velocity (equ. 6.45) as

$$v_{\rm pol} = \sqrt{\frac{GM}{R_0}}\sqrt{\delta_0^2(2\lambda_p - 1) - 2 + \beta + \chi}. \tag{6.54}$$

If χ is much larger than δ_0^2, 2, and β (i.e., if the toroidal magnetic energy flux at the footpoint of the jet is much larger than any other energy flux along the magnetic field line), then $v_{\rm pol}$ only depends on χ. However, because Rv_ϕ is χ-independent, there is no correlation between $v_{\rm pol}$ and Rv_ϕ. This is the case for the jet in our model: the vertical distribution in Fig. 6.15(a) and (e) shows the lack of correlation between $v_{\rm pol}$ and Rv_ϕ. As a consequence, measuring $v_{\rm pol}$ and Rv_ϕ does not directly yield the launching radius of the jet produced in our simulation. This is not surprising in hindsight because our jet is launched by the twisting of the magnetic field anchored on highly dynamic, fast-infalling, elevated avalanche accretion streams, which is very different from the conditions envisioned in the steady-state MHD wind launched from

the surface of a slowly accreting, geometrically thin disk [2].

If χ is comparable to, but does not dominate over, δ_0^2, we can reinterpret χ by defining a characteristic radius r_* such that $\omega_s = \Omega_*$, the angular velocity at r_*. The interpretation of equ. 6.44 and 6.45 would not change assuming all values estimated for the footpoint of the outflow are at r_* instead of r_0. Consequently, the estimated outflow-launching radius based on equ.6.44 and 6.45 will be r_*, which is less than the actual launching radius r_0. To connect our model with this interpretation, we assume at a large distance, all conserved quantities are dominated by the gas component, so the specific angular momentum is given by the conserved quantity l, and the poloidal velocity is calculated assuming poloidal kinetic energy dominates total energy, i.e.

$$v_{\rm pol} = \sqrt{2E}. \tag{6.55}$$

The extrapolation is performed for all points in Fig. 6.15(a), (b), (e), and (f), and the result is shown in Fig. 6.15(c), (d), (g), and (h) for the jet and disk wind in the upper and lower hemispheres. Most extrapolated points move a little towards the upper right corner, but the overall distribution stays around a similar position as in the original values. The vertical distribution of the jet remains, again showing the lack of correlation between specific angular momentum and poloidal velocity. The disk wind in our model now overlaps a little with the "disk wind regime" of the steady-state solution, with an estimated launching radius $r_0 \approx 0.6$ au, showing a reasonable estimate when χ is not dominating.

[2]We should note that there are other effects that can change the relation between $v_{\rm pol}$ and Rv_ϕ for outflows in general, independent of the driving mechanism, such as rapid flow deceleration, which can force part of the outflow to reverse its rotation direction (Sauty et al., 2012).

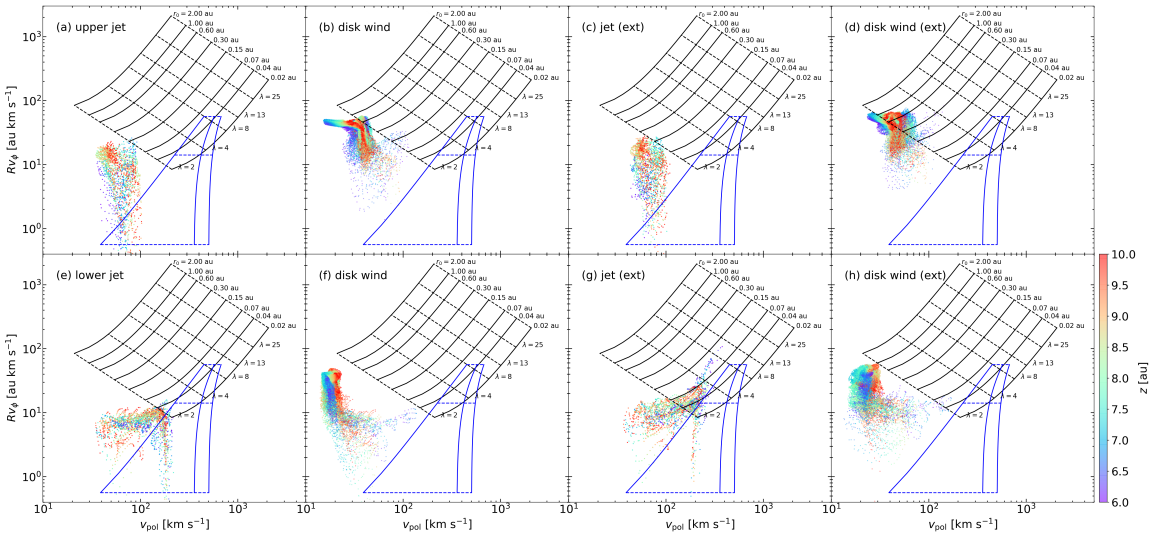


Figure 6.15: Comparison between the jet and disk wind in our model and the steady-state solutions from Ferreira et al. (2006). The outflow is divided into the jet and disk wind based on geometry (see sec. 6.5.3). Each cell is represented by a dot, colored according to its vertical distance from the disk midplane ($|z|$). **Panels (a) and (b)** show the jet and disk wind in the upper hemisphere, respectively; **panels (c) and (d)** show the same cells as a and b, but with values extrapolated assuming all angular momentum and kinetic energy carried by the magnetic field are released into the gas. The lower panels present the same quantities as the upper panels but use cells in the lower hemisphere.

6.6 Discussion

6.6.1 Mass and angular momentum fluxes carried by the jet and disk wind

In sec. 6.3, we demonstrated that the outflow can be divided into two distinct components: the fast-moving jet and the slower disk wind surrounding the jet. Between these, we identified an MRI-active turbulent disk wind region, which lacks a coherent flow structure, effectively separating the jet from the disk wind. The MRI-active turbulent disk wind becomes a laminar disk wind at a higher altitude where MRI can no longer be sustained.

This outflow-launching picture naturally produces a well-collimated jet, where centrifugal force is not important compared with magnetic force, and a wider angle disk-wind, where centrifugal force acts to widen the opening angle of the outflow. We stress that in this picture, centrifugal force is not responsible for launching the jet or the disk wind: its primary role is to widen the opening angle of the disk wind. However, it does not translate to the absence of angular momentum transportation. Both the jet and disk wind are super-Keplerian (panel [d] in fig. 6.3 and 6.5). To quantify the mass and angular momentum advected by the outflow, we show in Fig. 6.16(a) the temporal evolution of the disk accretion rate and outflow mass flux at $z = \pm 10$ au, the outer simulation boundary in the vertical direction. The horizontal lines show the averaged values between 4.0 yr and 10.0 yr. The mass flux is defined as

$$\Phi_m = \int \rho \boldsymbol{v} \cdot d\boldsymbol{A}, \tag{6.56}$$

where $\boldsymbol{A}$ is the area that the flow passes through. For accretion, $\boldsymbol{A}$ is the sphere

at 0.03 au, and for the outflow, $\boldsymbol{A}$ is the planes at $z = \pm 10$ au. A negative sign is added to the accretion mass flux, so all values are positive. The mass flux in the jet (gas moving at $v_z^p > 10^7$ cm s^{-1}) is about 2×10^{-11} $M_\odot$ yr^{-1}, whereas the disk wind outflow mass flux ($v_z^p > 10^6$ cm s^{-1} and $R < 4$ au) is 10^{-9} $M_\odot$ yr^{-1}; the latter is consistent with the empirical relation that the outflow-accretion mass flux ratio is about 1 : 10 (Watson et al., 2016; Pascucci et al., 2023). The relatively low mass flux in the fast jet may indicate that the magnetic field strength adopted in this paper in the inner disk may be too low to drive a fast jet with a much higher mass flux. For example, similar simulations but with a dynamically opened stellar magnetosphere that provides a much stronger field threading the inner disk can drive a fast jet with a much higher mass flux (Tu et al. 2025, in prep).

To quantify the angular momentum flux, we note that the momentum flux is defined as

$$\Phi_l = \int \rho v_\phi R \boldsymbol{v} \cdot d\boldsymbol{A}. \tag{6.57}$$

To connect the outflow momentum flux to the angular momentum on a Keplerian disk, we can define a "Keplerian angular momentum radius" R_a such that

$$v_K(R_a) R_a = \frac{\Phi_l}{\Phi_m}, \tag{6.58}$$

or, equivalently

$$R_a = \frac{1}{GM} \Big(\frac{\Phi_l}{\Phi_m} \Big)^2. \tag{6.59}$$

Fig. 6.16(b) shows the R_a for the jet and the disk wind, respectively. The average R_a for the jet is about 0.3 au. Since the base of the jet is at $\lesssim 0.1$ au, the jet transports angular momentum per unit mass a few times higher than the specific angular momentum at their footpoint, consistent with the magnetic domination of

the angular momentum near the base of the jet (see, e.g., Fig. 6.13[e]). In contrast, the disk wind R_a is about 1.0 au, which is consistent with the interpretation of the steady-state solution (sec. 6.5.3) and its launching radii, which range from ~ 0.1 au to ~ 1.5 au, encompassing the disk wind R_a of 1.0 au.

Angular momentum transport in the disk wind does not necessarily imply the magneto-centrifugal mechanism (which is, in contrary to the usual interpretation in literature, e.g., Gressel et al., 2020), which relies on the centrifugal force to launch an outflow. In particular, the dominance of the "tension energy advection" term (equ. 6.31) over the "pressure energy advection" term (equ. 6.30) of the Bernoulli invariant (sometimes used as direct evidence for the magneto-centrifugal mechanism) does not mean the magnetic tension force dominates over magnetic pressure force in the $\hat{z}$ direction. Fig. 6.17 shows a comparison between the energy flux ratio $S^{\rm eff}_{\rm BT}/S^{\rm eff}_{\rm BE}$ and the force ratios $a^{\rm eff}_{\rm z,tens}/a^{\rm eff}_{\rm z,pres}$ (defined in equ. 6.24 and equ. 6.23), respectively. While it is true that the tension energy advection dominates over the pressure energy advection at the base of the disk wind, the magnetic pressure force overwhelmingly dominates the magnetic tension force. This contrast is not surprising as the kinetic-$\beta > 1$ in the disk wind region (Fig. 6.5), so the tension energy advection, which includes the contribution from v_ϕ, can appear significant without contributing to acceleration in the $\hat{z}$-direction. Moreover, the tension force itself points toward the disk midplane, making it inherently incapable of driving an outflow (see fig. 6.4 and sec. 6.4.1). The region where tension energy advection dominates is located at a small altitude. The flow transitions to magnetic pressure energy advection dominated at a larger altitude. The transition occurs when the gas switches from a predominantly horizontal motion along the cylindrical $\hat{R}$ direction to a predominantly vertical motion.

In contrast, the jet is toroidal magnetic pressure dominated in both force and energy advection (as it is overwhelmingly magnetically dominated, see Fig. 6.3), so

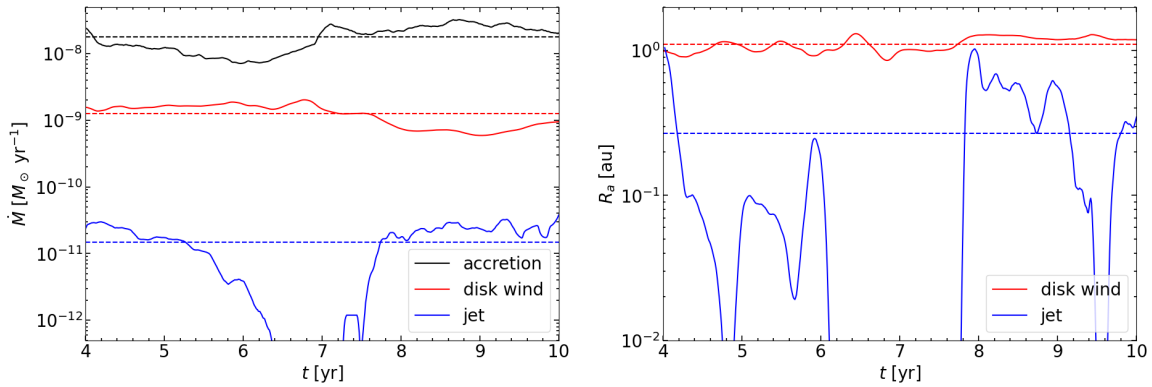


Figure 6.16: **Left panel:** Disk accretion rate and outflow mass flux. A negative sign is added to the accretion rate, so the values are positive. **Right panel:** The "Keplerian angular momentum radius" R_a (defined in equ. 6.59) for the jet and the disk wind. The horizontal lines in both panels are the averaged values between 4.0 yr and 10.0 yr for each line.

the acceleration is primarily in the $\hat{z}$ direction and the opening angle of the jet stays small. We stress here again that efficient angular momentum transport is *not* evidence for the magneto-centrifugal mechanism. For the jet, angular momentum transport does not directly contribute to the flow acceleration (the two are related through the toroidal magnetic field generated by field line twisting near the jet base, however); for the disk wind, angular momentum in the wind increases the opening angle of the outflow through the centrifugal force.

6.6.2 In-situ toroidal field generation

We have shown the importance of the toroidal magnetic field in accelerating the jet and the disk wind. In this subsection, we demonstrate how the toroidal field is generated and advected in the jet-launching region.

Toroidal magnetic generation is governed by the induction equation (equ. 6.3). In the magnetically active zone of the disk and the jet-launching region, the gas is in the ideal MHD limit, so we can ignore the second (Ohmic dissipation) term in equ. 6.3. The right-hand side of equ. 6.3 in cylindrical coordinate in the azimuthal direction

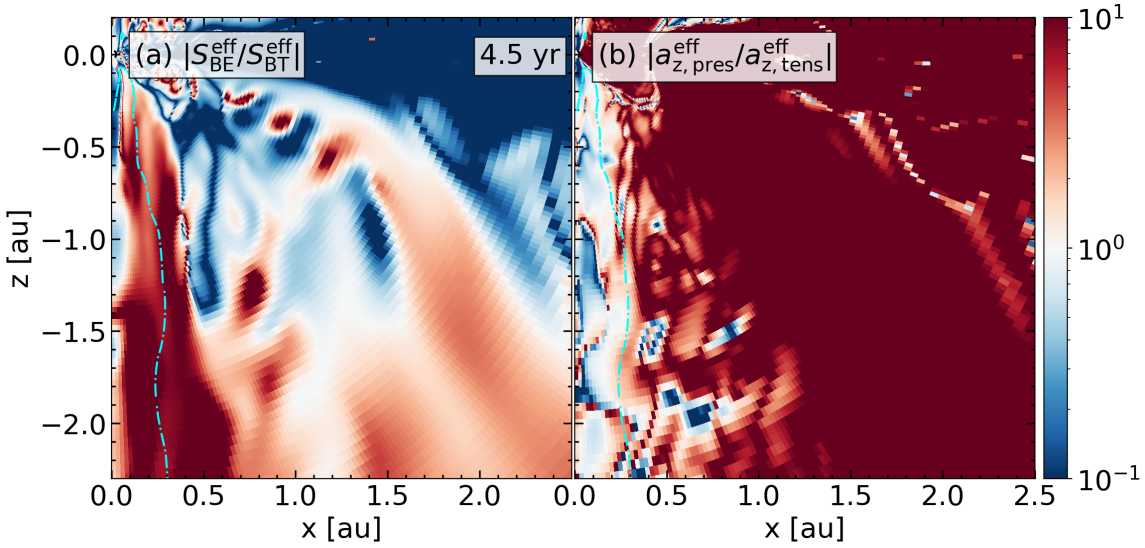


Figure 6.17: Ratios of energy advection rates and forces for the *disk wind*. The magnetic tension component of the Poynting flux (equ. 6.31) dominates over the magnetic pressure component (equ. 6.30) in transporting energy in the $\hat{z}$ direction near the outflow base at small radii (left panel). However, the dominance in energy transport does not translate to a dominance in force: magnetic pressure force dominates over magnetic tension force everywhere in the disk wind (right panel).

can be decomposed into two terms:

$$\left.\frac{\partial B_\phi}{\partial t}\right|_{\rm gen} = \frac{\partial (v_\phi B_z)}{\partial z} + \frac{\partial (v_\phi B_R)}{\partial R} \tag{6.60}$$

$$\left.\frac{\partial B_\phi}{\partial t}\right|_{\rm adv} = -\frac{\partial (v_z B_\phi)}{\partial z} - \frac{\partial (v_R B_\phi)}{\partial R} \tag{6.61}$$

where equ. 6.60 describes the generation of B_ϕ through differential twisting of the poloidal field and equ. 6.61 describes the advection of B_ϕ through poloidal gas motion. To show the evolution of the toroidal magnetic field, we show in Fig. 6.18 the toroidal magnetic field strength, and its generation and advection rates in panels (a), (b), and (c), respectively. As discussed in sec. 6.4.4, the jet in the lower hemisphere is accelerated in the $B_\phi > 0$ region. The generation of the jet-launching toroidal magnetic field occurs around the transition from $B_\phi < 0$ in the disk to $B_\phi > 0$ in the

jet-launching cavity, where $\left.\frac{\partial B_\phi}{\partial t}\right|_{\rm gen} \approx 10^3$ G yr^{-1}, which, for a typical field strength of ~ 1 G in the region, corresponds to a very short timescale of only $\sim 10^{-3}$ yr! The generated toroidal magnetic field is efficiently removed by advection at a comparable rate. A portion of this field is transported to the inner boundary via the avalanche accretion stream, which occurs where B_ϕ transitions from negative to positive (see Section 6.4.3). The remaining portion of the field, situated outside the accretion stream, releases its energy into the low-density gas, propelling it in the (negative) $\hat{z}$-direction to form a toroidal magnetic pressure-driven jet in the lower hemisphere.

The rapid generation of the toroidal magnetic field is facilitated by the presence of a mass-dominated avalanche accretion stream. Within this stream, differential rotation twists the poloidal magnetic field, efficiently converting it into a toroidal magnetic field. The dominance by the kinetic energy is illustrated by the green line in Fig. 6.18, which shows where $\beta_K = 1$(defined in equ. 6.19, see Fig. 6.3(c) for a 2D slice of β_K). The gas-dominated region, where $\beta_K > 1$, lies above the green line in the lower hemisphere and includes the fastest toroidal magnetic field generation region. On the other side of the green line, the toroidal field can still be generated *in situ* for a brief period within the magnetically-dominated region. This localized rapid toroidal field generation at the base of the polar cavity ensures a continuous supply of toroidal magnetic field, which provides the magnetic pressure (and the outward-going Poynting flux) needed to accelerate the low-density gas in the cavity to a high speed and form a fast jet.

6.7 Conclusions

We performed a 3D non-ideal MHD simulation of outflow-launching from the inner region of a circumstellar disk threaded by open magnetic field lines. Our model includes a magnetically active disk zone surrounded by a magnetically dead zone.

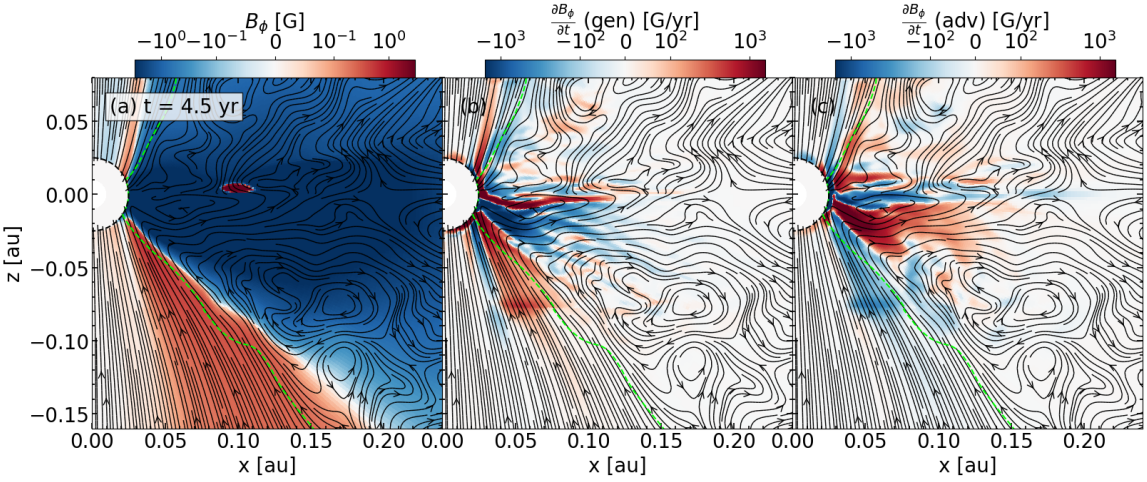


Figure 6.18: Azimuthally averaged magnetic field strength, generation, and advection. **Left panel:** azimuthal magnetic field B_ϕ at the representative time. **Middle panel**: generation of azimuthal magnetic field through differential rotation, as defined in equ. 6.60; **Right panel:** advection of azimuthal magnetic field through gas motion, as defined in equ. 6.61. The green line in each panel shows where $\beta_K = 1$ (defined in equ. 6.19), with the polar regions being magnetically dominated ($\beta_K < 1$). Note that a negative generation or advection rate in a negative B_ϕ region is an *increase* in magnetic field strength.

Although the jet in our model shares some similarities with the magneto-centrifugal model and the steady-state outflow solutions, the jet in our model is *not* driven magneto-centrifugally and has some key differences from the steady-state solutions. Our main conclusions are as follows

1. The outflow can be divided into three components: (1) a jet–the collimated fast, lightly loaded outflow near the polar axis; (2) an MRI-active turbulent disk wind surrounding the jet where the flow is turbulent due to MRI at low latitudes but becomes laminar at high altitude where MRI can no longer be sustained; an (3) a disk wind, a laminar high-density slow outflow surrounding both the jet and the MRI-active turbulent disk wind. It merges with the upper part of the MRI-active turbulent disk wind at high altitudes when the flow becomes laminar.

2. The jet and the disk wind are both driven by toroidal magnetic pressure. A toroidal magnetic field is generated in the mass-dominated disk, where differential rotation twists the poloidal field into a toroidal field. The toroidal field generated at the surface of the disk releases its energy to the low-density gas in the polar cavity, producing the fast lightly loaded jet. Gas rotation plays a negligible role in driving the jet due to the dominance of magnetic field energy over both kinetic and thermal energies (both kinetic-β and plasma-β are $\ll 1$) in the jet acceleration region.

3. In some extreme cases, the jet can be choked by the MRI-active turbulent disk wind when this wind fills the polar cavity with dense gas. The avalanche accretion stream is present only in one hemisphere due to the magnetic field geometry-facilitates jet launching by creating an interface between the turbulent disk wind and the polar cavity. This interface allows magnetic energy to be

efficiently transferred to a small amount of gas, enabling jet acceleration. In the opposite hemisphere, where the avalanche stream is absent, the jet is more likely to be suppressed by the dense gas accumulated from the MRI-active wind. Nevertheless, the disk wind itself remains bipolar, as it is more heavily mass-loaded and does not rely on a polar cavity to be launched.

4. The disk wind is also accelerated by the toroidal magnetic pressure, but unlike the jet, which is overwhelmingly magnetically dominated, the disk wind is kinetically dominated, so the centrifugal force can effectively widen the opening angle of the outflow.

5. The jet in our model shares several similarities with the classic magneto-centrifugal model. Firstly, angular momentum is efficiently transported from the disk to the jet; second, the jet is lightly loaded; and thirdly, the jet transitions from sub-Alfvénic to super-Alfvénic along a magnetic field line. However, the poloidal magnetic field lines in our jet are inclined by more than 60 degrees from the disk midplane, unlike the field configuration required for the initial flow acceleration from a geometrically thin disk in the standard lightly-loaded magneto-centrifugal wind. More importantly, even though our jet is lightly mass-loaded, it is primarily accelerated vertically by the unwinding of constantly twisted magnetic fields rather than horizontally by centrifugal force as “beads on a wire" as envisioned in the classic magneto-centrifugal wind model.

6. The jet in our model also differs from the expectations of steady-state axisymmetric outflow solutions. Due to the highly variable and non-magneto-centrifugal nature of the outflow acceleration region near the jet base (where the jet is primarily powered by the unsteady magnetic field twisting from differ-

ential rotaton in high-altitude fast accretion streams), at a large distance where the flow is dominated by the gas, there is no correlation between the gas poloidal velocity and its specific angular momentum, so the poloidal velocity-angular momentum relation should not be used as an indicator of the jet-launching radius. This correlation can be used, with caution, to estimate the launching radius of the disk wind, as the disk wind is less magnetically dominated.

6.8 ACKNOWLEDGMENTS

YT acknowledges support from the interdisciplinary fellowship at UVA. CYH acknowledges support from NASA SOFIA grant SOF-10_0505 and NRAO ALMA Student Observing Support (SOS). We acknowledge computing resources from UVA research computing (RIVANNA), NASA High-Performance Computing, and NSF's ACCESS computing allocation AST200032. ZYL is supported in part by NASA 80NSSC20K0533, NSF AST-2307199, and the Virginia Institute of Theoretical Astronomy (VITA). Z.Z. acknowledges support from NSF award 2408207, 2429732 and NASA grant 80NSSC24K1285.

Chapter 7

YSO Jets Driven by Magnetic Pressure Generated through Stellar Magnetosphere–Disk Interaction

The work presented in this chapter will be submitted for publication to the Astrophysical Journal (ApJ) with Zhi-Yun Li, Zhaohuan Zhu, Xiao Hu, and Chun-Yen Hsu as coauthors.

Abstract: The origin of jets in young stellar objects (YSOs) remains a subject of active investigation. We present a 3D non-ideal magnetohydrodynamic simulation of jet launching in YSOs, focusing on the interaction between the stellar magnetosphere and the circumstellar disk. At the beginning of the simulation, the magnetosphere partially opens, forming two oppositely directed magnetic field regions: one threading the star and the other threading the inner disk. The latter dominates over the original disk field at small radii and contributes to launching a disk wind. In our model, the jet is launched from the interface between these regions by toroidal magnetic pressure generated along "two-legged" field lines, anchored at a magnetically dominated stellar footpoint and a mass-dominated point on the disk surface. Outflows are driven along these lines via a "load-fire-reload" cycle: in the "load" stage, differential rotation between the stellar and disk footpoints generates a toroidal magnetic field; in the "fire" stage, vertical gradients in toroidal field strength drive the outflow and release magnetic energy; and in the "reload" stage, magnetic reconnection between oppositely directed field lines resets the configuration, enabling the cycle to repeat. This process occurs rapidly and asynchronously across azimuthal angles, producing a continuous, large-scale outflow. From an energetic perspective, Poynting flux transports the toroidal field from the vicinity of the star into the polar cavity, powering the jet. Comparison with a disk-only model shows that the stellar magnetosphere promotes bipolar jet launching by shaping a magnetic field geometry favorable to symmetric outflows.

7.1 INTRODUCTION

Star formation is often viewed as a collapse process, where a dense core, typically several to tens of thousands of AUs in size, collapses to form a young stellar object (YSO) consisting of a central star, a circumstellar disk, and, ultimately, planets.

However, the reverse process, outflow, is also a fundamental aspect of the formation and evolution of YSOs. Outflows play a crucial role in shaping the chemical and dust distribution within individual star-forming systems (Tsukamoto et al., 2021; Cacciapuoti et al., 2024; Morbidelli et al., 2024) and influence the formation of nearby stars and planets by regulating the dynamics of molecular clouds (André et al., 2014; Guszejnov et al., 2021; Hsieh et al., 2023).

The most energetic component of the outflow is the jet, a highly collimated stream of gas traveling at speeds exceeding 10^7 cm s^{-1}, often extending thousands of AU or more in length (Podio et al., 2015; Ray & Ferreira, 2021). Recent observations have provided greater insight into the structure of jets and their surrounding environments (e.g., Codella et al., 2014; de Valon et al., 2020; Lee et al., 2021; Whelan et al., 2024; Assani et al., 2024; López-Vázquez et al., 2024b; Hsu et al., 2024; Delabrosse et al., 2024). Accompanying the jet is a slower, more massive outflow known as the disk wind, which typically surrounds the jet with a wider opening angle (Tabone et al., 2017; Pascucci et al., 2023). Since both the jet and disk wind significantly impact both local and global star formation processes, understanding their driving mechanisms is crucial to understanding star formation. A key open question is whether the jet and disk wind share a common driving mechanism, particularly what powers the jet itself.

It is becoming a consensus that the jets and outflows are most likely magnetically driven. One commonly used model is the class of magnetocentrifugal models (Shu et al., 1995; Krasnopolsky et al., 1999; Ustyugova et al., 1999; Krasnopolsky et al., 2003; Anderson et al., 2005, 2006; Bai & Stone, 2013), where the centrifugal force launches outflows as a result of angular momentum transportation along a magnetic field line. While the magneto-centrifugal model and its variants, including the "disk wind" (Blandford & Payne, 1982; Pudritz & Norman, 1983) and "X-wind" (Shu et al., 1994, 2000; Shang et al., 2002; Cai et al., 2008) models, can effectively explain the

excessive angular momentum carried by the jet, how the exact launching conditions can be met under observational and theoretical constraints remains unclear (Desch et al., 2010; Bjerkeli et al., 2016).

Another class of models is the Poynting flux-driven jet model, where the outflow is launched by a predominantly toroidal magnetic field that transfers energy and angular momentum to the gas (Shibata & Uchida, 1986; Lovelace et al., 2001; Lovelace & Romanova, 2009; Guan et al., 2014). A related model is the "magnetic-tower" model (Lynden-Bell, 1996, 2003; Kato et al., 2004; Nakamura et al., 2007), where the loop-like toroidal magnetic fields stack on top of each other, forming a magnetic loop tower. This class of models is usually more mass-loaded than the magneto-centrifugal model, resulting in a more gradual acceleration. Although this class of models provides an alternative method of acceleration, the stability of the required magnetic condition and the necessary external pressure to collimate the jet pose challenges to this model (Moll et al., 2008; Huarte-Espinosa et al., 2012).

Either launching mechanism relies on energy and angular momentum extraction from its base, which is typically believed to be rooted in the inner disk or the star. One possibility is that the jet is driven by the disk alone. Since the YSO disk is expected to be magnetized, particularly during the early phase of disk evolution (Wurster & Li, 2018; Vlemmings et al., 2019; Galametz et al., 2020; Lankhaar et al., 2022; Yen et al., 2024; Tu et al., 2024a; Ohashi et al., 2025), the magnetic field in the disk could channel the disk's rotational energy and momentum to a large distance, forming a jet. Previous studies have investigated this possibility (e.g. Casse & Keppens, 2002; Kato et al., 2002; Anderson et al., 2006; Tzeferacos et al., 2009; Fendt et al., 2011; Fendt & Sheikhnezami, 2013; Stepanovs & Fendt, 2016; Béthune et al., 2017; Zhu & Stone, 2018; Ramsey & Clarke, 2019; Mattia & Fendt, 2020a,b; Mishra et al., 2020; Jacquemin-Ide et al., 2021; Jannaud et al., 2023; Takaishi et al., 2024; Tu et al.,

2025b,a; Takasao et al., 2025), but the jet-launching problem remains. Although a jet can be launched by the disk alone, the jet is typically weak and variable, sometimes prone to being unipolar. Thus, it is unclear how general this jet-launching mechanism is in explaining observed bipolar outflows.

One key ingredient missing in these disk-only jet models is the star, which can be connected to the inner disk through its magnetosphere. Observations have shown that YSOs could have a strong magnetosphere, and previous studies and simulations have primarily focused on how the magnetosphere influences the disk accreting onto the star (Bardou & Heyvaerts, 1996; Miller & Stone, 1997; Romanova et al., 2009, 2012; Lai, 2014; Takasao et al., 2019; Romanova et al., 2021, 2025; Zhu et al., 2024; Zhu, 2025). Outflow launching from the magnetosphere-disk boundary has been examined primarily in 2D (e.g., Goodson & Winglee, 1999; Romanova et al., 2005; Lovelace et al., 2013; Čemeljić et al., 2013; Lovelace et al., 2014), and less in 3D (e.g., Romanova et al., 2009; Takasao et al., 2022), showing the possibility of jet launching. Yet, how the magnetosphere participates in jet launching and how it interacts with the disk field remains uncertain. This paper focuses on modeling these key processes in a self-consistent 3D non-ideal magneto-hydrodynamic global model.

This study is an extension of Tu et al. (2025b) and Tu et al. (2025a), who studied outflow launching using the disk gas and disk magnetic field alone. Tu et al. (2025b) performed a 2D axisymmetric model and identified a key ingredient in jet launching, the “avalanche accretion stream" along the disk surface, which actively provides the energy and momentum to the jet-launching gas. Tu et al. (2025a) extended the models to 3D and identified a light-loaded magnetic-pressure-driven jet model in a disk-only case, whose jet is highly variable and asymmetric in both disk hemispheres. In this study, we follow the disk setup in Tu et al. (2025a) and include the stellar magnetosphere to examine the effect of the magnetosphere on jet launching.

This paper is organized as follows. Sec. 7.2 describes the simulation setup and model parameters. Sec. 7.3 gives an overview of the simulation result and identifies the key components of the modeled jet-launching system. The jet-launching mechanism is described in detail in Sec. 7.4, followed by a discussion of this mechanism in the context of the star formation literature in Sec. 7.5. We conclude in Sec. 7.6.

7.2 METHOD

The following set of non-ideal MHD equations governs the evolution of the circumstellar disk threaded by open magnetic field lines with the inner disk truncated by the stellar magnetosphere:

$$\frac{\partial \rho}{\partial t} + \nabla \cdot (\rho \boldsymbol{v}) = 0, \tag{7.1}$$

$$\rho \frac{\partial \boldsymbol{v}}{\partial t} + \rho(\boldsymbol{v} \cdot \nabla)\boldsymbol{v} = -\nabla P + \frac{1}{c}\boldsymbol{J} \times \boldsymbol{B} - \rho \boldsymbol{g}, \tag{7.2}$$

$$\frac{\partial \boldsymbol{B}}{\partial t} = \nabla \times (\boldsymbol{v} \times \boldsymbol{B}) - \frac{4\pi}{c}\nabla \times [\eta_O(\boldsymbol{J} \times \hat{\boldsymbol{B}})], \tag{7.3}$$

where $\boldsymbol{J} = (c/4\pi)\nabla \times \boldsymbol{B}$ is the current density, and η_O the Ohmic Dissipation coefficient. Other symbols have their usual meanings.

We use the `Athena++` code (Stone et al., 2020) to solve the governing equations in Cartesian coordinates with static mesh refinement (SMR). The initial condition setup is similar to Tu et al. (2025a), with the addition of the stellar magnetosphere. We refer the readers to Tu et al. (2025a) for a detailed description of the hydro, ionization, and non-ideal MHD setup, which are briefly summarized here.

We adopt a power law $\rho \propto r^{-1.35}$ for the density of the disk midplane, following Tu et al. (2025b). To model the truncation of the disk due to the stellar magnetosphere,

the midplane density decreases as

$$\rho(r < r_{\rm trun}) = \rho\Big(\frac{r}{r_{\rm trun}}\Big)^{p}, \tag{7.4}$$

where $r_{\rm trun} = 0.1$ au and $p = -10$. The remainder of the density is prescribed by assuming the disk is in isothermal hydrostatic equilibrium. To minimize numerical problems and ensure runability, we implement a similar density floor as in Tu et al. (2025b):

$$\rho_{\rm floor}(r) = \begin{cases} \rho_f; & r < r_f, \\ \rho_f (r/r_f)^{q_f}; & \text{otherwise}, \end{cases} \tag{7.5}$$

where $\rho_f = 6 \times 10^{-12}$ g cm^{-3}, $r_f = 0.015$ au. $q_f = -5$ allows a rapid drop in the density floor towards a large radius where a density floor is unnecessary. To speed up the simulation during the later stages, we increase the density floor coefficient ρ_f to 2.4×10^{-11} g cm^{-3} after $t = 1.0$ yr. The thermal and non-ideal MHD setup is identical to Tu et al. (2025a).

To quantify and trace the amount of mass introduced by the density floor, we utilize the "passive scalars" in `Athena++` to differentiate between the real gas in the simulation (defined as all the mass present in the active domain at initialization) and the added gas introduced by the density floor. The real gas dominates the outflow and outflow-launching region throughout the simulation. In contrast, the added mass primarily resides in the low-altitude infalling region around the polar axis (i.e., the polar region shown in Figure 7.5) and the inner magnetosphere, where the star rapidly accretes it.

Following Zhu et al. (2024) and Zhu (2025), we incorporate a dense "star" at the center of the simulation to minimize numerical diffusion of the stellar magnetosphere.

This approach leverages the Cartesian coordinate system, which avoids the presence of voids within the simulation domain. The stellar radius is $R_\star = 0.015$ au (about 3.2 $R_\odot$), with a central density of 1.4 g cm^{-3}. The remainder of the stellar density is calculated assuming the star is in isothermal hydrostatic equilibrium. To avoid numerical problems due to too large a density gradient at the stellar surface, we separate the star from the remainder of the simulation domain by setting a "fixing radius" $r_{\rm fix} = 0.018$ au, within which the hydro quantities are reset to their initial values at each time step, while the magnetic field remains untouched. The passive scalars are set to 0 within $r_{\rm fix}$ at every time step. The gas in $r_{\rm fix}$ is assumed to rotate as a solid body with a rotational period of 12 days (corresponding to the Keplerian rotation period at 0.1 au).

The gravitational force is modeled by assuming that stellar gravity dominates the gravitational acceleration everywhere in the simulation. The stellar gravity is modeled as a point-source gravity, with a smoothing towards $r = 0$ to avoid the singularity

$$a_g(r) = \begin{cases} 0; & r < r_s, \\ -\frac{GM_\star}{r^2}\frac{(r-r_s)^2}{(r-r_s)^2+r_s^2}\hat{\boldsymbol{r}}; & \text{otherwise}, \end{cases} \tag{7.6}$$

where $r_s = 0.012$ au.

To ensure divergence-free initial condition and model both the open magnetic field lines threading the disk and the stellar magnetosphere, the global vector potential is the sum of the vector potential of the magnetosphere and the open disk field, i.e.

$$\boldsymbol{A} = \boldsymbol{A}_{\rm disk} + \boldsymbol{A}_{\rm mag}, \tag{7.7}$$

where $\boldsymbol{A}_{\rm disk}$ is the same as the vector potential used in Tu et al. (2025a). The stellar

magnetosphere is modeled following Zhu et al. (2024), using a vector potential

$$\boldsymbol{A}_{\rm mag} = \frac{\bar{\boldsymbol{m}} \times \boldsymbol{r}}{r_c^3}, \tag{7.8}$$

where $r_c = \max(r, r_s/2)$. $\bar{\boldsymbol{m}}$ is chosen to be in the $-\hat{z}$ direction and of such magnitude that the initial magnetic field strength at the surface of the star is about 2000 Gauss. This choice of $\bar{\boldsymbol{m}}$ ensures that the magnetic field of the magnetosphere points upward on the disk midplane, aligned with the direction of the initial open disk field.

The computation domain and mesh refinement are chosen to best resolve the disk and the outflow-launching polar region while keeping a reasonable computational cost. The simulation domain spans ± 10 au in the $\hat{x}$ and $\hat{y}$ directions, and ± 20 au in the $\hat{z}$ direction. The root grid has a resolution of $64 \times 64 \times 128$, ensuring all cells are cubic. Nine levels of refinements are applied in the simulation, with the finest level applied in the disk (±0.04 au in the $\hat{x}$ and $\hat{y}$ directions, and ±0.02 au in the $\hat{z}$ direction), and in the outflow region (±0.02 au in the $\hat{x}$ and $\hat{y}$ directions, and ±0.04 au in the $\hat{z}$ direction). The remainder of the grid is generated automatically by applying the condition that adjacent meshblocks can only differ by at most 1 level of refinement. To reduce numerical diffusion within the star but not add too much computational cost, we apply two additional levels of refinement inside the star: level 10 covers ±0.01 AU, and level 11 resolves the central ±0.005 au. This refinement strategy keeps the stellar magnetosphere stable throughout the simulation. As a result of the mesh refinement, the finest cell size is $(0.0006 \text{ au})^3$ in the active domain, and $(0.00015 \text{ au})^3$ inside the star.

7.3 RESULT

In this section, we present an overview of our simulation results, highlighting key features of the jet structure. Figure 7.1 shows a 3D rendering of the jet in our model, where blue and red contours represent the outflow in the upper and lower hemispheres, respectively. Each hemisphere contains two layers: the outer layer encloses gas moving at speeds exceeding ± 100 km s^{-1}, while the inner layer highlights gas with speeds exceeding ± 200 km s^{-1}, illustrating the presence of a powerful bipolar jet. To avoid obscuring the jet, the disk is visualized as a toroidal structure around the midplane, with most of its mass removed for clarity. The white lines represent magnetic fieldlines, and velocity streamlines are shown by the black lines.

The partial opening of the magnetosphere during the early stages of simulations involving a stellar dipole is a well-known process (e.g. Goodson & Winglee, 1999; Romanova et al., 2009; Lii et al., 2014). In this phase, the initially closed outer dipole field lines that thread the disk inflate and eject poloidal magnetic loops. This magnetic ejection results in the partial opening of the magnetosphere as the system undergoes its initial adjustment.

The initial adjustment results in a characteristic magnetic field geometry. To illustrate the magnetic field geometry and its relationship with the outflow, we show in Figure 7.2 the magnetic fieldlines overplotted on the projected $\hat{z}$-direction velocity v_z^p, defined as

$$v_z^p = v_z \frac{z}{|z|}, \tag{7.9}$$

so outflow in both the upper and lower hemispheres is positive whereas inflow is negative. The magnetic field geometry can be crudely divided into four zones: the permanently closed stellar magnetosphere near the star (enclosed by the magenta

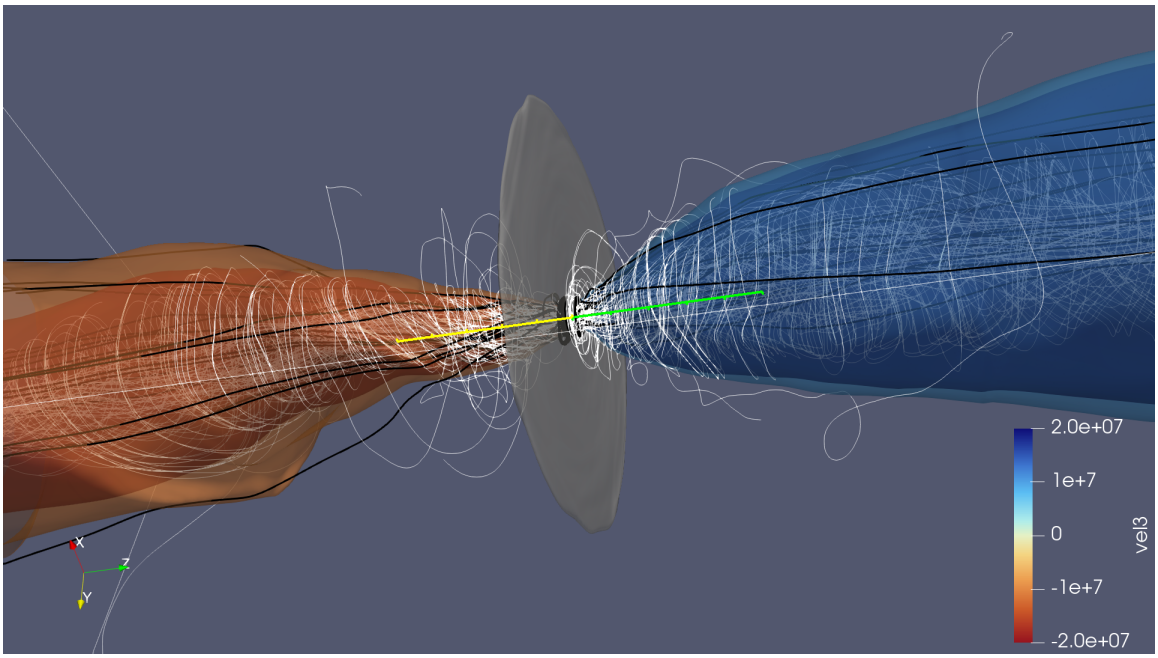


Figure 7.1: 3D rendition of the bipolar jet launched in our model. The outer red and blue shells are isosurface contours at 100 km s^{-1}, whereas the inner ones are at 200 km s^{-1}. The gray structure on the equatorial plane represents the disk. For reference, the green and yellow lines each have a length of 5 au, illustrating the physical scale of the system. An animated version of this figure can be found at: `https://virginia.box.com/s/uctiv36qbwj4tgr5bbjfs8kq4jzu3zwb`. The movie is 27 seconds long, highlighting the strong bipolar outflow from the simulation's beginning (0 yr) to the end (5.5 yr).

line in Figure 7.2), the $-\hat{z}$ direction opened stellar field attached to the star (roughly enclosed by the cyan lines), the large-scale open $+\hat{z}$-direction field (similar to the original disk field, the outer region marked by the green lines), and the less ordered field lines lying in between the former two (between the green and cyan lines). This overall magnetic field structure remains consistent throughout the simulation after the initial adjustment. Since the magnetic field configuration plays a crucial role in launching the outflow, we first examine its properties before discussing each outflow component in detail.

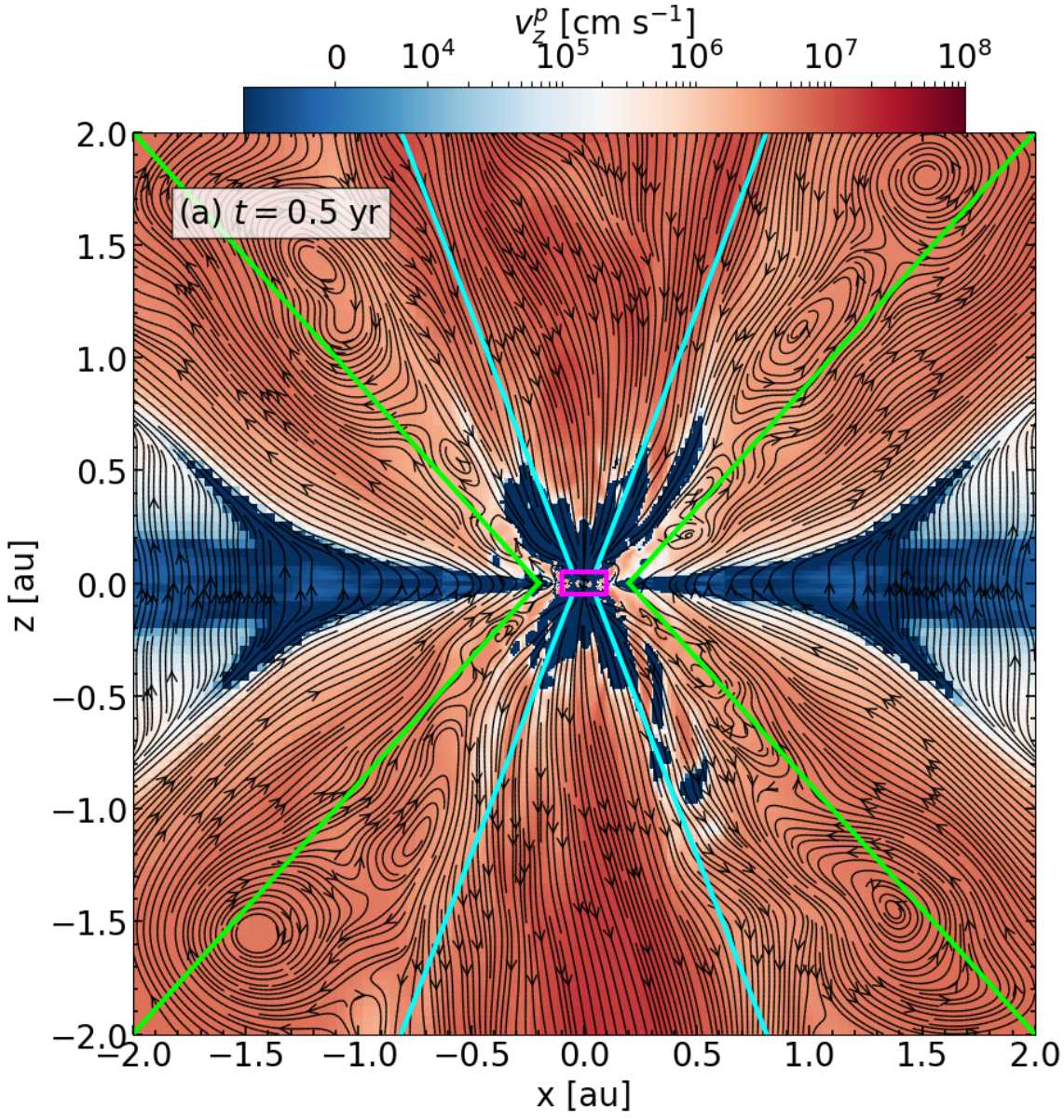


Figure 7.2: Magnetic field geometry after the initial adjustment in the simulation. The background color map shows the projected $\hat{z}$-direction velocity v_z^p (equ. 7.9). The magnetic field structure can be roughly divided into four distinct zones, delineated by the magenta, cyan, and green lines. The magenta line encloses the permanently closed stellar magnetosphere; the cyan line marks the boundary of opened stellar field lines that still thread the star; the green line outlines the extent of the large-scale magnetic field lines threading the disk. The region between the cyan and green lines corresponds to a reconnecting, outflow-driving zone where the interaction between stellar and disk fields powers the outflow.

7.3.1 Magnetic flux evolution

To quantify the opening of the magnetosphere field during simulation, Figure 7.3 shows the downward magnetic flux ($-\hat{z}$ direction) at $z = \pm 5$ au as a function of time for the upper and lower hemispheres, respectively. Since the disk's magnetic field is oriented upward, any downward flux at these heights must originate from the opening of the stellar magnetosphere. For reference, Figure 7.3 also shows the total stellar magnetospheric flux, defined as the total downward magnetic flux at the midplane. Due to magnetic reconnection of the innermost magnetospheric loops inside the star, the total stellar magnetic flux decreases slightly at the beginning of the simulation before stabilizing at approximately -8×10^{26} G cm^2. The opened magnetospheric flux remains around -8×10^{25} G cm^2, accounting for about 10% of the total magnetospheric flux.

The opened magnetic flux dominates the magnetic field of the inner disk. It is equivalent to the total initial flux of the disk within $r \approx 7$ au, and diffuses outward gradually. Figure 7.3 illustrates the evolution of the net magnetic flux enclosed within a given radius on the midplane over time. Due to the strong, negative magnetic field inside the star, the enclosed flux initially drops to a highly negative value at small radii, then gradually returns to positive as more upward-directed field lines are included. The zero-crossing point marking the approximate boundary between the original disk field and the stellar field slowly expands outward, reaching ~ 1 au by $t = 4.0$ yr.

Although the newly opened field lines within 1 au originate from the stellar magnetosphere rather than the original disk field, they thread the disk vertically and link the dense midplane to the less dense surface layers, just as the original disk field. This connection facilitates the launching of a slower disk wind at larger cylindrical

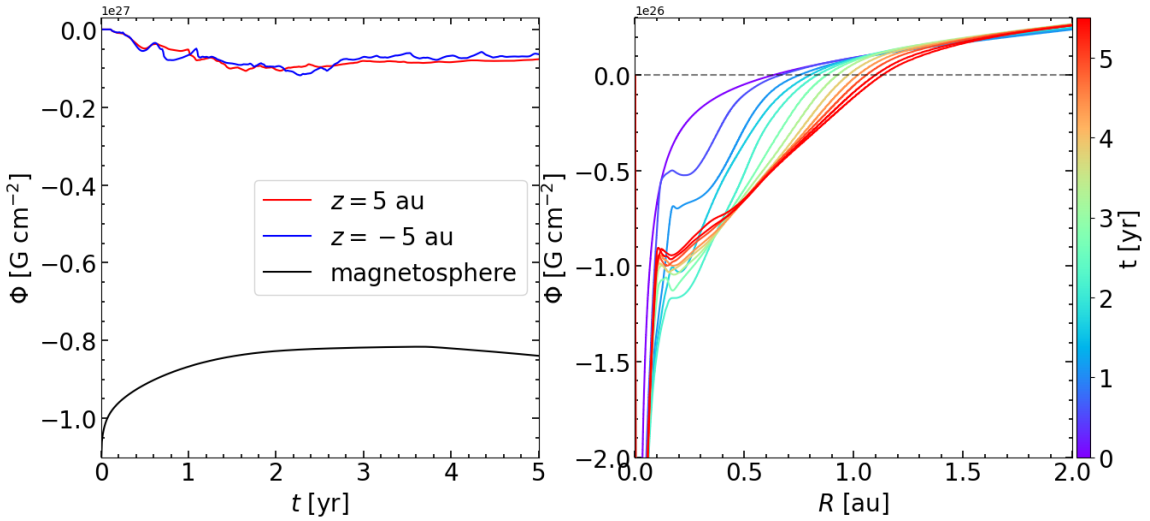


Figure 7.3: Magnetic flux evolution in the simulation. **The left panel** shows the total magnetospheric flux (black line), defined as the maximum magnitude of the total downward $\hat{z}$-directed magnetic flux integrated azimuthally at each cylindrical radius. The red and blue lines indicate the amount of opened stellar magnetosphere flux, measured as the maximum magnitude of azimuthally-integrated downward B_z at $z = \pm 5$ au above and below the disk midplane, respectively. **The right panel** shows the time evolution of the enclosed magnetic flux at each cylindrical radius at the midplane. The stellar magnetosphere primarily contributes to the negative flux at small radii, while the disk field dominates the positive flux at larger radii.

radii, which we examine in the following subsection.

7.3.2 Disk Wind from Opened Magnetospheric Field

The disk wind is a slower, high-density outflow at large cylindrical radius compared to the jet (see § 7.3.4 below). To illustrate the properties and launching mechanism of the disk wind, we show in Figure 7.4 the azimuthally averaged quantities in the disk wind region. Panels (a) and (b) show the density and the projected $\hat{z}$-direction velocity, respectively. Any outflow away from the disk midplane has a positive value. The disk wind has a density $\approx 10^{-13}$ g cm^{-3} near the base (around $r \approx 0.5$ au), and a density of $\approx 10^{-14}$ g cm^{-3} at higher altitudes. The outflow velocity of the disk wind is around 10^6 cm s^{-1}, slower than the jet but still above the escape velocity at high

altitudes.

Tu et al. (2025a) identify two components for the disk wind: an MRI-active disk wind and a laminar disk wind. In their case, the inner disk wind is MRI-unstable, leading to a turbulent outflow, whereas the outer disk wind is MRI-stable, resulting in a laminar wind. The MRI stability is measured using the dimensionless parameter (Tu et al., 2025a)

$$q \equiv \frac{\lambda}{H}, \tag{7.10}$$

where $H = R/10$ is the disk scale height and λ is the most unstable MRI wavelength given by (Zhu & Stone, 2018)

$$\lambda = 2\pi\sqrt{\frac{16}{15}}\frac{v_A}{\Omega}. \tag{7.11}$$

Here, v_A is the Alfvén speed and Ω is the local orbital frequency. Following Tu et al. (2025a), we choose the range $0.1 < q < 10$ to denote where MRI is most efficient.

Figure 7.4(c) shows this q parameter, illustrating a zone between the jet and the disk wind in both hemispheres where q is within the optimal range. The disk wind can thus be divided into the MRI-active disk wind at a small cylindrical radius and the MRI-stable disk wind at a larger cylindrical radius, particularly along the upper hemisphere. However, similar to Tu et al. (2025a), the MRI-active disk wind eventually merges with the laminar disk wind at high altitudes, where MRI can no longer be sustained. As a result, at these altitudes, the primary distinction is between the jet and the disk wind.

To illustrate the kinematics of the disk wind, we show the plasma-β and the kinetic-β in Figure 7.4(d) and (e), respectively. They are defined as

$$\beta = \frac{P}{B^2/8\pi}, \tag{7.12}$$

$$\beta_K = \frac{\rho v^2/2}{B^2/8\pi}, \tag{7.13}$$

measuring the ratios between the thermal and ram pressures and the magnetic pressure. The plasma-$\beta < 1$ in the disk wind indicates that thermal energy is negligible compared to magnetic energy. Kinetic-$\beta > 1$ in the disk indicates that kinetic energy (primarily from rotation) dominates the magnetic energy.

The dominance of kinetic energy results in the centrifugal force outweighing the magnetic force in the cylindrical-$\hat{R}$ direction. Figure 7.4(f) and (g) show the ratio between magnetic and centrifugal forces, and the magnitude of the magnetic force in the cylindrical-$\hat{R}$ direction, respectively. While the magnetic force generally points in the $-\hat{R}$ direction (towards the axis), its magnitude is insufficient to counteract the outward centrifugal force. This imbalance leads to an increasing opening angle of the disk wind.

The magnetic force is primarily responsible for driving the outflow in the $\hat{z}$ direction. Figure 7.4(h), (i), and (j) show the projected total magnetic force in the $\hat{z}$ direction, the effective magnetic pressure component, and the effective magnetic tension component, respectively. The projected total magnetic force is given by

$$a^p_{B,z} = \frac{z}{|z|}\Big[\frac{1}{4\pi\rho}(\nabla \times \boldsymbol{B}) \times \boldsymbol{B}\Big]_z, \tag{7.14}$$

and following Tu et al. (2025a), we define the projected effective magnetic pressure and tension forces in cylindrical coordinates by removing the $B_z \frac{dB_z}{dz}$ term that does not contribute to overall acceleration:

$$a^{p,\mathrm{eff}}_{z,\mathrm{pres}} \equiv -\frac{z}{|z|}\frac{1}{4\pi\rho}\Big(\frac{\partial B_\phi}{\partial z}B_\phi + \frac{\partial B_R}{\partial z}B_R\Big), \tag{7.15}$$

$$a_{\rm z,tens}^{p,\rm eff} = \frac{z}{|z|}\frac{1}{4\pi\rho}\Big(\frac{\partial B_z}{\partial R}B_R + \frac{\partial B_z}{\partial \phi}B_\phi\Big). \tag{7.16}$$

It is evident that magnetic pressure drives the disk wind outflow, not the magnetic tension force. This result is consistent with the geometric argument and conclusion in Tu et al. (2025a) that only magnetic pressure can drive an outflow when open magnetic field lines thread the disk.

7.3.3 Opened Stellar Field

As discussed in Sec. 7.3.1, part of the stellar magnetospheric field opens up. Half of the opened field threads the disk and becomes a "disk field"; the other half remains attached to the star and becomes an opened stellar field.

To illustrate the geometry of the opened stellar magnetic field, Figure 7.5(a) presents a density slice through the meridional plane, overlaid with magnetic field lines. On the displayed scale, the magnetic field in the polar regions above and below the star points in the $-\hat{z}$ direction, opposite to the field threading the disk (e.g., Figure 7.4), as expected.

The properties of this downward magnetic field and the gas kinematics are shown in Figure 7.5(b) and (c), respectively. The magnetic field strength is particularly strong in the polar cavity, reaching approximately 20 Gauss at $z = \pm 0.1$ au. The gas in the polar cavity immediately above and below the stellar magnetosphere rapidly falls toward the star because of strong gravity and insufficient rotational support. Given the low density and strong magnetic field in this region, it is unsurprising that the polar cavity is entirely magnetically dominated, with plasma-β and kinetic-β values much lower than 1 (Figure 7.5[d] and [e]).

Although the majority of the open stellar field does not directly contribute to jet launching, it serves as a structural backbone for the jet in the magnetically dominated

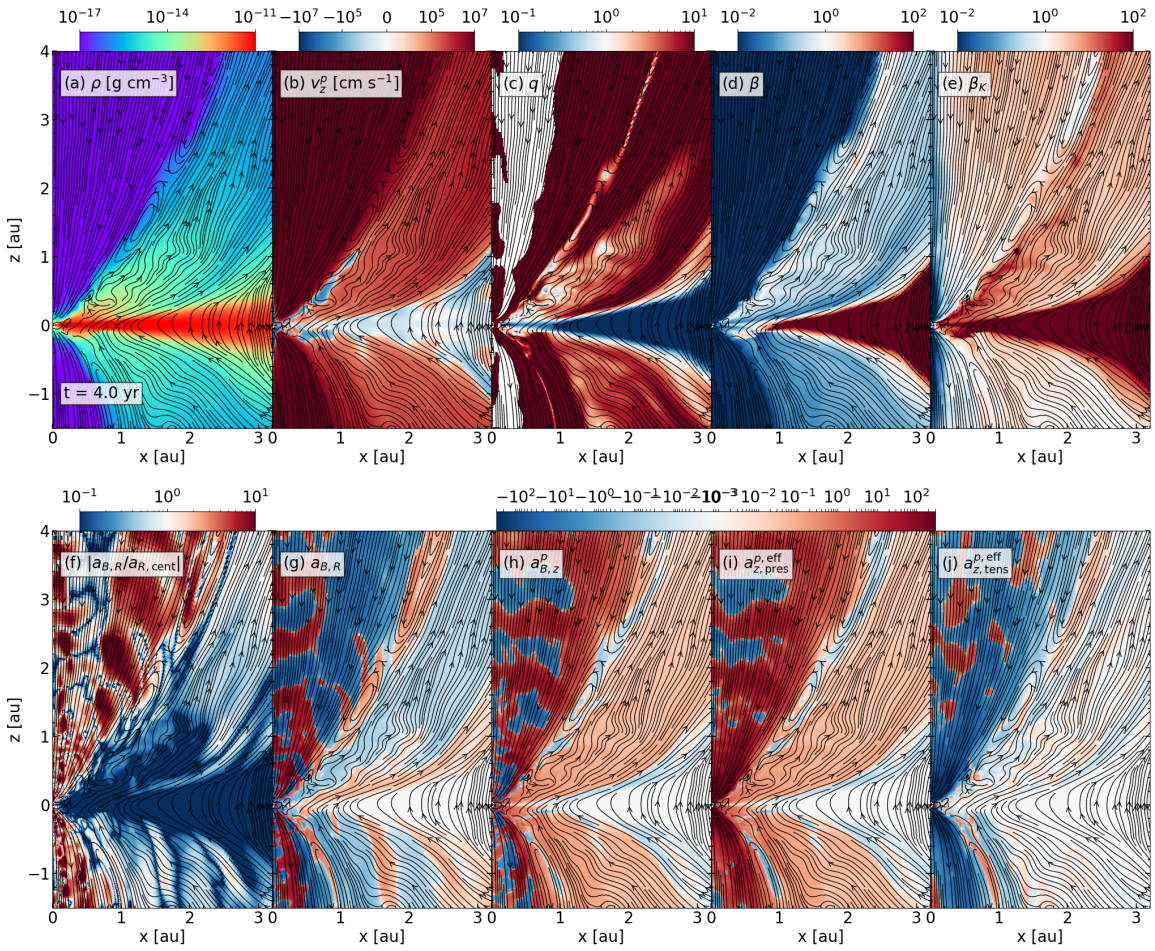


Figure 7.4: Overview of the outflow, particularly the disk wind at a large cylindrical radius surrounding the jet. **Panel (a) and (b)** show the density and projected $\hat{z}$-direction velocity (v_z^p, equ. 7.9) respectively; **panel (c)** shows the normalized MRI-turbulence wavelength (equ. 7.10; **panel (d) and (e)** show the plasma-β and (equ. 7.12) kinetic-β (equ. 7.13) respectively. The lower panels compare different force components in the disk wind. **Panel (f)** shows the ratio between the cylindrical-$\hat{R}$ direction magnetic force and centrifugal force. **Panel (g), (h), (i), and (j)** show the magnitude of the gas acceleration due to magnetic forces. The quantities are total gas acceleration in cylindrical-$\hat{R}$ direction, total magnetic acceleration in $\hat{z}$- irection, the effective magnetic pressure component (equ. 7.15), and the effective magnetic tension component (equ. 7.16) respectively. These disk wind properties and forces show that the disk wind in this model is very similar to the disk wind in Tu et al. (2025a).

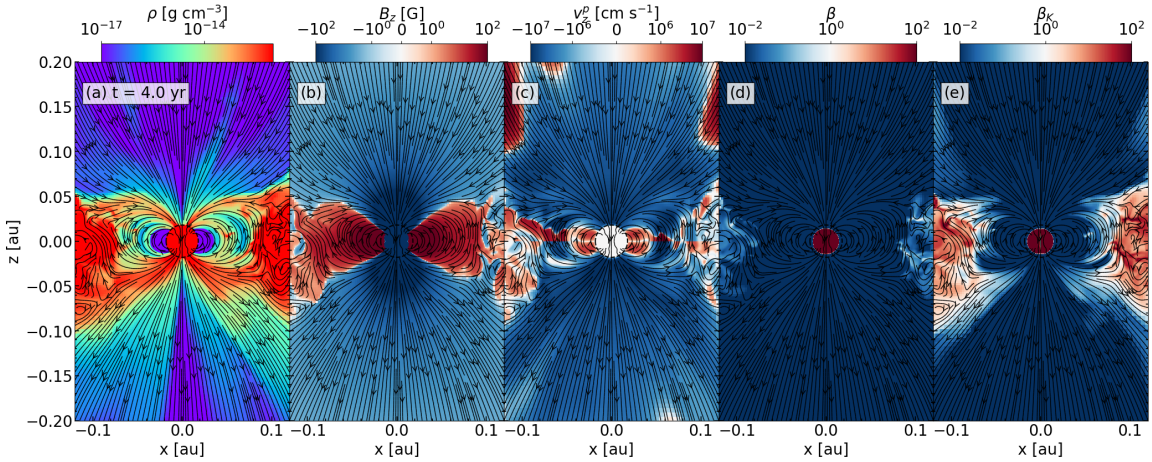


Figure 7.5: A zoom-in view focusing on the permanently closed stellar magnetosphere (around the midplane) and the opened stellar magnetic field threading the star (in the polar region above and below the star). **Panel (a)** shows the real density traced by the "passive scalars", highlighting the magnetospheric accretion streams. The sphere in the middle is the inner boundary $r_{\rm fix}$, where a star resides (see sec. 7.2 for a more detailed description of the setup). **Panels (b) and (c)** show the B_z field strength and v_z^p (equ. 7.9) respectively, illustrating the magnetic and dynamical properties of the region close to the star. **Panels (d) and (e)** show the plasma-β (equ. 7.12) and kinetic-β (equ. 7.13) respectively, indicating the magnetosphere and the polar cavity are both magnetically dominated.

region. As we demonstrate in Section 7.3.4, the jet is primarily driven by toroidal magnetic pressure. However, a magnetic tower consisting predominantly of toroidal loops is inherently susceptible to kink instabilities (Moll et al., 2008; Huarte-Espinosa et al., 2012). The strong open stellar magnetic field in the polar region, which accounts for most of the open stellar flux, helps stabilize the jet by threading these loops along the polar axis, mitigating instabilities.

7.3.4 Magnetospheric jet

The jet is launched from the interaction between the star, its magnetosphere, and the surrounding disk, and propagates in the low-density polar cavity. Figure 7.6 outlines the jet's location and key characteristics. At lower altitudes ($\lesssim 0.5$ au), the

jet is confined between the opened stellar field near the polar axis (approximately delineated by the magenta line) and the disk wind/atmosphere at larger cylindrical radii (indicated by the green dashed line). At higher altitudes, the jet expands to fill the polar cavity, as shown in Figure 7.4[b].

To assess the relative contributions of various energy components in the jet-launching region—namely, gas thermal energy, gas kinetic energy, and magnetic energy—we examine the plasma-β and kinetic-β in Figure 7.6(c) and (d). As expected, the plasma-β remains well below unity throughout the jet region, except in the disk midplane, indicating that magnetic energy dominates over thermal energy. The kinetic-β is also less than 1 inside the jet-launching polar cavity, but rises above 1 just outside the jet boundary. This transition is a key feature in the launching process and is analyzed in more detail in Section 7.4.

Since both plasma-β and kinetic-β are below order unity in the jet-launching polar cavity, we focus on the magnetic forces to establish a foundation for our detailed examination of the jet-launching mechanism in section 7.4. The lower panels of Figure 7.6 illustrate the magnetic forces in the jet region. Figure 7.6[e] shows the total magnetic force, revealing that the acceleration of the outflow occurs primarily along the surface of the vertically extended disk, which also marks the boundary of the jet-launching cavity. Above approximately 1 au in both hemispheres, acceleration becomes less coherent (with alternating regions of acceleration and deceleration), indicating that the bulk of the flow acceleration has largely completed beyond this altitude. This is confirmed by velocities in the $\hat{z}$ direction reaching several 10^7 cm s^{-1} below 1 au, with minimal subsequent increase in velocity above this height.

As demonstrated in Tu et al. (2025a), in systems with ordered, large-scale magnetic fields threading the disk, only magnetic pressure forces, not magnetic tension forces, can launch outflows in global models. Our simulations confirm this finding.

Figure 7.6(f) and (g) display the effective magnetic tension acceleration (equ. 7.16) and effective magnetic pressure acceleration (equ. 7.15), respectively. Magnetic tension acceleration generally points toward the midplane, while magnetic pressure acceleration points away from it. More specifically, Figure 7.6(h) shows the acceleration due to toroidal magnetic pressure gradient, defined as

$$a_{z,\mathrm{pres}}^{p,\mathrm{tor}} = -\frac{z}{|z|}\frac{1}{4\pi\rho}\frac{dB_\phi}{dz}B_\phi. \tag{7.17}$$

The toroidal magnetic pressure accounts for most of the magnetic pressure-driven jet acceleration. In the following section, we will examine the mechanism generating this crucial toroidal magnetic field (Section 7.4).

7.4 Jet launching mechanism: "Load-fire-reload"

This section presents a detailed description and analysis of the jet-launching mechanism in our model. The jet is launched through a cyclic process comprising three distinct phases: load, fire, and reload. Each phase corresponds to characteristic changes in the magnetic field configuration and dynamics. In the following subsections, we describe each step in detail and analyze how they collectively drive the jet-launching behavior observed in the simulation.

7.4.1 Load: charging B_ϕ by star-disk differential rotation

To illustrate the jet-launching mechanism, we zoom in on the inner part of the simulation in Figure 7.7, which shows the azimuthally averaged gas and magnetic field properties. Panels (a), (b), and (c) show the density, projected $\hat{z}$-direction velocity v_z^p, and kinetic-β, respectively. The jet resides in the low-density polar cavity, where

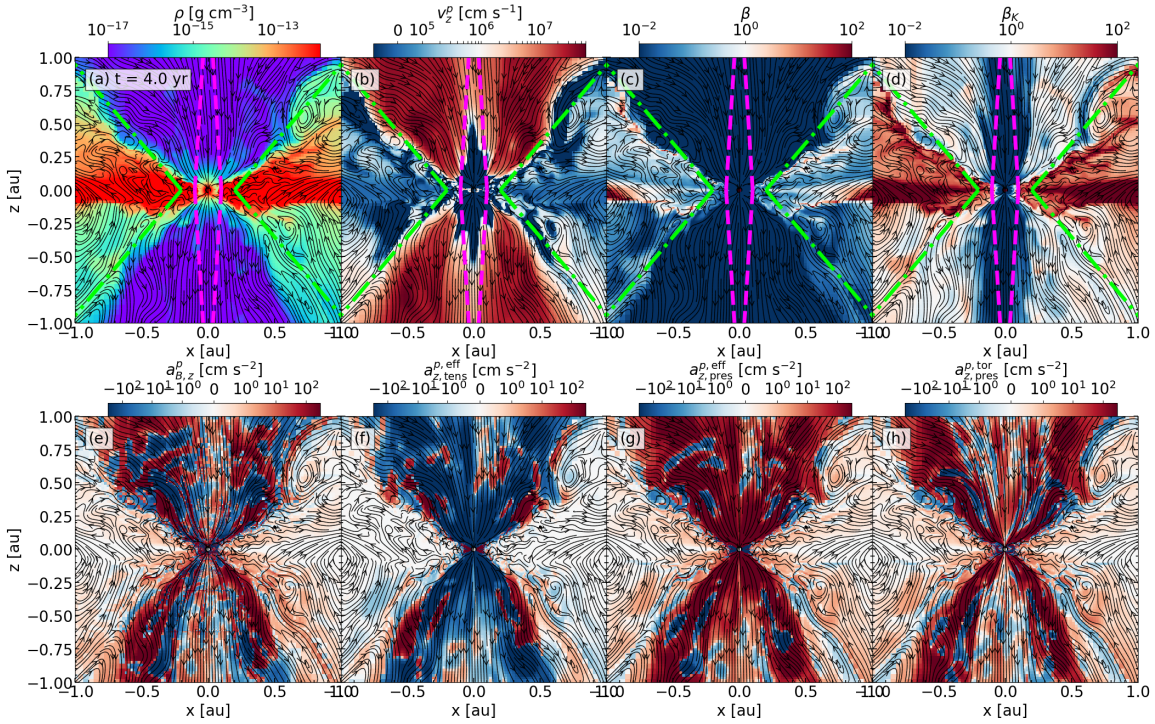


Figure 7.6: Overview of the jet. Upper panels focus on the magneto-hydrodynamic properties of the jet; lower panels focus on the magnetic forces. **Panels (a) and (b)** show the density and projected $\hat{z}$-direction (v_z^p, equ. 7.9) respectively, showing the jet lies in the low-density polar cavity. **Panels (c) and (d)** show the plasma-β (equ. 7.12) and kinetic-β (equ. 7.13) respectively, showing the jet is a magnetically-dominated structure. **Panels (e), (f), (g), and (h)** show the total magnetic force, the effective magnetic tension force (equ. 7.16), the effective magnetic pressure force (equ. 7.15), and the toroidal magnetic pressure force (equ. 7.17) respectively.

$\rho \lesssim 10^{-14}$ g cm^{-3}, $v_z^p > 10^7$ cm s^{-1} and $\beta_K < 1$. The low β_K highlights the magnetic dominance in the jet-launching polar cavity. A black dashed contour traces $\beta_K = 1$, the rough boundary between the high-density disk wind/atmosphere and the low-density jet.

On the scale shown in Figure 7.6, the jet is driven by magnetic pressure force primarily along the polar cavity-disk boundary, with a strong toroidal magnetic field. Since a toroidal field can in principle be generated wherever there is differential rotation along a field line, the most preferred field lines for toroidal field generation are those threading both the star, where the magnetically-dominated segment of the field line rooted on the star surface co-rotates with the star, and the disk, where the gas dominates and the field lines are forced to move with the gas at the local Keplerian velocity. We will first focus on these field lines, followed by a generalization to all field lines that experience field-gas differential rotation.

The field lines threading both the star and the dense disk generate a toroidal field in situ by a change in the angular speed of the rotation along the field line, as shown in Figure 7.7(d), which presents the ratio between the local angular velocity Ω and the Keplerian angular velocity Ω_K. Across the $\beta_K = 1$ boundary, the angular velocity transitions from nearly Keplerian in the disk to super-Keplerian above the disk. It is indicative of the differential rotation along the field line that leads to the toroidal field generation through field line twisting.

To showcase a magnetic field participating in this process, Figure 7.7 shows a 2D projection of a 3D field line, highlighted in solid magenta. One end of this field line is anchored on the star, which transfers angular momentum to the gas via a strong magnetic field in the low plasma-β polar region to force the gas to rotate at a super-Keplerian rate. The other end is embedded in the gas-dominated disk, where the gas motion remains nearly Keplerian. The significant differential rotation along this field

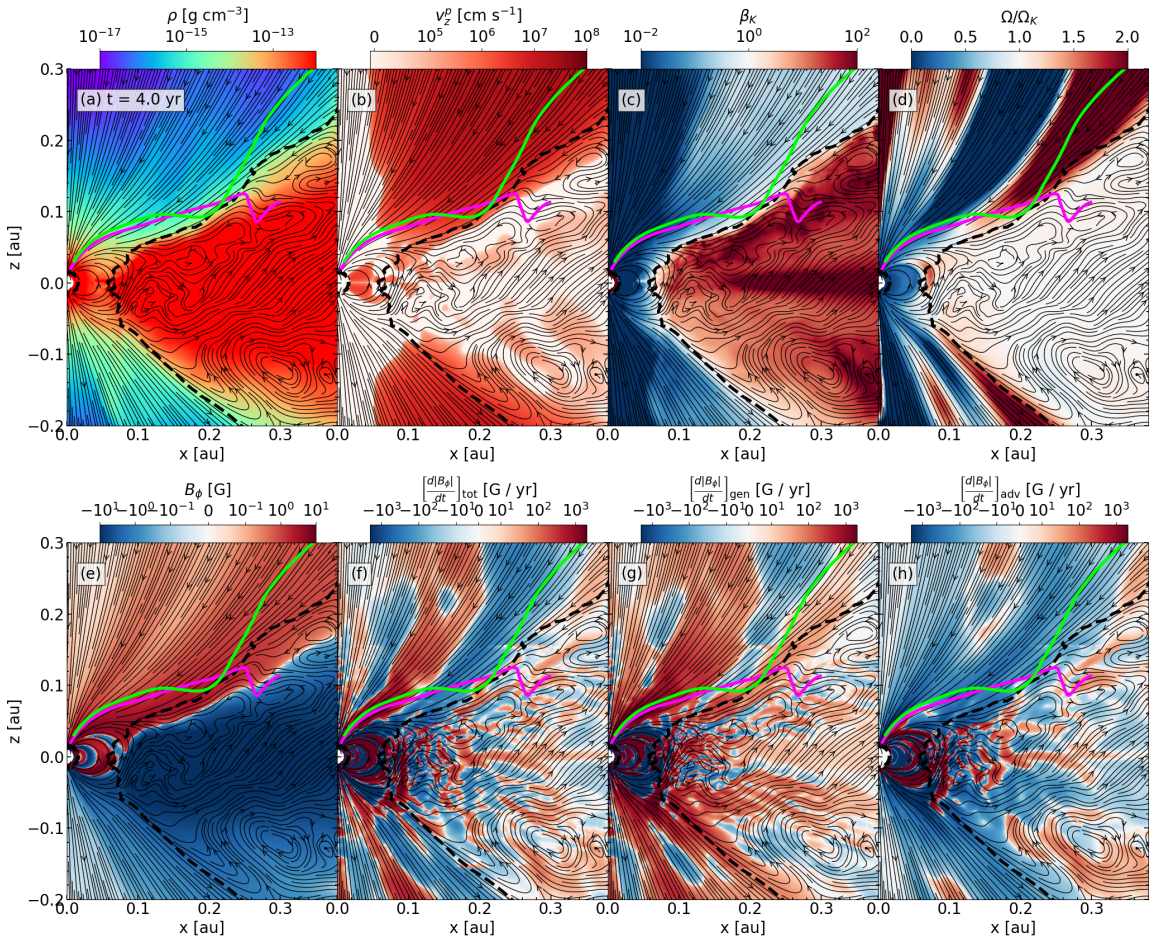


Figure 7.7: Toroidal magnetic field generation in the jet-launching region. The quantities plotted are azimuthally averaged. **Panel (a) and (b)** show the density and projected $\hat{z}$-direction velocity (v_z^p, equ. 7.9) respectively, showing the density structure and the location of the jet. **Panel (c)** shows the kinetic-β (equ. 7.13), highlighting the transition from the magnetically-dominated polar cavity to the mass-dominated disk. **Panel (d)** shows the angular velocity, normalized by the local Keplerian value. The lower panels show toroidal magnetic field dynamics. **Panel (e)** shows the toroidal magnetic field; **Panels (f), (g), and (h)** show the total change in toroidal field strength (equ. 7.20), toroidal field generation by differential rotation (equ. 7.18), and toroidal field advection by flux-freezing (equ. 7.19) respectively. The black dashed contour highlights the $\beta_K = 1$ surface. The magenta and green field lines are 2D projections of representative 3D field lines shown in Figure 7.8. An animated version is available at `https://virginia.box.com/s/ijkmmcxee9f6mchph57zp8zdptgbt07p`.

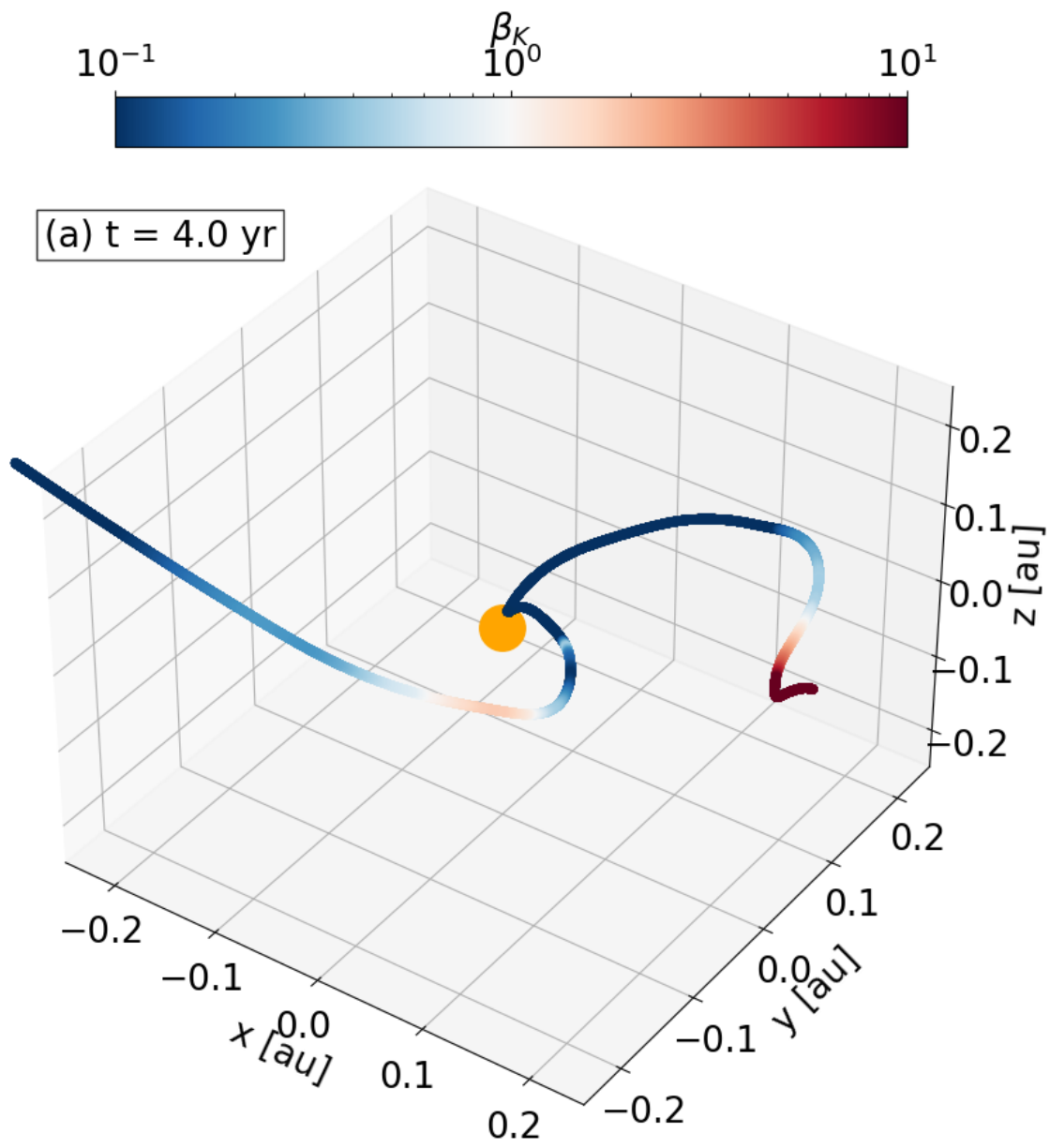


Figure 7.8: 3D rendition of the two fieldlines highlighted in Figure 7.7, colored by the local kinetic-β (equ. 7.13). The yellow sphere at the center represents the star. The magenta fieldline in Figure 7.7 is located on the right, with one low kinetic-β end on the star and one high kinetic-β end in the disk. The green field line from Figure7.7 is shown on the left: most of this field line resides in regions where $\beta_K < 1$, indicating magnetic dominance, except for a localized segment with $\beta_K > 1$, where kinetic energy becomes dominant.

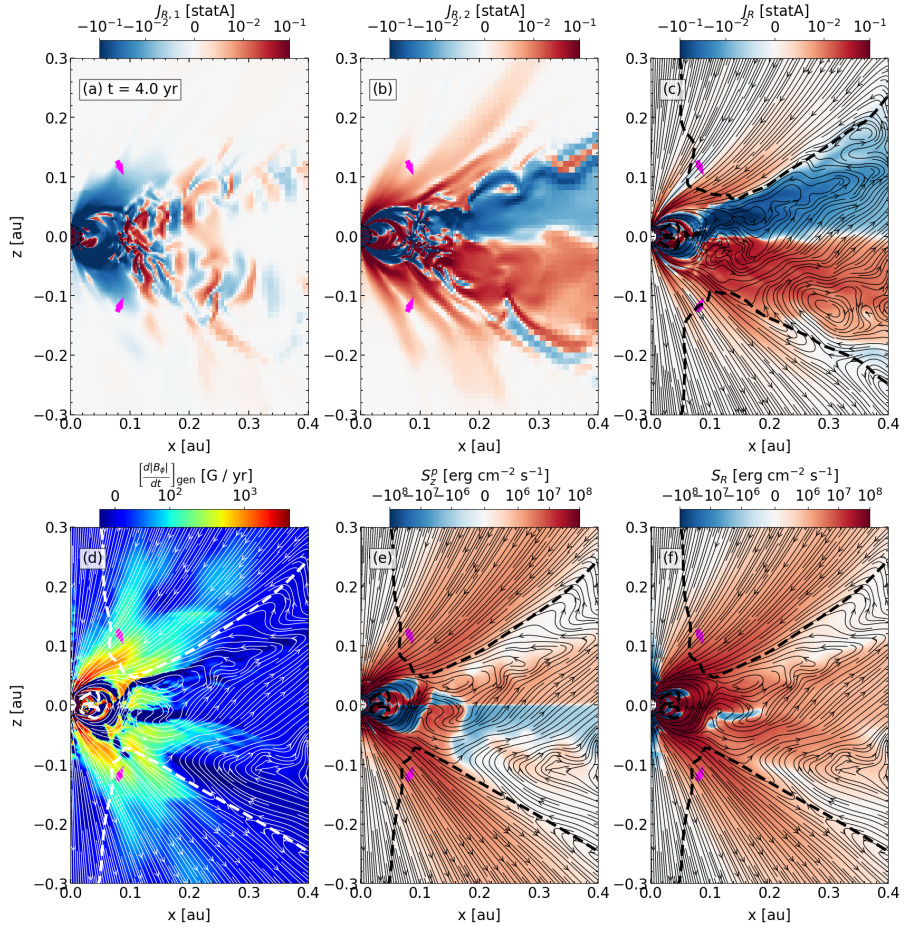


Figure 7.9: Magnetic energy evolution in the jet-launching region. The top panels illustrate the cylindrical $\hat{R}$-direction current and its components. Given the toroidal magnetic field structure (Figure 7.7[e]), a positive current is required to exert a force directly away from the disk. **Panels (a) and (b)** show meridional slices of the two components of the $\hat{R}$-directed current (equ. 7.22 and 7.23), respectively. The component due to azimuthal asymmetry (equ. 7.22) points toward the midplane, while the component arising from global field geometry (equ. 7.23) points away from the disk. **Panel (c)** shows the azimuthally averaged current at a representative time, revealing a positive current along the surfaces of both the magnetosphere and disk—sufficient to drive outflows. To reduce transient effects and emphasize large-scale features, panels (d), (e), and (f) present time-averaged (over ±0.1 yr centered on 4.0 yr) and azimuthally averaged quantities. **Panel (d)** shows toroidal field generation concentrated along narrow streams at the magnetosphere and disk surfaces, highlighting the origin of the current. **Panels (e) and (f)** display the projected Poynting flux in the $\hat{z}$- and $\hat{R}$-directions, respectively, demonstrating how magnetic energy generated near the star is transported outward to power the jet. The dashed contours in panels (c)–(f) outline the approximate extent of the jet.

line, particularly near where the field bends sharply, generates an azimuthal magnetic field, as shown in Figure 7.7(e).

The differential rotation along this field line generates the azimuthal magnetic field required for jet launching by magnetic pressure, accelerating the gas in the vertical $\hat{z}$-direction. Consequently, this azimuthal magnetic field is constantly advected away by gas motion. Quantitatively, magnetic field generation and removal in this nearly ideal MHD region (due to ionization by high temperature) are governed by the induction equation (equ. 7.3). In a cylindrical coordinate, the change in azimuthal magnetic field ($\left[\frac{\partial B_\phi}{\partial t}\right]_{\rm tot}$) can be divided into two processes: generation of B_ϕ from B_z and B_R by differential rotation,

$$\left[\frac{\partial B_\phi}{\partial t}\right]_{\rm gen} = \frac{\partial (v_\phi B_z)}{\partial z} + \frac{\partial (v_\phi B_R)}{\partial R}, \tag{7.18}$$

and advection of B_ϕ by gas motion,

$$\left[\frac{\partial B_\phi}{\partial t}\right]_{\rm adv} = -\frac{\partial (v_z B_\phi)}{\partial z} - \frac{\partial (v_R B_\phi)}{\partial R}. \tag{7.19}$$

Since the toroidal magnetic field strength (and the magnetic pressure associated with it) is what ultimately powers jet-launching, we focus on the change in toroidal magnetic field strength by defining

$$\frac{\partial |B_\phi|}{\partial t} \equiv \frac{B_\phi}{|B_\phi|}\frac{\partial B_\phi}{\partial t}, \tag{7.20}$$

where a positive value denotes an increase in the absolute value of the toroidal magnetic field strength and a negative value denotes a decrease. Figure 7.7(f), (g), and (h) shows $\left[\frac{\partial |B_\phi|}{\partial t}\right]_{\rm tot}$, $\left[\frac{\partial |B_\phi|}{\partial t}\right]_{\rm gen}$, and $\left[\frac{\partial |B_\phi|}{\partial t}\right]_{\rm adv}$ respectively. Although $|B_\phi|$ decreases in magnitude in a large part of the jet-launching region at the time shown, $|B_\phi|$ switches

rapidly between net gain and loss of strength over time, resulting in a quasi-steady state. The reader is encouraged to view the animated version of Figure 7.7 to see this rapid change between gaining and losing $|B_\phi|$.

The rapid change in the net change in $\left[\frac{\partial |B_\phi|}{\partial t}\right]_{\rm tot}$ does not translate to a rapid change in the $\left[\frac{\partial |B_\phi|}{\partial t}\right]_{\rm gen}$ nor $\left[\frac{\partial |B_\phi|}{\partial t}\right]_{\rm adv}$. Generation through differential rotation ($\left[\frac{\partial |B_\phi|}{\partial t}\right]_{\rm gen}$) stays mostly positive on the magnetically dominated side of the $\beta_K = 1$ boundary, and advection through gas motion ($\left[\frac{\partial |B_\phi|}{\partial t}\right]_{\rm adv}$) stays mostly negative, illustrating the required toroidal magnetic field for jet-launching is generated in situ by differential rotation along magnetic field lines.

The $\left[\frac{\partial |B_\phi|}{\partial t}\right]_{\rm gen}$ term being predominantly positive in the jet-launching region indicates that toroidal field generation is not limited to field lines like the magenta fieldline highlighted in Figure 7.7, where one footpoint is anchored in the disk and the other on the star. In fact, any differential rotation between the dense disk gas and the stellar magnetosphere can generate a toroidal magnetic field capable of launching an outflow, even if the field line is not fully embedded in the disk. An example of this is shown in Figure 7.8, where a segment along an otherwise open field line becomes kinetically dominated ($\beta_K > 1$) as it approaches the disk. This local interaction between the disk and the stellar field generates differential rotation, which in turn produces the toroidal field responsible for jet launching.

Similar field lines threading both the disk and the star to the one highlighted in Figure 7.7(d) can be found in the 3D plot (and the associated animation) of the field lines in the magnetosphere and surrounding regions (see Figure 7.10 below) along many azimuthal directions, allowing the jet to be driven continuously in the simulation.

Before discussing the release of toroidal magnetic energy during the "fire" phase, we first highlight that the most rapid generation of toroidal field occurs in the polar

region near the star. Although this may seem counterintuitive, since field lines in the magnetically dominated polar region are typically expected to remain relatively straight, this rapid winding arises because the star rotates faster along these field lines than the disk does. Specifically, for the "two-legged" field lines illustrated in Figures 7.7 and 7.8, the footpoint on the disk lies beyond the corotation radius of the star (approximately 0.1 au). As a result, the disk end of the field line rotates more slowly than the stellar end, causing the star to drag the field line forward. This differential rotation leads to significant field twisting near the stellar surface. Although the magnetic deformation is quickly removed by outgoing Alfvén waves (and their associated Poynting flux; see Figure 7.9 [e, f]) and does not remain near the star, it contributes to the magnetic energy buildup that eventually drives the jet, as we describe in the next subsection.

7.4.2 Fire: releasing magnetic energy by global field geometry

Another critical consequence of star-disk differential rotation is the emergence of strong current sheets, particularly in the cylindrical $\hat{R}$ direction, which are essential for converting magnetic energy stored in the toroidal field into jet-driving forces. Specifically, the abrupt change in magnetic field geometry by the differential rotation between the star and the disk leads to the generation of a significant radial current density, J_R, expressed as:

$$J_R = \frac{c}{4\pi}\Big(\frac{\partial B_z}{\partial \phi} - \frac{\partial B_\phi}{\partial z}\Big). \tag{7.21}$$

This current has two physically distinct contributions:

$$J_{R,1} = \frac{c}{4\pi}\frac{\partial B_z}{\partial \phi}, \tag{7.22}$$

arises from azimuthal asymmetries in B_z, while the second term,

$$J_{R,2} = -\frac{c}{4\pi}\frac{\partial B_\phi}{\partial z}, \tag{7.23}$$

stems from vertical gradients in the toroidal magnetic field. Since azimuthal averaging eliminates $J_{R,1}$ by construction, we examine both terms in meridional slices (see Figure 7.9[a,b]) to evaluate their roles in driving outflows.

For a magnetic force to support jet launching in both hemispheres, the condition $\frac{z}{|z|}J_R B_\phi > 0$ must be satisfied, such that the Lorentz force points away from the midplane. This is generally satisfied when $J_R > 0$, given the sign of B_ϕ in Figure 7.7[e], which is positive in the polar cavity of the upper hemisphere and negative in that of the lower hemisphere. While $J_{R,2}$ contributes positively to J_R and aligns with the outflow direction, $J_{R,1}$ tends to oppose the jet by introducing a restoring force toward the midplane. Moreover, $|J_{R,1}|$ is typically smaller than $|J_{R,2}|$, so the net current remains positive in the jet-launching region, as shown by the azimuthally-averaged J_R in Figure 7.9(c).

This jet-driving current is generated locally along the surface of the closed magnetosphere and the disk as a consequence of the rapid changes in the toroidal magnetic field geometry in the vertical direction. As discussed in Sec. 7.4.1, differential rotation between the star and the disk twists magnetic field lines most effectively when the field line has one end rooted in the star and the other embedded in the disk. A comparatively strong toroidal field is produced in this narrow layer where such "two-legged" field lines reside. Above this region, in the low-density polar cavity, the strong magnetic field keeps the fieldlines roughly poloidal, and the toroidal component remains weak. Below this region is the mass-dominated disk, where the magnetic effect is more diminished, providing a solid foundation for the outflow.

As a result, the field lines within this intermediate layer, subject to significant differential rotation, are continually over-twisted relative to those above and below. This localized over-twisting establishes steep vertical gradients in the toroidal magnetic field, giving rise to a strong radial current sheet (J_R) essential for jet launching. Because this differential twisting is inherently highly variable in space and time, we illustrate it in Figure 7.9(d) using the azimuthally and temporally averaged quantity $\left[\frac{\partial B_\phi}{\partial t}\right]_{\rm gen}$. The colormap highlights the toroidal magnetic field's generation rate in the layer above the closed magnetosphere and disk atmosphere, with more positive values indicating faster local toroidal field generation. The peaks in the toroidal field generation rate, pointed by arrows in Figure 7.9(d), align with the location of the J_R current sheet at the disk surface. However, as shown in Figure 7.9(d), the gas in the most rapid toroidal field generating region near the star is infalling, rather than outflowing (the outflow region is outlined in white in Figure 7.9[d]). This raises a natural question: how does the energy generated in this inner region reach the outflow zone to drive the jet?

The answer lies in the Poynting flux, which enables magnetic energy to travel faster than the gas itself. Even in regions of infall, magnetic fields can transport energy outward, effectively "advecting" it upstream into the jet-launching region. To illustrate this process, we show in Figure 7.9(d, e) the Poynting flux in $\hat{z}$ direction (S_z^p, projected in the same way as the $\hat{z}$ direction velocity v_z^p, equ. 7.9) and cylindrical-$\hat{R}$ directions (S_R), respectively. Even in the infall region around the polar axis, magnetic energy can be transported away from the star's vicinity to the outflow region.

In summary, the combined effect of the J_R current sheet (Figure 7.9[c]) and the amplified toroidal field (Figure 7.7[e]) generates a vertical ($\hat{z}$-direction) magnetic force, accelerating gas to high poloidal velocities.

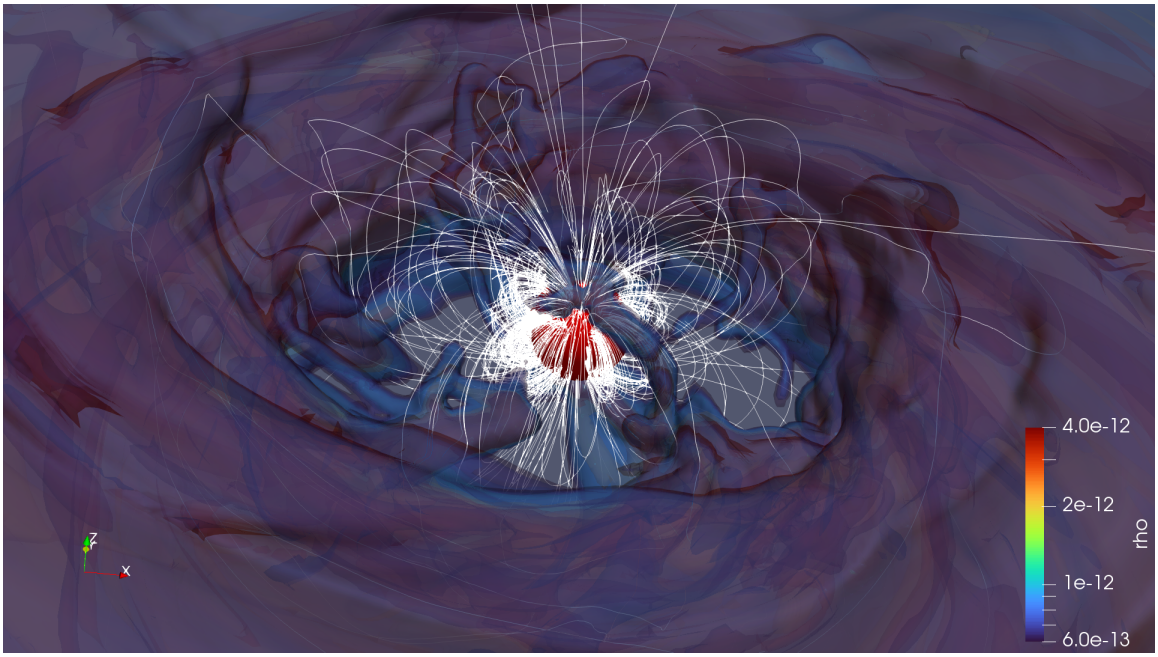


Figure 7.10: 3D rendition of the protostar, accreting magnetosphere, and magnetic field lines. The disk is shown as semi-transparent density isosurfaces at around 10^{-12} g cm^{-3}. The protostar is represented by the central red solid sphere. White lines depict magnetic field lines, including permanently closed magnetospheric loops and twisted field lines resulting from magnetosphere–disk interactions (e.g., the prominent twisted fieldline near the top-center of the image). An animated version of this figure is available at: `https://virginia.box.com/s/w3f0wjnpakciejrlxnurnvlaxwi24sdx`.

7.4.3 Reload: replenishing jet gas by magnetic reconnection

The "two-legged" magnetic field lines, such as those shown in Figure 7.7(e), stretch and may open during outflow launching. To sustain a continuous jet (Figure 7.1), these field lines must reconnect and revert to a "two-legged" configuration, "reloading" with mass by magnetic reconnection between oppositely directed field lines. As discussed in Sections 7.3.1 and 7.3.3, the global magnetic topology at late times when a persistent outflow is launched consists of downward-pointing original magnetospheric field lines that are opened but remain connected to the star (referred to as "the opened stellar field lines" for short) and upward-pointing original magnetospheric field lines that are opened but thread through the (inner) disk (but not the star). These oppositely directed open field lines are expected to preferentially reconnect at their interface. Although individual reconnection events are difficult to isolate in a highly variable 3D system, we present qualitative evidence below to confirm reconnection along this boundary.

Figure 7.11(a)-(d) presents the time evolution of the azimuthally averaged radial velocity v_r at t = 3.7, 3.8, 3.9, and 4.0 yr. To track the evolution of the magnetic field, we trace field lines using contours of the radial magnetic flux:

$$\Phi_{B,r}(r,\theta) = \int_0^{\theta}\int_0^{2\pi} B_r r^2 \sin\theta^{\star}\, d\phi d\theta^{\star}, \tag{7.24}$$

where constant $\Phi_{B,r}$ contours approximate field line locations, as indicated by the black dashed curves in Figure 7.11. These contours represent azimuthally averaged field configurations, capturing only the global magnetic evolution. In reality, three-dimensional reconnection events occur on much shorter timescales. Between t = 3.7 yr (panel [a]) and t = 4.0 yr (panel [d]), the same averaged field line transitions

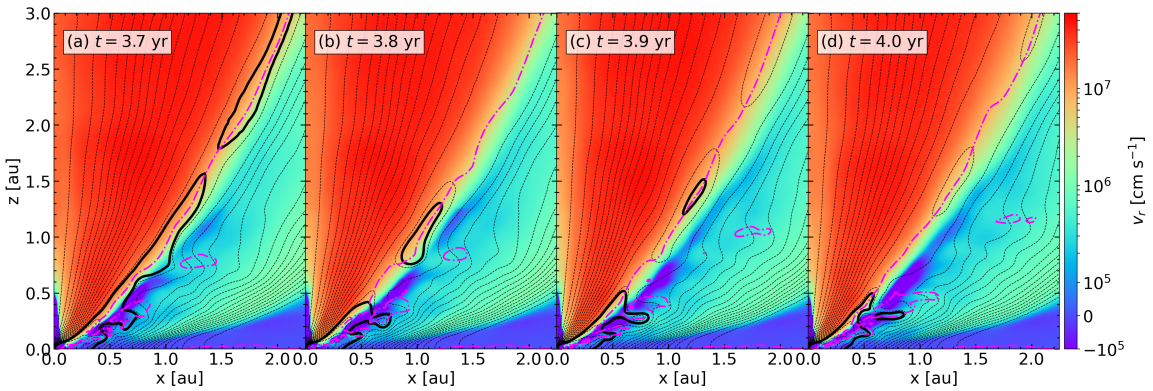


Figure 7.11: Illustration of the "reload" stage where magnetic reconnection resets the field geometry. While individual reconnection event occurs rapidly and is unrealistic to show explicitly in 3D simulations, we illustrate the cumulative effect using azimuthally integrated magnetic flux surfaces. The panels present a time sequence of the flux surface evolution. The background color shows the radial velocity in spherical coordinates (v_r), highlighting the jet's location. Black lines represent azimuthally averaged magnetic flux surfaces, which can also be interpreted as approximate magnetic field line locations. The thick black line shows magnetic reconnection by tracing a representative field line along the $B_r = 0$ surface, which is marked by the magenta dash-dot line.

from an extended state to a more compact (lower altitude) configuration. Given the continuous outflow during this interval, the contraction of the averaged field line suggests magnetic reconnection.

Reconnection primarily occurs along the $B_r = 0$ boundary (highlighted by the magenta contour in Figure 7.11) where the open field lines threading the star and disk meet. This process regulates the magnetic configuration at high altitudes, maintaining a quasi-steady state in the opened stellar magnetic flux (Figure 7.3[a]). In three dimensions, magnetic field stretching and localized reconnection events occur simultaneously at different heights and across multiple azimuthal sectors, ensuring quasi-continuous jet ejection.

To summarize, jet launching operates through a "load-fire-reload" cycle driven by differential rotation between the star and disk. The twisting of magnetospheric

field lines amplifies the toroidal magnetic field, generating a strong current sheet that accelerates the jet via the magnetic pressure force. Reconnection near the field reversal interface then resets the system, reforming field lines connecting the star and disk and reloading them with disk material for the next cycle. This process sustains a continuous outflow.

7.5 Discussion

7.5.1 Magnetospheric accretion and outflow

Although magnetospheric accretion is not the focus of this paper, we describe its general properties to set the stage for comparison with other jet-launching mechanisms.

Figure 7.12(a) shows a 3D rendering of the accretion streams onto the star (the red sphere at the center) The accretion streams are filamentary and follow the magnetospheric field lines. These "finger-like" accretion patterns result from the "interchange instability," a form of Rayleigh-Taylor instability in a magnetically dominated environment. Gas from the mass-dominated disk is loaded onto the strong magnetic field and subsequently accreted onto the star following the stellar magnetic field lines. This mechanism is established by theory (Arons & Lea, 1976; Spruit et al., 1995) and simulations (Romanova et al., 2008; Blinova et al., 2016; Takasao et al., 2022; Zhu et al., 2024).

These accretion streams originate from a mass-dominated disk whose boundary with the magnetically dominated magnetosphere marks the magnetospheric truncation radius R_T. We estimate the location of R_T in two ways.

First, we follow Zhu (2025) and define the corotation radius analytically using the

stellar parameters. The corotation radius is given by

$$R_{T,\mathrm{ana}} = R_\star \Big(\frac{B_\star^4 R_\star^5}{2GM_\star \dot{M}^2} \Big)^{1/7} = \Big(\frac{\bar{m}^4}{2GM_\star \dot{M}^2} \Big)^{1/7}, \tag{7.25}$$

where $B_\star$ and $R_\star$ are the magnetic field strength on the stellar surface and radius of the star, respectively, $M_\star, \dot{M}$ are the stellar mass and mass accretion rate, respectively. $\bar{m}$ is the coefficient used in setting the strength of the stellar magnetosphere (equ. 7.8). Note that our expression is slightly different from the one in Zhu (2025) because of the difference in the unit system. Using our simulation parameters and $\dot{M} = 10^{-7} M_\odot \ \mathrm{yr}^{-1}$ for the accretion rate at late times ($t \gtrsim 3$ yr) when the system settles to a quasi-steady state (see below, and Figure 7.12), the truncation radius $R_{T,\mathrm{ana}} \approx 0.088$ au.

Second, we follow Takasao et al. (2022) and define R_T as the smallest radius where $\beta_K = 1$. In our model, $R_{T,\,\beta_K}$ settles to a value ≈ 0.08 au($\approx 5R_\star$) at late times, slightly lower than the analytic estimate. Since the accretion stream is filamentary (Figure 7.12[a]), it is not surprising that the material with $\beta_K = 1$ can penetrate slightly into the magnetosphere. The truncation radius is comparable to the corotation radius ≈ 0.1 au. Our R_T is larger than Takasao et al. (2022) compared to the stellar radius, since our stellar magnetic field is stronger than theirs.

Most of the mass is accreted along magnetic field lines onto the star away from the midplane. To illustrate the landing locations of the gas on the star, we show in Figure 7.12(b) the averaged mass accretion rate per unit area at different polar angles $\frac{\partial \dot{M}}{\partial A}(\theta)$ between 3.0 yr and 5.5 yr in our model measured right outside r_{fix} (sec. 7.2) at 0.02 au. Most accretion occurs around $\sim 20°$-$40°$ from the polar axis, while the accretion around the midplane ($\theta = 90°$) is negligible.

The highly filamentary high-altitude accretion does not imply a strong variation in the accretion rate. Figure 7.12(c) shows that throughout the later stage of the

simulation between 3.0 yr and 5.5 yr, the total mass accretion rate remains around 1×10^{-7} $M_\odot$ yr^{-1}. In comparison, the jet outflow rate, defined as the total mass flux at ± 5 au with $v_z^p > 10^7$ cm s^{-1}, is about $2 \times 10^{-9} M_\odot$ yr^{-1}, around $2\% \sim 5\%$ of the gas accretion rate. The total mass outflow rate, measured at ± 5 au with gas velocity $> 10^6$ cm s^{-1}, is around $4 \times 10^{-8} M_\odot$ yr^{-1}. The total outflow rate is about 40% of the total accretion rate, similar to the ratio in Takasao et al. (2022) and Zhu et al. (2024), although the exact values differ mainly due to the difference in the chosen stellar magnetosphere magnetic field strength.

The outflow carries angular momentum. To connect the angular momentum transported with the disk Kerperian angular momentum, we define the "Keplerian angular momentum radius" following Tu et al. (2025a)

$$R_a = \frac{1}{GM}\left(\frac{\Phi_l}{\Phi_m}\right)^2, \tag{7.26}$$

where Φ_l and Φ_m are the angular momentum flux and mass flux in the outflow, respectively. Figure 7.12(d) shows R_a for the jet and the disk wind, respectively, measured at $z = 5$ au. The jet $R_a \approx 0.6$ au, much larger than its launch radius $\lesssim 0.2$ au. This shows an abundance of angular momentum carried by the jet, initially stored in the electromagnetic form associated with the twisting of the field lines. The disk wind $R_a \approx 1.3$ au, slightly larger than its launching radius $\lesssim 1$ au.

Both the jet and the disk wind carry significant angular momentum. In the following section (sec. 7.5.2), we will compare the accretion and outflow properties with those driven by the disk through the avalanche-accretion stream. Since the key distinction between the disk-driven outflow and our model is the presence of a stellar magnetosphere, we will discuss its impact on the overall dynamics of the system.

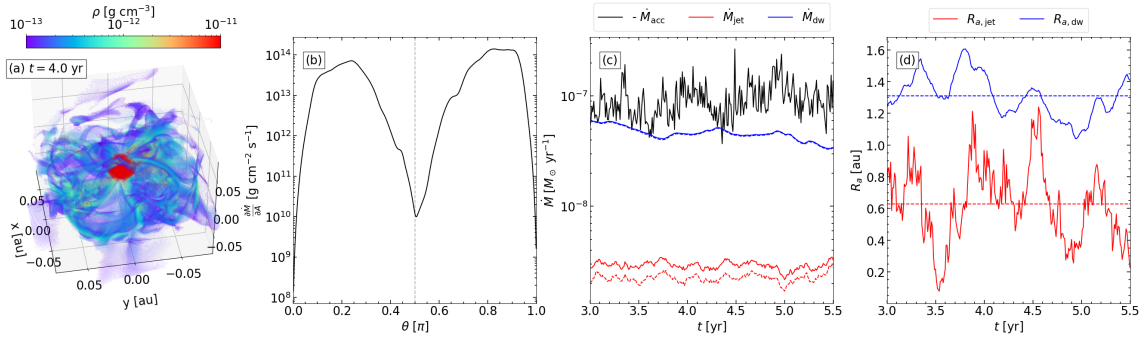


Figure 7.12: Accretion and outflow properties. **Panel (a)** shows a 3D rendition of the accretion streams by only choosing cells with real $\rho > 10^{-13}$ g cm^{-3} and kinetic-$\beta < 1$. **Panel (b)** quantifies the landing locations of the mass accretion rate streams on the star at each polar angle, showing off-midplane accretion along magnetosphere fieldlines. **Panel (c)** shows the total mass accretion rate (black line on top), jet outflow rate (red line at the bottom), and the disk wind outflow rate (blue line in the middle). The red dashed line is the jet outflow rate using the real gas only, showing the density floor's minimal effect on the outflow. **Panel (d)** shows the "Keplerian angular momentum radius" (R_a, equ. 7.26) of the jet (lower red line) and the disk wind (upper blue line). The horizontal dashed lines mark the averaged R_a over the time shown.

7.5.2 Comparing to the disk-field-only jet model

An alternative jet-launching mechanism involves jets driven solely by the disk magnetic field. Tu et al. (2025b) and Tu et al. (2025a) model outflows in the absence of a stellar magnetosphere and identify a mechanism in which jets are powered by the so-called "avalanche-accretion stream" in the magnetically elevated atmosphere of the disk. In this section, we compare the outflows driven by stellar magnetosphere-disk interactions with those produced by the disk magnetic field alone.

To set the stage for this comparison, we first summarize the disk-field-only jet-launching mechanism described in Tu et al. (2025b) and Tu et al. (2025a). In this scenario, the disk is threaded by a large-scale, open vertical magnetic field. Due to differential rotation and magnetic field geometry, the azimuthal magnetic field B_ϕ must switch sign somewhere between the upper and lower hemispheres, typically along

the disk surface on one side. This sign reversal leads to strong azimuthal magnetic braking, which removes angular momentum and drives an avalanche-accretion stream along the disk surface. The differential rotation between this stream and the open field lines rapidly amplifies the toroidal magnetic field, generating strong toroidal magnetic pressure that lifts a portion of the accretion stream vertically, launching a jet. A similar process drives a slower, more mass-loaded disk wind at larger cylindrical radii, though this does not require the formation of an avalanche-accretion stream. Some regions of the inner disk wind can be magnetorotational instability (MRI)-active, where turbulent gas is lifted to high altitudes before merging with the disk wind.

On the side of the disk without the azimuthal field sign change, the avalanche-accretion stream does not form, but jets can still emerge if the polar region remains relatively mass-free. However, MRI-active turbulent disk winds can fill the polar region with turbulent gas in many cases, overloading the outflow and effectively choking the jet. As a result, disk-field-only models frequently produce one-sided jets (see also, e.g., Béthune et al., 2017; Takaishi et al., 2024).

A key distinction between the disk-only model and our magnetosphere-disk model is the persistence of a bipolar jet in our simulations (see Figure 7.1). This difference arises from the global magnetic field geometry. In the presence of a stellar magnetosphere, the opening of the outer magnetosphere establishes a poloidal magnetic field structure with opposite directions between the polar region and its immediate surroundings. With differential rotation, this configuration produces a quadripartite global toroidal magnetic field topology, with bipartite in each hemisphere (as shown in Figure 7.13). Magnetic reconnection occurs along the boundary between the two magnetic partitions in each hemisphere, naturally limiting the disk's vertical expansion. This effect is analogous to the role of avalanche accretion streams in the disk-only

models. As a result, the magnetic configuration inherently supports the formation of a bipolar jet. In contrast, the disk-field-only model maintains a bipartite global toroidal field geometry (see, e.g., Figure 9 in Tu et al., 2025a), meaning that the toroidal field remains unipartite in each hemisphere. As a result, the avalanche accretion stream can develop only in the hemisphere where the toroidal field reverses direction. This asymmetry leads disk-field-only models to preferentially launch unipolar jets.

Another key distinction lies in how the toroidal magnetic field is generated. While both models rely on toroidal magnetic pressure to power the jet, the underlying mechanism for twisting the field differs significantly. In the disk field only model, the toroidal field is amplified by the differential rotation between the avalanche accretion stream of the disk surface and the slower-rotating gas above (and below) it. This configuration results in a toroidal twisting of the field where a faster-rotating layer below winds up a slower-rotating layer above.

In contrast, the disk-magnetosphere model produces the toroidal field in an opposite manner. Here, strong magnetic field lines anchored to the rotating star transfer angular momentum to the disk surface, spinning up the upper layers of the disk relative to the denser regions below. As a result, a toroidal field is generated by the differential rotation between the faster-rotating upper layers and slower-rotating lower layers of the disk.

There are several important consequences of these differences in the generation of toroidal magnetic fields. One immediate effect is on the geometry of the poloidal magnetic field that channels the jet. In the disk-field-only model, the avalanche-accretion stream drags magnetic field lines inward, resulting in an inward-pinched poloidal field configuration (see Figure 5 in Tu et al. 2025b). In contrast, in the magnetosphere-disk model, the pinching point of the field moves outward, leading to an outward-pinched poloidal magnetic field structure (Figure 7.7).

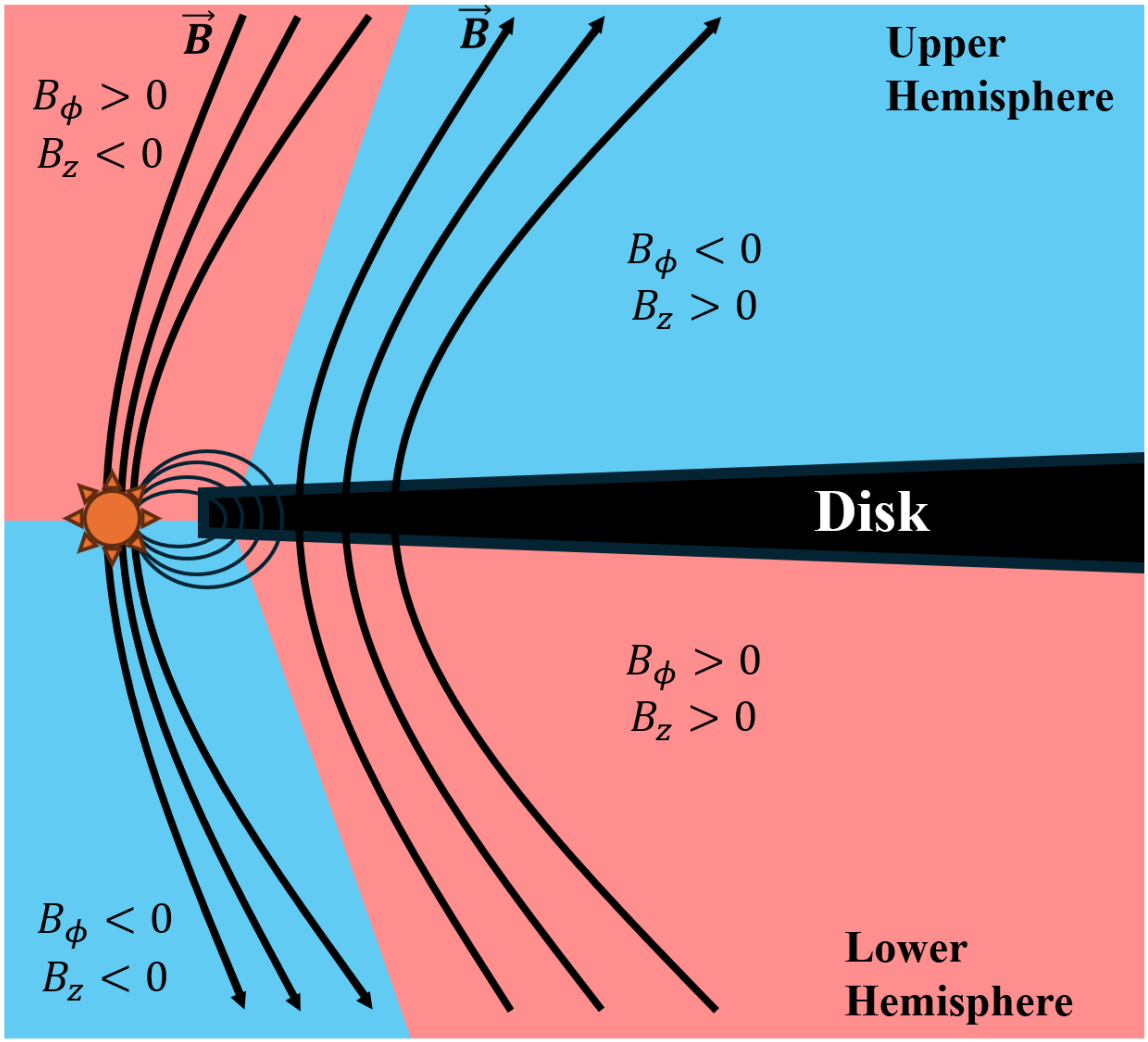


Figure 7.13: Illustration of the resulting large-scale toroidal magnetic field configuration, shaped by the poloidal field geometry established through the presence and partial opening of the stellar magnetosphere. In contrast to the disk-only case (Tu et al., 2025a), where the magnetic field direction reverses in only one hemisphere, both the poloidal and toroidal components exhibit reversal in both the upper and lower hemispheres in the case with a stellar magnetosphere.

The difference in magnetic field geometry stems from differences in the power source of the jet. In the disk-field-only model, the disk itself provides all the energy and angular momentum for the outflow. In contrast, in the magnetosphere-disk model, the field lines anchored on the rotating star provide an additional source of energy and angular momentum to power the jet. In addition, once opened, the magnetosphere supplies the inner disk with a much stronger open poloidal field than in the disk-field-only case, and provides a global field configuration with oppositely directed open poloidal fields near the (elevated) disk surface that is conducive to magnetic reconnection and jet mass loading. As a result, jets in the magnetosphere-disk model are both more energetic and more massive than those in the disk-field-only model from Tu et al. (2025a). Specifically, the jet in our simulations reaches velocities of several hundred km s^{-1}, compared to ≈ 100 km s^{-1} in the disk-field only case. The mass outflow rate is also higher, with $\dot{M}_{\rm jet} \approx 2 \times 10^{-9}\ M_\odot\ {\rm yr}^{-1}$ compared to $\approx 2 \times 10^{-11}\ M_\odot\ {\rm yr}^{-1}$. Additionally, the jet carries more angular momentum, with the Keplerian angular momentum radius (equ. 7.26) of $R_a \approx 0.6$ au, compared to 0.3 au in the disk-field-only model.

Similarly, the disk wind in the magnetosphere-disk model is stronger than in the disk-field-only model. This enhancement arises partly from the additional magnetic field strength in the disk due to the opening of the stellar magnetosphere. Moreover, some angular momentum in the disk wind originates from the star itself. When the magnetic field transfers energy and angular momentum to the jet, a portion of that angular momentum is fed into the disk. Although this effect is relatively minor in terms of driving outflows (since the disk remains gas-dominated), it contributes to the overall angular momentum budget of the disk wind.

In summary, the stellar magnetosphere plays two critical roles in shaping the outflow. First, the opening of the magnetosphere increases the field strength in the

jet-launching inner disk region and imposes a global field geometry that is conducive to jet mass loading through reconnection and resistant to the choking of the jet by the disk wind. Second, by transferring energy and angular momentum from the rotating star to the outflow, the magnetosphere strengthens both the jet and the disk wind, making them more energetic and angular-momentum rich than in the disk-field-only scenario.

7.5.3 Comparison with previous 2D models

The "load-fire-reload" jet-launching mechanism in our model shares many similarities with previous 2D models. Studies such as Goodson & Winglee (1999); Kuwabara et al. (2000); Fendt & Elstner (2000); Matt et al. (2002); Romanova et al. (2005); Fendt et al. (2011); Čemeljić et al. (2013); Zanni & Ferreira (2013) also observed the cyclic behavior of magnetic field lines, where outflows are launched before the field resets to its initial configuration for the next cycle. The formation of a current sheet due to differential rotation, as described in Sec. 7.4.2, is conceptually similar to the current sheet discussed in Uzdensky (2002).

However, our model differs from these 2D studies in two key ways: (1) the inclusion of the azimuthal dimension, and (2) the longer simulation runtime, allowing the system to reach a quasi-steady state. The additional dimension enables axisymmetric processes to break down, while the extended simulation duration ensures that transient effects from the initial conditions dissipate. These differences lead to three main consequences.

First, the jet can be launched continuously (see Figure 7.1) because magnetic expansion and reconnection can occur simultaneously at different azimuthal angles. This sustained flaring and reconnection stabilize the system into a quasi-steady state in the late simulation stages. Additionally, mass loading onto the jet-launching field

lines becomes more efficient due to reconnection along the disk surface-polar cavity boundary. The frequent localized magnetic reconnection and field expansion events alleviate the need for the global large-scale episodic outbursts often seen in 2D simulations.

Second, the magnetic field geometry associated with jet launching differs from 2D models. In our simulation, the field does not need to fully reconnect into closed loops across the disk midplane before another jet-launching event can occur: the only requirement is that the opened magnetosphere field lines threading the star touch and at least shallowly embedded in the disk atmosphere (as examplified by the green and magenta field lines in Fig. 7.7); the touch of the disk is facilitated by the elevation of the atmosphere of the disk, driven by the amplification of the toroidal field in the inner ideal MHD part of the disk (Oishi et al., 2020). As a result, only localized reconnection along the surface of the highly elevated and highly dynamic disk atmosphere is necessary to generate a jet, rather than global reconnection involving a coherent poloidal field threading the disk midplane.

These differences, particularly the suppression of large-scale temporal variations, are consistent with the findings of Takasao et al. (2022). While 2D models are valuable for developing first-step theories and characterizing general properties, these differences highlight the crucial role of 3D models in capturing additional key ingredients of the outflow-launching process.

7.5.4 Connection to the axisymmetric steady-state outflow

Although the outflow launching mechanism in our model is highly variable in space and time, it is still valuable to put our model in the context of the axisymmetric steady-state wind theory.

Four quantities are conserved along a magnetic field line in the axisymmetric

steady-state wind model. However, since our jet-launching mechanism (Sec. 7.4) involves the opening and reconnection of magnetic field lines, this "along a magnetic field line" picture is not strictly applicable. Nevertheless, we can reinterpret these conserved quantities to gain insight into the properties of the outflow.

The first conserved quantity,

$$k = \frac{4\pi\rho v_{\rm pol}}{B_{\rm pol}}, \tag{7.27}$$

characterizes the degree of mass loading of the outflow. Physically, k is the 4π times the ratio between the outflow mass flux $\dot{M}_{\rm out} = \rho v_{\rm pol} A$ and the magnetic flux $\Phi_B = B_{\rm pol} A$, where A is an area element perpendicular to the poloidal field.

The second is the conserved angular velocity:

$$\omega_s = \frac{v_\phi}{R} - \frac{k B_\phi}{4\pi\rho R}, \tag{7.28}$$

where the first term is the angular velocity of the gas and the second term can be interpreted as the magnetic contribution to the conserved angular velocity.

Similarly, the third quantity is the angular momentum, and the two terms are the angular momenta carried by the gas and magnetic field, respectively:

$$l = R v_\phi - \frac{R B_\phi}{k}. \tag{7.29}$$

The last is the energy

$$E = \frac{1}{2}v^2 + \Phi - \frac{\omega_s R B_\phi}{k} + h, \tag{7.30}$$

which is derived from Bernoulli's equation. The four terms are energy carried by gas advection, gravity, magnetic field, and gas internal energy, respectively. Since thermal

energy is negligible in the outflow (plasma-$\beta \ll 1$, Figure 7.4), the energy carried by the gas is essentially its kinetic energy.

To connect our model with these quantities, we show in Figure 7.14 the mass-weighted averaged quantities at every height z in the jet, defined as gas moving at a speed $v_z^p > 10^7$ cm s^{-1}. Note that while this analysis does not trace along individual magnetic field lines, the mass-weighted averaged quantities offer insight into the jet properties.

Figure 7.14(a) shows k, which is roughly constant along the jet. This indicates that the mass loading of the outflow remains approximately the same as the jet propagates outward.

Figure 7.14(b), (c), and (d) show ω_s, l, and E, and their gas and magnetic component, respectively. While the magnetic field dominates ω_s (the magnetic field is mostly toroidal) at large distances, gas dominates both angular momentum l and energy E. Only around the base of the jet $\lesssim 2$ au does the magnetic field dominate in angular momentum and energy, suggesting that energy and angular momentum are transferred from the magnetic field to the gas as the outflow propagates outward, and the outflow on the large scale is gas-dominated. These findings are consistent with, and similar to, the analysis along the field line in Tu et al. (2025b,a); Jacquemin-Ide et al. (2021).

To further quantify the outflow properties, we show in Figure 7.14(e) the plasma-β, kinetic-β (β_K), and the poloidal kinetic-β, defined as

$$\beta_{K,\mathrm{pol}} = \frac{\rho v_{\mathrm{pol}}^2}{B_{\mathrm{pol}}^2/4\pi}. \tag{7.31}$$

While plasma-β is confirmed to be much less than order unity, kinetic-β stays above 1 beyond the launching zone, emphasizing the gas dominance at large heights. The

$\beta_{K,\mathrm{pol}}$ is larger than β_K, highlighting the dominance of the poloidal gas motion over the poloidal magnetic field. Figure 7.14(f) further quantifies the velocity and magnetic field geometry, showing the ratio between the toroidal and the poloidal velocity or magnetic field. At a large height, the poloidal velocity dominates the toroidal velocity, but the magnetic field is mostly toroidal. This is consistent with the observation in Figure 7.1(3D figure), where the streamlines (black lines) are mainly poloidal, while the magnetic fields (white) are mainly toroidal on the plotted scales.

7.6 Conclusions

We performed a 3D non-ideal MHD simulation of outflow-launching involving a rotating protostar, the stellar magnetosphere, the circumstellar disk, and open magnetic field lines threading the disk. In our model, a fast, collimated bipolar jet is launched, surrounded by a slower, wider, but more mass-loaded disk wind. Our main conclusions are as follows.

1. During the early stages of the simulation, the stellar magnetosphere opens up, forming three distinct magnetic regions: (1) a polar region of open stellar field lines extending outward from the star; (2) a lower-latitude region of open stellar field lines threading into the disk, with field directions opposite to those in the polar region; and (3) an intermediate zone between the two, where oppositely directed poloidal magnetic fields coexist, a crucial region in the jet-launching process. In the inner disk, the open stellar field overwhelms the native disk field, facilitating the launch of a magnetically driven disk wind.

2. The jet is driven by toroidal magnetic pressure through a "load–fire–reload" cyclic process primarily involving magnetic field lines that connect the star and the vertically elevated disk surface. In the "load" stage, differential rotation

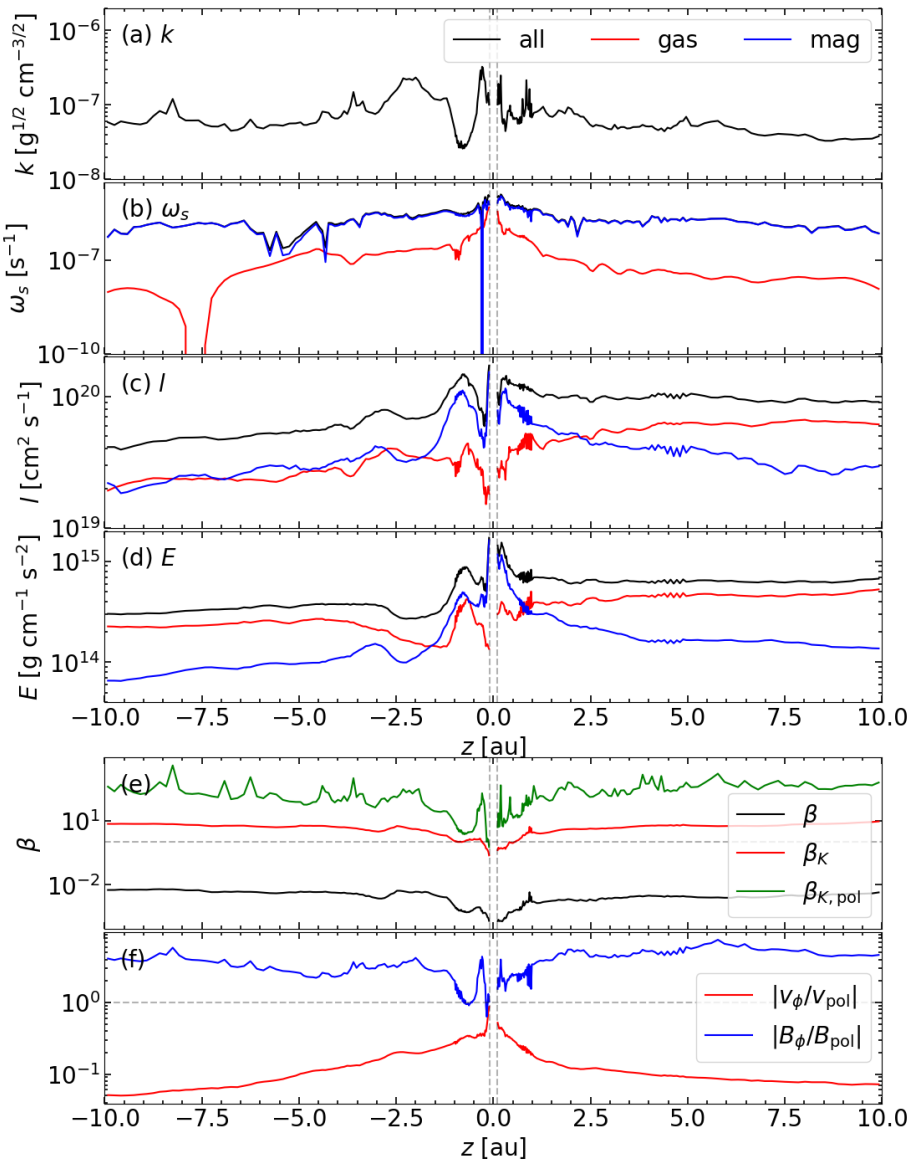


Figure 7.14: Mass-weighted average conserved quantities (upper four panels) and outflow properties (lower two panels) at different heights. **Panels (a), (b), (c), and (d)** show the mass loading parameter (equ. 7.27), angular velocity (equ. 7.28), angular momentum (equ. 7.29), and energy (equ. 7.30) respectively. **Panel (e)** shows the plasma-β (equ. 7.12), kinetic-β (equ. 7.13), and the poloidal kinetic-β (equ. 7.31). **Panel (f)** shows the ratios of toroidal to poloidal components for both velocity and magnetic field, illustrating the changing dominance of flow and field geometry with height.

along a magnetic field line between the star and the disk transfers rotational energy into the magnetic field, amplifying the toroidal component along field lines. This twisting is especially pronounced in a layer along the surfaces of the stellar magnetosphere and the disk, where it builds up a strong toroidal field. As the toroidal field strengthens in that layer, it generates a current in the cylindrical-$\hat{R}$ direction. This current, in turn, produces a vertical Lorentz force that propels the gas upward: the "firing stage" of the cycle. The release of toroidal magnetic energy drives the gas to expand in the $\hat{z}$ direction, launching the jet. Eventually, magnetic reconnection along the jet-launching field lines resets the field configuration, returning the magnetic field lines to the "two-legged" configuration, anchored at both the star and disk, ensuring that the system is continually "reloaded" for subsequent episodes of jet-launching.

3. Compared to the disk-only model presented in Tu et al. (2025a), both the jet and disk wind are stronger in the stellar magnetosphere model, exhibiting higher velocities and greater mass fluxes. The disk wind is stronger because the partially opened stellar magnetosphere provides additional open magnetic flux to the disk, which increases the field strength in the inner disk and facilitates a stronger disk wind. The rotating star provides an additional power source to power the jet, which, together with the stronger open magnetic field in the polar cavity, helps drive a stronger jet in the magnetosphere model.

4. The jet tends to be bipolar in the magnetosphere model, in contrast to the disk-only setup, where the jet tends to be unipolar. This difference arises primarily from the geometry of the global magnetic field. In the disk-only case, the magnetic field structure typically facilitates the opening of a jet-launching cavity in only one hemisphere, while the other hemisphere is more likely to be choked by

the disk wind. However, when a stellar magnetosphere is included, the toroidal magnetic field reverses signs in both hemispheres, enabling the formation of polar cavities on both sides of the midplane. Consequently, jets driven by the magnetosphere-disk interaction are more likely to be bipolar and symmetric.

7.7 ACKNOWLEDGMENTS

YT acknowledges support from the interdisciplinary fellowship at UVA. CYH acknowledges support from an ALMA Student Observing Support (SOS) from NRAO. We acknowledge computing resources from UVA research computing (RIVANNA), NASA High-Performance Computing, and NSF's ACCESS computing allocation AST200032 and PHY250098. ZYL, YT, and CYH are supported in part by NASA 80NSSC20K0533, NSF AST-2307199, JWST-GO-02104.002-A, and the Virginia Institute of Theoretical Astronomy (VITA). Z.Z. acknowledges support from NSF award 2408207, 2429732 and NASA grant 80NSSC24K1285.

Chapter 8

Arcturus: A post-process tracer and dust particle simulation framework

abstract: We present `Arcturus`, a flexible post-processing framework designed to trace the trajectories of passive tracer particles and dust grains in precomputed hydrodynamic and magnetohydrodynamic (MHD) simulations. By decoupling particle integration from the main simulation, `Arcturus` enables efficient and customizable studies of gas and dust dynamics, including the effects of aerodynamic drag and external forces such as gravity. Particle evolution is computed using a second-order Runge-Kutta scheme with temporally and spatially interpolated gas properties. The method supports adaptive time-stepping based on local flow conditions to ensure numerical stability and precision. We validate the framework through a series of benchmark tests, including solid-body rotation and gas drag slow-down, and demonstrate the key bottlenecks to numerical accuracy. Our results confirm that `Arcturus` achieves high precision with modest computational cost, offering a practical and scal-

able solution for Lagrangian analysis in astrophysical simulations.

8.1 Introduction

Modeling astrophysical systems is a challenging task. The complexity of the physical processes involved often renders analytic approaches insufficient, necessitating the use of sophisticated numerical simulations. However, the intricacy of the numerical methods and the substantial computational resources required pose significant challenges. Despite these obstacles, numerous simulation tools have been developed that demonstrate remarkable versatility, accuracy, and scalability.

Most modern codes are built upon the finite volume method, where the simulation domain is divided into discrete control volumes. Within each volume, hydrodynamic quantities are assumed to be uniform, and their evolution is computed by tracking fluxes across the boundaries. This ensures the conservation of mass, momentum, and energy—fundamental pillars of any reliable hydrodynamic simulation. Magnetic fields can also be incorporated within this framework through magnetohydrodynamics (MHD), where their evolution is computed via fluxes across cell faces.

Yet a persistent bottleneck remains: how can we track the history of individual gas parcels or dust particles? This is particularly important in contexts such as astrochemistry, where the physical history of a parcel—its trajectory, temperature, and density evolution—affects its chemical outcome. While it is possible to include tracer fluids or dust fluids directly in MHD simulations, doing so requires these components to be evolved concurrently with the simulation. This can be computationally expensive and inflexible, especially if one wishes to add new tracers or explore alternate initial conditions for the particles without rerunning the entire (gas) simulation.

Post-processing provides an elegant solution to this problem. By working with the output of a precomputed (magneto-)hydrodynamic simulation, one can reconstruct

the trajectories of tracer and dust particles without rerunning the full simulation. This not only greatly reduces computational cost but also offers significant flexibility: particle initial conditions can be specified as needed, and multiple models can be explored from a single simulation dataset. Despite these advantages, a general-purpose post-processing framework for this task has not been publicly available.

Here, we present such a post-processing framework, named `Arcturus`, which uses outputs from hydrodynamic or MHD simulations to reconstruct the motion of tracer and dust particles. Two early versions of this code are used in Chapter 2 and Chapter 4. This chapter is organized as follows: we describe the numerical algorithms in Section 8.2, validate the framework with benchmark tests in Section 8.3, and summarize key findings and best practices in Section 8.4.

8.2 Numerical method

The equation of motion of a tracer particle is given by

$$\frac{\partial \boldsymbol{x}}{\partial t} = \boldsymbol{v}_{\rm gas}, \tag{8.1}$$

where $\boldsymbol{v}_{\rm gas}$ is the gas speed at the location of the tracer.

Similarly, the equation of motion of a dust particle is given by

$$\frac{\partial^2 \boldsymbol{x}}{\partial t^2} = \boldsymbol{a}_{\rm drag} + \boldsymbol{a}_{\rm bulk}, \tag{8.2}$$

where $\boldsymbol{a}_{\rm drag}$ is the gas aerodynamic drag force and $\boldsymbol{a}_{\rm bulk}$ is the global force on the dust (such as gravity). Assuming the dust grains are spherical particles, in the context of protostellar and protoplanetary disks, the aerodynamic drag force is in the Epstein

regime (Epstein, 1924), given by

$$\boldsymbol{a}_{\rm drag} = \frac{\Delta \boldsymbol{v}}{t_s}, \tag{8.3}$$

, where $\Delta \boldsymbol{v} = \boldsymbol{v}_{\rm gas} - \boldsymbol{v}_{\rm dust}$; t_s is the "stopping time", given by

$$t_s = \frac{s\tilde{\rho}_{\rm dm}}{\rho_g v_{\rm th}}, \tag{8.4}$$

where s and $\tilde{\rho}_{\rm dm}$ are the dust grain size and dust material density respectively; ρ_g and $v_{\rm th} = \sqrt{\frac{8k_bT}{\mu m_{\rm H}}}$ are the gas density and gas thermal speed at the location of the dust grains respectively.

The global force $\boldsymbol{a}_{\rm bulk}$ in astrophysical context is mainly gravitational force $\boldsymbol{a}_{\rm grav}$.

The above equations are solved numerically forward in time using the Runge-Kutta 2nd-order integrator (RK2). To solve these equations, the gas properties at the location of the dust grain (e.g., gas velocity, density, and temperature) must be specified at every time step. Since this code uses the post-processing method, the gas information is obtained using both spatial and temporal interpolations.

Since the particle simulation time ($t^\star$) and dust position $\boldsymbol{x} = \langle x, y, z\rangle$ is known, we first determine two input hydro frames at t_1 and t_2 such that $t_1 \leq t^\star < t_2$. The hydro quantities are first spatially interpolated at t_1 and t_2 (denoted ρ_1 and ρ_2 respectively) using the dust spatial information and the Triangular Shaped Cloud algorithm (TSC, Hockney & Eastwood, 1981). The hydro information is then interpolated over time to the simulation time

$$\rho(t = t^\star) = \rho_1 \frac{t_2 - t^\star}{t_2 - t_1} + \rho_2 \frac{t^\star - t_1}{t_2 - t_1}. \tag{8.5}$$

The time step (dt) of integration must also be specified. Taking advantage that

the hydro information is known, the time step for each particle can be determined independently, and only synchronized when necessary (e.g., output to file). We name this time-stepping method "Adaptive Time Step". For each particle, the time step is determined by four criteria: firstly, the particle must not cross more than one cell in one time step ($dt_{\rm adv}$, criteria similar to the CFL condition in astrophysical fluid simulation context Courant et al., 1928), i.e.,

$$dt_{\rm adv} = \alpha \ \min\left(\frac{\Delta \boldsymbol{x}_{\rm cell}}{\boldsymbol{v}_{\rm dust}}\right), \tag{8.6}$$

where $\Delta \boldsymbol{x}_{\rm cell}$ is the cell size of the cell that the dust particle is in, $\alpha < 1$ is the user-defined number functioning similarly to the CFL number. We term α the "particle CFL number" hereafter.

Secondly, the time step needs to resolve the gas thermal speed

$$dt_{\rm thm} = \alpha \ \min\left(\frac{\Delta \boldsymbol{x}_{\rm cell}}{v_{\rm th}}\right). \tag{8.7}$$

Thirdly, the time step must not exceed α times the time between hydro inputs ($dt_{\rm frame}$) and the time to the next hydro frame

$$dt_{\rm hydro} = \min(\alpha \ dt_{\rm frame}, t_2 - t^\star), \tag{8.8}$$

and fourthly the time step is capped by some user-defined value ($dt_{\rm user}$) to avoid infinitely long time steps in some situations where dust is not moving and gas thermal speed is very short. The time step for the particle is the minimum of these four, i.e.,

$$dt = \min(dt_{\rm adv}, \ dt_{\rm thm}, \ dt_{\rm hydro}, \ dt_{\rm user}). \tag{8.9}$$

A post-process tracer particle or dust particle simulation can be performed with this information.

8.3 BENCHMARK TEST

To show the numerical accuracy of our algorithm, we carry out a series of tests in simple, controlled environments where we can compare our simulation results to analytic expectations.

8.3.1 Triangular Shaped Cloud

We first evaluate the numerical accuracy of the Triangular-Shaped Cloud (TSC) spatial interpolation algorithm. Since TSC is used to calculate gas properties at particle locations, its accuracy fundamentally limits the overall precision of the particle simulation.

To benchmark the interpolation performance, we use several commonly encountered algebraic functions in one-dimensional space. Given an analytic function $f(x)$ and its TSC-interpolated counterpart $T(x)$, the fractional error is defined as:

$$\text{fractional error} = \Big|\frac{f(x) - T(x)}{f(x)}\Big|. \tag{8.10}$$

Note that if $f(x) = kx^p$, the fractional error is independent of the constant k. Therefore, we only need to examine different values of the exponent p.

Because interpolation errors tend to be largest near $x = 0$, where the function varies most rapidly, we restrict our tests to the domain $0 \leq x \leq 1$. Fig. 8.1 shows the fractional error for four test functions: $f(x) = x^{0.5}$, $x^{-0.5}$, x^{-1}, and x^{-2}. These functions are representative of physical quantities commonly interpolated in simulations, such as those related to Keplerian rotation or gravitational forces. The black, red, and green lines in each panel represent numerical resolutions of $n = 32$, 64, and

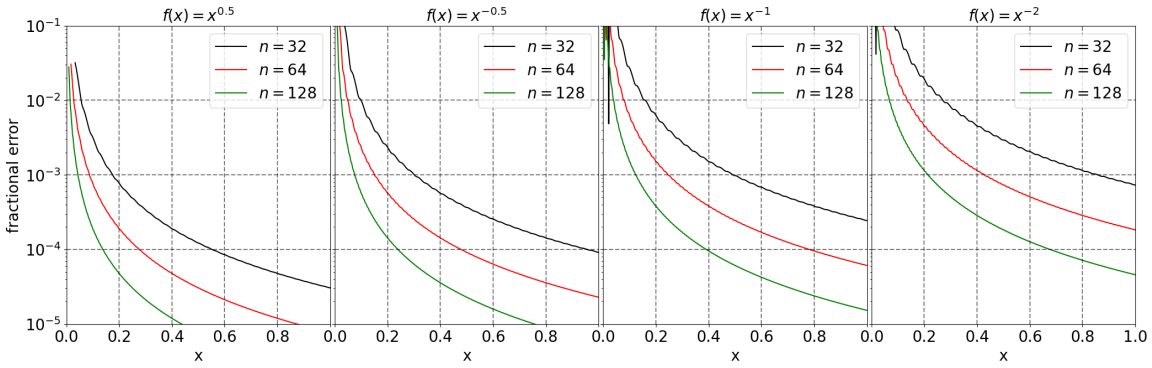


Figure 8.1: Numerical accuracy of the TSC interpolation algorithm with different functions $[f(x)]$, resolution between $[0, 1]$ (n), and distance from the origin (x).

128 grid cells over the interval $[0, 1]$, respectively.

As expected, the fractional error decreases with increasing distance from the origin and with decreasing function variability. Specifically, lower-order functions exhibit smaller interpolation errors. Notably, for all test cases, the fractional error decreases approximately linearly with increasing resolution. For instance, the error at a given x with resolution $n = 32$ matches the error at $x/2$ for $n = 64$. This implies that higher resolutions are required to maintain accuracy for functions with steeper gradients. For example, a fractional error of 10^{-4} at $x = 1$ is achieved with $n = 32$ for $f(x) = x^{-0.5}$, but requires $n \approx 128$ for $f(x) = x^{-2}$.

These results highlight the interpolation accuracy limits imposed by the TSC algorithm and establish the baseline precision for particle-based post-processing, which we examine further in the following subsections.

8.3.2 Tracer

We present a test of the tracer particle implementation. In the context of star formation and disk dynamics, a key component of the system is the circumstellar disk, where gas follows approximately circular orbits around a central object. To evaluate the tracer performance in such a setting, we conduct a test involving tracers in an

idealized circular flow.

The hydro is in steady-state, solid body rotation around $\hat{z}$ axis through the center. The hydro is modeled with a box from -1 to 1 in each direction, with a reference resolution 64^3. The gas is in a solid body rotation with a speed of 2π (i.e., the period is 1). The tracer particles are put in a uniform grid with 263^3 sampling the entire simulation domain. The particle CFL number is taken to be 0.3.

We compare the cylindrical radius of the tracer particles after one orbit $[R(t = 1)]$ with their initial cylindrical radius (R_0). As some particles near the edge leave the box during simulation, we only compare the ones that fully remain in the domain during the simulation domain. Fig. 8.2 shows the percentage difference as a function of the radius from the center, i.e.

$$\text{fractional error} = \frac{R(t = 1) - R_0}{R_0} \tag{8.11}$$

The black line shows the reference model. Beyond $r \approx 0.2$, the error in one orbit is less than 10^{-4}; beyond $r \approx 1$, the error reduces to $< 10^{-6}$.

The primary source of error in the tracer particle test is the resolution of the hydrodynamic grid, which shows a linear relationship with the interpolation error. This behavior is consistent with expectations based on the TSC algorithm. As illustrated by the red line in Fig. 8.2, increasing the hydro resolution to 128^3 reduces the error growth rate: the fractional error at radius 0.5 in the high-resolution model matches the error at radius 1.0 in the 64^3 model. Furthermore, we find that the error is insensitive to the gas rotation speed. A model with a rotation rate reduced by a factor of 10 produces virtually identical errors to those in the reference model, confirming that the error is primarily driven by spatial resolution rather than the dynamical timescale.

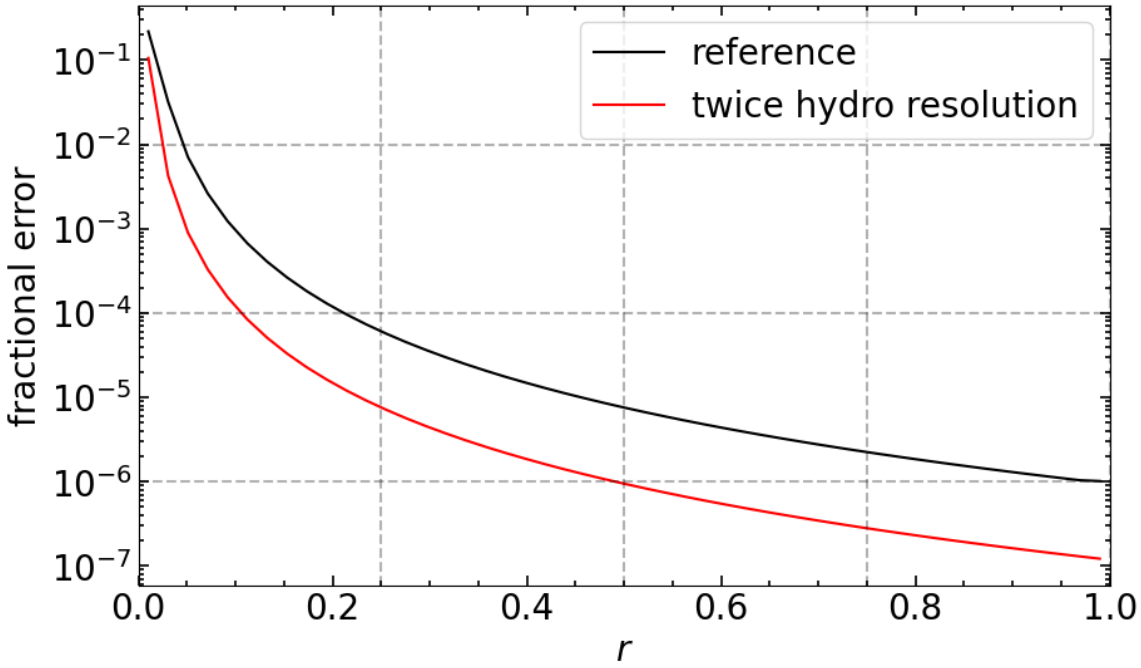


Figure 8.2: Fractional error in the tracer particle test as a function of radius in a model tracing circular orbits. The simulation setup is described in Section 8.3.2.

8.3.3 Dust particle

To test the accuracy of dust particles experiencing gas drag, we model dust particle slow-down due to gas drag by setting up a model where the dust has an initial speed $\boldsymbol{v} = v_0\ \hat{x}$ embedded in stationary gas (i.e., $|\boldsymbol{v}|_{\rm gas} = 0$). The equation of motion of these dust particles is given by

$$\frac{\partial^2 \boldsymbol{x}}{\partial t^2} = -\frac{1}{t_s}\frac{\partial \boldsymbol{x}}{\partial t}. \tag{8.12}$$

Given the initial conditions $\boldsymbol{x}(t=0) = \boldsymbol{x}_0$ and $\boldsymbol{v}(t=0) = v_0\ \hat{x}$, the location of the dust is analytically solvable as

$$\boldsymbol{x}(t) - \boldsymbol{x}_0 = \left[v_0 t_s - v_0 t_s \exp\left(-\frac{t}{t_s}\right)\right]\ \hat{x}. \tag{8.13}$$

The system is modeled using gas properties $\rho_g = 1$ and $v_{\rm th} = 1$; dust particles with $t_s = 1$. The initial speed varies between $v_0 = 0.1 \sim 10$. We compare our simulation result with the analytic solution at the characteristic time scale $t = t_s$. The hydro is modeled in a box with $\hat{x}$ from -1 to 10, and a resolution of 352 cells (equivalent to the 64^3 resolution used in the reference model in the tracer case, sec. 8.3.2). For the reference model, the particle CFL number is taken to be $\alpha = 0.3$. The particle is placed so its evolution is within the simulation domain.

Fig. 8.3.3 shows the fractional error compared to the analytic solution. The fraction error is defined as

$$\text{fractional error} = \frac{\Delta x_{\rm sim} - \Delta x_{\rm ana}}{\Delta x_{\rm ana}}, \tag{8.14}$$

where $\Delta x_{\rm sim}$ and $\Delta x_{\rm ana}$ are the displacement calculated by the simulation and analytic solution (equ. 8.13) respectively. When the dust particle's initial velocity is slower than the gas thermal speed ($v_0 < 1$), the fractional error is 2×10^{-3}; when the dust's initial speed increases beyond the gas thermal speed ($v_0 > 1$), the fractional error decreases.

The main source of the error is the time step in the simulation. In the case of the reference model, the faster dust has a smaller time step due to time-stepping criteria (see sec. 8.2). To show the source of the error more explicitly and quantitatively, we show in fig. 8.3 the fraction error in the same model setup but using particle CFL number $\alpha = 0.03$, ten times smaller than the reference model. The fractional error decreases by a factor of 10, linearly proportional to the time step.

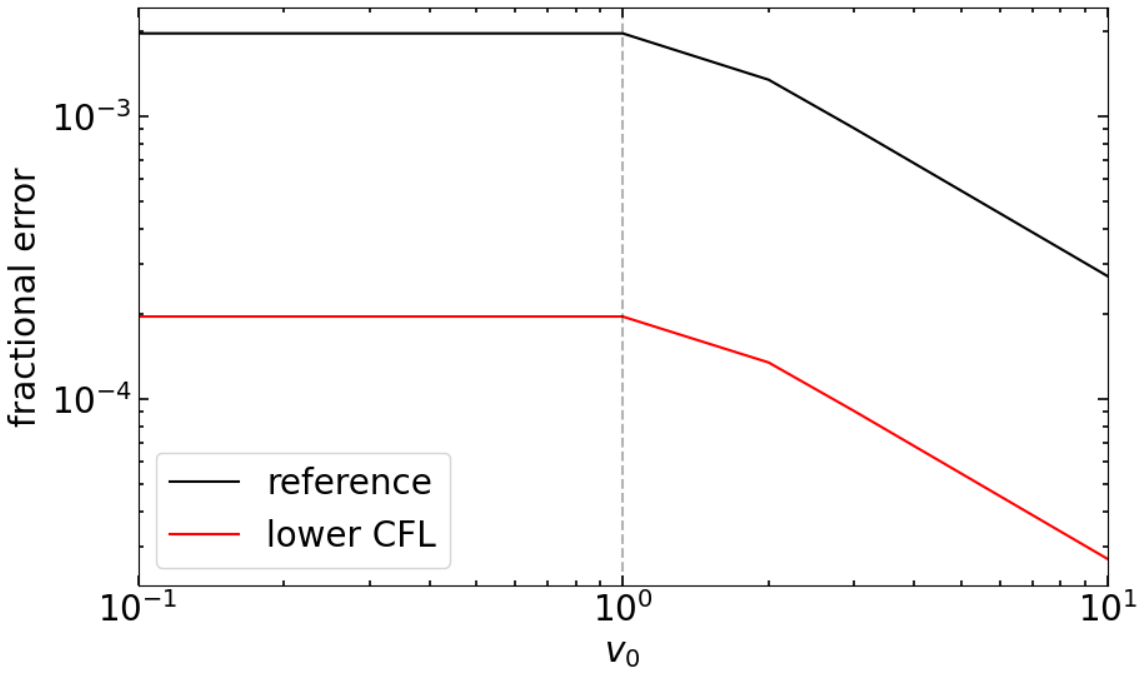


Figure 8.3: Fractional error in the dust particle test as a function of initial dust velocity in a model with stationary gas background. The simulation setup is described in Section 8.3.3.

8.3.4 Dust particle and gravity

The final test evaluates the gravity module, which applies gravitational forces to dust particles. In the context of protoplanetary disks, the dominant gravitational influence is from the central star, with both gas and dust orbiting in nearly Keplerian motion. To verify the accuracy of our gravity implementation, we test a scenario in which a dust particle follows a Keplerian orbit around a central star.

Since gravity is treated as part of the hydro input and interpolated in the same manner as other hydrodynamic quantities, we adopt a uniform hydro grid with a resolution of 128^3, spanning from -2 to 2 in all three spatial directions as our reference setup. To minimize the influence of gas drag— which is always present in the simulation— we use a low gas density and large dust grain size. Specifically, the gas density is set to $\rho_{\rm g} = 10^{-16}$ with a temperature of $T = 1$, while the dust grains have a size of $s = 10^{100}$ and a material density of $\tilde{\rho}_{\rm dm} = 1$, effectively rendering gas drag negligible. We model gravity using a central point mass of $M = 1/G$, such that the orbital period at $r = 1$ is 2π. The dust particles are initialized in Keplerian orbits on the midplane around the central mass.

We present the error in the cylindrical-$\hat{R}$ direction after $t = 2\pi$, corresponding to one orbital period at $r = 1$. Fig. 8.4 shows the fractional error, defined as:

$$\text{fractional error} = \frac{|R(t) - R_0|}{R_0} \tag{8.15}$$

The fractional error generally decreases with increasing radius, dropping below 10^{-3} beyond $r \gtrsim 0.5$. Notably, oscillations in the error as a function of radius are present, as indicated by the vertical dashed lines in Fig. 8.4. These low-error regions correspond to radii where the dust particle completes an integer number of orbits: the rightmost

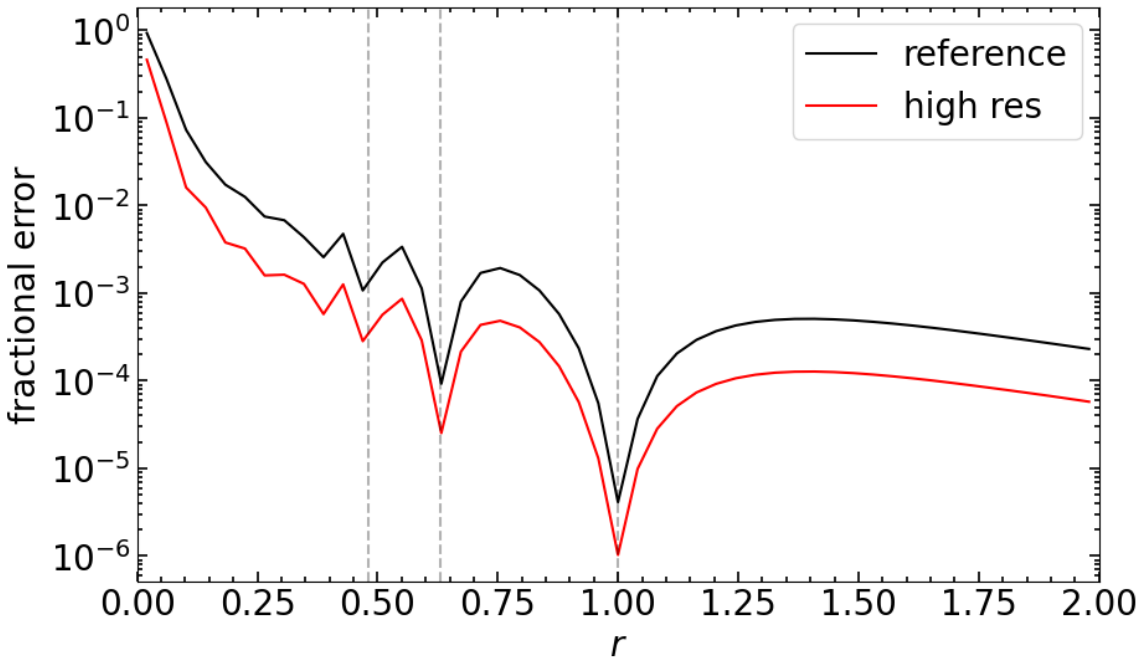


Figure 8.4: Fractional error in the gravity module of dust particle test as a function radius from the center in a model with minimal gas drag and the dust in Keplerian orbit around the center. The simulation setup is described in Section 8.3.4.

vertical dashed line at $r = 1$ is the simplest case; the second line from the right at $r = 0.5^{2/3}$ corresponds to two completed orbits; similarly, the third line near $r \approx 0.5$ marks three completed orbits. These features arise from the Keplerian motion being modeled on a Cartesian grid, where alignment with the grid axes introduces some expected discretization effects.

These numerical errors can be mitigated by increasing the hydro resolution. The red line in Fig. 8.4 shows the result for a setup identical to the fiducial case but with the hydro resolution doubled in all three spatial directions. The fractional error decreases by more than a factor of two, demonstrating improved orbital accuracy. However, the oscillatory pattern in the error remains, indicating that grid alignment effects persist even at higher resolution.

8.4 SUMMARY

We present a post-processing framework `Arcturus` for simulating tracer and dust particle trajectories based on hydrodynamic simulation outputs. This method is highly versatile and computationally efficient, as each particle can be evolved using its own adaptive time-step. We conducted a series of benchmark tests to assess numerical accuracy, leading to the following main conclusions:

1. Our numerical method achieves reasonable accuracy within the expected limits set by the TSC interpolation algorithm.

2. The hydrodynamic resolution is the primary factor governing the accuracy of both tracer and dust particle trajectories. Therefore, high-resolution hydro simulations are strongly recommended for post-processing applications.

3. For dust particles, reducing the integration time-step significantly improves accuracy, with errors decreasing approximately linearly with time-step size.

Chapter 9

Summary

The earliest phase of star formation lays the foundation for subsequent evolutionary stages. This thesis presents several studies to understand the key physical processes that shape this formative period.

In Chapter 2, I use 2D axisymmetric radiation hydrodynamics and dust evolution models to study the gas and dust dynamics, as well as grain growth, during the collapse of a dense molecular cloud core and the subsequent formation of a circumstellar disk. I show that grain growth is slow in the early protostellar phase, making the formation of mm/cm-sized grains unlikely unless the growth rate is enhanced by at least a factor of four. A semi-analytic solution to the Smoluchowski coagulation equation confirms this result, demonstrating that when the grain-grain relative speed scales linearly with grain size, the growth is primarily governed by the grain-grain collision speed and grain concentration. These findings offer a framework for estimating grain growth and provide direction for future studies in this area.

In Chapter 3, I use 3D non-ideal MHD simulations to model the collapse of a dense molecular cloud core leading to the formation of a single star and its circumstellar disk. In the case of a laminar dense cloud core, I confirm that the protostellar enve-

lope is dominated by the well-known pseudodisk—a thin, rapidly infalling structure confined to the equatorial plane. If the core is turbulent, the pseudodisk becomes 3D, dense, and flattened structures we term "gravo-magneto-sheetlets." These sheetlets, formed through the same physical processes as the pseudodisk, dominate the transport of mass, angular momentum, and magnetic flux within the envelope. However, unlike the pseudodisk, which delivers material to the outer edge of the forming disk, the sheetlets channel mass and angular momentum through the upper and lower disk surfaces, potentially facilitating disk substructure formation. Furthermore, I demonstrate the critical role of non-ideal MHD effects in shaping the protostellar disk formation: when the gas and magnetic field are tightly coupled, only a small and unstable disk forms, consistent with the scenario described by the traditional "magnetic braking catastrophe". In contrast, strong non-ideal MHD effects (particularly ambipolar diffusion) allow more angular momentum to be retained, enabling the formation of a larger and more persistent disk.

In Chapter 4, I extend the models from Chapter 3 to investigate multiple star formation by doubling the mass of the core and increasing its initial rotation rate. In the early stages of the simulation, a "gravo-magneto-sheetlet" structure, similar to those described in Chapter 3, forms alongside the first star-disk system. Between them, a new structure emerges: a dense, rotation-dominated region that is termed the "dense-rotation-dominated structure" (DROD). This structure is rotationally supported against infall toward the first star and is highly dynamic. Unlike a traditional disk, typically viewed as circular and flat, the DROD is intrinsically three-dimensional, containing spiral filaments. If sufficiently demagnetized through non-ideal MHD effects, collisions between these filaments can trigger the formation of companion stars. We refer to this mechanism as the "DROD fragmentation mechanism." A notable consequence of this process is the in-situ formation of misaligned,

$\sim$100 au-scale disks, which may explain systems such as the close multiple L1448 IRS3B.

Chapters 5, 6, and 7 focus on modeling outflows in protostellar environments. Chapters 5 and 6 investigate circumstellar disks threaded by large-scale vertical magnetic fields. The disk is structured into two distinct zones: an inner active zone, where thermal ionization enables strong coupling between the gas and magnetic field (ideal MHD limit), and an outer dead zone, where Ohmic dissipation decouples the magnetic field from the gas due to low ionization. The stellar magnetic field is excluded in these models to isolate the effects of the disk field.

Chapter 5 employs a 2D axisymmetric grid in spherical-polar coordinates. This setup provides high resolution in the meridional plane and allows for precise tracking of individual magnetic field lines. Leveraging these advantages, we show that the jet is driven by an "avalanche accretion stream" along the disk surface. This stream emerges from a positive feedback loop between infall, magnetic braking (which removes angular momentum), and the resulting lack of rotational support. The avalanche stream supplies angular momentum and energy to power the jet, which is launched from the upper surface of the disk.

Chapter 6 extends the 2D axisymmetric model into three dimensions, transitioning from spherical-polar to Cartesian coordinates. Although these 3D models are more computationally intensive and require compromises between resolution and cost, the absence of the polar axis and a hard inner boundary in Cartesian coordinates reduces uncertainties in jet modeling. With these 3D simulations, we show that the outflow consists of three components near the launching site: (1) a jet along the polar axis, (2) a laminar disk wind at large cylindrical radii, and (3) a turbulent disk wind driven by magneto-rotational instability (MRI), located between the jet and laminar wind. At larger altitudes, where MRI can no longer be sustained, the turbulent disk

wind merges with the laminar component, leaving only the jet and laminar wind distinguishable at large distances. Both the jet and the disk wind are launched by toroidal magnetic pressure, and we present a geometric argument showing that only magnetic pressure can drive an outflow in global models of protostellar environments. Additionally, the jet is lightly mass-loaded and requires a relatively mass-depleted polar cavity to propagate to large distances. This jet-launching mechanism differs fundamentally from the commonly invoked magneto-centrifugal model, and it calls into question the validity of using the poloidal-rotation velocity relation to infer the jet-launching radius, as is often done under the magneto-centrifugal paradigm. In our model, the jet can be one-sided: due to the global magnetic field geometry, the jet preferentially forms on the side where the toroidal magnetic field switches sign and an avalanche accretion stream is present. This stream sets a boundary to the disk's expansion, enabling the formation of a polar cavity and facilitating jet launching. On the opposite side, where the avalanche stream is absent, the expanding disk surface and MRI-active turbulent wind can fill the polar region with mass, choking jet formation. As a result, disk-only models can naturally produce one-sided jets.

Chapter 7 extends the models in Chapter 6 by including a stellar magnetosphere. Keeping the disk setup nearly identical to that in Chapter 6, the stellar magnetosphere is modeled as a dipole magnetic field anchored to a central star. In this model, a powerful and bipolar jet is launched through a "load–fire–reload" cycle. In the "load" stage, differential rotation along poloidal field lines threading both the star and the disk generates azimuthal magnetic fields. In the "fire" stage, the strong toroidal field gradient as a result of the differential rotation accelerates gas vertically, launching a jet and opening up the magnetic field. This is followed by the "reload" stage, in which magnetic reconnection resets the field geometry, allowing the cycle to repeat. Different stages of the cycle can occur simultaneously at different azimuthal angles, resulting in

a quasi-continuous outflow at large distances. Energetically, the generation of toroidal field can also be interpreted as the transfer of rotational energy into magnetic energy, which is then transported via Poynting flux from the stellar vicinity into the polar cavity to power the jet. Compared to the disk-only models in Chapters 5 and 6, the inclusion of the stellar magnetosphere promotes the launching of bipolar jets by shaping a magnetic field geometry conducive to symmetric outflows.

Finally, in Chapter 8, I present `Arcturus`, a post-processing tracer and dust simulation framework that reconstructs tracer or dust particle trajectories using outputs from (magneto-)hydrodynamic simulations. We demonstrate the robustness of the algorithm despite limitations arising from interpolation accuracy. With sufficiently frequent hydrodynamic outputs, this framework can be applied to investigate questions related to the evolutionary history of gas and dust parcels, as done in chapter 2 and chapter 4.

Appendix A

介绍

This appendix is a Chinese version of chapter 1 (Introduction)

行星系统的形成与演化——从我们的太阳系到遥远的系外行星——代表了天体物理学中最根本的科学探索之一。这些普遍存在的过程塑造了行星环境的物理条件，最终决定了其宜居性与生命潜力。数百年来，我们对行星系统的理解仅限于一个例子：我们自己的太阳系。这一局限在1995年被永远打破，随着51 Pegasi b 的发现(Mayor & Queloz, 1995)——首颗被确认绕类太阳恒星运行的系外行星。这项突破性发现打破了我们对行星系统结构的固有假设，并开启了天体物理发现的革命性新时代。通过研究行星、卫星及小天体如何形成与演化，我们不仅追溯宇宙的起源，还直面关于生命普遍性与人类宇宙地位的深刻问题。

从哲学角度来看，系外行星系统的显著多样性挑战了我们对地球特殊性的既有认知，迫使我们重新思考人类在宇宙中的角色。从生物学角度来看，这一研究方向力图揭示生命存在所需的具体物理与化学条件，为理解生命在宇宙中的潜在分布提供关键线索。从行星科学的视角出发，重建恒星系统的形成过程有助于解释恒星、行星及其残骸盘之间所呈现的多样性。从实践角度来看，这类知识具有不可或缺的应用价值——它直接指导我们对空间资源的勘探与利用，从近地小行星到外太阳系蕴藏的巨大潜力。

在这些领域取得进展，需要结合理论模型、先进数值模拟以及来自地面和空间观测设施的最前沿观测数据。这一研究不仅具有深远的学术意义，更在推动空间技术发展、奠定人类向地外可持续扩展的基础方面发挥着关键作用。

A.1 恒星与行星形成概述

行星系统的形成是一场起源于巨大分子云（Giant Molecular Clouds, GMCs）的宇宙之旅。作为星际介质中最寒冷、最致密的储库，这些庞大的结构横跨数百秒差距（1 秒差距约为3.26 光年），其总质量通常超过10^5 个太阳质量（$M_\odot$）(Großschedl et al., 2018)，是恒星形成的动态实验室。在其湍流主导的内部结构中，由重力不稳定性、磁场及恒星反馈共同驱动的超音速运动产生充满激波的混沌环境(Elmegreen & Scalo, 2004)。这些湍流过程在分子云中塑造出错综复杂的丝状结构，将气体和尘埃汇聚成密集的、延展的网络(Men'shchikov et al., 2010)。随着时间推移，引力不稳定性在这些丝状体中增强，导致局部物质聚集形成过密区域(Könyves et al., 2015)。这些高密度区域被称为分子云核心，是恒星诞生的关键前身(André et al., 2010)。当核心积累了足够的质量，其自引力将压倒热压、磁支撑和湍流运动等反作用力，进而触发级联式的塌缩过程。最终，这一演化过程导致原恒星系统的形成，可能进一步发展为单星、双星或小型星团；而原恒星盘中的残余物质则汇聚成行星、小行星和彗星(Könyves et al., 2015)。研究低质量恒星的形成过程对于理解类似太阳系的起源至关重要。这类恒星的质量通常不超过太阳质量的数倍，因此成为研究类太阳恒星与行星形成机制的理想范例。此外，许多低质量恒星形成区位于距地球较近的位置，为详细观测和分析这些形成过程提供了独特机遇。通过研究这些区域，我们可深入理解恒星早期演化阶段以及有利于行星形成的物理条件。

分子云核心向恒星与行星系统转化的过程通常被划分为四个演化阶段（Class 0、I、II、III，见图 1.1），这一分类最初基于观测特征提出，如今已被广泛接受为反映系统物理演化的时间序列(Barsony, 1994; Kristensen & Dunham,

2018)。Class 0 阶段最早通过其强烈的亚毫米辐射特征被识别，是密集核心初始塌缩的表现(Andre et al., 1993)。该阶段持续约10^4-10^5 年，原恒星仍深埋于其致密包层之中，大部分最终质量尚未积聚至中心天体。随后的Class I 阶段（持续约10^5 年）由包层进一步耗散并将物质输送至原恒星及其增长中的原行星盘，其光谱能量分布（SED）向红外波段移动，显示包层对中红外辐射的透光性增强。在此阶段，强烈准直的喷流和外流现象尤为显著，其由磁场引导、盘吸积驱动，以超音速速度喷出，重塑周围环境(Ray & Ferreira, 2021; Caratti o Garatti et al., 2024a)。

进入Class II 阶段（持续约10^6 年）后，包层基本被恒星与盘吸积或由喷流移除，留下一个拥有明亮原行星盘的前主序星，其在近红外波段具有强烈辐射[1]。在这一阶段，尘埃演化已相当显著，小尺度（微米级）尘粒逐渐聚集形成砾石与微行星体，盘面中往往出现环状与空隙结构，可能是原行星引力扰动或压力梯度诱导的结果(Dong et al., 2017; Dipierro et al., 2018; Lorek & Johansen, 2022)。最终，随着盘结构被光致蒸发和动力学过程（如恒星风作用）清除，系统进入Class III 阶段，仅存的残余物质构成碎片盘或年轻行星系统。气体被排出，行星迁移至稳定轨道，这一过程与早期太阳系的演化相类似(Lovell et al., 2021)。

这一演化序列已通过多波段观测得到了广泛验证，尤其是在距离地球较近的大质量分子云如金牛座、猎户座、蛇夫座和英仙座等分子云中，这些区域构成了研究年轻恒星天体的重要天体物理实验场。在所有阶段中，Class II 阶段的原恒星最为常见，由于其生命周期较长。其中最具代表性的是HL Tau (e.g. ALMA Partnership et al., 2015, 见图 1.2)，这是金牛座分子云中的一个Class I-II 系统[2]。该系统距离地球约140 秒差距，借助如ALMA（阿塔卡玛大型毫米/亚毫米阵列）等先进设备，其原行星盘已实现空间分辨成像，显示出多个同心环与空隙结构。这些特征被广泛解释为行星形成或盘内压力不稳定引发的结构重构(e.g. ALMA Partnership et al., 2015)。对HL Tau 及同类Class I-II 系统的高分辨率研究进一步揭示了其化学组

[1]在近红外和中红外波段，该原行星盘的亮度超过中心恒星。

[2]由于观测角度等因素限制，此类分类通常存在不确定性，因此并非绝对严格。

成(e.g., 检测到水分子， Facchini et al., 2024)与尘埃极化结构(Stephens et al., 2014, 2023)，为我们深入理解后期盘演化和行星形成机制提供了重要线索。

相比之下，对于Class 0 与早期Class I 阶段的观测研究仍相对有限，其根本原因在于两个方面：一是这些阶段的生命周期较短，二是中心天体通常被极致致密的尘埃包层遮蔽，使得其核心区域在可见光与近红外波段下难以探测。因此，研究者需依赖毫米/亚毫米（如ALMA）及近-中红外（如JWST、Spitzer）波段的观测，以穿透包层，获取关于吸积过程的线索。

VLA 1623 是Class 0 阶段的代表性原恒星系统（见图 1.3 左图），位于蛇夫座分子云中(Andre et al., 1993)。作为已知最年轻的原恒星之一，该系统由三个原恒星组成，共同从包层中吸积物质(Harris et al., 2018)。观测揭示其具有剧烈的、准直的双极外流，这些喷流由气体落入恒星时释放的能量驱动，以垂直于盘面的方向喷射而出。外流不仅是早期吸积活跃的标志，也是角动量重新分布的重要机制，常通过受激分子的辐射（如SiO）进行追踪(Codella et al., 2024)。进入Class I 阶段后，以IRAS 04302+2247 为例（该系统位于金牛座分子云，见图 1.3 右图），包层进一步稀薄，部分原行星盘结构在短波长下已可见(Lucas & Roche, 1998)。对该系统的高分辨率ALMA 观测显示，其尘埃粒子在垂直方向上尚未沉降至盘中面(Lin et al., 2023)，这表明系统内可能仍存在湍流或磁活动，有效抑制尘埃向中面沉降，与年老Class II 阶段中尘埃层已明显沉降的结构形成对比。

尽管观测手段持续进步，Class 0 和Class I 阶段所主导的物理机制仍然知之甚少。然则，这些阶段在恒星与行星系统的初始条件设定中扮演着基础性角色，影响着恒星及其原行星盘的质量、成分与动力学属性。在这些早期阶段中，众多相互耦合的物理过程交织演化：重力塌缩与湍流、磁场支撑相互竞争；气体与磁场的相互作用影响角动量传输；吸积驱动的喷流与正在坠落的包层物质交互；原行星盘在不对称、剧烈变化的环境中逐步成型。尽管观测“快照”提供了宝贵的时空截面，但由于系统演化时间远长于人类寿命，其静态图像往往难以揭示过程间的因果关系。同样，理想化的解析模型虽奠定理论基础，却常简化了这些阶段中的非线性反馈过程

（如气体演化与磁场牵引之间的相互作用）。

因此，为揭示这些复杂机制，数值模拟已成为不可或缺的工具。通过耦合磁流体力学（MHD）、辐射传输与化学演化，模拟可以在受控条件下进行“虚拟实验”，系统性改变初始参数（如湍流程度、磁场强度），追踪其在千年时间尺度下的演化结果。接下来的章节中，我们将介绍早期恒星形成中的关键科学问题，并阐述数值建模在这一领域中的核心作用。

A.2 原恒星与盘的形成

原恒星和原恒星盘（Class 0 和Class I）代表了恒星形成的最早阶段。尽管这个阶段相较于后期的原行星盘阶段相对较短，其动力学却在塑造新生系统的结构中扮演着关键角色——决定其是否演化为单星系统或多星系统。在此阶段中，前恒星核发生坍缩，形成恒星和环绕恒星的盘。大部分恒星质量在这一阶段被吸积，来源要么是直接从原恒星包层吸积，要么（更常见地）通过原恒星盘吸积(Fiorellino et al., 2023)。这个阶段也为后续盘的演化奠定基础，其物理特性将影响原行星盘的进一步演化，并最终决定是否能形成行星。

磁场是原恒星系统的基本组成部分，在恒星形成的各个阶段都能观测到其存在(Liu et al., 2022; Seifried et al., 2014)。在天体物理系统中，磁场如同“弹性绳”，在系统各组成部分之间提供动态耦合。例如，角动量可以通过磁场从旋转较快的气体传递到旋转较慢的部分（通常称为“磁制动”）。磁场也可以随着气体的流动而运动，从而影响整个系统的演化。在理想磁流体力学（MHD）近似下，假设磁场冻结在气体中，即磁场与气体共运动、无法分离。然而，在实际情况中，非理想MHD（non-ideal MHD）效应可能使磁场与气体解耦，从而允许它们相互独立地运动。三种主要的非理想MHD效应是：双极性扩散、霍尔效应和欧姆耗散。这些效应的重要性依赖于局部环境，例如气体密度、电离程度和磁场强度，这些因素影响了气体与磁场之间的耦合程度。原恒星阶段的磁场演化尤为重要(参见，例如, Tsukamoto, 2016)，非理想MHD过程可以重新分布或消除磁场，从而影响从原恒星

阶段向原行星盘阶段传递的磁通量，并决定原行星盘初期可能的磁场强度。

在恒星形成过程中观测磁场是非常具有挑战性的，尤其是在原恒星环境中，其磁场强度相较于恒星表面强磁场较弱。目前的直接观测主要依赖于塞曼效应（Zeeman effect），即在磁场作用下光谱线出现分裂现象(综述见 Crutcher & Kemball, 2019)。尽管该方法可用于检测磁场，但其信号通常非常微弱，需高灵敏度仪器和长时间观测，接近当前观测能力的极限。作为替代手段，也可通过测量尘埃偏振来间接推断磁场(e.g. Ohashi et al., 2025)。细长形状的尘埃颗粒会将自旋轴排列至与磁场方向一致，从而以特定方式发射偏振光(e.g., Le Gouellec et al., 2023, 图 1.4)。然而，该方法默认尘埃确实是沿磁场方向对齐的，而实际上气体阻力等过程也可能导致尘埃对齐方向的偏差，这一假设存在不确定性(Lin et al., 2024)。此外，这种方法主要提供磁场几何结构的信息，对磁场强度的约束较弱。因此，在星体形成过程中约束磁场及其演化十分困难，再加上非理想MHD带来的时间演化效应，其观测结果又添一层不确定性。为了弥合观测到的气体动力学与磁场行为之间的差距，非理想MHD模拟成为理解这些环境中磁场演化的关键工具。

另一个增加我们理解恒星形成复杂性的因素是湍流。在恒星形成的前恒星核中，湍流来源于尺度更大的巨大分子云，在那里，强烈的超音速湍流是普遍存在的(e.g., Mac Low & Klessen, 2004; Orkisz et al., 2017)。虽然湍流在前恒星核中通常减弱并变为亚音速(Chen et al., 2019)，但其对气体动力学和磁场演化的影响仍然重要且不确定。对于气体而言，湍流会扰乱前恒星核的层流式坍缩，改变气流的结构，进而影响新系统的构建。湍流还会改变磁场的几何结构，从而增强磁重联现象，即方向相反的磁力线发生重联并重新组织磁场结构。这一过程可能显著影响系统中磁通量的再分布。由于湍流、气体动力学和磁场之间的相互作用，仅依靠解析理论难以描述清楚这些过程，因此数值模拟对于捕捉局部过程以及研究其对恒星形成的整体影响至关重要。数值方法和模拟结果将在后续章节中详细讨论。

A.3 尘埃动力学与颗粒生长

类地行星（如水星、金星、地球和火星）以及太阳系中的小行星主要由固体物质构成，包括岩石和金属。在致密的分子云核心中，这些固体（以尘埃的形式存在）相对于气体而言是相当稀少的，其典型质量比为尘埃:气体= 1 : 100 (Bohlin et al., 1978)。此外，在致密核心中这些尘埃的尺寸非常小，通常在1微米（10^{-4} cm）或更小(Mathis et al., 1977a; Weingartner & Draine, 2001)。这些微小的尘埃颗粒是如何相互聚集并最终形成我们所居住的行星（6.4×10^8 cm）仍是一个未解之谜。

当前主流的行星形成模型遵循自下而上的路径，即固体颗粒从小尺寸逐渐成长至大尺寸。该过程包括若干阶段（见图 1.5）。第一阶段为“颗粒凝聚”，即小的（微米级）尘埃颗粒通过碰撞黏结形成更大的聚集体。当尘埃成长至毫米至厘米级时，其与气体的相互作用可能触发“流体不稳定性（streaming instability）”，进而导致尘埃聚集并坍缩为尺度从几公里到几十公里不等的天体(Youdin & Goodman, 2005a)。这些百公里级的天体随后通过“卵石吸积”（pebble accretion）方式吸积更小的尘埃颗粒(Bitsch et al., 2015; Visser & Ormel, 2016)，或通过与其他百公里级天体碰撞(Gabriel & Cambioni, 2023) 继续增长。通过这些过程，它们最终形成类地行星或太阳系中如木星和土星这样的巨行星核心。

然而，颗粒初始凝聚阶段的具体过程仍不明确，导致后续演化过程也存在不确定性。其中一个尚未解决的关键问题是：“颗粒生长，也就是颗粒凝聚而变大，主要发生在哪一个演化阶段（即哪一类天体）？”尽管当前逐渐形成共识认为颗粒生长在Class 0阶段或Class I阶段早期便已开始，但观测上对于是否在Class 0和Class I盘中存在大颗粒（毫米或厘米级）却仍存在冲突的证据，比如有些观察认为大颗粒在早期已经形成(Zamponi et al., 2024; Han et al., 2023; Kwon et al., 2009; Chiang et al., 2012; Jørgensen et al., 2007)，而另一些研究则未发现这些大颗粒(Ohashi et al., 2022; Zamponi et al., 2021)。因此，理解颗粒生长的物理过程和机制是十分

重要的，以便用理论指导对观测数据的解释。

在气体主导的环境中，颗粒生长面临的主要挑战之一是小尘埃颗粒由于气体阻尼作用与气体高度共动，导致彼此碰撞频率较低，从而抑制了其生长。当颗粒尺寸小于周围气体分子的平均自由程时，气体对尘埃的阻力加速度（在尘气相对速度Δv 下）满足Epstein阻力模型(Epstein, 1924)：

$$a_{\rm drag} = \frac{\Delta v}{t_s}, \tag{A.1}$$

其中t_s 是"停止时间"，描述了尘埃与气体之间的耦合程度：当颗粒很小时，t_s 也很小，意味着气尘耦合强。

判断t_s 是否很小并不总是直观，因此引入与气体特征动力学时间的比较更为有用。这就引出了"斯托克斯数（Stokes number）"的定义：

$$\mathrm{St} = \frac{t_s}{t_L} \tag{A.2}$$

其中t_L 是典型的气体周转时间——通常是气体完成一次完整旋转或循环所需的时间，具体定义视情境而定。在环星盘中，t_L 通常取为尘埃所处位置的局部环绕恒星的周期。而在湍流主导的小尺度动力学中，t_L 一般被定义为涡旋的周转时间，其值取决于湍流强度。如果在层流环境中观测到颗粒生长无法解释的颗粒尺寸，通常需要引入湍流以增强颗粒生长速率。

然而，将湍流引入颗粒生长模型也面临重大挑战。其中一个难点是斯托克斯数与颗粒碰撞速度之间存在高度非线性的关系，而碰撞速度又是决定颗粒生长效率的关键参数(参见例如 Voelk et al., 1980; Markiewicz et al., 1991a; Pan & Padoan, 2013, 2015)。虽然已有许多研究采用解析模型和局部数值模拟探讨这一关系，但迄今为止仍缺乏一个完整的理论框架来描述湍流条件下的颗粒碰撞。

进一步增加复杂性的是，湍流中颗粒动力学的局部模型仅提供有限信息，而颗

粒生长本质上是一个非局部过程。随着颗粒不断增大（即St 上升），其将逐渐与气体脱耦，并相对于气体产生漂移，导致颗粒集中或耗竭——这些效应只能通过全局模型捕捉(e.g. Birnstiel et al., 2010, 2012)。由于全局模型计算开销巨大，通常需要参数化和简化处理，从而引入结果不确定性。

在进一步考虑颗粒的内部结构、表面化学特性以及颗粒碰撞结果的多样性后，问题变得更加复杂。尽管模型中常将颗粒视为完美球体，但实际上其形状和结构可能远为复杂，例如具有孔隙度等特征，这会影响其物理行为(Dominik & Tielens, 1997; Blum, 2004)。此外，在早期、低温环境中，颗粒表面可能会被冰层覆盖，从而改变尘气相互作用并影响碰撞结果(Potapov et al., 2020)。

颗粒碰撞的结果通常分为三类：凝聚（即颗粒黏结并质量增长）、反弹（碰撞但保持原有尺寸）以及破碎（碰撞产生更小颗粒）。这些结果已通过理论模型(如描述颗粒表面力学的JKRS理论 Johnson et al., 1971; Sperling, 1964)以及实验手段（如在模拟失重环境的落塔实验中）进行研究(e.g. Blum & Münch, 1993; Weidling et al., 2012)。然而，由于颗粒结构和碰撞参数的复杂性，这些预测仍存在较大不确定性。

尽管存在诸多挑战，理解颗粒生长过程仍对揭示行星形成早期阶段至关重要，并为后续演化打下基础。例如，流体不稳定性（Streaming Instability）通常要求局部尘气质量比超过1 (Zhu & Yang, 2020)——这比致密分子云核心中的典型值高出一百倍。实现如此高的增强可能需要尘气显著脱耦，而这往往依赖于颗粒的增长。因此，目前仍有大量研究从多个角度探讨颗粒生长，旨在弥合理论模型、数值模拟、实验结果和观测数据之间的差距。

A.4 外流动力学

恒星和行星的形成通常被认为是由吸积驱动的过程（如图 1.1 所示），但其反向过程——外流——在塑造恒星形成过程中同样重要，甚至更为关键。

外流在恒星和行星形成环境中起着重新分配角动量的关键作用，影响恒星、盘

和行星的演化。在最早的吸积阶段（Class 0早期至中期），如果气体吸积过程是有序的(Basu et al., 2024)，外流可在恒星盘外被驱动（通过对内包层吸积旋转气体的磁制动作用），因此即便在最早的Class 0吸积阶段也能启动外流，从而实现角动量的传输（如sec. A.2 中讨论）。在Class 0和Class I阶段，外流可以从恒星或盘中发射，将角动量从其各自的源头带走。如果是由恒星驱动的，外流有助于调节恒星的自转；若没有外流，恒星的旋转速度将远高于观测值。例如，太阳的自转周期为24天，若未经历角动量损失，它本应拥有更短的自转周期。类似地，绕恒星盘的演化也依赖于角动量的传输(Hartmann, 1998; Goodson & Winglee, 1999; Mellon & Li, 2008)；若没有高效的角动量再分配，盘的吸积过程及随后的行星形成将会停滞。

观测上，由于喷流和外流在某些波段的尺度和亮度较大(例如观测铁II，见Assani et al., 2024)，它们成为可探测的恒星形成探针(Ray & Ferreira, 2021; Lee et al., 2018, 例如见图 1.6)。高分辨率的观测不断改善我们对其结构的理解，同时也提出了关于其起源的新问题(Pascucci et al., 2023)。磁场作为连接并调控跨尺度气体动力学的关键因素，被认为是喷流和外流的主要驱动者。由于喷流的尺度和结构较容易观测，而其发射区（恒星或内盘附近）难以直接探测，因此研究外流可以为约束其形成机制和条件提供重要的间接信息。理解喷流的发射机制对于解释观测结果和理解其背后的物理过程至关重要。

外流的影响远不止于恒星和行星形成。外流的主要组成部分是喷流，它是年轻恒星天体（YSO）外流中最具能量的形式。在高质量恒星形成中（$\gtrsim 10M_{\odot}$），喷流可延伸数个秒差距(e.g., Fedriani et al., 2018)；而在低质量恒星形成中（$\simeq 1M_{\odot}$），喷流可以达到超过10^4 au 的距离(e.g., Caratti o Garatti et al., 2024b)。这些喷流中的气体以高超音速（> 100 km s^{-1}）运动，将大量能量注入周围的星际介质（ISM）。在大尺度上，这些长距离传播的喷流会改变周围分子云核的条件，可能阻止这些核心中的恒星形成(Federrath, 2016)。这对初始质量函数（IMF，即在巨分子云尺度上新形成恒星的统计质量分布）具有显著影响，而IMF又是星系形成

与演化中的关键参数(Guszejnov et al., 2021)。

理解喷流的驱动机制对于评估其在各个尺度上的影响至关重要。喷流通常被认为起源于恒星附近，但恒星本身并不能单独驱动喷流——这可以通过我们太阳和其它孤立恒星周围缺乏喷流现象来证明。这表明内盘在喷流的发射中起着核心作用。其中一种可能机制是光蒸发风，即恒星辐射加热盘表面并热驱动出流。然而，光蒸发过程通常不足以产生观测到的高准直性和高速度的喷流，特别是那些速度超过100 km/s的喷流(Macías et al., 2016; Rodenkirch et al., 2020)。

相反，盘中的磁场——无论是从分子云核继承来的，还是受到恒星磁场的影响——都被认为是驱动喷流的关键因素。由于磁场可以动态耦合系统中的不同组分，它们原则上可以介导盘的旋转能量并将其转化为驱动喷流的能量。然而，这一过程的确切机制仍不确定。

喷流旋转的观测加强了一个观点：磁场提取并转换旋转能量驱动外流(Chrysostomou et al., 2008)。目前主要的模型类别之一是离心驱动机制(包括磁离心盘风模型和X风模型，参见例如 Blandford & Payne, 1982; Pudritz & Norman, 1983; Shu et al., 1994, 2000)，其中角动量通过近似刚性的磁力线从盘传递到气体，使得气体加速到超克卜勒旋转速度，从而由离心力驱动出流。另一类模型关注旋转能量的传输(例如Poynting通量喷流和磁塔喷流模型，见 Shibata & Uchida, 1986; Lovelace et al., 2001; Lynden-Bell, 2003, 1996)，其中旋转能量首先转移到磁场，形成强大的环向磁场分量，在盘上方产生显著的Poynting通量，进而将能量重新注入气体中，推动出流。尽管这两类模型已被广泛研究，但一个能够自洽地再现喷流能量学、形态和准直性等关键观测特征的完整框架仍未建立。

外流的另一个重要组成部分是盘风。相较于喷流，盘风的速度较低（几千米每秒），开角更大（数十度）(Pascucci et al., 2023)。虽然它对巨分子云尺度的反馈较弱，但却主导了外流中的质量传输，因此在调节盘的演化中起着关键作用(Tabone et al., 2020)，特别是在角动量的转移方面。与喷流一样，盘风也被认为是由磁流体动力（MHD）机制驱动的，但其与喷流之间的确切关系仍不清楚。尤

其是盘风与喷流内部是否存在子结构(de Valon et al., 2022)，若存在，这些子结构又是如何形成的，仍是一个未解之谜。

喷流发射区的动力学不仅自身具有重要意义，还对理解太阳系的形成与演化至关重要。太阳系早期演化的证据——包括太阳早期喷流可能存在的迹象——保存在小行星和陨石中。这些天体的性质和组成为我们研究早期太阳星云的历史提供了独特的探针。外流特别可能影响球粒陨石，这类石陨石中包含小球状的粒子（球粒）嵌入在硅酸盐基质中。这些球粒通常为毫米级，具有典型的球形形态。

一种特殊的球粒类型是钙铝富包体（Calcium-Aluminum-rich Inclusion，CAI）。与主要由镁铁硅酸盐组成的普通球粒不同，CAI富含高升华温度的耐火元素(Lodders, 2003)。在年轻太阳附近的高温环境下，所有元素均会被汽化为气态；而随着气体冷却，元素会按照其凝结温度的先后顺序重新凝结。由于CAI的成分具有较高的凝结温度，因此它们是最早重新出现的固体，形成于靠近年轻恒星的区域(Woitke et al., 2024)。

陨石证据也表明，CAI是最早在原行星盘中形成的固体，形成时间可能追溯到太阳星云的Class I或早期Class II阶段(参见例如 Bekaert et al., 2021)。然而，一个长期存在的问题仍未解决：CAI如何在靠近年轻太阳的区域形成，却最终被运输至太阳系的外部区域，并被包含在后来落入地球的陨石中？一种被提出的外输机制是湍流扩散，在该机制中，盘中的湍流随机地将粒子扩散到远离其形成位置的区域(Brownlee et al., 2006; Cuzzi et al., 2003)。另一个可能的机制是由喷流和外流输运，考虑到其与原恒星和内盘的直接连接，它们有可能将CAI向外输运，同时塑造原行星盘的结构(Ciesla, 2009)。

A.5 数值方法

天体物理系统的复杂性常常需要借助数值模拟来揭示其背后的主导机制。尽管本论文不打算对各种模拟技术进行详尽回顾，我们在此简要总结这些计算工具的概念基础，并概述其在天体物理研究中应用的基本原则。

天体物理系统——从分子云到星系——主要由气体构成，这是大多数模型中的主要组成部分。根据所研究的物理环境，不同的附加过程可能会被纳入模拟中，例如磁流体力学（MHD）、引力相互作用、相对论效应以及辐射过程。为了提升模型的真实性，还可以加入尘埃、化学成分和带电粒子等额外成分，尽管这些扩展会显著增加模拟的复杂性与计算成本。在恒星与行星形成的研究中，气体（包括尘埃）的动力学与磁场之间的相互作用尤为重要，因此我们将重点关注用于模拟这些过程的计算方法。

天体物理模拟的基石是对守恒定律的严格遵守：质量、动量与能量必须在时间演化中保持不变。考虑到天体系统所涵盖的巨大空间尺度与演化时间尺度，即使是极小的数值误差也可能在长期演化中积累为灾难性的偏差。因此，准确守恒这些物理量是不可妥协的要求。尽管平滑粒子流体动力学（SPH）方法也被广泛使用(e.g., Price et al., 2018)，有限体积法（FVM）因其天然对五个基本守恒量——质量、三个方向上的动量与能量——的守恒性而成为天体物理中的首选数值方法(e.g., Fryxell et al., 2000; Teyssier, 2002; Stone et al., 2020)。

有限体积法（Finite Volume Method, FVM）通过将模拟区域划分为离散的网格单元（控制体积）来工作，每个单元足够小，可认为其内部气体性质均匀。在每一个时间步，FVM 通过求解黎曼问题来决定守恒量在相邻单元之间的传输——黎曼问题描述了两个状态之间由间断面分隔的流体相互作用。例如，当一个单元的气压高于相邻单元时，它们之间的相互作用会产生波动（如激波或膨胀波），从而重新分布质量与能量。Godunov 类求解器在每个单元界面上逼近这些波动行为，计算跨越单元边界的守恒量通量。这种方法不仅严格守恒，而且能够自然捕捉到如超新星激波前沿或恒星形成云团内湍流等不连续结构(Toro, 2009)。

磁场在许多天体系统中扮演着关键角色，如今已被常规地纳入现代模拟中。磁场演化的准确性依赖于维持零散度条件（$\nabla \cdot \mathbf{B} = 0$），这是由麦克斯韦方程组导出的基本约束。最先进的“约束传输”（Constrained Transport, CT）算法从设计上保证这一条件的成立，确保每个单元内磁通量随时间始终为零(Evans &

Hawley, 1988)。CT 算法通过在交错网格上演化磁场分量——即磁场存储于单元面上——并利用边缘处电场的旋度来更新磁场。该几何方法从离散角度天然地保持了$\nabla \cdot \mathbf{B} = 0$，无需像清散度方法那样依赖人工修正。通过将流体动力学与磁场演化耦合，MHD 模拟可以捕捉到诸如喷流发射、吸积盘稳定性以及星际介质湍流等关键现象。

与连续介质方法不同，离散系统（例如行星轨道或气体中尘埃粒子的轨迹）的模拟则侧重于逐个求解点质量的运动方程(e.g., Rein & Liu, 2012)。例如，尘埃粒子的运动轨迹由牛顿第二定律控制：

$$\frac{d^2\boldsymbol{x}}{dt^2} = \mathbf{a}(\boldsymbol{x}, t), \tag{A.3}$$

其中$\mathbf{a}(\boldsymbol{x}, t)$ 表示粒子所受的合加速度（如引力或气体阻力）。当与气体动力学耦合时，这种粒子追踪方法可以用于研究原行星盘中的尘气耦合或行星在演化系统中的迁移过程。

A.6 论文结构

本论文旨在解答第 A.2节、第 A.3节以及第 A.4节中提出的若干关键科学问题。接下来的各章将通过一系列数值模拟与理论分析对这些问题进行详细探讨。第 2章模拟了原恒星环境中的尘粒动力学与颗粒增长，展示了在层流原恒星盘中尘粒增长较为缓慢。第 3章与第 4章模拟了原恒星核心的塌缩过程及其引发的恒星与盘的形成，重点研究了原恒星包层的结构、非理想MHD 对盘形成的影响，以及 ∼100 au 距离处多恒星系统及其错列盘结构的形成机制。第 5章、第 6章与第 7章探讨了喷流与外流的发射机制，其中第 5章与第 6章使用二维轴对称与三维模型研究了由盘磁场独立驱动的喷流发射过程。第 7章在模型中加入了恒星磁层，并进一步探讨磁层与盘的相互作用如何改变喷流发射行为。除此之外，第 8章介绍了一个用于后处理的示踪剂与尘埃模拟框架`Arcturus`，它被应用于第 2章与第 4章中，以突出各研

究情境中的关键物理过程。

Appendix B

Additional Information for Chapter 2

B.1 Brownian motion

Brownian motion was shown to be important for the growth of small, (sub)μm-sized grains (e.g., Suttner & Yorke, 2001; Tanaka et al., 2005). In this Appendix, we consider the effects of the Brownian motion on the grain growth in the two simulations shown in Fig. 2.5. The relative speed induced by Brownian motion on two dust particles of mass m_1 and m_2 is given by

$$\Delta v_{\rm BM} = \sqrt{\frac{8k_bT}{\pi}\frac{m_1+m_2}{m_1m_2}}. \tag{B.1}$$

It is added to the relative speed induced by the dust-gas drift in grain coagulation calculation. The results are shown in Fig. B.1, where the cumulative mass of the grain up to a certain grain size is plotted as a function of the grain size for both the reference run without any enhanced collision speed ($\chi = 1$) and with an enhancement factor of $\chi = 4$ and with and without the Brownian motion. It is clear that the

Brownian motion increases the grain sizes at a given time somewhat, but the increase is relatively modest. This is to be expected because the later grain growth to larger sizes is relatively insensitive to the size distribution of the smallest grains that are most affected by the Brownian motion. We conclude that the inclusion of the Brownian motion cannot explain the abundance of large mm/cm sized grains that are inferred in young protostellar disks and additional pieces of physics are needed.

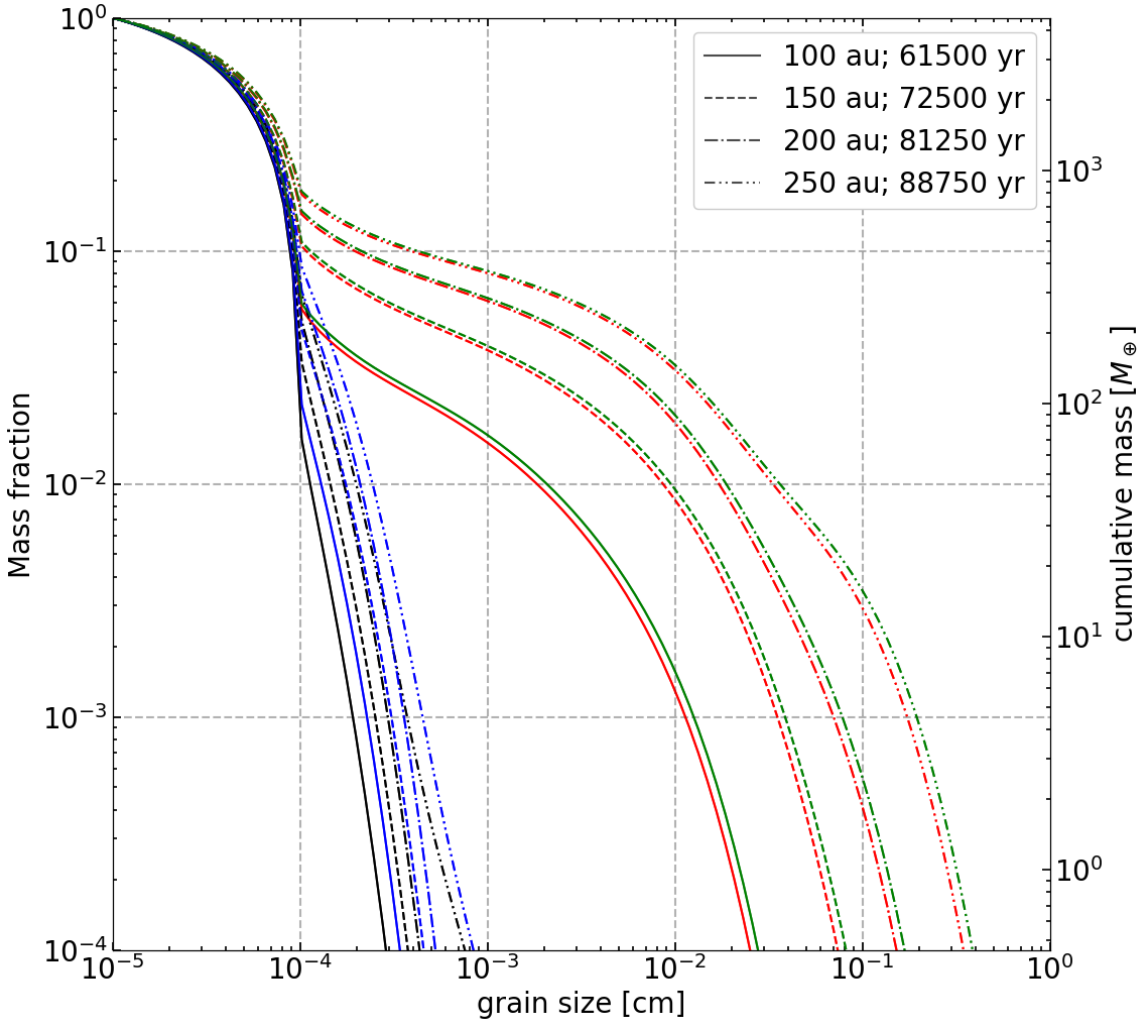


Figure B.1: Cumulative grain mass as a function of grain size similar to Fig. 2.5 but with the Brownian motion included. The mass includes both the grains in the active computational domain and those advected through the inner boundary. The black and red lines are the baseline models for $\chi = 1$ and 4 respectively without Brownian motion; the blue and green lines are the corresponding models with Brownian motion included.

Appendix C

Additional Information for Chapter 4

C.1 3D Visualization with Unity

To better visualize the formation of a multiple-star system, we use the Unity Engine (Unity Technologies, 2024), a 3D game engine, to generate movie-like videos of our simulation.

We visualize the reference model (M1.0AD2.0 model in chapter 4). The gas is visualized with spheres, with each sphere representing the same gas mass. The colors of the spheres follow the rainbow color scheme (similar to panel a of fig. 4.10), representing the gas density at their locations. Blue means lower density and red means higher density. The gas particle trajectories are calculated with the post-process Lagrangian tracer particle code described in sec. 4.2.1. The sizes of the stars are proportional to their masses. To account for the stellar illumination on gas for artistic purposes, each star is accompanied by a white light source at its location after its formation. For artistic purposes, the post-process Lagrangian simulation is modified in two ways.

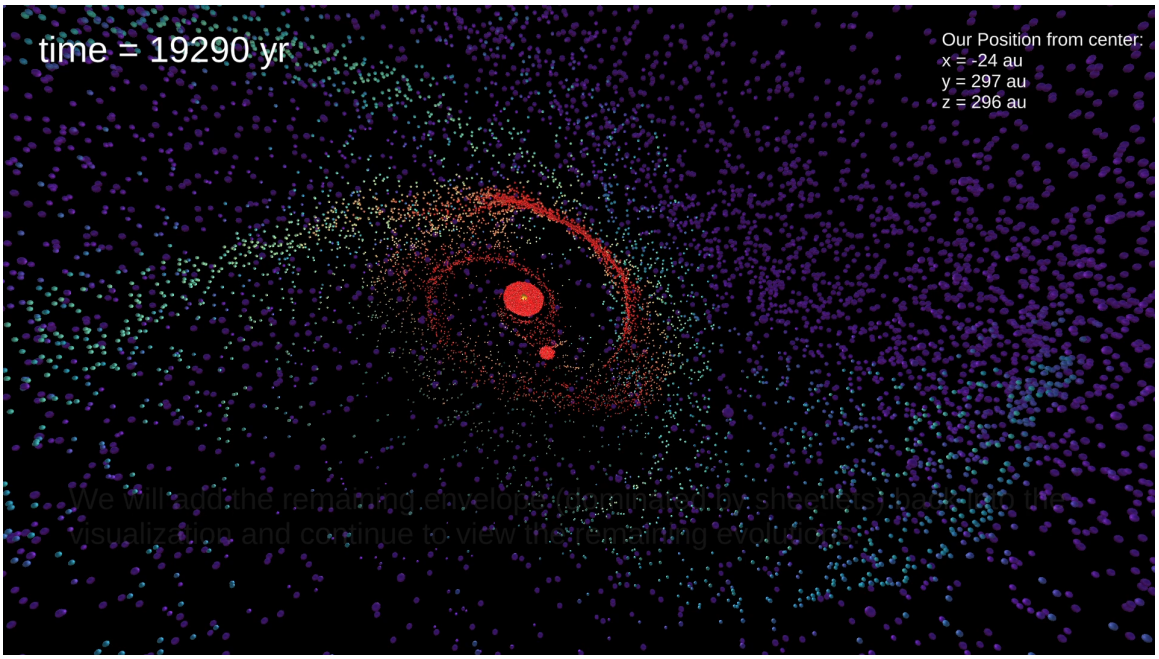


Figure C.1: One representative frame of the artistic rendering of the M1.0AD2.0 model with Unity (Unity Technologies, 2024). The movie can be found on YouTube at `https://www.youtube.com/watch?v=s-eHv7cAObw`

First, to better visualize the disk and minimize the impact of the relatively low MHD output frame rate, we force the gas particle to orbit in Keplerian orbit around a star if the particle is in the vicinity of the star (typically within 25au from the star) and the particle orbital velocity is > 0.7 local Keplerian velocity relative to its host star. Second, the second companion is not shown in the movie because it merged with the first companion.

The movie can be on YouTube at `https://www.youtube.com/watch?v=s-eHv7cAObw`. We show a representative frame of the movie in fig. C.1.

Appendix D

Additional Information for Chapter 5

D.1 Limits on the toroidal magnetic field strength in the active disk zone

For disk simulations like ours (those presented in chapter 5) that start with a relatively weak poloidal magnetic field, the toroidal field is generated by differential twisting of the poloidal magnetic field. We can estimate the strength of the steady-state toroidal field strength from the induction equation under several simplifying assumptions. For this simple estimate, we will assume that the toroial field is generated by the vertical differential twist of a vertical magnetic field B_z and removed by radial advection of a magnetically braked accretion flow. In this case, the induction equation for B_ϕ simplifies to

$$B_z \frac{\partial v_\phi}{\partial z} \approx B_\phi \frac{\partial v_R}{\partial R} \tag{D.1}$$

where R is the cylindrical radius. We assume that v_ϕ is close to the Keplerian value:

$$v_\phi(R,z) \approx v_K(R,z) = \frac{(GM)^{1/2}R}{(R^2+z^2)^{3/4}} \tag{D.2}$$

so that

$$\frac{\partial v_\phi(R,z)}{\partial z} = -\frac{3z\ v_K}{2(R^2+z^2)}. \tag{D.3}$$

We further assume that the radial flow v_R is caused by magnetic braking, which yields:

$$v_R = \frac{R}{2\pi\rho v_K}\frac{\partial B_\phi}{\partial z}B_z. \tag{D.4}$$

If the radial variation of v_R is on the scale of radius R and the vertical variation of B_ϕ is on the scale of z_b, we can combine equations (D.1)-(D.4) to eliminate B_z (it cancels out because the toroidal field generation and removal rates both depend linearly on it) and estimate the ratio of the magnetic energy density of the toroidal field and the kinetic energy density from Keplerian rotation

$$\frac{B_\phi^2/(8\pi)}{\rho\ v_K^2/2} \approx \frac{3zz_b}{4R^2}, \tag{D.5}$$

which is expected to be substantially less than unity inside the disk where both z and z_b are expected to be less than R, consistent with what we find in the simulation.

Appendix E

Additional Information for Chapter 6

E.1 Insensitivity to the inner boundary condition

In this Appendix, we demonstrate that our results in chapter 6 are insensitive to the prescribed rotation at the inner boundary by comparing the NOROT model (where the inner boundary is stationary) and the STROT model (where the inner boundary rotates as a solid body with a 2.9-day period). While these models are not expected to be identical due to their turbulent nature, we show that they are qualitatively similar.

Figure E.1 presents the azimuthally averaged density, v_z^p, B_ϕ, and $B_\phi^2/(8\pi\rho)$ for both the NOROT (upper row) and STROT (lower row) models. Readers are encouraged to view the animated version for a clearer understanding of their similarities over time. In both models, the density structure features a magnetically expanded active zone near the midplane ($\lesssim 0.15$ au), a more laminar magnetic dead zone at larger radii

($\geq$ 0.15 au), and an outflow extending above the disk in both hemispheres. At the time shown, the jet in the NOROT model is dominant in the upper hemisphere, while in the STROT model, it is stronger in the lower hemisphere. The disk wind (sec. 6.3.2) and MRI-active disk wind (sec. 6.3.3) are prominent at large cylindrical radii in both hemispheres for both models.

The magnetic field configurations in the two models are consistent with the geometric arguments in Section 6.4.1: the azimuthal magnetic field B_ϕ is negative in the upper hemisphere and positive in the lower hemisphere. Although the hemisphere where B_ϕ switches sign differs—upper hemisphere in NOROT and lower hemisphere in STROT—the jet-launching side is always aligned with the region where B_ϕ switches sign. Consequently, the magnetic energy per unit mass (fig. E.1[d], [h]) is larger on the jet-launching side. This supports the conclusion that the disk surface avalanche accretion stream facilitates jet launching by creating an outflow cavity, a process that is robust and independent of the inner boundary's rotation.

The similarity between the two models might seem counterintuitive at first, as one might expect the additional differential rotation in the STROT model to strengthen the outflow. However, in our simulations, the poloidal field lines threading the inner boundary do not exhibit significant differential rotation because the magnetic field dominates over gas motion immediately above and below the boundary. As the gas near the boundary adjusts to its motion, no additional differential rotation is introduced, causing the magnetic field lines in the polar regions to remain mostly vertical in both models. As a result, the STROT model is qualitatively similar to the NOROT model. While the early jet in the STROT model ($\lesssim$ 3yr in the animated version of Fig.E.1) is indeed stronger, the two models converge to a qualitatively similar behavior in their later evolution.

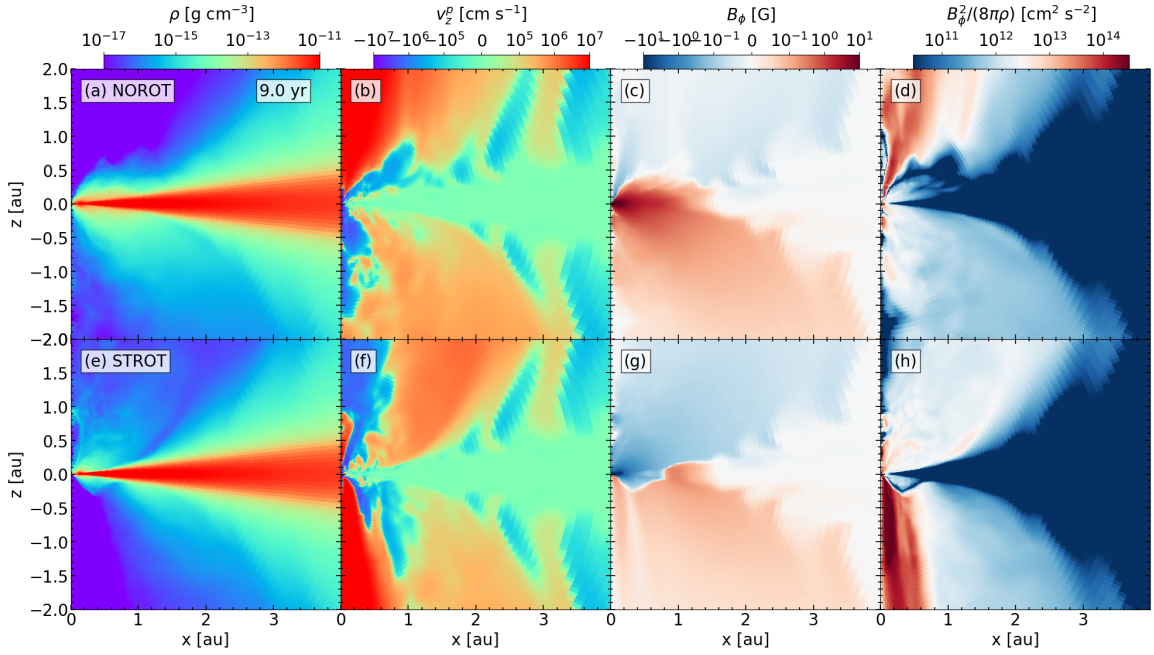


Figure E.1: Comparison between the NOROT and STROT at the same time (9.0 yr). The upper row shows a slice through the NOROT model and the lower row shows the STROT model. The four columns show density, projected z-direction velocity (v_z^p, equ. 6.18), azimuthal magnetic field, and magnetic energy per unit mass, respectively. Although these two models are not expected to be identical due to their turbulent nature, they are qualitatively similar. An animated showing the evolution can be found at `https://figshare.com/s/04e8a31b7f92218f24bb`. The animated version is 50 seconds long, showing the evolution of the NOROT and STROT models from the initial condition to 10 yrs. The animation shows the qualitative similarities between these two models.

References

Acheson, D., & Acheson, F. 1990, Elementary Fluid Dynamics, Comparative Pathobiology - Studies in the Postmodern Theory of Education (Clarendon Press). https://books.google.com/books?id=GgC69-WUTs0C

Aikawa, Y., Cataldi, G., Yamato, Y., et al. 2021, The Astrophysical Journal Supplement Series, 257, 13, doi: 10.3847/1538-4365/ac143c

ALMA Partnership, Brogan, C. L., Pérez, L. M., et al. 2015, The Astrophysical Journal Letters, 808, L3, doi: 10.1088/2041-8205/808/1/L3

Anderson, J. M., Li, Z.-Y., Krasnopolsky, R., & Blandford, R. D. 2005, The Astrophysical Journal, 630, 945, doi: 10.1086/432040

—. 2006, The Astrophysical Journal Letters, 653, L33, doi: 10.1086/510307

André, P., Di Francesco, J., Ward-Thompson, D., et al. 2014, in Protostars and Planets VI, ed. H. Beuther, R. S. Klessen, C. P. Dullemond, & T. Henning, 27–51, doi: 10.2458/azu_uapress_9780816531240-ch002

Andre, P., Ward-Thompson, D., & Barsony, M. 1993, The Astrophysical Journal, 406, 122, doi: 10.1086/172425

André, P., Men'shchikov, A., Bontemps, S., et al. 2010, Astronomy and Astrophysics, 518, L102, doi: 10.1051/0004-6361/201014666

Andrews, S. M. 2020, Annual Review of Astronomy and Astrophysics, 58, 483, doi: 10.1146/annurev-astro-031220-010302

Andrews, S. M., Huang, J., Pérez, L. M., et al. 2018, The Astrophysical Journal, 869, L41, doi: 10.3847/2041-8213/aaf741

Armitage, P. J. 2015, arXiv e-prints, arXiv:1509.06382. https://arxiv.org/abs/1509.06382

Arons, J., & Lea, S. M. 1976, The Astrophysical Journal, 207, 914, doi: 10.1086/154562

Artymowicz, P., & Lubow, S. H. 1994, The Astrophysical Journal, 421, 651, doi: 10.1086/173679

Aso, Y., Ohashi, N., Saigo, K., et al. 2015, The Astrophysical Journal, 812, 27, doi: 10.1088/0004-637X/812/1/27

Asplund, M., Grevesse, N., Sauval, A. J., & Scott, P. 2009, Annual Review of Astronomy and Astrophysics, 47, 481, doi: 10.1146/annurev.astro.46.060407.145222

Assani, K. D., Harsono, D., Ramsey, J. P., et al. 2024, Astronomy and Astrophysics, 688, A26, doi: 10.1051/0004-6361/202449745

Bai, X.-N. 2011, The Astrophysical Journal, 739, 50, doi: 10.1088/0004-637X/739/1/50

Bai, X.-N., & Stone, J. M. 2013, The Astrophysical Journal, 769, 76, doi: 10.1088/0004-637X/769/1/76

Bai, X.-N., Ye, J., Goodman, J., & Yuan, F. 2016, The Astrophysical Journal, 818, 152, doi: 10.3847/0004-637X/818/2/152

Balbus, S. A., & Hawley, J. F. 1991, The Astrophysical Journal, 376, 214, doi: 10.1086/170270

Banzatti, A., Abernathy, K. M., Brittain, S., et al. 2022, The Astronomical Journal, 163, 174, doi: 10.3847/1538-3881/ac52f0

Bardou, A., & Heyvaerts, J. 1996, Astronomy and Astrophysics, 307, 1009

Barsony, M. 1994, in Astronomical Society of the Pacific Conference Series, Vol. 65, Clouds, Cores, and Low Mass Stars, ed. D. P. Clemens & R. Barvainis, 197

Basu, S., Sharkawi, M., & Machida, M. N. 2024, The Astrophysical Journal, 964, 116, doi: 10.3847/1538-4357/ad1bf3

Bate, M. R., & Lorén-Aguilar, P. 2016, Monthly Notices of the Royal Astronomical Society, 465, 1089, doi: 10.1093/mnras/stw2853

Beckwith, K., Hawley, J. F., & Krolik, J. H. 2009, The Astrophysical Journal, 707, 428, doi: 10.1088/0004-637X/707/1/428

Beckwith, S. V. W. 1999, in NATO Advanced Study Institute (ASI) Series C, Vol. 540, The Origin of Stars and Planetary Systems, ed. C. J. Lada & N. D. Kylafis, 579. https://arxiv.org/abs/astro-ph/9905003

Bekaert, D. V., Auro, M., Shollenberger, Q. R., et al. 2021, Science Advances, 7, eabg8329, doi: 10.1126/sciadv.abg8329

Bergin, E. A., & Tafalla, M. 2007, Annual Review of Astronomy and Astrophysics, 45, 339, doi: 10.1146/annurev.astro.45.071206.100404

Béthune, W., Lesur, G., & Ferreira, J. 2017, Astronomy and Astrophysics, 600, A75, doi: 10.1051/0004-6361/201630056

Birnstiel, T., Dullemond, C. P., & Brauer, F. 2010, Astronomy and Astrophysics, 513, A79, doi: 10.1051/0004-6361/200913731

Birnstiel, T., Klahr, H., & Ercolano, B. 2012, Astronomy and Astrophysics, 539, A148, doi: 10.1051/0004-6361/201118136

Bitsch, B., Lambrechts, M., & Johansen, A. 2015, Astronomy and Astrophysics, 582, A112, doi: 10.1051/0004-6361/201526463

Bjerkeli, P., van der Wiel, M. H., Harsono, D., Ramsey, J. P., & Jørgensen, J. K. 2016, Nature, 540, 406

Blandford, R. D., & Payne, D. G. 1982, Monthly Notices of the Royal Astronomical Society, 199, 883, doi: 10.1093/mnras/199.4.883

Blandford, R. D., & Znajek, R. L. 1977, Monthly Notices of the Royal Astronomical Society, 179, 433, doi: 10.1093/mnras/179.3.433

Blinova, A. A., Romanova, M. M., & Lovelace, R. V. E. 2016, Monthly Notices of the Royal Astronomical Society, 459, 2354, doi: 10.1093/mnras/stw786

Blum, J. 2004, in Astronomical Society of the Pacific Conference Series, Vol. 309, Astrophysics of Dust, ed. A. N. Witt, G. C. Clayton, & B. T. Draine, 369

Blum, J., & Münch, M. 1993, Icarus, 106, 151, doi: 10.1006/icar.1993.1163

Bohlin, R. C., Savage, B. D., & Drake, J. F. 1978, The Astrophysical Journal, 224, 132, doi: 10.1086/156357

Boss, A. P., & Keiser, S. A. 2013, The Astrophysical Journal, 764, 136, doi: 10.1088/0004-637X/764/2/136

Bouvier, J., Alencar, S. H. P., Harries, T. J., Johns-Krull, C. M., & Romanova, M. M. 2007, in Protostars and Planets V, ed. B. Reipurth, D. Jewitt, & K. Keil, 479, doi: 10.48550/arXiv.astro-ph/0603498

Brownlee, D., Tsou, P., Aléon, J., et al. 2006, Science, 314, 1711, doi: 10.1126/science.1135840

Cacciapuoti, L., Testi, L., Podio, L., et al. 2024, The Astrophysical Journal, 961, 90, doi: 10.3847/1538-4357/ad0f17

Cai, M. J., Shang, H., Lin, H.-H., & Shu, F. H. 2008, The Astrophysical Journal, 672, 489, doi: 10.1086/523788

Caratti o Garatti, A., Ray, T. P., Kavanagh, P. J., et al. 2024a, Astronomy and Astrophysics, 691, A134, doi: 10.1051/0004-6361/202451350

—. 2024b, Astronomy and Astrophysics, 691, A134, doi: 10.1051/0004-6361/202451350

Casse, F., & Keppens, R. 2002, The Astrophysical Journal, 581, 988, doi: 10.1086/344340

Chandler, C. J., Barsony, M., & Moore, T. J. T. 1998, Monthly Notices of the Royal Astronomical Society, 299, 789, doi: 10.1046/j.1365-8711.1998.01818.x

Chang, P., Davis, S. W., & Jiang, Y.-F. 2020, Monthly Notices of the Royal Astronomical Society, 493, 5397, doi: 10.1093/mnras/staa573

Chauhan, M., Samal, M., Tej, A., & Froebrich, D. 2024, Monthly Notices of the Royal Astronomical Society, 530, 515, doi: 10.1093/mnras/stae846

Chen, H. H.-H., Pineda, J. E., Goodman, A. A., et al. 2019, The Astrophysical Journal, 877, 93, doi: 10.3847/1538-4357/ab1a40

Chiang, H.-F., Looney, L. W., & Tobin, J. J. 2012, The Astrophysical Journal, 756, 168, doi: 10.1088/0004-637X/756/2/168

Chrysostomou, A., Bacciotti, F., Nisini, B., et al. 2008, Astronomy and Astrophysics, 482, 575, doi: 10.1051/0004-6361:20078494

Ciesla, F. J. 2009, Meteoritics & Planetary Science, doi: 10.1111/j.1945-5100.2009.tb01197.x

Cleeves, L. I., Adams, F. C., & Bergin, E. A. 2013, The Astrophysical Journal, 772, 5, doi: 10.1088/0004-637X/772/1/5

Codella, C., Cabrit, S., Gueth, F., et al. 2014, Astronomy and Astrophysics, 568, L5, doi: 10.1051/0004-6361/201424103

Codella, C., Podio, L., De Simone, M., et al. 2024, Monthly Notices of the Royal Astronomical Society, 528, 7383, doi: 10.1093/mnras/stae472

Contopoulos, J. 1995, The Astrophysical Journal, 450, 616, doi: 10.1086/176170

Courant, R., Friedrichs, K., & Lewy, H. 1928, Mathematische Annalen, 100, 32, doi: 10.1007/BF01448839

Cridland, A. J., Rosotti, G. P., Tabone, B., et al. 2022, Astronomy and Astrophysics, 662, A90, doi: 10.1051/0004-6361/202142207

Crutcher, R. M., & Kemball, A. J. 2019, Frontiers in Astronomy and Space Sciences, 6, 66, doi: 10.3389/fspas.2019.00066

Cuzzi, J. N., Davis, S. S., & Dobrovolskis, A. R. 2003, Icarus, 166, 385, doi: https://doi.org/10.1016/j.icarus.2003.08.016

de Valon, A., Dougados, C., Cabrit, S., et al. 2020, Astronomy and Astrophysics, 634, L12, doi: 10.1051/0004-6361/201936950

—. 2022, Astronomy and Astrophysics, 668, A78, doi: 10.1051/0004-6361/202141316

Delabrosse, V., Dougados, C., Cabrit, S., et al. 2024, Astronomy and Astrophysics, 688, A173, doi: 10.1051/0004-6361/202449176

Desch, S. J., Morris, M. A., Connolly, H. C., J., & Boss, A. P. 2010, The Astrophysical Journal, 725, 692, doi: 10.1088/0004-637X/725/1/692

Dipierro, G., Ricci, L., Pérez, L., et al. 2018, Monthly Notices of the Royal Astronomical Society, 475, 5296, doi: 10.1093/mnras/sty181

Dominik, C., & Tielens, A. G. G. M. 1997, The Astrophysical Journal, 480, 647, doi: 10.1086/303996

Dong, R., Li, S., Chiang, E., & Li, H. 2017, The Astrophysical Journal, 843, 127, doi: 10.3847/1538-4357/aa72f2

Draine, B. T. 2006, The Astrophysical Journal, 636, 1114, doi: 10.1086/498130

Draine, B. T., Roberge, W. G., & Dalgarno, A. 1983, The Astrophysical Journal, 264, 485, doi: 10.1086/160617

Elmegreen, B. G., & Scalo, J. 2004, Annual Review of Astronomy and Astrophysics, 42, 211, doi: 10.1146/annurev.astro.41.011802.094859

Epstein, P. S. 1924, Phys. Rev., 23, 710, doi: 10.1103/PhysRev.23.710

Evans, C. R., & Hawley, J. F. 1988, The Astrophysical Journal, 332, 659, doi: 10.1086/166684

Evans, Neal J., I., Dunham, M. M., Jørgensen, J. K., et al. 2009, The Astrophysical Journal Supplement Series, 181, 321, doi: 10.1088/0067-0049/181/2/321

Facchini, S., Testi, L., Humphreys, E., et al. 2024, Nature Astronomy, 8, 587, doi: 10.1038/s41550-024-02207-w

Fedele, D., Tazzari, M., Booth, R., et al. 2018, A&A, 610, A24, doi: 10.1051/0004-6361/201731978

Federrath, C. 2016, Monthly Notices of the Royal Astronomical Society, 457, 375, doi: 10.1093/mnras/stv2880

Fedriani, R., Caratti o Garatti, A., Coffey, D., et al. 2018, Astronomy and Astrophysics, 616, A126, doi: 10.1051/0004-6361/201732180

Fendt, C., & Elstner, D. 2000, Astronomy and Astrophysics, 363, 208, doi: 10.48550/arXiv.astro-ph/0010607

Fendt, C., & Sheikhnezami, S. 2013, The Astrophysical Journal, 774, 12, doi: 10.1088/0004-637X/774/1/12

Fendt, C., Vaidya, B., Porth, O., & Nezami, S. S. 2011, in IAU Symposium, Vol. 275, Jets at All Scales, ed. G. E. Romero, R. A. Sunyaev, & T. Belloni, 383–391, doi: 10.1017/S1743921310016443

Ferreira, J. 1997, Astronomy and Astrophysics, 319, 340, doi: 10.48550/arXiv.astro-ph/9607057

Ferreira, J., Dougados, C., & Cabrit, S. 2006, Astronomy and Astrophysics, 453, 785, doi: 10.1051/0004-6361:20054231

Ferreira, J., & Pelletier, G. 1993, Astronomy and Astrophysics, 276, 625

Ferreira, J., Pelletier, G., & Appl, S. 2000, Monthly Notices of the Royal Astronomical Society, 312, 387, doi: 10.1046/j.1365-8711.2000.03215.x

Fiorellino, E., Tychoniec, L., Cruz-Saenz de Miera, F., et al. 2023, The Astrophysical Journal, 944, 135, doi: 10.3847/1538-4357/aca320

Flock, M., Fromang, S., Turner, N. J., & Benisty, M. 2016, The Astrophysical Journal, 827, 144, doi: 10.3847/0004-637X/827/2/144

Frank, A., Ray, T. P., Cabrit, S., et al. 2014, in Protostars and Planets VI, ed. H. Beuther, R. S. Klessen, C. P. Dullemond, & T. Henning, 451–474, doi: 10.2458/azu_uapress_9780816531240-ch020

Fryxell, B., Olson, K., Ricker, P., et al. 2000, The Astrophysical Journal Supplement Series, 131, 273, doi: 10.1086/317361

Gabriel, T. S. J., & Cambioni, S. 2023, Annual Review of Earth and Planetary Sciences, 51, 671, doi: 10.1146/annurev-earth-031621-055545

Galametz, M., Maury, A. J., Valdivia, V., et al. 2019, Astronomy and Astrophysics, 632, A5, doi: 10.1051/0004-6361/201936342

Galametz, M., Maury, A., Girart, J. M., et al. 2020, Astronomy and Astrophysics, 644, A47, doi: 10.1051/0004-6361/202038854

Galli, D., & Shu, F. H. 1993a, The Astrophysical Journal, 417, 243, doi: 10.1086/173306

—. 1993b, The Astrophysical Journal, 417, 220, doi: 10.1086/173305

Gammie, C. F. 1996, The Astrophysical Journal, 457, 355, doi: 10.1086/176735

Gong, H., & Ostriker, E. C. 2011, The Astrophysical Journal, 729, 120, doi: 10.1088/0004-637X/729/2/120

Goodson, A. P., & Winglee, R. M. 1999, The Astrophysical Journal, 524, 159, doi: 10.1086/307780

Gray, W. J., McKee, C. F., & Klein, R. I. 2018, Monthly Notices of the Royal Astronomical Society, 473, 2124, doi: 10.1093/mnras/stx2406

Gressel, O., Ramsey, J. P., Brinch, C., et al. 2020, The Astrophysical Journal, 896, 126, doi: 10.3847/1538-4357/ab91b7

Großschedl, J. E., Alves, J., Meingast, S., et al. 2018, Astronomy and Astrophysics, 619, A106, doi: 10.1051/0004-6361/201833901

Guan, X., Li, H., & Li, S. 2014, The Astrophysical Journal, 781, 48, doi: 10.1088/0004-637X/781/1/48

Guillet, V., Hennebelle, P., Pineau des Forêts, G., et al. 2020, Astronomy and Astrophysics, 643, A17, doi: 10.1051/0004-6361/201937387

Guszejnov, D., Grudić, M. Y., Hopkins, P. F., Offner, S. S. R., & Faucher-Giguère, C.-A. 2021, Monthly Notices of the Royal Astronomical Society, 502, 3646, doi: 10.1093/mnras/stab278

Haffert, S. Y., Bohn, A. J., de Boer, J., et al. 2019, Nature Astronomy, 3, 749, doi: 10.1038/s41550-019-0780-5

Han, I., Kwon, W., Aso, Y., Bae, J., & Sheehan, P. 2023, The Astrophysical Journal, 956, 9, doi: 10.3847/1538-4357/acf853

Harada, N., Hirano, S., Machida, M. N., & Hosokawa, T. 2021, Monthly Notices of the Royal Astronomical Society, 508, 3730, doi: 10.1093/mnras/stab2780

Harris, R. J., Cox, E. G., Looney, L. W., et al. 2018, The Astrophysical Journal, 861, 91, doi: 10.3847/1538-4357/aac6ec

Harrison, R. E., Looney, L. W., Stephens, I. W., et al. 2021, The Astrophysical Journal, 908, 141, doi: 10.3847/1538-4357/abd94e

Hartmann, L. 1998, Accretion Processes in Star Formation (Cambridge University Press)

Hasegawa, Y., Suzuki, T. K., Tanaka, H., Kobayashi, H., & Wada, K. 2021, The Astrophysical Journal, 915, 22, doi: 10.3847/1538-4357/abf6cf

Hawley, J. F., & Balbus, S. A. 1991, The Astrophysical Journal, 376, 223, doi: 10.1086/170271

Hawley, J. F., Fendt, C., Hardcastle, M., Nokhrina, E., & Tchekhovskoy, A. 2015, Space Science Reviews, 191, 441, doi: 10.1007/s11214-015-0174-7

Hennebelle, P., Commerçon, B., Lee, Y.-N., & Charnoz, S. 2020, Astronomy and Astrophysics, 635, A67, doi: 10.1051/0004-6361/201936714

Hennebelle, P., Commerçon, B., Chabrier, G., & Marchand, P. 2016a, The Astrophysical Journal Letters, 830, L8, doi: 10.3847/2041-8205/830/1/L8

—. 2016b, The Astrophysical Journal Letters, 830, L8, doi: 10.3847/2041-8205/830/1/L8

Hennebelle, P., & Fromang, S. 2008, Astronomy and Astrophysics, 477, 9, doi: 10.1051/0004-6361:20078309

Herbst, W., Eislöffel, J., Mundt, R., & Scholz, A. 2007, in Protostars and Planets V, ed. B. Reipurth, D. Jewitt, & K. Keil, 297, doi: 10.48550/arXiv.astro-ph/0603673

Hirashita, H., & Li, Z. Y. 2013, Monthly Notices of the Royal Astronomical Society, 434, L70, doi: 10.1093/mnrasl/slt081

Hockney, R. W., & Eastwood, J. W. 1981, Computer Simulation Using Particles (McGraw-Hill International Book Company)

Hosokawa, T., & Omukai, K. 2009, The Astrophysical Journal, 691, 823, doi: 10.1088/0004-637X/691/1/823

Hsieh, C.-H., Lai, S.-P., Cheong, P.-I., et al. 2020, The Astrophysical Journal, 894, 23, doi: 10.3847/1538-4357/ab7b69

Hsieh, C.-H., Arce, H. G., Li, Z.-Y., et al. 2023, The Astrophysical Journal, 947, 25, doi: 10.3847/1538-4357/acba13

Hsu, S.-Y., Lee, C.-F., Liu, S.-Y., et al. 2024, The Astrophysical Journal, 976, 29, doi: 10.3847/1538-4357/ad7e25

Huarte-Espinosa, M., Frank, A., Blackman, E. G., et al. 2012, The Astrophysical Journal, 757, 66, doi: 10.1088/0004-637X/757/1/66

Igumenshchev, I. V. 2008, The Astrophysical Journal, 677, 317, doi: 10.1086/529025

Ireland, L. G., Zanni, C., Matt, S. P., & Pantolmos, G. 2021, The Astrophysical Journal, 906, 4, doi: 10.3847/1538-4357/abc828

Isella, A., Guidi, G., Testi, L., et al. 2016, Phys. Rev. Lett., 117, 251101, doi: 10.1103/PhysRevLett.117.251101

Jacquemin-Ide, J., Ferreira, J., & Lesur, G. 2019, Monthly Notices of the Royal Astronomical Society, 490, 3112, doi: 10.1093/mnras/stz2749

Jacquemin-Ide, J., Lesur, G., & Ferreira, J. 2021, Astronomy and Astrophysics, 647, A192, doi: 10.1051/0004-6361/202039322

Jannaud, T., Zanni, C., & Ferreira, J. 2023, Astronomy and Astrophysics, 669, A159, doi: 10.1051/0004-6361/202244311

Jensen, E. L. N., & Akeson, R. 2014, Nature, 511, 567, doi: 10.1038/nature13521

Johnson, K. L., Kendall, K., & Roberts, A. D. 1971, Proceedings of the Royal Society of London. Series A, Mathematical and Physical Sciences, 324, 301. http://www.jstor.org/stable/78058

Jørgensen, J. K., Bourke, T. L., Myers, P. C., et al. 2007, The Astrophysical Journal, 659, 479, doi: 10.1086/512230

Kato, S. X., Kudoh, T., & Shibata, K. 2002, The Astrophysical Journal, 565, 1035, doi: 10.1086/324776

Kato, Y., Mineshige, S., & Shibata, K. 2004, The Astrophysical Journal, 605, 307, doi: 10.1086/381234

Kim, W.-T., & Ostriker, E. C. 2001, The Astrophysical Journal, 559, 70, doi: 10.1086/322330

Klaassen, P. D., Juhasz, A., Mathews, G. S., et al. 2013, Astronomy and Astrophysics, 555, A73, doi: 10.1051/0004-6361/201321129

Kobayashi, H., & Tanaka, H. 2010, Icarus, 206, 735, doi: 10.1016/j.icarus.2009.10.004

—. 2021, The Astrophysical Journal, 922, 16, doi: 10.3847/1538-4357/ac289c

Kobayashi, H., Tanaka, H., & Okuzumi, S. 2016, The Astrophysical Journal, 817, 105, doi: 10.3847/0004-637X/817/2/105

Kolmogorov, A. 1941, Akademiia Nauk SSSR Doklady, 30, 301

Konigl, A., & Pudritz, R. E. 2000, in Protostars and Planets IV, ed. V. Mannings, A. P. Boss, & S. S. Russell, 759, doi: 10.48550/arXiv.astro-ph/9903168

Könyves, V., André, P., Men'shchikov, A., et al. 2015, Astronomy and Astrophysics, 584, A91, doi: 10.1051/0004-6361/201525861

Krasnopolsky, R., Li, Z.-Y., & Blandford, R. 1999, The Astrophysical Journal, 526, 631, doi: 10.1086/308023

Krasnopolsky, R., Li, Z.-Y., & Blandford, R. D. 2003, The Astrophysical Journal, 595, 631, doi: 10.1086/377494

Kratter, K. M., Matzner, C. D., Krumholz, M. R., & Klein, R. I. 2010, The Astrophysical Journal, 708, 1585, doi: 10.1088/0004-637X/708/2/1585

Kristensen, L. E., & Dunham, M. M. 2018, Astronomy and Astrophysics, 618, A158, doi: 10.1051/0004-6361/201731584

Kudoh, T., Matsumoto, R., & Shibata, K. 1998, The Astrophysical Journal, 508, 186, doi: 10.1086/306377

Kuffmeier, M., Calcutt, H., & Kristensen, L. E. 2019, Astronomy and Astrophysics, 628, A112, doi: 10.1051/0004-6361/201935504

Kuffmeier, M., Haugbølle, T., & Nordlund, Å. 2017, The Astrophysical Journal, 846, 7, doi: 10.3847/1538-4357/aa7c64

Kuffmeier, M., Haugbølle, T., & Åke Nordlund. 2017, The Astrophysical Journal, 846, 7, doi: 10.3847/1538-4357/aa7c64

Kuffmeier, M., Zhao, B., & Caselli, P. 2020, Astronomy and Astrophysics, 639, A86, doi: 10.1051/0004-6361/201937328

Kuiper, R., Klahr, H., Beuther, H., & Henning, T. 2010, The Astrophysical Journal, 722, 1556, doi: 10.1088/0004-637X/722/2/1556

Kuwabara, T., Shibata, K., Kudoh, T., & Matsumoto, R. 2000, Publications of the Astronomical Society of Japan, 52, 1109, doi: 10.1093/pasj/52.6.1109

Kuznetsova, A., Bae, J., Hartmann, L., & Mac Low, M.-M. 2022, The Astrophysical Journal, 928, 92, doi: 10.3847/1538-4357/ac54a8

Kwon, W., Looney, L. W., Mundy, L. G., Chiang, H.-F., & Kemball, A. J. 2009, The Astrophysical Journal, 696, 841, doi: 10.1088/0004-637X/696/1/841

Kwon, W., Looney, L. W., Mundy, L. G., & Welch, W. J. 2015, The Astrophysical Journal, 808, 102, doi: 10.1088/0004-637x/808/1/102

Lada, C. J. 1987, in IAU Symposium, Vol. 115, Star Forming Regions, ed. M. Peimbert & J. Jugaku, 1

Lai, D. 2014, in European Physical Journal Web of Conferences, Vol. 64, European Physical Journal Web of Conferences, 01001, doi: 10.1051/epjconf/20136401001

Lam, K. H., Li, Z.-Y., Chen, C.-Y., Tomida, K., & Zhao, B. 2019, Monthly Notices of the Royal Astronomical Society, 489, 5326, doi: 10.1093/mnras/stz2436

Lankhaar, B., Vlemmings, W., & Bjerkeli, P. 2022, Astronomy and Astrophysics, 657, A106, doi: 10.1051/0004-6361/202141285

Laor, A., & Draine, B. T. 1993, The Astrophysical Journal, 402, 441, doi: 10.1086/172149

Launhardt, R., Pavlyuchenkov, Y. N., Akimkin, V. V., et al. 2023, Astronomy and Astrophysics, 678, A135, doi: 10.1051/0004-6361/202347483

Le Gouellec, V. J. M., Maury, A. J., & Hull, C. L. H. 2023, Astronomy and Astrophysics, 671, A167, doi: 10.1051/0004-6361/202244865

Lebreuilly, U., Hennebelle, P., Colman, T., et al. 2021, The Astrophysical Journal Letters, 917, L10, doi: 10.3847/2041-8213/ac158c

Lee, C.-F., Hwang, H.-C., Ching, T.-C., et al. 2018, Nature Communications, 9, 4636, doi: 10.1038/s41467-018-07143-8

Lee, C.-F., Li, Z.-Y., & Turner, N. J. 2020, Nature Astronomy, 4, 142, doi: 10.1038/s41550-019-0905-x

Lee, Y.-N., Charnoz, S., & Hennebelle, P. 2021, Astronomy and Astrophysics, 648, A101, doi: 10.1051/0004-6361/202038105

Lesur, G. 2021, Journal of Plasma Physics, 87, 205870101, doi: 10.1017/S0022377820001002

Lesur, G., Flock, M., Ercolano, B., et al. 2023, in Astronomical Society of the Pacific Conference Series, Vol. 534, Astronomical Society of the Pacific Conference Series, ed. S. Inutsuka, Y. Aikawa, T. Muto, K. Tomida, & M. Tamura, 465

Li, Z.-Y. 1995, The Astrophysical Journal, 444, 848, doi: 10.1086/175657

—. 1996, The Astrophysical Journal, 473, 873, doi: 10.1086/178199

Li, Z. Y., Banerjee, R., Pudritz, R. E., et al. 2014a, in Protostars and Planets VI, ed. H. Beuther, R. S. Klessen, C. P. Dullemond, & T. Henning, 173, doi: 10.2458/azu_uapress_9780816531240-ch008

Li, Z. Y., Banerjee, R., Pudritz, R. E., et al. 2014b, in Protostars and Planets VI, ed. H. Beuther, R. S. Klessen, C. P. Dullemond, & T. Henning, 173–194, doi: 10.2458/azu_uapress_9780816531240-ch008

Li, Z.-Y., Krasnopolsky, R., Shang, H., & Zhao, B. 2014c, The Astrophysical Journal, 793, 130, doi: 10.1088/0004-637X/793/2/130

Lii, P. S., Romanova, M. M., Ustyugova, G. V., Koldoba, A. V., & Lovelace, R. V. E. 2014, Monthly Notices of the Royal Astronomical Society, 441, 86, doi: 10.1093/mnras/stu495

Lin, Z.-Y. D., Li, Z.-Y., Yang, H., et al. 2024, Monthly Notices of the Royal Astronomical Society, 534, 3713, doi: 10.1093/mnras/stae2248

Lin, Z.-Y. D., Li, Z.-Y., Tobin, J. J., et al. 2023, The Astrophysical Journal, 951, 9, doi: 10.3847/1538-4357/acd5c9

Liu, J., Zhang, Q., & Qiu, K. 2022, Frontiers in Astronomy and Space Sciences, 9, 943556, doi: 10.3389/fspas.2022.943556

Lodders, K. 2003, The Astrophysical Journal, 591, 1220, doi: 10.1086/375492

Lombart, M., & Laibe, G. 2021, Monthly Notices of the Royal Astronomical Society, 501, 4298, doi: 10.1093/mnras/staa3682

López-Vázquez, J. A., Lee, C.-F., Shang, H., et al. 2024a, The Astrophysical Journal, 977, 126, doi: 10.3847/1538-4357/ad8eb4

—. 2024b, The Astrophysical Journal, 977, 126, doi: 10.3847/1538-4357/ad8eb4

Lorek, S., & Johansen, A. 2022, Astronomy and Astrophysics, 666, A108, doi: 10.1051/0004-6361/202244333

Lovelace, R. V. E., Li, H., Ustyugova, G. V., Romanova, M. M., & Colgate, S. A. 2001, in American Institute of Physics Conference Series, Vol. 586, 20th Texas Symposium on relativistic astrophysics, ed. J. C. Wheeler & H. Martel (AIP), 426–432, doi: 10.1063/1.1419587

Lovelace, R. V. E., & Romanova, M. M. 2009, arXiv e-prints, arXiv:0901.4753, doi: 10.48550/arXiv.0901.4753

Lovelace, R. V. E., Romanova, M. M., & Lii, P. 2013, arXiv e-prints, arXiv:1306.1160, doi: 10.48550/arXiv.1306.1160

Lovelace, R. V. E., Romanova, M. M., Lii, P., & Dyda, S. 2014, Computational Astrophysics and Cosmology, 1, 3, doi: 10.1186/s40668-014-0003-5

Lovell, J. B., Wyatt, M. C., Ansdell, M., et al. 2021, Monthly Notices of the Royal Astronomical Society, 500, 4878, doi: 10.1093/mnras/staa3335

Lubow, S. H., Papaloizou, J. C. B., & Pringle, J. E. 1994, Monthly Notices of the Royal Astronomical Society, 267, 235, doi: 10.1093/mnras/267.2.235

Lucas, P. W., & Roche, P. F. 1998, Monthly Notices of the Royal Astronomical Society, 299, 723, doi: 10.1046/j.1365-8711.1998.01798.x

Lynden-Bell, D. 1996, Monthly Notices of the Royal Astronomical Society, 279, 389, doi: 10.1093/mnras/279.2.389

Lynden-Bell, D. 2003, Monthly Notices of the Royal Astronomical Society, 341, 1360, doi: 10.1046/j.1365-8711.2003.06506.x

Mac Low, M.-M., & Klessen, R. S. 2004, Reviews of Modern Physics, 76, 125, doi: 10.1103/RevModPhys.76.125

Machida, M. N., Tomisaka, K., Matsumoto, T., & Inutsuka, S.-i. 2008, The Astrophysical Journal, 677, 327, doi: 10.1086/529133

Macías, E., Anglada, G., Osorio, M., et al. 2016, The Astrophysical Journal, 829, 1, doi: 10.3847/0004-637X/829/1/1

Marchand, P., Masson, J., Chabrier, G., et al. 2016, Astronomy and Astrophysics, 592, A18, doi: 10.1051/0004-6361/201526780

Markiewicz, W. J., Mizuno, H., & Voelk, H. J. 1991a, Astronomy and Astrophysics, 242, 286

—. 1991b, Astronomy and Astrophysics, 242, 286

Martel, É., & Lesur, G. 2022, Astronomy and Astrophysics, 667, A17, doi: 10.1051/0004-6361/202142946

Masson, J., Chabrier, G., Hennebelle, P., Vaytet, N., & Commerçon, B. 2016, Astronomy and Astrophysics, 587, A32, doi: 10.1051/0004-6361/201526371

Mathis, J. S., Rumpl, W., & Nordsieck, K. H. 1977a, The Astrophysical Journal, 217, 425, doi: 10.1086/155591

—. 1977b, The Astrophysical Journal, 217, 425, doi: 10.1086/155591

Matsumoto, R., Uchida, Y., Hirose, S., et al. 1996, The Astrophysical Journal, 461, 115, doi: 10.1086/177041

Matsumoto, T., Machida, M. N., & Inutsuka, S.-i. 2017, The Astrophysical Journal, 839, 69, doi: 10.3847/1538-4357/aa6a1c

Matt, S., Goodson, A. P., Winglee, R. M., & Böhm, K.-H. 2002, The Astrophysical Journal, 574, 232, doi: 10.1086/340896

Mattia, G., & Fendt, C. 2020a, The Astrophysical Journal, 900, 59, doi: 10.3847/1538-4357/aba9d7

—. 2020b, The Astrophysical Journal, 900, 60, doi: 10.3847/1538-4357/aba9d6

Mauxion, J., Lesur, G., & Maret, S. 2024, Astronomy and Astrophysics, 686, A253, doi: 10.1051/0004-6361/202348405

Mayor, M., & Queloz, D. 1995, Nature, 378, 355, doi: 10.1038/378355a0

Mazzei, R., Cleeves, L. I., & Li, Z.-Y. 2020, The Astrophysical Journal, 903, 20, doi: 10.3847/1538-4357/abb67a

McGroarty, F., & Ray, T. P. 2004, Astronomy and Astrophysics, 420, 975, doi: 10.1051/0004-6361:20041124

McKinney, J. C., & Blandford, R. D. 2009, Monthly Notices of the Royal Astronomical Society: Letters, 394, L126, doi: 10.1111/j.1745-3933.2009.00625.x

McKinney, J. C., & Narayan, R. 2007, Monthly Notices of the Royal Astronomical Society, 375, 513, doi: 10.1111/j.1365-2966.2006.11301.x

Meech, K., & Raymond, S. N. 2020, in Planetary Astrobiology, ed. V. S. Meadows, G. N. Arney, B. E. Schmidt, & D. J. Des Marais (University of Arizona Press), 325, doi: 10.2458/azu_uapress_9780816540068

Mellon, R. R., & Li, Z.-Y. 2008, The Astrophysical Journal, 681, 1356, doi: 10.1086/587542

Men'shchikov, A., André, P., Didelon, P., et al. 2010, Astronomy and Astrophysics, 518, L103, doi: 10.1051/0004-6361/201014668

Meskini, C., Sauty, C., Marcowith, A., Vlahakis, N., & Brunn, V. 2024, Astronomy and Astrophysics, 686, A287, doi: 10.1051/0004-6361/202449219

Mestel, L., & Spitzer, L., J. 1956, Monthly Notices of the Royal Astronomical Society, 116, 503, doi: 10.1093/mnras/116.5.503

Mignon-Risse, R., González, M., & Commerçon, B. 2023, Astronomy and Astrophysics, 673, A134, doi: 10.1051/0004-6361/202345845

Mignon-Risse, R., González, M., Commerçon, B., & Rosdahl, J. 2021, Astronomy and Astrophysics, 652, A69, doi: 10.1051/0004-6361/202140617

Miller, K. A., & Stone, J. M. 1997, The Astrophysical Journal, 489, 890, doi: 10.1086/304825

Mishra, B., Begelman, M. C., Armitage, P. J., & Simon, J. B. 2020, Monthly Notices of the Royal Astronomical Society, 492, 1855, doi: 10.1093/mnras/stz3572

Moll, R., Spruit, H. C., & Obergaulinger, M. 2008, Astronomy and Astrophysics, 492, 621, doi: 10.1051/0004-6361:200810523

Morbidelli, A., Marrocchi, Y., Ali Ahmad, A., et al. 2024, Astronomy and Astrophysics, 691, A147, doi: 10.1051/0004-6361/202451388

Morfill, G., Roeser, S., Voelk, H., & Tscharnuter, W. 1978, Moon and Planets, 19, 211, doi: 10.1007/BF00896994

Murillo, N. M., van Dishoeck, E. F., Hacar, A., Harsono, D., & Jørgensen, J. K. 2022, Astronomy and Astrophysics, 658, A53, doi: 10.1051/0004-6361/202141250

Murphy, G. C., Ferreira, J., & Zanni, C. 2010, Astronomy and Astrophysics, 512, A82, doi: 10.1051/0004-6361/200912633

Nakagawa, Y., Nakazawa, K., & Hayashi, C. 1981, Icarus, 45, 517, doi: 10.1016/0019-1035(81)90018-X

Nakagawa, Y., Sekiya, M., & Hayashi, C. 1986, Icarus, 67, 375, doi: 10.1016/0019-1035(86)90121-1

Nakamura, M., Li, H., & Li, S. 2007, The Astrophysical Journal, 656, 721, doi: 10.1086/510361

NASA. 2023, HH 211 (NIRCam Image). https://webbtelescope.org/contents/media/images/2023/141/01H9NWH9JEBFPKVD3M1RRTGGQJ

Noble, S. C., Krolik, J. H., & Hawley, J. F. 2010, The Astrophysical Journal, 711, 959, doi: 10.1088/0004-637X/711/2/959

Offner, S. S. R., Clark, P. C., Hennebelle, P., et al. 2014, in Protostars and Planets VI, ed. H. Beuther, R. S. Klessen, C. P. Dullemond, & T. Henning, 53–75, doi: 10.2458/azu_uapress_9780816531240-ch003

Offner, S. S. R., Dunham, M. M., Lee, K. I., Arce, H. G., & Fielding, D. B. 2016, The Astrophysical Journal Letters, 827, L11, doi: 10.3847/2041-8205/827/1/L11

Offner, S. S. R., Gaches, B. A. L., & Holdship, J. R. 2019, The Astrophysical Journal, 883, 121, doi: 10.3847/1538-4357/ab3e02

Offner, S. S. R., Kratter, K. M., Matzner, C. D., Krumholz, M. R., & Klein, R. I. 2010, The Astrophysical Journal, 725, 1485, doi: 10.1088/0004-637X/725/2/1485

Offner, S. S. R., Moe, M., Kratter, K. M., et al. 2023, in Astronomical Society of the Pacific Conference Series, Vol. 534, Protostars and Planets VII, ed. S. Inutsuka, Y. Aikawa, T. Muto, K. Tomida, & M. Tamura, 275, doi: 10.48550/arXiv.2203.10066

Ohashi, N., Saigo, K., Aso, Y., et al. 2014, The Astrophysical Journal, 796, 131, doi: 10.1088/0004-637X/796/2/131

Ohashi, N., Tobin, J. J., Jørgensen, J. K., et al. 2023, The Astrophysical Journal, 951, 8, doi: 10.3847/1538-4357/acd384

Ohashi, S., Muto, T., Tsukamoto, Y., et al. 2025, Nature Astronomy, doi: 10.1038/s41550-024-02454-x

Ohashi, S., Nakatani, R., Liu, H. B., et al. 2022, The Astrophysical Journal, 934, 163, doi: 10.3847/1538-4357/ac794e

Ohashi, S., Kobayashi, H., Nakatani, R., et al. 2021, The Astrophysical Journal, 907, 80, doi: 10.3847/1538-4357/abd0fa

Ohashi, S., Codella, C., Sakai, N., et al. 2022, The Astrophysical Journal, 927, 54, doi: 10.3847/1538-4357/ac4cae

Oishi, J. S., Vasil, G. M., Baxter, M., et al. 2020, Proceedings of the Royal Society of London Series A, 476, 20190622, doi: 10.1098/rspa.2019.0622

Orkisz, J. H., Pety, J., Gerin, M., et al. 2017, Astronomy and Astrophysics, 599, A99, doi: 10.1051/0004-6361/201629220

Ormel, C. W., & Cuzzi, J. N. 2007, Astronomy and Astrophysics, 466, 413, doi: 10.1051/0004-6361:20066899

Ormel, C. W., Paszun, D., Dominik, C., & Tielens, A. G. G. M. 2009, Astronomy and Astrophysics, 502, 845, doi: 10.1051/0004-6361/200811158

Ostriker, E. C., & Shu, F. H. 1995, The Astrophysical Journal, 447, 813, doi: 10.1086/175920

Padovani, M., Ivlev, A. V., Galli, D., & Caselli, P. 2018, Astronomy and Astrophysics, 614, A111, doi: 10.1051/0004-6361/201732202

Pan, L., & Padoan, P. 2013, The Astrophysical Journal, 776, 12, doi: 10.1088/0004-637X/776/1/12

—. 2015, The Astrophysical Journal, 812, 10, doi: 10.1088/0004-637X/812/1/10

Pantolmos, G., Zanni, C., & Bouvier, J. 2020, Astronomy and Astrophysics, 643, A129, doi: 10.1051/0004-6361/202038569

Parfrey, K., & Tchekhovskoy, A. 2023, arXiv e-prints, arXiv:2311.04291, doi: 10.48550/arXiv.2311.04291

Pascucci, I., Cabrit, S., Edwards, S., et al. 2023, in Astronomical Society of the Pacific Conference Series, Vol. 534, Protostars and Planets VII, ed. S. Inutsuka, Y. Aikawa, T. Muto, K. Tomida, & M. Tamura, 567, doi: 10.48550/arXiv.2203.10068

Pattle, K., Fissel, L., Tahani, M., Liu, T., & Ntormousi, E. 2023a, in Astronomical Society of the Pacific Conference Series, Vol. 534, Astronomical Society of the Pacific Conference Series, ed. S. Inutsuka, Y. Aikawa, T. Muto, K. Tomida, & M. Tamura, 193

Pattle, K., Fissel, L., Tahani, M., Liu, T., & Ntormousi, E. 2023b, in Astronomical Society of the Pacific Conference Series, Vol. 534, Protostars and Planets VII, ed. S. Inutsuka, Y. Aikawa, T. Muto, K. Tomida, & M. Tamura, 193, doi: 10.48550/arXiv.2203.11179

Persson, M. V. 2014, Current view of protostellar evolution (ENG), Figshare, doi: https://doi.org/10.6084/m9.figshare.654555.v7

Pineda, J. E., Segura-Cox, D., Caselli, P., et al. 2020, Nature Astronomy, 4, 1158, doi: 10.1038/s41550-020-1150-z

Podio, L., Codella, C., Gueth, F., et al. 2015, Astronomy and Astrophysics, 581, A85, doi: 10.1051/0004-6361/201525778

Porth, O., Mizuno, Y., Younsi, Z., & Fromm, C. M. 2021, Monthly Notices of the Royal Astronomical Society, 502, 2023, doi: 10.1093/mnras/stab163

Potapov, A., Jäger, C., & Henning, T. 2020, Phys. Rev. Lett., 124, 221103, doi: 10.1103/PhysRevLett.124.221103

Price, D. J., & Bate, M. R. 2008, Monthly Notices of the Royal Astronomical Society, 385, 1820, doi: 10.1111/j.1365-2966.2008.12976.x

Price, D. J., Wurster, J., Tricco, T. S., et al. 2018, Publications of the Astronomical Society of Australia, 35, e031, doi: 10.1017/pasa.2018.25

Pudritz, R. E., & Norman, C. A. 1983, The Astrophysical Journal, 274, 677, doi: 10.1086/161481

Pudritz, R. E., Ouyed, R., Fendt, C., & Brandenburg, A. 2007, in Protostars and Planets V, ed. B. Reipurth, D. Jewitt, & K. Keil, 277, doi: 10.48550/arXiv.astro-ph/0603592

Ramsey, J. P., & Clarke, D. A. 2019, Monthly Notices of the Royal Astronomical Society, 484, 2364, doi: 10.1093/mnras/stz116

Ray, T., & Ferreira, J. 2021, New Astronomy Reviews, 93, 101615, doi: https://doi.org/10.1016/j.newar.2021.101615

Rein, H., & Liu, S. F. 2012, Astronomy and Astrophysics, 537, A128, doi: 10.1051/0004-6361/201118085

Reynolds, N. K., Tobin, J. J., Sheehan, P., et al. 2021, The Astrophysical Journal Letters, 907, L10, doi: 10.3847/2041-8213/abcc02

Rodenkirch, P. J., Klahr, H., Fendt, C., & Dullemond, C. P. 2020, Astronomy and Astrophysics, 633, A21, doi: 10.1051/0004-6361/201834945

Romanova, M. M., Espaillat, C. C., Wendeborn, J., et al. 2025, Monthly Notices of the Royal Astronomical Society, 538, 480, doi: 10.1093/mnras/staf148

Romanova, M. M., Koldoba, A. V., Ustyugova, G. V., et al. 2021, Monthly Notices of the Royal Astronomical Society, 506, 372, doi: 10.1093/mnras/stab1724

Romanova, M. M., Kulkarni, A. K., & Lovelace, R. V. E. 2008, The Astrophysical Journal, 673, L171, doi: 10.1086/527298

Romanova, M. M., Ustyugova, G. V., Koldoba, A. V., & Lovelace, R. V. E. 2005, The Astrophysical Journal Letters, 635, L165, doi: 10.1086/499560

—. 2009, Monthly Notices of the Royal Astronomical Society, 399, 1802, doi: 10.1111/j.1365-2966.2009.15413.x

—. 2012, Monthly Notices of the Royal Astronomical Society, 421, 63, doi: 10.1111/j.1365-2966.2011.20055.x

Sadavoy, S. I., Sheehan, P., Tobin, J. J., et al. 2024, Astronomy and Astrophysics, 687, A308, doi: 10.1051/0004-6361/202348859

Salmeron, R., Königl, A., & Wardle, M. 2011, Monthly Notices of the Royal Astronomical Society, 412, 1162, doi: 10.1111/j.1365-2966.2010.17974.x

Sanhueza, P., Girart, J. M., Padovani, M., et al. 2021, The Astrophysical Journal Letters, 915, L10, doi: 10.3847/2041-8213/ac081c

Santos-Lima, R., de Gouveia Dal Pino, E. M., & Lazarian, A. 2012, The Astrophysical Journal, 747, 21, doi: 10.1088/0004-637X/747/1/21

Sauty, C., Cayatte, V., Lima, J. J. G., Matsakos, T., & Tsinganos, K. 2012, The Astrophysical Journal Letters, 759, L1, doi: 10.1088/2041-8205/759/1/L1

Segura-Cox, D. M., Schmiedeke, A., Pineda, J. E., et al. 2020, Nature, 586, 228, doi: 10.1038/s41586-020-2779-6

Seifried, D., Banerjee, R., Pudritz, R. E., & Klessen, R. S. 2013, Monthly Notices of the Royal Astronomical Society, 432, 3320, doi: 10.1093/mnras/stt682

—. 2014, Monthly Notices of the Royal Astronomical Society, 446, 2776, doi: 10.1093/mnras/stu2282

Seifried, D., Banerjee, R., Pudritz, R. E., & Klessen, R. S. 2015, Monthly Notices of the Royal Astronomical Society, 446, 2776, doi: 10.1093/mnras/stu2282

Shang, H., Glassgold, A. E., Shu, F. H., & Lizano, S. 2002, The Astrophysical Journal, 564, 853, doi: 10.1086/324197

Shang, H., Li, Z. Y., & Hirano, N. 2007, in Protostars and Planets V, ed. B. Reipurth, D. Jewitt, & K. Keil, 261

Sheehan, P. D., & Eisner, J. A. 2018, The Astrophysical Journal, 857, 18, doi: 10.3847/1538-4357/aaae65

Sheehan, P. D., Tobin, J. J., Federman, S., Megeath, S. T., & Looney, L. W. 2020, The Astrophysical Journal, 902, 141, doi: 10.3847/1538-4357/abbad5

Shibata, K., & Uchida, Y. 1986, Publications of the Astronomical Society of Japan, 38, 631

Shu, F. 1991, The Physics of Astrophysics: Gas dynamics, Series of books in astronomy (University Science Books). https://books.google.com/books?id=50VYSc56URUC

Shu, F., Najita, J., Ostriker, E., et al. 1994, The Astrophysical Journal, 429, 781, doi: 10.1086/174363

Shu, F. H. 1977, The Astrophysical Journal, 214, 488, doi: 10.1086/155274

Shu, F. H., Najita, J., Ostriker, E. C., & Shang, H. 1995, The Astrophysical Journal Letters, 455, L155, doi: 10.1086/309838

Shu, F. H., Najita, J. R., Shang, H., & Li, Z. Y. 2000, in Protostars and Planets IV, ed. V. Mannings, A. P. Boss, & S. S. Russell, 789–814

Shu, F. H., Shang, H., Gounelle, M., Glassgold, A. E., & Lee, T. 2001, The Astrophysical Journal, 548, 1029, doi: 10.1086/319018

Smoluchowski, M. V. 1916, Zeitschrift fur Physik, 17, 557

Sperling, G. 1964, PhD thesis, -

Spruit, H. 2006, in VI Microquasar Workshop: Microquasars and Beyond, 44.1, doi: 10.22323/1.033.0044

Spruit, H. C. 2010, in Lecture Notes in Physics, Berlin Springer Verlag, ed. T. Belloni, Vol. 794 (Springer-Verlag Berlin Heidelberg), 233, doi: 10.1007/978-3-540-76937-8_9

Spruit, H. C., Stehle, R., & Papaloizou, J. C. B. 1995, Monthly Notices of the Royal Astronomical Society, 275, 1223, doi: 10.1093/mnras/275.4.1223

Steinacker, J., Pagani, L., Bacmann, A., & Guieu, S. 2010, Astronomy and Astrophysics, 511, A9, doi: 10.1051/0004-6361/200912835

Stepanovs, D., & Fendt, C. 2016, The Astrophysical Journal, 825, 14, doi: 10.3847/0004-637X/825/1/14

Stephens, I. W., Looney, L. W., Kwon, W., et al. 2014, Nature, 514, 597, doi: 10.1038/nature13850

Stephens, I. W., Lin, Z.-Y. D., Fernández-López, M., et al. 2023, Nature, 623, 705, doi: 10.1038/s41586-023-06648-7

Stone, J. M., Gardiner, T. A., Teuben, P., Hawley, J. F., & Simon, J. B. 2008, The Astrophysical Journal Supplement Series, 178, 137, doi: 10.1086/588755

Stone, J. M., Tomida, K., White, C. J., & Felker, K. G. 2020, The Astrophysical Journal Supplement Series, 249, 4, doi: 10.3847/1538-4365/ab929b

Suriano, S. S., Li, Z.-Y., Krasnopolsky, R., & Shang, H. 2017, Monthly Notices of the Royal Astronomical Society, 468, 3850, doi: 10.1093/mnras/stx735

—. 2018, Monthly Notices of the Royal Astronomical Society, 477, 1239, doi: 10.1093/mnras/sty717

Suttner, G., & Yorke, H. W. 2001, The Astrophysical Journal, 551, 461, doi: 10.1086/320061

Tabone, B., Cabrit, S., Bianchi, E., et al. 2017, Astronomy and Astrophysics, 607, L6, doi: 10.1051/0004-6361/201731691

Tabone, B., Cabrit, S., Pineau des Forêts, G., et al. 2020, Astronomy and Astrophysics, 640, A82, doi: 10.1051/0004-6361/201834377

Takaishi, D., Tsukamoto, Y., Kido, M., et al. 2024, The Astrophysical Journal, 963, 20, doi: 10.3847/1538-4357/ad187a

Takasao, S., Hosokawa, T., Tomida, K., & Iwasaki, K. 2025, arXiv e-prints, arXiv:2503.15350. https://arxiv.org/abs/2503.15350

Takasao, S., Tomida, K., Iwasaki, K., & Suzuki, T. K. 2018, The Astrophysical Journal, 857, 4, doi: 10.3847/1538-4357/aab5b3

—. 2019, The Astrophysical Journal Letters, 878, L10, doi: 10.3847/2041-8213/ab22bb

—. 2022, The Astrophysical Journal, 941, 73, doi: 10.3847/1538-4357/ac9eb1

Tanaka, H., Himeno, Y., & Ida, S. 2005, The Astrophysical Journal, 625, 414, doi: 10.1086/429658

Testi, L., Birnstiel, T., Ricci, L., et al. 2014, in Protostars and Planets VI, ed. H. Beuther, R. S. Klessen, C. P. Dullemond, & T. Henning, 339, doi: 10.2458/azu_uapress_9780816531240-ch015

Teyssier, R. 2002, Astronomy and Astrophysics, 385, 337, doi: 10.1051/0004-6361:20011817

Thieme, T. J., Lai, S.-P., Lin, S.-J., et al. 2022, The Astrophysical Journal, 925, 32, doi: 10.3847/1538-4357/ac382b

Tobin, J. J., Chandler, C. J., Wilner, D. J., et al. 2013, The Astrophysical Journal, 779, 93, doi: 10.1088/0004-637x/779/2/93

Tobin, J. J., Dunham, M. M., Looney, L. W., et al. 2015, The Astrophysical Journal, 798, 61, doi: 10.1088/0004-637X/798/1/61

Tobin, J. J., Kratter, K. M., Persson, M. V., et al. 2016a, Nature, 538, 483, doi: 10.1038/nature20094

Tobin, J. J., Looney, L. W., Li, Z.-Y., et al. 2016b, The Astrophysical Journal, 818, 73, doi: 10.3847/0004-637X/818/1/73

Tohline, J. E. 2002, Annual Review of Astronomy and Astrophysics, 40, 349, doi: 10.1146/annurev.astro.40.060401.093810

Tomida, K., & Stone, J. M. 2023, The Astrophysical Journal Supplement Series, 266, 7, doi: 10.3847/1538-4365/acc2c0

Tomida, K., Tomisaka, K., Matsumoto, T., et al. 2013, The Astrophysical Journal, 763, 6, doi: 10.1088/0004-637X/763/1/6

Toomre, A. 1964, The Astrophysical Journal, 139, 1217, doi: 10.1086/147861

Toro, E. F. 2009, Riemann Solvers and Numerical Methods for Fluid Dynamics, 3rd edn. (Berlin Heidelberg: Springer-Verlag)

Tsukamoto, Y. 2016, Publications of the Astronomical Society of Australia, 33, e010, doi: 10.1017/pasa.2016.6

Tsukamoto, Y., Machida, M. N., & Inutsuka, S.-i. 2021, The Astrophysical Journal Letters, 920, L35, doi: 10.3847/2041-8213/ac2b2f

—. 2023a, arXiv e-prints, arXiv:2303.10419, doi: 10.48550/arXiv.2303.10419

Tsukamoto, Y., Maury, A., Commercon, B., et al. 2023b, in Astronomical Society of the Pacific Conference Series, Vol. 534, Astronomical Society of the Pacific Conference Series, ed. S. Inutsuka, Y. Aikawa, T. Muto, K. Tomida, & M. Tamura, 317

Tu, Y., Li, Z.-Y., & Lam, K. H. 2022, Monthly Notices of the Royal Astronomical Society, 515, 4780, doi: 10.1093/mnras/stac2030

Tu, Y., Li, Z.-Y., Lam, K. H., Tomida, K., & Hsu, C.-Y. 2024a, Monthly Notices of the Royal Astronomical Society, 527, 10131, doi: 10.1093/mnras/stad3843

Tu, Y., Li, Z.-Y., Zhu, Z., & Hsu, C.-Y. 2024b, Monthly Notices of the Royal Astronomical Society, 532, 3135, doi: 10.1093/mnras/stae1639

Tu, Y., Li, Z.-Y., Zhu, Z., Hsu, C.-Y., & Hu, X. 2025a, arXiv e-prints, arXiv:2502.20495, doi: 10.48550/arXiv.2502.20495

Tu, Y., Li, Z.-Y., Zhu, Z., Hu, X., & Hsu, C.-Y. 2025b, The Astrophysical Journal, 978, 84, doi: 10.3847/1538-4357/ad927b

—. 2025c, The Astrophysical Journal, 978, 84, doi: 10.3847/1538-4357/ad927b

Tzeferacos, P., Ferrari, A., Mignone, A., et al. 2009, Monthly Notices of the Royal Astronomical Society, 400, 820, doi: 10.1111/j.1365-2966.2009.15502.x

Umebayashi, T., & Nakano, T. 2009, The Astrophysical Journal, 690, 69, doi: 10.1088/0004-637X/690/1/69

Unity Technologies. 2024, Unity Engine, 2023.2.12. https://unity.com/

Ustyugova, G. V., Koldoba, A. V., Romanova, M. M., Chechetkin, V. M., & Lovelace, R. V. E. 1999, The Astrophysical Journal, 516, 221, doi: 10.1086/307093

Ustyugova, G. V., Lovelace, R. V. E., Romanova, M. M., Li, H., & Colgate, S. A. 2000, The Astrophysical Journal Letters, 541, L21, doi: 10.1086/312890

Uzdensky, D. A. 2002, The Astrophysical Journal, 572, 432, doi: 10.1086/340308

Valdivia-Mena, M. T., Pineda, J. E., Segura-Cox, D. M., et al. 2022, Astronomy and Astrophysics, 667, A12, doi: 10.1051/0004-6361/202243310

Čemeljić, M., Shang, H., & Chiang, T. Y. 2013, The Astrophysical Journal, 768, 5, doi: 10.1088/0004-637X/768/1/5

Visser, R. G., & Ormel, C. W. 2016, Astronomy and Astrophysics, 586, A66, doi: 10.1051/0004-6361/201527361

Vlemmings, W. H. T., Lankhaar, B., Cazzoletti, P., et al. 2019, Astronomy and Astrophysics, 624, L7, doi: 10.1051/0004-6361/201935459

Voelk, H. J., Jones, F. C., Morfill, G. E., & Roeser, S. 1980, Astronomy and Astrophysics, 85, 316

Wang, L., Bai, X.-N., & Goodman, J. 2019, The Astrophysical Journal, 874, 90, doi: 10.3847/1538-4357/ab06fd

Wardle, M., & Koenigl, A. 1993, The Astrophysical Journal, 410, 218, doi: 10.1086/172739

Watson, D. M., Calvet, N. P., Fischer, W. J., et al. 2016, The Astrophysical Journal, 828, 52, doi: 10.3847/0004-637X/828/1/52

Weber, E. J., & Davis, Leverett, J. 1967, The Astrophysical Journal, 148, 217, doi: 10.1086/149138

Weidling, R., Güttler, C., & Blum, J. 2012, Icarus, 218, 688, doi: 10.1016/j.icarus.2011.10.002

Weingartner, J. C., & Draine, B. T. 2001, The Astrophysical Journal, 548, 296, doi: 10.1086/318651

Whelan, E. T., Keppler, M., Turner, N. J., et al. 2024, The Astrophysical Journal, 974, 293, doi: 10.3847/1538-4357/ad6c4e

Woitke, P., Drążkowska, J., Lammer, H., Kadam, K., & Marigo, P. 2024, Astronomy and Astrophysics, 687, A65, doi: 10.1051/0004-6361/202450289

Wong, Y. H. V., Hirashita, H., & Li, Z.-Y. 2016, Publications of the Astronomical Society of Japan, 68, 67, doi: 10.1093/pasj/psw066

Wurster, J., & Bate, M. R. 2019, Monthly Notices of the Royal Astronomical Society, 486, 2587, doi: 10.1093/mnras/stz1023

Wurster, J., & Lewis, B. T. 2020a, Monthly Notices of the Royal Astronomical Society, 495, 3795, doi: 10.1093/mnras/staa1339

—. 2020b, Monthly Notices of the Royal Astronomical Society, 495, 3807, doi: 10.1093/mnras/staa1340

Wurster, J., & Li, Z.-Y. 2018, Frontiers in Astronomy and Space Sciences, 5, 39, doi: 10.3389/fspas.2018.00039

Xu, W., & Kunz, M. W. 2021a, Monthly Notices of the Royal Astronomical Society, 508, 2142, doi: 10.1093/mnras/stab2715

—. 2021b, Monthly Notices of the Royal Astronomical Society, 502, 4911, doi: 10.1093/mnras/stab314

Yang, H., & Bai, X.-N. 2021, The Astrophysical Journal, 922, 201, doi: 10.3847/1538-4357/ac250a

Yen, H.-W., Koch, P. M., Takakuwa, S., et al. 2017, The Astrophysical Journal, 834, 178, doi: 10.3847/1538-4357/834/2/178

Yen, H.-W., Takakuwa, S., Gu, P.-G., et al. 2019, Astronomy and Astrophysics, 623, A96, doi: 10.1051/0004-6361/201834209

Yen, H.-W., Takakuwa, S., Ohashi, N., et al. 2014, The Astrophysical Journal, 793, 1, doi: 10.1088/0004-637X/793/1/1

Yen, H.-W., Williams, J. P., Sai, J., et al. 2024, The Astrophysical Journal, 969, 125, doi: 10.3847/1538-4357/ad4c6b

Youdin, A. N., & Goodman, J. 2005a, The Astrophysical Journal, 620, 459, doi: 10.1086/426895

—. 2005b, The Astrophysical Journal, 620, 459, doi: 10.1086/426895

Zamponi, J., Maureira, M. J., Liu, H. B., et al. 2024, Astronomy and Astrophysics, 682, A56, doi: 10.1051/0004-6361/202244628

Zamponi, J., Maureira, M. J., Zhao, B., et al. 2021, Monthly Notices of the Royal Astronomical Society, 508, 2583, doi: 10.1093/mnras/stab2657

Zanni, C., & Ferreira, J. 2009, Astronomy and Astrophysics, 508, 1117, doi: 10.1051/0004-6361/200912879

—. 2013, Astronomy and Astrophysics, 550, A99, doi: 10.1051/0004-6361/201220168

Zhang, K., Bergin, E. A., Blake, G. A., et al. 2016, The Astrophysical Journal, 818, L16, doi: 10.3847/2041-8205/818/1/l16

Zhao, B., & Li, Z.-Y. 2013, The Astrophysical Journal, 763, 7, doi: 10.1088/0004-637X/763/1/7

Zhao, B., Li, Z.-Y., Nakamura, F., Krasnopolsky, R., & Shang, H. 2011, The Astrophysical Journal, 742, 10, doi: 10.1088/0004-637X/742/1/10

Zhao, B., Tomida, K., Hennebelle, P., et al. 2020, Space Science Reviews, 216, 43, doi: 10.1007/s11214-020-00664-z

Zhu, Z. 2025, Monthly Notices of the Royal Astronomical Society, 537, 3701, doi: 10.1093/mnras/staf250

Zhu, Z., & Stone, J. M. 2018, The Astrophysical Journal, 857, 34, doi: 10.3847/1538-4357/aaafc9

Zhu, Z., Stone, J. M., & Calvet, N. 2024, Monthly Notices of the Royal Astronomical Society, 528, 2883, doi: 10.1093/mnras/stad3712

Zhu, Z., & Yang, C.-C. 2020, Monthly Notices of the Royal Astronomical Society, 501, 467, doi: 10.1093/mnras/staa3628

Zimniak, N., Ferreira, J., & Jacquemin-Ide, J. 2024, Astronomy and Astrophysics, 692, A99, doi: 10.1051/0004-6361/202450501